

Astronomy and Astrophysics Library

Maurizio Spurio



# Particles and Astrophysics

A Multi-Messenger Approach



# **Astronomy and Astrophysics Library**

## **Series editors**

Gerhard Börner, Garching, Germany

Andreas Burkert, München, Germany

W.B. Burton, Charlottesville, VA, USA

A. Coustenis, Meudon, France

Michael A. Dopita, Canberra, ACT, Australia

Bruno Leibundgut, Garching, Germany

Georges Meynet, Versoix, Switzerland

Peter Schneider, Bonn, Germany

Virginia Trimble, Irvine, CA, USA

Derek Ward-Thompson, Preston, UK

Ian Robson, Edinburgh, UK



More information about this series at <http://www.springer.com/series/848>

Maurizio Spurio

# Particles and Astrophysics

A Multi-Messenger Approach

 Springer

Maurizio Spurio  
Department of Physics and Astronomy  
University of Bologna and Istituto  
Nazionale di Fisica Nucleare (INFN)  
Bologna  
Italy

Additional material to this book can be downloaded from <http://extras.springer.com/>

ISSN 0941-7834                      ISSN 2196-9698 (electronic)  
ISBN 978-3-319-08050-5            ISBN 978-3-319-08051-2 (eBook)  
DOI 10.1007/978-3-319-08051-2

Library of Congress Control Number: 2014947687

Springer Cham Heidelberg New York Dordrecht London

© Springer International Publishing Switzerland 2015

This work is subject to copyright. All rights are reserved by the Publisher, whether the whole or part of the material is concerned, specifically the rights of translation, reprinting, reuse of illustrations, recitation, broadcasting, reproduction on microfilms or in any other physical way, and transmission or information storage and retrieval, electronic adaptation, computer software, or by similar or dissimilar methodology now known or hereafter developed. Exempted from this legal reservation are brief excerpts in connection with reviews or scholarly analysis or material supplied specifically for the purpose of being entered and executed on a computer system, for exclusive use by the purchaser of the work. Duplication of this publication or parts thereof is permitted only under the provisions of the Copyright Law of the Publisher's location, in its current version, and permission for use must always be obtained from Springer. Permissions for use may be obtained through RightsLink at the Copyright Clearance Center. Violations are liable to prosecution under the respective Copyright Law. The use of general descriptive names, registered names, trademarks, service marks, etc. in this publication does not imply, even in the absence of a specific statement, that such names are exempt from the relevant protective laws and regulations and therefore free for general use.

While the advice and information in this book are believed to be true and accurate at the date of publication, neither the authors nor the editors nor the publisher can accept any legal responsibility for any errors or omissions that may be made. The publisher makes no warranty, express or implied, with respect to the material contained herein.

Printed on acid-free paper

Springer is part of Springer Science+Business Media ([www.springer.com](http://www.springer.com))

*A Mariagrazia,  
Eleonora e Federico*

*Du siehst, mein Sohn,  
zum Raum wird hier die Zeit.*

# Preface

This book aims to introduce the many different aspects that correlate particle physics with astrophysics and cosmology and to introduce astrophysics by means of the experimental results recently obtained through the study of charged and neutral high-energy particles (including GeV and TeV photons).

The Standard Model of particle physics, which includes the theory of electro-weak interaction and quantum chromodynamics for the strong interaction, explains quite well all available experimental results. The theory was recently crowned by the discovery of the last missing piece: the Higgs boson. A parallel Standard Model has been derived from observational cosmology, which describes the evolution of the Universe as a whole as well as the objects within it.

“Multimessenger” astrophysics, connecting traditional astronomy with cosmic ray,  $\gamma$ -ray, and neutrino observations, has been made possible by the availability of experimental techniques and detectors used in particle physics. These developments have allowed the construction and operation of experiments in space borrowing from the techniques used at accelerators. This has made possible, with space-based experiments, the study of cosmic matter and antimatter, and the detection of high-energy  $\gamma$ -rays with good pointing capabilities. Underground laboratories, created to test particle physics beyond the Standard Model, offer an ideal low-background environment to detect neutrinos produced by the nucleosynthesis in the Sun, or by the gravitational core-collapse of a massive star. Deep underwater/ice neutrino telescopes have started to provide information on cosmic accelerators, while at the same time allowing tests of several physical properties of neutrinos.

This book is aimed primarily at those undertaking postgraduate courses, Ph.D. students, and postdoc researchers involved in high-energy physics or astrophysics research. It is also aimed at senior particle physicists usually interested in accelerator/collider physics, eager to understand and appreciate the mechanisms of the largest accelerators in the Universe. The reader is assumed to know, at an introductory level, particle and nuclear physics. Additional material (referred to as “Extras”) is freely available on the Springer website of this book.

The book is based on my lecture experiences at the University of Bologna on *Astroparticle Physics*. I have adopted here a systematic approach to cover the

experimental aspects, as well as to introduce the theoretical background. In particular, I dedicated a large effort to obtain first-order estimates of all the relevant processes described, referring to more advanced readings for deeper developments. The interpretations of experimental results of modern experiments rely in most cases on data comparison with model predictions obtained via Monte Carlo methods. These computational techniques are usually very detailed. It is important that researchers acquire the habit to critically understand the physical results of advanced simulation tools, also with simple back-of-the-envelope estimates. In this optic, I devoted great care to specify the measurement units of all relevant quantities, to develop toy-models to derive observable quantities from intuitive physics processes, and to compare the results of these simple predictions with published data.

Two words of warning about the literature: I usually quoted review papers. They are usually easier to read and helpful in introducing the reader to the inherent physics than specific research papers. Reviews, in turn, contain a detailed indication for further readings (on average, more than 200 citations for each review paper). For the permission to reproduce or adapt photographs and diagrams, I am grateful to all authors, collaborations, institutions, and laboratories quoted in each figure caption. I made every effort to secure necessary permissions to reproduce the copyright material in this work. If any omissions are brought to my notice, I will be happy to include appropriate acknowledgments on reprinting.

I thank many colleagues for their cooperation and suggestions: the friends of the ANTARES and OPERA groups at Bologna University and of the former MACRO experiment, and in particular S. Cecchini, A. Margiotta, and Prof. G. Giacomelli (who recently passed away); the colleagues of the Istituto Nazionale di Fisica Nucleare, especially the representatives of the National Committee 2—who are mainly involved in astroparticle physics—for instructive discussions sometimes used in the content of this book. A particular mention of the Ph.D. students, those in our group and those with whom I interacted during the last 15 years in my research activity for a neutrino telescope in the Mediterranean Sea. Special thanks to all members of the ANTARES collaboration. I am grateful to many students who read the manuscript under the form of didactic material, for their suggestions and questions that have allowed me to set this work in a way that I hope will be useful for many.

Finally, I have to deeply and sincerely thank Prof. Vincenzo Flaminio, University of Pisa, who read critically and in-depth the manuscript. He has been a severe, knowledgeable, and affable reviewer, whose opinion was an important support for the author, which has contributed to significantly improve the final version.

I would also very much appreciate any corrections to mistakes or misprints (including the trivial ones), and also comments or simple observations. Please address them to: maurizio.spurio@unibo.it.

# Contents

<b>1</b>	<b>An Overview of Astroparticle Physics</b> . . . . .	1
1.1	Introduction . . . . .	1
1.1.1	Astrophysics and Astroparticle Physics . . . . .	3
1.1.2	Discoveries and Experiments Not Covered in This Book . . . . .	6
1.2	Cosmic Rays . . . . .	7
1.3	Gamma-Rays of GeV and TeV Energies . . . . .	10
1.4	Neutrino Astrophysics . . . . .	11
1.5	The Dark Universe . . . . .	15
1.6	Laboratories and Detectors for Astroparticle Physics . . . . .	16
1.6.1	Space Experiments . . . . .	16
1.6.2	Experiments in the Atmosphere . . . . .	17
1.6.3	Ground-Based Experiments . . . . .	18
1.7	Underground Laboratories for Rare Events . . . . .	18
	References . . . . .	21
<b>2</b>	<b>The Cosmic Rays and Our Galaxy</b> . . . . .	23
2.1	The Discovery of Cosmic Rays . . . . .	23
2.2	Cosmic Rays and the Early Days of Particle Physics . . . . .	26
2.3	The Discovery of the Positron and Particle Detectors . . . . .	27
2.3.1	The Motion in a Magnetic Field and the Particle Rigidity . . . . .	27
2.3.2	The Identification of the Positron . . . . .	29
2.4	A Toy Telescope for Primary Cosmic Rays . . . . .	32
2.5	Differential and Integral Flux . . . . .	34
2.6	The Energy Spectrum of Primary Cosmic Rays . . . . .	37
2.7	The Physical Properties of the Galaxy . . . . .	40
2.7.1	The Galactic Magnetic Field . . . . .	42
2.7.2	The Interstellar Matter Distribution . . . . .	44
2.8	Low-Energy Cosmic Rays from the Sun . . . . .	45
2.9	The Effect of the Geomagnetic Field . . . . .	47

2.10	Number and Energy Density of the Cosmic Rays . . . . .	50
2.11	Energy Considerations on Cosmic Ray Sources . . . . .	52
	References. . . . .	53
<b>3</b>	<b>Direct Cosmic Rays Detection: Protons, Nuclei, Electrons and Antimatter . . . . .</b>	<b>55</b>
3.1	Generalities on Direct Measurements . . . . .	56
3.2	The Calorimetric Technique . . . . .	57
3.2.1	Hadronic Interaction Length and Mean Free Path . . . . .	58
3.2.2	The Electromagnetic Radiation Length . . . . .	59
3.2.3	Hadronic Interaction Length and Mean Free Path in the Atmosphere. . . . .	60
3.3	Balloon Experiments . . . . .	61
3.4	Satellite Experiments . . . . .	64
3.4.1	The IMP Experiments . . . . .	64
3.4.2	The PAMELA Experiment. . . . .	66
3.5	The AMS-02 Experiment on the International Space Station. . . . .	67
3.6	Abundances of Elements in the Solar System and in CRs . . . . .	70
3.6.1	Cosmic Abundances of Elements . . . . .	73
3.7	Energy Spectrum of CR Protons and Nuclei. . . . .	76
3.8	Antimatter in Our Galaxy . . . . .	78
3.9	Electrons and Positrons . . . . .	80
3.9.1	The Positron Component . . . . .	82
3.9.2	Considerations on the $e^+$ , $e^-$ Components . . . . .	84
	References. . . . .	85
<b>4</b>	<b>Indirect Cosmic Rays Detection: Particle Showers in the Atmosphere . . . . .</b>	<b>87</b>
4.1	Introduction and Historical Information . . . . .	88
4.2	The Structure of the Atmosphere . . . . .	89
4.3	The Electromagnetic (EM) Cascade. . . . .	92
4.3.1	Heitler's Model of EM Showers . . . . .	93
4.3.2	Analytic Solutions. . . . .	95
4.4	Showers Initiated by Protons and Nuclei . . . . .	99
4.4.1	The Muon Component in a Proton-Initiated Cascade. . . . .	102
4.4.2	The EM Component in a Proton-Initiated Cascade . . . . .	103
4.4.3	Depth of the Shower Maximum for a Proton Shower . . . . .	106
4.4.4	Showers Induced by Nuclei: The Superposition Model . . . . .	107
4.5	The Monte Carlo Simulations of Showers . . . . .	110
4.6	Detectors of Extensive Air Showers at the Energy of the Knee . . . . .	112



4.6.1	A Toy Example of an EAS Array . . . . .	113
4.6.2	Some EAS Experiments. . . . .	116
4.6.3	Cherenkov Light Produced by EAS Showers . . . . .	118
4.7	The Time Profile of Cascades . . . . .	120
4.8	The Arrival Direction of CRs as Measured with EAS Arrays . . . . .	121
4.9	The CR Flux Measured with EAS Arrays . . . . .	124
4.10	Mass Composition of CRs Around the Knee . . . . .	126
4.10.1	The $N_e$ Versus $N_\mu$ Method. . . . .	127
4.10.2	Depth of the Shower Maximum . . . . .	128
	References. . . . .	130
<b>5</b>	<b>Diffusion of Cosmic Rays in the Galaxy . . . . .</b>	<b>133</b>
5.1	The Overabundance of Li, Be, and B in CRs . . . . .	134
5.1.1	Production of Li, Be, and B During Propagation. . . . .	135
5.2	Dating of Cosmic Rays with Radioactive Nuclei. . . . .	139
5.2.1	Unstable Secondary-to-Primary Ratios. . . . .	141
5.3	The Diffusion-Loss Equation . . . . .	142
5.3.1	The Diffusion Equation with Nuclear Spallation . . . . .	145
5.3.2	Numerical Estimate of the Diffusion Coefficient $D$ . . . . .	146
5.4	The Leaky box Model and its Evolutions. . . . .	147
5.5	Energy-Dependence of the Escape Time $\tau_{esc}$ . . . . .	149
5.6	Energy Spectrum of Cosmic Rays at the Sources . . . . .	151
5.7	Anisotropies due to the Diffusion . . . . .	152
5.7.1	The Compton–Getting Effect . . . . .	155
5.8	The Electron Energy Spectrum at the Sources . . . . .	155
5.8.1	Synchrotron Radiation . . . . .	156
5.8.2	Measured Energy Spectrum of Electrons . . . . .	160
5.8.3	Average Distance of Accelerators of Electrons . . . . .	161
	References. . . . .	162
<b>6</b>	<b>Acceleration Mechanisms and Galactic Cosmic Ray Sources. . . . .</b>	<b>165</b>
6.1	Second- and First-Order Fermi Acceleration Mechanisms. . . . .	166
6.1.1	Magnetic Mirrors . . . . .	167
6.1.2	The Second-Order Fermi Acceleration Mechanism . . . . .	169
6.1.3	The First-Order Fermi Acceleration Mechanism . . . . .	171
6.1.4	The Power-Law Energy Spectrum from the Fermi Model . . . . .	174
6.2	Diffusive Shock Acceleration in Strong Shock Waves. . . . .	174
6.2.1	Supernova Explosions and Cosmic Rays Acceleration . . . . .	176
6.2.2	Relevant Quantities in a Supernova Explosion . . . . .	177
6.3	Maximum Energy Attainable in the Supernova Model . . . . .	180
6.4	The Spectral Index of the Energy Spectrum . . . . .	182

6.4.1	The Escape Probability . . . . .	184
6.4.2	A Shock Front in a Mono-Atomic Gas . . . . .	185
6.5	Success and Limits of the Standard Model of Cosmic Ray Acceleration . . . . .	188
6.6	White Dwarfs and Neutron Stars. . . . .	190
6.6.1	White Dwarfs. . . . .	191
6.6.2	Neutron Stars and Pulsars . . . . .	193
6.7	Possible Galactic Sources of Cosmic Rays Above the Knee . . . . .	197
6.7.1	A Simple Model Involving Pulsars . . . . .	198
6.7.2	A Simple Model Involving Binary Systems . . . . .	199
	References. . . . .	200
<b>7</b>	<b>Ultra High Energy Cosmic Rays . . . . .</b>	<b>203</b>
7.1	The Observational Cosmology and the Universe. . . . .	204
7.2	The Large-Scale Structure of the Universe . . . . .	206
7.3	Anisotropy of UHECRs: The Extragalactic Magnetic Fields . . . . .	208
7.4	The Quest for Extragalactic Sources of UHECRs . . . . .	210
7.5	Propagation of UHECRs . . . . .	215
7.5.1	The Adiabatic Energy Loss . . . . .	215
7.5.2	The Propagation in the CMB: The GZK Cut-Off . . . . .	215
7.5.3	$e^\pm$ Pair Production by Protons on the CMB. . . . .	218
7.5.4	Propagation in the Extragalactic Magnetic Field . . . . .	219
7.6	The Fluorescence Light and Fluorescence Detectors . . . . .	220
7.7	UHECR Measurements with a Single Technique. . . . .	225
7.7.1	Results from HiRes and AGASA . . . . .	226
7.8	Large Hybrid Observatories of UHECRs . . . . .	228
7.9	The Flux of UHECRs . . . . .	233
7.10	The Chemical Composition of UHECRs . . . . .	234
7.11	Correlation of UHECRs with Astrophysical Objects . . . . .	236
7.12	Constraints on Top-Down Models. . . . .	238
7.13	Summary and Discussion of the Results . . . . .	239
	References. . . . .	241
<b>8</b>	<b>The Sky Seen in <math>\gamma</math>-rays . . . . .</b>	<b>243</b>
8.1	The Spectral Energy Distribution (SED) and Multiwavelength Observations . . . . .	244
8.2	Astrophysical $\gamma$ -rays: The Hadronic Model . . . . .	246
8.2.1	Energy Spectrum of $\gamma$ -rays from $\pi^0$ Decay . . . . .	247
8.3	Galactic Sources and $\gamma$ -rays . . . . .	249
8.3.1	A Simple Estimate of the $\gamma$ -ray Flux from a Galactic Source . . . . .	250

8.4	Astrophysical $\gamma$ -rays: The Leptonic Model . . . . .	251
8.4.1	The Synchrotron Radiation from a Power-Law Spectrum . . . . .	252
8.4.2	Synchrotron Self-Absorption . . . . .	254
8.4.3	Inverse Compton Scattering and SSC . . . . .	255
8.5	The Compton Gamma Ray Observatory Legacy . . . . .	259
8.5.1	The EGRET $\gamma$ -ray Sky . . . . .	259
8.6	Fermi-LAT and Other Experiments for $\gamma$ -ray Astronomy . . . . .	262
8.6.1	The Fermi-LAT . . . . .	262
8.6.2	AGILE and Swift . . . . .	264
8.7	Diffuse $\gamma$ -rays in the Galactic Plane . . . . .	264
8.7.1	An Estimate of the Diffuse $\gamma$ -ray Flux. . . . .	267
8.8	The Fermi-LAT Catalogs . . . . .	268
8.9	Gamma Ray Bursts . . . . .	273
8.9.1	Classification of GRBs . . . . .	276
8.10	Limits of $\gamma$ -ray Observations from Space. . . . .	279
	References. . . . .	280
<b>9</b>	<b>The TeV Sky and Multiwavelength Astrophysics . . . . .</b>	<b>281</b>
9.1	The Imaging Cherenkov Technique. . . . .	282
9.1.1	Gamma-Ray Versus Charged CR Discrimination . . . . .	284
9.1.2	HESS, VERITAS and MAGIC. . . . .	285
9.2	EAS Arrays for $\gamma$ -astronomy . . . . .	288
9.2.1	Sensitivity of $\gamma$ -ray Experiments. . . . .	289
9.3	TeV Astronomy: The Catalog . . . . .	290
9.4	Gamma-Rays from Pulsars . . . . .	293
9.5	The CRAB Pulsar and Nebula . . . . .	294
9.6	The Problem of the Identification of Galactic CR Sources . . . . .	296
9.7	Extended Supernova Remnants. . . . .	297
9.7.1	The SED of Some Peculiar SNRs. . . . .	299
9.8	Summary of the Study of Galactic Accelerators . . . . .	303
9.9	Active Galaxies . . . . .	304
9.10	The Extragalactic $\gamma$ -ray Sky . . . . .	307
9.11	The Spectral Energy Distributions of Blazars . . . . .	308
9.11.1	Quasi-Simultaneous SEDs of Fermi-LAT Blazars . . . . .	309
9.11.2	Simultaneous SED Campaigns and Mrk 421 . . . . .	311
9.12	Jets in Astrophysics . . . . .	313
9.12.1	Time Variability in Jets . . . . .	314
9.13	The Extragalactic Background Light . . . . .	315
	References. . . . .	319
<b>10</b>	<b>High-Energy Neutrino Astrophysics. . . . .</b>	<b>321</b>
10.1	The CRs, $\gamma$ -rays and Neutrino Connection . . . . .	322
10.1.1	Neutrino Detection Principle . . . . .	323

10.2	Background in Large Volume Neutrino Detectors . . . . .	325
10.3	Neutrino Detectors and Neutrino Telescopes. . . . .	327
	10.3.1 Muon Neutrino Detection . . . . .	328
	10.3.2 Showering Events . . . . .	330
10.4	Cosmic Neutrino Flux Estimates . . . . .	331
	10.4.1 A Reference Neutrino Flux from a Galactic Source. . .	331
	10.4.2 Extragalactic Diffuse Neutrino Flux . . . . .	333
	10.4.3 Neutrinos from GRBs . . . . .	335
	10.4.4 Cosmogenic Neutrinos. . . . .	338
10.5	Why km <sup>3</sup> -Scale Telescopes . . . . .	338
	10.5.1 The Neutrino Effective Area of Real Detectors. . . . .	341
	10.5.2 Number of Optical Sensors in a Neutrino Telescope . . . . .	342
10.6	Water and Ice Properties . . . . .	343
10.7	Operating Neutrino Telescopes . . . . .	345
	10.7.1 A Telescope in the Antarctic Ice. . . . .	345
	10.7.2 A Telescope in the Mediterranean Sea. . . . .	347
10.8	Results from Neutrino Telescopes . . . . .	349
	10.8.1 Point-Like Sources . . . . .	349
	10.8.2 Limits from GRBs and Unresolved Sources . . . . .	352
10.9	The First Measurement of Cosmic Neutrinos . . . . .	353
	References. . . . .	357
<b>11</b>	<b>Atmospheric Muons and Neutrinos . . . . .</b>	<b>359</b>
11.1	Nucleons in the Atmosphere. . . . .	360
11.2	Secondary Mesons in the Atmosphere . . . . .	363
11.3	Muons and Neutrinos from Charged Meson Decays . . . . .	367
	11.3.1 The Conventional Atmospheric Neutrino Flux . . . . .	369
	11.3.2 The Prompt Component in the Muon and Neutrino Flux. . . . .	369
11.4	The Particle Flux at Sea Level . . . . .	370
11.5	Measurements of Muons at Sea Level . . . . .	373
11.6	Underground Muons . . . . .	374
	11.6.1 The Depth–Intensity Relation . . . . .	375
	11.6.2 Characteristics of Underground/Underwater Muons . . .	375
11.7	Atmospheric Neutrinos . . . . .	377
	11.7.1 Early Experiments. . . . .	379
11.8	Oscillations of Atmospheric Neutrinos. . . . .	381
11.9	Measurement of Atmospheric $\nu_\mu$ Oscillations in Underground Experiments . . . . .	382
	11.9.1 Event Topologies in Super-Kamiokande . . . . .	382
	11.9.2 The Iron Calorimeter Soudan 2 Experiment . . . . .	387
	11.9.3 Upward-Going Muons and MACRO . . . . .	388

11.10 Atmospheric $\nu_\mu$ Oscillations and Accelerator Confirmations . . . . .	391
11.11 Atmospheric Neutrino Flux at Higher Energies . . . . .	393
References . . . . .	394
<b>12 Connections Between Physics and Astrophysics of Neutrinos . . . .</b>	<b>397</b>
12.1 Stellar Evolution of Solar Mass Stars . . . . .	398
12.2 The Standard Solar Model and Neutrinos . . . . .	400
12.3 Solar Neutrino Detection . . . . .	405
12.4 The SNO Measurement of the Total Neutrino Flux . . . . .	409
12.5 Oscillations and Solar Neutrinos . . . . .	412
12.6 Oscillations Among Three Neutrino Families . . . . .	414
12.6.1 Three Flavor Oscillation and KamLAND . . . . .	416
12.6.2 Measurements of $\theta_{13}$ . . . . .	417
12.7 Matter Effect and Experimental Results . . . . .	418
12.8 Summary of Experimental Results and Consequences for Neutrino Astrophysics . . . . .	421
12.8.1 Effects of Neutrino Mixing on Cosmic Neutrinos . . . . .	422
12.9 Formation of Heavy Elements in Massive Stars . . . . .	424
12.10 Stellae Novae . . . . .	425
12.11 Core-Collapse Supernovae (Type II) . . . . .	426
12.11.1 GRB Supernovae . . . . .	431
12.12 Neutrino Signal from a Core-Collapse SN . . . . .	431
12.12.1 Supernova Rate and Location . . . . .	431
12.12.2 The Neutrino Signal . . . . .	432
12.12.3 Detection of Supernova Neutrinos . . . . .	433
12.13 The SN1987A . . . . .	436
12.14 Stellar Nucleosynthesis of Trans-Fe Elements . . . . .	437
References . . . . .	438
<b>13 Microcosm and Macrocosm . . . . .</b>	<b>441</b>
13.1 The Standard Model of the Microcosm: The Big Bang . . . . .	442
13.2 The Standard Model of Particle Physics and Beyond . . . . .	445
13.3 Gravitational Evidence of Dark Matter . . . . .	446
13.4 Dark Matter . . . . .	448
13.5 Supersymmetry . . . . .	450
13.5.1 Minimal Standard Supersymmetric Model . . . . .	451
13.5.2 Cosmological Constraints and WIMP . . . . .	452
13.6 Interactions of WIMPs with Ordinary Matter . . . . .	454
13.6.1 WIMPs Annihilation . . . . .	455
13.6.2 WIMPs Elastic Scattering . . . . .	456
13.7 Direct Detection of Dark Matter: Event Rates . . . . .	458
13.8 WIMPs Direct Detection . . . . .	461

- 13.8.1 Solid-State Cryogenic Detectors . . . . . 462
- 13.8.2 Scintillating Crystals . . . . . 463
- 13.8.3 Noble Liquid Detectors . . . . . 464
- 13.8.4 Present Experimental Results and the Future . . . . . 465
- 13.9 Indirect WIMPs Detection . . . . . 467
  - 13.9.1 Neutrinos from WIMP Annihilation  
in Massive Objects . . . . . 467
  - 13.9.2 Gamma-Rays from WIMPs . . . . . 470
  - 13.9.3 The Positron Excess: A WIMP Signature? . . . . . 471
- 13.10 What's Next? . . . . . 473
- References. . . . . 475
- Index** . . . . . 477

# Chapter 1

## An Overview of Astroparticle Physics

### 1.1 Introduction

The Standard Model (SM) of particle physics, which includes the theory of electro-weak interaction and quantum chromodynamics for strong interaction, explains quite well all available experimental results in particle physics (Braibant et al. 2011, 2012). The SM predictions had precise confirmations from the measurements performed at the LEP and SLAC electron-positron colliders, with the discovery of the top quark at the Tevatron  $p\bar{p}$  collider. The theory was recently crowned by the discovery at the LHC of the last missing piece of the theory: the Higgs boson.

On the other hand, few physicists believe that the SM is the ultimate theory. Some considerations show that the SM is incomplete and represents a sort of low energy limit of a more fundamental theory, which should reveal itself at higher energies. These considerations are based upon the facts that:

- the SM has many free parameters which need an experimental input (the masses of leptons, quarks, and gauge bosons; the mass of the Higgs boson; the coupling constants;...);
- the three-family structure of lepton and quarks remains unexplained;
- the SM does not contain gravity;
- there are several unresolved “fine-tuning” problems;
- there are several unresolved “aesthetic” problems, such as the fact that the electric charge of the fundamental fermions and bosons is quantized in multiples of  $\frac{1}{3}e$ , without a deeper justification;

The threshold for this higher energy limit could be so high that no accelerator on Earth, also in the far future, will be able to reach it. For instance, Grand Unified Theories (GUTs) of electroweak and strong interactions predict that new physics would appear at extremely high energies,  $> 10^{14}$  GeV. It is in this context that astroparticle physics plays a fundamental role.

There are important connections between astrophysics, particle physics, and cosmology, in particular in the early Universe, which is commonly described as a gas of

very energetic particles. As time proceeded, the Universe, Following the the Universe expanded, the energy per particle decreased, phase transitions took place, the nature of particles changed, and there was a symmetry breaking from unified to nonunified interactions, Fig. 1.1. In recent years, some indication from the study of the early Universe pointed out some features that are completely outside the SM, namely:

- a large fraction (about 70%) of the mass-energy is made of an unknown form of dark energy;

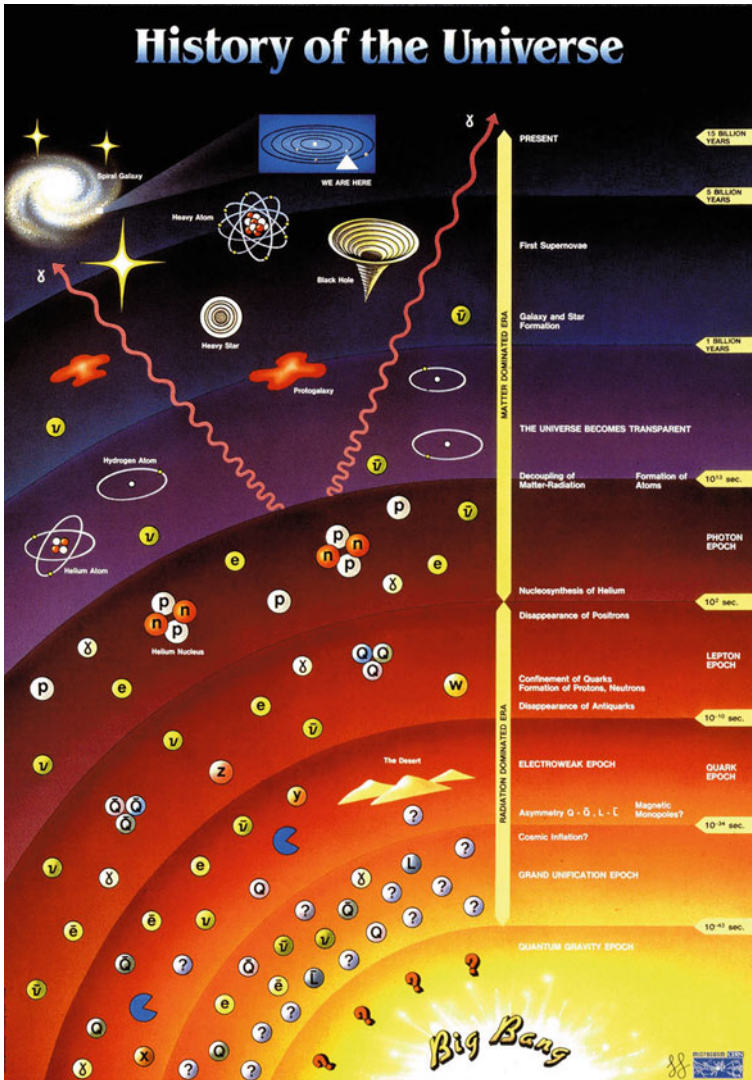


Fig. 1.1 An idealized sketch of the evolution of the Universe: from Big Bang to the present. The drawing was made by Giorgio Giacomelli



- a large fraction of the mass-energy (about 25 %) is made of an unknown form of *dark matter*;
- the matter–antimatter asymmetry observed in the Universe is not fully justified by the charge-parity (CP) violation allowed within the SM.

Grand Unification Theories foresee the nonconservation of the baryon and lepton numbers. Some models in the 1980s predicted proton lifetimes of the order of  $10^{30}$  years. This lifetime is much longer than the age of the Universe, but experimentally measurable. This motivated the construction of large detectors aimed at a search for proton decay. The experiments contained more than 1 ton ( $\sim 10^{33}$  nucleons) of material, and were located underground to shield the experiment from the radiation due to cosmic rays. Only the penetrating component of secondary radiation, namely muons and neutrinos, is able to reach the detectors at such depths. Contrary to the optimistic expectation, no proton decays were observed (actually, the measured lifetime turned out to be longer than  $\sim 10^{33}$  y) but the background events induced by the atmospheric neutrinos were particularly important. The events induced by atmospheric  $\nu_e + \bar{\nu}_e$  were roughly in agreement with the expectation. However, the number of events induced by  $\nu_\mu + \bar{\nu}_\mu$  was lower than expected. This was attributed to the phenomenon of neutrino oscillations, caused by a quantum-mechanical mixing between massive neutrinos. The definitive discovery of a nonzero neutrino mass in 1998 using atmospheric neutrinos was the result of long experimental investigation. This represented the first experimental hint for physics beyond the Standard Model.

### 1.1.1 Astrophysics and Astroparticle Physics

Both astrophysics and astroparticle physics study the nature of cosmic objects, but using different experimental techniques. We currently use the term *astrophysics* when the studied astronomical messenger is the electromagnetic radiation, see Fig. 1.2.

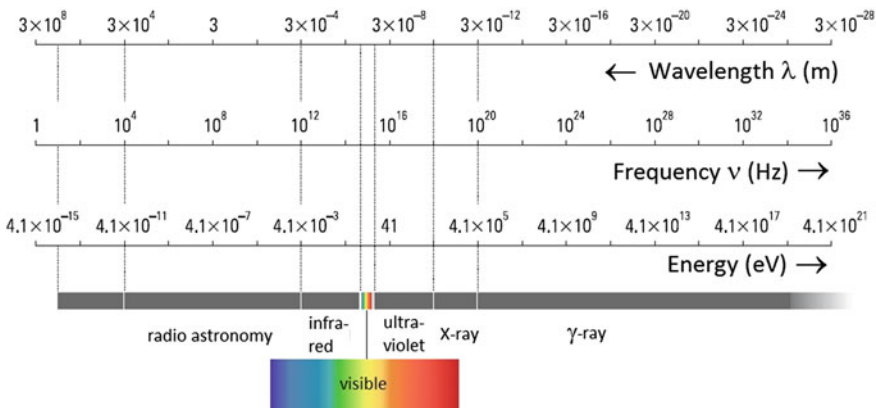


Fig. 1.2 Spectral range of electromagnetic radiation

We use *astroparticle physics* when the cosmic objects are studied with experimental techniques similar to those used in high-energy physics. Astronomical messenger probes observed by astroparticle detectors are charged cosmic rays, neutrinos, high energy  $\gamma$ -rays. Astroparticle physics searches include that for unknown dark matter, for other relic primordial, or exotic particles, the study of rare phenomena in a low-radioactivity environment.

Experimental *astroparticle physicists* usually can swap from nonaccelerator experiments to accelerator or collider experiments; they are readily found in the Physics departments of universities or research agencies as well as at the major high-energy accelerator laboratories all over the world, as the European Laboratory for Particle Physics (CERN). *Astrophysicists* usually they are readily found in Astronomy sections of Physics and Astronomy departments and observatories. Also, the journals where astroparticle and astrophysics papers are published are in most cases different. Consequently, there exists a cultural difference between the astrophysics and the particle physics communities.

To test if your educational background is more similar to that of an *astrophysicist* or to an *astroparticle physicist*, have a look at Fig. 1.2. If you are more familiar with the nomenclature of the electromagnetic spectrum through the electron Volt (eV) energy scale, you behave as an *astroparticle physicist*. On the other hand, if you prefer to classify the electromagnetic radiation according to the wavelength or frequency, you are closer to an *astrophysicist*.

Astroparticle physics dates since the discovery of the cosmic radiation by Hess in 1912. One of the most important open questions is the nature of cosmic accelerators. After the discovery of radioactivity by Becquerel in 1896, it soon became evident that part of natural radioactivity does not originate on Earth, but has an extraterrestrial origin. Today, we know that cosmic objects exist that are able to accelerate protons and nuclei, the Cosmic Rays (CRs), up to  $10^{20}$  eV. The bulk of the CRs is believed to be of galactic origin. Supernova remnants are the likely sites where CR acceleration occurs. Models exist which predict that a fraction (up to  $\sim 10\%$ ) of the kinetic energy released in the supernova explosions is used to accelerate to high energy charged particles (protons, heavier nuclei, and electrons). The identification of these galactic engines (or class of galactic engines) able to accelerate protons to energy orders of magnitude larger than in the LHC is one of the major aims of astroparticle physics.

At the high-energy tail of the CR spectrum, the number of particles reaching the Earth atmosphere is very low. At  $E \sim 10^{20}$  eV, the flux is only about one particle per square kilometer per century. Experiments covering huge surfaces are needed to collect a reasonable number of events. One of the challenges of these experiments is the measurement, in addition to the primary CR energy, of its nuclear charge/mass. This information is necessary to understand which kind of galactic or extragalactic engine is at work in the acceleration process.

Astronomy (in the sense of the localization in the sky of peculiar cosmic objects) with charged particles is inhibited by the presence of irregular interstellar and intergalactic magnetic fields, which randomize the directions of charged CRs. Only particles at very high energies ( $> 10^{19}$  eV) travel along approximately straight lines through magnetic fields.

Historically, astrophysics was born when spectroscopy techniques were applied to optical observations of light from stars. As experimental techniques improved and new detectors were developed during the last century, other different radiation wavelengths were used to improve the knowledge of astrophysical objects. The measurement of neutrinos from the Sun and the detection in 1987 of a neutrino burst from a stellar gravitational collapse occurred in the Large Magellanic Cloud opened the field of *neutrino astrophysics*.

The *multimessenger astronomy* connects different kinds of observations of the same astrophysical event or system. A certain degree of mixture between astronomers and physicists exists in experiments studying the electromagnetic radiation above the  $\sim 10$  MeV range.<sup>1</sup> Multimessenger astronomy is a relatively recent experimental opportunity, connecting traditional astrophysics observations with the new observational windows opened by  $\gamma$ -ray and neutrino detectors. In the near future, also gravitational wave observatories will be part of the game. All these astrophysical branches have been made possible by the availability of experimental techniques and detectors mainly developed in particle physics. These developments have allowed the realization of sensible detectors in space able to detect  $\gamma$ -rays up to hundreds of GeV with good pointing capabilities, deep underground detectors able to catch neutrinos emitted in the core of the Sun, or during the gravitational core-collapse of a massive star. Deep underwater neutrino telescopes start to provide information about high-energy neutrinos emitted from astrophysical accelerators.

The observation in different electromagnetic bands and/or with different probes may not just be an advantage; it may be a necessity for solving some of the outstanding problems in particle physics and astrophysics:

- Can we definitively prove that the galactic CR acceleration mechanism is provided by supernovae shock waves?
- Are there galactic objects able to accelerate CRs up to  $10^{18-19}$  eV?
- Are the Active Galactic Nuclei, the Gamma Ray Bursts, or some other still unknown mechanism the sources of CRs at  $\sim 10^{20}$  eV?
- What is the mechanism(s) that triggers (trigger) the GRBs?
- Is the antimatter detected outside the Earth atmosphere produced by secondary processes only? Is there antimatter of primary origin, or produced by non-Standard Model mechanisms?
- Are there fossil or primordial particles in cosmic radiation?
- Can we directly or indirectly detect dark matter and understand its nature?
- Is the proton really stable?
- What can we possibly learn from neutrino astronomy?

Gravitation is not included at present in the Standard Model of particle physics, and the *graviton* enters only marginally on the Review of Particle Physics (Beringer et al. 2012). The physics of gravitational waves and their experimental searches are not included in this book. Also, the problem of the nature of *dark energy*, which

---

<sup>1</sup> In this book the units of energy for electromagnetic radiation, instead of frequency and wavelength, are normally used.

seems to dominate the energy content of the Universe, seems at present outside the field of particle physics.

### 1.1.2 Discoveries and Experiments Not Covered in This Book

Since ancient ages, visible light was the only means to explore the Universe. Only in the **twentieth century** we were able to **open new observational windows** in other regions of electromagnetic radiation. This **information revolution** started in the **1940s with radio waves**, with the opening of observations at radio wavelengths, exploded with the start of the space age in the 1960s.

**Most of the electromagnetic radiation is blocked by the Earth's atmosphere** and therefore space observatories or some form of indirect detection is required, Fig. 1.3. The launch of the **first artificial satellite in 1957** opened new opportunities for astrophysics studies. The observation of **X-rays sources and gamma radiation** was made possible a few years later with dedicated instruments on-board satellites. **For X-rays**, we should mention **Uhuru (1970)**, the **Einstein Observatory (1978)**, **Exosat (1983)**. The successful launch of the **ROSAT, in 1990**, paved the way for the discovery of numerous X-ray sources. More recent satellites include the **XMM-Newton** observatory (low to mid energy X-rays 0.1–15 keV) and the **INTEGRAL** satellite (high energy X-rays 15–60 keV). Both were launched by the European Space Agency

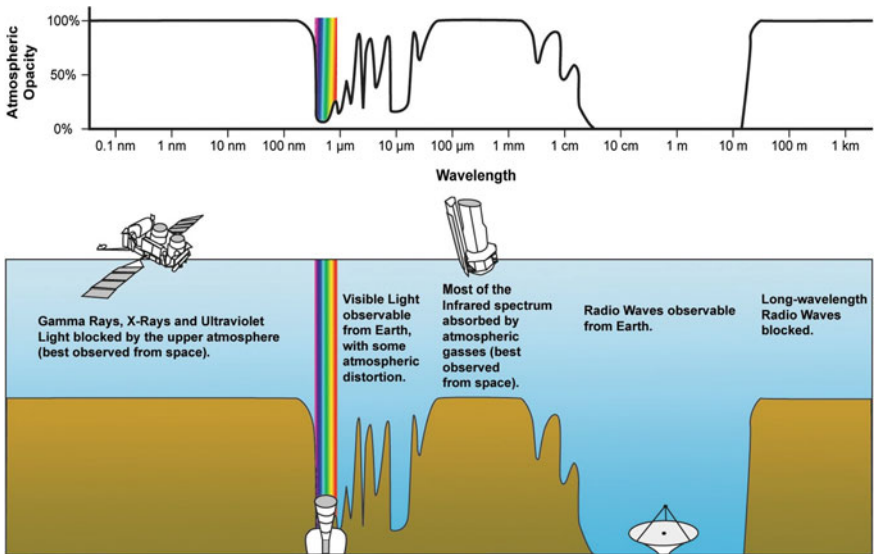


**Fig. 1.3** The atmosphere opacity as a function of the wavelength is presented in the *upper part*. Opacity is represented by the percentage of electromagnetic radiation, which does not reach the ground. Space experiments are widely used to detect electromagnetic radiation not reaching the Earth's surface. Note that the scale is in terms of the logarithm of the wavelength, so the energy scale decreases from left to right. Credit: NASA

(ESA). The National Aeronautics and Space Administration (NASA) has launched the *RXTE* and the *Chandra* observatories.

In the optical range, the *Hubble space telescope* (which was launched by NASA in 1990), provided optical images of stars and galaxies of unprecedented quality, the figure error of the primary mirror had in 1993 by a spectacular repair in space.

The interest on the study of astrophysical sources through detection of their  $\gamma$ -ray emission started at the end of the 1950s. We should mention the following satellites: *Vela* (1967), *OSO-3* (1969), *SAS-2* (1972), *COS-B* (1975). At the beginning of the 1970s the first firm detections of  $\gamma$ -rays from space came with the *OSO-3* (Kraushaar et al. 1973) observation of radiation from the plane of our Galaxy. Real breakthrough events for  $\gamma$ -ray astronomy were the launch in 1991 of the *Compton Gamma-Ray Observatory* (*CGRO*), which was designed to include the major advances in detector technology during the 1980s. The satellite carried four major instruments (*BATSE*, *OSSE*, *COMPTEL*, *EGRET*) which greatly improved the spatial and temporal resolution of  $\gamma$ -ray observations. *EGRET* was the first detector for tens of MeV  $\gamma$ -rays, opening the field of observation for very high energy  $\gamma$ -rays, which is a subject covered in this book.

All new observation windows provided a wealth of new data, new discoveries inaccessible in other spectral range which widely improved our understanding of the high-energy processes in our Universe. All experiments covering the electromagnetic spectrum below the GeV are only marginally referred to in this book. Dedicated textbooks on these subjects are recommended (Gruppen 2005; Mészáros 2010; Longair 2011; Rai Choudhuri 2012; Lang 2013).

## 1.2 Cosmic Rays

The nature of cosmic accelerators is one of the major unsolved astrophysical problems. It is an important subject, as the sites of cosmic ray acceleration in our Galaxy are strictly correlated with the dynamics of formation of massive stars, stellar evolution, and finally supernova explosions. In some sense, the study of cosmic radiation helps to understand the formation of our own solar system.

The physics of cosmic rays is dealt with in some detail in this book. Chapter 2 introduces the physics of primary cosmic rays. Primary CRs are high-energy protons and nuclei (plus a minority electron component) produced in astrophysical environments, filling the galactic space and arriving on Earth. Primary CRs can be identified if measured before they interact with the atmosphere. Secondary CRs are those particles produced in interactions of the primaries with interstellar gas or with nuclei in the Earth's atmosphere. Nuclei such as lithium, beryllium, and boron (which are very rare end-products of stellar nucleosynthesis) are secondary particles, as well as antiprotons and positrons.

Chapter 3 deals with the experimental techniques used for the measurement of primary CRs below  $\sim 10^{14}$  eV (*direct measurements*). Experiments mounted on balloons and satellites (and recently on the *International Space Station*) allow a *direct study* of the CRs impinging on the top of the atmosphere, before the first interaction with Earth

matter. This enables measurement of the so-called *chemical composition of cosmic rays*, which is the relative fraction of different nuclei present in cosmic radiation, and in some cases of their isotopic composition.

When *entering the Earth's atmosphere*, CRs collide with nucleons of atmospheric nuclei (mainly oxygen and nitrogen) and produce a cascade of secondary particles, the so-called *air shower* (Gaisser 1991). The basic mechanism of air shower production of a CR proton on a nucleon  $N$  is the reaction:



The decays of short-lived hadrons lead to a cascade of high-energy photons, electrons, and positrons (the electromagnetic component) and a penetrating component of muons and neutrinos. The measurement of the secondary particles with ground-based detectors (*indirect measurements*) allows the knowledge of the CR flux up to the highest energies, as described in Chap. 4.

Figure 1.4 shows the flux of primary CRs as measured by *direct* and *indirect* experiments. Each experiment measures the CR flux in a given energy range. Different

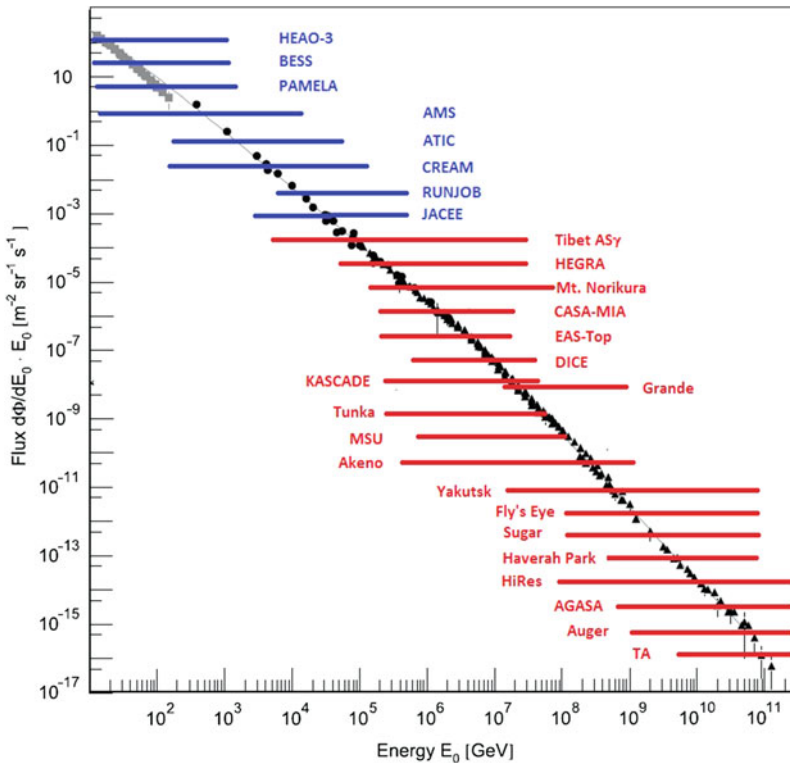


**Fig. 1.4** Flux of cosmic rays as a function of energy. Below few GeV, the contribution of particles coming from the Sun is not negligible. The energy range of the CR flux measured by some direct experiments is shown as a *blue line* and that measured by some indirect experiments as a *red line*

kinds of experiments cover more than 10 decades of energy. In the lower energy part of this spectrum, the Sun contributes with low energy cosmic rays (below the GeV scale), mainly associated with solar flares. In this book, we do not consider charged particles of solar origin. We focus on the origin, propagation, and detection of CRs with energies above several GeV, which are originated outside the solar system. On the opposite region of the CR spectrum, the highest-energy cosmic rays ( $\sim 10^{20}$  eV) correspond to 16 J, i.e., to a mass of 1 kg moving at a speed of almost  $6 \text{ ms}^{-1}$ ! Their origin is likely to be associated with the most energetic processes in the Universe.

The CR flux of Fig. 1.4 is shown in a double-logarithmic representation. We meet this situation in a large number of cases; for the spectra of  $\gamma$ -rays, secondary particles in the atmosphere, atmospheric muons, and neutrinos.... In general, nonthermal particle spectra can usually be approximated by power laws of the type

$$\frac{d\Phi}{dE} = A \cdot E^{-\alpha}. \quad (1.2)$$

In a double-logarithmic representation, these power laws are represented by straight lines:

$$\log \left[ \frac{d\Phi}{dE} \right] = \log[A \cdot E^{-\alpha}] = \log[A] - \alpha \cdot \log[E]. \quad (1.3)$$

The spectral index  $\alpha$  corresponds to the slope of the line and the normalization  $A$  to the intercept with the  $y$ -axis. Since many spectra are steep ( $d\Phi/dE \sim E^{-2} - E^{-4}$ ), it is useful to weight the  $y$ -axis with a power of the energy,  $E^\beta$ . In this way the straight line has a different slope:

$$\log \left[ E^\beta \cdot \frac{d\Phi}{dE} \right] = \log[A \cdot E^{-\alpha+\beta}] = \log[A] - (\alpha - \beta) \cdot \log[E]. \quad (1.4)$$

For instance, if  $\alpha = 2.7$  (as for the differential spectrum of primary CRs), the choice of  $E^\beta = E^{2.7}$  allows to represent the flux with a flat line parallel to the  $x$ -axis. The double-logarithmic representation with a weight is chosen to simplify reading off fluxes characterized by a fast decrease in energy.

The propagation of primary CRs in interstellar space, continuously deflected by galactic magnetic fields, is an important piece of information necessary to understand the nature of cosmic accelerators and it is studied in Chap. 5. During propagation of primary particles in the Galaxy, secondary CRs as well as antiparticles are produced by interactions with interstellar matter. Detailed modeling of this diffusion process with the production of secondary particles is of fundamental importance to understand if anomalous signals eventually detected in the cosmic radiation could be a signal of physics beyond the Standard Model, indicating some evidence for Dark Matter. In the last two decades, excitement was induced by different results successively discarded as evidence of a dark matter signal, as a claimed excess of diffuse  $\gamma$ -rays in the GeV range. At present, the most intriguing deviation from the expectation from secondary CR production is an excess of positrons, detected with different space experiments.



The sources of CRs are still unidentified. Astronomy with charged CRs is prevented by the presence of galactic magnetic fields. Only neutral probes (such as photons and neutrinos) can unambiguously point to a potential source or class of sources. There are however different astrophysical candidate CR sources. Starting from the 1960s, models of cosmic acceleration at astrophysical shocks were developed. This led to a sort of standard model of cosmic rays acceleration known as the *diffusive shock acceleration model*, discussed in Chap. 6. In this model, about 5–10% of the nonrelativistic kinetic energy connected with shocks powered by supernovae explosions in our Galaxy is transferred to a few particles that become relativistic, cosmic rays. The key feature is that an energy power-law spectrum of the type  $\sim E^{-2}$  is produced. The model is consistent with the balance between the energy transferred to the accelerated particles and the energy loss due to the escape of CRs out of the Galaxy.

It is plausible that the feature in the CR spectrum at  $\sim 10^{15}$  eV, known as the *knee*, represents a transition between different classes of galactic CR accelerators. Details of acceleration mechanism and propagation of CRs at high energies are not completely understood. Some peculiar sources should transfer additional energy to already accelerated protons or nuclei through conventional electromagnetic or gravitational processes at the sites of acceleration to justify energies larger than that corresponding to the knee. However, the presence of galactic objects able to accelerate CRs to energies greater than  $\sim 10^{19}$  eV seems unlikely.

Huge detector arrays are needed to measure the *Ultra High Energy Cosmic Rays (UHECRs)* with energies exceeding  $10^{18}$  eV (Sokolsky 2004). At the highest energies, CRs are probably of extragalactic origin. The experimental techniques, results, and hypotheses in support of an extragalactic origin of these UHECRs are described in Chap. 7. Above  $\sim 50$  EeV ( $1 \text{ EeV} = 10^{18} \text{ eV}$ ), the arrival directions of electrically charged cosmic rays are no longer significantly affected by galactic magnetic fields. It is still possible that the arrival directions of the highest energy cosmic rays provide information about the location of their sources. Proton astronomy at energies larger than the EeV range would be probably possible and it may also provide indirect information about extragalactic magnetic fields. The determination of the strength of these magnetic fields is a challenging issue for conventional astronomical methods.

### 1.3 Gamma-Rays of GeV and TeV Energies

High-energy processes in general manifest themselves with a *nonthermal spectrum* (i.e., their emission is not that of a black body with a given temperature). The measured diffuse photon flux indicates that the energy content in X- and  $\gamma$ -rays, produced by violent phenomena, is comparable to that associated with low-energy phenomena.

Gamma-ray astronomy at energies above some tens of MeV is an experimental discipline that reached full maturity during the last 10 years, which is described in Chap. 8. The Earth's atmosphere is not transparent to high-energy photons (Fig. 1.3) and  $\gamma$ -rays must be detected either outside the atmosphere or exploiting the production of a cascade of secondary particles, following interactions in the atmosphere.



In the GeV range, the Fermi-LAT experiment (launched in 2008) is made possible by the availability of new detectors coming from technologies typical of experimental particle physics. Fermi-LAT has opened a new window in the observation of the sky. Unlike that in the visible, the  $\gamma$ -ray sky is dominated by a diffuse galactic radiation. The majority of about 2000 galactic and extragalactic sources present in the Fermi-LAT catalog appear as point-like, i.e., with angular dimensions smaller than the resolution of the detector. These discoveries have a strong impact on several topical areas of modern astrophysics and cosmology. Finally, the BeppoSAX experiment (launched in 1996 and deorbited in 2003) predominantly studied X-ray sources, but also increased significantly our understanding of  $\gamma$ -ray bursts, as well as the successive Swift.

At energies above some hundreds of GeV the  $\gamma$ -ray flux is too low to be detected by satellite detectors. As for charged CRs, the Earth's atmosphere itself can be used as a detector for these very high-energy photons. After a long preparatory phase (Aharonian et al. 2008), the parallel branch of  $\gamma$ -ray astrophysics using ground-based detectors started to observe a large number of sources since mid-2000, as studied in Chap. 9. When  $\gamma$ -rays collide with matter at the top of the atmosphere, they produce showers of particles emitting Cherenkov radiation which can be detected with Imaging Atmospheric Cherenkov Telescopes (IACTs) on ground. A milestone in this indirect way to conduct  $\gamma$ -ray astrophysics was reached in 1989 with high-confidence level detection of the Crab Nebula by the Whipple Observatory.

At present, the catalog of objects emitting in the TeV energy range counts almost 150 galactic and extragalactic objects. Most of them are point-like, but extended emission originating from shells of supernova remnants (SNRs) has also been observed. This emission could be interpreted as originating from hadronic interactions of CRs with energies up to  $10^{14}$  eV in cosmic regions where CRs are accelerated.

Unlike charged CRs, once  $\gamma$ -rays emerge from the production regions they are largely unaffected in the propagation. However, the Universe is not completely transparent to photons of TeV energy and above. For instance, PeV ( $=10^3$  TeV;  $1 \text{ TeV} = 10^{12}$  eV) energy photons produced at the edge of our own Galaxy cannot be detected because they will convert into an electron/positron pair when interacting with a Cosmic Microwave Background (CMB) photon during their journey to Earth.

## 1.4 Neutrino Astrophysics

The messengers of the high-energy Universe are protons and heavier nuclei, electrons,  $\gamma$ -rays, and neutrinos.<sup>2</sup> Neutrinos are *elusive particles*, but they are abundant in the Universe (Fig. 1.5). Neutrinos are special particles: they are several orders of magnitude lighter than all other fermions, Neutrinos are electrically neutral, do not feel strong interactions, and interact only weakly. For example, the (anti)neutrinos

<sup>2</sup> Since some astrophysical objects are connected to the acceleration of huge macroscopic masses, also the detection of gravitational waves could play a role in the future.

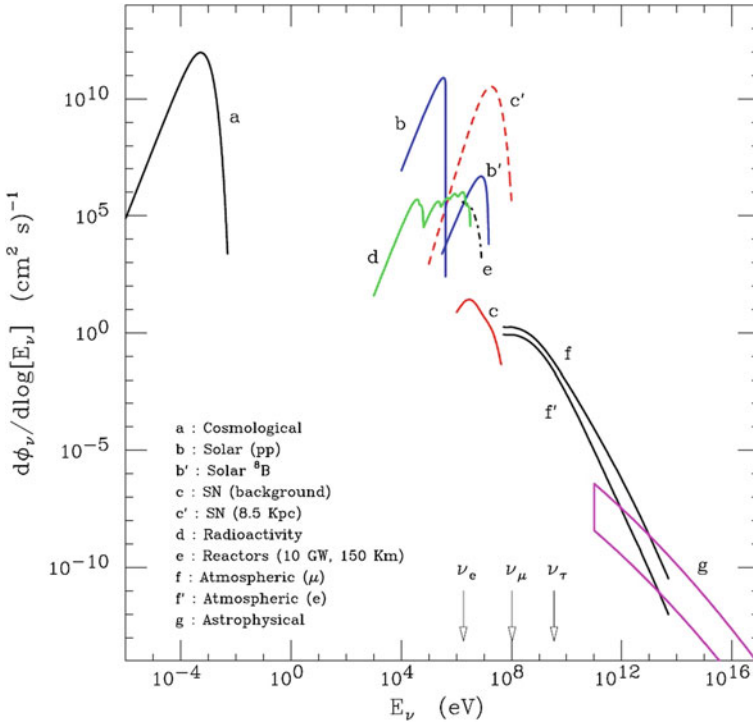


**Fig. 1.5** Flux of neutrinos at the surface of the Earth. The three *arrows* near the *x*-axis indicate the energy thresholds for producing the corresponding charged lepton through charged current interactions on a free proton target. The line **a** that refers to cosmological neutrinos assumes that the neutrino mass is vanishing small. For solar neutrinos **b**, only  $\nu_e$  from the  $pp$  and  ${}^8\text{B}$  reactions are considered, see Sect. 12.2. The *lines* that refer to diffuse supernova neutrinos **c** and a supernova burst lasting 10 s (**c'**) correspond to  $\bar{\nu}_e$  (Sect. 12.10). The other neutrino species have similar spectra, with differences that cannot be appreciated in the figure. The line **d** that describes geophysical neutrinos from radioactive decays include the  ${}^{238}\text{U}$  and  ${}^{232}\text{Th}$  decay chains, whose flux depends weakly on the geographical location. The  $\bar{\nu}_e$  produced by a 10 GW power reactor located at a distance of 150 km are considered **e**. The atmospheric muon and electron neutrino fluxes (**f**, **f'**, respectively) are calculated for Kamioka (Japan) location. Only the lowest energy part depends on the location. A range of predictions for the flux of astrophysical neutrinos **g** is shown. Courtesy of P. Lipari (Lipari 2006)

produced in nuclear reactors with  $\sim 1 \text{ MeV}$  energy, for example, have a cross-section of  $\sim 10^{-44} \text{ cm}^2$ . This corresponds to the fact that one neutrino out of  $10^{11}$  will interact when traveling the Earth along the diameter.

The fact that the neutrino interaction cross-section is so small is the reason that neutrino astronomy is a very recent discipline. In fact, massive and expensive detectors are required to achieve appreciable event rates. On the other hand, a small cross-section is also an extraordinary opportunity, because neutrinos can emerge from deep inside the core of astrophysical objects, revealing directly the physical processes in

operation there. The appealing feature of neutrinos with respect to protons and  $\gamma$ -rays, is that they can travel through the Universe without being deflected or absorbed. In addition, differently from the highest energy  $\gamma$ -rays, neutrinos of any energy can reach us practically without attenuation from the edge of the Universe.

The idea of a telescope for high-energy neutrinos based on the detection of secondary particles produced by neutrino interactions was first formulated in the 1960s by Markov. The basic principle of a neutrino telescope is a matrix of light detectors in water or ice, which offers large volume of free target for neutrino interactions while providing at the same time a shielding against secondary CRs.

The relativistic charged particles produced by neutrino interaction emit Cherenkov radiation in the transparent medium. A detector must measure with high precision the number and arrival time of these photons on a three-dimensional array of Photo Multiplier Tubes (PMTs), from which some of the properties of the neutrino (flavor, direction, energy) can be inferred.

At present, two large detectors exist in the world. In the Southern hemisphere, equipped with 86 detection strings embedded in the Antarctic ice, IceCube is taking data in its full configuration since 2011. In the Northern hemisphere, in the Mediterranean Sea, ANTARES has proved the detection technique with a 12 string apparatus completed in 2008. Presently, the community effort is aimed at the construction of a km<sup>3</sup>-scale detector, named KM3NeT, in the Mediterranean Sea. The status of neutrino telescopes, their physical goals, and the very recent (2013) first observation of cosmic neutrinos by IceCube are the subject of Chap. 10.

Atmospheric neutrinos represent the irreducible background for neutrino telescopes. The study of atmospheric neutrinos started in the 1980s, with the advent of large underground laboratories for the study of phenomena predicted by Grand Unification Theories. This study allowed the discovery of neutrino oscillations. All neutrino flavors undergo the mechanism of neutrino oscillations, and  $\nu_\mu$  disappearance was reported using atmospheric neutrinos in 1998 by the Super-Kamiokande and MACRO collaborations using completely different experimental techniques (Chap. 11). The discovery that neutrinos are massive particles is the main contribution of astroparticle to particle physics since the discovery of the positron and the muon in atmospheric showers.

As a necessary counterpart to neutrinos in most decays ruled by weak interactions, there is a penetrating component in the cascade initiated by protons and nuclei, that of atmospheric muons. Relatively few high-energy muons are present in the cascade induced by a primary CR; these muons can penetrate more than 10 km of water and are measured by underground or underwater detectors. Atmospheric muons represent a background for all measurements, which need a very low background, usually located in underground laboratories.

Among experiments that need a low-background rate there are those devoted to neutrinos emitted by the Sun and by gravitational core-collapse bursts. The role of neutrinos for the comprehension of energy mechanisms that fuel the Sun, the main sequence stars and the core-collapse of massive stars is the subject of Chap. 12.

The Sun (like all main sequence stars) produces energy by fusion (Bachall 1989). The first reaction in the cycle occurs through weak interaction, that is,  $p + p \rightarrow {}^2_1\text{H} + e^+ + \nu_e$ ; the Sun and the stars are sources of electron neutrinos. Approximately  $6 \times 10^{10}$  solar  $\nu_e$  cross a surface of one square centimeter on Earth every second. The measurement of solar neutrinos represents the only experimental method for a detailed understanding of nuclear processes inside the Sun, a representative of the main sequence stars. Solar  $\nu_e$ 's come from nuclear fusion reactions in the inner core and directly tell us about the source of energy in the Sun. Photons in the  $\sim\text{MeV}$  energy range are also emitted by the same nuclear reactions. It takes them at least  $10^5$  years to reach the solar photosphere, where they are emitted from the surface with a black body spectrum.

A major experimental milestone in astroparticle physics was the start in 1967 of the measurement of solar neutrinos by a radiochemical experiment in the Homestake Mine (the Davis experiment). This experiment, after a few years of data taking, indicated a deficit in the flux of solar neutrinos, which was confirmed by successive experiments, GALLEX/GNO, SAGE, Kamiokande, and later Super-Kamiokande. After a long experimental struggle, we learned that the neutrino deficit measured by the above experiments was not due to experimental problems or a deficit in the understanding of the astrophysical properties of stellar objects. It was due to oscillations of electron neutrinos during their travel from the Sun to the Earth.

The Sudbury Neutrino Observatory (SNO), which ended its data taking in 2006, was finally able to firmly confirm the oscillation scenario of solar neutrinos using heavy water. SNO showed that the total neutrino flux (the flavor-independent sum of the  $\nu_e$ ,  $\nu_\mu$ ,  $\nu_\tau$ ) from the Sun as measured on Earth was consistent with the total number of expected neutrinos predicted by the so-called *Standard Solar Model*. SNO demonstrated that 2/3 of the solar electron neutrinos had oscillated into neutrinos with different flavor ( $\nu_\mu$  or  $\nu_\tau$ ), whose energy is below the threshold for charged current interactions (see the arrow positions in Fig. 1.5).

An enormous number of neutrinos (some  $10^{58}$ ) are emitted in a few seconds following the gravitational collapse of a massive star that triggers the *supernova explosion*. The closest visible supernova over the last three centuries (the SN1987A), occurred in the Large Magellanic Cloud at about 50 kpc from Earth. It was observed in 1987 when some sufficiently large neutrino detectors were in operation. They were able to observe about 20 neutrino interactions, which allowed a first-order experimental confirmation of theoretical models on the supernova explosion mechanism. At present, new and larger detectors are in operation; the occurrence of a new galactic supernova (few per century are expected) will open a new era on neutrino astrophysics and on the understanding of the stellar gravitational collapse.

Finally, it should be mentioned that, similar to the cosmological microwave background radiation, we are immersed in a bath of cosmological neutrinos produced when the Universe was hot and young. The average number density ( $\sim 340 \text{ cm}^{-3}$ ) of cosmological neutrinos is slightly smaller than that of cosmic microwave background photons. As they are of extremely low energy (meV, see Fig. 1.5), there is at present no reliable technique for their detection.

## 1.5 The Dark Universe

Another still unsolved question in astroparticle physics is the nature of *dark matter*. From the observation of orbital velocities of stars in nearby galaxies, and of the velocities of galaxies in galactic clusters, the conclusion emerges that the energy density of visible matter in the Universe is too low to correctly describe the dynamics. A common effort between astroparticle and particle physics concerns searches for *dark matter* candidates, as described in Chap. 13. Exotic, currently unknown, particles or additional massive neutrino species may contribute to the missing matter of the Universe.

The framework became even more complicated after the discovery, started in 1998, of the accelerating expansion of the Universe through observations of distant supernovae. The growing rate of expansion implies that the Universe is being pushed apart by an unknown form of energy embedded in empty space. This unknown *dark energy* (or vacuum energy density) makes up a large part (more than 70%) of the energy density of the Universe and probably plays a decisive function in the dynamics and evolution of the Universe. The *dark energy* is an enigma, perhaps the greatest in cosmology today, which we do not consider in this book.

Dark matter candidates outside particle accelerators can be searched for in a *direct* or *indirect* way. Direct detection experiments typically operate in deep underground laboratories to reduce the background from cosmic rays.

Indirect experiments are looking for products of Weakly Interacting Massive Particle (WIMP) annihilations. These searches assume that WIMPs are Majorana particles (particles coinciding with their own antiparticles), or that WIMPs and anti-WIMPs exist. If two WIMPs (or WIMP and anti-WIMP) collide, they could annihilate to produce ordinary particle–antiparticle pairs or  $\gamma$ -rays. This could produce a significant number of  $\gamma$ -rays or particles with a characteristic energy distribution. Searches for  $\gamma$ -ray lines or an excess of  $e^+$  or  $e^-$  over the known background are in progress mainly in space experiments.

WIMPs are expected to be gravitationally trapped inside massive objects, with a consequent possible increasing rate of WIMP-antiWIMP annihilation. Underground/water/ice experiments look for an excess of events induced by neutrinos from the direction of massive objects (as the Sun or the Earth core, and the galactic center).

Following the observations, the Universe has an age of about 13.7 billion years and consists of about 100 billion galaxies; each galaxy is made of about 100 billion stars. Taking into account the mass of each star, the observable Universe is made of about  $10^{80}$  protons. However, this should account for less than 5% of matter and energy; most of the matter/energy is still invisible to us. The number of cosmic background radiation photons is about a billion times the number of protons.

## 1.6 Laboratories and Detectors for Astroparticle Physics

Astroparticle physics experiments, which are described in the following chapters of this book, are located underground, on the Earth's surface, in the atmosphere, and in space.

The direct detection of the CRs flux, the measurement of GeV  $\gamma$ -rays, the search for antimatter in the Universe, the indirect searches for WIMP-antiWIMP annihilation producing  $\gamma$ -rays or  $e^+e^-$  pairs takes place in space experiments.

As the cosmic ray flux strongly decreases with increasing energy, the study of CRs around and above the knee is done by measuring with different techniques the secondary particles produced in the atmosphere and reaching ground level.

The searches for rare phenomena benefit in the reduction of secondary CR flux in underground laboratories, Sect. 1.7. This is also true for very large and/or massive experiments needed to study neutrino physics and astrophysics, to search for proton decay and for relic particles from the Big Bang. A similar noise reduction is necessary for high-energy neutrino telescopes that use huge volumes of transparent medium, as the Antarctic ice and the deep-seawater, to detect charged leptons produced by charged current neutrino interactions.

### 1.6.1 Space Experiments

The Earth's atmosphere corresponds to an absorption layer of about 25 radiation lengths. For this reason, the detection of particles interacting electromagnetically (including the high-energy photons) must be performed outside the atmosphere itself, on-board satellites or on-board the International Space Station (ISS).

The space environment has many unique advantages for research, which cannot be realized on Earth. On-board satellites and on the ISS, it is characterized by microgravity, high vacuum, space radiation, and a wide field of view. Weightlessness (i.e. almost no gravity) means that buoyancy, sedimentation, static pressure, and thermal convection processes do not occur.

The ISS is a space station, corresponding to a habitable artificial satellite in a low Earth orbit. The ISS is the largest artificial body in orbit, and it can often be seen at the appropriate time with the naked eye from Earth. It is a modular structure, whose first component was launched in 1998, consisting of pressurized modules, external trusses, solar arrays, and other components. ISS components have been launched by USA Space Shuttles as well as by Russian Proton and Soyuz rockets. The ISS serves as a microgravity and space environment research laboratory. Crew members can conduct experiments in physics, astronomy, meteorology as well as biology, medicine, and other fields. The station is suited for the testing of spacecraft systems and equipment required for space missions.

Of particular relevance is the study of the possibility of a long-term permanence of humans in space. The space environment is hostile to life. Unprotected presence in space is characterized by the intense radiation due to charged CRs and other charged



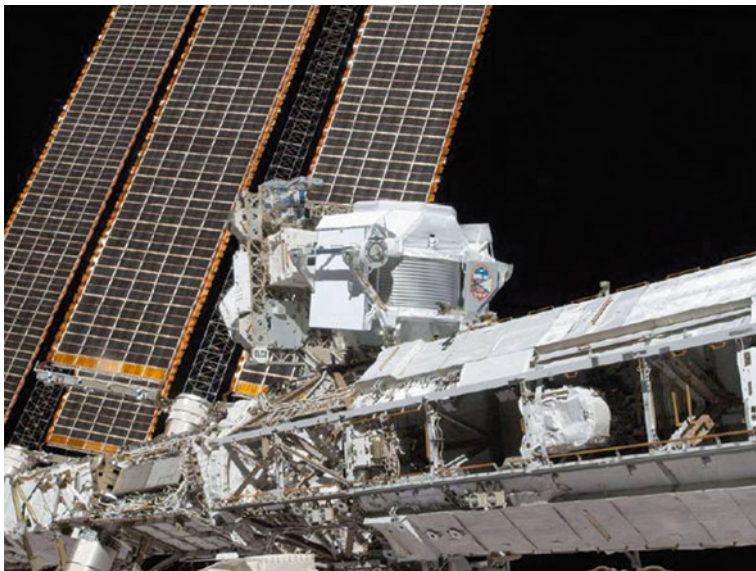


**Fig. 1.6** The Alpha Magnetic Spectrometer (AMS) detector on-board of the International Space Station (Photo: courtesy AMS-02 Collaboration)

particles from the solar wind, high vacuum, extreme temperatures, and microgravity. In addition to AMS-02, other future detectors can be installed on the ISS.

The requirements for a space-borne high-energy physics experiment are extremely challenging. Several constraints are imposed on experiments that have to be launched using satellites or transported on the ISS. For instance, the Alpha Magnetic Spectrometer (AMS-02, Fig. 1.6) has flown with the Space Shuttle with the strict weight limit of 7 tons. For permanence on the ISS, the requirements are power consumption less than 2 kW (as a normal hairdryer) and data rate limited to 2 Mbits per second. In addition, the AMS-02 experiment must work properly in space without any external operation for many years, has survived accelerations up to 9 g and vibrations up to 150 dB during the shuttle launch, and withstand cyclic temperature variations between  $-80^{\circ}$  and  $50^{\circ}$  C in vacuum. Each subsystem and electronic component was produced in prototypes (engineering, qualifications, and flight models) tested to provide the expected physics performance and the mandatory space safety.

### 1.6.2 Experiments in the Atmosphere

Scientific ballooning contributed significantly to the space science program, both directly with physics results coming from measurements made by balloon-borne instruments, and indirectly by serving as a test platform on which instruments have been tested that were subsequently flown on more constrained space missions.

One of the most widely recognized use of ballooning was for the study of anisotropy in the 2.7 K CMB in the millimeter wavelengths. Almost 20 flights have paved the way for the extremely successful measurements of the COBE, WMAP and Planck satellites.

The atmosphere itself has an important role in the development of showers induced by primary CRs. During propagation in the atmosphere, charged particles can emit Cherenkov light and/or excite the fluorescence<sup>3</sup> of nitrogen atoms. Experiments placed on ground are able to measure TeV scale  $\gamma$ -rays and the ultra-high energy cosmic ray particles through the measurement of the light emission.

### 1.6.3 Ground-Based Experiments

The flux of primary CRs from  $\sim 10^{15}$  eV up to more than  $10^{20}$  eV is measured through the detection of secondary particles. The *Extensive Air-Showers Arrays* (EAS) are composed of a collection of detectors distributed over a large area. Scintillators or water-Cherenkov counters are typically used to detect charged particles reaching the ground. Other techniques include the *Cherenkov telescopes*, which detect the Cherenkov light emitted by the electrons in the atmosphere and the *fluorescence detectors*, which observe the fluorescence light emitted by atmospheric nitrogen excited by the shower particles. These detectors can estimate many characteristics of the shower: the number of secondary particles, related to the primary CR energy; the shower lateral distribution with respect to the axis; the primary CR direction of incidence.

## 1.7 Underground Laboratories for Rare Events

In the Standard Model of particle physics quarks and leptons are placed in separate multiplets and the baryon number conservation forbids proton decay. However, there is no known gauge symmetry that generates baryon number conservation, which must be then considered as an open experimental question. Starting from the 1980s, the search for proton decay was the main reason for constructing underground laboratories and large detectors. The simplest GUT model, SU(5), predicts a proton lifetime of  $\tau_p \sim 10^{30}$  years for the process  $p \rightarrow e^+ \pi^0$  that corresponds to many proton decay events in a kiloton-scale detector, if the background from secondary CRs, in particular from atmospheric neutrinos, is reduced by a large shield of surrounding matter.

Water Cherenkov (IMB, Kamiokande) and tracking calorimeters (KGF, NUSEX, Soudan) were the pioneering experiments in the search for proton decay. The Cherenkov detection allows for larger masses, while tracking calorimeters provide better space resolution and good identification of the proton decay products, as elec-

---

<sup>3</sup> The term “fluorescence” refers to the process by which atoms absorb photons of one wavelength and emit photons at a longer wavelength.



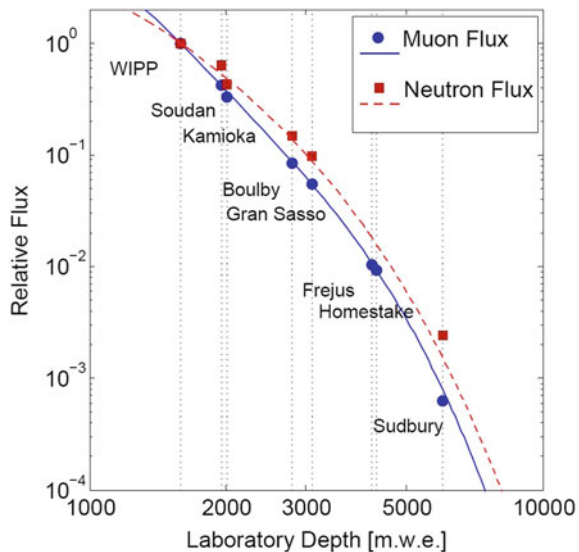
trons, muons, and charged kaons. The limits provided by these experiments ruled out beyond doubt the simplest GUT models.

Since these early experiments, it was easily realized that underground laboratories offer an ideal environmental situation for different experimental studies:

- the detection of low energy phenomena, such as solar neutrinos, neutrinos from stellar gravitational collapses, neutrinoless double-beta decay, and searches for rare phenomena. The main problem for all these experiments is the environmental purity of material and the radioactivity background; refined detectors, often of large mass, are needed. For detection of low energy neutrinos, the most important parameters are the detector mass and the energy threshold;
- the study of  $\sim 1$  GeV events, such as nucleon decays and neutrino oscillations. The main feature of a detector is its mass (1–50 kt) and the capability of identifying neutrino events;
- the detection of through-going particles, high-energy muons, magnetic monopole candidates, etc. The main feature of these detectors is the surface coverage.

The muon flux decreases with the thickness of the rock overburden as shown in Fig. 1.7, which reports also the depth of some large national or international underground facilities (Saab 2014). Operations at deep underground sites also reduce the flux of energetic neutrons, which are created by the interaction of atmospheric muons within the materials and structures surrounding the experiment. This neutron flux represents a penetrating component which does not release a signal in most veto detectors, used for the above-mentioned rare event searches. Regardless of the experimental technique used in rare event searches, reducing the rate of background events plays an essential role. For instance, in the searches for WIMPs, energetic neutrons lead to interactions in a detector that are indistinguishable from a WIMP signal.

**Fig. 1.7** Relative cosmic ray muons (blue) and energetic neutrons ( $>10$  MeV, red) flux at some underground laboratories as a function of laboratory depth. The muon and neutron flux is assumed =1 at the depth of the Waste Isolation Pilot Plant (WIPP), a geological repository for radioactive waste in USA. The blue and red points correspond to measured values, while the lines show a functional fit. Courtesy Prof. T. Saab



**Underground laboratories differ in many other important aspects:** horizontal or vertical access, interference with nearby activities (mine work, road traffic, etc.), quality of the support infrastructures (laboratories, office space, assembly halls, etc.) and personnel on the surface, degree of internationality of the user community, policy of space and time allocation, etc. Scientific sectors different from astroparticle physics, such as biology, geology, and engineering can also profit from the very special underground environment provided by the laboratories and their facilities.

**At present, there are a large number of underground experiments,** with a dominant role of Europe, located in mines or in underground halls close to a highway tunnel. We give in the following a list of the major underground laboratories where some of the experiments described in this book are located.

- The **Baksan** Neutrino Observatory, in **Russia** at depth of about 2,100 m.w.e., where the SAGE and Baksan experiments were located. It was one of the older underground laboratories, started in 1966. It is managed as an observatory, with very long-duration experiments.
- The **Gran Sasso** Laboratory (LNGS). L'Aquila (**Italy**). Is the largest underground facility, the older in Europe after Baksan, located on the highway Roma-Teramo, 120 km east of Rome in Italy. The LNGS are operated by the Istituto Nazionale di Fisica Nucleare (INFN), Italy. The laboratory consists of three underground tunnels, each about 100 m long; it is at an altitude of 963 m above sealevel, is well shielded from secondary CRs by an average amount of rock equivalent to 3,700 m of water (or 3,700 m.w.e.), and has a low activity environment. It hosted and hosts many important experiments (MACRO, Gallex/GNO, Icarus, Opera, DAMA, LVD, Borexino, Xenon...).
- The **Kamioka** Observatory (**Japan**). Is the largest and most important underground laboratory in Asia. The Kamioka Observatory was established in 1983 by M. Koshiba and is operated by the Institute for Cosmic Ray Research, University of Tokyo. The coverage corresponds to 2,700 m.w.e. It hosted or hosts the **Kamiokande** experiment, **Super-Kamiokande**, **KamLAND**, and **XMASS**.
- The **SNO**-laboratory. **Sudbury** (Northern Ontario, **Canada**). It hosted the SNO experiment at a depth of about 6,000 m.w.e.; SNO will be replaced by SNO+, a new kilo-ton scale liquid scintillator detector that will study neutrinos. New structures are being excavated.
- The **Soudan** Underground Laboratory (Minnesota, **USA**). It hosted in two different halls the Soudan experiment, the CDMS dark matter experiment, and the MINOS long baseline experiment.
- The **Homestake** mine in South Dakota was a deep underground gold mine where the Chlorine (or Davis) experiment took data until the mine closure in 2002. A proposed Deep Underground Science and Engineering Laboratory (DUSEL) was a major project under consideration by founding agencies in **USA**.
- **Other infrastructures in Europe** are: BUL, the Boulby Palmer Laboratory (UK); Canfranc (Spain); Modane (France) that hosted the Frejus proton decay experiment; Pyhäsalmi (Finland), under construction; the SUL, Solotvina Underground Laboratory (Ukraine).

- **Other infrastructures in Asia** are: the OTO-Cosmo Observatory (Japan); Y2L, Operated by the Dark Matter Research Centre (DMRC), Korea; INO, the India based Neutrino Observatory (India).

A complete review of the available facilities can be found in Bettini (2007).

## References

- F. Aharonian, J. Buckley, T. Kifune, G. Sinnis, High energy astrophysics with ground-based gamma ray detectors. *Rep. Prog. Phys.* **71**, 096901 (2008)
- J.N. Bachall, *Neutrino Astrophysics* (Cambridge University Press, Cambridge, 1989)
- J. Beringer et al. (Particle Data Group), The review of particle physics. *Phys. Rev. D* **86**, 010001, 1–6 (2012). <http://pdg.lbl.gov/>
- A. Bettini, The world underground scientific facilities. A compendium (2007). [arXiv:0712.1051](https://arxiv.org/abs/0712.1051)
- S. Braibant, G. Giacomelli, M. Spurio, *Particle and Fundamental Interactions* (Springer, Berlin, 2011). ISBN: 978-9400724631
- S. Braibant, G. Giacomelli, M. Spurio, *Particles and Fundamental Interactions: Supplements, Problems and Solutions* (Springer, 2012). ISBN 978-9400741355
- T.K. Gaisser, *Cosmic Rays and Particle Physics* (Cambridge University Press, Cambridge, 1991). ISBN 978-0521339315
- C. Grupen, *Astroparticle Physics* (Springer, Berlin, 2005). ISBN: 978-3540253129
- W.L. Kraushaar, G.W. Clark, G.P. Garmire, R. Borke, P. Higbie, C. Leong, T. Thorsos, High-energy cosmic gamma-ray observations from the OSO-3 satellite. *Astrophys. J.* **186**, 401–402 (1973)
- K.R. Lang, *Essential Astrophysics* (Springer, Berlin, 2013). ISBN 978-3642359637
- P. Lipari, *Introduction to Neutrino Physics* (2006). <http://cds.cern.ch/record/677618/files/p115.pdf>
- M.S. Longair, *High Energy Astrophysics*, 3rd edn. (Cambridge University Press, Cambridge, 2011). ISBN 978-0521756181
- P. Mészáros, The High Energy Universe, *Ultra-High Energy Events in Astrophysics and Cosmology* (Cambridge University Press, Cambridge, 2010)
- A. Rai Choudhuri, *Astrophysics for Physicists* (Cambridge University Press, Cambridge, 2012). ISBN 978-1107024137
- T. Saab, An Introduction to Dark Matter Direct Detection Searches and Techniques (2014). [arXiv:1203.2566](https://arxiv.org/abs/1203.2566)
- P. Sokolsky, *Introduction to Ultrahigh Energy Cosmic Ray Physics* (Westview Press, Colorado, 2004). ISBN: 978-0813342122

# Chapter 2

## The Cosmic Rays and Our Galaxy

Primary *Cosmic Rays* (CRs) are fully ionized atomic nuclei and other particles accelerated at astrophysical sources and reaching the Earth. In this book, usually we indicate with the acronym “CRs” protons and nuclei in the cosmic radiation. The electron,  $\gamma$ -ray, and neutrino components of CRs will be always specified. The discovery of CRs (Sects. 2.1 and 2.2) made it possible to verify both the Einstein relation between particle’s mass and energy and the Dirac theory about the existence of antimatter (Sect. 2.3). Particle detectors play (Sect. 2.4) a fundamental role in this history.

Some quantitative aspect of the CRs, as the differential and integral flux, are defined in Sect. 2.5 and the measured energy spectrum of the primary cosmic rays are presented in Sect. 2.6. Most CRs originate outside the solar system and the physical properties of the Galaxy (dimension, matter density, magnetic fields), described in Sect. 2.7) have an effect on their journey from sources to the Earth. Only low-energy particles (below few GeV) are of solar origin (Sect. 2.8). The intensity of this ionizing radiation is modulated by the solar activity. Below few tens of GeV, the primary CR flux depends also from the magnetic latitude as it is affected by the geomagnetic field (Sect. 2.9).

The theoretical models on the origin of CRs rely on many astrophysical parameters and experimental observations about nature, energy density, confinement time, and chemical composition of CRs as a function of their energy. Supernova remnants are recognized as candidates for the acceleration of galactic CRs. The main motivation is the relation (described in Sect. 2.11) between the loss in kinetic energy due to CRs escape from the galactic disk and the energy released by supernova shock waves. The details of the physical mechanisms through which kinetic energy is transferred to high-energy particles will be described in Chap. 6.

### 2.1 The Discovery of Cosmic Rays

The discovery of CRs is commonly attributed to Victor Hess (1912). After the discovery of radioactivity in 1896 by Henri Becquerel, while studying phosphorescent materials, it was known that some materials can produce ionizations. These

substances are called *radioactive materials*, for their similarity with the radium ( $^{88}\text{Ra}$ ). In the presence of a radioactive material, a charged *electroscope* promptly discharges, while their golden leaves can stay apart from each other if the ionization level of the surrounding material is low. Radioactive elements emit charged particles, which ionize the gas therein, thus causing the discharge of electroscopes. The discharge rate was used at the beginning of the last century to measure the level of radioactivity.

Around 1900, Wilson and others developed a new technique for the insulation of electroscopes in a closed vessel, thus improving the sensitivity of the electroscope itself. As the discharge was present also when no radioactive elements were present inside the electroscope shielding, the presence of ionizing agents coming from outside the vessel was assumed. The questions concerned the Earth or the extraterrestrial origin of such radiation. An experimental confirmation of one of the two hypotheses, however, seemed hard to achieve.

The original idea to perform a measurement far from any terrestrial material seems to be due to Theodor Wulf. In 1909, using an improved electroscope in which two metalized silicon glass wires replaced the two golden leaves, Wulf measured the rate of ionization at the top of the Eiffel Tower in Paris (300 m above ground). According to the hypothesis of the terrestrial origin of most of the radiation, a smaller ionization rate was expected at the top of the tower than on ground. The measured ionization rate was, however, too similar to that on ground to allow a confirmation of the extraterrestrial origin of a part of the radiation.

The first measurement using a balloon (by K. Bergwitz) was made in the same year; the ionization at 1,300 m altitude was found to be only about 24% than ground level. The final answer to the problem was given by the Austrian physicist Victor Hess (Fig. 2.1). After many balloon flights (starting from 1911) and different instruments on board, finally in 1912 he reached an altitude of 5,200 m. The results clearly showed that the ionization, after going through a minimum, increased considerably with height. Hess concluded that the increase of the ionization with height was originated by radiation coming from space. He also noticed the absence of day–night variations and thus he excluded the Sun as the direct source of this hypothetical penetrating radiation.

The results by Hess were later confirmed by W. Kolhörster in a number of flights up to 9,200 m. Hess was awarded the Nobel Prize in physics in 1936 for the discovery of the cosmic rays.

It should also be mentioned that several important contributions to the discovery of the origin of CRs have been forgotten. In particular that of D. Pacini, who in an earlier paper (Pacini 1912) wrote (in Italian) that *a sizable cause of ionization exists in the atmosphere, originating from penetrating radiation, independent of the direct action of radioactive substances in the soil*. A recommended historical overview of the early age of the history of cosmic rays is in Carlson and De Angelis (2010) and references therein.

After the discovery of CRs, a long scientific debate started about the nature of such an extraterrestrial radiation. Most believed at the beginning that cosmic rays were  $\gamma$ -rays because of their huge penetrating power. In particular, R.A. Millikan

**Fig. 2.1** Historical photograph of Hess preparing for a balloon flight (American Physical Society)



hypothesized that those extraterrestrial  $\gamma$ -rays were produced during the formation of helium nuclei in the interstellar space, starting from the combination of protons and electrons.

In 1927, J. Clay found evidence of a variation of the cosmic ray intensity with latitude. As this deflection was attributed to the presence of the geomagnetic field, the only plausible interpretation was that the primary cosmic rays were charged particles, not photons. This interpretation was principally due to Bruno Rossi, who in 1930 predicted a difference between the intensities of CRs arriving from the East and the West assuming positively charged particles. A world-wide survey was performed in 1932 by Compton, which verified the Rossi prediction of the so-called “East-West effect” and rejected the Millikan theory.

In 1938–1939 (in Paris first and then in the Alps mountains), P. Auger and collaborators showed that groups of particles could arrive in time coincidence on detectors separated by distances as large as 200 m. This was the first indication that the observed particles in atmosphere were secondary particles induced from a common primary CR (Auger et al. 1939). They concluded that there exist in the Universe mechanisms able to accelerate particles up to an energy of  $10^{15}$  eV. Note that at that time the largest energies from natural radioactivity or artificial acceleration were just a few MeV. Only in 1941 it was established (Schein et al. 1941) that CRs were mostly protons.

In 1962, John Linsley observed an event interpreted due to a cosmic ray of energy  $10^{20}$  eV (Linsley 1962). This event was measured by an array of scintillation counters spread over  $8 \text{ km}^2$  in a desert of New Mexico (USA).

## 2.2 Cosmic Rays and the Early Days of Particle Physics

CRs are very-high-energy particles entering the atmosphere, making it possible before the advent of particle accelerators the creation of new, unstable particles through the Einstein relation between energy and mass. Around 1920, only the proton, the electron, and the photon were known as elementary particles. Before the advent of particles accelerators, up to the 1950s, the study and discovery of new particles and the study of the fundamental interactions between elementary particles was performed mainly using cosmic rays.

Since the 1930s, the experimental techniques for the detection and measurement of some physical quantities (e.g., electric charge, mass, lifetime) of the particles present in the secondary cosmic rays started to become more refined. Particularly, P. Blackett (Nobel laureate in 1948) used a cloud chamber inside a magnetic field that bent the trajectory of charged particles. Experimental techniques using CRs remained useful until well after the end of the Second World War, when particle accelerators started to be developed.

Using Blackett's experimental techniques, in 1932, C. Anderson (Nobel laureate in 1936) discovered a particle having the same mass as the electron, though with opposite electric charge (Fig. 2.2). It was the antielectron (or positron), that is, the antiparticle predicted by the relativistic quantum theory of the electron developed a few years before by P.A.M. Dirac (Nobel laureate in 1933). Immediately afterwards, in 1934, J. Chadwick (Nobel laureate in 1935) experimentally identified a particle with a mass similar to that of the proton, though without electric charge: the neutron.

In 1937, C. Anderson and S. Neddermeyer discovered a particle of intermediate mass between that of the proton and of the electron: they called this new particle the meson. For some time, it was thought that this particle was that necessary to glue protons and neutrons in nuclei. A theoretical model due to H. Yukawa (Nobel laureate in 1949) predicted the existence of a particle with a mass very close to that of the just discovered meson. Nevertheless, during World War II in Rome, M. Conversi, E. Pancini and O. Piccioni demonstrated in a famous experiment using secondary cosmic rays that the meson of Anderson and Neddermeyer (nowadays called the muon) was not the particle predicted by Yukawa. Even if the theory of Yukawa does not properly describe the physics of nuclei, the predicted particle (the pion) was discovered in 1947 by C. Lattes, G. Occhialini and G. Powell in secondary cosmic rays using nuclear emulsions (i.e., sophisticated photographic films) at high altitudes.

In 1947, in the interactions of cosmic rays in a cloud chamber with magnetic field, particles with a particularly strange behavior were discovered. They were thus named strange particles. Many years later [see Chap. 7 of Braibant et al. (2011)], it



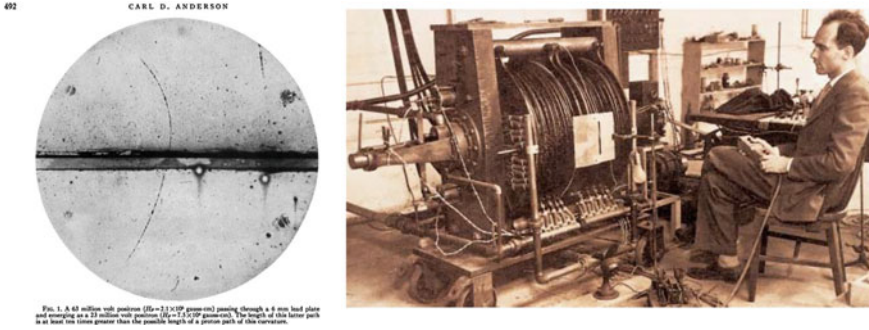


**Fig. 2.2** *Left* The first image of a positron obtained by Anderson in a cloud chamber (Anderson 1933). A charged particle interacting with the supersaturated vapor of the mixture inside the chamber produces ionization. The resulting ions act as condensation centers, around which a mist will form. Due to many ions being produced along the path of the charged particle, the tracks of particles having electric charge  $Ze = 1$  or  $2$  have distinctive shapes (an alpha particle’s track is broad, while an electron’s is thinner and straight). The particle in this event has the same electric charge of the electron but opposite sign, Sect. 2.3. *Right* Carl D. Anderson, Nobel Prize for Physics in 1936, with its detector: a cloud chamber inside an electromagnet

was realized that **strange particles**, as protons and neutrons, **are composite** objects. **Protons** and **neutrons**, and other short-lived particles with semi-integer spin, are **made of three  $u$  and  $d$  quarks**. The **pions**, as other mesons with null or integer spin, are **made of a quark and an antiquark**. **Strange particles contain a new, heavier quark called  $s$  (for *strange*)**. With the advent of accelerators, the fields of particle physics and that of cosmic rays parted ways, though they have actually reconnected in recent years.

### 2.3 The Discovery of the Positron and Particle Detectors

In this section, we will use the Anderson’s picture of the detected positron to introduce how particles are identified with the help of an external magnetic field.

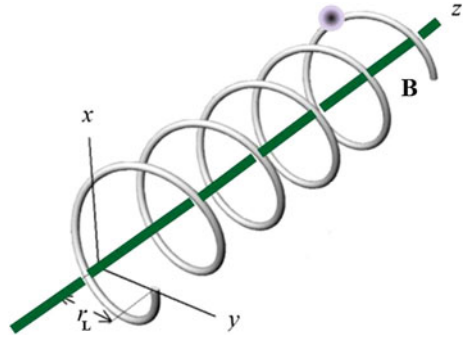
#### 2.3.1 The Motion in a Magnetic Field and the Particle Rigidity

**The Lorentz force** exerted by the magnetic field  $\mathbf{B}$  on a particle with charge  $q$ , mass  $m$ , and velocity  $\mathbf{v}$  is (in c.g.s. units)

$$\Gamma m \frac{d\mathbf{v}}{dt} = \frac{q}{c} \mathbf{v} \times \mathbf{B} \tag{2.1}$$



**Fig. 2.3** The motion of a charged particle along the  $\mathbf{B}$  field line



where  $\Gamma^1$  is the Lorentz factor:

$$\Gamma \equiv \frac{1}{\sqrt{1 - v^2/c^2}} = \frac{E}{mc^2} \tag{2.2}$$

Since the acceleration is perpendicular to both the magnetic field and velocity vectors, in the case of a static uniform field, the orbit is a circle, plus a uniform motion along the direction of  $\mathbf{B}$ . The resulting helicoidal motion is shown in Fig. 2.3. The integration of Eq. (2.1) yields for a static and uniform magnetic field:

$$\mathbf{v} = \mathbf{r} \times \frac{q\mathbf{B}}{\Gamma mc} \equiv \mathbf{r} \times \boldsymbol{\omega}_L \tag{2.3}$$

The angular frequency of the circular motion is

$$\omega_L = \frac{2\pi}{T_L} = \frac{qB}{\Gamma mc} \tag{2.4}$$

The radius of the orbit is called the cyclotron radius or Larmor radius. For  $q = Ze$ , where  $e$  is the electric charge of the proton,<sup>2</sup> the Larmor radius is:

$$r_L = \frac{v}{\omega_L} = \frac{\Gamma m v c}{ZeB} = \frac{pc}{ZeB} \approx \frac{E}{ZeB} \tag{2.5}$$

The last equality holds only for relativistic particles (as in most cases in this textbook). The cyclotron radius decreases with the increase of the charge  $Z$  of a nucleus, in units of the proton electric charge. As the effect of a magnetic field on a particle depends

<sup>1</sup> In the book, we use the  $\Gamma$  (uppercase) for the Lorentz factor to avoid confusion with the  $\gamma$ -ray.  
<sup>2</sup> A major difference between the c.g.s. and SI units is in the definition of the unit of charge. The c.g.s. unit of electrical charge (the statcoulomb, statC) can be written entirely as a dimensional combination of the mechanical units (gram, centimeter, second). In this book, we use the notation that  $e = 4.8 \times 10^{-10}$  statC is the proton charge;  $-e$  will be the electron charge.

on the ratio between momentum and electric charge, the particle rigidity  $R$  is defined as:

$$R \equiv \frac{pc}{Ze} \approx \frac{E}{Ze} = \frac{1.6 \times 10^{-12}(\text{eV/erg})E(\text{erg})}{4.8 \times 10^{-12}(\text{statC})} = \frac{1}{300} E \quad [\text{V}] \quad (2.6)$$

when the energy is measured in eV. By definition, the eV is the product of an electric charge and a potential difference, and the rigidity is measured in Volts. If a multiple of the eV is used (for instance, the GeV), the rigidity is automatically expressed in the same multiple (GV).

### 2.3.2 The Identification of the Positron

Let us consider the picture in Fig. 2.2. The additional information which we have are:

- a 6 mm-thick lead plate is located in the middle of the chamber. A particle, while crossing the plate, loses energy;
- the intensity of the magnetic field inside the electromagnet in the region of the cloud chamber is 15 kG;
- the magnetic field is perpendicular to the plane of the paper;
- by comparing the number of ionization centers in the chamber with that released by radioactive nuclei emitting  $\alpha$  (helium nuclei with charge =  $2e$ ) or  $\beta$  radiation, the particle has an electric charge  $+e$  or  $-e$ .

The simplest interpretation (an electron with charge  $-e$  entering from above) is wrong. To demonstrate it, we draw in Fig. 2.4 two circles which interpolate the ionization points before and after the lead layer. The picture represents the projection on a plane of the 3-D particle trajectory<sup>3</sup> and our drawing is only approximate. In any case, we are lucky enough that the trajectory of the particle is mainly in the plane of the picture. Observing the circles, it is evident that the radius of curvature is larger in the bottom region. From (2.5), we conclude that the energy of the particle is larger in the region below the lead. Thus:

- the particle must have entered the chamber from below;

As we know the directions of the particle velocity and of the magnetic field (entering the plane), using the relation  $\mathbf{F} \propto \mathbf{v} \times \mathbf{B}$  we obtain that

- the particle has suffered a force toward the left. Thus, it is a positively charged particle.

It remains to show that

<sup>3</sup> For these reasons, in later *bubble chamber* techniques two or more views of the event were used.

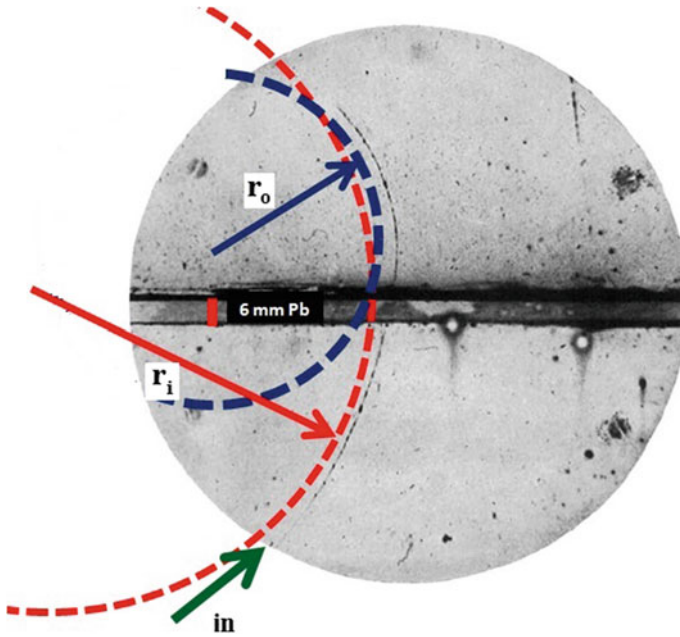


**Fig. 2.4** The Anderson’s positron picture interpolated with two arcs of circle (slightly shifted to the left, to show the original track). The energy loss in the Pb plate is that characteristic of an electron-like particle (see text). The fact that  $r_o < r_i$  indicates that the particle energy is  $E_o < E_i$  and thus that it enters from below (arrow). However, from the knowledge of the magnetic field direction, the sign of the charge of this particle must be positive. It cannot be an electron

- the particle in the figure cannot be a proton and has almost the same mass as the electron. Thus, is a positron, the particle foreseen by the quantum Dirac theory of the electron.

For this last step, we use the measurement of the radius of curvature of the two circles drawn in Fig. 2.4. The ruler in the figure is provided by the 6 mm Pb plate. The radius of the two circles can be scaled using this ruler in a way independent of the magnification of the picture. Our estimate is  $r_i = 14 \text{ cm}$ ,  $r_o = 7 \text{ cm}$  for the particle when it enters and exits the cloud chamber, respectively. From (2.5), we obtain the respective particle momentum:

$$\begin{aligned}
 p_i c &= r_i e B = 14 \times (4.8 \times 10^{-10}) \times (1.5 \times 10^4) = 1.0 \times 10^{-4} \text{ erg} \\
 p_i &= 63 \text{ MeV}/c
 \end{aligned}
 \tag{2.7a}$$

using the relation  $1 \text{ erg} = 1.6 \times 10^{-12} \text{ eV}$ . Similarly, after the plate<sup>4</sup>:

<sup>4</sup> In his work (Anderson 1933), Anderson reported a 63 million volt positron passing through a 6mm lead plate and emerging as a 23 million volt positron. Our result is not so bad.

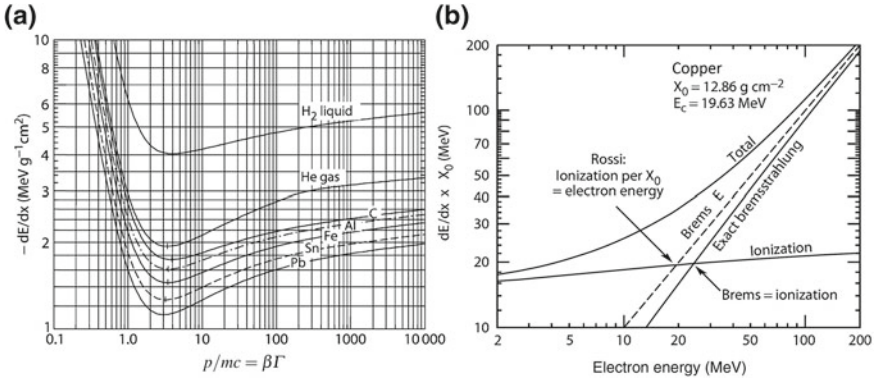


**Fig. 2.5** **a** Mean energy loss in different materials of charged particles due to the electromagnetic interactions (excitation and ionization) with the electrons of the medium. The *horizontal scale* is in  $\beta\Gamma$  units, which is independent of the incident particle type. **b** Electron energy loss in copper as a function of the electron energy. The excitation and ionization contribution remains roughly constant with increasing energy. Instead, the term due to the electron energy loss through interactions with nuclei (bremsstrahlung) increases. The intersecting point of the two curves defines the critical energy. In this figure, it corresponds to about 20 MeV. *Credit* the Particle Data Group (Beringer et al. 2012)

$$p_o = r_o e B / c = 32 \text{ MeV}/c \tag{2.7b}$$

The energy loss of charged particles through excitation and ionization of a material is given by the Bethe-Bloch formula as a function of the particle momentum  $p$ . It depends on the charge  $Ze$  and velocity  $\beta = v/c$  of the incoming particle and only weakly from the properties of the crossed material. When  $p$  is expressed in terms of the adimensional Lorentz factors  $p/mc = \beta\Gamma$ , the energy loss assumes the behavior shown in Fig. 2.5a. The energy loss curves have a minimum for  $\beta\Gamma \sim 3$ , that is,  $pc = 3mc^2$ . Neglecting the logarithmic rise when  $E \sim pc \gg mc^2$ , the Bethe-Block formula can be approximated as:

$$-\frac{dE}{dx} = \frac{Z^2}{\beta^2} \left( \frac{dE}{dx} \right)_{\min} ; \text{ with } \left( \frac{dE}{dx} \right)_{\min} \sim 2 \text{ MeV g}^{-1} \text{ cm}^2 \tag{2.8}$$

Let us consider the energy loss under the hypothesis of an incoming proton ( $m_p c^2 = 938 \text{ MeV}$ ) with momentum  $p_i$  and

$$\beta\Gamma = \frac{p_i c}{m_p c^2} = \frac{63 \text{ MeV}}{938 \text{ MeV}} \sim 0.07. \tag{2.9}$$

The energy loss for such a low momentum is outside the scale of Fig. 2.5a. The energy loss can be estimated from (2.8), assuming  $\beta\Gamma \sim \beta = 0.07$ . The specific energy loss in lead (density  $\rho_{Pb} = 11 \text{ g cm}^{-3}$ ) corresponds to

$$-\frac{dE}{dx} = (0.07)^{-2} \times 2 (\text{MeV cm}^2/\text{g}) \times 11 (\text{g cm}^{-3}) \simeq 5,000 \text{ MeV/cm}.$$

To cross 6 mm of lead, a proton would lose  $\sim 3,000 \text{ MeV}$ . This is by far inconsistent with the observed variation of energy  $\Delta E = E_i - E_o = 1.5 \text{ MeV}$ , assuming an incoming proton having  $p_i = 63 \text{ MeV}/c$  and  $p_o = 32 \text{ MeV}/c$ . The positively charged particle in the picture cannot thus be a proton!

Let us consider the case of a *positive electron*. From the Dirac theory, its mass is identical to that of the electron ( $m_e c^2 = 0.511 \text{ MeV}$ ), so that:

$$\beta\Gamma = \frac{p_i c}{m_e c^2} = \frac{63 \text{ MeV}}{0.511 \text{ MeV}} \simeq 123 \quad (2.10)$$

In the case of the electron, in addition to the excitation-ionization energy loss, also the *bremsstrahlung* (hard Coulomb scattering with atomic nuclei) process must be considered. The electron energy loss in copper is given in Fig. 2.5b. Copper has a radiation length  $X_0 \sim 12.9 \text{ g cm}^{-2}$ , Sect. 3.3. From the figure, to an electron with  $p = 63 \text{ MeV}/c$  corresponds an energy  $E = 63 \text{ MeV}$  and thus:

$$\frac{dE}{dx} \times X_0 \simeq 70 \text{ MeV} \rightarrow \frac{dE}{dx} \simeq 70/12.9 = 5.4 \text{ MeV/g cm}^{-2}$$

Thus, assuming the usual 6 mm of lead i.e.  $\Delta x = 6.6 \text{ g cm}^{-2}$ :

$$\Delta E \sim 5.4 \times 6.6 = 36 \text{ MeV}. \quad (2.11)$$

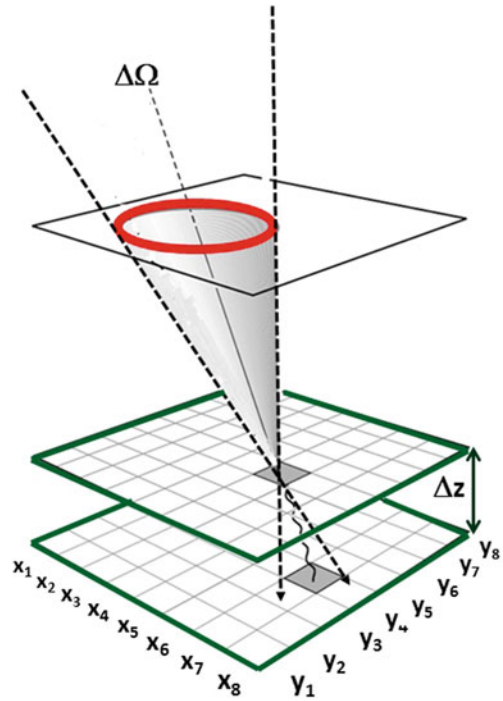
As the electron is relativistic, the energy loss from the picture is simply  $E_i - E_o \simeq p_i c - p_o c = 31 \text{ MeV}$  in the 6 mm of lead, very close to the value obtained using (2.11). The mass and energy loss properties of the particle are compatible with that of the electron!<sup>5</sup>

## 2.4 A Toy Telescope for Primary Cosmic Rays

The aforementioned example of the positron discovery, although using very simple devices, is an example of how detectors for particle identification operate. Any experimental apparatus for CRs detection should: (i) identify the particle, (ii) measure its electric charge, and (iii) measure its energy and momentum. We illustrate in the following how the *flux* of particles can be measured with a simple experimental device. The techniques used by modern experiments for the direct measurement of CRs are presented in the next chapter.

<sup>5</sup> At the time of the Anderson picture, only protons and electrons were known as charged particles. Try to work out that the observed particle cannot be a charged  $\pi^+$  meson, with  $m_\pi = 139.6 \text{ MeV}/c^2$ .

**Fig. 2.6** Layout of a simple telescope for the measurement of CRs. The two counter's layers are assumed to be segmented both in the  $x$  and  $y$  axis. A CR arriving within the solid angle  $\Delta\Omega$  will produce one hit on each layer (see text)



Our ideal experiment (a *toy telescope for charged CRs*) is made of **two layers of counters** of a given area  $A$  separated by the distance  $\Delta z$  (see Fig. 2.6). Each counter's layer is segmented with a characteristic spatial resolution. **The signal** in the counter is **provided by the excitation/ionization energy loss** of through-going charged particles, see Chap. 2 of Braibant et al. (2011). **The excitation/ionization energy loss (2.8) is proportional to the square of the electric charge  $Z$  of the particle.** With **proportional counters the amplitude  $I$  of the signal depends thus on  $Z^2$ .** This method to measure the electric charge of the incoming particle through Eq. (2.8) will be referred in the following as  **$dE/dx$  measurement**. Primary CRs can be measured if the telescope is carried to the top of the atmosphere by a balloon or outside the atmosphere by a satellite.

In Fig. 2.6 we **assume that** a charged **particle** crossing the **lower counter induces a signal at** the position labeled  $(x_7, y_4)$ . **Additional information** are the  **$z$ -position  $z_1$**  of the layer, the **crossing time ( $t_1$ )** and the **amplitude  $I_1$**  of the signal. The **complete set** of information (a **hit**) can be represented as  $(x_7, y_4; z_1, t_1, I_1)$ . The hits are stored as digital information on a *online* computer.

Each particle detector has some advantage/disadvantage with respect to others: some of them have good spatial resolution and poor timing resolution, and vice versa [see Sect. 2.7 of Braibant et al. (2011)]. The design of a modern experiment is a compromise between the requirements necessary to have the best performances in

terms of physics results, and the cost, dimension, power dissipation, weight, etc. of each sub-detector.

A major requirement of any experiment is the *trigger logic*. This is a mandatory task, because the *probability of a fake signal on a single counter is high*. Due to the presence (for instance) of radioactive elements in the surrounding materials, or due to electronic noise, there are spurious signals in each detector plane with usually larger rates. By definition, these *spurious hits are not correlated with a crossing particle and constitute the background*.

In our simple example, a trigger is given by a *coincidence between planes*. This corresponds to have *a signal both on the  $z_1$  and  $z_2$  layers within a given time interval  $T$* . A condition on amplitudes  $I_1, I_2$  can also be added. The hits are permanently stored in the computer for further analysis if  $|t_1 - t_2| \leq T$ . The combination of signals in both planes, without constraints on time difference, will usually provide a too large event rate with respect to the real CR rate.

Relativistic particles in vacuum cover 1 m in  $\sim 3.3$  ns. Typical distances  $\Delta z$  between layers in CR telescopes (as in our example) are of the order of 1–2 m. The *timing resolution* of the detectors must be of the *order of a ns* (or better) to have the possibility to *distinguish between upward-*(with  $t_2 - t_1 > 0$ ) and *downward-*(with  $t_2 - t_1 < 0$ ) going cosmic rays. In this case, a *time-of-flight* (ToF) measurement is performed. A very good timing resolution is characteristic for instance of most *scintillation counters*. Scintillation counters can be arranged in order to have sufficient spatial resolution to distinguish different directions (as in our telescope). In addition, *their response depends on the ionization energy loss*, and thus on the *particle  $Z^2$* . Many ToF systems are also *used to measure the  $Z$  of the detected particle*.

In many real detectors a *uniform magnetic field* in the region *between the counters performing a ToF is present*. The *magnetic field allows the measurement of the particle momentum* (if  $|Ze|$  is known) and *sign of the charge*, as charged *particles are deflected according to their rigidity*. To measure the curved particle trajectory, additional detectors are needed inside the magnetic field region. If the magnetic field is along the  $y$  axis,  $\mathbf{B} = B\hat{y}$ , the deflection is expected along the  $x$ -axis for particles entering with velocity along  $\hat{z}$ . In this case, *detectors with good spatial resolution inside the magnetic field* (*tracking systems*) are used *to accurately measure the  $x$  coordinate*. *The combination of the magnetic field and tracking detectors forms a magnetic spectrometer*.

Finally, depending on some constraints (for instance, the total weight of the payload on a satellite or balloon) *a calorimeter* or other devices *for the measurement of the particle energy* can be added (see Chap. 3 for real experiments in space or in the upper atmosphere).

## 2.5 Differential and Integral Flux

The simple CR telescope of Fig. 2.6 is useful for the *definition* of the quantities related to the measurement of the *number  $N$  of incident particles per unit time* on the *detector surface  $A$*  at a given *solid angle  $d\Omega$* . Usually, the area seen by particles

depends upon their arrival direction (corresponding to a given zenith and azimuth angles  $\theta$  and  $\phi$ , respectively) in a small angular region  $d\Omega = \sin\theta d\phi d\theta$  and thus  $A = A(\theta, \phi) = A(\Omega)$ . The quantity:

$$A\Omega \equiv \int A(\Omega) \cdot d\Omega \quad [\text{cm}^2 \text{sr}] \quad (2.12)$$

is called *the geometrical factor*. The event rate in a detector (i.e. the number of events per second) is given by the particle flux (see below) times the geometrical factor.

The *intensity vs. energy* is determined using detectors able to measure the energy of the incoming particle. Thus the *number of CRs* arriving in a *given energy interval*  $dE$  and *solid angle*  $d\Omega$  represents the *differential intensity of particles of a given energy in the given solid angle*:

$$\Phi(E) \equiv \frac{d^2\varphi}{dEd\Omega}(E) \equiv \frac{dN}{A \cdot T \cdot d\Omega \cdot dE} \quad \frac{\text{particles}}{\text{cm}^2 \text{sr s GeV}} \quad (2.13)$$

Sometimes, particles can be measured only if their energy is larger than a given energy *threshold*  $E_0$ . Equivalently, we could be interested in all particles measured with energy larger than  $E_0$ . In both cases:

$$\Phi(>E_0) \equiv \frac{d\varphi}{d\Omega}(E) = \int_{E_0}^{\infty} \frac{d^2\varphi}{dEd\Omega} dE \quad \frac{\text{particles}}{\text{cm}^2 \text{sr s}} \quad (2.14)$$

represents the *integral intensity of particles with energy*  $> E_0$ , i.e. the measurement of the CR intensity for particles with energy larger than the given threshold.

According to the literature, the quantities  $\Phi(E)$  (2.13) and  $\Phi(>E_0)$  (2.14) are sometime called the *differential flux* and the *integral flux* of particles, respectively. Note the different units in the two cases. In the following chapters an index could appear: for instance,  $\Phi_{\text{CR}}, \Phi_e, \Phi_\gamma, \Phi_\nu$  will indicate the *flux of primary CRs, electrons, gamma-rays and neutrinos*, respectively. Nuclei correspond to an important fraction of CRs. If the detector can measure the *electric charge*  $i = Ze$  of the incoming nucleus, the *flux*  $\Phi_i$  of the *particular nuclear species* can be defined, as for instance in Fig. 3.10.

The arrival direction of CRs is largely isotropic. The particles' flux trough a spherical surface is simply given by the integration over the solid angle of (2.14):

$$\frac{d\varphi}{dE}(E) = 4\pi \frac{d^2\varphi}{dEd\Omega}(E) = 4\pi \Phi(E) \quad \frac{\text{particles}}{\text{cm}^2 \text{s GeV}} \quad (2.15)$$

In most cases (as for our ideal experiment of Fig. 2.6) we are interested in the flux through a planar surface. The differential particles flux through a planar detector from one hemisphere is:

$$\mathcal{F}(E) = \int \frac{d^2\varphi}{dEd\Omega} \cos\theta d\Omega \quad \frac{\text{particles}}{\text{cm}^2 \text{s GeV}} \quad (2.16)$$



$d\Omega$  is as usual the elemental solid angle,  $\theta$  the angle between the vector perpendicular to the area  $A$  and the direction of the incoming particle. For isotropic radiation (as in the case of the primary CRs) the flux on a plane is:

$$\begin{aligned}\mathcal{F}(E) &= \Phi(E) \int_0^{2\pi} d\phi \int_0^{\pi/2} d\theta \sin\theta \cos\theta \\ &= \pi \Phi(E) \int_0^{\pi/2} d\theta \sin 2\theta = \pi \Phi(E) \frac{\text{particles}}{\text{cm}^2 \text{ s GeV}}.\end{aligned}\quad (2.17a)$$

Note that the form of the surface changes the numerical coefficient in front of  $\Phi$  with respect to (2.15). Integrating (2.17a) over energies, we obtain the quantity:

$$\mathcal{F}( > E) = \pi \Phi( > E) \frac{\text{particles}}{\text{cm}^2 \text{ s}}.\quad (2.17b)$$

An important quantity in astrophysics is the *number density* (units:  $\text{cm}^{-3}$ ) of CRs moving with velocity  $v$ . The number density corresponds to the number of particles present in a given volume at a given time. The setup of Fig. 2.6 for instance is continuously crossed by CRs at given rate. If we imagine of taking a snapshot of the particles present in the detector volume at a given time and counting them, we could derive the number density of particles in the detector volume.

Using *dimensional arguments*, the number density can be easily obtained from the integral flux (2.14) integrated over the solid angle and divided by the velocity (cm/s). It is easy to work out that for an isotropic flux the *particle number density* is:

$$n = \frac{4\pi}{v} \Phi( > E) \frac{\text{particles}}{\text{cm}^3}.\quad (2.18a)$$

If the flux is not isotropic, the integration over the solid angle gives a factor different from  $4\pi$ . If the particle velocity are not constant, an integration over the velocity distribution spectrum is also needed.

Sometimes we are interested in the *differential number density* of cosmic rays. Using (2.13) we obtain:

$$\frac{dn}{dE} = \frac{4\pi}{v} \Phi(E) \frac{\text{particles}}{\text{GeV cm}^3}.\quad (2.18b)$$

In this book, we are dealing practically always with relativistic particles, and  $v \simeq c$ .

## 2.6 The Energy Spectrum of Primary Cosmic Rays

After more than 100 years of research, we know that the solar system is permanently bombarded by a flux of highly energetic particles. Their energies extend from the MeV range to  $10^{20}$  eV. The primary component arriving on the top of the atmosphere includes all stable charged particles and nuclei. Also some unstable nuclei (with lifetimes larger than  $10^6$  years) are found. This (small) fraction of radioactive nuclei is important to estimate the escape time of CRs (Sect. 5.1).

Figure 1.4 shows the integral intensity of CRs as measured by a large number of different experiments, from small detectors on board of balloon and satellites to huge air shower arrays on ground, covering surfaces of more than  $3,000 \text{ km}^2$ . Each experiment has measured the integral flux (2.14) in a given energy interval. The analytic interpolation of all available data shown in Fig. 1.4 is usually referred to as the integral energy spectrum.

The distribution of the differential flux (2.13) covering the whole energy interval of CRs is usually referred as the differential energy spectrum (or simply the energy spectrum) of CRs and it is shown in Fig. 2.7.

The energy spectrum falls steeply as a function of energy. The integral flux (2.17b) corresponding to different energy thresholds gives

$$\mathcal{F}(>10^9 \text{ eV}) \simeq 1,000 \text{ particles/s m}^2 \tag{2.19a}$$

$$\mathcal{F}(>10^{15} \text{ eV}) \simeq 1 \text{ particle/year m}^2 \tag{2.19b}$$

$$\mathcal{F}(>10^{20} \text{ eV}) \simeq 1 \text{ particle/century km}^2. \tag{2.19c}$$

Figure 2.7 seems almost featureless, but two transition points (where the slope of the spectrum changes) are clearly visible. This feature defines three energy intervals in the CR spectrum. The transition point at  $\sim 3 \times 10^6 \text{ GeV}$  is called the knee. Below the knee, the integral CR flux decreases by a factor  $\sim 50$  when the energy increases by an order of magnitude.

At energies larger than few GeV (where the contribution of particles coming from the Sun, Sect. 2.8, is negligible) the energy spectrum can be described by a power-law:

$$\Phi(E) = K \left( \frac{E}{1 \text{ GeV}} \right)^{-\alpha} \frac{\text{particles}}{\text{cm}^2 \text{ s sr GeV}} \tag{2.20a}$$

$$\Phi(>E) = \frac{K}{(\alpha - 1)} \left( \frac{E}{1 \text{ GeV}} \right)^{-\alpha+1} = \frac{K}{(\alpha - 1)} \left( \frac{E}{1 \text{ GeV}} \right)^{-\gamma} \frac{\text{particles}}{\text{cm}^2 \text{ s sr}}. \tag{2.20b}$$

The parameter  $\alpha$  is the differential spectral index of the cosmic ray flux (or the slope of the CR spectrum) and  $K$  a normalization factor;  $\gamma \equiv \alpha - 1$  is the integral

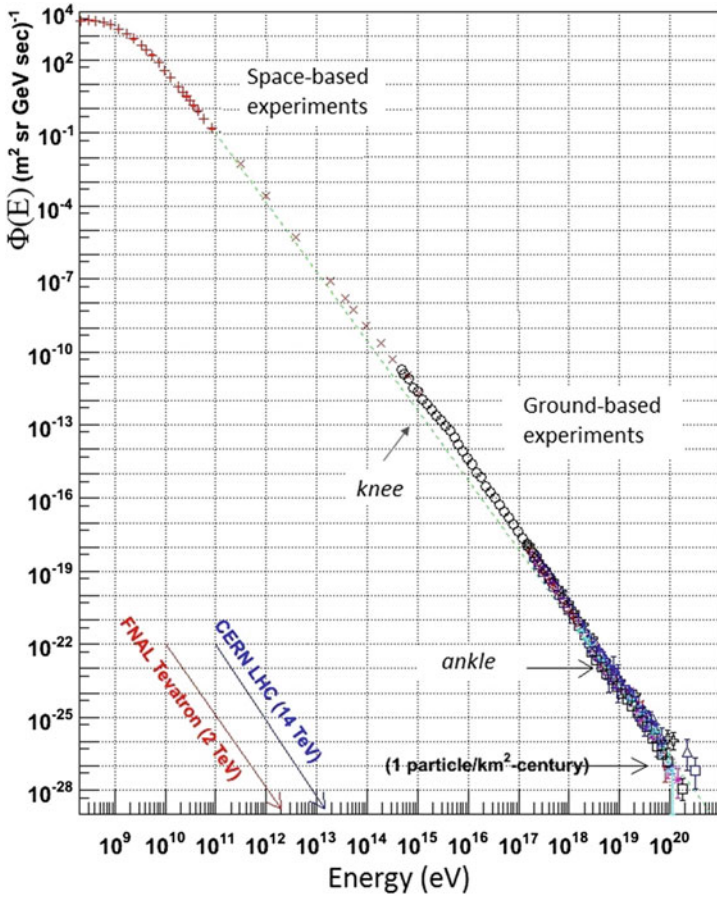


**Fig. 2.7** The differential energy spectrum  $\Phi(E)$  (units: particles/m<sup>2</sup> sr s GeV) of cosmic rays over eleven decades of energy. The red/blue arrows indicate the equivalent center of mass energy reached at the Tevatron collider at Fermilab and at the LHC collider at CERN. Note that the spectrum is remarkably continuous over the whole energy interval, and that the flux on the y-axis covers 33 decades. The dashed line shows a  $E^{-3}$  spectrum

**spectral index.** The numerical values of the parameters are determined through a fit to experimental data.

Different compilations of data exist which determine the parameters  $K$ ,  $\alpha$  using direct measurements of the CR flux (Chap. 3). These compilations give results in agreement within  $\sim 30\%$ . In the energy range from several GeV to  $\sim 10^{15}$  eV, we use that obtained in Wiebel-Sooth et al. (1998), with

$$K = 3.01; \quad \alpha = 2.68 \tag{2.20c}$$

that includes the contribution of protons ( $\sim 90\%$ ) and heavier nuclei. The compilation of Hörandel (2003) in the same energy region gives  $K = 2.16, \alpha = 2.66$ . The Beringer et al. (2012) gives the proton flux in terms of *energy-per-nucleon*, with  $K = 1.8, \alpha = 2.7$ .

The *energy-per-nucleon* is the *energy-per-nucleus*, divided by the number of nucleons. Conventionally, the two quantities can be distinguished by the indication that the *energy-per-nucleus* is measured in [GeV], while the *energy-per-nucleon* in [GeV/nucleon] or [GeV/A], where the “A” stands for “nucleons”. The *energy-per-nucleon* can be assessed only through *direct* experiments, when both  $E$  and  $Z \sim A/2$  are measured. When the atmosphere is used as a calorimeter in air shower experiments, generally the *energy-per-nucleus* is measured.

Above the knee, the CR flux decreases by a factor  $\sim 100$  when the energy increases by a factor of 10. The spectral index of the CR spectrum becomes steeper,  $\alpha \sim 3.1$ . The measurements of the CR spectrum above the knee are presented in Chap. 4. At the energy of  $\sim 10^{10}$  GeV the spectrum becomes flatter again in correspondence of the second transition point, called the *ankle*. CRs above the ankle are thought to have an extragalactic origin (Chap. 7).

The *knee* and *ankle* structures are more evident in Fig. 2.8. It shows almost the same data set as in Fig. 2.7. The main difference is that the *y-axis variable is multiplied*

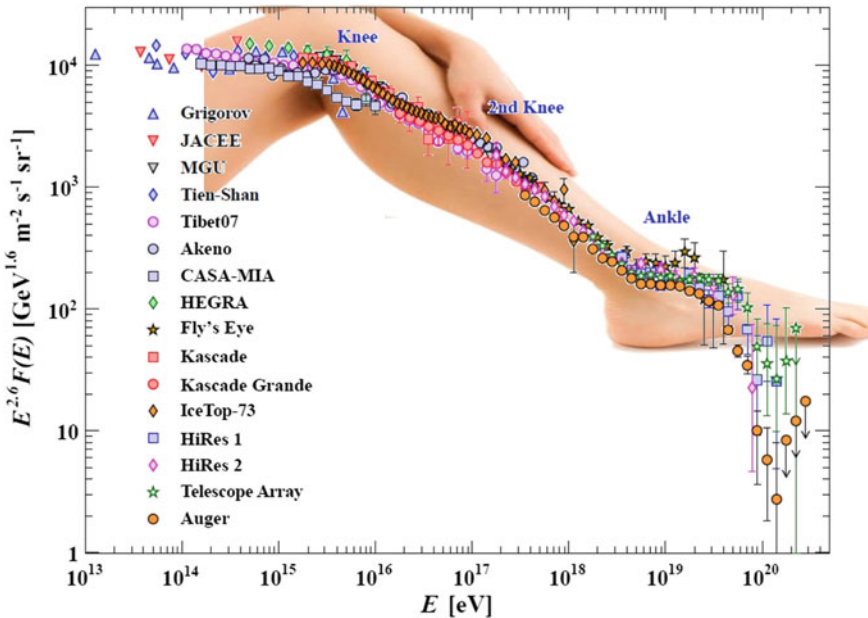


**Fig. 2.8** The differential CR flux  $\Phi(E)$  as measured by many *direct* and *indirect* CR experiments over eight decades of energy, almost the same as Fig. 2.7. Here the flux is multiplied by a power of the energy:  $\Phi(E) \times E^{2.6}$ . The structures of the knee and ankle are more evident as well as point-to-point differences between different experiments (most due to systematic uncertainties on the energy calibration). Adapted from a figure from Sect. 27: Cosmic Rays of Beringer et al. (2012)

by  $E^{2.6}$ . As explained in Sect. 1.2, this enhances the visibility for structures in the spectrum.

About 79 % of the primary nucleons are free protons and about 70 % of the rest are nucleons bound in helium nuclei (see Sect. 3.7). The flux of electrons corresponds to less than 1 % of that of protons and nuclei at the same energy. This does not correspond to a charge-asymmetry in the CR sources. Electrons (as explained in the following chapters) suffer larger energy losses that reduce the number of those arriving with high energies on Earth. In general, fluxes of CR particles as measured on Earth are influenced by their travel through the galactic interstellar medium and magnetic field. In the next section, a description of the main properties of the Galaxy is given.

## 2.7 The Physical Properties of the Galaxy

Today it is an established fact that the Sun is part of a system of stars, the *Galaxy* (or *Milky Way*), which is very similar to the spiral galaxies that we observe in the Universe. This conclusion was a sort of larger scale *Copernican revolution* and was thus a nontrivial fact, also from the observational point of view.

The determination of the shape and the size of the Galaxy with optical measurements only has been difficult because of the position of the solar system within the Galaxy. In this context, it was very important the observation of distant galaxies, which revealed large-scale structures that were not visible in our Galaxy, due to light absorption by interstellar dust. Only around 1930 it became unmistakably clear that the Galaxy is similar to objects at that time called *spiral nebulae*.

The recent images of the Galaxy using observations at different wavelengths show that it is basically a disk with a central bulge surrounded by a halo of globular clusters. It is convenient to distinguish two components: a *spheroidal* and a *disk* structure. Both contain stellar populations and other material with very different characteristics. These two components have different chemical compositions, kinematic and dynamic properties and a diverse evolutionary history.

Distances and sizes are usually expressed by astronomers in *parsec* (symbol: *pc*). One parsec corresponds to about 3.26 light-years or to

$$1 \text{ pc} = 3.086 \times 10^{18} \text{ cm} \quad (2.21)$$

The spheroidal component has a very massive nucleus (smaller than 3 pc of radius) with a *black hole* at its center, with mass  $2 \times 10^6 M_{\odot}$ ,<sup>6</sup> a bulge with radius of  $\sim 3$  kpc and an extended halo of about 30 kpc. These three regions are approximately concentric. The disk is very thin ( $\sim 200$ – $300$  pc thick) and a radius of about 15 kpc. The Sun is about 8.5 kpc from the center.

<sup>6</sup> The subscript  $\odot$  conventionally represents the Sun and  $\oplus$  the Earth.

The galactic volume, assuming a flat disk having a radius of  $\sim 15$  kpc and a thickness of  $\sim 300$  pc, corresponds to:

$$\mathcal{V}_G = [\pi(15 \times 10^3)^2 \times 300] \times (3 \times 10^{18})^3 = 5 \times 10^{66} \text{ cm}^3 \quad (2.22)$$

The volume of the galactic halo is more than an order of magnitude larger.

Stars and globular clusters are the characteristic components of the spherical region, where gas and dust are relatively scarce. Spectroscopy indicates that the stars in the spheroid component are *metal-poor*<sup>7</sup> (stars of population II). Metal-poor stars consist of material that has not undergone much recycling through previous generations of stars, are very old and represent the typical population of globular clusters.

The disk is instead characterized by the presence of large amounts of dust and gas, which give rise to absorption of the interstellar radiation, and by young and metal-rich stars (Population I). These stars may be distributed more or less uniformly, or grouped in stellar associations along the spiral arms. These considerations suggest that the disk is made entirely of materials already processed in previous generations of stars. This situation is analogous to that observed in other spiral galaxies.

An estimate of the total number of stars in the Galaxy is about  $10^{10}$ .

Important information on the Galaxy have become available after the advent of radio astronomy. At low frequencies (150 MHz) the emission from the Galaxy shows a maximum of intensity along the galactic plane. The emission decreases steadily with increasing galactic latitude  $b$ ,<sup>8</sup> covering the whole sky. The diffused radio emission is usually described in terms of two distinct structures: (i) a disk (which coincides with the optical disk) with an angular aperture of about  $\pm 5^\circ$  in galactic latitude  $b$ ; (ii) an ellipsoidal shaped halo which extends at high galactic latitudes and up to the poles. From the study of the emission spectrum, it can be inferred that the diffuse radiation is composed of a nonthermal component and a thermal one from the disk. The nonthermal component is due to synchrotron radiation of electrons moving in the galactic magnetic field. The luminosity<sup>9</sup> of the component from the disk, integrated over the whole radio band, is equal to:

$$\mathcal{L} \sim 10^{38} \text{ erg/s} . \quad (2.23)$$

The luminosity from the emission of the halo is subject to greater uncertainty, but corresponds (within a factor of 2) to that of the disk.

Superimposed to the thermal emission, discrete radio sources are observed. They are divided in two populations: (1) objects of large angular size, concentrated along

<sup>7</sup> In the language of astronomers, all elements heavier than He are often called metals.

<sup>8</sup> See *Extras # 2* for the astronomical coordinate systems.

<sup>9</sup> In astronomy, the luminosity measures the total amount of energy emitted by a star or other astronomical object per unit time over the whole electromagnetic spectrum or a defined part of it.

the galactic plane; they are supernova remnants, surrounded by regions with a high concentration of ionized hydrogen. (2) radio sources of small angular diameter isotropically distributed and attributed to extragalactic objects. In both cases, the spectrum of the radiation is that typical of synchrotron emission.

### 2.7.1 The Galactic Magnetic Field

The presence of a magnetic field inside the Galaxy was discovered (1949) when it was realized that the observed light from the stars has a high degree of polarization. This polarization is correlated with the attenuation of starlight due to the presence of dust (Brown 2010).

Precise information on the galactic magnetic field comes from radio astronomy. Radio telescopes can measure the Faraday rotation angle and the extent of dispersion of the radiation emitted by pulsars and the Zeeman effect on the 21 cm line of neutral hydrogen.

The Faraday rotation effect is based on the fact that the plane of polarization of linearly polarized electromagnetic waves rotates when they propagate in the presence of a magnetic field  $B$  in a medium with electron density  $n_e$  [ $\text{cm}^{-3}$ ]. The rotation depends on the square of the wavelength  $\lambda$ , and on the parallel component of the magnetic field  $B_{\parallel}$  along the line of sight to the source:

$$\text{RM} = \int_0^L B_{\parallel} n_e dr \quad (2.24)$$

where  $L$  is the distance traveled by the radiation. By measuring the variation of the angle of polarization as a function of the wavelength  $\lambda$  from radio pulsars, RM can be estimated. From independent estimates of  $n_e$  and  $L$ , the value of  $B$  in the traversed region can be deduced.

Different estimates exist on the average intensity of the regular galactic magnetic field, which depends on the distance from the galactic center (Fig. 2.9). We assume approximately:

$$B \simeq 4 \mu\text{G} \quad (2.25)$$

The galactic field is oriented mainly parallel to the plane, with a small vertical component along the  $z$ -axis ( $B_z \sim 0.2\text{--}0.3 \mu\text{G}$  in the vicinity of the Sun).

The models of the large-scale structure of the galactic magnetic field provide a regular distribution of the  $\mathbf{B}$  lines that follows the distribution of matter, i.e. a spiral shape (Stanev 2010). The spatial extension of regions in which the magnetic field is coherent is of the order of 1–10 pc. Figure 2.10 shows the direction and strength of the regular magnetic field in the galactic plane. The large-scale structure of the galactic



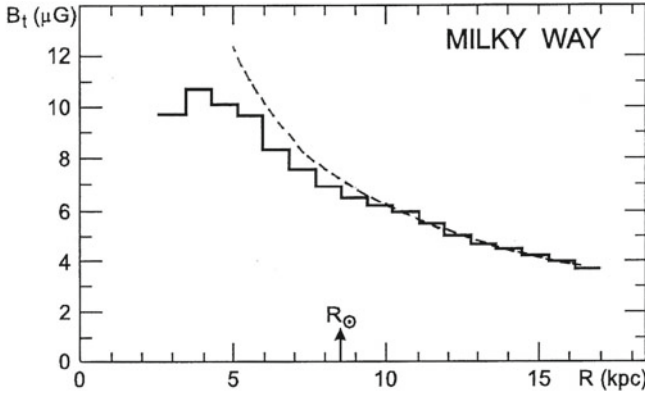
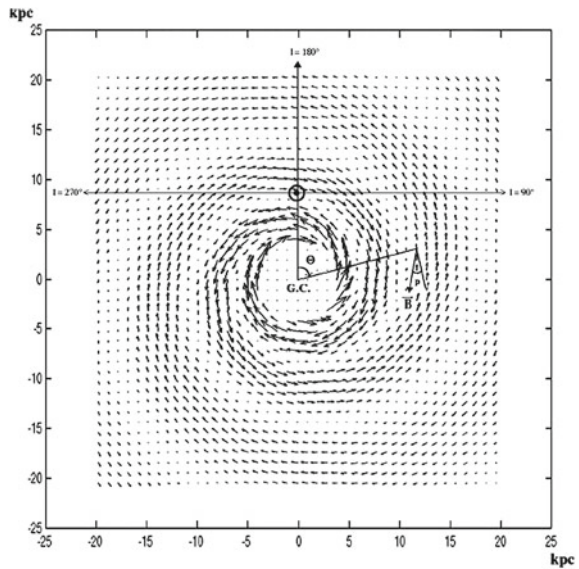


**Fig. 2.9** Total magnetic field strength in the Galaxy as a function of the distance from the galactic center. The position of the Sun is indicated by the arrow (Battaner et al. 2007). Courtesy of Prof. E. Battaner

**Fig. 2.10** The direction and strength of the regular magnetic field in the Galactic plane is represented by the length and direction of the arrows. The intensity of the field inside the circle of radius 4 kpc representing the bulge is assumed to be  $6.4 \mu\text{G}$  (Prouza and Smída 2003). Courtesy Dr. M. Prouza and Dr. R. Smída



magnetic field strongly influences the motion of charged particles. An example of this influence on charged particles with three different energies is visible in Fig. 7.3.

An **important problem**, which is far from being solved, is the **galactic magnetic halo**, i.e., the extension of the magnetic field above and below the galactic plane. Recent measurements indicate an extended halo that can contribute significantly to the cosmic ray confinement.

As **the Galaxy** is filled with **a magnetic field** whose **average intensity** is  $B \sim 4 \mu\text{G}$ , we obtain using (2.5) the following Larmor radii for protons at different energies:



$$\begin{aligned}
 r_L(E = 10^{12} \text{ eV}) &\simeq 10^{15} \text{ cm} = 3 \times 10^{-4} \text{ pc} \\
 r_L(E = 10^{15} \text{ eV}) &\simeq 10^{18} \text{ cm} = 0.3 \text{ pc} \\
 r_L(E = 10^{18} \text{ eV}) &\simeq 10^{21} \text{ cm} = 300 \text{ pc}
 \end{aligned}
 \tag{2.26}$$

These values of  $r_L$  should be compared with the Galaxy dimensions. Particles below  $10^{18}$  eV are strongly constrained inside the galactic volume by the galactic magnetic field.

### 2.7.2 The Interstellar Matter Distribution

In outlying regions of the Galaxy, the ratio of the distance between stars and their diameter is of the order of  $\sim 1$  pc: ( $10^6$  km)  $\simeq 3 \times 10^7$ . Thus only a small fraction of the space ( $\sim 4 \times 10^{-23}$ ) is occupied by matter in the form of stars. The rest is filled with large masses of gas (molecules, atoms, ions) and tiny solid particles, the interstellar dust. Dusts are made up of ice grains of various species, graphite, silicates and perhaps metals. The gas is revealed by the presence of absorption and emission lines, both in the optical and in radio. Dusts are observed only as large dark clouds obscuring the view of the stars behind, or in reflection nebulae which shine for the presence of nearby stars. Another tracer of the presence of dust is the infrared emission in the vicinity of very hot stars.

As a whole, this gas and dust is called *InterStellar Matter (ISM)*. It represents 5–10% of the total mass of the Galaxy. The average density of this medium is (Ferriere 2001)

$$n_{\text{ISM}} \sim 1 \text{ proton/cm}^3 = 1.6 \times 10^{-24} \text{ g/cm}^3 \tag{2.27}$$

It is hard to detect the ISM in the visible range of the electromagnetic radiation, and it has been studied mostly using radio-astronomy techniques. Most of the ISM is made of neutral (HI) and molecular ( $\text{H}_2$ ) hydrogen.

Neutral hydrogen is the main component of the ISM, with an average density of approximately  $0.4 \text{ atoms/cm}^3$ . The presence of HI is revealed in the radio band through the 21 cm line. The line was measured in emission mainly along the galactic plane, and with smaller intensity at all galactic latitudes. The linear dimension of the regions in which neutral hydrogen is present is of the order of 100–150 pc.

The emission is due to the fact that the ground state of the hydrogen atom consists of two hyperfine levels. They correspond to configurations with spin of the proton and electron parallel (higher level) and antiparallel (lower level). The emission is due to the transition between levels, whose energy difference corresponds to an electromagnetic emission with frequency  $\nu_H = 1,420.40575 \text{ MHz}$ , or  $\lambda_H = 21.1049 \text{ cm}$ . In thermodynamic equilibrium, the population of each level depends on its energy according to the Boltzmann law. The transition between the two levels has a lifetime  $\tau \sim 1.1 \times 10^7 \text{ y}$ . Although this corresponds to a very low transition probability, there is such a large quantity of hydrogen in the Galaxy that the line is clearly detectable.

In addition to the emission, the line can also be seen in *absorption* when a cloud of hydrogen is located on the line of sight between the observer and a radio source that emits a continuous spectrum.

About 1% of interstellar hydrogen is ionized (HII). It is generally found in the form of clouds with a density that exceeds  $10 \text{ atoms/cm}^3$ . The ionization is due to the presence of very hot stars that emit photons of energy larger than the ionization energy of hydrogen (13.6 eV). The HII emission is due to *free-free* (or *thermal bremsstrahlung*) transitions, which produces a continuous spectrum.

Radio telescopes have revealed the presence in the ISM of the characteristic lines of many molecules. Molecules emit through their vibrational modes. For example, the simple OH molecule can rotate with respect to the axis that joins the two nuclei, or around an axis perpendicular to it. The vibrational modes of the molecules are quantized, and this allows the identification of the molecules themselves.

About 50% of the mass of the interstellar medium is in molecular form, and most of this seems to be  $\text{H}_2$ . Unfortunately, the  $\text{H}_2$  molecule has no rotational energy levels in the radio band, and the estimates of its presence in the Galaxy are rather uncertain. A large fraction is gathered in clouds, both compact and diffuse, with dimensions that reach 50 pc, and with high densities (up to  $10^{10} \text{ molecules/cm}^3$ ). The temperatures of these clouds can reach up to thousands of degrees. These clouds correspond to the star forming regions.

In addition to the  $\text{H}_2$  molecule, almost a hundred different molecules and molecular radicals were identified in the ISM. The more complex molecular systems have up to 13 atoms. Most of the complex molecules are organic. None of the inorganic molecules (except the ammonia,  $\text{NH}_3$ ) contain more than three atoms. Apparently, as on Earth, the bond with carbon is the key for the formation of complex molecules!

One of the most interesting molecules detectable in the radio is the CO, which is the most abundant molecule after  $\text{H}_2$ . It has three emission lines (with  $\lambda$  between 1 and 3 mm). The CO is a tracer for molecular hydrogen, because its main excitation source is due precisely to collisions with the  $\text{H}_2$  molecule.

## 2.8 Low-Energy Cosmic Rays from the Sun

The Sun is the main source of CRs of energy below  $\sim 4 \text{ GeV}$ . Episodic solar activities and the corresponding increase of the low-energy CR flux have a number of effects that are of practical interest. A radiation dose from energetic particles is an occasional hazard for astronauts and for electronics on satellites.<sup>10</sup> Such disturbances

<sup>10</sup> I was always fascinated by “2001: A Space Odyssey”, a science fiction film produced and directed in 1968 by Stanley Kubrick. A space voyage to Jupiter tracing a signal emitted by an unknown object (a monolith) was organized with a spaceship. Most of spaceship’ operations are controlled by a computer on board, HAL 9000 (or simply “Hal”, as Hal interacts and speaks with the human crew), and double-checked by a twin computer on Earth. Hal states that he is “foolproof and incapable of error”. The main problem arises when Hal foresees an imminent failure on a device. The twin computer on Earth is of the contrary advice. Humans on board of the spaceship discover that Hal is

may damage power systems, disrupt communications, degrade high-tech navigation systems, or create the spectacular aurora.

Cosmic rays originated from the Sun were first observed in the early 1940s. They consist of protons, electrons, and heavy ions with energy ranging from a few tens of keV to few GeV. They are originated mainly by solar flares.

A solar flare is a sudden brightening observed over the Sun's surface, which is interpreted as a large energy release. Flares occur in active regions around sunspots, where intense magnetic fields penetrate the photosphere to link the corona to the solar interior.

The Sun activity influences also the probability that CRs with energy below few GeV reach the Earth. When CRs enter our solar system, they must overcome the outward-flowing solar wind. This wind is a stream of charged particles continuously released from the upper atmosphere of the Sun and it consists mostly of electrons and protons with energies usually between 1.5 and 10 keV.

The flux of galactic CR nuclei with energies below  $\sim 1$  GeV/nucleon is strongly modulated by their interaction with the magnetic field carried by the expanding solar wind. The expanding magnetized plasma generated by the Sun decelerates and partially excludes the lower energy particles from the inner solar system. Consequently the low-energy component of the CR flux undergoes a sizable variation over the solar cycle. This effect is known as solar modulation.

The magnetic activity and the solar modulations are manifested through sunspots, which have a 11 year cycle. Most solar flares and coronal mass ejections originate in magnetically active regions around visible sunspot groupings. It should be noted that the earliest surviving record of sunspot observation dates from 364 BC, based on comments by Chinese astronomers (Early Astronomy and the Beginnings of a Mathematical Science, University of Cambridge, NRICH, 2007, <http://rich.maths.org/6843>). From 28 BC, sunspot observations were regularly recorded by Chinese astronomers in official imperial records.

The intensity of low-energy CRs at Earth is measured through ground-based detectors called neutron monitors. Their measurements are anti-correlated with the level of solar activity, i.e., when solar activity is high many sunspots are visible, the CR intensity at Earth is low, and vice versa. Neutron monitors are designed to measure neutrons produced by the interactions of CRs with the atmospheric nuclei. If the primary CR that started the cascade has energy over  $\sim 500$  MeV, some of its secondary by-products (including neutrons) will reach ground level. Figure. 2.11 shows the correlation between the number of observed sunspots (which measure the phase of the 11 y solar activity) and the number of neutrons detected at ground.

---

(Footnote 10 continued)

really wrong. They decide to disconnect it and to assign the spaceship operations to the computer on Earth. This decision induces a fight between humans and Hal. We are interested on the reason why there is a discrepancy between the prevision of the failure carried out by Hal and by the twin computer on Earth. The only plausible reason is the fact that the processor units of the Hal on board of the spaceship were damaged by cosmic rays. Although it is a science fiction movie, it fully grasped one of the main problems for long time permanence of humans in space. Computer failures can be prevented by increasing the number of units. This solution cannot be adopted for humans.

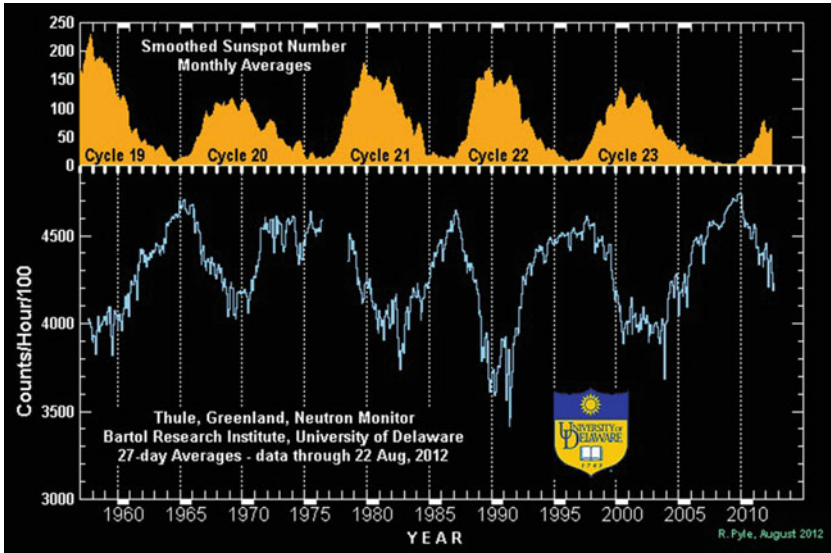


Fig. 2.11 The solar modulation cycle (<http://www.bartol.udel.edu/gp/neutron/>). The rate of the neutron monitor is updated monthly), which correlate the sunspot number (on the top) with the neutron rate measured at the McMurdo station (bottom of the figure). Credit the Bartol Research Institute

The correlation of the CR flux for energies below few GeV with the solar phase is clearly visible in Fig. 2.12. Here, the flux of protons as measured by the PAMELA experiment (Sect. 3.4.2) in four different years is shown (Adriani 2013). A higher proton flux at energies below few GeV is evident during 2009, when the number of monthly sunspots in Fig. 2.11 was almost zero.

## 2.9 The Effect of the Geomagnetic Field

To reach the top of the atmosphere, particles and nuclei below the GeV range are guided by the Earth dipolar magnetic field. Thus the intensity of any low-energy component of the cosmic radiation depends both on the location and time.

For certain magnetic field configurations, there exist regions of space for which the arrival of particles below a certain energy threshold is forbidden. These regions of space are said to be shielded from such particles. Using the concept of a magnetic potential barrier, Störmer showed first (around the 1920s) the existence of a shielded region for the Earth dipole magnetic field configuration. A simple condition which is necessary for a particle to reach the Earth atmosphere is that all trajectories starting from the point considered on Earth (after reversing the charge of the particle) reach  $r = \infty$ . At low enough energies, this condition may be violated, because trajectories

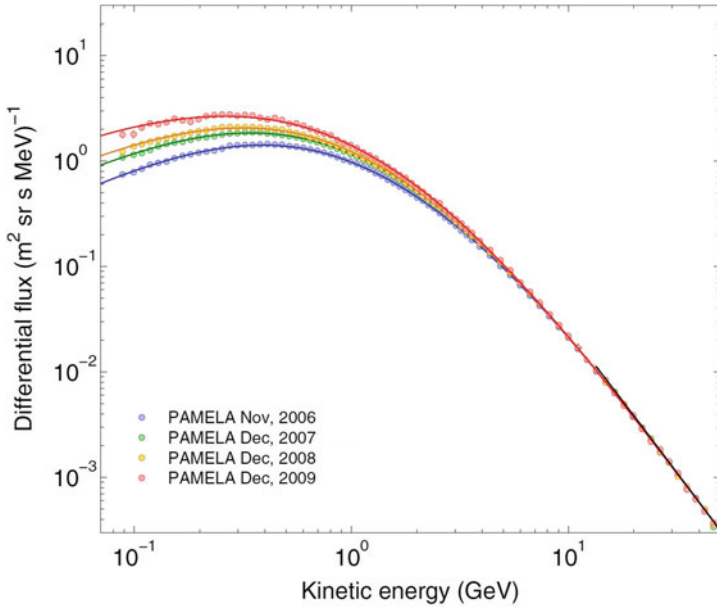


**Fig. 2.12** The yearly proton energy spectrum measured by the PAMELA experiment (Sect. 3.4.2) from the beginning of the space mission in mid of 2006 till end of 2009. Compare the phase of the solar activity with Fig. 2.11. The variation of the solar activity does not affect CRs with energy larger than few GeV. Courtesy of the PAMELA collaboration

can be deflected back to the Earth or stay within a finite distance. In this case, the magnetic field does induce anisotropies in the observed flux.

Consider a particle of charge  $Ze$  with orbit in the equatorial plane of the dipole-like Earth magnetic field. Equating the centrifugal and the Lorentz force gives (note that we express the following equations in the I.S. units):

$$\frac{mv^2}{r} = Ze|\mathbf{v} \times \mathbf{B}| \tag{2.28}$$

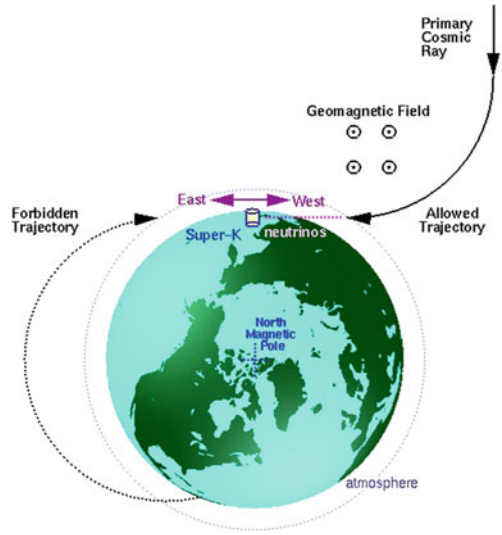
The Earth magnetic field is induced by the Earth magnetic moment  $\mathcal{M}$ :

$$\mathbf{B} = \frac{\mu_0 \mathcal{M}}{4\pi r^3} \tag{2.29}$$

At the surface ( $r = R_{\oplus} = 6.38 \times 10^6 \text{ m}$ ) the measured value is  $B = 0.307 \times 10^{-4} \text{ T}$ , therefore  $\mathcal{M} = 7.94 \times 10^{22} \text{ Am}^2$ . It is easy work out from (2.28) and (2.29) the radius of the orbit:

$$r = \left( \frac{\mu_0 Ze \mathcal{M}}{4\pi p} \right)^{1/2} \tag{2.30}$$

**Fig. 2.13** Primary CRs with energy below  $\sim 60$  GeV are influenced by the Earth magnetic field. In particular, low-energy cosmic rays from the East are suppressed compared to those from the West. The Earth itself effectively shadows certain trajectories, which are therefore forbidden (Futagami et al. 1999). This East-West effect was first detected in the 1930s and was used to infer that the charge sign of the primary cosmic rays is positive. Courtesy of Prof. E. Kearns



where  $p$  is the particle momentum. Using the numerical values for  $r = R_{\oplus}$ :

$$\frac{p}{Ze} = \frac{\mu_0 \mathcal{M}}{4\pi R_{\oplus}^2} \sim 59.6 \text{ GV}. \tag{2.31}$$

This value corresponds to the minimum rigidity for a particle to be able to reach the Earth from the East, if its orbit is exactly in the (magnetic) equatorial plane (see Fig. 2.13). In fact, the radius of curvature of the trajectory labeled as *forbidden trajectory* does not reach  $\infty$  starting from ground. Toward the poles, the influence of the dipole field becomes weaker (as the arriving particle velocity is almost parallel to  $\mathbf{B}$ ), and the cutoff rigidity (2.31) becomes smaller. The integrated CR intensity increases with the latitude for charged particles (*latitude effect*). This is exactly the property measured by Compton in 1932 which demonstrated that CRs are positively charged (as we mentioned in Sect. 2.1). The East-West effect influences also the production of low-energy atmospheric neutrinos detected in underground experiments (Chap. 11).

The Earth dipole-like magnetic field induces also another relevant effect known as the *Van Allen radiation belts* (named after its discoverer, J. Van Allen). They are two torus-shaped layers of energetic charged particles around the Earth, located in the inner region of the magnetosphere, and held in place by the magnetic field, Fig. 2.14. The belt extends from an altitude of about 1,000–60,000 km above the surface. The outer belt consists mainly of energetic electrons, while the inner belt is formed by a combination of protons and electrons. The belts pose a hazard to satellites, which must protect their sensitive components with adequate shielding if their orbit spends a significant time inside the radiation belts.

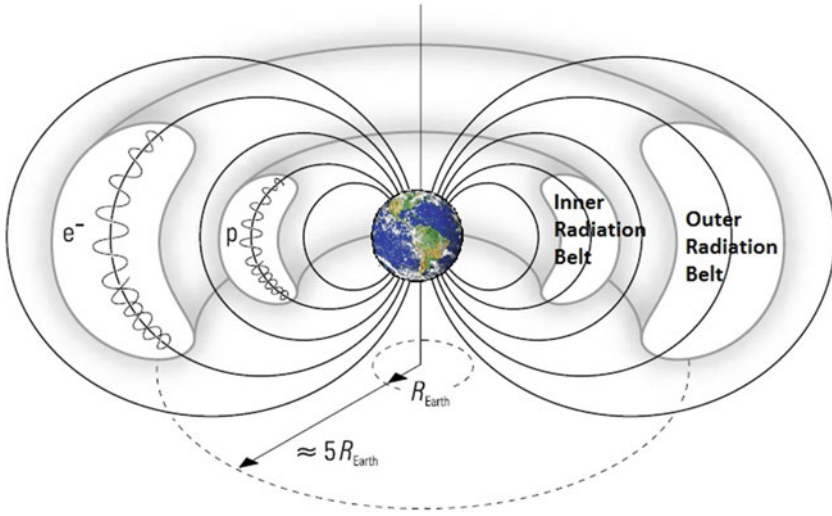


Fig. 2.14 Sketch of the van Allen radiation belts

### 2.10 Number and Energy Density of the Cosmic Rays

After this long journey in the environment in which CR propagate, let us now evaluate the **number density of CRs**, according to the definition (2.18a) for  $v \simeq c$ . We use the experimental flux as parameterized in (2.20b):

$$n_{CR} = \frac{4\pi}{c} \Phi(>E_0) = \frac{4\pi \cdot K / (\alpha - 1)}{3 \times 10^{10}} \cdot E_0^{-\gamma} \tag{2.32a}$$

The **numerical value depends** on the **threshold energy  $E_0$** . We **assume** that the **parameterization (2.20a)** holds down to  $E_0 \simeq 3 \text{ GeV}$  where (somewhat **arbitrarily**) we **put the threshold for the solar wind's contribution**. This is confirmed also from Fig. 2.12 which shows no dependence on solar modulations for energies larger than this threshold. **Using the values of (2.20c) and  $E_0 = 3 \text{ GeV}$ :**

$$n_{CR} \simeq 1 \times 10^{-10} \text{ cm}^{-3} \tag{2.32b}$$

A second important quantity is the **kinetic energy density** (or, simply, the **energy density**) of CRs. It can be obtained by the integration of (2.13) assuming the flux given by (2.20a):



$$\begin{aligned} \rho_{\text{CR}} &\equiv \frac{1}{c} \int_{E_0}^{\infty} E \frac{d^2\varphi}{dE d\Omega} dE d\Omega \quad [\text{GeV cm}^{-3}] \\ &= \frac{4\pi}{c} \int_{E_0}^{\infty} 3.01 E^{-\alpha+1} dE = \frac{4\pi}{c} \left[ \frac{3.01}{\alpha-2} E^{-\alpha+2} \right]_{E_0}^{\infty} \end{aligned} \quad (2.33a)$$

The numerical value depends on the threshold energy  $E_0$ . As above using  $E_0 = 3$  GeV we obtain:

$$\rho_{\text{CR}} \simeq 1 \text{ eV/cm}^3. \quad (2.33b)$$

We need to compare (2.32b) and (2.33b) with some other astrophysical quantities, in order to understand if they represent “small” or “large” quantities. The number density (2.32b) of CRs can be compared with the average number density of the interstellar matter (2.27). Thus, only about one proton out of  $\sim 10^{10}$  not bound in stars in the Galaxy is a relativistic particle, i.e. a cosmic ray.

Concerning the energy density (2.33a), let us consider the following astrophysical quantities.

**The energy density of the interstellar magnetic field.** To any magnetic field region is associated a corresponding energy density that in the Gauss system corresponds to:

$$\rho_B = \frac{1}{8\pi} B^2 \text{ erg/cm}^3 \quad (2.34)$$

(the relation in the I.S. is  $1/(2\mu_0)B^2 \text{ J/m}^3$ ). Using the numerical values for the average interstellar magnetic field ( $B \sim 4 \mu\text{G}$ ) we obtain:

$$\rho_B = \frac{(4 \times 10^{-6})^2}{8\pi} = 6 \times 10^{-13} \text{ erg/cm}^3 \simeq 1 \text{ eV/cm}^3 \quad (2.35)$$

The coincidence within a small factor between (2.33b) and (2.35) suggests a connection between galactic magnetic field and CRs.

**The starlight density.** From photometric measurements of the light coming from galactic stars, astronomers have evaluated the visible photon density:

$$n_{\gamma_{\text{vis}}} \simeq 2 \times 10^{-2} \text{ cm}^{-3} \quad \Rightarrow \quad \rho_{\gamma_{\text{vis}}} \simeq 4 \times 10^{-2} \text{ eV/cm}^3 \quad (2.36)$$

assuming 2 eV/photon for the visible light. This is a much smaller value than (2.33b)

**The density of the Cosmic Microwave Background Radiation.** The CMB radiation is the thermal radiation filling almost uniformly the observable Universe. A precise measurement of CMB radiation is extremely important to cosmology, since any proposed model of the Universe must explain this radiation. The CMB radiation has a thermal black body spectrum at a temperature of 2.725 K (Fixsen 2009),



which corresponds to an energy of  $E_{\text{CMB}} \sim 3kT = 7 \times 10^{-4} \text{ eV}$ , where  $k = 8.61 \times 10^{-5} \text{ eV K}^{-1}$  is the Boltzmann constant. Using the measured number density of the CMB radiation:

$$n_{\gamma\text{CMB}} \sim 400 \text{ cm}^{-3} \quad \Rightarrow \quad \rho_{\gamma\text{CMB}} \sim 0.3 \text{ eV/cm}^{-3}. \quad (2.37)$$

In this particular case, in spite of the similarity between (2.33b) and (2.37), there is no argued connection between the two phenomena.

## 2.11 Energy Considerations on Cosmic Ray Sources

Supernova remnants are energetically suitable candidates for the acceleration of CRs with energy below the knee. The main motivation is the equilibrium (firstly hypothesized by Baade and Zwicky in 1934) between the loss of CRs due to their escape out of the galactic volume and the energy provided by supernova shock waves.

The Galaxy is uniformly filled with the relativistic radiation we detect on Earth. The CR sources are uniformly distributed in the Galaxy and the CRs are trapped by the galactic magnetic fields. According to the present observations, the total kinetic energy of CRs corresponds to:

$$\rho_{\text{CR}} \times \mathcal{V}_G = 8 \cdot 10^{54} \text{ erg}. \quad (2.38)$$

where the energy density  $\rho_{\text{CR}}$  is given in (2.33b) and the galactic volume ( $\mathcal{V}_G \sim 5 \times 10^{66} \text{ cm}^3$ ) in (2.22). If the particles are completely confined inside the galactic volume, this number should increase with time in the presence of new galactic core-collapse supernova explosions. This process that represents the candidate injection mechanism for galactic CRs have started very long time ago, as discussed in Chap. 6. Each supernova burst contribute to increase the galactic CR density  $\rho_{\text{CR}}$ . A competitive effect which induces a decrease of  $\rho_{\text{CR}}$  is due to the escape of CRs out of the Galaxy with a characteristic escape time (or confinement time)  $\tau_{\text{esc}}$ . This quantity corresponds to the average time needed for a CR, trapped by the galactic magnetic field, to reach the galactic boundary. From here, the particle can freely escape, because the magnetic field outside the galactic plane is negligible.

Anticipating the results which we derive in Sect. 5.2, the confinement time is  $\tau_{\text{esc}} \simeq 10^7 \text{ y} = 3 \times 10^{14} \text{ s}$ . Assuming an almost steady value of the energy density  $\rho_{\text{CR}}$ , the energy loss rate due to the escape of CR out of the galactic volume is:

$$P_{\text{CR}} \simeq \frac{\rho_{\text{CR}} \times \mathcal{V}_G}{\tau_{\text{esc}}} = \frac{8 \cdot 10^{54}}{3 \cdot 10^{14}} = 3 \times 10^{40} \text{ erg/s}. \quad (2.39)$$

Thus, the power required by cosmic accelerators to replenish the galactic volume corresponds to  $P_{\text{CR}}$ .

This number has a large uncertainty. The assumption of  $\rho_{\text{CR}} \sim \text{const}$  for a time scale  $\gg \tau_{\text{esc}}$  is completely reasonable from the astrophysical point of view. It is not expected a large variation in the supernova rate in the last, say, billion years. Another uncertainty arises from the galactic volume, which is bigger if the magnetic halo is considered. As this magnetic field is poorly known, a galactic volume about  $10\% V_G$  could be considered. In this case, the matter density in this extended volume is a factor of  $\sim 3$  smaller. Compressively, the quantity estimated in (2.39) could be a factor of three larger, and  $P_{\text{CR}} \simeq 10^{41}$  erg/s. Are these powers energetically compatible with the energy released by supernova explosions?

A supernova explosion of 10 solar masses ( $10 M_\odot$ ) releases about  $10^{53}$  erg, 99% in form of neutrinos (Sect. 12.10) and 1% in form of kinetic energy of expanding particles (shock wave). The supernova rate  $f_{\text{SN}}$  in a galaxy like our own is about 3 per century ( $f_{\text{SN}} \sim 10^{-9} \text{ s}^{-1}$ ). If a physical process able to accelerate charged particles exists, it transfers energy from the kinetic energy of the shock wave to CRs with an efficiency  $\eta$ :

$$P_{\text{SN}} \simeq \eta \times f_{\text{SN}} \times 10^{51} = \eta \times 10^{42} \text{ erg/s.} \quad (2.40)$$

By requiring that  $P_{\text{CR}} = P_{\text{SN}}$ , the quantity  $\eta$  must be of the order of a few percent. In this case, the shock waves from supernova explosions are able to refurbish the Galaxy with new accelerated particles and maintain the stationary energy content of CRs. This condition makes the supernova model energetically compatible with the observations. A transfer mechanism with efficiency of few % is known and it will be described in Sect. 6.2. With a rate of about three supernovae per century in a typical Galaxy, the energy required could be provided by a small fraction ( $\sim 5\text{--}10\%$ ) of the kinetic energy released by supernova explosions.

## References

- O. Adriani et al., Time dependence of the proton flux measured by PAMELA during the 2006 July-2009 December solar minimum. *Astrophys. J.* **765**, 91 (2013)
- C. Anderson, The positive electron. *Phys. Rev.* **43**, 491 (1933)
- P. Auger et al., Extensive cosmic-ray showers. *Rev. Mod. Phys.* **11**, 288–291 (1939)
- W. Baade, F. Zwicky, Remarks on Super-Novae and cosmic rays. *Phys. Rev.* **46**, 76 (1934)
- E. Battaner et al., Magnetic fields in galaxies, in lecture notes and essays in astrophysics. III Astrophysics Symposium (2007), <http://www.slac.stanford.edu/econf/C07091016/>
- J. Beringer et al. (Particle Data Group), The review of particle physics. *Phys. Rev. D* **86**, 010001 (2012). <http://pdg.lbl.gov/>
- S. Braibant, G. Giacomelli, M. Spurio, *Particle and Fundamental Interactions* (Springer, Berlin, 2011). ISBN 978-9400724631
- J.C. Brown, The magnetic field of the milky way galaxy (2010), [arXiv:1012.2932v1](https://arxiv.org/abs/1012.2932v1)
- P. Carlson, A. De Angelis, Nationalism and internationalism in science: the case of the discovery of cosmic rays. *Eur. Phys. J. H* **35**, 309–329 (2010)
- K. Ferriere, The interstellar environment of our galaxy. *Rev. Mod. Phys.* **73**, 1031–1066 (2001)

- D.J. Fixsen, The temperature of the cosmic microwave background. *Astrophys. J.* **707**(2), 916–920 (2009), doi:[10.1088/0004-637X/707/2/916](https://doi.org/10.1088/0004-637X/707/2/916)
- T. Futagami et al. (The SK Collab.), Observation of the East-West anisotropy of the atmospheric, neutrino flux. *Phys. Rev. Lett.* **82**, 5194–5197 (1999). <http://hep.bu.edu/superk/ew-effect.html>
- J.R. Hörandel, On the knee in the energy spectrum of cosmic rays. *Astropart. Phys.* **19**, 193–220 (2003)
- J. Linsley, Evidence for a primary cosmic-ray particle with energy  $10^{20}$  eV. *Phys. Rev. Lett.* **10**, 146 (1962)
- D. Pacini, La radiazione penetrante alla superficie ed in seno alle acque. *Nuovo Cimento VI/3* (1912) 93. Translated and commented by Alessandro De Angelis: Penetrating radiation at the surface of and in water. [arXiv:1002.1810](https://arxiv.org/abs/1002.1810)
- M. Prouza, R. Smída, The galactic magnetic field and propagation of ultra-high energy cosmic rays. *Astron. Astrophys.* **410**, 1–10 (2003)
- M. Schein, W.P. Jesse, E.O. Wollan, The nature of the primary cosmic radiation and the origin of the mesotron. *Phys. Rev.* **59**, 615–633 (1941)
- T. Stanev, *High Energy Cosmic Rays* (Springer Praxis Books, 2010). ISBN 9783540851486
- B. Wiebel-Sooth, P.L. Biermann, H. Meyer, Cosmic rays. VII. individual element spectra: prediction and data. *Astron. Astrophys.* **330**, 389–398 (1998)

## Chapter 3

# Direct Cosmic Rays Detection: Protons, Nuclei, Electrons and Antimatter

The **relative percentage** of protons and heavier nuclei in the cosmic radiation is usually referred as the **chemical composition of CRs**. A **detailed knowledge** of the chemical composition up to the highest energies is of **crucial importance** for the **understanding** of astrophysical **sources** of CRs and their **propagation** in the Galaxy. The **chemical composition of CRs** can be accurately **measured** through **experiments** carried at a negligible residual atmospheric depth or **outside the atmosphere**. When arriving at the top of the atmosphere, primary CRs start to interact with nuclei of air molecules, producing a cascade of secondary particles. **Primary nuclei** undergo **fragmentation** processes and the **information** about their **mass** cannot easily be derived from the **indirect measurements** that are the subject of the next chapter.

In this chapter, we deal about the **techniques**, Sects. 3.1, 3.2, and the **experimental results** of **direct measurements** performed with **balloons** (Sect. 3.3) and **space missions** (Sect. 3.4). They **measured** accurately the **flux** and the **chemical composition** of CRs up to  $\sim 100$  TeV (Sects. 3.6, 3.7), allowing the formulation of models about their galactic origin and propagation. One of the features predicted by the **standard model of CR acceleration** is that the **CR spectra** are well described by **power laws**, with **similar spectral indices** for **protons** and **heavier nuclei**, up to energies of  $\sim 10^{15}$  eV. The **CR sources** are thought to be **concentrated near the galactic disk**, with a **radial distribution** similar to that of supernova remnants. The **propagation of CRs** in the Galaxy is usually studied with a **diffusion differential equation**. The theoretical models of CR acceleration and propagation in the interstellar medium presented in the following chapters are based on the data described here.

Measurements from **early space-borne experiments** refer mostly to energies **lower than 1 GeV**. They provided relevant information concerning the energy part of CRs affected by the **dependence of the Sun activity**. Important information on the **energy spectra** of **protons**, **helium**, and **heavier nuclei** arise from the **PAMELA satellite**, launched in 2006. Even more important are the physical outputs of the **AMS-02 experiment**, launched in 2011 with the Space Shuttle and taking data on the **International Space Station (ISS)**. AMS-02 (Sect. 3.5) represents the **most sophisticated particle detector ever sent into space**, incorporating all the **characteristics of the very large detectors** used at large **particle accelerators**. AMS-02 is providing fundamental

and detailed information concerning the **chemical composition** of the cosmic radiation and the presence of primary antiparticles.

An important **feature of the new experiments**, including PAMELA and AMS-02, is the presence of **magnetic spectrometers** which enable the **search for antiparticles and antimatter in space**. Experimental evidence indicates that **our Galaxy is made of matter**. Antiparticles can be **created as secondary particles by CRs interactions with the interstellar medium** in our Galaxy. **Whether or not there is significant amount of primary antimatter** is one of the **fundamental questions** of the origin and nature of the Universe. For instance, the **observation of only one antihelium nucleus** would provide **evidence** for the **existence of antimatter in space**. At present, **searches for  $\bar{p}$  and heavier antinuclei** (Sect. 3.8) give **no indication of primary sources of antimatter** in our Galaxy. On the contrary, the **measurements of electrons and positrons**, Sect. 3.9, show **unexpected features**. In particular, an **excess of positrons** with respect to the expectation from secondary production **reported with large statistical significance** from PAMELA and AMS-02, has opened theoretical **scenarios** about the possible **origin from dark matter annihilations**. This scenario will be discussed in Chap. 13.

### 3.1 Generalities on Direct Measurements

In the **low energy region, up to** about **1 GeV/n**, detectors on **satellites** can identify **individual CRs**. In **some case** (as described in Sect. 3.4.1) **different isotopes** of the same element can be **separated**, fully characterized by **simultaneous measurements** of their **energy, charge, and mass ( $E, Z, A$ )**. The **charge** and the **time of flight (ToF)** can be measured with the  **$dE/dx$**  method described in Sect. 2.4. Usually the **ToF system provides** also the **trigger** for other **subdetectors**.

Experimentally **more challenging** is the measurement of the **energy**, usually obtained with a **homogeneous calorimeter** (Sect. 3.2), **selecting noninteracting stopping particles**. For this reason, this technique **works up to energies of a few GeV** only and the spurious **production of daughter nuclei** by **nuclear spallation** of heavier nuclei is the **main source of contamination**.

In the **energy range from the GeV to  $\sim 1$  TeV**, the **energy** can be **measured** using **magnetic spectrometers** or **Cherenkov detectors**. **Individual elements** are identified, characterized by their **charge  $Z$  through the  $dE/dx$  method**. At **high energy**, also **Transition Radiation Detectors (TRDs)** are used (Boezio and Mocchiutti 2012).

In **calorimeters**, the **particles** need to be (at least partly) **absorbed**. Calorimeters of limited dimension have been used because of weight and size constraints of balloon and space experiments. The weight of a detector with a **thickness of one hadronic interaction length** (Sect. 3.2.1) and **area of  $1 \text{ m}^2$**  amounts to  **$\sim 1$  ton**. In some cases, **multiple energy measurements** are **needed** in order to cover the **largest possible energy range** and to perform a **cross-calibration** of detectors with different systematic uncertainties.

Some experiments have **redundant detectors** also for the **measurement** of the **electric charge**, in particular if they are interested for the searches of **antiparticles**. The redundancy is mandatory to **discriminate** for instance **positrons** from the

more abundant CR protons when positively charged particles are detected. The measurement of the charge  $Z$  with different methods makes the nuclei selection very clean. However, the determination of the efficiency in the particles selection is usually a difficult task. Nuclei can interact within the detector (or in the atmosphere above the detector, for balloon experiments) producing a hadronic shower and undergoing a fragmentation into lighter nuclei. The corresponding systematic uncertainties are thus important and sometimes difficult to assess.

**Magnetic spectrometers** consist of a tracking device system inside a region with a magnetic field generated by a solenoid (either permanent or superconductive). Magnetic spectrometers can measure the particle rigidity up to a maximum value that depends on the magnetic field and on the precision of the measurement of the curvature of particles traversing the magnet. The maximum detectable rigidity is reached when they are poorly described by arcs, and appear to be straight lines. The mass constraints on payloads limit these measurements to about  $\sim 10-100$  GV for experiments carried by balloon, 1 TV in PAMELA and 2 TV in AMS-02.

**Transition radiation detector (TRD)** In some recent experiments, TRDs have been used to measure the  $\Gamma$  Lorentz factor of the incident particle and thus the energy instead of bulky and heavy hadronic calorimeters. The information from a TRD allows, together with data from other detectors, a separation of different nuclear species. Radiation (in the X-ray band, and usually denoted as *transition radiation*) could be produced when a particle with high  $\Gamma$  crosses several interfaces characterized by an abrupt change of the refraction index. Particles with large  $\Gamma$  induce X-rays with large probability. For a given energy, this allows a discrimination between light and heavy particle, as  $\Gamma = E/mc^2$ . A TRD contains many layers of transparent materials with different indices of refraction  $n$  in order to increase the photon emission probability of a single layer.

**The Ring-imaging Cherenkov detector (RICH)** estimates the particle velocity  $\beta = v/c$  with a high accuracy. The  $\beta$  derives from pattern recognition of photons distributed over geometrical shapes as circles, ellipses, arcs, or crescents produced by the Cherenkov effect. Charge measurement derives from the total amount of collected photons. Higher is the charge, higher is the number of photons.

## 3.2 The Calorimetric Technique

The *calorimetric calorimeter* technique is another method used for the energy determination of CRs. The calorimeters on board of balloons or satellites are very similar to those widely used in high-energy physics experiments at accelerators, although with limits on payload weight.

In a *calorimeter*, the kinetic energy of the incident particle is converted inside an absorber into a cascade of many secondary particles (the *shower*). At the end, the

primary energy of the incident particle is dissipated via excitation/ionization of the absorbing material.

A primary CR interacting with a nucleus produces a large number of secondary hadrons. They deposit energy through ionization/excitation of the medium and through successive interactions with nuclei, see Eq. (1.1), yielding lower energy hadrons, the *hadronic cascade*. Neutral mesons produced in the cascade, mainly  $\pi^0$ , immediately decay into  $\gamma\gamma$  pairs. In matter, each high-energy photon converts into an electron-positron pairs; each  $e^-$  ( $e^+$ ) is able to radiate energetic photons through bremsstrahlung. These radiated photons can convert into pairs that, in turn, radiate. In conclusion, one has an *electromagnetic shower* (*electromagnetic cascade*) with a large number of photons, electrons, and positrons.

### 3.2.1 Hadronic Interaction Length and Mean Free Path

The development of the hadronic cascade depends on the material medium through the nuclear (or hadronic) interaction length  $\lambda$ . This quantity corresponds to the mean path length after which the number of hadrons is reduced by the factor  $e$ , the Neper's constant. It is inversely proportional to the interaction cross-section  $\sigma$  and the medium number density  $n$  [ $\text{cm}^{-3}$ ]:

$$\lambda = \frac{1}{n\sigma} \quad [\text{cm}]. \quad (3.1)$$

As the number density depends on the matter density  $\rho$  ( $\text{g cm}^{-3}$ ), more frequently the nuclear interaction length for a nucleus with mass number  $A$  is expressed in units [ $\text{g cm}^{-2}$ ] as:

$$\lambda_I = \frac{\rho}{n\sigma} = \frac{Am_p}{\sigma} \quad [\text{g cm}^{-2}] \quad (3.2)$$

where  $m_p$  is the proton mass.

In the simplest model, the nuclear cross-sections are assumed energy-independent and proportional to the geometrical area of the interacting nuclei:

$$\sigma = \pi R^2 \quad \text{with} \quad R \simeq R_T + R_P - r_o \quad (3.3)$$

where  $R_P$  and  $R_T$  are the projectile ( $P$ ) and target ( $T$ ) radii. From nuclear models, the radius of a nucleus with mass  $A$  is:

$$R_A = r_o A^{1/3} \quad \text{with} \quad r_o \simeq 1.2 \times 10^{-13} \text{cm} \quad (3.4)$$

where  $r_o$  is the proton radius. This model is confirmed by the experimental fact that the proton-proton cross-section ( $\sigma_{pp}$ ) outside the region of the resonances is almost constant [see Sects. 7.3 and 7.4 of Braibant et al. (2011)] at the value given by the geometrical cross-section,  $\sigma_{pp} = \pi r_o^2 = 45 \text{mb}$ .

**Table 3.1** Main characteristics of detectors and absorber materials used in calorimeters

Material		$X_0$ (g cm <sup>-2</sup> )	$\lambda_I$ (g cm <sup>-2</sup> )	$E_c$ (MeV)
Active detectors	NaI	9.5	151	12.5
	BGO	8.0	157	7
Passive absorbers	Fe	13.8	132	28
	Pb	6.4	194	9.5
	U	6.0	199	9
Air [STP]	Mixture	36.7	90	86

For air, the Standard Temperature and Pressure (STP) conditions are considered.  $X_0$  = radiation length,  $\lambda_I$  = interaction length for protons,  $E_c$  critical energy = energy where energy loss through radiation equals that due to excitation/ionization

The cross-section for a proton in a medium with mass number  $A$  is:

$$\sigma \simeq \pi[r_0 A^{1/3}]^2 = \sigma_{pp} A^{2/3}. \tag{3.5}$$

Some typical values of interaction lengths, Eq. (3.2), using the above proton cross-sections are given in Table 3.1.

### 3.2.2 The Electromagnetic Radiation Length

In the electromagnetic component of the cascade, the electron and positron energy losses are mainly due to the excitation/ionization and bremsstrahlung processes, Fig. 2.5b, which can be parameterized as:

$$-\frac{dE}{dX} \simeq \alpha(E) + \frac{E}{X_0} \tag{3.6}$$

where the depth  $X$  is measured in units of (g cm<sup>-2</sup>), the term  $\alpha(E)$  due to the excitation/ionization energy loss is only slightly energy dependent and the radiation length  $X_0$  depends on the material. The quantity  $X_0$  corresponds to the length after which the energy  $E_0$  of the incident electron is reduced to  $E_0/e$ . Typical values of radiation lengths  $X_0$  for some materials are listed in Table 3.1.

The development of the electromagnetic cascade continues until the energies of the electrons and positrons fall below the critical energy  $E_c$ . Below the critical energy  $e^+$ ,  $e^-$  lose energy mainly through the excitation/ionization process. In a medium with high  $Z$ , such a cascade has limited longitudinal and transverse dimension, as illustrated in Fig. 3.1a. An electromagnetic calorimeter measures the total energy produced through excitation/ionization due to  $e^+$ ,  $e^-$ ,  $\gamma$ .

**Calorimeters for space experiments** The most appropriate material for an electromagnetic calorimeter would be one with a short  $X_0$ . A hadron calorimeter should



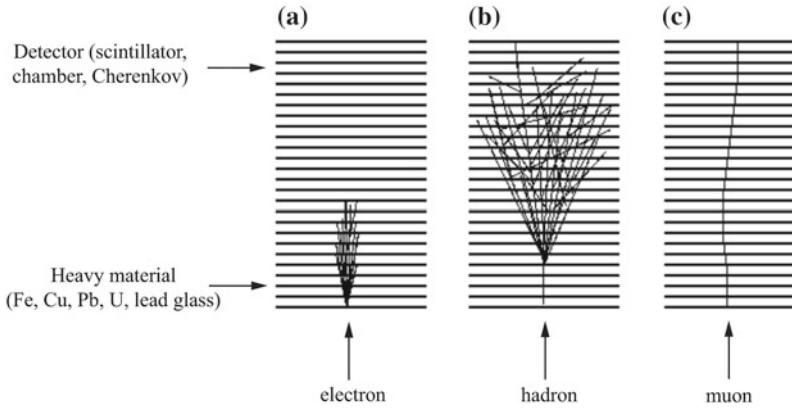


**Fig. 3.1** Behavior **a** of an **electromagnetic cascade**, **b** of a **hadronic cascade** and **c** of a **muon** when traversing a sampling calorimeter constituted of interleaved detector and absorber layers of heavy material. A muon behaves as a minimum ionizing particle and can be easily identified (Braibant et al. 2011)

have a **short interaction length  $\lambda_I$**  to force hadronic interactions as the particle enters the detector and to completely absorb the cascade. The **hadronic cascade is wider and longer than that electromagnetic** (see Fig. 3.1b). Usually, a calorimeter for hadrons (or **hadronic calorimeter**) must have **larger dimensions** than one for electromagnetic showers (or **EM calorimeter**) and in accelerator experiments, it has **usually** a thickness of **six nuclear interaction lengths  $\lambda_I$** . Calorimeters carried by balloons on the top of the atmosphere (or outside the atmosphere by satellites) are limited in absorber thickness due to weight restrictions. The **minimum depth depends on the energy resolution required** for a particular experiment but, typically, the electromagnetic component is reliably measured up to the energy for which the maximum of the shower is contained within the calorimeter.

### 3.2.3 Hadronic Interaction Length and Mean Free Path in the Atmosphere

The **Earth atmosphere** itself (**vertical thickness  $X_v^{\text{atm}} = 1,030 \text{ g cm}^{-2}$** , Sect. 4.2) acts like a **calorimeter** of variable density with  **$\sim 11$  interaction lengths and 28 radiation lengths** (compare with Table 3.1). For this reason, **direct CR measurements can occur only outside the atmosphere**, or at a **very large height**.

If the considered **medium** is the **Earth atmosphere**, with  **$A \simeq A_{\text{atm}} = 14.5$**  we obtain:

$$\sigma_{\text{atm}} = 270 \text{ mb} = 0.27 \times 10^{-24} \text{ cm}^2. \quad (3.7)$$

Using (3.2) the mean free path for CR protons in the atmosphere is:

$$\lambda_I \simeq \frac{14.5 \cdot 1.6 \times 10^{-24}}{0.27 \times 10^{-24}} = 85 \text{ g cm}^{-2} \quad (3.8a)$$

An interesting consequence of the hadron quark model is that the cross-section for a secondary pion is  $\sigma_\pi \simeq 2/3\sigma_p$  [see Sect. 7.14.3 of Braibant et al. (2011)]. Thus, the mean free path of secondary pions in the atmosphere is:

$$\lambda_I^\pi \simeq 120 \text{ g cm}^{-2}. \quad (3.8b)$$

Finally, for a heavy CR nucleus (e.g. Iron, with  $A_{\text{Fe}} = 56$ ) using the fact that  $\sigma_{\text{Fe}} \simeq \pi r_c^2 (A_{\text{Fe}}^{2/3} + A_{\text{Atm}}^{2/3})$  we obtain:

$$\frac{\sigma_{\text{Fe}}}{\sigma_p} \simeq \frac{(A_{\text{Fe}}^{2/3} + A_{\text{Atm}}^{2/3})}{A_{\text{Atm}}^{2/3}} = 3.5 \quad \text{and thus} \quad \lambda_I^{\text{Fe}} \simeq \frac{85}{3.5} = 24 \text{ g cm}^{-2}. \quad (3.8c)$$

### 3.3 Balloon Experiments

The hypothesis of the existence of an extraterrestrial radiation was confirmed with experiments using balloon ascensions. Balloon experiments were always important during the CR history. As a curiosity, in the early 1930s stratospheric flights were made with huge rubberized fabric balloons. Aeronauts in sealed, airtight capsules were able to survive up to a record altitude of 22 km (in 1935). Scientific balloons used today (for instance for the NASA flights) are made of 20  $\mu\text{m}$  thick polyethylene film; they are as large as a football stadium with a diameter of about 140 m and a volume larger than 1.1 million cubic meters filled with helium gas. They can carry experiments (payloads) up to 3,600 kg and fly at altitudes up to 42 km. The payloads are attached to a parachute. The flights are terminated by remotely firing an explosive squib that separates the payload from the balloon. The experiment descends slowly, suspended by the parachute, and it is recovered and refurbished for future flights.

In the early 1990s, remarkably successful long flights around Antarctica (1–2 weeks) were started (Seo 2012). The duration of conventional 1–2 day flights was limited due to altitude excursions during day–night transitions. The continuous solar heating during local summer in the polar region ensures nearly constant altitudes with essentially no ballasting. From 2005 to 2010, the CREAM payload flew six times, for a cumulative exposure of 162 days and with a record duration of almost 40 days, while circumnavigating Antarctica three times (Fig. 3.2).

Apart from the measurement of the cosmic ray composition in the region below the knee (presented in this chapter), balloon experiments as well as detectors on satellites



**Fig. 3.2** **a** CREAM ballooncraft with the launch vehicle while a  $10^6 \text{ m}^3$  balloon is being inflated at the launch site, Williams field near McMurdo, Antarctica; **b** the balloon trajectory of a 37 day flight of CREAM, which was launched on December 1, 2009 and terminated on January 8, 2010 during about three rounds of the South Pole. Courtesy of Prof. E. Seo (CREAM Collaboration) (<http://cosmicray.umd.edu/cream/>)

are devoted to **searches for antimatter** (Sect. 3.8) and **dark matter** in our Galaxy (Chap. 13). Here, we mention only some recent and large statistics experiments.

The **improvement of flight duration** and **payload capability** allows carrying **complex and heavy experiments**. The major improvement was the use of **superconducting magnet spectrometers** with a **suite of particle detectors** to **identify antiparticles**. These experiments were the Balloon Experiment with a superconducting Solenoid Spectrometer (**BESS**), the Cosmic AntiParticle Ring-Imaging Cherenkov Experiment (**CAPRICE**) and the High-Energy Antimatter Telescope (**HEAT**). Usually, a date or an extension is used to distinguish different flights of the same detector when it flew more than once, sometimes with a slightly different configuration. For instance, BESS had nine successful flight campaigns since 1993, and the last one was denoted as BESS-polar.

In **BESS**, the **particle rigidity** (2.6) is measured in the superconducting spectrometer, where a **uniform magnetic field of  $\sim 10^4 \text{ G}$**  acts for 1 m on the particles. The

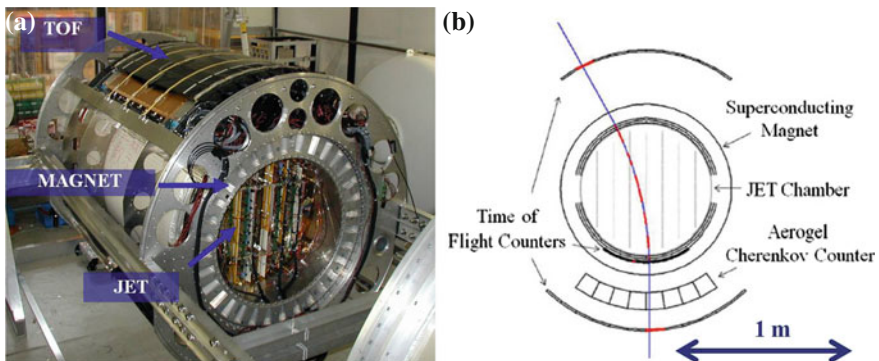


**Fig. 3.3** **a** A picture of the original BESS apparatus. **b** A cross-sectional view of the BESS-Polar instrument showing also a particle trajectory. Courtesy of Dr. J.W. Mitchell and Prof. A. Yamamoto (BESS Collaboration)

**Table 3.2** Comparison of balloon experiments for high-energy CR measurements

Instrument	Energy measurement	Charge range	Flight duration (days)	Amospheric overburden ( $\text{g}/\text{cm}^2$ )	Exposure ( $\text{m}^2 \text{ sr days}$ )	$N_p E > 6 \text{ TeV}$
ATIC	Calorimeter	$1 \leq Z \leq 28$	48	4.3	5	$\sim 720$
TRACER	TRD	$8 \leq Z \leq 28$	10	3.9	50	–
CREAM	Calorimeter	$1 \leq Z \leq 28$	160	3.9	48	$\sim 5,000$
CREAM	TRD	$3 \leq Z \leq 28$	42	3.9	55	–
JACEE	Emulsion	$1 \leq Z \leq 28$	60	5.3	10	$\sim 700$
RUNJOB	Emulsion	$1 \leq Z \leq 28$	60	10	24	$\sim 700$

The energy measurement techniques are identified in Column 2; the range of the electric charge measurement in Column 3. The charge resolution was  $\sim \Delta Z = 0.3$  for all experiments, apart JACEE and RUNJOBS

sagitta is measured with the central tracker made of *drift chambers*, having a *spatial resolution of  $\sim 150 \mu\text{m}$* . The *ToF system* provides the measurement of the *particle direction, velocity  $\beta = v/c$  and electric charge  $Ze$* . Figure 3.3a shows a picture of the BESS apparatus, where the magnetic barrel is visible. The cross-sectional view of the instrument and a charged particle trajectory is sketched on the right side of the figure.

The Advanced Thin Ionization Calorimeter (ATIC) was configured with a homogeneous Bismuth Germanium Oxide (BGO) calorimeter with about  $20 X_0$ . The calorimeter is preceded by a silicon matrix for the measurement of the particle electric charge. Since December 2000, ATIC had three successful flights from McMurdo, Antarctica, see Table 3.2. One of the main results of the ATIC flights was the reported excess of electrons and positrons around 600 GeV (see Sect. 3.9). Concerning the measurement of primary CRs composition, the ATIC data filled the gap for elements from protons ( $Z = 1$ ) to iron ( $Z = 26$ ) of the measurements made by experiments using spectrometers and higher energy data from emulsion-based experiments.

Pioneering calorimeters using emulsions for measurements of CRs above 2 TeV were made by the Japanese-American Collaborative Emulsion Experiment (JACEE) and the RUssian-Nippon JOint Balloon Experiment (RUNJOB) collaborations. Both detectors had limited charge resolution and measured groups of nuclei with close electric charge. The experiments used the passive calorimetric techniques of emulsions and of X-ray films. These passive techniques limit the exposures because of the integrating effects of the background. Long exposures of experiments which use passive detectors would require frequent replacement of the emulsion plates and X-ray films.

The Transition Radiation Array for Cosmic Energetic Radiation (TRACER) experiment extended the flux measurements of heavy nuclei to higher energies. TRACER was configured with two layers of plastic scintillators ( $2 \times 2 \text{ m}^2$ ) which measured the electric charge, and a TRD to determine the  $\Gamma$  of the incident particle. The TRD characteristics of this experiment preclude the measurement of light nuclei. In addition to the TRD, a Cherenkov counter (made of acrylic plastic) at the bottom of the detector was used to reject nonrelativistic particles. TRACER reported

elemental spectra from oxygen ( $Z = 8$ ) to iron ( $Z = 26$ ) from a flight in Antarctica in 2003 (Table 3.2), and from boron ( $Z = 5$ ) to iron in a second flight in 2006.

The Cosmic Ray Energetics and Mass Balloon Experiment (CREAM) used both a calorimeter (with 20 radiation lengths  $X_0$  and half interaction length  $\lambda_I$ ) and a TRD for the measurements of the CRs energy. The two subdetectors had different systematic biases in determining the particle energy allowing an in-flight cross-calibration of the two techniques for particles with  $Z \geq 4$ . The CREAM calorimeter measured all elements, including nuclei with  $Z = 1$  and 2, up to  $\sim 10^{14}$  eV with energy resolution better than 45% for all energies. The highly segmented detectors comprising the instrument had about  $10^4$  electronic channels. The CREAM calorimeter was designed to be large enough to collect adequate statistics, within the weight limit for a balloon flight. It used a tungsten absorber (tungsten has high  $Z$  and a small radiation length,  $X_0/\rho = 0.35$  cm) and thin scintillating fibers.

Table 3.2 compares the quoted balloon experiments for high-energy measurements: CREAM (Ahn et al. 2007), ATIC (Ganel et al. 2005), TRACER (Ave et al. 2008), JACEE (Asakimori et al. 1998) and RUNJOB (Derbina et al. 2005).

### 3.4 Satellite Experiments

Primary CR data from early space experiments refer mostly to energies lower than 1 GeV. Of particular important was the first measurement of isotopic Li, Be, and B flux with experiments on satellites in the 1970s (Garcia-Munoz et al. 1975) with the Interplanetary Monitoring Platform-7 and -8 (IMP) spacecrafts, who measured CRs up to  $\sim 100$  MeV. The IMP was a series of 10 scientific satellites launched by NASA between 1963 and 1973. These experiments were sensible mainly in an energy region where the solar wind significantly affects CRs, and provided relevant information concerning the solar activity. Other space experiments were on board the High-Energy Astrophysics Observatory (HEAO-3) satellite and the Cosmic Ray Nuclei (CRN) experiment who flew for nine days on the Space Shuttle. The PAMELA experiment is a powerful particle identifier using a permanent magnet spectrometer with a variety of specialized detectors that accurately measures with high sensitivity the abundance and energy spectra of CR electrons, positrons, antiprotons and light nuclei over a very large range of energies from 50 MeV to hundreds of GeV.

In the following, we describe the Be isotopes flux measurement done by one of the first space experiments in the early 1970s, and the experiments representing the status of the art after 40 years of research: PAMELA and AMS-02.

#### 3.4.1 The IMP Experiments

Among the different physics studies performed by the IMP-7 (launched in 1972) and IMP-8 (launched in 1973) experiments, a very important result was the detection of the  $^{10}\text{Be}$  (Garcia-Munoz et al. 1977). This was the first measurement of this

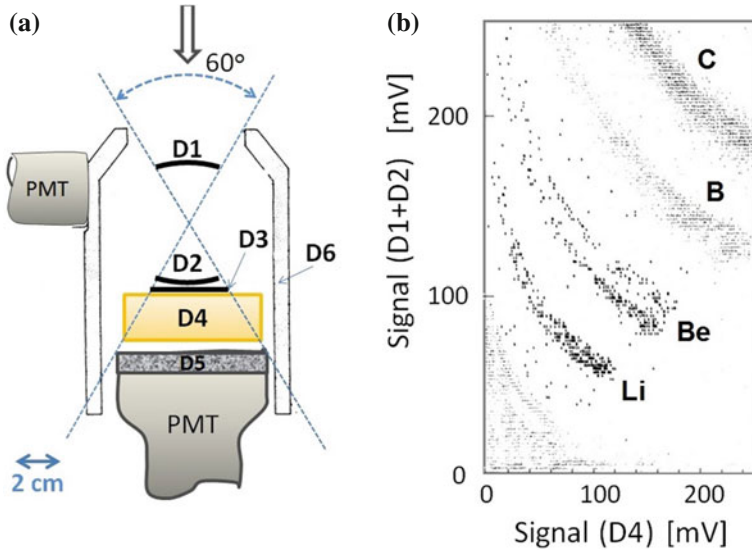


**Fig. 3.4** **a** Layout of the telescope on board IMP-7, -8. The silicon detectors (denoted as D1, D2, D3) measure the particle energy loss. D4 is a CsI (Tl) scintillator viewed by four photodiodes. D5 and D6 are two additional scintillator. **b** Result from IMP-8 (data collected between 1974 and 1975). On the y-axis, the signal is proportional to the energy loss  $\propto Z^2/\beta^2$  measured in (D1 + D2), on the x-axis, to the residual energy of the particle measured in D4. At a given energy, the value on the y-axis increases as  $Z^2$ . For a given  $Z$  and energy, nuclei with larger  $A$  have smaller  $\beta$  and undergo larger energy losses in D4

isotope (important for the determination of the “age” of CRs) which was repeated on successive satellite missions (Voyager, Ulysses, CRIS), Sect. 5.2.

The general layout of the telescope is shown in left side of Fig. 3.4. It is a small-scale version of our toy telescope, described in Sect. 2.4. Particles passing through the detector layers D1, D2, D3, and which have come to rest in D4 are considered. Counters D5 and D6 act as veto, to confirm that the particle is stopped in D4. The separation between different chemical species and isotopes is achieved using the  $dE/dx$  technique (measured in D1, D2) as a function of the total energy released in D4. The events due to each isotope are located along distinct lines that are approximately equilateral hyperbolae, as shown on the right side of Fig. 3.4 (from IMP-8). Nuclei with different  $Z$  are well separated by their energy loss, which depends on  $(Z/\beta)^2$  of the particle. At a given total energy (proportional to the signal D4) of a nucleus with a given  $Z$ , the velocity  $v = \beta c$  is smaller for the isotope with a larger  $A$ . Thus,  $^{10}\text{Be}$  produces a larger signal in D1, D2 than the other isotopes  $^7\text{Be}$  and  $^9\text{Be}$ .

Very few  $^{10}\text{Be}$  nuclei were collected by these small acceptance experiments. Assuming that all the Be isotopes are produced during propagation in the Galaxy of C, N, and O nuclei with the production cross-sections as estimated using accelerator



data (see discussion in Sect. 5.1 and Table 5.1), we would expect a ratio between the three elements as:

$${}^7\text{Be} : {}^9\text{Be} : {}^{10}\text{Be} = 9.7 : 4.3 : 2.3 \quad (\text{expected}) \quad (3.9)$$

The IMP measurements of the different Be isotopes give

$${}^7\text{Be} : {}^9\text{Be} : {}^{10}\text{Be} = 329 : 177 : 15 \quad (\text{measured}) \quad (3.10)$$

By comparison between expected and measured values, the ratio  ${}^7\text{Be} : {}^9\text{Be}$  is almost equal to the ratio of production cross-sections.  ${}^{10}\text{Be}$  is instead largely suppressed, and the only explanation is that a large fraction of this unstable isotope had time to decay after being originated, before detection. This allow the measurement of the CR escape time, as discussed in Sect. 5.1.

### 3.4.2 The PAMELA Experiment

The Payload for Antimatter Matter Exploration and Light-nuclei Astrophysics (PAMELA) is an experiment mainly devoted to antimatter studies up to the hundreds GeV region. Its size and flight durations are such as to allow an accurate measurement of the neutral and charged components of CRs up to the TeV region. PAMELA was launched by a Soyuz-U rocket from the Baikonur cosmodrome in Kazakhstan in June 2006.

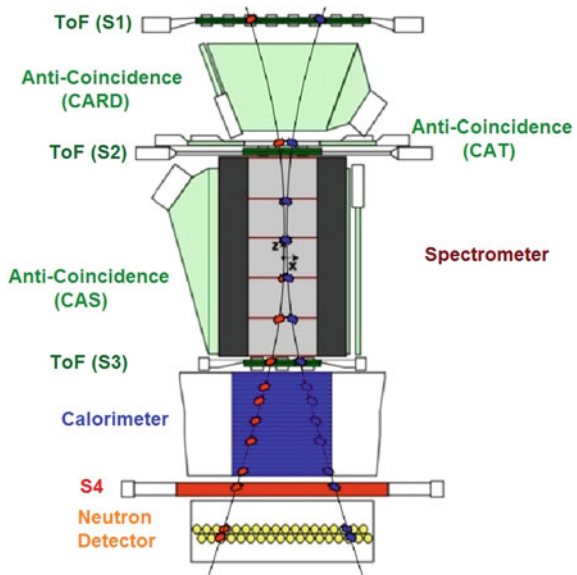
The apparatus is composed of different subdetectors. Figure 3.5 shows from top to bottom:

- a time of flight system, ToF (S1, S2, S3);
- an anticoincidence system (denoted in the figure as CARD, CAT, CAS);
- a magnetic spectrometer;
- an electromagnetic imaging calorimeter;
- a shower tail catcher scintillator (S4);
- a neutron detector.

The ToF system comprises six layers of fast plastic scintillators arranged in three double planes (S1, S2 and S3). It provides a fast signal used to trigger the data acquisition and to measure the time-of-flight and  $dE/dx$  of traversing particles. The ToF resolution of  $\sim 0.3$  ns allows  $e^-$  ( $e^+$ ) to be separated from  $\bar{p}$  ( $p$ ), up to 1 GeV/c. Due to this very accurate time resolution, particles traversing the detector from the bottom (albedo particles) can also be rejected with a large statistical significance.

The central part of the PAMELA apparatus is the magnetic spectrometer, consisting of a 0.43 T permanent magnet and a microstrip silicon tracking system, with a spatial resolution of 3  $\mu\text{m}$ . The maximum detectable rigidity is around 1 TV. The dimensions of the magnet define the geometrical factor, Eq. (2.12), to be 21.5  $\text{cm}^2$  sr. Ionization losses are measured in the ToF scintillator planes, in the silicon planes

**Fig. 3.5** Cross-section of the PAMELA detector with two opposite-sign charged particles. Combined measurements from the magnetic spectrometer, calorimeter, time of flight (ToF) system, and neutron detectors shown here distinguish the incident particles by their charge, momentum, and mass. Credit: PAMELA Collaboration (<http://pamela.roma2.infn.it>)



of the tracking system and in the first silicon plane of the calorimeter, allowing a measurement of the electric charge up to  $Z = 8$ .

The sampling electromagnetic calorimeter comprises 44 silicon planes interleaved with 22 plates of tungsten absorber. The total depth of the calorimeter is 16.3 radiation lengths and 0.6 interaction lengths. A plastic scintillator system mounted beneath the calorimeter helps in the identification of high-energy electrons; it is followed by a neutron detection system, which complements the electromagnetic/hadronic discrimination capabilities of the calorimeter by detecting the increased neutron production associated with hadronic showers compared to electromagnetic ones in the calorimeter.

### 3.5 The AMS-02 Experiment on the International Space Station

The AMS-02 is the largest particle physics detector ever carried outside the atmosphere (Fig. 3.6). It was designed to operate as an external module on the International Space Station (ISS), Fig. 1.6. It studies with an unprecedented precision the cosmic ray composition and flux. In addition, it could open new information on the Universe and its origin by searching for antimatter and dark matter candidates. Concisely, AMS-02 utilizes 15 among particle detectors and supporting subsystems in a volume of  $64 \text{ m}^3$ ; its weight is 8,500 kg and it dissipates 2.5 kW. It has a data downlink bandwidth of 9.6 Mbps. It was launched on 16th May 2011 on board of the shuttle Endeavour. The mission duration is expected to coincide with the lifetime of



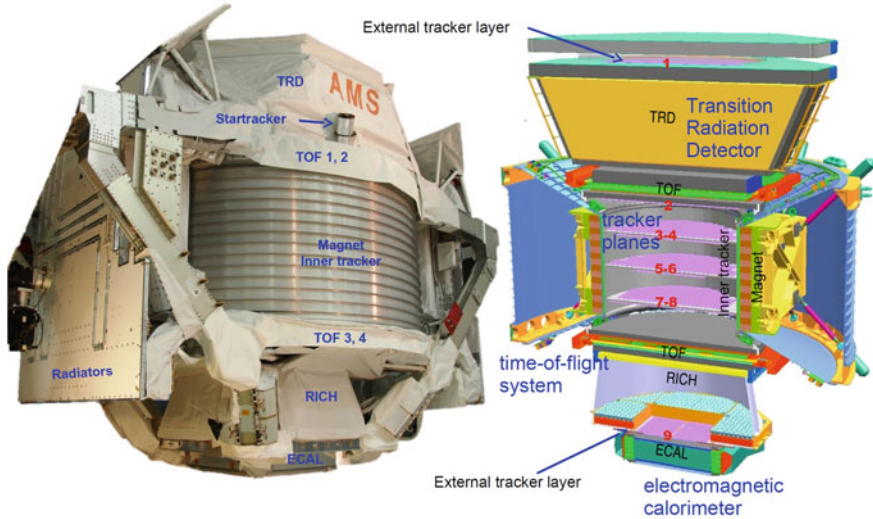


**Fig. 3.6** The AMS-02 detector. See text for the details of different subdetectors. Credit: AMS-02 Collaboration (<http://www.ams02.org/>)

the ISS (2020 or longer): the detector will not come back to Earth. Its subdetector system is a sort of compendium of devices carried by preceding satellites and balloon experiments. For this reason, we describe it with some details.

The AMS-02 prototype was designated as AMS-01. It was a simplified version of the detector, which flew into space aboard the Space Shuttle Discovery in June 1998 for about 10 days. AMS-01 proved that the detector concept worked in space and provided some measurements quoted in the following sections.

AMS-02 uses a very large permanent magnet (which is the heart of the detector) operating at ambient temperature, consisting of 6,000 Ne–Fe–B pieces carefully magnetized and assembled. This magnet was successfully flown on the AMS-01 mission. The use in AMS-02 of a superconducting magnet was also tested, but this solution was discarded. The currently available technology does not allow keeping a superconducting magnet operational on the ISS for more than 2–3 years. The configuration of the magnet has a negligible net dipole moment, to avoid coupling with the Earth magnetic field, which would disturb the orbit of the ISS. The Nd–Fe–B magnets are the strongest permanent magnets, and that of AMS generates a magnetic field of 1.5 kg.

Inside the magnet, the central Tracker is able to precisely measure the curvature of the particles traversing the magnet and determine the particle rigidity. The tracker records the coordinate of a particle at eight different positions with a precision of  $\sim 10 \mu\text{m}$  at each point. The radius of the best circular trajectory passing through the points defines the particle curvature, used to evaluate the rigidity through Eq. (2.6). The Tracker is made of 2,264 double-sided microstrip sensors ( $7.2 \times 4.1 \text{ cm}^2$ ,  $300 \mu\text{m}$  thick) assembled in 192 read-out units, totaling 200,000 read-out channels. The large number of channels generates about 200 W of heat, which must be dissipated.

The **maximum detectable rigidity** for the **AMS-02 Tracker** is about **2 TV**, a very high value with respect to other space experiments.

The exact position of each module is of fundamental importance for the trajectory determination. The procedure that determines the modules misplacements is called **alignment**. The **AMS-02 Tracker** was **aligned in 2010** using a **straight proton beam at CERN**. The proton beam was used as **reference**. Translation and rotation constants for all Tracker modules have been determined with respect to it. Thermal conditions may change rapidly in space. This fact can introduce mechanical deformations and misalignments, which will affect the rigidity measurement. A **Tracker Alignment System (TAS)** made of **laser beams** that mimic straight tracks provide a fast and reliable monitoring of the Tracker geometrical stability during the AMS-02 mission. Therefore, systematic effects due to misalignments can be monitored and corrected.

The **time of flight (ToF) system** is able to measure with precision of  **$\sim 0.15$  ns** the particle transit time through the detector and provides trigger for the other subdetectors. Since the distance between the upper and lower ToF planes is approximately 1.2 m, the ToF is able to resolve **particles velocity up to 0.98 c**. It is composed by four planes of scintillation counters two above and two below the magnet. Each ToF plane consists of *paddles* aligned along the  $x$  and  $y$  coordinates, respectively. A ToF paddle consists of 1 cm thick plastic scintillator of dimension approximately  $12 \times 120$  cm<sup>2</sup>. The scintillators are coupled at both ends via light guides to photomultipliers.

The **ToF** system is also **important** for **antimatter** discrimination as it is able to **discriminate up-going/down-going** particles with a rejection factor of  $10^{-9}$ . In a magnetic field, the trajectory of an upward going electron is equivalent to that of a downward going positron and a wrong assignment of the direction of a particle would induce a wrong charge assignment.

The **TRD** of AMS-02 is made by **many layers of plastic** or **felt** and **vacuum**. The X-rays are measured by a gas detector (straw tubes) filled with a special Xe:CO<sub>2</sub> (80:20 %) mixture regulated by a gas recirculation system. The TRD system is placed on top of the magnet vacuum case. This system provides the **measurement of the  $\Gamma$**  factor for protons and electrons of a given energy, improving the redundancy on the discrimination of positrons against CR protons.

The **Electromagnetic CALorimeter (ECAL)** helps to have the highest **rejection** between **protons and positrons at high energy**. It is a pancake consisting of nine superlayers for an active area of  $\sim 65 \times 65$  cm<sup>2</sup>, and a total thickness of 16.65 cm. Each superlayer (1.85 cm thick) is made of 11 grooved lead foils interleaved with layers of scintillating fibers, glued together. The detector imaging capability is obtained by stacking superlayers with fibers alternatively parallel to two orthogonal axis. The pancake has an average density of 6.9 g cm<sup>-3</sup>, **16 radiation lengths** for a total weight of 496 kg.

The **calorimeter** is able to **reconstruct a 3D shower profile** at 18 different depths. These measurements will give an accurate description of the **longitudinal** and **transverse shower shape** allowing the **positron/proton showers separation** with an identification power of one  $e^+$  over  $10^5 p$ . From the shower shape, it is **also possible to reconstruct the direction of the incident particle**. The ECAL can reach **angular precisions of few degrees**. This is very important for the measurement of  $\gamma$ -rays

converting inside the calorimeter. The  $\gamma$ -rays detected in the ECAL are complemented by those producing pair conversions in the Tracker. Both these measurements provide the  $\gamma$ -ray energy and direction with respect to the AMS-02 coordinate system.

The *Star Tracker* system uses a Global Positioning System receiver and it is necessary to determine the orientation of the detector in the sky. This information is needed to measure the arrival direction of particles in the sidereal reference frame, i.e., with respect to fixed stars. The system provides continuous synchronization between the data acquisition and the Coordinated Universal Time (UTC).

AMS-02 has the maximum analyzing power for particles traversing the instrument from top to bottom. Particles with a high incidence angle cannot be well measured, and an *Anticoincidence Counter* (ACC) is used to reject them. The ACC is a barrel of scintillation counters around the tracker and it is important for the rejection of events with bad topology. Indeed high-energy particles incident on AMS-02 materials could interact inelastically. The result of such interaction is the production of a hadronic shower that will confuse the tracker pattern recognition. These events could be a significant background for the search of antimatter signals.

A particle from top to bottom of the detector will give a signal in the ToF and not on the ACC. Conversely, a horizontal particle may give a signal on the ACC and not in the ToF. Then, an event should be recorded following the logic: (ToF) AND NOT (ACC). This restrictive condition can be released under particular conditions. In general, the *Level 1 trigger* of AMS-02 is constructed using information from ToF (for charged particles), ACC (as veto for high inclination particles) and ECAL (for neutral particles).

Because of the high levels of radiation in space, the electronics used for AMS-02 is also particularly challenging. The number of electronics channels for the correct operation is about 3,00,000 and it is equivalent to all remaining electronics channels on ISS. The data are supervised by more than 600 separate computers using special radiation-tolerant chips. Redundancy is systematically implemented: there are at least two of every card, cable, and connector.

Real-time transmission of data from AMS-02 to the NASA ground facilities occurs through a high-rate downlink system. The operations of the detector are monitored in a Science operation center at CERN. During the period 19 May 2011 to August 2013 about  $36.5 \times 10^9$  CRs were collected. First results on the measurement of the positron fraction in primary CRs were released in April 2013 (Aguilar et al. 2013), followed by results on charged cosmic nuclei (protons, helium, boron, carbon) and on the fluxes, ratios, and anisotropies of leptons.

### 3.6 Abundances of Elements in the Solar System and in CRs

At low energies, the chemical composition of the CRs has been measured with the abundance of nuclei arriving above the Earth atmosphere. Table 3.3 shows the relative abundances (*R.A.*) between the different components of the cosmic radiation

**Table 3.3** Composition of the different CR components

Element (Z)	Group Z	R.A. $E_T > 2.5$ GeV	R.A. $E_T > 10.6$ GeV/n	Number of particles per 100 Si	
				CRs	SS
H (1)		26000	540	$1.9 \times 10^5$	$2.93 \times 10^6$
He (2)		3600	26	$2.63 \times 10^4$	$2.47 \times 10^5$
Li (3)	$\mathcal{L}$	18	0.121	130	$5.6 \times 10^{-3}$
Be (4)		10.5	0.09	76	$6.1 \times 10^{-5}$
B (5)		28	0.19	202	$1.9 \times 10^{-3}$
C (6)	$\mathcal{M}$	100	0.99	720	$7.2 \times 10^2$
N (7)		25	0.22	180	$2.1 \times 10^2$
O (8)		91	1	655	$1.6 \times 10^3$
F (9)	$\mathcal{H}$	1.7	0.015	12	$8.0 \times 10^{-2}$
Ne (10)		16	0.152	115	330
Na (11)		2.7	0.026	20	5.8
Mg (12)		19	0.197	137	103
Al (13)		2.8	0.031	20	8.5
Si (14)		14	0.163	100	100
P (15)		0.6	0.005	4.3	0.8
S (16)		3	0.030	22	42
Cl (17)		0.5	0.005	3.6	0.5
Ar (18)		1.5	0.009	11	9.3
K (19)		0.8	0.006	5.7	0.4
Ca (20)		2.2	0.018	15.8	6.0
Sc (21)	$\mathcal{V} \mathcal{H}$	0.4	0.003	2.9	$3.4 \times 10^{-3}$
Ti (22)		1.7	0.010	12.2	0.25
V (23)		0.7	0.005	5.0	$2.9 \times 10^{-2}$
Cr (24)		1.5	0.011	10.8	1.3
Mn (25)		0.9	0.009	6.5	0.9
Fe (16)		10.8	0.110	78	84.8
Co (27)		<0.2	$4 \times 10^{-4}$	–	0.23
Ni (28)		0.4	0.007	2.9	4.9
(29–30)		–	–	–	0.2
(>30)	$\mathcal{U} \mathcal{H}$	$5 \times 10^{-3}$	–	0.02	0.02
(–1)	$e^-$	260	5	$3 \times 10^4$	$2.93 \times 10^6$

The relative abundances (R.A.) measured with different methods and energy thresholds are reported in column 3 (Grieder 2001) and 4 (Engelmann et al. 1990). The corresponding relative CR abundances (column 5) are compared with that of the solar system (SS, column 6) (Lodders et al. 2009). The last two columns are arbitrary normalized to 100 for Si

above the energy threshold  $E_T$  of 2.5 GeV (column 3) and of  $E_T > 10.6$  GeV/n (column 4), where the solar contribution can be neglected. Nuclei heavier than helium only contribute about a few percent of the total flux on Earth. However, the relative

abundance of these elements is an essential piece of information to understand the origin and history of accelerated particles, in particular when compared with the nuclear composition of the solar system (column 6).

A remarkable **resemblance** between the measured **CR abundances of nuclear species** and the **abundances** found in the **solar system** can be noticed. The **latter** are also representative of the **cosmic abundances of elements**, see Sect. 3.6.1. The relative abundances of elements in CRs as a function of the nuclear charge  $Z$  for all elements are shown in Fig. 3.7 and are compared with the solar system abundances. It is interesting to note that **all the elements** in the periodic table **are present** in the solar system, and have been found in cosmic rays as well. Elements up to the iron are much more abundant than trans-iron elements. A peculiarity observed in Fig. 3.7 is the alternation between **relative abundance and scarcity of adjacent atomic numbers**. This pattern is very **similar** to that expected from the **energy levels of adjacent nuclei** in the **nuclear binding energy curve**, see next section. Data shown in Fig. 3.7 and Table 3.3 represent probably one of the most important pieces of information about the nature of CR sources.

The **two samples** (CRs and solar system abundances) exhibit a **striking similarity**, in most cases the differences being **within 20%**. The first conclusion from the data shown in Fig. 3.7 is that the **accelerated matter** arriving on Earth is **sampled** from a **region** whose surrounding material has the **same chemical composition of our Solar System**. This material is plausibly originated by the same mechanism that originated the Sun and the planets.

However, some **remarkable differences** between the two exist. The most relevant corresponds to the overabundance of **Li, Be, B** elements in CRs with respect to the

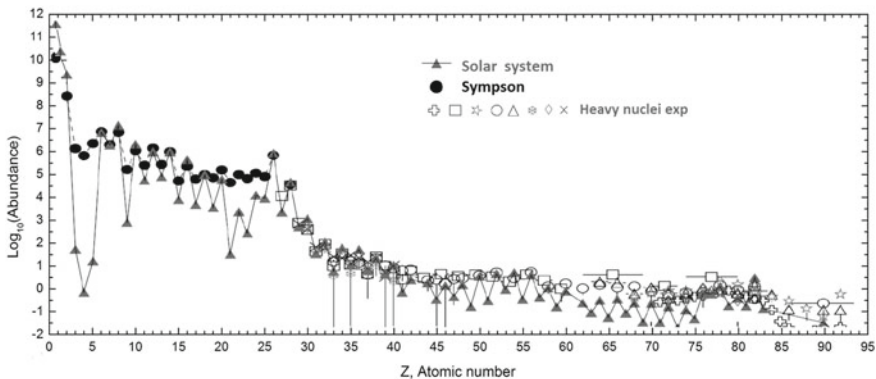


**Fig. 3.7** Relative abundance of nuclei in cosmic rays as a function of their nuclear charge number  $Z$  at energies around 1 GeV/n, normalized to Si = 100. Abundance for nuclei with  $Z \leq 28$  are (drawn according to Simpson 1983). Heavier nuclei are measured by different experiments [as reported in Blümer (2009)]. The abundance of elements (*triangles*) in the solar system according to Lodders (2003) is also shown

cosmic chemical composition. The observed abundance ratio  $(\text{Li} + \text{Be} + \text{B})/(\text{C} + \text{N} + \text{O})$  in CRs exceeds the value found in solar system material by a factor of  $\sim 10^5$ , see Table 3.3. A similar excess occurs for the elements below the iron ( $Z = 26$ ) and the lead ( $Z = 82$ ) peaks. This difference is interpreted as due to the effect of the propagation in the Galaxy (Sect. 5.1) and provide a measure of the material that CRs have encountered since they were accelerated. Carbon, nitrogen, and oxygen are considered primary cosmic rays, produced and accelerated by astrophysical sources. Lithium, beryllium, and boron are secondary components produced by fragmentation reactions of the heavier C, N and O elements during the journey of CRs in the interstellar medium. As the spallation cross-section of the relevant nuclei is known at GeV energies, the ratio of secondary to primary cosmic rays will be used in Sect. 5.1 to infer the average escape time  $\tau_{\text{esc}}$  of CRs in the Galaxy.

In addition to stable isotopes, CRs contain long-lived radioactive nuclides, mostly of secondary origin. The observed abundances of these isotopes can be used for establishing various time scales related to the origin of CRs. In particular, secondary isotopes which decay through  $\beta^\pm$  emission have been used (Sect. 5.2) as a second method to measure  $\tau_{\text{esc}}$ .

### 3.6.1 Cosmic Abundances of Elements

The chemical elements existing in nature are a finite number: they are those that appear in the periodic table of elements. The observed stable nuclei are 264; the number of the unstable ones is more than 1,500. The latter number is increasing every year, as improved experimental techniques are developed, allowing the measurements of shorter and shorter nuclear lifetimes.

The nuclei can be classified in terms of the number of protons  $Z$  (the atomic number), the number of neutrons  $N$  and the number of nucleons  $A$  (the mass number)  $A = Z + N = Z$  protons plus  $N$  neutrons. By sorting the nuclei on the basis of  $Z$  and  $N$ , the stable nuclei are distributed as shown in Table 3.4. The largest number of stable nuclei occur when both  $Z$  and  $N$  are even. The number of nuclei with  $Z$  even and  $N$  odd is approximately equal to that with  $Z$  odd and  $N$  even. The content of Table 3.4 reflects to the fact that the nuclear force is independent of whether the nucleons are protons or neutrons.

**Table 3.4** Number of stable nuclei according to the parity of  $Z$  and  $N$

$Z$	$N = A - Z$	Number of stable nuclei
Even	Even	157
Even	Odd	53
Odd	Even	50
Odd	Odd	4
	Total	264

In the formation of a nucleus, binding energy is gained because a more stable system is obtained. The energy released should be compensated by the decrease of the final mass, with respect to the sum of the initial masses of the constituents. For example, the bound state with the smallest nuclear mass is the deuterium nucleus (deuteron); the deuteron is a hydrogen isotope consisting of one proton and one neutron ( $Z = 1, A = 2$ ). In this case, the mass deficit is 2.224 MeV, a small amount compared to  $m_p + m_n$ , but not quite negligible ( $\sim 0.2\% m_p$ ).

The binding energy (BE) is defined as the difference between the mass of the nucleus and the sum of the masses of the constituent nucleons:

$$M_A = \sum_{k=1}^A m_k - BE = (Zm_p + Nm_n) - BE. \quad (3.11)$$

The helium nucleus  ${}^4_2\text{He}$  (also called  $\alpha$  particle) is a particularly stable configuration whose binding energy is equal to 28.298 MeV. The binding energy of nuclei with small mass is not a regular function of  $A$ . For  $A > 12$ , the binding energy is approximately proportional to the number of nucleons (Fig. 3.8), with  $BE/A \sim 8$  MeV/nucleon. The elemental abundances in the Universe as a function, the mass number  $A$  are determined by the stellar nucleosynthesis and by the nuclear binding energies. The curve of Fig. 3.8 increases up to  $A \sim 60$  (the so-called iron peak). After the maximum, it decreases and ends at  $A \sim 220$  (the last stable nucleus).

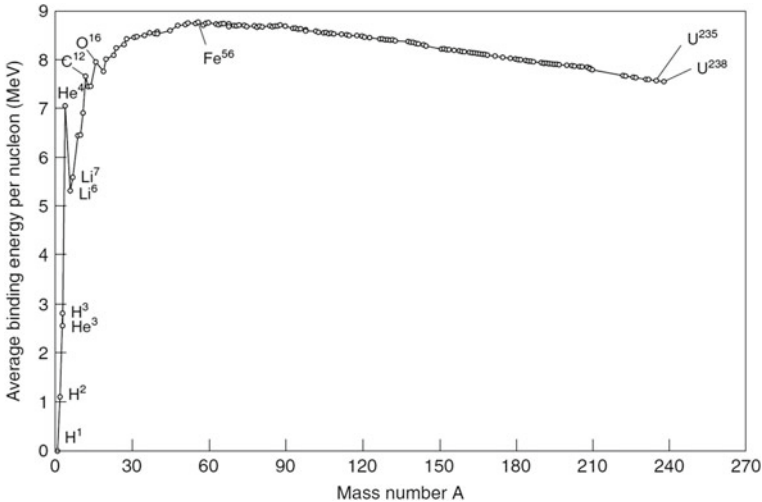


**Fig. 3.8** The binding energy per nucleon,  $BE/A$ , of stable nuclei measured as a function of  $A$ . The binding energy is defined by Eq. (3.11). The peaks correspond to particularly stable nuclei. The curve has a maximum at  $A \sim 60$



When the nuclear binding energy is plotted as a function of the nuclear charge  $Z$ , a characteristic alternation between low and high values is evident. This is caused by the higher relative binding energy of even atomic numbers with respect to odd atomic numbers, as explained by the Pauli exclusion principle. The nuclear drop model [Sect. 14.3.2 of Braibant et al. (2011)] provides a theoretical explanation for the above observations.

The cosmochemistry or chemical cosmology is the study of the chemical composition of matter in the Universe and the processes that led to the observed compositions. Meteorites are one of the most important tools for studying the chemical nature of the Solar System. Many meteorites come from material that is as old as the Solar System itself, and thus provides scientists with a record from the early solar nebula. Carbonaceous (C) chondrites<sup>1</sup> are especially primitive. C chondrites represent only a small proportion (4.6%) of meteorite falls. They have retained many of their chemical properties since their formation in the solar system about 5 billion years ago, and are therefore a major focus of cosmochemical investigations. In addition to meteoritic data, the abundances of elements in the solar system are derived from photospheric measurements on the light from the Sun. It has been known for some time that abundances determined from lines in the Sun's spectrum and abundances in CI-type carbonaceous meteorites agree quite well when normalized to the same scale. The CIs (named after the Ivuna meteorite) are a particular and rare type of chondrites. The element abundances determined from solar photospheric measurements and meteoritic CI chondrite are summarized in Fig. 3.7 and compared with the chemical composition of CRs.

The abundance of elements in the solar system is believed to be determined by the original matter composition after the Big Bang (roughly 76% hydrogen and 24% helium) and the nucleosynthesis in a number of progenitor supernova stars. For this reason, the chemical composition of the solar system is representative of the part of the Galaxy (the disk) with equal evolution history and the term cosmic abundances is sometimes used as a synonym for solar system abundances. For the relatively abundant elements (up to nickel), energy spectra for individual elements have been measured.

The fundamental properties of nuclear physics necessary to explain the binding energies as a function of  $A$  shown in Fig. 3.8 are more complicated than those necessary to understand atomic physics. However, our knowledge of nuclear interactions is advanced enough to conclude that the chemical elements everywhere in the Universe are the same as those found on Earth. It does not exist, therefore, some elusive stable element with physical properties unknown on Earth (e.g., the unobtainium on the Pandora planet of the *Avatar* movie). This is proved also by the fact that the chemical composition of CRs is not different from that found on our Solar System.

---

<sup>1</sup> Chondrites are stony meteorites that have not been modified due to melting or differentiation of the parent body.



### 3.7 Energy Spectrum of CR Protons and Nuclei

The **fluxes of nuclei** in the cosmic radiation follow a **power law** with a fast decrease with increasing energy. For **all nuclear species**, the dependence on energy is of the type

$$\Phi_i = K_i (E/\text{GeV})^{\alpha_i} \text{cm}^{-2} \text{s}^{-1} \text{sr}^{-1} \text{GeV}^{-1} \quad (3.12)$$

as in Fig. 2.7.  $E$  can be **either** expressed in terms of **energy-per-nucleon** or **energy-per-nucleus** as defined in Sect. 2.6. The parameters  $K_i, \alpha_i$  are obtained from a fit to experimental data. Different compilations (based on experiments in which groups of nucleus are clumped together) exist and the interested reader can refer to Wiebel-Sooth et al. (1998) and Hörandel (2003). When all the nuclear species are

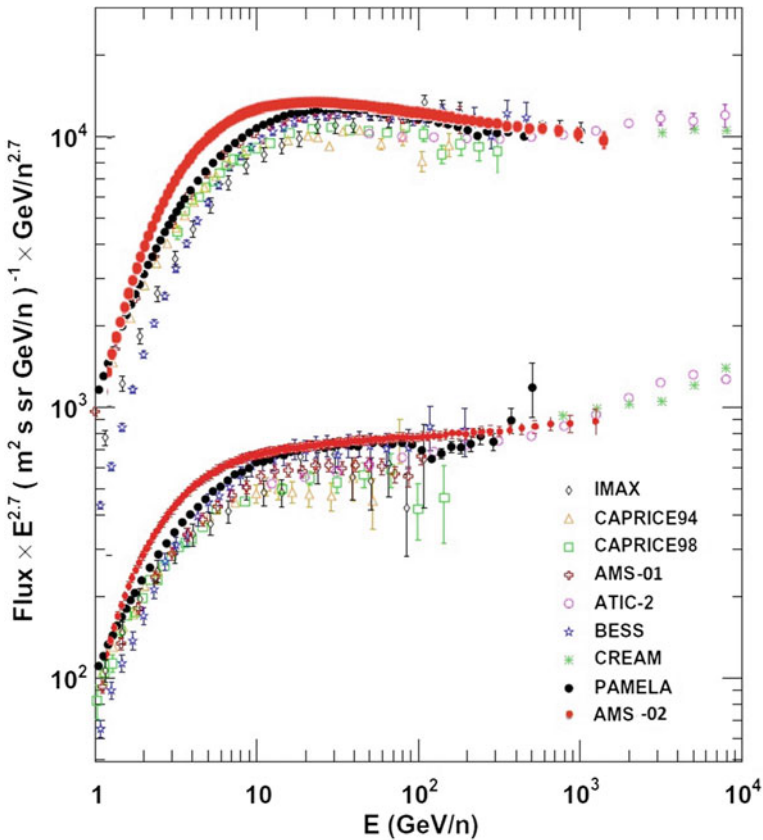


**Fig. 3.9** **Proton (upper set)** and **helium (lower set)** energy spectra above 1 GeV/n obtained by balloon-borne [CAPRICE 94 (Boezio et al. 1999) and CAPRICE 98 (Boezio et al. 2003), IMAX (Menn et al. 2000), BESS (Haino et al. 2004), ATIC-2 (Wefel et al. 2007), CREAM (Ahn et al. 2010) and space-borne AMS-01 (Alcaraz et al. 2000), AMS-02 (Haino 2013), PAMELA (Adriani et al. 2011)] experiments. Courtesy Dr. M. Boezio

summed together, we have the so-called *all-particle spectrum*, whose parameters are given in (2.20c).

Figure 3.9 shows the *proton* and *helium energy spectra* (the flux is multiplied by  $E^{2.7}$  here) above 1 GeV/n measured by recent balloon and space experiments. The recent data from AMS-02, PAMELA and CREAM show a *difference in the spectral index of proton and helium nuclei*. In addition, a *change of the slope above  $\sim 1$  TeV/n* is evident in the ATIC-2 and PAMELA data. On the contrary, *this behavior is not observed by AMS-02*.

Below 10 GeV/n, the difference among experiments is mainly due to solar modulations. At high energies, some differences well beyond the quoted statistical-only errors are present. In particular, the differences between the helium spectra

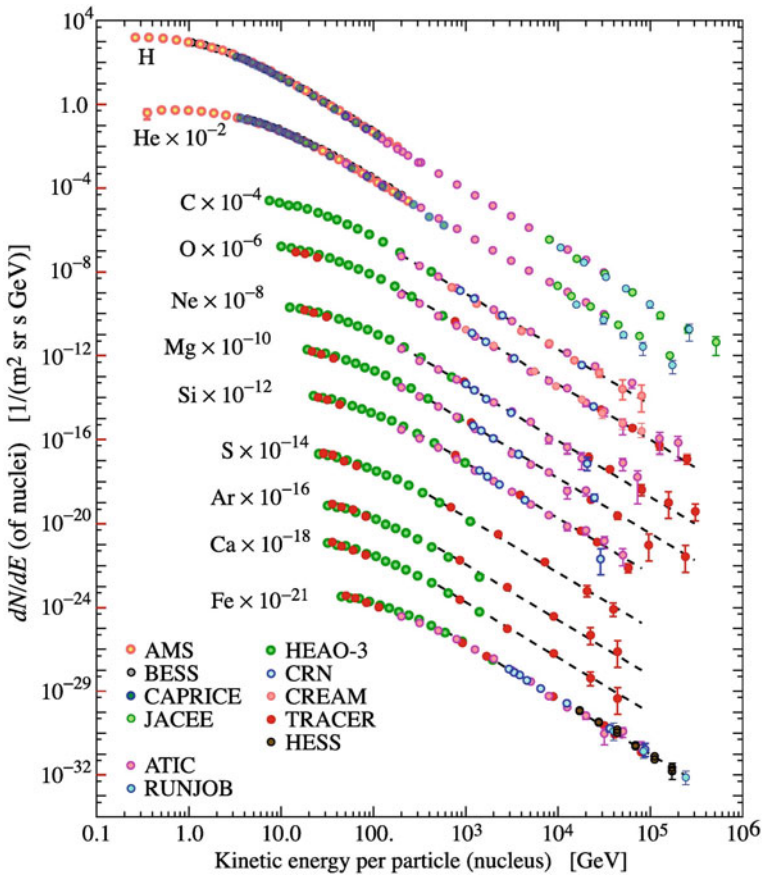


**Fig. 3.10** Fluxes  $\Phi_i$  of CR nuclei  $i = Ze$  are plotted vs. energy-per-nucleus using data from direct experiments. For a better understanding of the figure, the flux of each nuclear species is multiplied for a scaling factor. Figure due to P. Boyle and D. Muller, Sect.27: Cosmic Rays of Beringer et al. (2012)

measured by AMS-01 and PAMELA cannot be explained by statistical fluctuations. The AMS-02 data are more in agreement with PAMELA than AMS-01.

Likely, the **main sources of discrepancy** arise from the evaluation of the detector and selection **efficiencies** and from the **technique used in the determination of the energy**. In experiments using magnetic spectrometers (as AMS and PAMELA) the rigidity (and then the energy) is determined by measuring the curvature of charged particles. Consequently, the energy resolution depends on the spatial resolution of the tracking devices inserted in the magnetic field and on the topology of the event. The tracking alignment is a major ingredient for the correct energy assignment. In fact, a wrong assumption on the absolute position of the tracking sensor with respect to the magnetic field would result in a measurement affected by a systematic bias.

**Figure 3.10** shows the **major nuclear components in CRs** as a **function** of the **energy-per-nucleus**. The **exponent  $\alpha_i$**  is almost the same for all nuclear species shown in **Fig. 3.10**, **apart from protons**. This fact is of primary importance for the theories studying the acceleration mechanisms of CRs. It is also to be noticed that the data reported in **Fig. 3.10** have been obtained mainly by balloon-borne experiments (CREAM, ATIC and TRACER) with a good agreement between the different measurements. At the highest energies, the measurement is usually limited by statistics. The results of AMS-02 have not been made public yet.

In the late 2014, it is foreseen the launch and the installation of a modified version of the CREAM detector on the ISS. The detector is being reconfigured to reduce risks due to the launch, providing an order of magnitude increase in the exposure factor. A 3-year exposure on the ISS will extend measurements to energies beyond any reach possible with balloon flights and greatly reduce the statistical uncertainties on the primary flux up to the iron (Seo et al. 2014).

### 3.8 Antimatter in Our Galaxy

Equal amounts of matter and antimatter should have been produced at the beginning of the Universe as described by the Big Bang theory. The fact that **there seems to be only matter around us** is one of the **major unknown facts in cosmology** and in particle physics. The **possible presence of cosmological antimatter in the Universe** is a fundamental physics issue, which can be faced from the experimental point of view.

**Antiprotons**, as well as **positrons**, are a component of the **cosmic radiation** being **produced in the interaction** between CRs and the interstellar matter. **Positrons in CRs** were already observed in **1964** and **antiprotons** in **1979** with balloon-borne magnetic spectrometers. Secondary **antiprotons** are mainly **produced by CR protons interacting with ISM protons**



**This reaction** was used in **1955** by E. **Segrè** and O. **Chamberlain** (**Nobel Prize in 1959**) at the **Berkeley Bevatron**, and occurs above the threshold of  $E'' \gtrsim 7 \text{ GeV}$

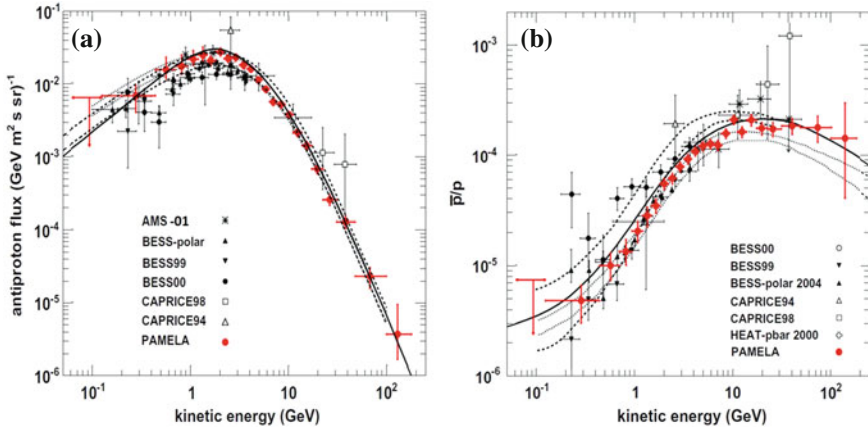


**Fig. 3.11** Measurements of the antiproton energy spectrum (a) and of the antiproton-to-proton flux ratio (b) provided by space and balloon experiments. The dotted lines indicate the upper and lower limits calculated using the model of CR propagation and interaction, including uncertainties on propagation parameters and antiproton production cross-sections, respectively. Courtesy Dr. M. Boezio and the PAMELA Collaboration

of the relativistic proton against the proton at rest. To give a first-order estimate of the antiproton flux in CRs, we should consider the  $E^{\text{tr}}$  and the steeply falling of the primary flux with energy,  $\Phi(E) \propto E^{-2.7}$ . Comparing the flux of secondary antiprotons at the threshold of  $\sim 0.1$  GeV with that of protons at  $E \sim 0.1$  GeV (where there is the maximum, see Fig. 3.10), the expected under-abundance is of factor

$$\frac{\Phi_{\bar{p}}}{\Phi_p} \sim \left(\frac{0.1}{7}\right)^{2.7} \sim 10^{-5} \tag{3.14}$$

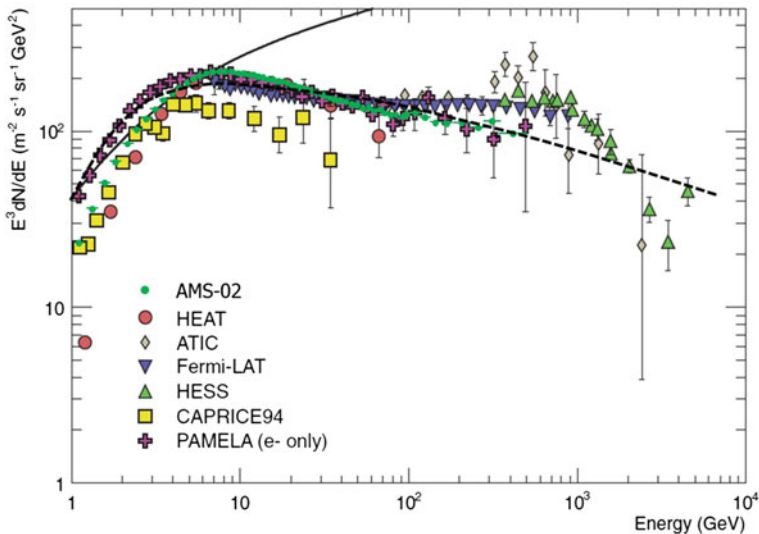
Being exactly the same as particles except for their opposite charge sign, antiparticles are readily distinguished as they bend in opposite directions in the magnetic field. Magnetic spectrometers provide a clear and simple particle/antiparticle separation and probe the existence of antimatter in our Galaxy. Waiting for the AMS-02 results, at present the best constraints on antiproton data come from the BESS and PAMELA experiments (Boezio and Mocchiutti 2012).

Figure 3.11 left shows the antiproton energy spectrum measured by recent CR experiments. On the right side, we show the antiproton-to-proton flux ratio as a function of energy. This ratio is in agreement with the simple estimate (3.14). In the figure, the results of detailed theoretical calculations (see Sect. 5.4), which assume pure secondary production of antiprotons during the propagation of CRs in the Galaxy, are also reported. The measured spectrum agrees with calculations, consistently with the hypothesis that the observed antiprotons are secondary particles produced by CR interactions with the interstellar medium.

No heavier antinuclei have been detected so far. The BESS experiment provides the lowest upper limit to date on the **relative antihelium-to-helium ratio,  $7 \times 10^{-8}$** , in the **rigidity range 1–14 GV**. BESS also provides the **lowest upper limit** for the **antideuteron flux of  $2 \times 10^{-4}(\text{m}^2\text{s sr GeV/n})^{-1}$**  at the 95 % confidence level, between 0.17 and 1.15 GeV/n. The detection of a single antideuteron or antihelium nucleus would impact our understanding of the matter/antimatter asymmetry of the Universe.

### 3.9 Electrons and Positrons

**Electrons and positrons** constitute about **1% of the CRs**, as shown in Table 3.3. This component provides additional information on the acceleration sites and CR propagation in the Galaxy. High-energy electrons are **subject to a number of electromagnetic energy loss processes** already in **proximity of the sources**, where the **matter density** and the **magnetic fields** are **large**. The **accelerated electrons** are the **source of most of the nonthermal electromagnetic radiation** measured by astronomers from **radio to X-rays**, as presented in Sect. 5.8 and widely discussed in Chap. 8. These processes cause distortions of  $e^-$  injection energy spectra as they propagate through the interstellar medium from their sources and they potentially provide information



**Fig. 3.12** **The electron plus positron energy spectrum** from different space-based, balloon, and ground-based experiments. The flux is multiplied by  $E^3$ . The **black full line** shows for reference the proton spectrum. The theoretical calculation (**dashed line**) is based on the prediction of secondary electrons produced by the interaction of CRs with the interstellar matter. Figure adapted from the Sect. 27. Cosmic Rays of Beringer et al. (2012) and references therein. The AMS-02 data have been extracted from Aguilar et al. (2013)

on the propagation, confinement, and production mechanisms of high-energy particles. Electrons **directly produced at accelerator sites** are called *primary electrons*.

In recent years, the knowledge of the leptonic component in the CRs has gained greatly from new experimental results from the ATIC balloon-borne experiment (Chang et al. 2008), the Fermi-LAT (Ackermann et al. 2012) and PAMELA (Adriani et al. 2011) satellite-based experiments. The **Fermi-LAT** experiment, Sect. 8.6.1, is mainly devoted to  **$\gamma$ -ray astronomy** and is also performing CR measurements (Thompson et al. 2012). It is **not instrumented with a magnetic spectrometer**; **electron and positron** components are **measured separately** by exploiting **Earth's shadow**, which is offset in opposite directions for opposite charges due to the **magnetic field of the Earth** (Ackermann et al. 2012).

Finally, the **AMS-02** (Aguilar et al. 2013) experiment has recently reported results on the **largest sample** of measured **CR leptons**. Their results on **fluxes, ratios, and anisotropies** of  $e^\pm$  represent a fundamental step towards the comprehension of the lepton component of CRs. The measurement is based on data collected during the first two years of operation, with  $6.8 \times 10^6$   $e^\pm$  events in the energy range 0.5–350 GeV.

Figure 3.12 shows the **electron plus positron energy spectrum multiplied by  $E^3$**  as measured by different experiments. Within systematic errors the **entire electron spectrum** from few GeV to 1 TeV can be fitted by a **power law  $\Phi_e(E) \propto E^{-3.1}$** . If electrons are **emitted** by astrophysical sources **with a spectral index  $\alpha_e$** , a **steepening of the spectrum by one power is expected** because of the **electron radiation losses**, as we will show in Sect. 5.8. The **measured spectral index  $\sim 3$**  indicates a **spectral index of CR sources  $\alpha_e \sim 2$** .

The presence of a **structure** in a smooth spectrum of the lepton component would represent an important **signature for unexpected physics**. In particular, from **annihilation of dark matter candidates** (Sect. 13.6) or from the **presence of sources of nearby and active galactic accelerator** of CR electrons. An excess of electrons in the range 300–700 GeV with respect to that expected from conventional diffuse electron sources has been reported by ATIC and PPB-BETS (a long duration balloon flight using the Polar Patrol Balloon in Antarctica). Fermi-LAT has observed a spectral flattening of the  $e^\pm$  spectrum between 70–200 GeV and a milder excess at higher energies with respect to those of ATIC and PPB-BETS. AMS-02 data has produced **no evidence of structures** in the electron energy spectrum, at present **up to 350 GeV**. However, a change in the spectral distribution with increasing energies is seen, compatible with the increases in the positron component discussed below.

Secondary  $e^+$  and  $e^-$  are produced by CR interactions with the interstellar matter, as end products of the decay of short lived secondary particles (mostly pions via the decay  $\pi^\pm \rightarrow \mu^\pm \rightarrow e^\pm$ ). These secondary  $e^\pm$  add to primary electrons accelerated at sources.

In Fig. 3.12, the dashed line refers to a **theoretical calculation of the electron plus positron spectrum** based on the propagation of CRs in the Galaxy. This computer-code calculation (**GALPROP**, Sect. 5.4) describes in detail the propagation of primary particles (protons, electrons, and nuclei) from the sources through the interstellar medium.

### 3.9.1 The Positron Component

Experiments using magnetic spectrometers can distinguish the sign of the electric charge. This allows the measurement of the positron fraction in the  $e^\pm$  component of CRs as a function of the energy. The dominant background is represented by misidentified CR protons. Unlike electrons, which are present as primary component in CR sources, the vast majority of positrons arise as secondary products of CR interactions in our Galaxy.

Figure 3.13 shows the positron energy spectrum  $E^3 \Phi_{e^+}(E)$  as a function of the energy  $E$ . The dashed line shows the prediction from the aforementioned computer code of primary propagation in the interstellar medium (Sect. 5.4). Above few GeV, a significant excess with respect to the secondary production by CR propagation is observed. PAMELA first (Adriani et al. 2009) and then Fermi-LAT observed that the  $E^3 \Phi_{e^+}(E)$  flattens up to  $\sim 30$  GeV, before rising again above 30 GeV.

This behavior has been recently confirmed with high statistics and extended up to 350 GeV by AMS-02. In this experiment, the background is efficiently suppressed by requiring a minimal amount of material crossed in the TRD and ToF detectors. In addition, a good match between the particle momentum reconstructed in the nine tracker layers of the silicon spectrometer and the energy measured in the electromagnetic calorimeter is required. The performance of the TRD results in a proton rejection efficiency larger than  $10^3$  keeping 90 % of positrons. The calorimeter provides a rejection factor better than  $10^3$  for protons with momentum up to 1 TeV/c.

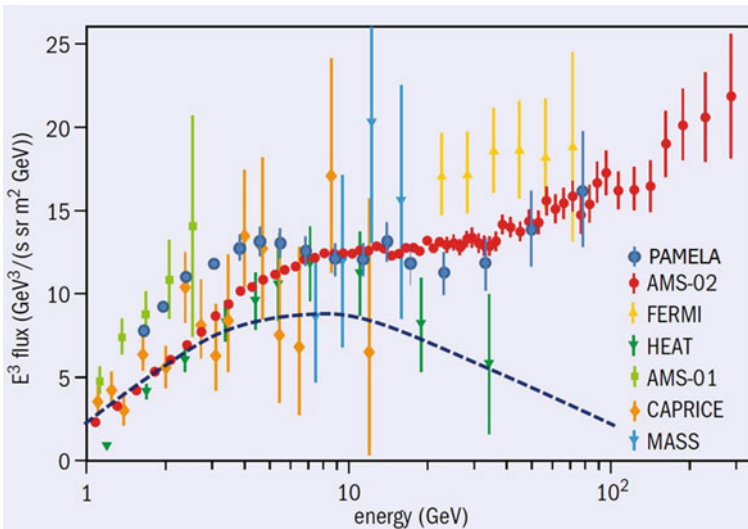


**Fig. 3.13** The positron energy spectrum multiplies for  $E^3$  measured by different balloon-borne (CAPRICE, HEAT, MASS) and space-borne (AMS-01, AMS-02, PAMELA, Fermi-LAT) experiments. The dashed lines show the calculation using the GALPROP program. Courtesy of prof. Manuel Aguilar Benítez. See Aguilar et al. (2013) and references therein



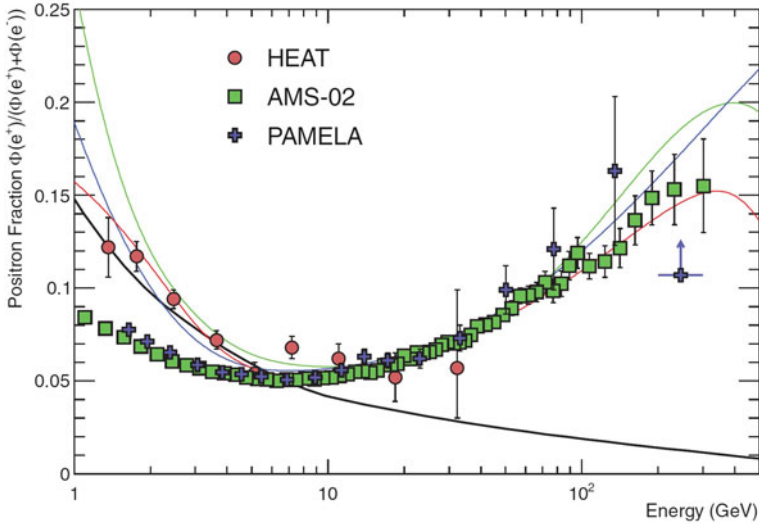


**Fig. 3.14** The **positron fraction** (ratio of the flux of  $e^+$  to the total flux of  $e^+ + e^-$ ) as a function of the energy measured HEAT, PAMELA, and AMS-02. The heavy **black line** is a model of pure secondary production using a detailed propagation model of CRs (Sect. 5.4). The **three thin lines** show three representative **attempts to model** the positron excess with different phenomena discussed in Sect. 13.9.3: **dark matter decay (green)**; **propagation physics (blue)**; **production in pulsars (red)**. The ratio below 10 GeV is dependent on the polarity of the solar magnetic field. Figure from the Sect. 27. Cosmic Rays of Beringer et al. (2012)

The combination of the two factors leads to an overall proton-to-positron rejection power of  $\sim 10^6$  for most of the energy range under study.

The **increase of the positron component** is still more **evident** in Fig. 3.14, which shows the positron fraction, i.e. the **ratio between  $\Phi_{e^+}/(\Phi_{e^+} + \Phi_{e^-})$**  measured by HEAT (Beatty et al. 2004), PAMELA (Adriani et al. 2013), and AMS-02 (Aguilar et al. 2013) as a function of the energy  $E$ . The **positron-fraction spectrum does not exhibit fine structures** and **steadily increases** in the region between **10 and 250 GeV**. In the high statistics AMS-02 sample the ratio is of the order of  $\sim 10\%$  above a few tens of GeV. As a consequence, since positrons are always created in pair with an electron,<sup>2</sup> **about 90% of the observed electrons must be of primary origin**.

The positron fraction at energies below  $\sim 10$  GeV is systematically lower than data collected during the 1990s by other experiments. This discrepancy is well interpreted because of solar modulation effects. At high energies (above 10 GeV) the positron fraction increases significantly with energy. This increase is well above that expected

<sup>2</sup> This is exact in the case of conversion of a  $\gamma$ -ray. Positrons can be produced as the end stage of hadronic interactions by the decay chain  $\pi^+ \rightarrow \mu^+ \rightarrow e^+$ . On average, isotopic spin invariance on  $\pi^\pm$  production guarantees the presence of an electron through the decay  $\pi^- \rightarrow \mu^- \rightarrow e^-$  with equal rate. However due to the fact that CRs are positively charged, secondary positrons are in slight excess over electrons.



from a model in which all positrons are of secondary origin: the heavy black line in Fig. 3.14 shows the result of a calculation based on such an assumption.

### 3.9.2 Considerations on the $e^+$ , $e^-$ Components

The  $\bar{p}/p$  ratio ( $\sim 10^{-5}$ – $10^{-4}$ ) shown in Fig. 3.11 demonstrated that the antiproton flux is in overall agreement with a pure secondary component. The electron component declines faster with increasing energy than the baryonic one. At 1 TeV, the ratio between CR electrons and protons is  $\sim 10^{-3}$ . The  $e^+/(e^- + e^+)$  ratio (about 10%) indicates that also most of the detected electrons are of primary origin, although the fraction of secondary leptons is much larger than that of secondary baryons. This is an important information concerning the astrophysical origin of the leptonic component. Due to the presence of magnetic fields, the typical distance over which 1 TeV electrons lose half its total energy is estimated to be 300–400 pc when they propagate within  $\sim 1$  kpc of the Sun (Aharonian et al. 1995). Electrons are affected more readily by energy-dependent diffusive losses, convective processes in the interstellar medium, and perhaps reacceleration during propagation from their sources to us. For these reasons, at energies above a few hundred GeV, the majority of electrons is supposed to be originated by sources closer than a few hundred pc. We will return on this estimate in Sect. 5.8, after having presented the synchrotron energy loss. High-energy CR electrons really probe CR production and propagation in the nearby region of our Galaxy.

In conclusion, due to their large energy losses, it seems not plausible (contrary to the case of protons and nuclei) that the observed electrons originate from a uniform distribution of sources in the Galaxy. If the source is too far, the probability that an electron reaches the Earth is extremely small. More likely, primary high-energy electrons observed on Earth originate from a small number of sources well localized in space and relatively close (on a scale of galactic distances) to the Solar System.

Concerning the measured data on the positron fraction above 10 GeV (Fig. 3.14), it has stimulated a large scientific debate. The  $e^+/(e^- + e^+)$  ratio cannot in fact be understood by models describing the production of secondary CRs during propagation in the Galaxy (see Chap. 5). Several theoretical explanations have been proposed to explain the observed excess: an astrophysical origin, such as nearby pulsars or microquasars, or exotic sources, as for instance the annihilation of dark matter particles in the proximity of our Galaxy. We will return of the subject in Chap. 13. The agreement between PAMELA, Fermi-LAT and AMS-02 data reduces the possibility of a systematic bias and gives confidence that the increase of the positron flux is to be ascribed to a physical, still unknown, effect. A detailed description of astrophysical models which can explain the origin of the positron excess can be found in Serpico (2012). It is possible that a final word will be given by the increased statistics from the AMS-02 experiment. The present data set covers only about 10% of the expected number of leptons. AMS-02 represents undoubtedly the leading experiment for the direct study of the cosmic radiation in coming years.

## References

- M. Ackermann et al., Measurement of separate cosmic-ray electron and positron spectra with the Fermi-LAT. *Phys. Rev. Lett.* **108**, 011103 (2012)
- O. Adriani et al., (PAMELA Collaboration). The cosmic-ray positron energy spectrum measured by PAMELA. *Phys. Rev. Lett.* **111** (2013) 081102. Also: [arXiv:1308.0133](https://arxiv.org/abs/1308.0133)
- O. Adriani et al., *Science* **106**, 201101 (2011)
- O. Adriani et al., (PAMELA Coll.) Observation of an anomalous positron abundance in the cosmic radiation. *Nature* **458**, 607–609 (2009)
- O. Adriani et al., (PAMELA Coll.) The cosmic-ray electron flux measured by the PAMELA experiment between 1 and 625 GeV. *Phys. Rev. Lett.* **106**, 201101 (2011)
- M. Aguilar (AMS-02 collaboration) AMS-02 provides a precise measure of cosmic rays. *CERN Courier* 53 (2013) 8, 23–26. Also: B. Bertucci ICRC 2013 (ID 1267)
- M. Aguilar et al., (AMS-02 Collaboration) First result from the alpha magnetic spectrometer on the ISS: Precision measurement of the positron fraction in primary cosmic rays of 0.5–350 GeV. *Phys. Rev. Lett.* **110**, 14–141102 (2013)
- F.A. Aharonian, A.M. Atoyan, H.J. Voelk, High energy electrons and positrons in cosmic rays as an indicator of the existence of a nearby cosmic Tevatron. *Astron. Astrophys.* **294**, L41 (1995)
- H.S. Ahn et al., *Astrophys. J. Lett.* **714**, L89 (2010)
- H.S. Ahn et al., (CREAM Coll.) The cosmic ray energetics and mass (CREAM) instrument. *T. Nucl. Instrum. Methods A* **579**, 1034–1053 (2007)
- J. Alcaraz et al., *Phys. Lett. B* **490**, 27 (2000)
- K. Asakimori et al., Cosmic-ray proton and helium spectra: results from the JACEE experiment. *Astrophys. J.* **502**, 278–283 (1998)
- M. Ave et al., Composition of primary cosmic-ray nuclei at high energies. *Astrophys. J.* **678**, 262–273 (2008)
- J.J. Beatty et al., New measurement of the cosmic-ray positron fraction from 5 to 15 GeV. *Phys. Rev. Lett.* **93**, 24112 (2004)
- J. Beringer et al., (Particle Data Group). The Review of Particle Physics. *Phys. Rev. D* **86** (2012) 010001 and 2013 partial update for the 2014 edition
- J. Blümer, R. Engel, J. Hörandel, Cosmic rays from the knee to the highest energies. *Prog. Part. Nucl. Phys.* **63**, 293–338 (2009)
- M. Boezio et al., *Astropart. Phys.* **19**, 583 (2003)
- M. Boezio et al., *Astrophys. J.* **518**, 457 (1999)
- M. Boezio, E. Mocchiutti, Chemical composition of galactic cosmic rays with space experiments. *Astropart. Phys.* **39–40**, 95–108 (2012)
- S. Braibant, G. Giacomelli, M. Spurio, *Particle and Fundamental Interaction* (Springer, Berlin, 2011). ISBN 978-9400724631
- J. Chang et al., An excess of cosmic ray electrons at energies of 300–800 GeV. *Nature* **456**, 362 (2008)
- V.A. Derbina et al., Cosmic-ray spectra and composition in the energy range of 10–1000 TeV per particle obtained by the RUNJOB experiment. *Astrophys. J.* **628**, L41–L44 (2005)
- J.J. Engelmann et al., Charge composition and energy spectra of CR nuclei for elements from Be to Ni. results from HEAO-3-C2. *Astr. Astroph.* **233** (1990) 96
- O. Ganel et al., Beam tests of the balloon-borne ATIC experiment. *Nucl. Instrum. Methods A* **552**(3), 409–419 (2005)
- M. Garcia-Munoz, G.M. Mason, J.A. Simpson, The cosmic-ray age deduced from the Be-10 abundance. *Astrophys. J.* **201**, L145 (1975)
- M. Garcia-Munoz, G.M. Mason, J.A. Simpson, The age of galactic cosmic rays derived. *Astrophys. J.* **217**, 859–877 (1977)
- P.K.F. Grieder, *Cosmic Rays at Earth* (Elsevier, New York, 2001). ISBN 978-0444507105
- S. Haino (ID 1265) and V. Choutko (ID 1262) ICRC 2013
- S. Haino et al., *Phys. Lett. B* **594**, 35 (2004)

- J.R. Hörandel, On the knee in the energy spectrum of cosmic rays. *Astropart. Phys.* **19**, 193–220 (2003)
- J. Hörandel, Cosmic-ray composition and its relation to shock acceleration by supernova remnants. *Adv. Space Res.* **41**, 442 (2008)
- K. Lodders, H. Palme, H.P. Gail. Abundances of the elements in the solar system. Chapter 4 of *Landolt-Börnstein, New Series, Astronomy and Astrophysics*, Springer, Berlin (2009). Also: [arXiv:0901.1149](https://arxiv.org/abs/0901.1149)
- K. Lodders, Solar system abundances and condensation temperatures of the elements. *Astrophys. J.* **591**, 1220 (2003)
- W. Menn et al., *Astrophys. J.* **533**, 281 (2000)
- E.S. Seo, Direct measurements of cosmic rays using balloon borne experiments. *Astropart. Phys.* **39–40**, 76–87 (2012)
- E.S. Seo et al., Cosmic ray energetics and mass for the international space station (ISS-CREAM). *Adv. Space Res.* **53**, 1451–1455 (2014)
- P.D. Serpico, Astrophysical models for the origin of the positron “excess”. *Astropart. Phys.* **39–40**, 2–11 (2012)
- J. Simpson, Elemental and isotopic composition of the galactic cosmic rays. *Ann. Rev. Nucl. Part. Sci.* **33**, 323–382 (1983)
- D.J. Thompson, L. Baldini, Y. Uchiyama, Cosmic ray studies with the Fermi gamma-ray space telescope Large Area Telescope. *Astropart. Phys.* **39–40**, 22–32 (2012)
- J.P. Wefel et al., ICRC Conference 2007 (Vol. 2, p. 31)
- B. Wiebel-Sooth, P.L. Biermann, H. Meyer, Cosmic rays. VII. individual element spectra: prediction and data. *Astron. Astrophys.* **330**, 389–398 (1998)

## Chapter 4

# Indirect Cosmic Rays Detection: Particle Showers in the Atmosphere

Above  $10^{15}$  eV, the CR flux drops below a few tens of particles per  $\text{m}^2$ -year. It is no longer possible to detect the incident particles above the atmosphere before they interact. Direct experiments (characterized by a small geometrical factor  $A \cdot \Delta\Omega$  [ $\text{cm}^2 \text{ sr}$ ]) must be replaced by ground-based instruments that cover up to several thousands of  $\text{km}^2$ , the extensive air shower (EAS) arrays. They use a completely different approach to CR measurements, started by pioneering experiments soon after World War II by Auger, Kohlhörster and Rossi.

The EAS arrays are in most cases large area and long duration experiments studying, as accurately as possible, the nature, flux, mass, direction of primary CRs up to the highest energies. Air showers are initiated by primary CRs, through the interaction with a nucleus in the atmosphere. In addition to the hadronic component the decays of short-lived hadrons lead to a shower of particles: photons, electrons, and positrons constitute the electromagnetic (EM) component; muons and neutrinos constitute the penetrating component. All these particles travel at the speed of light in the atmosphere approximately along the direction of the primary CR.

High energy primary  $\gamma$ -rays induce an almost pure EM cascade. In Sect. 4.3 we present a simple model for the EM cascade initiated by a  $\gamma$ -ray, which can be mathematically treated using differential transport equations of  $e^\pm$  and  $\gamma$  in the atmosphere. Some simple features, as derived from approximate solutions of the cascade equations, are presented. The cascades initiated by primary CR protons or nuclei have additional features. They are also characterized by large event-to-event fluctuations. Their description is today achieved using full Monte Carlo simulations, which follow the details of the development of the EM and muonic components. It is interesting, however, to obtain (Sect. 4.4) a first-order estimate of the quantities, which can be measured by experiments, both for the muonic and the EM components. In the first sections of the chapter, we enumerate the main showers features (denoted as SF1, SF2, ... , SF12), which characterize EM and muonic component of the cascade initiated by  $\gamma$ -rays, protons and heavier nuclei. These characteristics are

---

<sup>1</sup> For historical reasons, photons with energy in the MeV scale and beyond are called  $\gamma$ -rays.

confirmed by detailed Monte Carlo simulations of air showers in the atmosphere (Sect. 4.5), which are used by the experiments to interpret their observations.

EAS arrays are installed on ground and are sometimes referred to as indirect detection experiments. Modern shower arrays employ complementary techniques (Sect. 4.6) such as scintillators, air Cherenkov detectors, etc. to measure simultaneously as many shower parameters as possible, in order to reduce the model dependence in the energy and mass number  $A$  determination.

The features of the EM and muonic cascades will be used in Sects. 4.8, 4.9 and 4.10 to illustrate how indirect experiments can derive the CR flux and properties in the energy region around the *knee* of CRs.

## 4.1 Introduction and Historical Information

Air showers are the particle cascades produced by the interaction of a cosmic ray with a nucleus in the atmosphere. The term “shower” is the English translation done by P. Blackett of the Italian expression *sciame* first used by B. Rossi. The atmosphere (Sect. 4.2) acts as a calorimeter and becomes part of the detection system. As this is not a fully controlled environment, in some cases the atmospheric conditions are carefully monitored and recorded along with the air-shower array data.

The main techniques used to measure EAS can be classified as follows: detectors that measure the particle content of the shower at ground; detectors that measure the light produced by the propagation of the EAS itself in the atmosphere. The main disadvantage of the experiments detecting light is that they can only take data on dark, moonless nights, with a duty cycle of  $\sim 5\text{--}10\%$ . In EAS arrays, usually the CR direction is inferred by the relative arrival times of the signals on different counters, the energy from the integration of the measured density of secondary particles (the electromagnetic cascade, the muons or the visible light induced by the shower of charged particle in the atmosphere) at the detector level. The estimate of the mass of the incoming CR is a much more difficult task.

Direct measurements of the CR flux have provided a power law dependence for the CR energy spectrum up to  $\sim 10^{15}$  eV. Observations in 1959 of EAS indicated a steepening at around  $3 \times 10^{15}$  eV (the knee). In 1963, observations made with the first large shower array discovered another structure just above  $10^{18}$  eV. For the early years of indirect measurements, see the recent review (Kampert and Watson 2012).

The main drawback of EAS experiments is that the interpretation of the observations depends on the model used to describe the hadronic interactions of CRs with air nuclei (Anchordoqui et al. 2004). Uncertainties in the development of cascades generated by CRs with energies above  $10^{16}\text{--}10^{17}$  eV are unavoidable. In addition, relevant quantities for shower development (as the number of secondary hadrons and

their momentum distribution occur in the very forward direction and are not accessible at collider experiments.<sup>2</sup>

One has, therefore, to rely on phenomenological interaction models, which differ in their predictions, making the task of retrieving information from air shower data even more difficult at increasing energies. Other uncertainties are related to the structure of the atmosphere, which is not a homogeneous calorimeter, and to its variations.

EAS arrays measure the overall cosmic ray spectrum summing up the contribution of all nuclear species. The measurement of the total energy of a primary CR through the observation of the induced cascades relies on a much firmer theoretical basis than the measurement of its mass. Uncertainties in the hadronic physics make it hard to separate the observable quantities produced by protons or by iron nuclei. No EAS experiment has measured up to now the primary composition of cosmic rays on an event-by-event basis. Instead, through the measurement of one or more of the observables, which are sensitive to the mass (Sect. 4.10), the flux of groups of nuclei as a function of the energy was estimated using statistical techniques.

## 4.2 The Structure of the Atmosphere

The main parameter concerning the development of a cascade of secondary CRs is the amount of matter above any atmospheric layer, in which the primary CR has interacted. This quantity is called the (vertical) atmospheric depth,  $X_v$ . This depth is the integral in altitude of the atmospheric density  $\rho$  above the observation level  $h$  (see Fig. 4.1):

$$X_v \equiv \int_h^\infty \rho(h') dh' \tag{4.1}$$

The variation of the atmospheric density with altitude is a very important information for the modeling of shower cascades in the atmosphere, and for the competition between interaction and decay of secondary mesons.

The dependence of density on  $h$ ,  $\rho(h)$ , can be determined using thermodynamics. The pressure  $p$  (atmospheric weight per unit of surface  $S$ ) at the depth  $X_v$  is  $p = \frac{mg}{S} = \frac{g}{S} \int_h^\infty \rho(h') \cdot S dh' = gX_v$  while, from (4.1),  $\rho = -dX_v/dh$  (the  $-$  represent

---

<sup>2</sup> Before the LHC physics runs, someone expressed concerns over the safety, and attempted to halt the beginning of the experiments through petitions to the US and European Courts. These opponents asserted that the LHC experiments have the potential to create micro black holes that could grow in mass or release dangerous radiation leading to doomsday scenarios, such as the destruction of the Earth. Any doomsday scenario at the LHC was ruled out before starting of the physics runs simply noting that the physical conditions and events created in the LHC experiments occur naturally and routinely in the Universe without hazardous consequences. In particular, ultra high energy CRs that are impacting on Earth with energies considerably higher than those reached in any man-made collider have never destroyed the Earth!

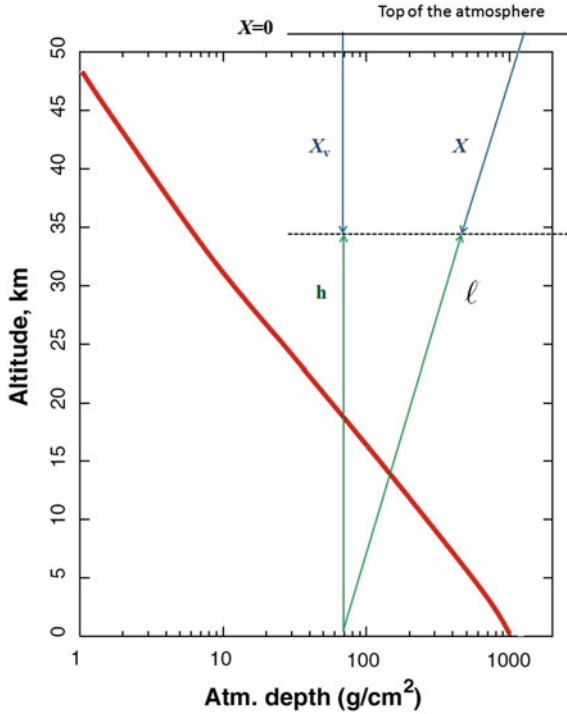


Fig. 4.1 The red curve represents the altitude in km, which corresponds to a given residual atmospheric depth  $X_v$ . For a proton, the interaction length is  $\sim 85 \text{ g cm}^{-2}$ ; this is the amount of material crossed by a proton that reaches a height of about 20 km above ground. The atmospheric depth  $X$  for non-vertical directions is usually denoted as slant atmospheric depth. The total depth of the atmosphere is  $X_v^{atm} \simeq 1,030 \text{ g cm}^{-2}$ . It is easy to verify that this corresponds to  $\sim 10 \text{ m}$  of a material with the density of water (meter of water equivalent = m.w.e). Sometimes, it is useful to measure the atmospheric depth in terms of m.w.e. The geometrical definitions of the quantities given in the text ( $X_v, X, h$  and  $\ell$ ) are also sketched in the figure

the fact that  $\rho$  decreases as  $h$  increases). Assuming the atmosphere as a perfect gas:

$$\rho = \frac{Mp}{kT} \tag{4.2}$$

where  $k$  is the Boltzmann constant,  $M$  is the mean molecular mass of air. The average mass of the atmosphere, composed mainly by nitrogen (78%) and oxygen (21%), is  $\langle A \rangle = A_{atm} \simeq 14.5$ . However, this average mass strongly depends on the altitude. As most molecules are biatomic,  $M = 2A_{atm} \times m_p = 4.8 \times 10^{-23} \text{ g}$  and:

$$T(h) = \frac{M p}{k \rho} = - \frac{M}{k} \frac{gX_v}{dX_v/dh} \tag{4.3}$$

where  $T(h)$  is the temperature at the height  $h$  in the atmosphere. The temperature of the troposphere (extending from ground up to 10–20 km of height) decreases approximately with increasing altitude at a rate  $\sim -6.5\text{K/km}$ . Nevertheless, to a first approximation, the atmosphere is considered as an isothermal gas with  $T(h) = \text{const}$ . Under this *isothermal approximation*, Eq. (4.3) can be easily integrated and:

$$X_v = X_v^{\text{atm}} e^{-h/h_0}; \quad \text{with} \quad X_v^{\text{atm}} = 1,030 \text{ g cm}^{-2}. \quad (4.4)$$

The *atmospheric scale height*  $h_0$  is defined as:

$$h_0 = \frac{kT}{Mg} \quad (4.5)$$

Using the numerical value of  $M$ , at the surface of Earth ( $T \simeq 290 \text{ K}$ ),  $h_0 \simeq 8.4 \text{ km}$ . In the region where CRs interact, the temperature is between 210–240 K, and  $h_0 \simeq 6\text{--}7 \text{ km}$ . The vertical thickness of the atmosphere  $X_v^{\text{atm}}$  corresponds for incoming CRs to a calorimeter of variable density with  $\sim 11$  interaction lengths and 28 radiation lengths (compare with Table 3.1).

If we consider that the temperature decreases with increasing altitude  $h$ , some analytical parameterizations are obtained [see for instance Gaisser (1991) and Stanev (2010)]. They are useful as input for Monte Carlo simulations of the CR cascades. Figure 4.1 shows the dependence of  $X_v$  (here along the  $x$ -axis) upon  $h$  as derived with the parameterization reported in Stanev (2010).

Considering the curvature of the Earth ( $R_\oplus$  is the Earth radius) and a non-vertical direction (zenith angle  $\theta$ ), the relation between  $h$  and path length  $\ell$  in the atmosphere is:

$$h = \ell \cos \theta + \frac{1}{2} \frac{\ell^2}{R_\oplus} \sin^2 \theta. \quad (4.6)$$

The atmospheric depth for such an inclined direction is called the *slant depth* and corresponds to:

$$X = \int_{\ell}^{\infty} \rho(h) d\ell \quad (4.7)$$

For zenith angles  $\theta < 60^\circ$  one can scale the slant depth as

$$X \simeq X_v \cos \theta \quad \text{and} \quad \rho = \frac{X_v}{h_0} \simeq \frac{X \cos \theta}{h_0} \quad (4.8)$$

(flat Earth approximation). For horizontal directions, the slant depth corresponds to about  $X(\theta = 90^\circ) = 36,000 \text{ g cm}^{-2}$ .



### 4.3 The Electromagnetic (EM) Cascade

The showers containing only  $e^+$ ,  $e^-$  and  $\gamma$ -rays (called *EM showers* henceforth) and initiated by photons or electrons are mathematically described using *differential transport equations*, which include the particle energy losses and particle production. The most popular description of the EM shower was developed in the 1930s by Rossi and Greisen.

EM showers are governed mainly by (i) bremsstrahlung of electrons (here, we refer as *electrons* both to electrons and positrons) and (ii) pair production by photons. In addition to bremsstrahlung, electrons are subject to excitation/ionization energy loss. The total energy loss  $dE/dX$  of electrons is described by Eq. (3.6). The *radiation length*,  $X_0$ , is defined as: (a) the mean free path of a high-energy electron, corresponding to the distance over which it loses all but  $1/e$  of its energy by bremsstrahlung, and (b)  $7/9$  of the mean free path for pair production by a high-energy photon. The factor  $7/9$  arises from QED arguments. For this reason, Eq. (3.6) can formally be used to describe also the propagation of high-energy photons in a medium.

The radiation length,  $X_0$  and the *critical energy* (the energy at which radiation energy losses equal those deriving from excitation/ionization) depend on the material. From Table 3.1 for electrons in air:

$$X_0 \simeq 37 \text{ g cm}^{-2}; \quad E_c \simeq 86 \text{ MeV}. \quad (4.9)$$

The bremsstrahlung (dominant for  $E > E_c$ ) and the excitation/ionization energy loss (dominant for  $E < E_c$ ) are competing processes in showers.

As a matter of nomenclature, in the following we indicate with:

1.  $N_e^i, N_\gamma^i, N_\pi^i, N_\mu^i$  the number of electrons, hard photons (=  $\gamma$ -rays), pions and muons present in the cascade induced by a primary particle  $i$ . The index  $i = \gamma, p, A$  corresponds to a primary  $\gamma$ -ray, proton or nucleus with mass  $A$ , respectively;
2.  $N_{e_{\max}}^i$  corresponds to the number of  $e^\pm$  at the maximum of the EM shower induced by a primary particle ( $i = \gamma, p, A$ );
3.  $X_{\max}^i$  corresponds to the atmospheric depth (Sect. 4.2) in  $\text{g cm}^{-2}$  where the maximum of the EM shower induced by a primary particle ( $i = \gamma, p, A$ ) occurs in the atmosphere.

As shown in Sect. 3.9 the flux of electrons drops sharply at energies above 1 TeV. On the contrary, pure electromagnetic showers initiated by  $\gamma$ -rays are increasingly interesting due to a sizeable flux above the TeV observed through Imaging Cherenkov telescopes (Chap. 9). The main difference between a shower initiated by a photon and that induced by a primary proton or nucleus is the presence in the latter of a hadronic component, which develops a significant muon cascade (Sect. 4.4.1).

### 4.3.1 Heitler’s Model of EM Showers

Some properties of EM showers can already be understood within the very simple model due to Heitler (Heitler 1944). In this model, the evolution of electromagnetic cascades is described as a perfect binary tree (Fig. 4.2). An incoming electron interacts in the atmosphere after traveling a certain “step” and produces two new particles, each with half the energy of the initial particle. Similarly, a photon converts into an electron-positron pair if its energy  $> 2m_e$ . In the following, the cross sections of the two processes are assumed equal, independent of the energy and additional energy loss mechanisms are ignored. The radiation length  $X_0$  represents both photon’s and electron’s mean free paths in the matter, neglecting for the former the factor  $7/9$ . In more detailed models for shower developments the energy distribution of the bremsstrahlung photons should be considered [see Gaisser (1991)].

Let us now quantify the length of the “step”. The important quantity is the product  $X = x\rho$  ( $\text{g cm}^{-2}$ ) of the distance  $x$  (cm) traversed in a medium and the medium density  $\rho$  ( $\text{g cm}^{-3}$ ). The energy loss of bremsstrahlung corresponds to the second term of (3.6). In the energy regime where excitation/ionization processes can be neglected ( $\alpha = 0$ ) the solution of (3.6) is simply:

$$E(X) = E_0 e^{-X/X_0} \tag{4.10}$$

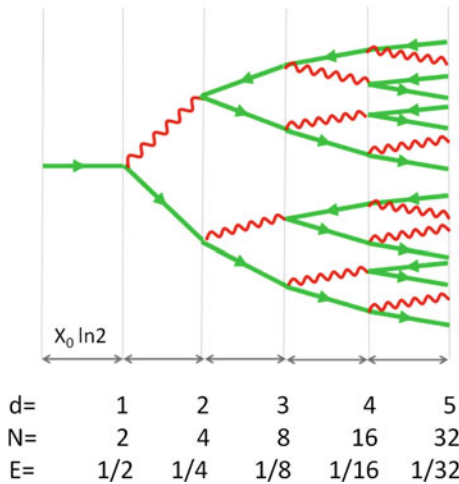


Fig. 4.2 Toy model evolution of an electromagnetic cascade. At each step of the cascade the number of particles is multiplied by two, through either pair creation or single photon bremsstrahlung. Backward arrows indicate a positron, as in Feynman diagrams. The evolution stops when individual particle energies fall below the critical energy  $E_c$ . The number  $N$  of particles at each step  $d$  and the average particle energy  $E$  in the Heitler’s model are also indicated. Adapted from (<http://www.borborigmi.org/>)

where  $E_0$  is the energy of the particle initiating the shower. Let us define the “step”  $d$  as:

$$d = \ln 2 \cdot X_0 \quad (4.11)$$

By inserting (4.11) into (4.10) we have:

$$\frac{E(X=d)}{E_0} = \exp\left(\frac{-X_0 \ln 2}{X_0}\right) = \frac{1}{2} \quad (4.12)$$

Statistically, at each step electrons halve their energy via bremsstrahlung emission of a single photon while photons produce an electron-positron pair each with half the energy of the photon. Therefore, at each step the energy of each particle decreases by a factor of two and the total number of particles increases by a factor of two.

After  $k$  generations, the number of particles is  $N_k = 2^k$  and their individual energy is  $E_0/2^k$ . This development continues until at the step  $k^*$  the individual energy drops below the critical energy  $E_c$ . At such an energy the multiplication process show down and soon after stops altogether. At  $k^*$  the number of secondary particles reaches, therefore, a maximum (the so-called *shower maximum*):

$$N_{\max} = 2^{k^*} \simeq \frac{E_0}{E_c} \quad (4.13)$$

According to (4.13) and recalling (4.9), a 10 TeV photon reaching the top of the atmosphere produces in the Heitler’s model  $\sim 10^5$  secondary particles at the shower maximum.

The depth in the atmosphere (in  $\text{g cm}^{-2}$ ) where the maximum of the electromagnetic cascade occurs can be obtained from (4.13) and is given by

$$X_{\max}^\gamma = X_f + k^* \cdot d = X_f + k^* \ln 2 \cdot X_0 = X_f + X_0 \ln\left(\frac{E_0}{E_c}\right) \quad (4.14)$$

where  $X_f$  is the atmospheric depth where the cascade starts. More detailed computations, which consider the energy distribution of particles in the shower, agree with (4.14) with  $X_f = X_0/2$  as an appropriate value.

The position of the shower maximum depends on the energy  $E_0$  and the quantity:

$$D_{10} \equiv \frac{dX_{\max}^\gamma}{d(\log_{10} E_0)} = 2.3 \frac{dX_{\max}^\gamma}{d(\ln E_0)} \quad (4.15)$$

is called the *elongation rate*. In this simple model, from (4.15) we obtain  $D_{10} = 2.3X_0$ , expressing the fact that  $D_{10}$  is proportional to the radiation length of the medium. This elongation rate corresponds to the slope of the curves representing the depth of the EM maximum as a function of the primary energy  $E_0$  as shown in Figs. 4.7 and 4.20 together with the experimental data.

The Heitler's model, although oversimplified, illustrates some important features of the electromagnetic component of the air showers. More accurate analytical modeling (Sect. 4.3.2) and Monte Carlo simulations (Sect. 4.5) confirm the properties of Heitler's model, although the particle number at maximum is overestimated by factors  $\sim 2-3$ . Here (see Fig. 4.2), the ratio electrons to photons is  $N_e/N_\gamma = 2$ , while direct measurements of showers in air report a value  $N_e/N_\gamma \sim 1/6$ , also confirmed by Monte Carlo simulations. This is explained by the fact that during the bremsstrahlung process, multiple photons are emitted and electrons lose energy through additional channels.

### 4.3.2 Analytic Solutions

Purely EM showers were historically studied by coupled differential equations, which describe the evolution of the number of photons,  $N_\gamma$  and of the number of electrons,  $N_e$  as a function of the atmospheric depth  $X$  (Rossi and Greisen 1941; Kamata and Nishimura 1958). They are sometimes expressed in terms of the adimensional variable  $t \equiv X/X_0$ . The equations governing  $N_e(t)$ ,  $N_\gamma(t)$  (which are called the electron and photon sizes, respectively) are coupled by the production processes. An electron can radiate a photon and a photon can create an  $e^\pm$  pair with energy dependent cross sections. We do not present the mathematical details of these coupled differential equations [see for instance Gaisser (1991) and a recent review Lipari (2009)]. The resulting analytical solutions<sup>3</sup> are more complicated but similar to those that we will present in Sect. 5.1 for the production of light Li, Be, and B nuclei during CR propagation. These solutions are combinations of exponential functions and contain an important parameter denoted as  $s$ , the shower age. The concept of shower age derives from the observation that all showers at the maximum of their development have similar characteristics (that is have the same "age").

The  $N_e(t)$ ,  $N_\gamma(t)$  solutions from the analytical description increase as  $t$  increases, reach a maximum, and then decrease. As in Heitler's model, Eq. (4.13), the number of particles at the maximum are directly correlated with the energy  $E_0$  of the primary particle.

Based on the solutions of the cascade equations, Greisen developed a compact and still often used parameterization of the mean number of charged particles as a function of atmospheric depth  $X$  (Greisen 1960) for a  $\gamma$ -ray induced shower:

$$N_e^\gamma(X) = \frac{0.31}{\sqrt{\ln(E_0/E_c)}} \exp\left[\left(1 - \frac{3}{2} \ln s\right) \frac{X}{X_0}\right]. \quad (4.16)$$

<sup>3</sup> Two solutions exist denoted as Approximation A when the electron excitation/ionization losses are neglected and Approximation B when they are included.

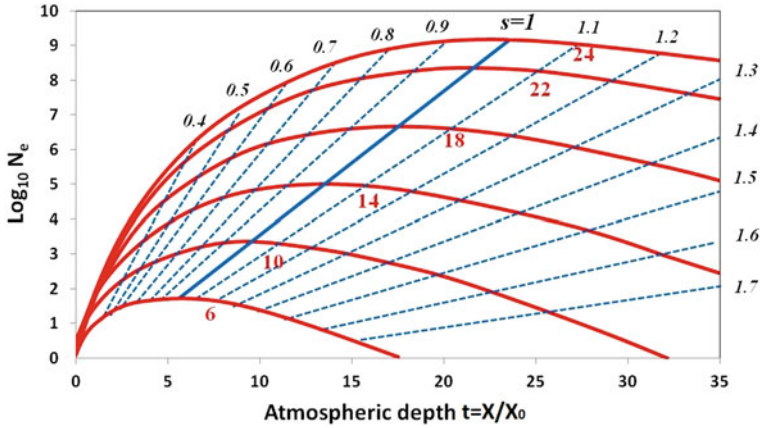


**Fig. 4.3** Shower size  $N_e(t)$  as a function of the atmospheric depth  $t = X/X_0$  (the longitudinal variable in units of radiation lengths) for primary CR photons. The numbers in red, close to the line  $s = 1.1$  are the values of  $\ln(E_0/E_c)$  where  $E_c$  is the critical energy. The corresponding six energies  $E_0$  are in increasing order: 0.035, 2, 100 TeV; 5.7, 320, 2,300 PeV. The diagonal line connecting the maxima of the different curves is labeled with  $s = 1$ . The different age values are shown by the numbers in black. The dashed diagonal lines indicates the positions in the atmosphere with constant age  $s$ . The sea level corresponds to  $t \approx 27$ .

The Greisen approximation for the shower size contains the shower age parameter  $s$ :

$$s \approx \frac{3X}{X + 2X_{\max}^\gamma} \tag{4.17}$$

Figure 4.3 shows the electron size  $N_e$  as a function of  $t$  obtained from (4.16) and for different energies  $E_0$  of the incoming particle. The shapes of the curves describing the electron size for showers initiated by primary photons with different energies  $E_0$  as a function of  $t$  look very similar. Showers have age  $s = 1$  at maximum and age  $s < 1$  before the maximum (“young” showers). “Old” showers have  $s > 1$ .

At shower maximum (4.16) corresponds by definition to  $N_{e_{\max}}^\gamma$ , and thus:

$$N_{e_{\max}}^\gamma = \frac{0.31}{\sqrt{\ln(E_0/E_c)}} \exp\left[\frac{X_{\max}^\gamma}{X_0}\right] \tag{4.18}$$

Using (4.14) and neglecting the term  $X_f$ , we obtain:

$$N_{e_{\max}}^\gamma = \frac{0.31}{\sqrt{\ln(E_0/E_c)}} \left(\frac{E_0}{E_c}\right) = \frac{1}{g} \left(\frac{E_0}{E_c}\right) \tag{4.19}$$

where  $g \equiv \sqrt{\ln(E_0/E_c)}/0.31$ . In the Greisen approximation  $g$  is weakly dependent on the primary energy. To a first approximation, in the energy range ( $E_0 \approx 10^{15} - 10^{18}$  eV) we deal with in this Chapter, the approximate value  $g \approx 10$  can be

used. Thus, the EM size at maximum is about 10% of the total size (4.13) obtained from the Heitler's model.

The Greisen profile describes accurately the average development of purely electromagnetic showers, and can be adapted for the description of proton and nucleus-induced showers, as presented in the following section. It cannot be easily adapted for the description of neutrino-induced showers (Lipari 2009).

From the analytical solution, it also follows that, for  $E \geq E_c$ , the energy spectrum of secondary particles in a shower is approximately described by a power law:

$$\frac{dN_e}{dE} \sim E^{-(s+1)} \tag{4.20}$$

where  $s$  denotes the shower age parameter. Near maximum ( $s = 1$ ) the energy spectrum is  $dN_e/dE \propto E^{-2}$ . As the shower becomes older, the energy spectrum of secondary electrons becomes softer: the fraction of high energy electrons decreases. Young showers have a harder spectral index. This nomenclature of soft and hard spectral index is quite common in astrophysics. A harder spectrum has a larger component of high-energy particles.

From the experimental point of view, detectors are able to measure charged particles above a given energy threshold  $E_t$ . Detectors are located at a fixed height in the atmosphere and for each primary CR they sample showers having different ages. This has an effect because the energy distribution of electrons depends on the age  $s$ , and older showers have a smaller fraction of electrons contributing to the signal.

The detection of high-energy photons relies on the fact that they can produce charged particles (through pair creation or Compton Effect). For this reason, the effective EM size measured by EAS experiments is  $N = N_e(> E_t) + \varepsilon N_\gamma$ , where  $0 \leq \varepsilon \leq 1$  is the probability of  $\gamma \rightarrow e$  conversion in the detector. In some detectors (for instance in thin layers of scintillator counters)  $\varepsilon \simeq 0$  while  $E_t$  is very low and the measured EM size corresponds to  $N_e$ . For this reason, in the following we specialize on the electronic component of the EM shower, and to its number  $N_{e_{\max}}$  at the position of the maximum.

The particle density as a function of the distance  $r$  to the shower core (the lateral particle distribution) is a measured quantity in most air shower experiments. The lateral particle distribution is mainly determined by multiple Coulomb scattering of electrons.<sup>4</sup> Results of detailed calculations of the lateral particle distribution by Nishimura and Kamata (Kamata and Nishimura 1958) were parameterized by Greisen (Greisen 1960) as:

$$\frac{dN_e}{rdrd\phi} = N_e(X) \cdot \frac{C(s)}{2\pi r_1^2} \left(\frac{r}{r_1}\right)^{s-2} \left(1 + \frac{r}{r_1}\right)^{s-4.5} \frac{\text{particles}}{\text{m}^2} \tag{4.21}$$

<sup>4</sup> A charged particle traversing a medium is deflected by many small-angle scatters. This deflection is due to the superposition of many Coulomb scatterings from individual nuclei, and hence the effect is called multiple Coulomb scattering. The Coulomb scattering distribution is well represented by a Gaussian distribution. At larger angles the distribution shows larger tails and the behavior is more similar to that of Rutherford scattering.

$C(s) = \Gamma(4.5 - s) / [\Gamma(s)\Gamma(4.5 - 2s)]$  is a normalization constant<sup>5</sup> obtained by imposing that  $\frac{2\pi}{N_e(X)} \int_0^\infty r \frac{dN_e}{dr} dr = 1$ . The quantity  $r_1$  is the Molière unit:

$$r_1 = X_0 \left( \frac{E_s}{E_c} \right) \simeq 9.2 \text{ g cm}^{-2} \quad (4.22)$$

in air, where  $E_c$  is the critical energy and  $E_s = m_e c^2 \sqrt{4\pi/\alpha} \simeq 21 \text{ MeV}$ ,  $m_e$  is the electron mass and  $\alpha \simeq 1/137$  the electromagnetic coupling constant. Note the units of this definition of  $r_1$ . When measured in units of length (dividing by the material density  $\rho$  in  $\text{g cm}^{-3}$ ), the Molière radius

$$r_M = \frac{r_1}{\rho} \text{ cm} \quad (4.23)$$

is different for different materials. In air, it increases with decreasing air density in the atmosphere. At sea level  $r_M \sim 80 \text{ m}$  and at the position of the shower maximum  $r_M \sim 200 \text{ m}$ . Showers developing at higher altitudes have larger lateral dimensions. Equation (4.21) is called the Nishimura-Kamata-Greisen (NKG) function.

The main properties of the EM component can be summarized as follow:

- SF1** The number of particles at shower maximum is approximately proportional to the primary energy, Eq. (4.19).
- SF2** The depth in the atmosphere of the shower maximum increases logarithmically with energy, Eq. (4.14).

Cascades initiated by  $\gamma$ -rays are almost pure EM showers ( $=e^\pm, \gamma$ ), without other particles. For instance, muon production depends on mechanisms such as the Drell-Yan process, characterized by a small cross section [refer to Sect. 7.14 of Braibant et al. (2011)]. Thus, an additional characteristic is that:

- SF3** In  $\gamma$ -ray induced showers very few muons are expected, and to a first approximation  $N_\mu^> = 0$ .

Monte Carlo simulations of the cascades confirm that the EM component of the showers exhibits a number of universality features. In particular, EM cascades induced by primary photons, electrons, protons and nuclei have properties, which are independent of the primary type and rather insensitive to the primary energy. These features are:

- SF4** the longitudinal development of EM cascades depends on two parameters: the energy  $E_0$  of the primary nucleus and the shower age  $s$ . They can also be described in terms of analytical formulas like that of Greisen, Eq. (4.16).
- SF5** Near the shower core, the electron energy distribution is a universal function of the age parameter as in Eq. (4.20).

<sup>5</sup> The  $\Gamma$  function is an extension for positive real numbers of the factorial.

**SF6** The lateral distribution of the EM cascade, Eq. (4.21), at a given age  $s$  is a universal function if the lateral distance is measured in Molière units  $r_1$ , Eq. (4.22).

#### 4.4 Showers Initiated by Protons and Nuclei

CRs are mainly protons and heavier nuclei, which initiate a *hadronic shower* by interacting with atmospheric nuclei after traversing on average one interaction length  $\lambda_I$ . The multiplicity of charged particles produced in the interaction increases with the center of mass energy  $\sqrt{s}$ . When expressed in terms of the laboratory energy  $E_0$ , the number of charged hadrons,  $n_{\text{ch}}$ , as found in  $p\bar{p}$  and  $pp$  data (Eidelman et al. 2004) increases as:

$$n_{\text{ch}} \propto E_0^{0.2}. \quad (4.24)$$

The same is true for  $\pi^+$  collisions: the multiplicity in  $\pi^+{}^{14}\text{N}$  collisions increases with energy and one finds:  $n_{\text{ch}} \simeq 5, 11,$  and  $27$  at  $10, 100,$  and  $10^4$  GeV, respectively (Hörandel 2007). After the first interaction, the  $n_h = 3/2n_{\text{ch}}$  produced hadrons (including the neutral ones, which are  $n_0 = 1/2n_{\text{ch}}$ ) carry a fraction  $\kappa$  of the primary CR energy  $E_0$ . They are mainly pions [see Sect. 10.9 of Braibant et al. (2011)]. As indicative value for the following first-order estimates we fix<sup>6</sup>  $n_{\text{ch}} = 10$ . The parameter  $\kappa \simeq 0.7$  is usually referred to as the *inelasticity*. It takes into account the fact that a significant fraction of the total energy is carried away by a single *leading particle* and is defined as:

$$\kappa = \frac{E_0 - E'}{E_0 + M_T} \quad (4.25)$$

where  $E'$  is the residual energy of the nucleon after the collision and  $M_T$  the mass of the target nucleon (which can be neglected in our energy regime). The residual energy  $E'$  is used by the leading particle for a successive interaction after traversing on average one more  $\lambda_I$ . After  $k$  iterations, the leading particle carries a fraction  $(1 - \kappa)^k$  of the initial energy  $E_0$ . In the following, the inelasticity will not be considered. See Matthews (2005) for more details. The process continues (see Fig. 4.4) until the hadron energy falls below an *interaction threshold*. Neutral pions in the cascade have a lifetime  $\tau_{\pi^0} = 8.4 \times 10^{-17}$  s characteristic of the electromagnetic interactions and decay:

$$\pi^0 \rightarrow \gamma\gamma \quad \text{with} \quad d_{\pi^0}^{\prime} = \Gamma c \tau_{\pi^0} = \Gamma \cdot 2.5 \times 10^{-6} \text{ cm} \quad (4.26)$$

<sup>6</sup> The quantity  $n_{\text{ch}}$  is more easily measured in accelerator experiments than  $n_h$ .



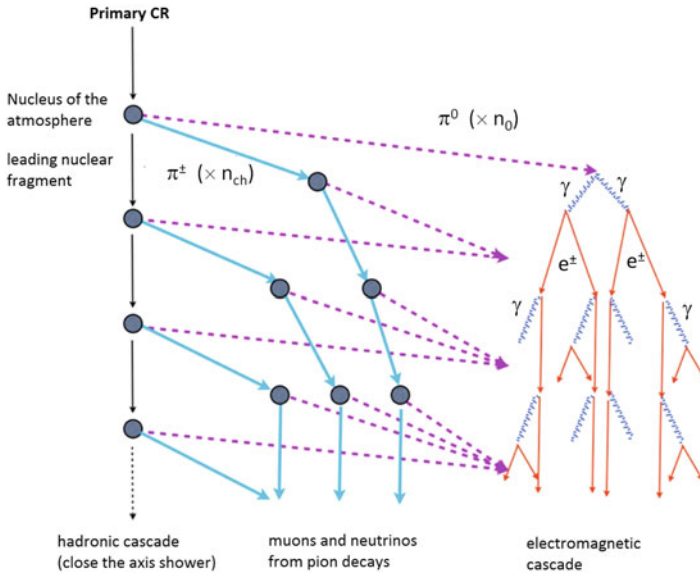


**Fig. 4.4** Schematic evolution of cascades initiated by hadrons. At each step roughly 1/3 of the energy is transferred from the hadronic cascade to the electromagnetic one (Letessier-Selvon and Stanev 2011)

$d'_{\pi^0}$  is the neutral pion decay length, i.e., the distance in the laboratory frame traversed at the light speed during one lifetime. The decay length in (4.26) is denoted as  $d'$  when measured in cm, and as  $d = d' \rho$  when multiplied by the material density and measured in  $g\ cm^{-2}$ . As usual, we indicate with  $\Gamma$  the relativistic Lorentz factor, to avoid confusion with the symbol used for the  $\gamma$ -ray. The daughter  $\gamma$ -rays start an electromagnetic cascade practically at the first interaction point.

Charged pions decay through weak interactions with a longer lifetime ( $\tau_{\pi^\pm} = 2.6 \times 10^{-8}$  s):



and, when considering the density  $\rho$  of the medium,

$$d_{\pi^\pm} = d'_{\pi^\pm} \cdot \rho\ \text{g}\ \text{cm}^{-2} \quad (4.28)$$

is the charged pion decay length. The interaction length (3.2) of pions is  $\lambda_I^\pi \simeq 120\ \text{g}\ \text{cm}^{-2}$ . For this reason, once produced  $\pi^\pm$  can either decay or interact with air nuclei. Whether decay or interaction dominates depends upon which of the two,  $d_{\pi^\pm}$  or  $\lambda_I^\pi$ , is smaller. The role of the two processes is also complicated by the fact that the interaction probability depends on the material density, which in the atmosphere depends in turn on the height  $h$ . High energy  $\pi^\pm$  prevalently interact because the

relativistic Lorentz factor  $\Gamma$  is high, while low energy pions decay. At high altitudes, pions are more likely to decay than at low altitudes, where the atmosphere is denser. The stochastic interaction/decay competition of all charged mesons determines the details of the development of hadronic showers, Chap. 11.

In our first-order model [following Matthews (2005)] we assume that  $\pi^\pm$  always interact if their energy is above a certain threshold energy  $E_{\text{dec}}^\pi$ , and decay if the energy is below  $E_{\text{dec}}^\pi$ . In the case of interaction, additional  $n_h = n_{\text{ch}} + n_0$  hadrons of lower energy are produced. Here, we assume that all  $n_h$  are pions. We estimate  $E_{\text{dec}}^\pi$  as the energy at which the decay length of a charged pion, Eq. (4.28), becomes equal to their interaction length, Eq. (3.8b). The decay length depends, through the Lorentz factor, on the pion energy. The  $E_{\text{dec}}^\pi$  can be derived by imposing:

$$\lambda_I^\pi = d'_{\pi^\pm} \cdot \rho = \left( \frac{E_{\text{dec}}^\pi}{m_\pi c^2} \right) c \tau_{\pi^\pm} \cdot \rho \quad (4.29)$$

and thus, using  $\rho \simeq 10^{-3} \text{ g cm}^{-2}$ :

$$E_{\text{dec}}^\pi = \frac{\lambda_I^\pi}{c \tau_{\pi^\pm} \cdot \rho} \cdot (m_\pi c^2) \simeq 160 \cdot (m_\pi c^2) \simeq 20 \text{ GeV}. \quad (4.30)$$

The energy transferred to the EM component can be estimated within this simple model, neglecting the correction factor due to the inelasticity. In each hadronic interaction, 2/3 of the initial energy is transferred to the hadronic component. After  $k$  generations the energies of the hadronic ( $E_h$ ) and EM ( $E_{EM}$ ) components are given by:

$$E_h = \left( \frac{2}{3} \right)^k E_0 ; \quad E_{EM} = E_0 - E_h. \quad (4.31)$$

Hence, after  $k$  interactions the energy per pion is  $E = E_0 / (n_h)^k$ . At a certain value  $k^*$ ,  $E$  becomes smaller than  $E_{\text{dec}}^\pi$ . The number of interactions needed to reach  $E = E_{\text{dec}}^\pi$  is:

$$k^* = \frac{\ln(E_0/E_{\text{dec}}^\pi)}{\ln n_h}. \quad (4.32)$$

In the energy range we are considering ( $10^{15} - 10^{18}$  eV), the value of  $k^*$  ranges from 4 to 6.

The basic properties of a cascade induced by a primary hadron with energy  $E_0$  can be easily understood assuming the decay channels (4.26) and (4.27) for neutral and charged pions, respectively. Our simple cascade model consists of two interrelated processes: the development of a hadronic shower, whose observables are mostly the daughter muons, and an EM shower. The primary energy  $E_0$  at the maximum of the shower is finally shared between  $N_\mu^p$  muons and  $N_{\text{max}}^p$  electrons/photons. By analogy

to Eq. (4.13), the total energy in this case is

$$E_0 = E_c N_{\max}^p + E_{\text{dec}}^\pi N_\mu^p. \quad (4.33)$$

Scaling to the electron size using (4.19),  $N_{e_{\max}}^p = N_{\max}^p/g$ :

$$E_0 = g E_c \left( N_{e_{\max}}^p + \frac{E_{\text{dec}}^\pi}{g E_c} N_\mu^p \right) \sim 0.85 [\text{GeV}] (N_{e_{\max}}^p + 24 N_\mu^p). \quad (4.34)$$

The relative magnitude of the contributions from  $N_\mu^p$  and  $N_{e_{\max}}^p$  depends on their respective critical energies, the energy scales at which electromagnetic and hadronic multiplication ceases. Different primaries produce different numbers of muons and  $e^\pm$ , affected also by shower-to-shower statistical fluctuations.

#### 4.4.1 The Muon Component in a Proton-Initiated Cascade

Let us consider now the dependence of the number of muons in the cascade on  $E_0$ . Muons are produced in the decay of the  $k^*$  generation of charged pions, when  $\pi^\pm$  reach an energy below the threshold  $E_{\text{dec}}^\pi$  and all decay into a muon-neutrino pair. Thus:

$$N_\mu^p = N_\pi^p = (n_{\text{ch}})^{k^*}. \quad (4.35)$$

Using (4.32) and the properties of logarithms we have:

$$\ln N_\mu^p = k^* \ln n_{\text{ch}} = \ln \left( \frac{E_0}{E_{\text{dec}}^\pi} \right) \cdot \frac{\ln n_{\text{ch}}}{\ln n_h} \quad (4.36)$$

returning from logarithms to numbers:

$$N_\mu^p = \left( \frac{E_0}{E_{\text{dec}}^\pi} \right)^\beta \quad \text{where } \beta \equiv \ln n_{\text{ch}} / \ln n_h. \quad (4.37)$$

Eq. (4.37) represents a first order estimate, with many approximations hidden inside the two parameters  $\beta$  and  $E_{\text{dec}}^\pi$ . The value  $\beta \sim 0.85$  is obtained for  $n_{\text{ch}} = 10$ . When the contribution of the inelasticity  $\kappa$  is included,  $\beta \sim 0.9$ . It should be noted that the number of secondary pions depends (slowly) on energy as the shower develops, and  $\beta$  can range between  $\sim 0.85$ – $0.95$ . Only Monte Carlo computations can correctly reproduce the shower. The numerical values of  $\beta$  and  $E_{\text{dec}}^\pi$  for different particles and hadronic interaction models are given in Alvarez-Muniz et al. (2002). The

hadronic energy in (4.31) can be completely accounted for in the muon component as:

$$E_h = N_\mu^p E_{dec}^\pi \tag{4.38}$$

The average energy of each muon in such a model is of the order of  $E_{dec}^\pi/2 \sim 10$  GeV. At such an energy the muon energy loss is  $dE_\mu/dx \sim 2 \times 10^{-3} \text{ GeV g}^{-1} \text{ cm}^2$ . Thus, most muons have enough energy to cross the entire atmospheric depth ( $\sim 1,000 \text{ g cm}^{-2}$ ). Only muons with energy below few GeV have a large decay probability, as the muon decay length is

$$d_\mu^p = \Gamma \cdot c \cdot \tau_\mu = \Gamma \cdot 0.66 \text{ km} \tag{4.39}$$

for the process  $\mu^- \rightarrow e^- \nu_\mu \bar{\nu}_e$  and  $\mu^+ \rightarrow e^+ \bar{\nu}_\mu \nu_e$ . For example, approximately 20 % of 1 GeV muons ( $\Gamma \sim 10$ ) produced at a height of 10km will reach the sea level before decaying. Thus, the number of muons reaching the detection level (usually at depths between  $800\text{--}1,000 \text{ g cm}^{-2}$ ) is only slightly depleted with respect to  $N_\mu^p$  at the position of the maximum.

### 4.4.2 The EM Component in a Proton-Initiated Cascade

The number of electrons is estimated using the relation  $E_0 = E_{EM} + E_h$ , where the hadronic energy is given by (4.38). The energy fraction carried by the electromagnetic component is

$$\frac{E_{EM}}{E_0} = \frac{E_0 - N_\mu^p E_{dec}^\pi}{E_0} = 1 - \left( \frac{E_0}{E_{dec}^\pi} \right)^{\beta-1} \tag{4.40}$$

The number of electrons at maximum can be obtained with simple arguments. There are  $n_0$  independent showers started by the EM decay of each neutral pion, each carrying  $E_0/n_h$  of the primary energy. Equation (4.19) can be traduced for a proton-induced shower to

$$N_{e_{max}}^p = n_0 \cdot \frac{1}{g} \left( \frac{E_0/n_h}{E_c} \right) = \left( \frac{E_0}{3gE_c} \right) = 4 \times 10^5 \left( \frac{E_0}{\text{PeV}} \right) \tag{4.41}$$

using the fact that  $n_0/n_h = 1/3$ . In the last equality, we inserted the numerical values  $g = 10$ ,  $E_c = 86 \text{ MeV}$  and  $1 \text{ PeV} = 10^9 \text{ MeV}$ . This value underestimates by  $\sim 30\%$  the electron size due to the additional contribution of successive interactions of the leading particle and of charged pions, producing additional neutral particles. A better estimate can be derived using Eq. (4.40), and it is left as an exercise; see Hörandel (2007) for an hint. This gives

$$N_{e_{max}}^p = 6 \times 10^5 \left( \frac{E_0}{\text{PeV}} \right)^{1.046} \tag{4.42}$$

The number of electrons at maximum grows as function of energy slightly faster than exactly linear.

Monte Carlo simulations show that the fraction of energy transferred to the EM component at shower maximum increases from about 70% at  $10^{15}$  eV to 90–95% at  $10^{20}$  eV. For instance, a  $10^{19}$  eV proton striking vertically the top of the atmosphere produces at sea level about  $3 \times 10^{10}$  particles with energy larger than 200 keV, 99% of these particles are photons and electrons. Their energy is mostly in the range of 1–10 MeV and they transport 85% of the total energy. The remaining particles are either muons with an average energy of about 4 GeV (carrying about 10% of the total energy), few GeV pions (about 4% of the total energy), and, in smaller proportions, neutrinos and baryons. The shower footprint on ground extends over a few  $\text{km}^2$ .

The average energy of electrons at the position of the maximum is below  $E_c$ , and thus, of the order of tens of MeV. After the maximum, the energy of the EM cascade degrades faster than that of muons, due to the different energy loss of electrons and muons. The model yielding Eq. (4.42) does not take into account electron energy losses in the atmosphere and the size  $N_e(X)$  is valid only at shower maximum. After the maximum, it reduces exponentially along the path to the detection level. Figure 4.5 shows the energy fraction (both in linear and logarithmic scales) of the electromagnetic, hadronic, muonic and neutrino components as functions of the atmospheric depth, as obtained with a full Monte Carlo simulation (CORSIKA, see Sect. 4.5) for a primary proton with  $E_0 = 10^{19}$  eV. The energy released into air refers to the energy fraction transferred from high-energy particles to the excitation and ionization of the medium.

Figure 4.6 shows the number of muons  $N_\mu^p$  and of electrons/positrons,  $N_{e\text{max}}^p$ , using our simplified estimate for proton and iron primaries. The main features of the EM and muonic components produced by a proton are summarized as follow:

- SF7** The number of muons (4.37) produced in an air shower increases almost linearly with the proton energy  $E_0$ , as  $N_\mu^p \propto E_0^\beta$  with  $\beta \sim 0.9$ .
- SF8** The energy  $E_0$  of a primary can be simply estimated if both  $N_e$  and  $N_\mu$  are measured, Eq. (4.34). The relation is linear and almost insensitive to fluctuations on the EM and muonic size. If more primary energy than the average is on the muonic component, the EM one is depleted keeping constant their sum, and viceversa. It is also insensitive to primary particle type—see below. If only the EM size is measured, by inversion of (4.42) we obtain  $E_0 \simeq (1.5\text{GeV})(N_{e\text{max}})^{0.97}$ . This is much dependent of the relative fluctuation of the EM/muonic size.

The results are in agreement with detailed Monte Carlo simulations (Sect. 4.5).

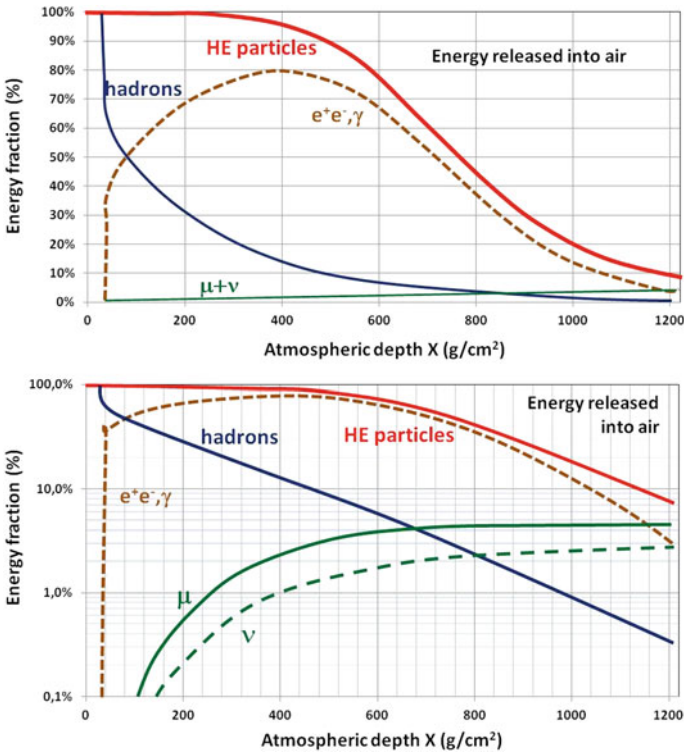


Fig. 4.5 Fraction of energy transferred to the different components of the cascade induced by a primary proton of  $10^{19}$  eV. Part of the energy is released into air by excitation/ionization processes. The top graph uses a linear scale for the energy fraction; the bottom uses a log scale for a better visualization of the “older” part of the shower

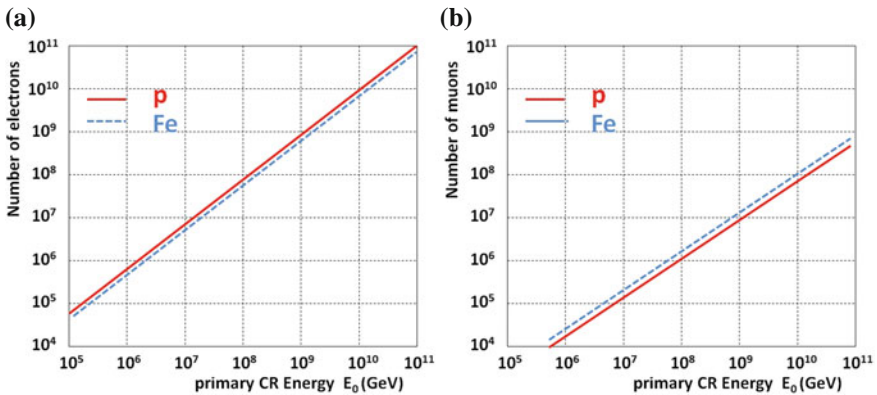


Fig. 4.6 Number of electrons a and number of muons b at shower maximum as a function of energy for primary protons and iron nuclei. The proton lines (red) are obtained using Eqs. (4.37) and (4.42)

### 4.4.3 Depth of the Shower Maximum for a Proton Shower

The atmospheric depth at which the electromagnetic component of a proton-induced shower reaches its maximum is denoted as  $X_{\max}^p$ . The cascade is provided by the superposition of many individual showers. The  $n_0 = 1/3n_h$  neutral pions produced in the first interaction generate (through  $\pi^0 \rightarrow \gamma\gamma$  decay)  $2n_0$   $\gamma$ -rays starting the EM cascade at the same position in the atmosphere. For a primary proton the first interaction occurs on average at an atmospheric depth  $X_f = \lambda_I$ . Each  $\gamma$ -ray carries  $E_0/2n_h$  of the primary energy. A simple estimate of  $X_{\max}^p$  can be obtained using the result (4.14) for a shower initiated by a  $\gamma$ -ray with the substitutions  $X_f \rightarrow \lambda_I$  and  $E_0 \rightarrow E_0/2n_h$ :

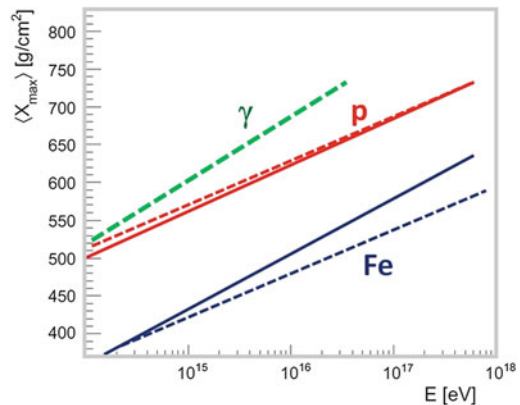
$$X_{\max}^p \simeq \lambda_I + X_0 \cdot \ln\left(\frac{E_0}{2n_h E_c}\right). \quad (4.43)$$

Let us estimate the difference between (4.43) and (4.14), i.e. between the position of the maximum in the atmosphere for a proton or a  $\gamma$ -ray initiated shower of the same energy  $E_0$ . The first interaction point for the proton is deeper in the atmosphere,  $\lambda_I \simeq 2.5X_0$ , using (3.8a). Then (4.43) can be written as

$$X_{\max}^p = \lambda_I + X_0 \cdot \left[ \ln\left(\frac{E_0}{E_c}\right) - \ln(2n_h) \right] \simeq 2.5X_0 + (X_{\max}^\gamma - X_0/2) - 3.4X_0 \quad (4.44)$$

the last numerical factor ( $\ln(2n_h) \simeq 3.4$ ) is obtained with  $n_h = (3/2)n_{ch} = 15$ . Numerically,  $X_{\max}^\gamma - X_{\max}^p \simeq 1.4X_0$ , corresponding to about  $50 \text{ g cm}^{-2}$  in atmosphere. The maximum of the EM shower induced by a proton occurs higher in the atmosphere than that induced by a photon of the same energy  $E_0$ . Also the elongation rates, Eq. (4.15), are slightly different for protons and photons, as shown in Fig. 4.7. The difference  $X_{\max}^\gamma - X_{\max}^p$  is thus dependent on energy. A correction arises on the fact

**Fig. 4.7** Depth of maximum versus primary energy for the EM component of air showers. Green dotted showers induced by a photon primary. Dashed showers induced by proton (red) and iron (blue) primaries. They are uniformly shifted by  $150 \text{ g cm}^{-2}$  according to Eq. (4.48). Red and blue solid lines are from full MC simulations of p and Fe showers



that in (4.44) only the first-generation pions are accounted for, and the sub-showers generated in the following steps are neglected.

### 4.4.4 Showers Induced by Nuclei: The Superposition Model

To extend the simple approach from primary protons to nuclei, the *superposition model* is used. This assumes that a nucleus with atomic mass number  $A$  and energy  $E_0$  is equivalent to  $A$  individual single nucleons, each having an energy  $E_0/A$ , and acting independently. The resulting EAS is treated as the sum of  $A$  individual proton induced showers, all starting at the same point. The corresponding shower features are obtained by replacing  $E_0 \rightarrow E_0/A$  in the expressions derived for proton showers and summing  $A$  such showers.

The number of the  $e^\pm, \gamma$  (the EM component) at the maximum of the shower induced by a primary nucleus can be derived from (4.41) with the above assumptions:

$$N_{e_{\max}}^A = A \times \left( \frac{E_0/A}{3gE_c} \right) = N_{e_{\max}}^p \tag{4.45}$$

This is an important result, which has important implications for experiments: from the measurement of the electromagnetic size, it is hard to distinguish a proton with energy  $E_0$  from a nucleus  $A$  of the same energy  $E_0$ , as can also be deduced from the left panel of Fig. 4.6.

The corresponding number of muons in nucleus-induced showers can be obtained from (4.37):

$$N_\mu^A \simeq A \times \left( \frac{E_0/A}{E_{\text{dec}}^\pi} \right)^\beta = A^{1-\beta} \cdot N_\mu^p \tag{4.46}$$

The important feature is that  $N_\mu^A$  increases slowly as function of the mass  $A$  of the primary particle as  $N_\mu \propto A^{0.1}$ . The heavier the shower-initiating particle is the more muons are expected for a given primary energy. For instance, using (4.46) with  $\beta = 0.9$ , the number of muons in a He ( $A = 4$ ), O ( $A = 16$ ) and Fe ( $A = 56$ ) induced shower is 14, 32 and 50% larger than that induced by a primary proton of the same energy. Compare with the right panel of Fig. 4.6 for the case of Fe.

To evaluate the average depth of the shower maximum from a nucleus of mass  $A$  we must use (4.43) assuming that the shower is originated from a nucleon in the nucleus with energy  $E_0/A$ . Thus, replacing  $E_0 \rightarrow E_0/A$  and  $\lambda_l \rightarrow \lambda_l^A$  in Eq. (4.43)

$$X_{\max}^A \simeq \lambda_l^A + X_0 \cdot \ln \left( \frac{E_0}{2An_h E_c} \right) \tag{4.47}$$



from which we obtain:

$$X_{\max}^A = \lambda_I^A + X_0 \cdot \ln\left(\frac{E_0}{2n_h E_c}\right) - X_0 \ln A \simeq X_{\max}^p - X_0 \ln A \quad (4.48)$$

(neglecting in the last equality the difference between  $\lambda_I$  and  $\lambda_I^A$ ). Using this relation, an air shower initiated by a He, O and Fe nucleus of the same total energy reaches its maximum  $\sim 50, 100$  and  $150 \text{ g/cm}^2$  earlier than that initiated by a proton with the same energy. The depth of the maximum as a function of the primary energy for proton and iron showers is presented in Fig. 4.7 as dashed lines. When a Monte Carlo simulation is used the differences  $X_{\max}^A - X_{\max}^p$  are smaller and with a mild dependence on the CR energy, as shown with the full lines in Fig. 4.7. A slightly difference in the elongation rate is predicted from different interaction models, Sect. 4.5, used to estimate the hadron production in the simulation. This is visible in Fig. 4.20, which will be discussed in the following and compared with the experimental data.

The main qualitative results and properties of our first-order estimate for nucleus-induced showers are summarized below. They are confirmed by detailed simulations independently from the interaction models used in the Monte Carlo simulation (see next section).

- SF9** The electromagnetic size is equal for a cascade initiated by a proton with energy  $E_0$  and by a nucleus  $A$  of energy  $E_0$ , Eq. (4.45);
- SF10** the number of muons in a nucleus-induced shower depends on  $A$  as  $N_{\mu}^A \propto A^{1-\beta} \sim A^{0.1}$ , Eq. (4.46);
- SF11** the depth of maximum of the EM component of a nucleus-induced shower differs from that of a proton-induced shower as  $X_{\max}^A \simeq X_{\max}^p - X_0 \ln A$ , Eq. (4.48).

This feature is evident in Fig. 4.8, which shows the longitudinal profile for two showers initiated by a proton (left) and an iron nucleus (right) with energy  $E_0 = 10^{14} \text{ eV}$  obtained using a CORSIKA-based Monte Carlo simulation (see next section). The different components of the cascade, the electromagnetic ( $e/\gamma$ ), the muonic ( $\mu$ ) and the hadronic ( $h$ ), are shown in different colors.

- SF12** Due to the larger cross section of a nucleus  $A$  one has  $\lambda_I^A \sim \lambda_I/A^{2/3}$  and the fluctuations on  $X_{\max}^A$  are much smaller than those on  $X_{\max}^p$ . As a consequence the root mean square fluctuation  $\sigma(X_{\max}^A)$  on the position of the maximum of the EM component induced by a heavy nucleus is smaller than  $\sigma(X_{\max}^p)$ .

This peculiarity is noticeable in Fig. 4.9 which shows the number of charged EM particles from the simulation of 50 different showers induced by protons and iron nuclei of the same energy ( $E_0 = 10^{19} \text{ eV}$ ) as a function of the atmospheric depth. Shower-to-shower fluctuations of the position of the maximum depth are present, although more evident in the case of protons. From this figure, the average atmospheric depth and its root mean square are  $X_{\max}^p \simeq 770 \pm 60 \text{ g cm}^{-2}$  for p-induced showers and  $X_{\max}^{Fe} \simeq 700 \pm 20 \text{ g cm}^{-2}$  for iron-induced showers.

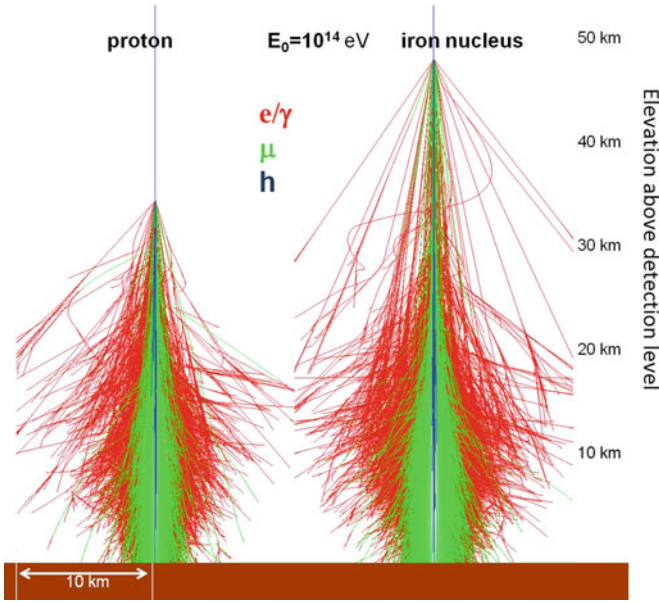


**Fig. 4.8** Longitudinal profile for two showers with energy  $E_0 = 10^{14}$  eV from a full MC simulation based on the CORSIKA code. *Left* shower initialized by a proton. *Right* shower initialized by an iron nucleus

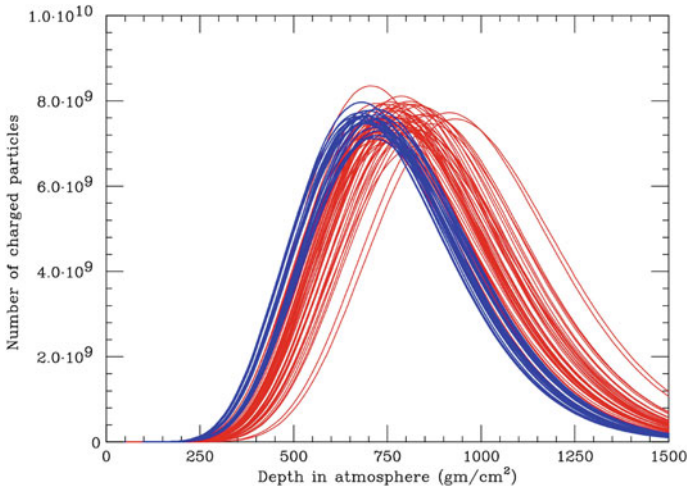


**Fig. 4.9** Simulation of the longitudinal profile produced with the CORSIKA code for 50 proton-induced (*red*) and 50 iron-induced (*blue*) showers. The same total energy of  $10^{19}$  eV is assumed. Shower-to-shower fluctuations on  $N_{e_{max}}$  and  $X_{max}$  are evident. Courtesy of prof. J.W. Cronin

Information from detailed Monte Carlo simulations are used by EAS experiments to estimate the parameters of the CR spectrum at energies around and above the knee. The properties of the primary CRs are deduced from the shape and the particle content of the EAS. The energy of the primary depends on the total number of secondaries produced and information on the chemical composition can be deduced from the relative  $N_\mu, N_e$  contributions or from  $X_{\max}$ .

## 4.5 The Monte Carlo Simulations of Showers

EAS experiments cannot be exposed to a test beam for calibration. The interpretations of their measurements rely on comparison of the experimental data with model predictions of the shower development in the atmosphere obtained via Monte Carlo (MC) simulation of particle interactions and transport in the atmosphere.

While the electromagnetic and the weak interactions are rather well understood, the major uncertainties in MC simulations of EAS arise from the hadronic interaction model. The properties of an EAS for a given energy and primary are strongly dependent on the inelastic cross sections  $\sigma_{\text{inel}}$  of primary and secondary particles with air nuclei.

At the present level of theoretical understanding, Quantum Chromo-Dynamics (QCD) cannot be applied to calculate the hadronic inelastic cross section and the number of secondary particles from first principles. Therefore, hadronic interaction models are usually a mixture of basic theoretical ideas and empirical parameterizations tuned to describe the experimental data where measurements exist.

The data from the LHC at CERN allow detailed tests of interaction models up to center-of-mass energies which are equivalent to CR energies of  $\sim 10^{17}$  eV, but an appreciable amount of extrapolation of the properties of hadronic interactions is still needed to interpret the air shower data. In fact, because of the low transverse momentum ( $p_t$ ) of secondary particles produced in hadronic interactions and because of momentum conservation, most secondaries are moving in the same direction as the primary CR (forward production). Due to the unavoidable presence of the beam pipe in accelerators, none of the collider experiments registers particles emitted into the extreme forward direction (that of the beam), and the available information in this kinematic region is very poor. These low- $p_t$  particles carry most of the hadronic energy and are of the greatest importance in the EAS development, since they transport a large energy fraction deep into the atmosphere.

Present models for the  $\sigma_{\text{inel}}$ , for the multiplicity distribution of secondary hadrons and their momenta distributions have to be extrapolated well beyond the range of knowledge. These model uncertainties are the dominant source of systematic uncertainties for the study for ultra-high energy CRs, as we discuss in Chap. 7.

A widely used Monte Carlo code, simulating in great detail the EAS initiated by photons, nucleons, or nuclei is the CORSIKA program (Heck 1998; Knapp and Heck 1993; Engel and Heck 2011). Each produced particle is propagated (tracked) along the atmosphere. All physics processes are considered: energy loss, deflection due to

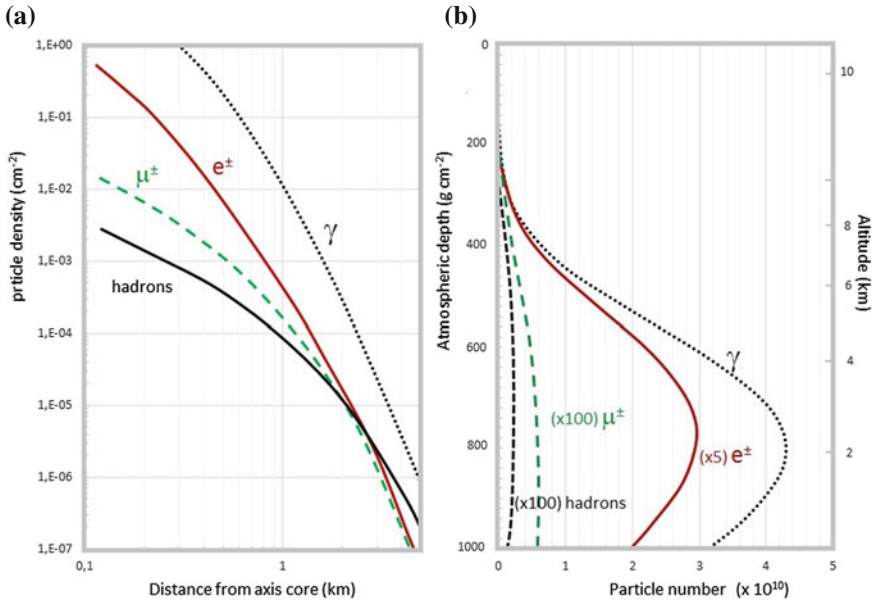


**Fig. 4.10** Average **a** lateral and **b** longitudinal shower profiles of the hadronic, muonic and electromagnetic components generated with the CORSIKA code. The shower are induced by vertical protons of energy  $10^{19}$  eV. The lateral distribution of the particles at ground level is calculated for  $870 \text{ g cm}^{-2}$ , the depth of the Pierre Auger Observatory, Sect. 7.8. Only photons and  $e^{\pm}$  with energy larger than 0.25 MeV are followed in the simulation. For muons and hadrons, the energy threshold is 100 MeV

multiple scattering and to the Earth’s magnetic field, decay modes (for unstable particles) and electromagnetic and hadronic interactions. Figure 4.10 shows the lateral and longitudinal profiles of all the components induced by a vertical CR proton of  $10^{19}$  eV.

CORSIKA contains various computer codes for the hadronic interaction modeling of nucleons and nuclei, which allow a comparison and an estimate of systematic errors. The available hadronic models are VENUS, QGSJET, DPMJET, SIBYLL, HDPM, and EPOS (see Extras # 3).

Detailed comparisons of the models available in CORSIKA have been performed revealing differences on the 25–40% level. Some of the models are unable to describe all aspects of the experimental results. Most of the figures shown in this chapter contain predictions derived from the CORSIKA code with one or more of the quoted hadronic interaction models (usually, different versions and releases of the same code exist).

## 4.6 Detectors of Extensive Air Showers at the Energy of the Knee

Extensive air showers induced by CRs with energies above  $\sim 10^{14}$  eV can be detected with arrays of sensors (scintillators, water Cherenkov tanks, muon detectors, Cherenkov telescopes, etc.) spread over a large area. When a CR falls within the array boundary, the subsample of detectors placed near enough to the shower core will observe the radiation reaching the detection level.

The accuracy of the description and reconstruction of EAS characteristics (energy, nature of the primary, direction) results from a compromise between the financial budget and the number of sensors distributed over the largest area  $A$  with the smallest detector spacing. The instrumented area  $A$  should meet the condition that  $\Phi(>E) \cdot A \cdot \Delta\Omega \cdot T$  gives a reasonable number of events in a given observational time period  $T$ . The quantity  $\Delta\Omega$  is the covered solid angle and the integral intensity  $\Phi(>E)$  has units  $\text{cm}^{-2}\text{s}^{-1}\text{sr}^{-1}$  as usual. The number of secondary particles crossing each detector within a given time windows are counted. Detector spacing of the order of few tens of meters appears optimal for  $10^{15}$  eV CRs. At higher energies the spacing must be increased to increase the instrumented area with sustainable economic budgets.

Most particles observed at ground level are close (about 200–300 m corresponding to 2–3 Molière radii) to the shower axis. At the highest energies ( $> 10^{18}$  eV), particles can be observed up to some kilometers away. The incident CR direction and energy are measured assuming that the shower has an axial symmetry in the plane perpendicular to the shower axis. This assumption is valid for zenith angles  $\theta < 60^\circ$  and not too far from the axis.

In addition to the EM and muonic cascades, relativistic charged particles emit visible photons through the Cherenkov effect in the atmosphere. These visible photons are concentrated around the shower axis, reach the ground essentially unaltered. Cherenkov light array detectors can measure the time and intensity profile of the emitted light, which carries memory of its production point along the shower axis. Another method used to detect CRs of energy larger than  $10^{18}$  eV exploits the excitation of nitrogen molecules by the particles in the shower and the associated fluorescence emission of light. The light is detected by photomultipliers and the profile of the shower in the atmosphere can be inferred rather directly. This method will be discussed in Chap. 7.

Figure 1.4 shows the flux of primary CRs as measured by direct and indirect experiments. Each EAS experiment measures the CR flux in a given energy range. Different kinds of experiments cover more than 8 decades of energy.

Many arrays were built in different countries to study CRs in the region of the knee between  $10^{14}$ – $10^{17}$  eV, giving important contributions. The early measurements have been replicated with superior statistics in the modern arrays built in Germany (KASCADE and KASCADE-Grande), in Italy (EAS-TOP) and in Tibet. EAS arrays are normally located at atmospheric depths between  $800 \text{ g cm}^{-2}$  and the sea level. Some exceptions exist, as the Tibet air-shower array, built at Yangbajing (altitude 4,300 m above sea level), with an atmospheric depth of  $606 \text{ g cm}^{-2}$ .

The first of the giant shower arrays operating at the beginning of 1960s was built by J. Linsley, L. Scarsi and B. Rossi at Volcano Ranch, New Mexico. The array was constituted of 20 scintillators  $3\text{ m}^2$  each and 900 m apart, covering a total surface area of about  $8\text{ km}^2$ . Scintillator arrays are usually made of flat pieces of plastic scintillators displaced on the ground and connected by cables. As most of the EAS experiments are in remote regions, serious problems for power supply, safety, data transmission, communication etc. usually exist. Plastic scintillator are robust, cheap, easy to handle and simple to use and deploy; they are equally sensitive to all charged particles, thus they mostly measure the dominant EM component of the cascade. The sensitivity of an array of flat scintillators for inclined CRs drops quickly towards the horizontal direction because of the decrease of their effective surface and because of the absorption of the EM component. Usually, data of scintillator arrays are restricted to zenith angles below  $45^\circ$ .

An alternative to scintillator counters are water Cherenkov tanks. The pioneering largest EAS using this technique was the Haverah Park array, operating in England from 1964 to 1987, made of water tanks of various sizes spread over about  $12\text{ km}^2$ . In water, charged particles emit Cherenkov radiation. These detectors are heavy and require extra pure water with excellent protection against contamination. In addition, they are not as easy to deploy as scintillators. These disadvantages are compensated by the fact that the Cherenkov light generated in water is proportional to the path length of the particle. For this reason, water tanks are sensitive to both the electromagnetic and the muon components. On average (the correct numbers depend on the exact detector geometry) a muon releases about 10 times more light than a single 20 MeV electron. Because of their height (typically of the order of 1 m), water tanks also offer a nonzero effective surface for horizontal showers.

### 4.6.1 A Toy Example of an EAS Array

We use a toy model (Fig. 4.11) to illustrate some interesting features of the detection of the EM component using an EAS array. The figure on the left shows the footprint of a vertical shower generated by a primary iron nucleus with  $E_* = 4 \times 10^{15}\text{ eV}$ . We assume a detector at 2000 m above sea level, corresponding to about  $820\text{ g cm}^{-2}$ . At this depth, the corresponding shower size is  $N_e = 8 \times 10^5$  (as can be obtained from Fig. 4.3). The array consists of  $14 \times 14$  counters (plastic scintillator for instance,  $1\text{ m}^2$  each and spaced by 15 m). We have superimposed on each counter the number of shower particles crossing it. The total instrumented surface is  $A = 4 \times 10^8\text{ cm}^2$ ; the total surface of the detectors is  $A_{\text{det}} = 196 \times 10^4\text{ cm}^2$ , the ratio between  $A_{\text{det}}/A = 5 \times 10^{-3}$ .

The counters of this array detect mainly electrons and positrons; few photons convert in the detector. To a first approximation each electron crossing a counter loses the same amount of energy  $\xi$ . A counter measures the total energy  $\Delta E$  released by incoming particles in a given time window. Usually the employed detection technique and the data acquisition electronics give a linear response in a wide interval of  $\Delta E$ .



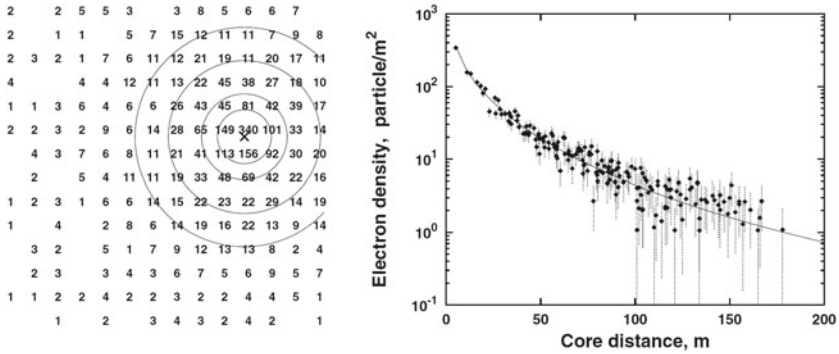


**Fig. 4.11** *Left* A simulated event on an ideal detector with 196 counters (each having a surface of  $1 \text{ m}^2$ ) on a  $15 \text{ m}$  grid. The geometry is similar to that of the KASCADE array. The lateral distribution was sampled from the NKG distribution, Eq. (4.21), with Poissonian fluctuations. At the position of each counter, we show the number of detected particles. Some empty counters are also present. The circles represent the regions within which the number of particles per counter exceeds 10, 20, 50 and  $100 \text{ m}^{-2}$ , respectively. *Right* The particle density as function of the distance from the shower axis for the event shown on the left. The line represents the average particle lateral distribution. From Stanev (2010)

In this case, the number of particles crossing the counter can be estimated as  $\Delta E/\xi$ . If the number of particles is too high, saturation effects can occur.

Each counter usually suffers for a continuous counting rate due to noise, mainly due to the environmental radioactivity. Such noise has a random nature and occurs on different counters at different times. To get rid of such spurious signals, a time coincidence among several counters is normally required. The arrival of a shower is therefore identified by the array when many counters register within a short time interval a signal well above that registered in the absence of a shower. A trigger usually consists of a minimum number (majority) of counters fired in the same time window. In the presence of a trigger, the information (number of particles, arrival time, ...) registered by each counter are stored on computer.

The expected rate of CRs with energy at least equal to  $E_* = 4 \times 10^{15} \text{ eV} = 4 \text{ PeV}$  producing events similar to that shown in Fig. 4.11 can be obtained from the particle flux (2.17b):

$$\dot{N}(> E_*) \equiv \mathcal{F} \cdot A = \Phi(> E_*) \times \frac{\pi}{2} \times A \times \varepsilon. \quad (4.49)$$

The factor  $\pi/2$  instead of  $\pi$  arises because only downward going particles reach the detector. We need to anticipate the result on the CR flux above the knee Sect. 4.8 and given in Eq. (4.53), i.e.  $\Phi(> E) = 2.2 \times 10^{-10}/E^{2.06}$  when the energy is expressed in PeV. Thus:

$$\dot{N}(> E_*) = \frac{2.2 \times 10^{-10}}{4^{2.06}} \times \frac{\pi}{2} \times [4 \cdot 10^8] \times \varepsilon \simeq 10^{-2} \times \varepsilon (\text{s}^{-1}) \simeq 10 \text{ events/h} \quad (4.50)$$

The quantity  $\epsilon$  represents the overall array efficiency, which includes the fraction of solid angle covered, the fact that showers near the detector edges could not trigger the detector, etc. A factor  $\epsilon \sim 0.3$  is assumed here.

Let us estimate the energy range in which this array can efficiently detect CRs. Let us start considering a primary CR having the same core axis as the one just considered and a tenth of the energy  $E_*$ . The corresponding shower will have a particle density smaller by an order of magnitude. Each number on Fig. 4.11 will be a factor of 10 smaller and the outer ring will have a particle density of  $1 \text{ m}^{-2}$ . About 70 counters will have fired and the energy and direction of the CR originating the shower can be reconstructed. A shower produced by a CR with energy  $E_*/100 = 4 \times 10^{13} \text{ eV}$  will have a density hundred times smaller than that of the event in Fig. 4.11. Now, the inner ring will have a particle density of  $1 \text{ m}^{-2}$ . The cascade will interest very few counters, below the majority needed to trigger the apparatus. We conclude that our EAS array is able to detect showers from primaries having energy  $\gtrsim 10^{14} \text{ eV}$ .

On the other side, a primary with energy  $10E_*$  will have such a large number of particles to fire all counters and some of them could saturate. As the integral flux decreases as  $E^{-2.06}$  in this energy range, the event rate reduces to  $\dot{N}( > 10E_*) = 10^{-2.06} \dot{N}( > E_*) = 3/\text{day}$ . A shower produced by a CR with energy larger by another decade covers a much larger surface and saturates almost all counters. Only a rough estimate of the primary energy can then be given. However, due to the flux decrease, the event rate reduces by an additional  $10^{-2.06}$  factor to few events/year. In conclusion the considered array could measure efficiently primary CRs in the energy range  $10^{14} \lesssim E_0 \lesssim 10^{17} \text{ eV}$ .

A viable solution to increase the maximum value of measurable energy keeping constant the number of counters would be to increase the distance between counters. This solution is almost costless if the apparatus does not interfere with civil, engineering or environmental constraints, for instance being installed in a desert region. It is intuitive that the same counters distributed over a larger area would increase the lowest measurable CR energy.

The right side of Fig. 4.11 shows the measured density distribution as a function of the distance from the shower axis. The position of the shower axis on the detection plane can be estimated in different ways, for instance finding the center of gravity of the counting rate. The counter measuring the highest particle number (340) is very close to the shower core. Each point corresponds to the measurement of one counter at a given distance from the core. The error band corresponds to the statistical error: for poissonian statistics, the error is the square root of the number of counted particles.

In the following we present some selected EAS experiments covering the energy range up to  $\sim 10^{18} \text{ eV}$  and discuss the ways in which direction, energy and mass of the primary can be derived from the data. For a review, see Nagano and Watson (2000); Blümer et al. (2009); Grieder (2010); Letessier-Selvon and Stanev (2011).



### 4.6.2 Some EAS Experiments

The **Extensive Air Shower on Top (EAS-TOP)** array was located at Campo Imperatore, in central Italy, at a height of 2,005 m (above the underground Gran Sasso laboratories), at  $820 \text{ g cm}^{-2}$  atmospheric depth. It has been in operation, in different configurations, between 1989 and 2000. Its EM detector was made of 35 scintillator modules,  $10 \text{ m}^2$  each, separated by 20 m in the central region and 80 m near the edges of the array. The detector was fully efficient for electromagnetic sizes  $N_e > 10^5$ . A central muon-hadron calorimetric detector, covering a surface of  $140 \text{ m}^2$  was also present. It consisted of 9 layers of 13 cm thick iron absorbers and limited streamer tubes as active elements. Muons were counted if their energy was  $> 1 \text{ GeV}$ .

The **KArlsruhe Shower Core and Array Detector (KASCADE)** experiment has been running successfully since 1996 and studies CRs in the range from  $10^{14}$  to  $10^{17} \text{ eV}$ . It detects a combination of observables: electrons, muons at four energy thresholds, and energy and number of hadrons (Antoni et al. 2003). The main components are the field array, a central detector and the muon-tracking detector. The field array measures electrons and muons ( $E_\mu > 230 \text{ MeV}$ ) in the shower separately using an array of 252 detector stations containing shielded and unshielded detectors, arranged on a square grid of  $200 \times 200 \text{ m}^2$  with a spacing of 13 m. Figure 4.12 displays a sketch of a detector station. The EM size is measured by the  $e/\gamma$  detectors, which are positioned over a lead/iron plate inside a wooden hut. Each  $e/\gamma$  detector consists of a liquid scintillator covered by a light collecting cone. On top, a light collector and a photomultiplier are mounted to read out the signals. The energy resolution reached

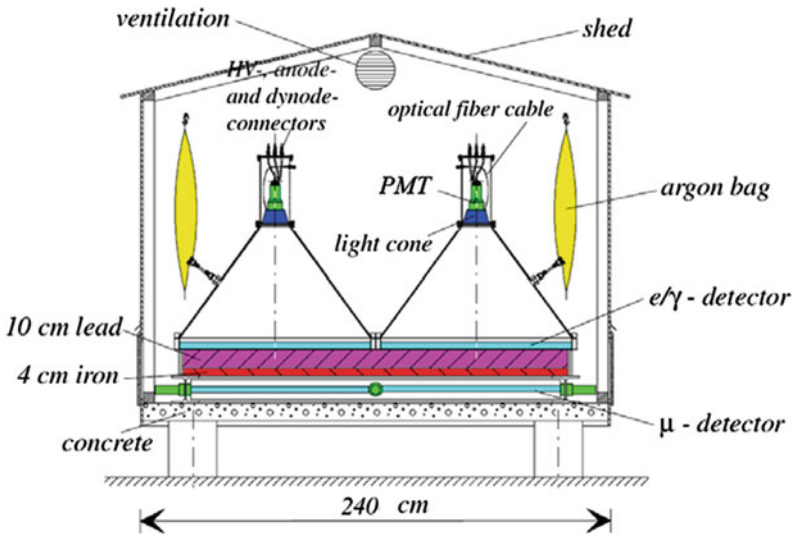


**Fig. 4.12** Schematic view of one of the 256 sample array detector stations of the KASCADE experiment. Courtesy of the KASCADE collaboration (<https://web.ikp.kit.edu/KASCADE/>)

is  $\sim 8\%$  at 12 MeV, which corresponds to the mean energy deposit of a minimum ionizing particle (m.i.p.). Energy deposits up to  $\sim 2000$  m.i.p. can be measured. The time resolution has been determined to be  $\sim 0.8$  ns.

In the 192 outer stations the muon detectors are installed underneath the  $e/\gamma$  detectors followed by a shielding of 10 cm lead and 4 cm iron, corresponding to 20 radiation lengths, which stop the EM component. Muons can cross the shielding, and the  $\mu$ -detector consists of four plastic scintillators of 3 cm thickness and  $0.8\text{ m}^2$  surface. The light is read out by 1.5-inch photomultipliers. The energy resolution has been determined to be about 10% at 8 MeV, the mean energy deposited by a muon.

The surface covered with detectors is 1.3 and 1.5% of the total area for the electromagnetic and the muonic detectors, respectively. This large fraction of instrumented surface and the small distance between counters allows the reconstruction of the incident angles, the lateral distributions and the measurement of the size of  $N_\mu$  and  $N_e$  for CRs down to  $10^{14}$  eV. The layout of the KASCADE detector is shown in Fig. 4.13 (right).

As an extension of KASCADE, **KASCADE-Grande** was built by reassembling 37 stations of the electromagnetic detectors of the former EAS-TOP experiment. The goal of this enlargement was to extend the measurement of primary CRs up to  $10^{18}$  eV. The area covered by the EM array is expanded to  $700 \times 700\text{ m}^2$  with the 37 stations,  $10\text{ m}^2$  each. The layout of the experiment is shown in Fig. 4.13 (left).

The **Yakutsk array** represents the most complex, and most northerly, of the early giant arrays. It was operated by the Institute of Cosmophysical Research and Aeronomy at Yakutsk, Siberia (105 m above sea level) since 1967 and was enlarged to

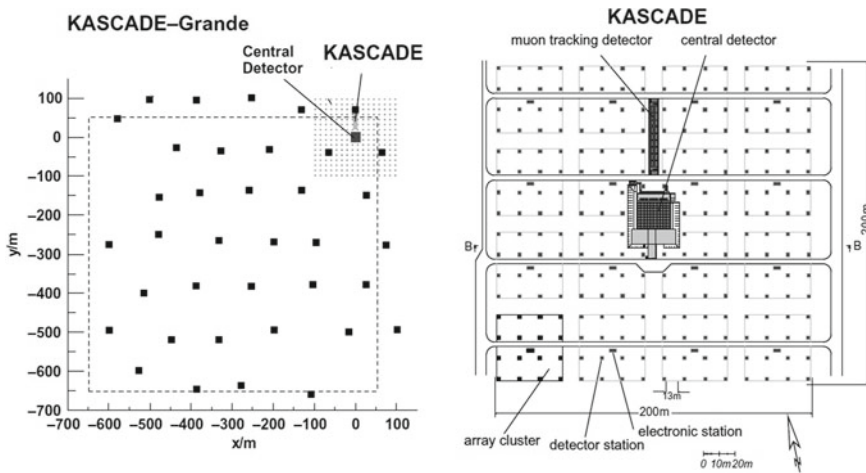


**Fig. 4.13** (Left) Schematic top view of the KASCADE-Grande experiment, with the KASCADE on the top right hand corner of the figure. (Right) Layout of the KASCADE experiment and its subdetectors. The figure also shows the organization of the KASCADE array into 16 clusters of 16 or 15 stations. The highlighted lower left cluster is equipped with Flash-ADC. Courtesy of the KASCADE collaboration (<https://web.ikp.kit.edu/KASCADE/>)

cover an area of  $18 \text{ km}^2$  in 1974. A particularly important feature was the presence of 35 Photo Multiplier Tube (PMT) systems of various areas to measure the air-Cherenkov radiation associated with the showers. These gave indirect information on the longitudinal development of showers and provided a calorimetric approach to the energy estimates for the primary particles. Measurements relating to CRs above  $10^{17} \text{ eV}$  have been reported.

The **Chicago Air Shower Array (CASA)** detector was an array of both surface and underground plastic scintillators, which measured the electromagnetic, and muon components of air showers. The array was located on Dugway Proving Grounds, Utah, USA and operated without interruption for the five year, from 1992 to 1997, measuring CRs in the energy range  $10^{14}$ – $10^{16} \text{ eV}$ . The 1089 CASA detectors were distributed on a regular grid with a 15 m spacing for the detection of the electromagnetic component. The area enclosed by CASA was  $0.23 \text{ km}^2$  and included **the Muon Array (MIA)** consisted of 1024 scintillation counters distributed in 16 patches of 64 counters each. The MIA counters were buried beneath approximately 3 m of earth and had a typical muon energy threshold of  $\sim 1 \text{ GeV}$ .

### 4.6.3 Cherenkov Light Produced by EAS Showers

The **majority of particles in EAS travel with relativistic velocities** through the atmosphere. **Cherenkov radiation** is emitted when a **particle has a speed exceeding that of light in the medium**. The **emitted radiation falls in the wavelength region of 300–350 nm (near ultraviolet)** that **matches** very well the **quantum efficiency of most photomultipliers**. Due to their low mass, **electrons (and positrons)** have a **low Cherenkov threshold**,  $E_T = 21 \text{ MeV}$  at sea level,  $35 \text{ MeV}$  at 8 km of altitude. The reason for the **change in  $E_T$**  is the **variation** of the Cherenkov **threshold velocity** with the **changing refraction index** of the atmosphere  $n = n(h)$ . For Standard Temperature and Pressure (STP) conditions,  $n = 1.00029$ ; as the **pressure varies with altitude**,  $n$  **decreases with increasing  $h$** . The **emission angle** of Cherenkov light with respect to the particle direction is given by:  $\theta_C = \cos^{-1}(1/n)$  with  $\theta_C = 1.3^\circ$  at STP.

The **angle increases** when the EM **shower propagates from the top of the atmosphere down to the ground level** (see Fig. 4.14).

For the **detection of Cherenkov light two techniques** have been used: **i) integrating detectors** (described below) consisting of arrays of photomultipliers looking upwards in the sky and distributed over a large area at ground level; **ii) imaging detectors or telescopes** (Chap. 9) composed of large area collection mirrors and a camera with segmented photomultiplier read-out. **Optical devices** such as **Cherenkov detectors** and **fluorescence detectors** can only be **operated during clear moon-less nights**. This restricts their **duty cycle to about 10 %**.

**Integrating detectors measure the lateral distribution of the Cherenkov light** (see the right side of Fig. 4.14) **with an array of PMTs**. The **longitudinal development** in the atmosphere can **also be measured**, in particular the **position  $X_{\text{max}}$**  of the **shower maximum**. These instruments are operating in most cases near array detectors measuring

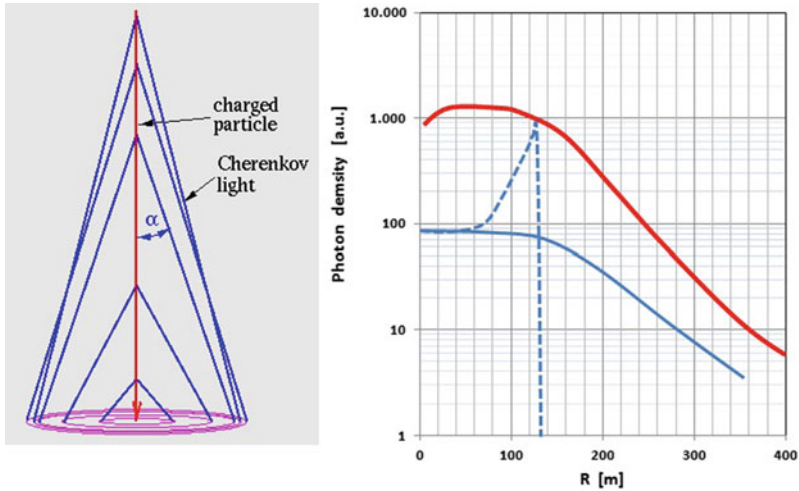


**Fig. 4.14** *Left* Cherenkov light emission from EAS at 5 different atmospheric heights, showing the changing Cherenkov emission angle as a function of the depth, related to the variation of the atmospheric refraction index (courtesy of dr. Konrad Bernloehr). *Right* Resultant photon density at ground level for two different primary energies differing by an order of magnitude. The *dashed line* represents the photon density for the case of no electron multiple scattering for lower energy shower

the EM and/or muonic component to increase the number of observed quantities of the same shower. This technique was **pioneered** by the **AIROBICC** experiment on the La Palma island.

The Broad Lateral Non-imaging Cherenkov Array (**BLANCA**) takes advantage of the CASA-MIA particle array installation by augmenting it with **144 Cherenkov detectors**. The Dugway atmospheric depth corresponds to  $870 \text{ g cm}^{-2}$  and BLANCA uses the CASA trigger (threshold at  $\sim 10^{14} \text{ eV}$ ) to collect Cherenkov light from CR in the knee region. Each BLANCA detector contains a light collecting cone (called *Winston cone*) to concentrates the light striking an  $880 \text{ cm}^2$  entrance aperture onto a PMT tube. The minimum detectable density of a typical BLANCA unit is approximately (one blue photon)/ $\text{cm}^2$ . BLANCA operated between 1997 and 1998, for a total of  $\sim 460 \text{ h}$  of Cherenkov observations.

The Dual Imaging Cherenkov Experiment (**DICE**) was a ground based air shower detector consisting of two telescopes located at the CASA-MIA site with an effective geometrical factor of  $\sim 3,300 \text{ m}^2 \text{ sr}$ . Each telescope used a 2 m diameter spherical mirror with a focal plane detector consisting of 256 close packed 40 mm hexagonal PMTs which provide  $\sim 1^\circ$  pixels in an overall field of view of  $16^\circ \times 13.5^\circ$  centered about the vertical. The telescopes were on fixed mounts separated by 100 m.

A Cherenkov detector array is also the **Tunka**, close to lake Baikal in Siberia, where 133 PMTs with 8 inches diameter distributed over a  $\sim 1 \text{ km}^2$  surface are operational from 2009, replacing an older 25 PMTs array.

## 4.7 The Time Profile of Cascades

The different developments of the EM and muonic components of EAS induce a difference in the arrival times of electrons and muons at the observation level. Therefore, an alternative to the use of dedicated muon detectors is the separation of the muon and EM components by an adequate cut on the particle arrival time. Muons are on average produced higher in the atmosphere and scatter far less than electrons do; they are heavier than electrons and are less affected by the geomagnetic field. Their paths to ground are nearly straight lines. Most  $e^\pm$  are on average produced deeper in the atmosphere and reach the observation point after multiple scattering. This generates longer path lengths and thus longer times of flight. The resulting effect of the different development is that muons arrive earlier at the observation level than the EM component.

These features, which can provide an interesting experimental tool to measure the two components using the same counter array, are confirmed by detailed Monte Carlo simulations. In fact, EAS detector arrays can be equipped with modern fast time resolving electronics to sample the time development of the detector responses. This offers an alternative method to determine the muon content of EAS.

A first measurement of such time delay was performed by the KASCADE-Grande array (Apel et al. 2008). The time structure of the EAS disk was analyzed as a function of the distance  $R$  from the shower axis up to  $R = 600$  m. A Flash-ADC<sup>7</sup> based data acquisition system installed on a cluster (see Fig. 4.13) of the KASCADE array samples detector signals of the  $e/\gamma$  and the  $\mu$ -detectors, respectively.

Figure 4.15 shows a sketch of the EM and muonic shower fronts. The quantity  $\langle t \rangle(R)$  represents the delay of the EAS with respect to a flat front as a function of the radial distance  $R$  from the shower core. The delay (in units: ns) increases with increasing  $R$  (measured in m) as  $\langle t \rangle[\text{ns}] \simeq 0.2R$  up to  $R \sim 500$  m. For  $R > 200$  m the electronic system of the KASCADE-Grande detector was able to separate the contributions from the EM and muonic components. Close to the shower core ( $R < 200$  m) the maximum difference in their average arrival time amounts to 4 ns.

The measurements confirm that a shower is a thin pancake of particles propagating near the core axis, and the thickness (indicated with  $\sigma(R)$  in Fig. 4.15) increases as increasing distance  $R$  from the shower axis. For  $R < 400$  m the thickness of the EM shower increases linearly according to the relation  $\sigma(R)$  [ns]  $\simeq 0.2R$  ( $R$  in [m]). For a particle propagating at the light speed, 1 m thickness corresponds to  $\sim 3$  ns. The muon shower disk is similar to that of the EM component.

The thickness of the high-energy components of the shower is expected to be very small. This has been measured using the arrival time of the penetrating component of

<sup>7</sup> Analog-to-Digital Converters (ADC) convert the height or the integral of an electronic signal into a digital number. For instance, the height of a signal between 0 and 5 V may be converted by a 10-bit ADC into a number between 0 and  $2^{10} - 1 = 1,023$ . Flash-ADCs are very fast compared to other ADC types, so a single flash-ADC can be used to analyze various channels in sequence, or to analyze in a time-sequence the development of a pulse, functioning in this way as a Waveform Analyzer (WFA).





The shower direction (defined by its zenith  $\theta$  and azimuth  $\phi$  angles) is the normal to the propagating shower front, that is approximately a plane in the proximity of the shower axis, but has a spherical-like shape away from, see Fig. 4.15. The direction of the incoming CR can be deduced from geometrical considerations by measuring the time delay  $\Delta t = T_i - T_j$  between different counters.

In principle, three counters are enough to identify a plane. However, due to uncertainties on timing, on statistical fluctuations and on the finite thickness of the shower front, a larger number of counters is necessary for a sufficiently precise measurement. For these reasons, the CR direction is usually derived from a chi-squared minimization or a maximum-likelihood procedure using the measured arrival time of the shower front in a large number of counters, assuming the shower core to lie in the plane perpendicular to the shower axis. The quality of the reconstruction degrades when the measurement is performed far from the axis, because the thickness of the particle disk grows and the density decreases.

The uncertainties on the zenith  $\theta$  and azimuth  $\phi$  angles depend on the time resolution of the detection technique used by the EAS array and on the cascade size. Typical detectors have time resolutions in the range from 0.5 ns up to a few ns. For instance, the angular resolution of the KASCADE detector improves from  $0.55^\circ$  for small showers with size  $N_e \sim 10^4$  to  $0.1^\circ$  for showers with  $N_e \sim 10^6$ .

After the shower core position and shower direction have been determined the shower size can be obtained from a fit of the experimental lateral distribution using the NKG function. We recall that  $dN_e/dr$  at a given distance  $r$  depends on the shower size  $N_e$ , on the Molière radius and on the shower age  $s$ . The difficulty is that  $s$  is not known and should be determined from the data themselves. Some experiments perform a global fitting procedure of the lateral distribution which includes as free parameters the axis position, direction and the age  $s$  (the Molière radius can be determined from the atmospheric density at the position of the array). Another possible solution is to use in the fit an average value of  $s$  appropriate for the detector altitude and array layout. This average  $s$  is usually computed through a Monte Carlo simulation or empirically derived from the data. Once also  $s$  is fixed, the shower size can be derived from (4.21) assuming azimuthal symmetry in the plane perpendicular to the shower:

$$N_e = \int_0^{\infty} \frac{dN_e}{dr} \cdot 2\pi r dr. \quad (4.51)$$

The size  $N_e$  is proportional to the primary CR energy  $E_0$ .

Figure 4.16 shows an example (from the EAS-TOP experiment) of the use of the NKG lateral distribution with a fixed value of  $s$  to fit the measured shower size as a function of the distance from the core. The agreement is good in every shower size interval; differences are at most 10% for large core distances. Other solutions are also adopted. The KASCADE experiment for instance found that the lateral distributions of the three shower components (electromagnetic, muonic, and hadronic) can all be parameterized using the NKG function. They fitted simultaneously the

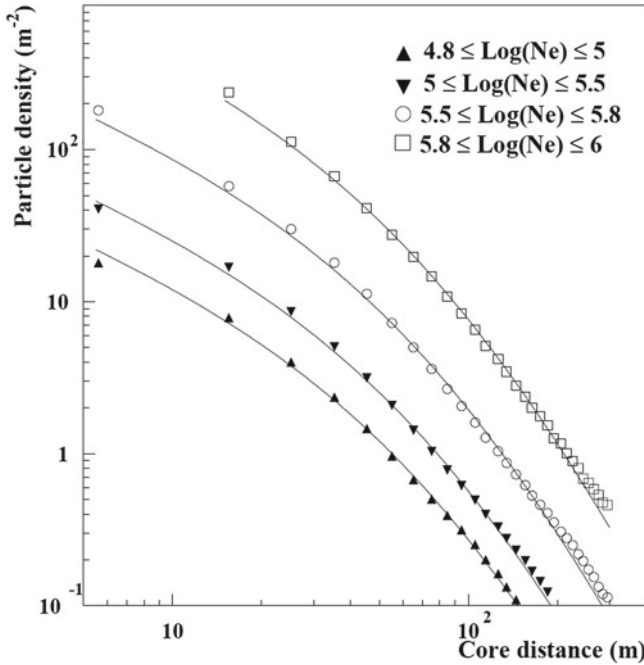


**Fig. 4.16** Experimental lateral distributions in different intervals of measured shower size  $N_e$ . The average particle density as a function of the distance is fitted with the NKG function (4.21) (solid lines), with  $r_1 = 100$  m and a fixed age parameter  $s = 1.21$ . Courtesy of EAS-Top Collaboration

parameters  $N_e$ ,  $r_1$  (4.22) and  $s$  finding that the measured lateral distributions of the electromagnetic component can be reproduced with an accuracy of about 1 %.

The arrival direction of charged CRs with primary energies between  $10^{14}$ – $10^{18}$  eV is remarkably isotropic. Different sky regions were observed by different EAS arrays both in the Northern and in Southern hemispheres. No excess of particles is measured from any particular direction in celestial coordinates. The trajectories of charged particles are largely tangled by regular and stochastic interstellar magnetic fields (Sect. 2.7.1). The EAS array measurements in the region between  $10^{14}$ – $10^{18}$  eV confirm that the CR flux on Earth is consistent with isotropy. No astronomy of charged CRs through the identification of an excess of events from a given direction is possible in this energy range.

A large-scale anisotropy that would reflect the general pattern of propagation of CRs in the Galactic environment is anyway expected, as presented in Sect. 5.7.



## 4.9 The CR Flux Measured with EAS Arrays

The CR flux in the region up to  $10^{18}$  eV is still dominated by protons and nuclei originating in our Galaxy. Many experiments provided measurements of the number of events as a function of the energy  $E_0$ , the so-called *all-particle spectrum* (Hörandel 2007). This represents the sum over all nuclear species present in cosmic rays, without any separation. The energy  $E_0$  can be derived through the measurement of the shower size. The experimental situation is complicated by the fact that surface detectors do not observe the number of electrons at shower maximum, but at a fixed depth  $X_{\text{det}}/\cos\theta$ , where  $\theta$  is the CR zenith angle. The number of particles  $N_e$  is calculated using (4.51) and the energy  $E_0$  by inversion of (4.42) or similar relations. The CASA-MIA group used the measured  $N_e$  and  $N_\mu$  sizes to derive the primary energy through (4.34). The KASCADE-Grande experiment found a more complex relation to estimate  $E_0$  as function of the observed number of electrons (with  $E_e > 3$  MeV) and muons (with  $E_\mu > 300$  MeV) at sea level. More accurate size-to-energy conversions are obtained from detector-dependent Monte Carlo simulations.

As an example of an individual experiment, let us consider the EM size  $N_e$  measured by EAS-Top (Aglietta et al. 1999). Figure 4.17 shows the measured size spectrum for showers from almost the vertical direction (up to  $17^\circ$ ). The statistical accuracy is better than a few percent in most bins. The size  $N_e$  is proportional to the primary energy  $E_0$ . From simulations (using CORSIKA with the HDPM hadron interaction

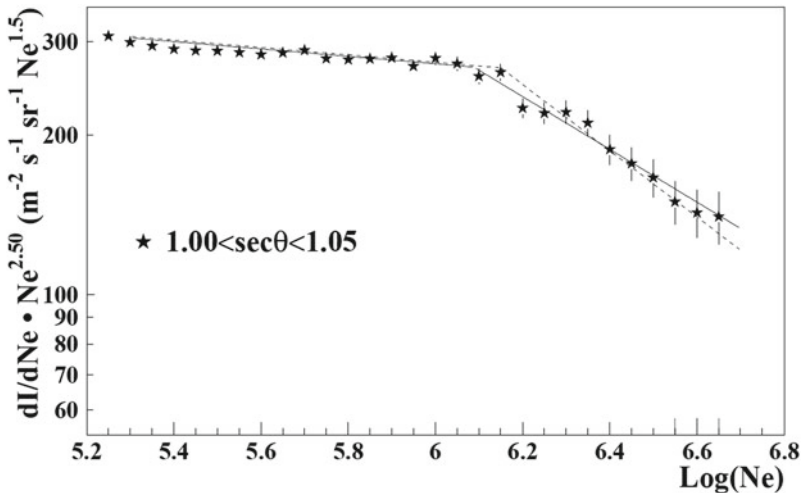


**Fig. 4.17** Flux of CRs with zenith angle  $\theta < 17^\circ$  as a function of the shower size  $N_e$  measured at the atmospheric depth of  $820 \text{ g cm}^{-2}$  by the EAS-Top experiment. An almost linear dependence between measured size and energy exists and the data on the  $x$ -axis, when converted to energy, range between  $0.9 \times 10^{15}$  and  $1.0 \times 10^{16}$  eV, covering the knee region. The flux has been multiplied by  $N_e^{2.5}$  to make evident the change of slope occurring at  $\log N_e \sim 6.1$ . Courtesy of EAS-Top Collaboration

model, Sect. 4.5), the energy interval of sensibility of the experiment was between  $(0.9 < E_0 < 10) \times 10^{15}$  eV, exactly the region around the knee. The size spectrum was multiplied by  $N_e^{2.5}$  (as  $N_e$  depends almost linearly on  $E_0$  this is equivalent to the multiplication by  $E_0^{2.5}$ ) to emphasize the change of slope at the knee.

The shower size  $N_e$  produced by primaries of a given energy will fluctuate from shower to shower because of differences in the stochastic development of the cascades. These considerations led Hillas to suggest that a more appropriate quantity to estimate the primary CR energy would be the measured particle density at a relatively large distance from the shower axis. Here the fluctuations are small and hence the density depends only on primary energy. Hillas proposed to use the signal at an optimal distance depending on the energy range and the array spacing. Monte Carlo simulations have confirmed that the density far from the shower axis depends only mildly on the used hadronic interaction model or on the primary composition, and may be used reliably as an estimator of the total energy. This method (Letessier-Selvon and Stanev 2011) was used for instance by the Haverah Park and AGASA experiments (Sect. 7.7).

A compilation of the results from a large number of different experiments is shown in Fig. 4.18. The y-scale variable has been multiplied again by  $E_0^{2.5}$ . At a fixed energy  $E_0$  there is some dispersion of the points. The red line in Fig. 4.18 shows the extrapolation up to the knee region of Eq. (2.20) obtained from a fit to direct measurements. The position of the knee is at  $\sim 4 \times 10^{15}$  eV. It is evident that the

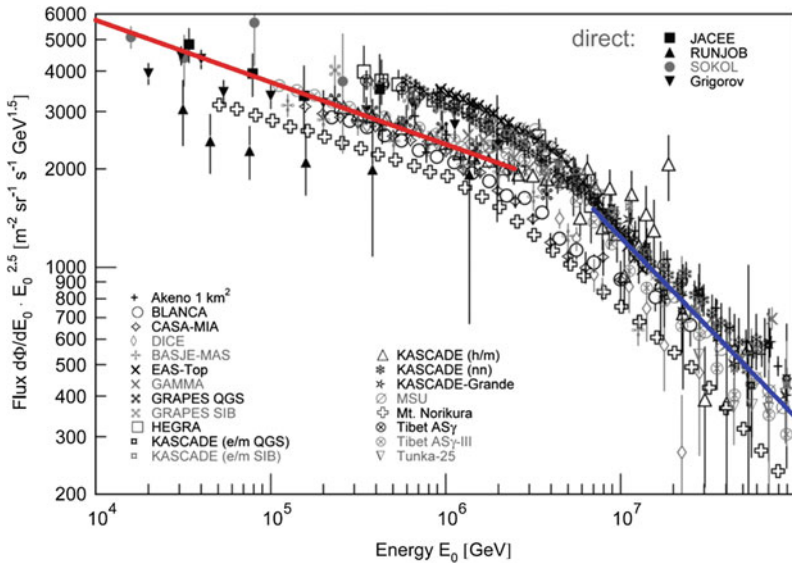


Fig. 4.18 All-particle energy spectra in the knee region from air shower experiments and few direct experiments. The red line below the knee refers to the power-law spectrum (2.20), while the blue line above the knee to (4.52). See Blümer et al. (2009) for the references to the quoted experiments

extrapolation of (2.20) around and above the knee is no longer valid. After a smooth transition in the knee region the new spectral index of the power-law function can be derived from EAS data in the energy region above  $10^{16}$  eV. The differential energy spectrum between  $10^{16} - 10^{18}$  eV can be expressed as:

$$\Phi(E) \sim 1026 \times \left( \frac{E}{1 \text{ GeV}} \right)^{-3.06} \frac{\text{particles}}{\text{cm}^2 \text{ s sr GeV}} \quad (4.52)$$

This function (when multiplied by  $E^{2.5}$ ) corresponds to the blue line in Fig. 4.18 and is derived from the data compilation of Hörandel (2003). Here, an energy-renormalized scale of the individual experiments has been applied. We will return on that in Sect. 7.7.3. The dispersion of the points from different EAS experiments at a fixed value of the flux is mainly due to systematic uncertainties on the absolute energy calibration of each individual experiment. These systematic uncertainties are mainly due to the conversion from size  $N_e$  to energy  $E_0$ . Typical values of the absolute energy scale of each EAS experiment are about 15 to 25%. Most data sets agree within systematic uncertainties; this is a remarkable result, despite the fact that different experimental techniques are used, that the detectors are installed at different atmospheric depths and that different interaction models to interpret the observed data are employed.

The integral spectrum above the knee (note that here the energy is expressed in PeV, i.e.  $10^{15}$  eV, which is a more natural unit for this energy range) corresponding to (4.52) is:

$$\Phi(> E) \sim 2.2 \times 10^{-10} \times \left( \frac{E}{1 \text{ PeV}} \right)^{-2.06} \frac{\text{particles}}{\text{cm}^2 \text{ s sr}} \quad (4.53)$$

The all-particle spectrum of Fig. 4.18 contains no information about the CR mass. The sensitivity of indirect measurements is far from allowing an estimate of the nuclear mass  $A$  for each individual shower. However, recently techniques have been developed for the measurement of the relative abundances as a function of the primary energy at least for groups of nuclear components.

## 4.10 Mass Composition of CRs Around the Knee

The mass  $A$  of the nucleus of energy  $E_0$  originating the shower is another important quantity because it is correlated with the nature of the accelerating astrophysical sources. At least two independent quantities have to be measured in order to estimate both energy and mass of the primary CR that initiated the EAS. In addition to the shower size  $N_e$  usually the position  $X_{\text{max}}$  of the maximum or the muon size  $N_\mu$  are observed (Swordy et al. 2002; Kampert and Unger 2012). However, it is particularly difficult to determine  $E_0$  and  $A$  on a shower-to-shower basis, because of the intrinsic

fluctuation (at a fixed  $N_e$ ) of the  $X_{\max}$  and  $N_\mu$  of each cascade. Those fluctuations arise from the stochastic nature of the interaction processes (in particular, the atmospheric depth at which the first interaction occurs) and from experimental limitations. The latter include the large spacing and limited sampling size of most EAS detectors.

The nuclear composition of CRs has recently been deduced on a statistical basis by some EAS experiments. These measurements rely to a large extent on the theoretical understanding of the shower development and on the modeling of the hadronic interactions generating the cascade.

### 4.10.1 The $N_e$ Versus $N_\mu$ Method

In the  $N_e$  versus  $N_\mu$  technique, the electron size  $N_e$  (or the weighted sum of electron and muon size) is a measure of the primary energy, while  $N_\mu$  relates to the primary mass, Eq. (4.46). The electron-muon discrimination is achieved by employing a combination of unshielded and shielded scintillation detectors at ground level, as the quoted examples of KASCADE, KASCADE-Grande and CASA-MIA.

The individual spectra of groups with different mass were first obtained by the KASCADE Collaboration (Antoni et al. 2005) with a two-dimensional unfolding technique. This approach yields a set of energy spectra of primary mass groups (three are considered in Fig. 4.19: [p+He], medium, heavy [Si+Fe]), such that their resulting simulated distribution of  $N_e$  and  $N_\mu$  resembles the observed one.

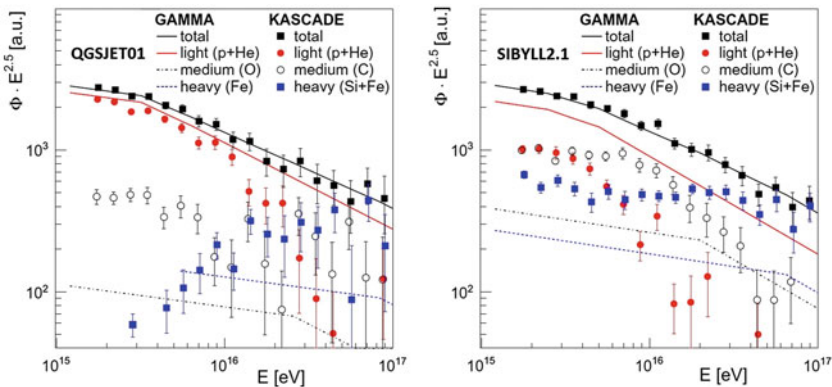


Fig. 4.19 Unfolded fluxes of different groups of nuclei as a function of the energy from the GAMMA and KASCADE experiments using two different interaction models (left QGSJET01; right SIBYLL2.1). The total represents the all-particle spectrum. Courtesy of Prof. Karl-Heinz Kampert

To solve the underlying mathematical equations the needed input is the so-called *response matrix (or kernel)* describing the correlation:

$$(E_0, A) \rightarrow (N_\mu, N_e)$$

including their *shower-to-shower fluctuations*. This relation means that to each simulated primary with given  $(E_0, A)$  corresponds an entry in the response matrix with a given number  $(N_\mu, N_e)$  of muons and electrons.

The *response matrix* will *depend* on the *chosen hadronic interaction model* employed in the EAS simulations and on the detector response, which is included in the simulation. The kernel establishes the connection between the searched quantities and the measured ones by inversion of the matrix filled with the measured quantities. *In the literature, it is known that a direct inversion of the matrix induces strong variations in the solution, mostly because of statistical fluctuations in the data.* Small changes in the contents of nearby bins in the observed distribution can produce huge fluctuations when inverting the response matrix. Methods which produce regularizations of the solution and iterative methods are known in the literature (Cowan 1998).

The level of systematic uncertainties imposed by the interaction models was studied by the KASCADE Collaboration constructing kernel functions using different hadronic interaction models and comparing the corresponding *unfolded results*. *Figure 4.19* shows the result obtained with *QGSJET-01* and *SIBYLL2.1*. They concluded that *neither model is able to describe the full range of energies consistently*. However, *they yield the same basic result: the CR composition at the knee is light (p-He dominated) with an evident change towards a heavy composition at higher energies*. Moreover, the data are consistent with the assumption of a rigidity dependent change of the knee energy. The figure reports also the result of the deconvolution from the data of the GAMMA Collaboration (Garyaka et al. 2007).

*Recently, data from the KASCADE-Grande experiment reached sufficient statistics to allow an extension of the unfolding analysis up to  $\sim 10^{18}$  eV.* The results (Apel et al. 2011) *confirm the earlier findings* of KASCADE and *indicate a very heavy composition at about  $10^{17}$  eV.*

### 4.10.2 Depth of the Shower Maximum

The *lateral distribution of Cherenkov light arriving on ground* is the result of a *convolution of the longitudinal profile of charged particles in the shower* (above the Cherenkov energy threshold  $E_T$ ) and the Cherenkov emission angle  $\theta_C$ . Both  $E_T, \theta_C$  *depend on the air density and thus on the height*. The *electron energy distribution and thus the number of electrons above  $E_T$  is an universal function of the shower age  $s$* , Eq. 4.20.

The *integrating Cherenkov technique provides a model independent method to measure both the calorimetric shower energy and  $X_{\max}$  in each individual CR cascade*

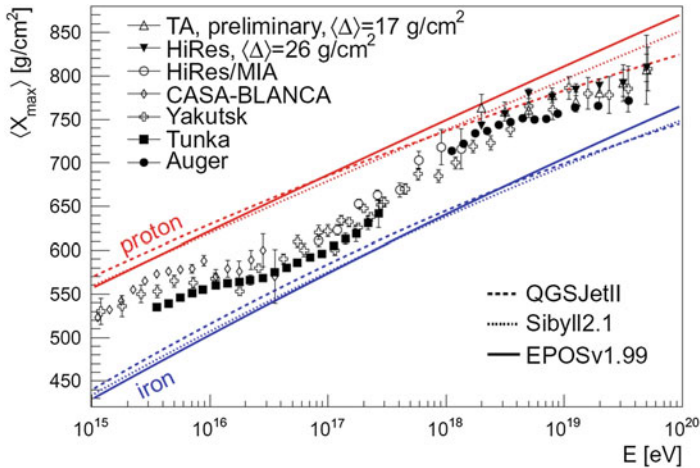


**Fig. 4.20** Measurements of  $X_{\max}$  with non-imaging Cherenkov detectors (Tunka, Yakutsk, CASA-BLANCA) and fluorescence (Sect. 7.6) detectors (HiRes/MIA, HiRes, Auger and TA). The results are compared to air shower simulations using three different hadronic interaction models (QGSJET, Sybyll, EPOS). Two extreme compositions are used: all showers induced by protons (red lines) or iron nuclei (blue lines). Courtesy of Prof. Karl-Heinz Kampert

with typical precision of a few tens of  $\text{g cm}^{-2}$ . The dependence of  $X_{\max}$  on energy  $E_0$  as measured by BLANCA, Tunka and Yakutsk is shown in Fig. 4.20. At low energies ( $E < 10^{16}$  eV) the three measurements disagree by up to  $40 \text{ g cm}^{-2}$ . The three detectors agree on a change towards a heavier composition before  $\sim 10^{16}$  eV. At  $\sim 10^{17}$  eV the values of  $X_{\max}$  from Tunka and Yakutsk are approaching the results of the simulations which use heavy primaries. Beyond that energy, the average shower maximum increases again towards the air shower predictions for light primaries. At even higher energies, approaching the region where the contribution of extragalactic CRs starts, only data from Yakutsk exist. Measurements above  $10^{18}$  eV will be discussed in Chap. 7.

The figure shows also the dependence of  $X_{\max}$  upon the energy  $E_0$  for different hadronic interaction models. It was assumed that all CRs are protons (red lines) or iron nuclei (blue lines). A variation of  $\sigma_{\text{inel}}$  and/or of the inelasticity parameter  $\kappa$  in the model would directly translate into uncertainties of the primary mass estimates obtained from the height of the shower maximum. Larger cross sections and higher inelasticity produce short showers, while smaller cross sections and lower inelasticity produce long showers penetrating deep into the atmosphere. The slopes of the curves represent the elongation rate defined in (4.15). The logarithmic increases of  $X_{\max}$  as a function of energy, Eq. (4.43), as well as the difference between  $X_{\max}^p$  and  $X_{\max}^{\text{Fe}}$ , Eq. (4.48), are evident.

We will continue the description of the highest energy component of the CRs, likely produced by extragalactic sources, in Chap. 7. The detection methods used to catch CRs up to  $\sim 10^{20}$  eV are similar to that described in this Chapter.

## References

- M. Aglietta et al., (EAS-TOP Coll.) The EAS size spectrum and the cosmic ray energy spectrum in the region  $10^{15} - 10^{16}$  eV. *Astropart. Phys.* **10**, 119 (1999)
- S.P. Ahlen et al., (MACRO Coll.). Arrival time distributions of very high energy cosmic ray muons in MACRO. *Nucl. Phys.* **B370**, 432–444 (1992)
- J. Alvarez-Muniz, R. Engel, T.K. Gaisser, J.A. Ortiz, T. Stanev, Hybrid simulations of extensive air showers. *Phys. Rev.* **D66**, 033011 (2002)
- L. Anchordoqui et al., High energy physics in the atmosphere: phenomenology of cosmic ray air showers. *Ann. Phys.* **314**, 145–207 (2004)
- T. Antoni et al., (KASCADE coll). The cosmic-ray experiment KASCADE. *Nucl. Instr. Methods* **A513**, 490–510 (2003)
- T. Antoni et al., KASCADE measurements of energy spectra for elemental groups of cosmic rays: results and open problems. *Astropart. Phys.* **24**, 1–25 (2005)
- W.D. Apel et al., Energy spectra of elemental groups of cosmic rays: update on the KASCADE unfolding analysis. *Astropart. Phys.* **31**, 86–91 (2009)
- W.D. Apel et al., Kneelike structure in the spectrum of the heavy component of cosmic rays observed with KASCADE-Grande. *Phys. Rev. Lett.* **107**, 171104 (2011)
- W.D. Apel et al., Time structure of the EAS electron and muon components measured by the KASCADE-Grande experiment. *Astropart. Phys.* **29**, 317–330 (2008)
- J. Blümer, R. Engel, J.R. Hörandel, Cosmic rays from the knee to the highest energies. *Prog. Part. Nucl. Phys.* **63**, 293–338 (2009)
- S. Braibant, G. Giacomelli, M. Spurio, *Particle and fundamental interactions*, (Springer, 2011), ISBN 978-9400724631
- G. Cowan, *Statistical Data Analysis*, (Oxford University Press, 1998). ISBN: 978-0198501558
- S. Eidelman et al., (Particle data group). Review of particle physics. *Phys. Lett. B* **592**, 1 (2004)
- R. Engel, D. Heck, T. Pierog, Extensive air showers and hadronic interactions at high energy. *Annu. Rev. Nucl. Part. Sci.* **61**, 467–489 (2011)
- T.K. Gaisser, *Cosmic Rays and Particle Physics* (Cambridge University Press, Cambridge, 1991)
- A. Garyaka et al., Rigidity-dependent cosmic ray energy spectra in the knee region obtained with the GAMMA experiment. *Astropart. Phys.* **28**, 169–181 (2007)
- K. Greisen, Cosmic ray showers. *Ann. Rev. Nucl. Part. Sci.* **10**, 63–108 (1960)
- P.K.F. Grieder, *Extensive Air Showers*, (Springer, 2010), ISBN 978-3-540-76940-8
- D. Heck, CORSIKA: A Monte Carlo Code to Simulate Extensive Air Showers. Forschungszentrum Karlsruhe FZKA 6019 (1998)
- W. Heitler, *Quantum Theory of Radiation* (Oxford University Press, Oxford, 1944)
- J.R. Hörandel, On the knee in the energy spectrum of cosmic rays. *Astropart. Phys.* **19**, 193–220 (2003)
- J. Hörandel, Cosmic rays from the knee to the second knee:  $10^{14}$ – $10^{18}$  eV. *Mod. Phys. Lett. A* **22**, 1533–1552 (2007)
- K. Kamata, J. Nishimura, *Progr. Theor. Phys.* **6**, 93 (1958)
- K.H. Kampert, M. Unger, Measurements of the cosmic ray composition with air shower experiments. *Astropart. Phys.* **35**, 660 (2012)
- K.-H. Kampert, A.A. Watson, Extensive air showers and ultra high-energy cosmic rays: a historical review. *Eur. Phys. J.* **H 37**, 359–412 (2012)
- J. Knapp, D. Heck, Extensive air shower simulation with CORSIKA: A User's Manual. Kernforschungszentrum Karlsruhe KfK 5196 B, 1993; for an up to date version see <http://www.wik.fzk.de/CORSIKA/>
- A. Letessier-Selvon, T. Stanev, Ultrahigh energy cosmic rays. *Rev. Mod. Phys.* **83**, 907 (2011)
- P. Lipari, The concepts of age and universality in cosmic ray showers. *Phys. Rev. D* **79**, 063001 (2009)
- J. Matthews, A Heitler model of extensive air showers. *Astropart. Phys.* **22**, 387–397 (2005)



- M. Nagano, A.A. Watson, Observations and implications of the ultrahigh-energy cosmic rays. *Rev. Mod. Phys.* **72**(3), 689–732 (2000)
- J. Nishimura, *Handbuch der Physik* **46**(2), 1 (1965)
- B. Rossi, K. Greisen, Cosmic ray theory. *Rev. Mod. Phys.* **13**, 240–309 (1941)
- T. Stanev, *High Energy Cosmic Rays*, (Springer, 2010), ISBN 9783540851486
- S.P. Swordy et al., The composition of cosmic rays at the knee. *Astropart. Phys.* **18**, 129–150 (2002)

# Chapter 5

## Diffusion of Cosmic Rays in the Galaxy

The observed spectra of CRs depend on two basic processes: the acceleration in the astrophysical sources and the propagation in the interstellar medium (ISM) of our Galaxy, described here. It is necessary to study first the latter (the propagation) in order to better understand the physics of acceleration mechanisms, subject of Chap. 6.

Upon leaving the source regions, charged energetic particles diffuse in the random galactic magnetic field that accounts for their high isotropy and relatively long confinement time. The galactic diffusion model explains the observations on energy spectra, composition, and anisotropy of CRs. It also provides a basis for the interpretation of radioastronomical, X-ray, and  $\gamma$ -ray measurements (Chap. 8) since a continuous radiation with a nonthermal spectrum is produced during propagation by the energetic electrons, protons, and nuclei.

Most information on CR propagation arise from the measurements of the abundances of some particular nuclei: the so-called *light elements* Li, Be, and B, that is elements with atomic number just below the abundant C, N, and O elements (*medium elements*). Light elements are mainly of *secondary* origin, i.e., produced as the result of interactions of heavier primary nuclei with the interstellar matter. The *stellar nucleosynthesis* processes explain the low cosmic abundance of Li, Be, and B. We use the observed ratio between light and medium elements to assess an analytic description of the problem (Sect. 5.1) and a first-order estimate of the *escape time* of CRs from our Galaxy. An independent method of “dating” the CR permanence in our Galaxy using radioactive nuclei is presented in Sect. 5.2.

The simple analytic description of CR propagation in the Galaxy will help us to build more general diffusion–convection equations for different cosmic ray species (Sect. 5.3). This *diffusion equation* incorporates also energy loss and gain processes in the interstellar medium, nuclear fragmentation, and radioactive decay of unstable nuclei. The galactic magnetic field randomizes the arrival direction of charged particles, making the *flux isotropic*.

Nowadays, the propagation process is well described by solving numerically (e.g., the GALPROP simulation code shown in Sect. 5.4) or analytically the diffusion equation. The empirical transport coefficients of CRs, the properties of the sources (namely the total power, energy spectra of different components, elemental

and isotopic composition), and the size of the confinement region of cosmic rays in the Galaxy are determined from fits to all available data on cosmic rays (Ptuskin 2012).

A knowledge of the effects of the propagation of CRs and the use of detailed diffusion models is very important not only to deduce the physical conditions at the sources, but also to estimate the dependence of the escape time upon particle energy. This is derived using the observed ratio of secondary to primary nuclei. For example, the boron to carbon ratio is decreasing with energy at  $E > 1$  GeV/nucleon, as shown in Sect. 5.5. The dependence of the escape time on energy provides a very important constraint on the spectral index of CRs at sources, as obtained in Sect. 5.6.

Small anisotropies are expected for the escape process of CRs out the Galaxy, or to the possible contribution of sources near to the solar system, or due to the motion of the solar system in the Galaxy. The expected amplitude and the status of experimental searches for large-scale anisotropies are in Sect. 5.7.

Electrons, as the lightest stable-charged particles, are subject to additional energy loss mechanisms with respect to protons and nuclei. The presence of magnetic fields induces synchrotron emission, which produces intense electromagnetic radiation in the proximity of the electron accelerators. In addition, a diffuse emission is produced during electron propagation in the galactic disk. As a consequence, severe limits on the electron energy spectrum and on the distance of CR electron sources can be derived Sect. 5.8.

## 5.1 The Overabundance of Li, Be, and B in CRs

The material formed in the early phase of the universe, at the time of the primordial nucleosynthesis, was in mass 3/4 protons and 1/4 helium nuclei. All heavier nuclei present in the periodic table of elements are produced by nucleosynthesis in stars, Chap. 12. Stellar nucleosynthesis is the process of nuclear fusions inside stars, producing energy to support their gravitational contraction.

Nuclear fusion in stars proceeds until the formation of nuclei with  $A \leq 60$ . The involved nuclear reactions, Sect. 12.1, does not increase the abundance of light nuclei (Lithium, Beryllium, and Boron) as these elements act as catalysts of nuclear reactions. The heavier elements up to iron are only synthesized in massive stars with  $M > 8M_{\odot}$ . Once Fe becomes the primary element in the core of a star, further compression does not ignite nuclear fusion anymore; the star is unable to thermodynamically support its outer envelope. This initiates the gravitational collapse (Sect. 12.11). All nuclei formed during stellar nucleosynthesis are released in the Galaxy and could be used for the formation of new stars.

Li, Be, and B act as catalysts of thermonuclear reactions in stars and a low abundance after a stellar collapse is expected, as the collapse occurs when material for fusion is no longer available. The Li, Be, and B abundances in the solar system (and in the Universe) are generally very small for this reason.

The bulk of CRs is believed to be accelerated by galactic supernova remnants, Chap. 6. A similarity between the chemical composition of the solar system and that of nuclei present in the cosmic radiation is thus expected, as discussed in Sect. 3.6. A clear difference between the relative abundances of the Li, Be, and B elements in the CRs with respect to those in the solar system is evident in Fig. 3.7 and from Table 3.3:

$$R_{CR} \simeq 0.25; \quad R_{SS} \sim 10^{-5}, \quad (5.1)$$

Here,  $R_{CR}$  represents the ratio between the abundance of Li, Be, and B and that of C, N, and O nuclei found in CRs, and  $R_{SS}$  the corresponding ratio found in the solar system.

The discrepancy between the ratios in (5.1) is explained as due to the CR propagation in the Galaxy before reaching the Earth. The interstellar medium is filled with matter (mainly hydrogen, Sect. 2.7) and Li, Be, and B elements are produced during the propagation as an effect of interactions of heavier nuclei with protons of the interstellar medium.

### 5.1.1 Production of Li, Be, and B During Propagation

To simplify the problem, let us globally identify the Li, Be, and B secondary elements with the symbol  $\mathcal{L}$  (which stands for *light elements*) and the C, N, and O primary elements with  $\mathcal{M}$ , *medium elements*. The (relatively) abundant  $\mathcal{M}$ -type CR nuclei propagate in the Galaxy, constantly deflected by galactic magnetic fields until, in a random way, they reach the galactic border and exit the confinement volume. Along the way,  $\mathcal{M}$  nuclei can interact with protons of the interstellar medium. This gives rise to the so-called *spallation process* (or *fragmentation process*)<sup>1</sup>; the result of this interaction process is the ejection of some nucleons from the nucleus that has been hit.

The production of secondaries by CRs distributed over the whole galactic volume depends on the nuclear cross-section, on the average density of the interstellar material,  $\rho_{ISM}$  ( $\text{g cm}^{-3}$ ) and on the distance  $x$  (cm) traveled between the production and the exit from the Galaxy. The relevant quantity for the production of secondaries is thus:

$$\xi = \rho_{ISM} \cdot x = c \cdot \rho_{ISM} \cdot \tau \quad [\text{g cm}^{-2}] \quad (5.2)$$

<sup>1</sup> “Spallation” refers to inelastic nuclear reactions that occur when energetic particles interact with an atomic nucleus. Cosmic ray physicists usually refer to reactions induced by cosmic rays as “fragmentation”. For our practical purposes, the two words are synonymous.

$\xi$  represents the *path length* or the *grammage*, while  $\tau$  represents a characteristic *time* of the phenomenon and  $c$  the *speed of light*, as the particles are assumed to be relativistic.

The *problem consists in finding the value of  $\xi = \xi_{\text{esc}}$  which reproduces the observed ratio  $R_{\text{CR}}$  between the  $\mathcal{L}$  and  $\mathcal{M}$  abundances given in (5.1). This value corresponds to the mean amount of interstellar matter traversed by CRs before escaping from the confinement volume. In the simple model derived in this section, we obtain that  $\xi_{\text{esc}} = \text{constant}$  independent from the energy. We will work out in § 5.4 that more precisely  $\xi_{\text{esc}}$  decreases with the increase of the particle energy.*

The *spallation of  $\mathcal{M}$  nuclei on protons produces  $\mathcal{L}$  nuclei and can be quantitatively studied with accelerator data using the reaction*



with a *high-energy proton interacting with a nucleus  $X$  at rest. In principle, the cross-section for the process (5.3) only depends on the center-of-mass energy of the initial system. It should be, therefore, equal to that for the process  $X + p \rightarrow Y + \text{anything}$  (where the proton  $p$  is at rest, as in the case of the interstellar matter) provided that the center-of-mass energy is the same in the two cases. We are, moreover, assuming the cross-section to be approximately independent from the energy.*

We are particularly interested in the *experimental value of the spallation cross-section for processes (5.3) where C, N, O nuclei correspond to the target  $X$  and the Li, Be, B isotopes are the fragments  $Y$ . The corresponding values for the spallation process are reported in Table 5.1 (Silberberg and Tsao 1990). From the table we can deduce, for instance, that a proton interacting on a carbon nucleus produces a  $^{11}_5\text{B}$  with a probability of  $31.5/252.4 = 12.5\%$ .*

From Table 5.1, we obtain the *average probability  $P_{\mathcal{M}\mathcal{L}} = 0.28$  that a medium  $\mathcal{M}$  element fragments into a lighter  $\mathcal{L}$  element. This value is obtained by summing*

**Table 5.1** Fragmentation cross-sections of C, N, and O nuclei hit by protons. The considered fragments are the isotopes of Li, Be, and B

Nuclear			Target (X)		
Fragment (Y)			Fragmentation cross-section (mb)		
	Z	A	C	N	O
Li	3	6	12.6	12.6	12.6
Li	3	7	11.4	11.4	11.4
Be	4	7	9.7	9.7	9.7
Be	4	9	4.3	4.3	4.3
Be	4	10	2.9	1.9	1.9
B	5	10	17.3	16.0	8.3
B	5	11	31.5	15.0	13.9
Total cross-section (mb)			252.4	280.9	308.8

We assume that fragmentation cross-section does not depend on the energy

all the partial cross-sections in the table, divided by  $252.4 + 280.9 + 308.8 \text{ mb}$ . Thus, during propagation:

$$N_{\mathcal{M}} + p \rightarrow N_{\mathcal{L}} + X \quad \text{with } P_{\mathcal{M}\mathcal{L}} = 0.28. \quad (5.4)$$

The mean free path of hadrons and nuclei in matter was defined in Eq. (3.2). In the case of propagation of nuclei in the interstellar medium (dominated by the presence of protons),  $A = 1$ . The nucleus-proton cross-sections correspond to that of the spallation processes, proportional to the geometrical area of the nuclei, Eq. (3.3). The nuclear radius is given by (3.4). For  $\mathcal{M}$  nuclei, the average value of the atomic mass is  $A_{\mathcal{M}} \simeq 14$ , while for  $\mathcal{L}$  nuclei we have  $A_{\mathcal{L}} \simeq 8.5$ . The target consists of protons with  $R_T = r_o$ . Using these values, for the cross-section and mean free path, we obtain:

$$\sigma_{\mathcal{M}} \simeq 280 \text{ mb} \quad \longrightarrow \quad \lambda_{\mathcal{M}} \simeq 6.0 \text{ g cm}^{-2} \quad (5.5)$$

$$\sigma_{\mathcal{L}} \simeq 200 \text{ mb} \quad \longrightarrow \quad \lambda_{\mathcal{L}} \simeq 8.4 \text{ g cm}^{-2} \quad (5.6)$$

To determine from (5.2), the escape length  $\xi_{\text{esc}}$  that reproduces the observed ratio between (Li, B, and Bo) and (C, N, and O) we need to set out a system of differential equations for the number of  $\mathcal{M}$  and  $\mathcal{L}$  nuclei as a function of  $\xi$ . The equation that describes the reduction of the number of  $\mathcal{M}$  nuclei during their journey is:

$$\frac{d}{d\xi} N_{\mathcal{M}}(\xi) = -\frac{N_{\mathcal{M}}(\xi)}{\lambda_{\mathcal{M}}}, \quad (5.7)$$

$\mathcal{L}$  nuclei in CRs are produced by spallation of heavier  $\mathcal{M}$  elements. Their number increases with increasing path length of  $\mathcal{M}$  nuclei. The differential equation that describes the number of secondary  $\mathcal{L}$  nuclei as a function of path length  $\xi$  contains a positive source term and a negative attenuation term:

$$\frac{d}{d\xi} N_{\mathcal{L}}(\xi) = +\frac{P_{\mathcal{M}\mathcal{L}}}{\lambda_{\mathcal{M}}} N_{\mathcal{M}}(\xi) - \frac{N_{\mathcal{L}}(\xi)}{\lambda_{\mathcal{L}}} \quad (5.8)$$

The source term increases with probability  $P_{\mathcal{M}\mathcal{L}}$  as the spallation of  $\mathcal{M}$  nuclei occurs during propagation. The attenuation term is similar to that affecting the  $\mathcal{M}$  nuclei. The boundary conditions are  $N_{\mathcal{L}}(\xi = 0) = 0$  and  $N_{\mathcal{M}}(\xi = 0) = N_{\mathcal{M}}^0$ . Here,  $N_{\mathcal{M}}^0$  is a dummy parameter representing the production rate of  $\mathcal{M}$  primary nuclei from astrophysical sources. It will disappear at the end when we compare the ratio between elements.

Equations (5.7) and (5.8) are coupled, since the number of  $\mathcal{L}$  nuclei depends on  $N_{\mathcal{M}}(\xi)$ . Equation (5.7) can be immediately solved as:

$$N_{\mathcal{M}}(\xi) = N_{\mathcal{M}}^0 e^{-\xi/\lambda_{\mathcal{M}}} \quad (5.9)$$

Some algebra is needed to solve (5.8). First, replace in it  $N_{\mathcal{M}}(\xi)$  with the value given by Eq. (5.9); then multiply both sides by  $e^{\xi/\lambda_{\mathcal{L}}}$ ; the two terms containing  $N_{\mathcal{L}}$  can be considered as the derivative of the product of two functions. As a result, (5.8) takes the form:

$$\frac{d}{d\xi}(N_{\mathcal{L}}(\xi) \cdot e^{\xi/\lambda_{\mathcal{L}}}) = \frac{P_{\mathcal{M}\mathcal{L}}}{\lambda_{\mathcal{M}}} N_{\mathcal{M}}^0 \cdot e^{(\xi/\lambda_{\mathcal{L}} - \xi/\lambda_{\mathcal{M}})}. \quad (5.10)$$

As the equation contains exponential functions, the ansatz is of the form  $N_{\mathcal{L}}(\xi) = c \cdot (e^{-\xi/\lambda_{\mathcal{L}}} - e^{-\xi/\lambda_{\mathcal{M}}})$  where  $c$  is a constant to be determined using the boundary conditions. By placing the test solution in Eq. (5.10), we obtain an identity if the constant  $c$  is  $c = \frac{P_{\mathcal{M}\mathcal{L}} \cdot N_{\mathcal{M}}^0}{\lambda_{\mathcal{M}}} \cdot \frac{\lambda_{\mathcal{M}} \lambda_{\mathcal{L}}}{\lambda_{\mathcal{L}} - \lambda_{\mathcal{M}}}$ . The solution of (5.8) is:

$$N_{\mathcal{L}}(\xi) = \frac{P_{\mathcal{M}\mathcal{L}}}{\lambda_{\mathcal{M}}} \cdot N_{\mathcal{M}}^0 \cdot \frac{\lambda_{\mathcal{M}} \lambda_{\mathcal{L}}}{\lambda_{\mathcal{L}} - \lambda_{\mathcal{M}}} \cdot (e^{-\xi/\lambda_{\mathcal{L}}} - e^{-\xi/\lambda_{\mathcal{M}}}). \quad (5.11)$$

The two functions (5.9) and (5.11) are shown in Fig. 5.1, where arbitrarily it is assumed  $N_{\mathcal{M}}^0 = 1$ .

The measured quantity is the ratio of  $R_{CR} = N_{\mathcal{L}}/N_{\mathcal{M}} = 0.25$ , which does not depend on  $N_{\mathcal{M}}^0$ . The value of  $\xi = \xi_{\text{esc}}$  which gives the measured value of  $R_{CR}$  is determined using the ratio between (5.9) and (5.11), or through inspection of Fig. 5.1:

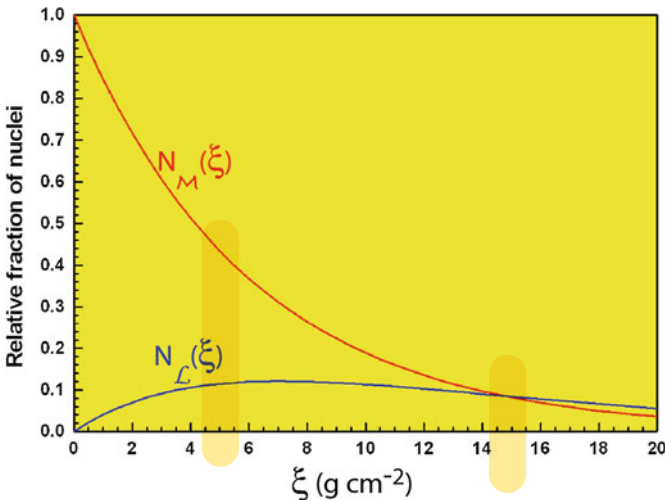


**Fig. 5.1** Evolution of the number of  $\mathcal{M}$  and  $\mathcal{L}$  nuclei as a function of the galactic path length  $\xi$ . Near the astrophysical accelerators ( $\xi = 0$ ), the  $\mathcal{L}$  nuclei are absent. As  $\xi$  increases,  $N_{\mathcal{L}}$  increases as light nuclei are produced by fragmentation of  $\mathcal{M}$  nuclei. For instance, if the path length is equal to  $\xi = 15 \text{ g cm}^{-2}$ , the ratio is  $N_{\mathcal{L}}/N_{\mathcal{M}} = 1$ . The measured ratio of  $N_{\mathcal{L}}/N_{\mathcal{M}} \simeq 1/4$  yields  $\xi_{\text{esc}} = x_{\text{esc}} \cdot \rho_{\text{ISM}} \simeq 5 \text{ g cm}^{-2}$



$$\xi_{\text{esc}} = x_{\text{esc}} \cdot \rho_{\text{ISM}} = 5 \text{ g cm}^{-2}. \quad (5.12)$$

This quantity is called the *average escape length* of CRs from our Galaxy. Since the value of the density of the interstellar material is  $\rho_{\text{ISM}} \sim 1 \text{ cm}^{-3} = 1.6 \times 10^{-24} \text{ g cm}^{-3}$ , the path  $x_{\text{esc}}$  corresponds to:

$$x_{\text{esc}} = \frac{\xi_{\text{esc}}}{\rho_{\text{ISM}}} = \frac{5 \text{ g cm}^{-2}}{1.6 \times 10^{-24} \text{ g cm}^{-3}} = 10^{25} \text{ cm} = 3 \text{ Mpc} \quad (5.13)$$

(1 parsec =  $3 \times 10^{18}$  cm). With a Galaxy having a radius of 15 kpc and a thickness of 300 pc, this result can be explained only if the propagation of cosmic rays resembles that of a *random walk*. Moreover, it suggests that the *propagation* and *acceleration* processes can be treated separately.

In Eq. (5.2) a characteristic time  $\tau$  was introduced. When  $\xi = \xi_{\text{esc}}$  this time corresponds to  $\tau = \tau_{\text{esc}}$ , the so-called *escape time*. It represents the average time of permanence of CRs inside the confinement volume before escaping our Galaxy. From (5.13):

$$\tau_{\text{esc}} = \frac{x_{\text{esc}}}{c} = \frac{10^{25} \text{ cm}}{3 \times 10^{10} \text{ cm/s}} \simeq 3 \times 10^{14} \text{ s} = 10^7 \text{ y}. \quad (5.14)$$

Since  $\xi_{\text{esc}}$  depends only on the ratio between the abundances of  $\mathcal{L}$  and  $\mathcal{M}$  nuclei, it does not depend on the observer's position: in any other position in the Galaxy, a hypothetical observer would measure the same  $N_{\mathcal{L}}/N_{\mathcal{M}}$  ratio, obtaining the same value of  $\tau_{\text{esc}}$ .

The value of  $x_{\text{esc}}$  (5.13) is orders of magnitude larger than the thickness of the galactic disk as a consequence of the tangled motion of charged particles in the galactic magnetic fields. As the gyromagnetic radius for a particle with charge  $Ze$ , energy  $E$ , in the magnetic field  $B$  is  $R \simeq \frac{E}{eZB}$ , Eq. (2.5), it is expected (Sect. 5.4) that the escape time  $\tau_{\text{esc}}$  decreases as the particle energy increases.

## 5.2 Dating of Cosmic Rays with Radioactive Nuclei

The escape time  $\tau_{\text{esc}}$  can be estimated using a completely different experimental method. The secondary-to-primary ratio described in the previous section provides a value of  $\xi_{\text{esc}}$  (or  $\tau_{\text{esc}}$ ) which critically depends on the assumed value of  $\rho_{\text{ISM}}$ . The decay of radioactive nuclei is used to derive  $\tau_{\text{esc}}$  in a way that is independent from the estimate of  $\rho_{\text{ISM}}$ . The dating technique with radioactive isotopes relies on the fact that the half-life of the nucleus should not be too small with respect to the age to be measured (Garcia-Munoz et al. 1977).

The radioactive isotope of carbon ( $^{14}\text{C}$  or *radiocarbon*) is the most commonly used element in the dating technique using radioactive isotopes. Radiocarbon is quite

important because it can be used to determine the age of matter which “lived” up to  $\sim 50,000$  years ago (Bowman 1990).

The interactions of cosmic rays with atmospheric nuclei (as in a hadronic calorimeter) produce showers of hadrons. Among the hadrons, the neutrons bombard the nitrogen nuclei,  ${}^{14}_7\text{N}$ , which represent the major constituent of the atmosphere. This induces the reaction:



Carbon has two stable isotopes:  ${}^{12}_6\text{C}$  and  ${}^{13}_6\text{C}$ . The  ${}^{14}_6\text{C}$  produced in the atmosphere has the (relatively) short half-life  $t_{1/2} = 5,730$  years. The amount of  ${}^{14}_6\text{C}$  in a sample is halved after 5,730 years due to radioactive beta-decay ( ${}^{14}_6\text{C} \rightarrow {}^{14}_7\text{N} + e^- + \bar{\nu}_e$ ).

Due to the steady cosmic ray flux on Earth, the production of  ${}^{14}_6\text{C}$  in the atmosphere has been constantly occurring at a fixed rate since a very long time, so there is a fairly constant ratio of  ${}^{14}_6\text{C}$  to  ${}^{12}_6\text{C}$  atoms in the atmosphere. This ratio is approximately  $(1.0-1.3) \times 10^{-12}$ .

When plants fix atmospheric carbon dioxide ( $\text{CO}_2$ ) into organic material during photosynthesis, they incorporate a given quantity of  ${}^{14}_6\text{C}$  corresponding to the level of its concentration in the atmosphere. After their “death,” plants are used to make textiles or are consumed by other organisms (humans or other animals). Due to the metabolism of living organisms, also humans and animals have a  ${}^{14}_6\text{C}$  to  ${}^{12}_6\text{C}$  ratio at the level of the atmospheric concentration. From the instant of the vegetal or animal death, the concentration of  ${}^{14}_6\text{C}$  nuclei in the organic material decreases due to its radioactive decay according to the law  $N(t) = N_0 e^{-t/\tau}$ . The quantity  $\tau$  is the lifetime which is related to the half-life,  $t_{1/2}$ , by the relation:  $t_{1/2} = \tau \ln 2$ .

After a time  $t$ , a measurement of the ratio  ${}^{14}_6\text{C}/{}^{12}_6\text{C}$  allows to derive the age of the sample. Its low activity limits the age determination by counting techniques to the order of 50,000 years.

As the level of atmospheric  ${}^{14}_6\text{C}$  is affected by variations in the cosmic ray intensity (which is in turn affected by variations in the Earth’s magnetic field), high-accuracy measurements can only be achieved through a fine calibration of raw, i.e., uncalibrated, radiocarbon dates. The available standard calibration curves are based on the comparison of radiocarbon dates of samples that can be dated independently by other methods such as the examination of tree growth rings, deep ocean or ice sediment cores, lake sediments, coral samples, and others. The most accurate curve extends back quite accurately up to 26,000 years. Any errors in the calibration curve do not contribute more than  $\pm 16$  y up to the last 6,000 y and no more than  $\pm 163$  y over the entire 26,000 years (Reimer Paula 2004).

Radiometric dating was extended to many other elements. For instance, the uranium–lead radiometric dating was used to date Earth rocks with a precision of less than 2 million years over a span of 4.5 billion years.

### 5.2.1 Unstable Secondary-to-Primary Ratios

The unstable secondary nuclei that live long enough to be useful probes of CRs propagation are  $^{10}\text{Be}$  ( $1.51 \times 10^6$  y),  $^{26}\text{Al}$  ( $8.7 \times 10^5$  y),  $^{36}\text{Cl}$  ( $3.1 \times 10^5$  y), and  $^{54}\text{Mn}$  ( $6.3 \times 10^5$  y) - in parenthesis their half-life. The most used one is the radioactive isotope  $^{10}\text{Be}$  which has a half-life similar to the escape time (5.14) and which is produced abundantly in the fragmentation of C, N, and O (see Table 5.1). The  $^{10}\text{Be}$  undergoes  $\beta$  decay into  $^{10}\text{B}$ . The relative abundances of the isotopes of Be and B provide a measure of whether or not all the  $^{10}\text{Be}$  has decayed and consequently an estimate of the time elapsed since production.

The experiments detecting  $^{10}\text{Be}$  were carried on satellites (IMP-7/8, ISEE-3, Voyager, Ulysses, CRIS). Let us try to derive an order-of-magnitude estimate  $t^*$  of the escape time using the data of the CR telescopes on board of the IMP-7 (Explorer 47) and IMP-8 (Explorer-50) satellites, reported in Sect. 3.4.1. We use the ratio between the  $^{10}\text{Be}$  and  $^7\text{Be}$ . The latter is stable, while the number of  $^{10}\text{Be}$  decreases with time:

$$N_{10}(t) = N_{10}^0 e^{-t/\tau_{10}} \quad ; \quad N_7(t) = N_7^0$$

with  $\tau_{10} = 1.51 \times 10^6 / \ln 2 \sim 2.2 \times 10^6$  y. At production, the ratio  $N_7^0/N_{10}^0 = 9.3/2.3 \sim 4$  depends only on the fragmentation cross-section, Eq. (3.9), obtained from the data in Table 5.1. Thus, at a time  $t^*$  after production, using the measured ratio  $r_{\text{mea}} = 15/329 = 0.045$  between the two isotopes derived from (3.10) we obtain

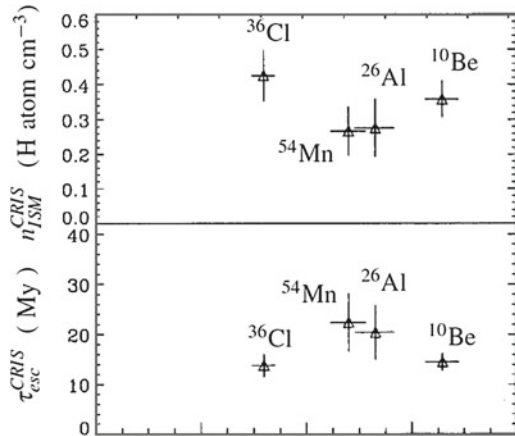
$$r_{\text{mea}} = \frac{N_{10}^0}{N_7^0} e^{-t^*/\tau_{10}} \quad \Rightarrow \quad \frac{t^*}{\tau_{10}} = -\ln\left(\frac{N_7^0}{N_{10}^0} r_{\text{mea}}\right) \sim 2$$

The time spent during propagation in the Galaxy corresponds to about  $t^* = 2\tau_{10} \sim 4 \times 10^6$  y. The statistical error on this quantity is as large as 50%. This rough estimate neglects some factors. The value obtained with a more detailed analysis in Garcia-Munoz et al. (1977) is  $t^* = 17_{-8}^{+24} \times 10^6$  y.

The most precise estimate of the CRs escape time using radioactive isotopes is due to the Cosmic Ray Isotope Spectrometer (CRIS) experiment, which was launched aboard NASA's Advanced Composition Explorer (ACE) satellite in 1997. The CRIS primary objective was to measure the isotopic abundances of nuclei in the charge range  $3 \leq Z \leq 30$  for energies below 500 MeV/n. The instrument consists of a scintillating fiber hodoscope, used as a tracking device, and four stacks of silicon wafers to measure the energy loss and the total energy. CRIS measured the abundances of the  $\beta$ -decay species  $^{10}\text{Be}$ ,  $^{26}\text{Al}$ ,  $^{36}\text{Cl}$ , and  $^{54}\text{Mn}$ . The determined values of  $\tau_{\text{esc}}$  for different radioactive isotopes are shown in Fig. 5.2. Averaged over the different isotopes, CRIS obtained a confinement  $\tau_{\text{esc}}^{\text{CRIS}} = 15.0 \pm 1.6$  My (Yanasak et al. 2001).

From the CRs escape time, CRIS estimated also the hydrogen number density,  $n_{\text{ISM}} = \rho_{\text{ISM}}/1.6 \times 10^{-24}$  g. The values corresponding to the different isotopes are shown in the upper plot of Fig. 5.2. The average value corresponds to

**Fig. 5.2** CRIS result on the measurement of the different  $\beta$ -decay isotopes. *Upper plot* mean ISM Hydrogen number density  $n_{\text{ISM}}$ . *Lower plot* the galactic confinement time  $\tau_{\text{esc}}$  derived from the CRIS observations. The different isotopes used for the measurements are shown in order of increasing half-live



$$n_{\text{ISM}}^{\text{CRIS}} = 0.34 \pm 0.04 \text{ H atom cm}^{-3} \quad (5.16)$$

The combination of the escape time and hydrogen number density measured by CRIS indicates an average escape length  $\xi_{\text{esc}}^{\text{CRIS}} \approx 7.6 \text{ g cm}^{-2}$ , to be compared with the value (5.12) obtained with our simple estimate.

The value (5.16) represents evidence that galactic CRs spend time in the galactic halo where the matter density is lower than the canonical value assumed for the number density in the disk ( $n_{\text{ISM}} \sim 1 \text{ H atom cm}^{-3}$ ). A magnetic field confining CRs must therefore be present also in the galactic halo.

### 5.3 The Diffusion-Loss Equation

CRs undergo a diffusion process through the interstellar medium from their sources until they exit the Galaxy. Occasionally, some CRs can be intercepted by detectors near the Earth. In this section, we derive a diffusion equation which will be used to describe the CRs journey in the Galaxy. This journey modifies also the CRs energy spectrum from the sources to the observer. As the solar system has nothing of peculiar with respect to any other point of our Galaxy, our observations are not influenced by the particular region where they are done. Particles having energies smaller than a few GeV, which are affected by the solar modulations, should not be considered. The galactic magnetic fields are the main factors which affect the CRs motion, as the Larmor radius for particles below the knee ( $E < 10^{15} \text{ eV}$ ) is much smaller than the typical spatial dimension over which the magnetic fields are coherent (Sect. 2.7.1). A random component in the motion is induced by the presence of irregularities, associated either with fluctuations in the fields or with the induction of instabilities due to the streaming motions of the charged particles themselves. During their diffusion, CRs are subject to energy-loss mechanisms and absorption

by dense media; nuclei may suffer spallation processes. Occasionally, CRs can gain energy by scattering with magnetized clouds.

To describe the changes due to this incoherent motion on the CR spectrum, a useful tool is to set a differential equation. This equation describes the energy spectrum at different points in the interstellar medium in the presence of diffusion (represented by a scalar diffusion coefficient  $D$ ), of energy losses, of fragmentation and other physics effects. To maintain secular equilibrium in the CR's density, a term that describes the input from astrophysical sources is needed.

We give a derivation of the diffusion-loss equation which closely follows the so-called coordinate space approach (Longair 2011).

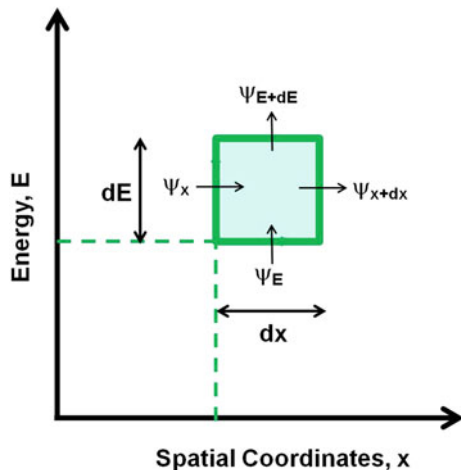
Let us consider a dummy state variable  $\psi$  which depends both on the spatial coordinates and on energy. Dummy means that it has no definite physical dimensions and it will disappear from the final result. The observable variable is  $\mathcal{N}$ , which has definite physical dimensions. For instance, it can represent the number of particles in a given volume and a given energy interval (units of  $\text{cm}^{-3} \text{GeV}^{-1}$ ). The state of the system can be described in a Cartesian coordinate system, in which the  $x$  variable represents the spatial coordinates and the energy  $E$  is plotted along the  $y$  axis, see Fig. 5.3. A change in the number of particles with a given energy  $E$  in a given region of space can be produced by two physical processes:

- (1) The diffusion of particles out of the considered region of space. The process is visualized in Fig. 5.3 as a movement along the  $x$ -axis. As  $\psi_x$  is the particle flux at a fixed point  $x$  through the energy window  $dE$ , the relation between  $\psi_x$  and  $\mathcal{N}$  is:

$$\psi_x \equiv -D \frac{\partial \mathcal{N}}{\partial x}. \tag{5.17}$$

$D$  is a scalar quantity and it represents the diffusion coefficient (units of  $\text{cm}^2 \text{s}^{-1}$ ).

**Fig. 5.3** The coordinate space diagram used in deriving the diffusion-loss equation. The spatial coordinates are along the  $x$ -axis, the energy along the  $y$ -axis



- (2) The **loss of energy** in a given time interval  $dt$ , due to processes as excitation/ionization, bremsstrahlung, etc. A **variation** can be induced **also** by **energy gain**, due to acceleration mechanisms. The **process** is visualized in Fig. 5.3 as a **flux along the y-axis**. The **relationship between the variable  $\psi_E$ , the number density  $\mathcal{N}$ , and the rate of energy change is:**

$$\psi_E \equiv \mathcal{N}(E) \frac{dE}{dt}, \quad (5.18)$$

We **assume** that **energy** is **lost** (or **gained**) at a **rate**:

$$-\frac{dE}{dt} = b(E) \quad (5.19)$$

The function  $b(E)$  is conventionally positive for energy losses, and negative for energy gains.

Considering the rectangle of Fig. 5.3, the **number of particles in the interval  $dx$  and energy interval between  $E$  to  $E + dE$**  is  $\mathcal{N}(E, x, t)dEdx$ . Therefore, the **rate of change** of particle density in the defined phase space is:

$$\begin{aligned} \frac{d}{dt} \mathcal{N}(E, x, t)dEdx &= [\psi_x(E, x, t) - \psi_{x+dx}(E, x + dx, t)]dE \\ &\quad + [\psi_E(E, x, t) - \psi_{E+dE}(E + dE, x, t)]dx \\ &\quad + Q(E, x, t)dEdx \end{aligned} \quad (5.20)$$

The quantity  $Q(E, x, t)$  represents a **source term** (units  $\text{cm}^{-3} \text{GeV}^{-1} \text{s}^{-1}$ ) if  $\mathcal{N}$  has units  $\text{cm}^{-3} \text{GeV}^{-1}$  and it represents the injection rate of particles per unit volume of coordinate space. After **simplifying the notation**:

$$\frac{d\mathcal{N}}{dt} = -\frac{\partial \psi_x}{\partial x} = \frac{\partial \psi_E}{\partial E} + Q. \quad (5.21)$$

Using (5.17) in (5.21) we get:

$$\frac{d\mathcal{N}}{dt} = D \frac{\partial^2 \mathcal{N}}{\partial x^2} = \frac{\partial \psi_E}{\partial E} + Q \quad (5.22)$$

which can be **generalized in a three dimensional space**:

$$\frac{d\mathcal{N}}{dt} = D \nabla^2 \mathcal{N} = \frac{\partial \psi_E}{\partial E} + Q. \quad (5.23)$$

The effect of **energy losses is included** by inserting (5.18) and (5.19) into (5.23) and thus:

$$\frac{d\mathcal{N}}{dt} = D\nabla^2\mathcal{N} + \frac{\partial}{\partial E}[b(E)\mathcal{N}(E)] + Q. \quad (5.24)$$

This represents the *diffusion-loss equation* for the time and spatial evolution of the energy spectrum of the particles. The *solution* of the most general case is in principle *extremely difficult*. *Additional terms* can be *added* to this equation to *include* other physical effects, as the *escape probability*, the *radioactive decay*, and the *spallation* of nuclei during the propagation of cosmic ray nuclei from sources to Earth. We will adopt some approximations in what follows when we shall need a solution of this differential equation.

### 5.3.1 The Diffusion Equation with Nuclear Spallation

The *production* of a *particular nucleus*  $Z_i$  by the *spallation process* depends on the *number of all nuclear species with  $Z > Z_i$* , on their *cross-sections*, and the *matter number density of the crossed medium*. In general, it is assumed that the spallation products have the same kinetic energy per nucleon as the progenitor and that the cross-section does not vary with energy. Mimicking what has been done for the case of Li, Be, B in (5.7) and (5.8), the diffusion equation (5.24) can *include* the *spallation process* with *two additional terms*:

$$\frac{d\mathcal{N}_i}{dt} = D\nabla^2\mathcal{N}_i + \frac{\partial}{\partial E}[b(E)\mathcal{N}_i(E)] + Q - \frac{\mathcal{N}_i}{\tau_i} + \sum_{j>i} \frac{P_{ji}}{\tau_j}\mathcal{N}_j. \quad (5.25)$$

$\tau_i$  and  $\tau_j$  are the *lifetimes* of particles of *species  $i$  and  $j$* . For the spallation process, they correspond to  $\tau_i = \lambda_i/c$  and  $\tau_j = \lambda_j/c$ , where  $\lambda_{i,j}$  are their *interaction lengths* (Sect. 3.2.3).  $P_{ji}$  is the *probability* that, in an *inelastic collision* involving the *destruction* of the nucleus  $j$ , the *nucleus  $i$  is produced*. The finite *lifetime*  $\tau_{\text{decay}}$  of *unstable elements* can also account for by simply *assuming* that:

$$\frac{1}{\tau_i} = \frac{1}{\tau_{\text{decay}}} + \frac{c}{\lambda_i} \quad (5.26)$$

where the smaller between  $\tau_{\text{decay}}$  and  $\lambda_i/c$  is the dominant term. In this way, both decay and interaction processes are taken into account.

The *diffusion equation* (5.25) is *time dependent*. Normally, we are interested in the *steady-state solution*, corresponding to  $d\mathcal{N}_i/dt = 0$ . Electrons, positrons, and antiproton propagation can be described as well by the diffusion equation. They constitute special cases, differing principally due to the energy losses and production rates of these particles, and can be fully described with numerical simulations (see Sect. 5.4).

A high degree of isotropy is a distinctive quality of CRs observed on Earth. The motion of high-energy charged particles is influenced by magnetic fields that make

isotropic the CR arrival distribution on Earth. The concept of CR diffusion explains why energetic charged particles are trapped in the Galaxy and have highly isotropic distributions. Before entering into the details of the techniques used to solve the problem let us try to understand the meaning of the diffusion coefficient  $D$  in (5.25).

### 5.3.2 Numerical Estimate of the Diffusion Coefficient $D$

The long path length obtained in (5.13) indicates a sort of random walk of CRs in the Galaxy. In a random walk, after  $N$  steps of the same length  $|\mathbf{l}_i| = l_0$ , a particle moving from the origin of a reference frame arrives at the position  $\mathbf{d} = \sum_{i=1}^N \mathbf{l}_i$ . Assuming that the direction of each step is randomly chosen:

$$d^2 = \mathbf{d} \cdot \mathbf{d} = \sum_{i=1}^N \sum_{j=1}^N \mathbf{l}_i \cdot \mathbf{l}_j = Nl_0^2 + 2l_0^2 \sum_{i=1}^N \sum_{j=1}^N \cos \theta_{ij} \simeq Nl_0^2 \quad (5.27)$$

as the angles  $\theta_{ij}$  between  $\mathbf{l}_i$  and  $\mathbf{l}_j$  are chosen randomly and thus the off-diagonal terms cancel.

Let us consider only the diffusion, the source and the time-dependent terms in (5.25):

$$\frac{d\mathcal{N}}{dt} - D\nabla^2 \mathcal{N} = Q. \quad (5.28)$$

Note that in this way the dependence on the energy variable is neglected and only the time variation of the spatial coordinates is taken into account. In addition, we assume a point-like source term  $Q$ , mathematically described as a Dirac delta function. Note that (5.28) can be formally transformed into the free Schrödinger equation with the substitutions  $D \rightarrow \hbar^2/(2m)$  and  $t \rightarrow -it$ . As the same equations have the same solutions, we can borrow the free propagator for a nonrelativistic particle as Green's function  $\mathcal{N} = G(r)$  for the diffusion equation assuming  $D$  as a constant parameter:

$$G(r) = \frac{1}{(4\pi Dt)^{3/2}} e^{-r^2/(4Dt)} \quad (5.29)$$

Thus the mean distance travelled from the origin in a time  $t$  is  $d \propto \sqrt{Dt}$ . In the random walk, we get  $d^2 \sim Nl_0^2$ . Connecting the two pictures, we obtain

$$D \simeq \frac{Nl_0^2}{t} \simeq vl_0; \quad \text{with } v = \frac{Nl_0}{t}. \quad (5.30)$$

Therefore, the diffusion coefficient  $D$  has the meaning of the product of the CRs velocity  $v \sim c$  times its mean free path  $l_0$ . An analysis in a 3-dimensional space gives more precisely:



$$D = \frac{vl_0}{3}. \quad (5.31)$$

An order of magnitude estimate for the diffusion coefficient  $D$  in a steady state problem can be determined from (5.28) by dimensional arguments. We replace the spatial derivative with a division by the characteristic length scale  $L$  and the time derivative with a division for a characteristic time  $\tau$ :

$$\frac{D\mathcal{N}}{L^2} \sim \frac{\mathcal{N}}{\tau} \quad (5.32)$$

Then, we assume that the dynamics of CRs occurs within the galactic disc; the particles should diffuse to a distance  $L$  roughly equal the thickness of the galactic disc, i.e.,  $L \simeq 300 \text{ pc} = 9 \times 10^{20} \text{ cm}$ . This occurs with a characteristic escape time given by Eq. (5.14), i.e.,  $\tau_{\text{esc}} = 10^7 \text{ years} = 3 \times 10^{14} \text{ s}$ . Thus:

$$D \simeq \frac{L^2}{\tau_{\text{esc}}} = 3 \times 10^{27} \text{ cm}^2 \text{ s}^{-1} \quad (5.33)$$

By using the relation (5.30), we can evaluate the length  $l_0$  of each step for charged particles moving in the Galaxy

$$l_0 = \frac{3D}{c} = \frac{9 \times 10^{27}}{3 \times 10^{10}} = 3 \times 10^{17} \text{ cm} = 0.1 \text{ pc} \quad (5.34)$$

In the literature, estimated values of  $D$  up to  $3 \times 10^{28} \text{ cm}^2 \text{ s}^{-1}$  are found using more refined computations. Thus the value of the step  $l_0$  in Eq. (5.27) lies in the range

$$l_0 = 0.1 - 1 \text{ pc}. \quad (5.35)$$

This quantity can be interpreted as the typical scale of magnetic inhomogeneities in the interstellar medium. On the microscopic level, the diffusion of CRs results from particle scattering on random magnetohydrodynamic waves and discontinuities. There is evidence of galactic irregularities on the scale given in (5.35), associated with supernova shells, regions of ionized hydrogen, and so on.

## 5.4 The Leaky box Model and its Evolutions

The framework in which CRs propagate freely in a containment volume is called the *leaky box model*. In this model, the diffusion term in the diffusion equation is approximated by a leakage term:

$$D\nabla^2 \mathcal{N} \rightarrow -\frac{\mathcal{N}}{\tau_{\text{esc}}}, \quad (5.36)$$

As the diffusion coefficient  $D$  should be energy dependent, also the characteristic escape time of CRs from the Galaxy  $\tau_{\text{esc}} = \tau_{\text{esc}}(E)$  is energy dependent. Consequently, (5.25) becomes:

$$\frac{d\mathcal{N}_i}{dt} = -\frac{\mathcal{N}_i}{\tau_{\text{esc}}} + \frac{\partial}{\partial E} [b(E)\mathcal{N}_i(E)] + Q - \frac{\mathcal{N}_i}{\tau_i} + \sum_{j>i} \frac{P_{ji}}{\tau_j} \mathcal{N}_j. \quad (5.37)$$

The leaky-box model provides the most common description of CR transport in the Galaxy at energies below  $\sim 10^{17}$  eV. The model is based on particles injected by sources  $Q$  distributed uniformly over the galactic volume (the *box*) filled with a uniform distribution of matter and radiation fields. The particles get-away from this volume with an escape time independent of their position in the box. The escape time  $\tau_{\text{esc}}(E)$  depends on the particle energy, charge, and mass number, but it does not depend on the spatial coordinates. Secondary nuclei are produced during the propagation as a function of the path length (5.2).

The general problem translates into a system of coupled transport equations for all isotopes involved in the process of nuclear fragmentation, extending that shown in Sect. 5.1 for the  $\mathcal{L}$  production from  $\mathcal{M}$  nuclei. The solution of the problem today relies on powerful computer calculations. Before the modern computer epoch, the *weighted-slab technique* (Strong et al. 2007), which consists of splitting the problem into astrophysical and nuclear parts, was used. The fragmentation part is solved in the *slab model*, where CRs traverse a thickness  $\xi$  of interstellar gas and these solutions are integrated over all values of  $\xi$ , weighted with a distribution function  $G(x)$  derived from an astrophysical propagation model. The solution of the leaky-box model has an exponential distribution of path lengths  $\xi$  as  $G(\xi) \propto \exp(-\xi/\xi_{\text{esc}})$ , where  $\xi_{\text{esc}}$  represents the mean escape length.

The complexities of propagation of CRs, and in particular of electrons and of secondary stable antiparticles (antiprotons and positrons), can be treated only through full computer simulations, because of their large energy and spatially-dependent energy losses. In this case, a numerical model named Galactic Propagation (GALPROP) provides the most advanced, explicit solution to date for the CR propagation problem.

The GALPROP code (Strong and Moskalenko 1998) enables simultaneous predictions of all relevant observations, including CR nuclei, electrons, antiparticles,  $\gamma$ -rays, and synchrotron radiation. The code [publicly available as a basis for further expansion (<http://galprop.stanford.edu/>)] incorporates current information on galactic structure and source distributions. Finally, the advances in computing power allow to overcome the limitations of analytical and semi-analytical methods when CR,  $\gamma$ -ray, and other data become more accurate.

The CR propagation (5.37) is solved numerically on a spatial grid, either in two dimensions with cylindrical symmetry in the Galaxy or in full three dimensions. The boundaries of the model in radius and height, and the grid spacing, are user definable. In addition, there is a grid in the space of momentum, which is the natural quantity for propagation. The distribution of CR sources can be specified, typically

to represent SNRs. **Interstellar gas distributions** are based on current **HI (21-cm atomic hydrogen emission)** and **CO (molecular emission used to trace molecular hydrogen)** surveys (see Sect. 2.7.2). **Nuclear cross-sections** are based on **extensive compilations** and **parameterizations**. The **numerical solution proceeds** in time until a **steady-state is reached**; a **time-dependent solution** is also a **possible** option. **Starting** with the **heaviest primary nucleus** considered (for example,  $^{64}\text{Ni}$ ), the propagation solution is used to compute the source term for its **spallation products** (which are then **propagated in turn**) **down to protons, secondary electrons and positrons, and antiprotons**. In this way, the production of secondaries, tertiaries, etc is included.

Due to the mentioned properties of the lightest leptons, **primary electrons are treated separately**. The important features of **diffuse  $\gamma$ -rays** and **synchrotron emission** (Sect. 8.7) are computed **using interstellar gas data** (for pion decay and bremsstrahlung), the **interstellar radiation field model** (for inverse Compton), and the **galactic magnetic field model**.

The prediction of this code compared with some experimental result is shown in Figs. 3.11, 3.12 and 3.14, and others. GALPROP has been adopted as the standard for diffuse galactic  $\gamma$ -ray emission in the analysis of the Fermi satellite data (Sect. 8.7) as well as by AMS, ACE, HEAT, and PAMELA among others.

## 5.5 Energy-Dependence of the Escape Time $\tau_{\text{esc}}$

An **energy dependence** of the CR **escape time** can be deduced from the measurement of the **secondary-to-primary ratios** of stable nuclei. The **reference ratio** is that between **boron and carbon (B/C)** because **B** is entirely secondary, i.e., produced by heavier primary CR nuclei. **C, N, and O** are the **major progenitors of B**, and the production **cross-section** is **better known than** those of **Be** and **Li**. A large number of different **measurements** exists **up to  $\sim 1$  TeV**.

Fig. 5.4 presents the **measurement** of the **B/C ratio** from different experiments as a function of energy. The figure shows a **mild increase** of the ratio **starting from low energies and up to  $\sim 1$  GeV/nucleon**. This is due to the **dependence**, at low energies, of the **nuclear cross-section** on the **relative velocity between nuclei**. At **higher energies**, the **fragmentation nuclear cross-section** is almost constant. At those energies, therefore, the **decrease of the B/C ratio** is only a consequence of different **path lengths  $\xi$**  for nuclei with different energies.

Empirically, we can **assume** a dependence of the path length on the **particle rigidity  $R$** . **Particles** with **low rigidity** suffer a **larger deflection** during the motion in a magnetic field because, according to (2.5), the **Larmor radius** is  $r_L = R/B$ . Thus, we assume that the **path length decreases when the rigidity  $R$  increases** as:

$$\xi_{\text{esc}}(R) = \xi_0 \left( \frac{R}{R_0} \right)^{-\delta} \quad (5.38)$$

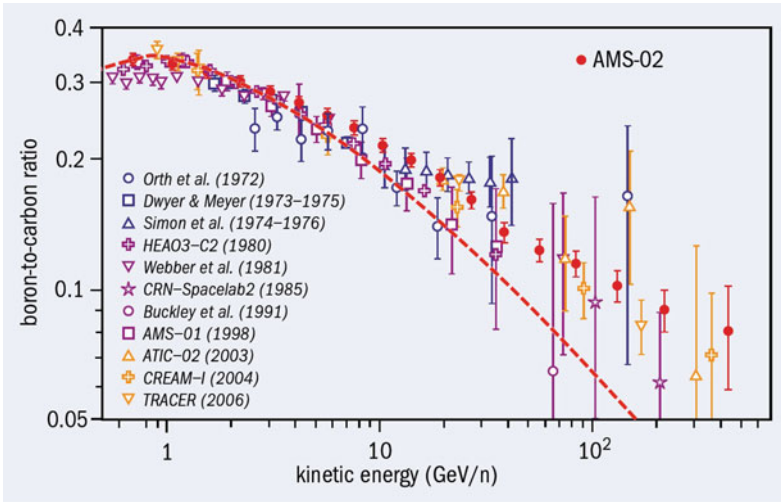


**Fig. 5.4** Observed boron to carbon abundance ratio, measured as a function of the kinetic energy per nucleon by different space and balloon experiments. The compilation is from the AMS-02 releases of data during the ICRC 2013 (Aguilar et al. 2013) (Courtesy of prof. Manuel Aguilar Benítez). See therein the references to other experiments. The dashed line represents the result of a prediction with the leaky box model, assuming an energy-dependent escape path length  $\xi_{\text{esc}} \equiv \Lambda \propto E^{-0.6}$  and was derived from Obermeier et al. (2012)

where  $\delta$ ,  $\xi_0$ ,  $R_0$  are parameters which must be derived from experimental data. Typical values obtained by fitting the data are:

$$\delta = 0.6; \quad \xi_0 = 11.8 \text{ g cm}^{-2}; \quad R_0 = 5 \text{ GV/c}. \quad (5.39)$$

Notice that these values differ slightly from others obtained using different data sets [see for instance Engelmann et al. (1990), Strong et al. (2007) and Obermeier et al. (2012)]. The result from the leaky-box model is also presented in Fig. 5.4. Here, the time-dependent escape time due to the energy-dependent diffusion in the galactic disk is shown with a dashed line.

Also iron produces secondary nuclei (Sc, Ti, and V) by fragmentation process during propagation. The ratio between secondary nuclei (Sc, Ti, and V) and Fe can be described by a dependence on  $R$  similar to that reported in (5.38). In particular, also the energy dependence of these ratios can be described using the value  $\delta \simeq 0.6$ .

This result is consistent with the general diffusion equation. In fact, as  $\tau_{\text{esc}} = \xi_{\text{esc}} / (c \cdot \rho_{\text{ISM}})$  we have that:

$$\tau_{\text{esc}} = \tau_0 \left( \frac{R}{R_0} \right)^{-0.6} = \tau_0 \left( \frac{E}{E_0} \right)^{-0.6} \quad (5.40)$$

as at high energy the rigidity is equal to the energy for particles of given electric charge. In the leaky-box equation (5.37), the energy dependence of the particles loss is accounted for by the escape time  $\tau_{\text{esc}}$  and, according to (5.40), the escape process dominates at high energy over fragmentation. In models using the diffusion coefficient  $D$ , this parameter becomes energy dependent,  $D = D(E)$ . Appropriate parameterizations are introduced when the diffusion equation in the form of (5.25) is used. This dependence of the  $\tau_{\text{esc}}$  (or  $D$ ) upon energy is of decisive importance to derive the energy spectrum of CRs in the proximity of the sources.

## 5.6 Energy Spectrum of Cosmic Rays at the Sources

Let us derive a constraint for the spectral index of the CR energy spectrum near acceleration sites starting from the diffusion equation (5.37). We consider primary protons and stable nuclei ( $\mathcal{N} = \mathcal{N}_P$ ) in a steady-state ( $d\mathcal{N}_P/dt = 0$ ), neglecting the fragmentation processes ( $P_{ij} = 0$ ). For primary protons and nuclei, the energy loss processes (excitation/ionization, bremsstrahlung, etc.) are negligible, and  $b(E) = 0$  (this is not true for electrons). The fragmentation processes can be neglected as well for the present purpose. Under these conditions from (5.26), we have  $\tau_i = \lambda/c$ , where  $\lambda$  is the interaction length of protons or nuclei in the ISM, and Eq. (5.37) becomes:

$$-\frac{\mathcal{N}_P(E)}{\tau_{\text{esc}}(E)} + Q_P(E) - \frac{\mathcal{N}_P \cdot c}{\lambda} = 0. \quad (5.41)$$

In § 5.3 we adopted for  $\mathcal{N}$  the units  $[\text{GeV}^{-1} \text{cm}^{-3}]$ . This quantity can reproduce the primary CR intensity when multiplied by  $c/4\pi$ . The quantity:

$$\frac{c\mathcal{N}_P}{4\pi} \equiv \Phi(E) \quad \text{has units } [\text{GeV}^{-1} \text{cm}^{-2} \text{s}^{-1} \text{sr}^{-1}]. \quad (5.42)$$

For CR protons, the mean free path is  $\lambda_p \simeq 40 \text{ g cm}^{-2}$  as obtained from (3.2) using  $A = A_{\text{ISM}} = 1$  and  $\sigma = \sigma_{pp} \simeq 45 \text{ mb}$ . The solution of (5.41) is:

$$\mathcal{N}_P(E) = \frac{Q_P(E) \cdot \tau_{\text{esc}}(E)}{1 + c\tau_{\text{esc}}(E)/\lambda_p} \quad (5.43)$$

as  $c\tau_{\text{esc}}(E) = \xi_{\text{esc}}(E) \sim \text{few g cm}^{-2}$ , the term  $c\tau_{\text{esc}}(E)/\lambda_p < 0.1$  and it can be neglected. Finally, remembering (5.40) and (5.42) we get:

$$\Phi(E) \propto Q_P(E) \cdot E^{-\delta} \quad (5.44)$$

The left-hand side of (5.44) represents the primary spectrum of CRs observed on Earth (2.20a),  $\Phi(E) \propto E^{-\alpha}$  and then:

$$Q_P(E) = \frac{\Phi(E)}{E^{-\delta}} \propto E^{-\alpha} \cdot E^{\delta} \quad (5.45)$$

Thus, as  $\alpha = 2.7$  below the knee ( $\sim 10^{15}$  eV), we get the important prediction for the energy spectrum of CRs at the sources:

$$Q_P(E) \propto E^{-\alpha+\delta} = E^{-2.1} \quad (5.46)$$

Models of CR sources should reproduce this energy dependence, with a spectral index  $\sim 2$ .

We note that (5.43) can give information concerning the energy spectrum of heavier nuclei. In general, the acceleration processes provide (almost) the same energy dependence  $Q(E)$  at the sources for protons and heavier nuclei. However, the nuclear cross-section increases as  $A^{2/3}$ ,  $A$  being the mass number. Consequently, the interaction length decreases as  $A^{-2/3}$ , and for Fe nuclei it becomes  $\lambda_I^{\text{Fe}} \sim 2.5 \text{ g cm}^{-2}$ . In this case, the effect of interactions in (5.43) cannot be neglected until  $c\tau_{\text{esc}}^{\text{Fe}}(E)/\lambda_I^{\text{Fe}} \ll 1$ . At sufficient high energy, the escape time for heavier nuclei is sufficiently small to reproduce the proton's behavior.

## 5.7 Anisotropies due to the Diffusion

The CR flux on Earth is consistent with isotropy when the low-energy particles affected by the Sun are neglected. Small anisotropies are expected due to the global leakage of CRs from the Galaxy, to the possible contribution of individual sources, and due to the motion of the solar system in the Galaxy.

We can estimate how anisotropic the flux of cosmic rays would be by estimating their net streaming velocity  $V$  because of the presence of the diffusion. Let us use again dimensional arguments on (5.28) in a region without sources ( $Q = 0$ ). Assuming the same approximation used before (5.32), we have

$$\frac{\mathcal{N}}{T} = D \frac{\mathcal{N}}{L^2} \quad \Rightarrow \quad \frac{L}{T} = V = \frac{D}{L} \sim 10^{-4} c. \quad (5.47)$$

The numerical value is obtained assuming for  $L$  the galactic disk height (300 pc) and the diffusion coefficient  $D$  in (5.33). Therefore, if we were located at the edge of the galactic disc, we would observe a net streaming velocity of about  $10^{-4} c$  which would correspond to an anisotropy of the CR flux.

In general, the presence of a cosmic ray anisotropy is strictly correlated with the streaming velocity  $V$  of the CR particles. This streaming velocity plays the same role as the drift velocity attained by electrons in the presence of an electric field. There

is an anisotropy only if there is a net streaming velocity, which can be expressed with a particular amplitude and phase. The amplitude of the CR anisotropy is defined as:

$$\delta \equiv \frac{I_{\max} - I_{\min}}{I_{\max} + I_{\min}} \quad (5.48)$$

where  $I_{\max}$ ,  $I_{\min}$  represent the maximum and minimum intensity of cosmic rays from a given direction. Usually, the arrival direction of CRs is referred to the equatorial coordinate system, see Extras # 2.

By simple dimensional arguments, the amplitude of the anisotropy depends on the streaming velocity amplitude as  $V \sim \delta c$ . It can be demonstrated using Lorentz invariance (Kachelriess 2008) that, for a flux of particles (such as the cosmic rays) with differential energy spectrum  $\Phi(E) \propto E^{-\alpha}$ , the streaming speed and the anisotropy amplitude are correlated through the spectral index  $\alpha$  by:

$$V = \left[ \frac{\delta}{(\alpha + 2)} \right] c \quad (5.49)$$

Because the CR escape probability increases with energy, Eq. (5.40), the diffusion coefficient  $D$  is energy dependent as well. This corresponds to an increase of the streaming velocity  $V$ , according to Eq. (5.47). The expectation from our simple considerations is that the amplitude  $\delta$  of the anisotropy increases with energy. This simple prediction is confirmed by accurate calculations (Candia et al. 2003). Values as large as  $\delta \sim 10^{-1}$  can be obtained, depending on particle energy and on the strength and structure of the galactic magnetic field.

Different predictions for an anisotropy amplitude of a dipole type (when the arrival CR directions are expressed in the equatorial coordinate system) as a function of the CR energies are reported in Fig. 5.5. A dipole anisotropy is a form of anisotropy due to the difference in the arrival intensity of particles from opposite directions, usually attributed to the motion of the observer relative to the source. As the CR diffusion depends on the modeling of the galactic magnetic fields, two predictions (labeled with “A” and “S” in the figure) refer to two different configurations of the galactic magnetic fields. In the region of Ultra High Energy Cosmic Rays, above  $\sim 10^{18}$  eV, a possible galactic origin of these particles (model labeled with “Gal”) would produce an anisotropy of large amplitude,  $\delta \sim 0.1$ . A much smaller anisotropy amplitude is expected if the sources of CR are of extragalactic origin, as indicated by the model labeled with “C-G Xgal.” The level of different anisotropy amplitudes can be tested with experiments measuring the arrival direction of CRs in the region around and above the knee.

From the experimental point of view, because of the small amplitude of the expected anisotropy, a large data sample is necessary in order to have a statistically significant measurement of (5.48). Many experimental studies on dipole anisotropies (also called large-scale anisotropies) are based on the fact that the exposure of the detectors is uniform in the right ascension coordinate RA. The uniformity in the exposure guarantees that there is not bias from any particular sky region due to experimental effects.

As an example, let us consider the  $n$  events that a particular experimental apparatus has classified as CRs in the energy range between  $E$  and  $E + \Delta E$ . The  $n$  events are then analyzed in terms of the so-called *Rayleigh formalism of harmonic analysis*. The *Rayleigh formalism* gives the amplitude  $A$  (that can be identified with the  $\delta$  given in Eq. 5.48) and phase  $\phi$  of the first harmonic, and additionally the probability  $P$  for detecting a spurious amplitude due to fluctuations from a sample of  $n$  events which are drawn from a uniform distribution (Mardia and Jupp 1999). Two quantities can be obtained from the dataset, with the sum includes  $n$  right ascension values  $RA_i$ :

$$S = \frac{2}{n} \sum_{i=1}^n \sin(RA_i), \quad C = \frac{2}{n} \sum_{i=1}^n \cos(RA_i). \quad (5.50)$$

If the CR arrival directions are completely random, clearly  $S = C = 0$ . In the presence of anisotropy, the amplitude  $A$  and the phase  $\phi$  of the first harmonic are given by:

$$A = \sqrt{C^2 + S^2}; \quad \phi = \arctan \frac{S}{C}. \quad (5.51)$$

The results of some experiments measuring CRs at different energies are reported in Fig. 5.5. Few evidences on large-scale anisotropies were reported from extensive

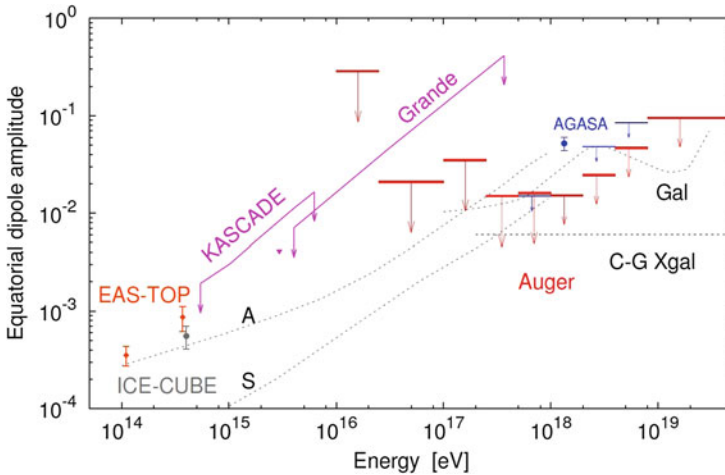


**Fig. 5.5** The anisotropy amplitude as a function of energy. In red are the limits obtained by the Auger Observatory over the full energy range as reported at the ICRC in 2013 [see Abreu et al. (2011) for the reference to the experiments]. The lines denoted as **A** and **S** up to 10<sup>18</sup> eV refer to predictions for two different galactic magnetic field models. The predictions for a purely galactic origin of ultra-high energy cosmic rays (UHECRs) is denoted as **(Gal)**, and the expectations from the Compton-Getting effect for an extragalactic component of CRs (**C-GXgal**). In this case, the CRs are assumed to be isotropic in the cosmic microwave background rest frame. Courtesy of the Pierre Auger Observatory



air shower experiments in the last two decades in the energy region  $10^{14} - 10^{15}$  eV. At high energy (when the asymmetry is larger), the CR flux is so low that it can be measured only by the largest shower array detectors, Sect. 7.8. Note that some theoretical models can already be strictly constrained by the established upper limits (lines with a down arrow). The experiments require the anisotropy to be smaller than the values shown in the graph. In particular, an older large anisotropy value around  $10^{18}$  eV reported by the AGASA experiment has been ruled out by the Pierre Auger Observatory.

The non-observation of an anisotropy in the arrival direction of UHECRs is the main motivation for the hypothesis of their extragalactic origin, Chap. 7.

### 5.7.1 The Compton–Getting Effect

A small anisotropy is expected also as a result the motion of the observer (on Earth) relative to the frame in which CRs have no bulk motion (the galactic disk). This effect is known since 1935 as the Compton–Getting effect. The Compton–Getting effect predicts that the intensity of CRs unaffected by the solar wind should be higher in the direction toward which Earth is moving. As the speed of the Sun (and consequently of the Earth) within the Galaxy is  $V_{\odot} \sim 220$  km/s, the expected anisotropy amplitude due to the Compton–Getting effect can be estimated using (5.49):

$$\delta_{CG} = \frac{V_{\odot}}{c} (\alpha + 2) \sim 10^{-3} \quad (5.52)$$

thus a difference between the strongest and weakest cosmic ray intensities of about 0.1% would result. The amplitude of the anisotropy is of the same order of magnitude of the diffusion out of the galactic plane discussed above. We note in passing that the phase should be completely different.

Several ground-based extensive air shower detectors and underground experiments detecting cosmic-ray muons (Chap. 11) have observed that CRs in the energy range up to 100 TeV show a large-scale anisotropy with an amplitude  $\delta_{CG} \sim 0.1\%$ . These observations seem to be related to the motion of the Earth in the Galaxy. The experimental values of  $\delta$  are very close to the predicted one. Fig. 5.5 depicts the point relative to the EAS-TOP (Aglietta et al. 2009) and IceCube (Abbasi et al. 2012) experiments for energies below  $10^{15}$  eV. For a compilation of results that includes lower energies, see Guillian et al. (2007).

## 5.8 The Electron Energy Spectrum at the Sources

In Sect. 5.6, using experimental observations, we derived that CR sources should have an energy spectrum of the type  $Q(E) \propto E^{-2}$ . The mechanism that provides accelerated particles with a  $E^{-2}$  spectrum will be described in Chap. 6, and it requires the existence of magnetic field regions in correspondence of sources.

Since ordinary matter in astrophysical environments is electrically neutral, we expect the presence of high-energy electrons, accelerated by the same mechanisms and with the same characteristics of protons. On the other hand, high-energy electrons are subject to additional energy loss processes, which cause distortions of their injection energy spectra. These distortions are mainly due to the presence of the magnetic fields itself, which induce *synchrotron radiation*. In addition, electrons can also interact with matter and radiation. Their energy loss processes due to excitation/ionization and bremsstrahlung can be parameterized as in Eq. (3.6).

Electrons accelerated in the presence of magnetic fields manifest the presence of acceleration regions through the production of electromagnetic radiation which is detected with different experimental techniques (from radio-telescopes through  $\gamma$ -ray satellites) as described in Chaps. 8 and 9. However, also the presence of the galactic magnetic field has some consequences, as the radiation emission during propagation provide constraints on the possible distance of electron sources. For this reason, we start here the presentation of the synchrotron radiation, which will be completed in Sect. 8.4.

### 5.8.1 Synchrotron Radiation

Synchrotron radiation is electromagnetic radiation generated by charged particles that are accelerated along a curved path or orbit. The radiation was named after its discovery in 1946 in a synchrotron accelerator where charged particles were accelerated.

Classically, any accelerated charged particle emits electromagnetic radiation. The radiated power is given by the relativistic Larmor formula (Jackson 1999) (in c.g.s. units):

$$P = -\frac{dE}{dt} = \frac{2e^2}{3c^3} a^2 \quad (5.53)$$

where  $a$  is the particle acceleration and  $E$  its energy. For a non-relativistic circular orbit, the acceleration is just the centripetal acceleration,  $v^2/R$ . The relativistic acceleration is obtained from its definition, where  $\tau = t/\Gamma$  is the proper time ( $\Gamma$  represents the Lorentz factor) and  $m_e$  the electron mass at rest:

$$a = \frac{1}{m_e} \frac{dp}{d\tau} = \frac{1}{m_e} \Gamma \frac{d(\Gamma m_e v)}{dt} = \Gamma^2 \frac{dv}{dt} = \Gamma^2 \frac{v^2}{R} \quad (5.54)$$

The radiated power (neglecting the time dependence of  $\Gamma$ ) is:

$$-\frac{dE}{dt} = \frac{2e^2}{3c^3} a^2 = \frac{2e^2}{3c^3} \left[ \Gamma^2 \frac{v^2}{R} \right]^2 = \frac{2e^2 \Gamma^4 v^4}{3c^3 R^2} \quad (5.55)$$

The velocity is  $v \rightarrow c$  for relativistic electrons. In the case of a fixed radius  $R$  (that of an accelerator), the term  $\Gamma^4 = [E/(m_e c^2)]^4$  depends on the fourth power of the particle energy. The radiated power is inversely proportional to the square of the accelerator radius  $R$ . Synchrotron radiation becomes the dominant factor in the energy loss rate [for instance, at the LEP  $e^+e^-$  collider at CERN (Braibant et al. 2012)] and is the limiting factor on the final beam energy that can be reached at such machines. The synchrotron radiation loss dependence suggests the construction of accelerators with a radius  $R$  as large as possible, or of linear accelerators.

In astrophysical environments, the radius of particles is dictated by the magnetic field itself. Using the Larmor radius (2.5)  $r_L = R = E/eB = \Gamma m_e c^2 / eB$  (for  $Z = 1$ ) in (5.55), we obtain

$$-\frac{dE}{dt} = \frac{2e^2 \Gamma^4 c^4}{3c^3 R^2} = \frac{2e^2 \Gamma^4 e^2 B^2}{3c^3 \Gamma^2 m_e^2} = \frac{2e^4}{3m_e^2 c^4} c \Gamma^2 B^2 \quad (5.56)$$

Making use of the definition of the Thomson cross-section,

$$\sigma_T \equiv \frac{8\pi r_e^2}{3} = \frac{8\pi e^4}{3m_e^2 c^4} = 0.66 \times 10^{-24} \text{ cm}^2 \quad (5.57)$$

(where  $r_e = e^2/m_e c^2$  is the classical electron radius), we can rewrite (5.56) as:

$$-\frac{dE}{dt} = \frac{\sigma_T}{4\pi} c \Gamma^2 B^2 = \frac{\sigma_T}{4\pi} c \frac{E^2}{m_e^2 c^4} B^2 \quad (5.58)$$

The electron energy loss rate depends on the square of its energy and on the square of the magnetic field. The latter corresponds to the energy density of the magnetic field,  $U_B = B^2/8\pi$ .

More generally, if the electron has a velocity that is not perpendicular to the magnetic field direction, it moves in a spiral path at a constant pitch angle  $\psi$  and

$$-\frac{dE}{dt} = \frac{\sigma_T}{4\pi} c \Gamma^2 B^2 \sin^2 \psi. \quad (5.59)$$

When considering a population of high-energy electrons, the distribution of pitch angles is expected to be isotropic because of the presence of irregularities in the magnetic field distribution and of random scattering processes during the motion of electrons. Averaging over an isotropic distribution of pitch angles and using the definition of the energy density of the magnetic field,  $U_B = B^2/8\pi$ , Eq. (5.59) becomes

$$-\frac{dE}{dt} = \frac{4}{3} \sigma_T c U_B \Gamma^2. \quad (5.60)$$

The general feature of synchrotron emission is that the radiation is beamed along the particle direction. The derivation of the synchrotron frequency spectrum of the

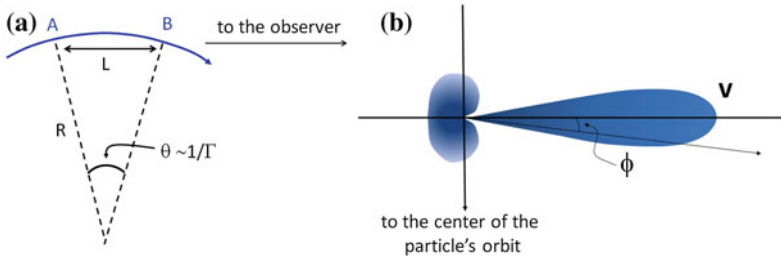


**Fig. 5.6 a** The geometry of the path of the electron during the time when the beamed radiation is observed by the distant observer. **b** The polar diagram of the radiation transformed into the laboratory frame of reference

radiation produced by a mono-energetic electron requires a considerable effort. We use here only a first-order approximation, remanding to Chap. 8 of Longair (2011) for a detailed derivation.

Relativistic beaming effects are associated with synchrotron radiation. A distant observer would receive the radiation only when the accelerated particle has a velocity toward the observer itself. This correspond to a “pulse of radiation” that the observer notices every time the electron’s velocity vector lies within a small angle. The duration of the pulse can be quantitatively derived with the help of Fig. 5.6a.

Consider an observer located at a distance  $D$  from the point A. The radiation from A, the leading edge, reaches the observer at time  $D/c$ . The radiation emitted at the point B occurs at a later time  $L/v$  and then travels a distance  $(D - L)$  at the speed of light to reach the observer. The final part (the trailing edge) of the pulse therefore arrives at a time  $L/v + (D - L)/c$ . The duration of the pulse as measured by the observer is therefore

$$\Delta t = \left[ \frac{L}{v} + \frac{(D - L)}{c} \right] - \frac{D}{c} = \frac{L}{v} \left[ 1 - \frac{v}{c} \right] \tag{5.61}$$

The observed duration of the pulse is much less than the time interval  $L/v$ , which is true only if light propagated at an infinite velocity. The factor  $1 - (v/c)$  in Eq. (5.61) takes into account the fact that the source of radiation is moving towards the observer, and it can be approximated with:

$$\left( 1 - \frac{v}{c} \right) = \frac{[1 - (v/c)][1 + (v/c)]}{[1 + (v/c)]} = \frac{[1 - (v^2/c^2)]}{[1 + (v/c)]} \simeq \frac{1}{2\Gamma^2} \tag{5.62}$$

The electromagnetic field for a relativistic particle with Lorentz factor  $\Gamma$  is such that the angular distribution of the intensity of radiation with respect to the acceleration vector in the instantaneous rest frame is similar to that shown in Fig. 5.6b [see Jackson (1999)]. In particular, the emitted radiation is beamed in the direction of motion of the electron within the angles  $-1/\Gamma < \phi < 1/\Gamma$ . The observer thus receive a pulse of radiation every time the electron’s velocity vector lies within an

angle of about  $\pm 1/\Gamma$ . This corresponds to the electron position in the trajectory characterized by the angle  $\theta$  (Fig. 5.6a). Thus, we can assume that the radiation reaches the observer when emitted in the angle

$$\theta \simeq \frac{1}{\Gamma} \quad (5.63)$$

Using the geometrical relations of Fig. 5.6a) we have

$$\frac{L}{v} \simeq \frac{R\theta}{v} \simeq \frac{1}{\Gamma\omega_r} \simeq \frac{1}{\omega_g} \quad (5.64)$$

Classically, the angular gyrofrequency for an electron moving with velocity  $v$  on a circumference of radius  $R$  is  $\omega_g = v/R$ . The frequency of the emitted radiation would be expected to be  $\nu_g = \omega_g/2\pi$ . The relativistic gyrofrequency is defined as  $\omega_r$ . Making use of (5.62) and (5.64), the relation (5.61) becomes:

$$\Delta t = \frac{L}{v} \left[ 1 - \frac{v}{c} \right] \simeq \frac{1}{2\Gamma^3\omega_r} \quad (5.65)$$

This means that the duration of the pulse as observed by a distant observer in the laboratory frame of reference is roughly  $1/\Gamma^2$  times shorter than the non-relativistic period  $2\pi/\omega_g$ .

The observed frequency (formally: the maximum Fourier component of the spectral decomposition of the observed pulse of radiation) corresponds to

$$\nu \simeq (\Delta t)^{-1} \simeq \Gamma^2 \nu_g = \Gamma^3 \nu_r = \frac{\Gamma^3 v}{2\pi R} \quad (5.66)$$

using the relation (5.64). This corresponds (for  $v \sim c$ ) to the critical frequency

$$2\pi \nu_c = \omega_c \equiv \frac{3\Gamma^3 c}{2R} \quad (5.67)$$

which includes the correction factor obtained from the average over all possible pitch angles between the velocity and the magnetic field. In general, we may interpret  $R$  as the instantaneous radius of curvature of the electron's trajectory and  $v/R$  as the angular frequency associated with it.

For order of magnitude calculations, it is sufficient to know that the total energy loss rate of the relativistic electron is given by (5.60) and that most of the radiation is emitted at a frequency given in (5.66). Figure 5.7 shows the shape of the spectrum of the synchrotron radiation (Longair 2011) emitted by a mono-energetic electron. The function is plotted in terms of the quantity  $\omega/\omega_c = v/v_c$  where  $\omega_c$  is the critical angular frequency (5.67). The spectrum presented in the figure has a broad maximum,  $\Delta\nu/\nu \sim 1$  centered roughly at the frequency  $\nu \sim \nu_c$ . The maximum of the emission spectrum corresponds to the value  $0.29\nu_c$ .

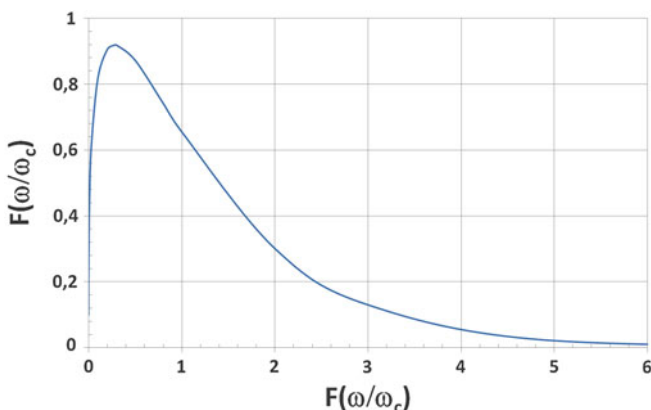


Fig. 5.7 Shape of the spectrum of the synchrotron radiation produced by a monoenergetic electron. The function is plotted in terms of the ratio  $\omega/\omega_c = v/v_c$  where  $\omega_c$  is the critical angular frequency

### 5.8.2 Measured Energy Spectrum of Electrons

The synchrotron emission of accelerated electrons near the sources generates radiation with an energy spectrum peaked in the infrared/X-ray range, as studied in Sect. 8.4. Here, we are interested on how the energy loss rate (5.60) affects the energy spectrum of CR electrons, in a way independent of the peculiar characteristics of a source. Let us adapt the leaky-box diffusion equation (5.37) for electrons:

$$\Phi_e(E) \equiv \frac{c}{4\pi} \mathcal{N}_e.$$

Most of the electron energy is lost near the sources because of the presence of magnetic fields. In this case, the dominant energy-loss process is due to the synchrotron radiation and Eq. (5.58) can be written as  $|dE_e/dt| = b_0 E^2$  with  $b_0 = \left(\frac{\sigma_T}{4\pi}\right) c \frac{B^2}{m_e^2 c^4}$ .

In the diffusion equation (5.37) the energy-dependent term becomes  $b(E) = b_0 E^2$ . Because this dependence on the squared energy, we can neglect the term due to diffusion and that due to other energy loss processes. Under these assumptions, all spatial dependences disappear from the diffusion-loss equation. As usual, we assume that the spectrum has reached a steady state ( $d\mathcal{N}_e/dt = 0$ ) under the continuous injection of particles described by an infinite, uniform distribution of sources, each pumping in high-energy electrons with an injection spectrum

$$Q_e(E) = \kappa E^{-\alpha_e} \quad (5.68)$$

Equation (5.37) reduces to:

$$\frac{d}{dE} [b(E) \mathcal{N}_e(E)] = -Q_e(E) \rightarrow \int d[b_0 E^2 \mathcal{N}_e(E)] = - \int Q_e(E) dE \quad (5.69)$$

Assuming  $\mathcal{N}_e(E) \rightarrow 0$  for energy  $E \rightarrow \infty$  the (5.69) can be integrated:

$$\mathcal{N}_e(E) = \frac{b_0}{(\alpha_e - 1)k} \cdot E^{-(\alpha_e+1)} \quad (5.70)$$

Thus, if synchrotron losses dominate

$$\Phi_e(E) \propto E^{-(\alpha_e+1)}, \quad (5.71)$$

i.e., the observed spectrum is steeper by one power of  $E$  with respect to the spectrum at the sources.

We expect the energy distribution of electrons accelerated at the sources to follow the same behavior as that CR protons and nuclei, thus  $\alpha_e \simeq 2$ . The measured energy spectrum of electrons follows in a wide energy interval a  $E^{-3}$  dependence (Fig. 3.12 in Sect. 3.9), demonstrating that most of the electron energy is released as electromagnetic radiation near the sources, where magnetic fields are large. The corresponding non-thermal electromagnetic radiation spectrum can be detected by means of different experiments.

### 5.8.3 Average Distance of Accelerators of Electrons

The presence of galactic magnetic fields induces synchrotron emission of electrons during the diffusion process of primary CR electrons in the Galaxy. This energy loss process constrains the maximum distance from which high-energy primary CR electrons can arrive on Earth.

An electron of energy  $E$  suffering energy loss processes  $|dE/dt|$  lost its energy within a typical time-scale  $\tau$  and typical path length-scale  $\ell$  of

$$\tau = \frac{E}{|dE/dt|}, \quad \ell = c\tau. \quad (5.72)$$

If the energy loss is due to synchrotron radiation, using Eq. (5.58) we obtain the typical path length-scale  $\ell_{\text{syn}}$ :

$$\ell_{\text{syn}} = \frac{4\pi m_e^2 c^4}{\sigma_T} \frac{1}{E} \frac{1}{B^2} = 1.25 \times 10^{13} \frac{1}{E [\text{erg}]} \frac{1}{B^2 [\text{G}]^2} [\text{cm}] \quad (5.73)$$

having inserted in the last equality the numerical constants to express energy in erg and the magnetic field in Gauss. For an electron of energy  $E = 1 \text{ TeV} = 1.6 \text{ erg}$  in the galactic magnetic field  $B \sim 4 \mu\text{G}$ , we have  $\ell_{\text{syn}} \simeq 5 \times 10^{23} \text{ cm} = 1.6 \times 10^5 \text{ pc}$ .

This path length-scale  $\ell_{\text{syn}}$  corresponds to a tangled trajectory in a diffusion process which can be considered as the sum of  $N_s$  steps of length  $l_0$ . If we consider for electrons the same value (5.35) for the dimension of magnetic inhomogeneities of the interstellar medium as for protons and nuclei, the number of steps corresponding to the length (5.73) is:

$$N_s(1 \text{ TeV}) = \frac{\ell_{\text{syn}}(1 \text{ TeV})}{l_0} \sim 1.6 \times 10^5 \quad \text{for } l_0 = 1 \text{ pc}. \quad (5.74)$$

Using Eq. (5.27), we can estimate the average distance  $d$  traveled in this random way:

$$d = \sqrt{N_s} \cdot l_0 \simeq 400 \text{ pc} \quad \text{for } l_0 = 1 \text{ pc}. \quad (5.75)$$

Due to the presence of galactic magnetic fields, primary TeV electrons lose half its total energy within a distance smaller than few hundreds of pc from the source. This distance is even smaller if we assume a smaller value for  $l_0$  or for higher energy electrons, due to the  $E^2$  dependence of synchrotron energy loss. The bound (5.75) has important consequences in modelling the propagation of CR electrons in computer program as GALPROP or in the interpretation of experimental results concerning the leptonic component of CRs. We will return on this in Sect. 13.9.3 in relation with the excess of positrons found by the PAMELA, AMS-02 and other experiments.

## References

- R. Abbasi et al., Observation of Anisotropy in the Galactic Cosmic-Ray Arrival Directions at 400 TeV with IceCube. *Astrophys J.* **746**, 33 (2012)
- P. Abreu et al., Search for first harmonic modulation in the right ascension distribution of cosmic rays detected at the Pierre Auger Observatory. *Astroparticle Physics* 34 (2011) 627–639. The results were updated at the ICRC 2013 (see: [arxiv:1310.4620](https://arxiv.org/abs/1310.4620))
- M. Aglietta et al., Evolution of the cosmic-ray anisotropy above  $10^{14}$  eV. *Astrophys. J. Lett.* **692**(2), L130–L133 (2009)
- M. Aguilar et al., (AMS-02 collaboration) AMS-02 provides a precise measure of cosmic rays. *CERN Courier* 53 (2013) 8, 23–26. Also: A. Oliva, ICRC 2013 (ID 1266)
- S. Bowman, *Radiocarbon Dating (Interpreting the Past)* University of California Press (1990). ISBN: 978-0520070370
- S. Braibant, G. Giacomelli, M. Spurio, *Particles and Fundamental Interactions: Supplements* (Springer, Problems and Solutions, 2012). ISBN 978-9400741355
- J. Candia, S. Mollerach, E. Roulet, Cosmic ray spectrum and anisotropies from the knee to the second knee. *Jou. Cosmol. Astropart. Phys.* **05**, 003 (2003)
- J.J. Engelmann et al., Charge composition and energy spectra of cosmic-ray nuclei for elements from Be to Ni. Results from HEAO-3-C2. *Astron. Astrophys.* **233**, 96–111 (1990)
- M. Garcia-Munoz, G.M. Mason, J.A. Simpson, The age of galactic cosmic rays derived. *Astrophys. J.* **217**, 859–877 (1977)
- G. Guillian et al., Observation of the anisotropy of 10 TeV primary cosmic ray nuclei flux with the super-Kamiokande-I detector. *Phys. Rev. D* **75**, 062003 (2007)
- J.D. Jackson, *Classical Electrodynamics* (Wiley, New York, 1999). ISBN 978-0471309321



- M. Kachelriess, Lecture Notes on High Energy Cosmic Rays (2008). [arXiv:0801.4376](https://arxiv.org/abs/0801.4376)
- M.S. Longair, *High Energy Astrophys.*, 3rd edn. (Cambridge University Press, Cambridge, 2011) ISBN: 978-0521756181
- V. Mardia, P. Jupp, *Directional statistics*, Wiley (1999). ISBN: 978-0471953333
- A. Obermeier et al., The boron-to-carbon abundance ratio and galactic propagation of cosmic radiation. *Astrophys J* **752**, 69 (2012)
- V. Ptuskin, Propagation of galactic cosmic rays. *Astropart. Phys.* **39–40**, 44–51 (2012)
- J. Reimer Paula, INTCAL04 Terrestrial Radiocarbon Age Calibration, 0–26 Cal Kyr BP. *Radiocarbon* **46**(3), 1029–1058 (2004)
- R. Silberberg, C.H. Tsao, Spallation processes and nuclear interaction products of cosmic rays. *Phys. Rep.* **191**, 351–408 (1990)
- A.W. Strong, I.V. Moskalenko, Propagation of cosmic-ray nucleons in the Galaxy. *Astrophys. J.* **509**, 212–228 (1998)
- A.W. Strong, I.V. Moskalenko, V.S. Ptuskin, Cosmic-ray propagation and interactions in the galaxy. *Annu. Rev. Nucl. Part. Sci.* **57**, 285–327 (2007)
- N.E. Yanasak et al., Cosmic-ray time scales using radioactive clocks. *Adv. Space Res.* **27**(4), 727–736 (2001)

# Chapter 6

## Acceleration Mechanisms and Galactic Cosmic Ray Sources

Cosmic Rays (CRs) are particles whose energies are typically much higher than the thermal energies found in astrophysical environments. By “nonthermal” emission we mean continuum emission that cannot be originated by blackbody radiation or thermal bremsstrahlung. Their acceleration processes have to explain the features observed in experimental data and discussed in the previous chapters, namely that:

- The energy spectrum of cosmic rays (protons, heavier nuclei and electrons) has the form  $\Phi(E) \propto E^{-\alpha}$  over a wide energy range (Sect. 2.6), indicating nonthermal acceleration processes;
- The measured exponent is  $\alpha \sim 2.7$  for protons and nuclei up to the knee region (several PeV); protons dominate this energy region;
- The observed chemical abundances of CRs below the knee are similar to the abundances of the elements as found in our Solar System, Sect. 3.6. This indicates that CRs are accelerated out of a sample of well-mixed interstellar matter. In other words, CRs are “normal” matter accelerated to extremely high energies;
- The observed exponent  $\alpha$  becomes  $\sim 3.1$  above the knee, Sect. 4.8. The chemical composition seems to become heavier, although at such energies no measurement of the mass number  $A$  of individual CRs is possible;
- After corrections of the measured spectral index  $\alpha$  for the effects due to the propagation in the Galaxy, the expected energy dependence near the sources should be  $E^{-\alpha_S}$ , with spectral index  $\alpha_S \sim 2$ , Sect. 5.6. This is true both for protons/nuclei and CR electrons;
- Above  $\sim 5 \times 10^{18}$  eV, the energy spectrum flattens again to form the ankle;
- The Larmor radius of particles with energy above the ankle is larger than the galactic disk thickness;
- No preferred directions from the galactic plane are observed for the ultra-high-energy CRs, Sect. 5.7. Their origin is thus probably extragalactic.

In addition, cosmic rays with energies up to  $\sim 10^{20}$  eV have been observed (Chap. 7). Theoretical calculation must consider sources and processes able to accelerate particles to these extraordinary energies. In most man-made accelerators, particles are accelerated by electric fields and deflected in circular orbits by magnetic

fields. The magnetic fields ensure also that the particles remain confined in the acceleration regions. This occurs also in an apparatus, like the tokamak, where high temperature plasma is confined. The plasma is the state of matter described as an electrically neutral and completely ionized medium of positive and negative particles.

In most astrophysical environments, static electric fields cannot be maintained because the matter is in the state of a plasma. Ionized gases have a very high electrical conductivity and any static electric field is rapidly short-circuited by the motion of free charges.

Cosmic rays below the knee are the dominant part of the energy density. In the standard model of CR production, they are accelerated by violent processes that produce shock waves and turbulences. The role of magnetized clouds is particularly important, Sect. 6.1. The bulk of CRs is believed to be accelerated in recursive stochastic mechanisms where low-energy particles, after a large number of interactions with a shock wave, will reach high energies, Sect. 6.2. In this model, supernova remnants could accelerate protons up to  $\sim 10^{15}$ – $10^{16}$  eV (Sect. 6.3), with a spectral energy index  $\alpha \sim 2$  (Sect. 6.4) as required by experimental data.

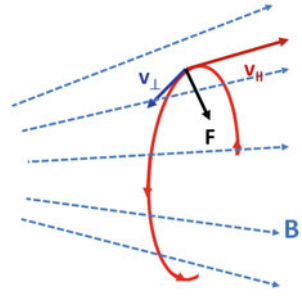
The standard model of galactic CR acceleration has some limitations, Sect. 6.5. In particular, it fails to describe the flux above the knee. Additional models have been put forward, as for instance particle acceleration through electromagnetic mechanisms associated with time-varying magnetic fields. Through Faraday's law some special, very efficient galactic accelerators, could explain the energy region of the CR spectrum above the knee. Some peculiar galactic objects can be involved in these processes, Sect. 6.7. At present, no firm experimental proof is evident for any point-like source of cosmic rays.

Due to the fact that the galactic magnetic field is not able to confine CRs with energy above  $\sim 10^{18}$  eV, they are believed to be of extragalactic origin. They may be accelerated at Active Galactic Nuclei (AGN), at radio galaxies, in Gamma Ray Bursts (GRBs), or in other powerful astrophysical systems.

## 6.1 Second- and First-Order Fermi Acceleration Mechanisms

In this section, we study the acceleration mechanism of charged particles in regions where very strong inhomogeneous magnetic fields exist. The process can be seen as the scattering of the particle by magnetic field irregularities (*magnetic mirrors*). In astrophysical situations, the magnetic field is provided by a “frozen” cloud of interstellar matter, with a density much higher than that of the surrounding material. In addition, the magnetic field frozen inside the cloud has a higher intensity with respect to the average. The scattering between the particle (with mass  $m$ ) and the magnetic cloud (with mass  $M \gg m$ ) is elastic in the reference frame in which the cloud is at rest.

**Fig. 6.1** Motion of a charged particle in a nonuniform magnetic field



### 6.1.1 Magnetic Mirrors

If a charged particle moves in a nonuniform magnetic field, important differences arise in comparison to the case of the simple helicoidal motion that takes place in a uniform field, as discussed in Sect. 2.3.1. We adopt here a very simple approach on this problem; we refer to Chen (1984) for a detailed description used in plasma physics.

In the observer system frame, the particle moves in a nonuniform and static magnetic field. Because of its own motion, in the reference system integral with the instantaneous center of curvature, Fig. 6.1, the particle feels a time-varying magnetic field. In this reference system, the particle experiences an induced electric field  $\mathcal{E}$ , given by Faraday's equation:

$$\nabla \times \mathcal{E} = -\frac{1}{c} \frac{\partial \mathbf{B}}{\partial t} \quad (\text{cgs units}) \quad (6.1)$$

The induced electric field modifies the energy  $E_{\perp}$  associated to the radial component of the velocity  $v_{\perp}$  by an amount equal to the work done by  $\mathcal{E}$ . During one orbit, the change is given by:

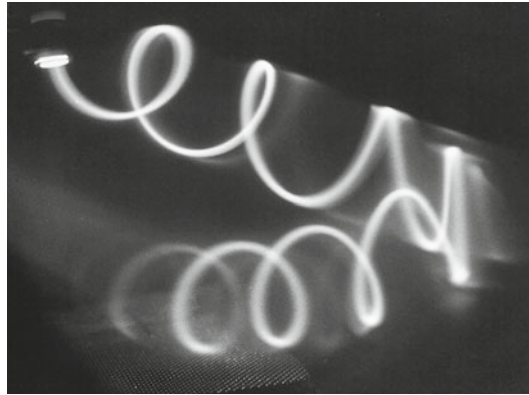
$$\Delta E_{\perp} = \Delta \left( \frac{1}{2} m v_{\perp}^2 \right) = \oint q \mathcal{E} \cdot d\ell = q \oint \nabla \times \mathcal{E} \cdot d\mathbf{S} = -\frac{q}{c} \oint -\frac{\partial \mathbf{B}}{\partial t} \cdot d\mathbf{S} \quad (6.2)$$

where Stokes' theorem has been used. The surface integrals are extended to the circle delimited by the (approximately) circular orbit covered by the particle during one rotation.

Assuming that the field changes by only a small amount over a Larmor period  $T_L = 2\pi/\omega_L$  ( $T_L$  is the time the particle takes to complete the circular orbit in the plane perpendicular to  $\mathbf{B}$ ), the quantity  $-\partial \mathbf{B}/\partial t$  can be approximated with  $\Delta B/T_L$ . From (6.2) we obtain:

$$\Delta E_{\perp} = \frac{q}{c} \Delta B \frac{\omega_L}{2\pi} (\pi r_L^2) = \left( \frac{1}{2} m v_{\perp}^2 \right) \frac{\Delta B}{B} = E_{\perp} \frac{\Delta B}{B} \quad (6.3)$$

**Fig. 6.2** Mirror reflection of an electron beam in a magnetic field that converges to the *right*. Note that the guiding center (axis of spiral) of the reflected beam does not coincide with that of the incident. This is due to the gradient and curvature drift in a nonuniform field. Courtesy of professor Reiner Stenzel (<http://www.physics.ucla.edu/plasma-exp/beam/>)



having used the relation<sup>1</sup>  $\omega_L = qB/mc$  and the fact that  $\omega_{LR}$  corresponds to the velocity  $v_{\perp}$  along the instantaneous center of curvature. We can rewrite the above relation as:

$$\Delta \left[ \ln \left( \frac{E_{\perp}}{B} \right) \right] = 0 \quad \Rightarrow \quad \frac{E_{\perp}}{B} = \text{const} \quad (6.4)$$

Inhomogeneities in the magnetic field therefore produce variations of  $E_{\perp}$ . Note that, in the observer reference frame, the motion occurs in a static field, where the Lorentz force does not produce work. The kinetic energy must then remain constant in time, and at every change of  $E_{\perp}$  must correspond an equal and opposite variation of  $E_{\parallel}$ . For example, if the motion occurs in a region where the magnetic field  $B$  increases, then, by (6.4) also  $E_{\perp}$  increases and  $E_{\parallel}$  must therefore decrease. A force is established that opposes the motion of the particle along the lines of increasing magnetic field - see Fig. 6.2.

Because  $v_{\perp} = v \sin \theta$ , where  $\theta$  is the angle between the velocity and magnetic field vectors and taking into account the fact that  $v$  is constant, Eq. (6.4) can be rewritten as:

$$\frac{\sin^2 \theta}{B} = \text{const} \quad \Rightarrow \quad \sin \theta = \sin \theta_0 \sqrt{\frac{B}{B_0}} \quad (6.5)$$

where  $B_0, \theta_0$  are the corresponding value at one reference, initial position. A relativistic particle in a magnetic field moves on a helicoidal trajectory, keeping constant the “adiabatic invariant”  $\sin^2 \theta / B$ . If during its journey the particle enters a region of increasing magnetic field, it will be reflected. Equation (6.5) says in fact that the angle  $\theta$  can increase up  $\pi/2$ . At this point the particle cannot further penetrate the region in which  $B$  increases and it must reverse its longitudinal direction of the motion and

<sup>1</sup> we assume here a nonrelativistic motion and therefore  $\Gamma = 1$  in Eq. (2.3).

start moving along the direction of decreasing  $B$ . The regions where the magnetic field undergoes a strong increase behaves as magnetic mirrors, for their property of reflecting the motion of charged particles. An electric charge between two magnetic mirrors will remain trapped in the region between the two mirrors. In the Earth's magnetic field, the trapped particles above the atmosphere constitute the van Allen radiation belts (Sect. 2.9).

### 6.1.2 The Second-Order Fermi Acceleration Mechanism

One of the first models for CRs acceleration was due to Enrico Fermi (Fermi 1949). He suggested a mechanism in which particles would be accelerated by collisions with moving clouds of gas.

Let us first consider the scattering between a particle with velocity  $\mathbf{v}$  and a cloud moving with velocity  $\mathbf{U}$ , both along the  $x$ -axis. Let also assume in addition that  $U \ll v$ . Two situations are possible, as sketched in Fig. 6.3. By applying energy-momentum conservation in the elastic scattering, it is straightforward to derive that the velocity  $v'$  of the particle after the interaction with the cloud is:

$$v' = \frac{(m - M)v + 2MU}{m + M} \rightarrow v' \simeq -v \pm 2U \tag{6.6}$$

assuming  $M \gg m$ . If  $\mathbf{U}$  is opposite to  $\mathbf{v}$  (type I collision, Fig. 6.3 left), then  $v'_I = -v - 2U$ . Otherwise, when  $\mathbf{U}$  and  $\mathbf{v}$  are parallel (type II collision, Fig. 6.3 right),  $v'_{II} = -v + 2U$ .

The kinetic energy (in the nonrelativistic case) of the particle before the collision is  $E = mv^2/2$ ; after the collision it is  $E^* = m(-v \pm 2|U|)^2/2$ . The sign  $-$  occurs for type I, and the sign  $+$  for type II collisions. The change in kinetic energy of the particle in first order in  $(U/v)$  during the collision is then:

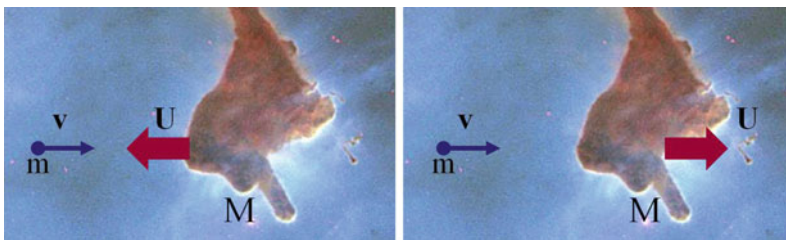


**Fig. 6.3** *Left* Type I collision. The particle and the cloud velocities are opposite in direction. The particle gains energy in head-on elastic scattering. *Right* Type II collision. The particle and the cloud velocities are in the same direction. The particle loses energy in the elastic scattering

$$\Delta E \simeq \pm 4 \frac{U}{v} \cdot E \quad (6.7)$$

(here and hereafter,  $U = |U|$ ). The variation can be either positive ( $\Delta E_I$ ) or negative ( $\Delta E_{II}$ ), according to whether the velocities of the particle and the cloud are opposite or in the same direction.

With a random distribution of clouds in both directions, the rates of type I and II interactions for a particle with positive velocity are respectively:

$$f_I = \frac{v+U}{\ell}; \quad f_{II} = \frac{v-U}{\ell}. \quad (6.8)$$

Here,  $\ell$  represents the particle mean free path. For this particular situation, the head-on collisions are thus more frequent than type-II collisions, and on average the particle will gain energy. The average energy gained stochastically in unit time will be:

$$\frac{\Delta E}{\Delta t} = f_I \Delta E_I + f_{II} \Delta E_{II} = 4 \cdot \frac{U}{v} \cdot E \cdot \frac{2U}{\ell} = \left( \frac{8U^2}{\ell v} \right) E. \quad (6.9)$$

We define here a constant  $\tau_F^n$  with the dimension of a time:

$$\tau_F^n \equiv \frac{\ell v}{8U^2} \quad (6.10)$$

which was first introduced by Fermi in the so-called *second-order Fermi process* (because (6.9) is quadratic in the cloud velocity  $U$ ).<sup>2</sup>

This second-order process describes a situation similar to the mixing of two gases (in our case, clouds and particles) with different temperatures (different kinetic energies). Because of interactions between the two gas components, they reach equilibrium, i.e., energy equipartition between the two species. Here, the particles gain energy despite their large velocities because the masses of the clouds are much larger.

In the 1949 paper, Fermi proposed that collisions with interstellar clouds were the main source of the CRs energy. Fermi himself soon realized that such a mechanism is very inefficient for the acceleration of particles to very high energies. In fact, random velocities of interstellar clouds in the Galaxy are very small ( $U/c \leq 10^{-4}$ ,  $U \leq 3 \times 10^6$  cm/s). Furthermore, the mean free path  $\ell$  for the scattering of cosmic rays corresponds to the typical scale of magnetic inhomogeneities in the interstellar medium (5.34), i.e.  $\ell \sim 0.1$  pc. The average time between two successive collisions (assuming relativistic velocities for the CRs) is

$$\Delta t_C \sim \frac{\ell}{c} = \frac{3 \times 10^{17} \text{ cm}}{3 \times 10^{10} \text{ cm/s}} = 10^7 \text{ s}, \quad (6.11)$$

<sup>2</sup> The coefficient 8 in Eqs. (6.9) and (6.10) is due to the uni-dimensional discussion. In the three-dimensional case, the correct coefficient is 2.

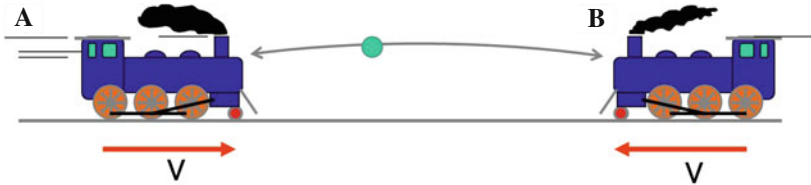


Fig. 6.4 Toy-model of a possible first-order Fermi acceleration mechanism

i.e. few collisions per year. The constant  $\tau_B^H = \frac{E v}{2U^2} = 10^9$  years corresponds to the fact that a sizeable energy increase of a CR particle could only be reached on cosmological timescales.

### 6.1.3 The First-Order Fermi Acceleration Mechanism

A higher efficiency [as Fermi realized in a second work (Fermi 1954)] is obtained if the accelerated particles are moving between two clouds mutually approaching or stellar material separated by a shock front.

The basic idea of this mechanism is easily illustrated using the toy example of two approaching trains, shown in Fig. 6.4. If a ball is thrown from train B towards train A, at a speed  $v$  in the rest frame of the train B, the speed of the ball in the laboratory frame will be  $v_1 = v + V$  and  $v_1^A = v + 2V$  in the rest frame of train A. Assuming the collision to be elastic, the ball will bounce back towards train B with speed  $v_2^A = v + 2V$  in the rest frame of train A and  $v_2 = v + 3V$  in the laboratory frame. Following the further collision of the ball with train B, it is easily seen that the ball will have a speed of  $v_2^B = v + 4V$ , in the rest frame of train B at the time of the new collision and will bounce back with a speed  $v_3 = v + 5V$  in the laboratory frame. As the gain in each collision is proportional to the train velocity  $V$ , if the process could continue for a long time, we may thus see that the ball could acquire a very large energy.

The “bouncing” back and forth of a proton or nucleus, between the material upstream and down-stream of a shock-front, has a strong similarity with the toy example described. We shall, to start with, compute the energy gained by a particle of velocity  $v$  that undergoes a single collision with a magnetic cloud moving at velocity  $U$  in a direction opposite (head-on collision) or equal (catching collision) to that of the particle. Assuming that, as a result on many collisions,  $v$  will eventually become  $\approx c \gg U$ , it is appropriate a relativistic approach. Let us define  $S$  the reference frame of the observer, with the cloud velocity directed along the  $x$ -axis, and  $S'$  the frame in which the cloud is at rest. Only the  $p_x$  component of the particle momentum is relevant in the problem, as the  $y, z$  components are conserved in the interaction.

The four-momentum describing the particle is  $(E, p_x)$  in the frame  $S$ , and  $(E', p'_x)$  in  $S'$ . From the Lorentz transformations:



$$E' = \Gamma(E + Up_x) \quad (6.12a)$$

$$p'_x = \Gamma\left(p_x + \frac{U}{c^2}E\right). \quad (6.12b)$$

The collision is *elastic* in the frame in which the cloud is at rest. This means that the energy and momentum after the collision are:

$$E' \xrightarrow{\text{collision}} E'; \quad p'_x \xrightarrow{\text{collision}} -p'_x. \quad (6.13)$$

The particle energy  $E^*$  after the scattering in the reference frame of the observer is obtained by inversion of (6.12a):

$$E = \Gamma(E' - Up'_x) \xrightarrow{\text{collision}} \Gamma(E' - U(-p'_x)) \equiv E^*. \quad (6.14)$$

Inserting (6.12a, 6.12b) into (6.14) we obtain:

$$E^* = \Gamma \left[ \Gamma(E + Up_x) + U\Gamma\left(p_x + \frac{U}{c^2}E\right) \right]. \quad (6.15)$$

Recalling that  $p_x = mv\Gamma \cos\theta$  and  $E = mc^2\Gamma$ :

$$\frac{p_x}{E} = \frac{mv\Gamma \cos\theta}{mc^2\Gamma} = \frac{v}{c^2} \cos\theta \quad (6.16)$$

then (6.15) becomes:

$$E^* = \Gamma^2 \left[ E + 2Up_x + \frac{U^2}{c^2}E \right] = \Gamma^2 E \left[ 1 + 2U\frac{p_x}{E} + \frac{U^2}{c^2} \right] = \Gamma^2 E \left[ 1 + 2U\frac{v \cos\theta}{c^2} + \frac{U^2}{c^2} \right]. \quad (6.17)$$

Using now the definition of the Lorentz factor  $\Gamma$  and its Taylor approximation:  $\Gamma^2 = [1 - (U/c)^2]^{-1} \simeq [1 + (U/c)^2]$  and at the second order in  $U/c$ :

$$E^* \simeq \left[ 1 + \frac{U^2}{c^2} \right] E \left[ 1 + 2U\frac{v \cos\theta}{c^2} + \frac{U^2}{c^2} \right] \simeq E \left[ 1 + 2\frac{Uv \cos\theta}{c^2} + 2\frac{U^2}{c^2} \right]. \quad (6.18)$$

The energy gained by the particle in the observer reference frame is:

$$\Delta E = E^* - E = \left[ 2\frac{Uv \cos\theta}{c^2} + 2\left(\frac{U}{c}\right)^2 E \right]. \quad (6.19)$$

The first term of (6.19) is null when averaged over all directions. Energy is gained in head-on collisions ( $\cos\theta > 0$ ) and lost in catching collisions when  $\cos\theta < 0$ . In this situation the energy gain is  $\Delta E \propto (U/c)^2$ , as derived in the previous section (second order Fermi model). The acceleration process is therefore rather inefficient.

Let us assume an astrophysical environment in which only head-on collisions occur (as in the toy situation of Fig. 6.4). In such conditions, the quadratic term in (6.19) can be neglected, since  $U/c \ll 1$ . Then, using also the fact that the particle is relativistic and  $v \sim c$ , (6.19) becomes:

$$\Delta E = E^* - E = \left(2 \frac{U \cos \theta}{c}\right) \cdot E, \quad E^* = \left(1 + 2 \frac{U}{c} \cos \theta\right) \cdot E. \quad (6.20)$$

The particle gains energy in each collision if  $\cos \theta > 0$ . We remind that the average value  $\langle x \rangle$  of a variable  $x$  distributed according to a function  $f(x)$  is:

$$\langle x \rangle = \frac{\int x \cdot f(x) \cdot d\Omega}{\int f(x) \cdot d\Omega}. \quad (6.21)$$

Here,  $x = \cos \theta$ ,  $d\Omega = d\phi \cos \theta d\theta = d\phi d \sin \theta$  is the differential solid angle and  $f(x)$  is given by (6.20). The average over all directions with  $\cos \theta > 0$  gives:

$$\langle \cos \theta \rangle = \frac{\int_0^1 \cos \theta \cdot \cos \theta \cdot d \sin \theta}{\int_0^1 \cos \theta \cdot d \sin \theta} = \frac{2}{3}. \quad (6.22)$$

Finally, when averaged over directions, (6.20) becomes:

$$\langle \Delta E \rangle = \left(\frac{4U}{3c}\right) \cdot \langle E \rangle \equiv \eta \cdot \langle E \rangle \quad (6.23a)$$

$$\langle E^* \rangle = \left(1 + \frac{4U}{3c}\right) \cdot \langle E \rangle \equiv \mathcal{B} \cdot \langle E \rangle \quad (6.23b)$$

The two quantities defined above,  $\eta$  and  $\mathcal{B}$ , are used in the following. A situation in which accelerated particles suffer only head-on collisions is assumed in the astrophysical diffusive shock acceleration model, which uses strong shock waves produced (for instance) by supernova explosions.

The above result can also trivially be obtained using (6.7) and (6.8) assuming only type I collisions. In this case, for  $v \sim c \gg U$ , (6.9) is simply:

$$\frac{\Delta E}{\Delta t} = f_I \Delta E_I = 4 \cdot \frac{U}{v} \cdot E \cdot \frac{U+v}{\ell} \simeq 4 \frac{U}{\ell} E = \frac{E}{\tau_F}. \quad (6.24)$$

The characteristic time

$$\tau_F' \equiv \frac{\ell}{4U} = 2\tau_F'' \frac{U}{c} \quad (6.25)$$

is now sensibly shorter than that expected in the second-order process (6.10).

### 6.1.4 The Power-Law Energy Spectrum from the Fermi Model

The important result of the Fermi mechanism is that it succeeded in deriving a power-law energy spectrum. To see this, let us use the diffusion-loss equation (5.37). As usual,  $\mathcal{N}$  represents the (energy dependent) number density of CRs. We are interested in a steady-state situation ( $d\mathcal{N}/dt = 0$ ) and neglecting sources,  $Q(E) = 0$ . Then (5.37) becomes:

$$\frac{\partial}{\partial E} [b(E)\mathcal{N}(E)] - \frac{\mathcal{N}(E)}{\tau_{\text{esc}}} = 0. \quad (6.26)$$

The term  $b(E) = -dE/dt$  represents now an energy gain term, obtained comparing Eq. (5.19) with (6.24) or (6.9):

$$\frac{dE}{dt} = \frac{E}{\tau_F} \quad \longrightarrow \quad b(E) = -E/\tau_F. \quad (6.27)$$

Therefore (6.26) reduces to:

$$-\frac{d}{dE} \left[ \frac{E}{\tau_F} \mathcal{N}(E) \right] - \frac{\mathcal{N}(E)}{\tau_{\text{esc}}} = 0. \quad (6.28)$$

After differentiation and rearrangement of the terms, (6.28) becomes:

$$-\frac{d\mathcal{N}(E)}{dE} = \frac{\tau_F}{E} \left[ \frac{1}{\tau_F} + \frac{1}{\tau_{\text{esc}}} \right] \mathcal{N}(E) = \frac{1}{E} \left[ 1 + \frac{\tau_F}{\tau_{\text{esc}}} \right] \mathcal{N}(E). \quad (6.29)$$

Therefore:

$$\mathcal{N}(E) = \text{constant} \times E^{-\alpha_S} \quad \text{with} \quad \alpha_S = 1 + \frac{\tau_F}{\tau_{\text{esc}}}. \quad (6.30)$$

The Fermi acceleration mechanism succeeded in deriving a power-law energy spectrum with spectral index  $\alpha_S$ . Note that in the above notation we have used  $\tau_F$ : it can represent both  $\tau_F''$  and  $\tau_F'$ . A power-law spectrum is thus obtained in both Fermi mechanisms. The efficiency of the two processes is completely different, and only the first order one can account for galactic CRs acceleration.

## 6.2 Diffusive Shock Acceleration in Strong Shock Waves

The first-order Fermi mechanism described in Sect. 6.1.3 is very efficient in accelerating particles if we consider regions where there are small-scale turbulences, for example, in the shells of young supernova remnants.

As this mechanism is associated with particle acceleration in strong shock waves, it is often referred to as *diffusive shock acceleration*. The key feature of this process is that the acceleration automatically results in a power-law energy spectrum (6.30) with spectral index  $\alpha_S \approx 2$ .

Different modeling of the diffusive shock acceleration exists, according to different authors which refined the model starting from the old first-order Fermi acceleration model (Axford et al. 1977; Krymsky 1977; Bell 1978; Blandford and Ostriker 1978; Drury 1983; Jokipii 1987; Jones and Ellison 1991). These works stimulated an enormous amount of interest, and different astrophysical environments are now considered as possible acceleration region candidates.

A shock wave carries energy and can propagate through a medium or in some cases in the absence of a material medium, through the electromagnetic field. Shock waves are characterized by an abrupt, nearly discontinuous change in the characteristics of the medium (Fig. 6.5a). Across a shock there is always an extremely rapid rise in pressure, temperature and density of the flow. In supersonic flows (as in the case of supernova explosions), the shock wave travels through the medium at a higher speed than an ordinary wave. The speed  $v_s$  of the shock front is much larger than the thermal velocities of particles ( $v_s \gg v_1$ ).

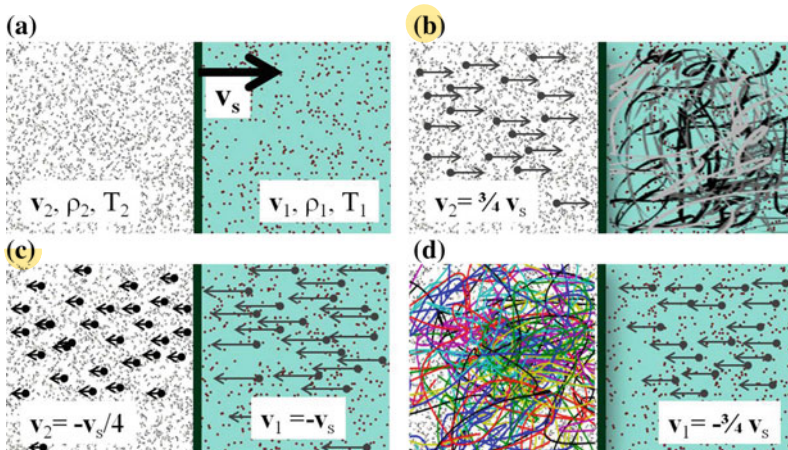


**Fig. 6.5** **a** Conditions on the down-stream (left) and the up-stream (right) side of a shock wave in the laboratory system. The shock front propagates at supersonic velocity  $v_s$  through stationary interstellar gas with density  $\rho_1$ , temperature  $T_1$  and particle velocities  $v_1 \ll v_s$ . Density, temperature and velocity behind the shock are  $\rho_2$ ,  $T_2$  and  $v_2$ , respectively. **b** The same situation seen in the reference frame in which the shock front is at rest. In this frame of reference, the ratio of the up-stream to the down-stream velocity is  $v_1/v_2 = R$ . For a fully ionized plasma,  $R = 4$ , as demonstrated in Sect. 6.4.2. **c** The flow of gas as observed in the frame of reference in which the up-stream gas is stationary and the velocity distribution of the high energy particles is isotropic. **d** The flow of gas as observed in the frame of reference in which the down-stream gas is stationary and the velocity distribution of high energy particles is isotropic

In the frame in which the shock front is at rest (Fig. 6.5b) the velocities of the material up-stream and down-stream are respectively  $\mathbf{v}_1 = -\mathbf{v}_s$  and  $\mathbf{v}_2 = \mathbf{v}_s/R$ . The constant  $R$  depends only on the gas composition, and for a mono-atomic gas  $R = 4$  (see the demonstration in Sect. 6.4.2).

Now consider high energy particles down-stream of the shock. Scattering ensures that the particle distribution is isotropic in the frame of reference in which the gas is at rest (Fig. 6.5c). The shock front moves at velocity  $v_s$  but the gas up-stream (i.e. behind) the shock advances at a speed  $U = (3/4)v_s$  relative to the material down-stream. When a particle crosses the shock front from right to left, an elastic collision occurs and the particle gains energy according to (6.23a). The velocity distribution of particles entered in the region behind the shock front will become isotropic with respect to that flow.

A symmetric situation occurs for a particle diffusing from up-stream the shock, moving towards the ahead region in front of the shock (Fig. 6.5d). The distribution of the particle velocities is isotropic behind the shock. When crossing the shock front, a particle encounters gas moving towards the shock front, again with speed  $U = (3/4)v_s$ . It receives the same increase in energy  $\eta$  on crossing the shock front from down-stream to up-stream as it did in traveling from up-stream to down-stream.

The fact that in every passage through the shock front the particle receives an increase of energy is the clever aspect of the first-order Fermi acceleration mechanism. In addition, the energy increment  $\eta = (4/3)U/c$  is the same in both directions. Then, according to (6.23b), the particle energy after each collision is incremented by a factor  $\mathcal{B}$ :

$$\mathcal{B} = 1 + \eta = 1 + \frac{4}{3} \frac{3v_s}{4c} = 1 + \frac{v_s}{c} \quad (6.31)$$

As  $v_s/c$  is small, many collisions is necessary to achieve a sizeable energy gain.

### 6.2.1 Supernova Explosions and Cosmic Rays Acceleration

Type II or core collapse supernovae occur at the end of the fusion process in very massive stars,  $M \geq 8M_\odot$ . These stars develop an onion-like structure (Fig. 12.9) with a degenerate Fe core. After the core is completely fused to iron, no further processes releasing energy are possible. Instead, photo-disintegration destroys the heavy nuclei, e.g. via  $\gamma + {}^{56}\text{Fe} \rightarrow 13{}^4\text{He} + 4n$ , and removes the thermal energy necessary to provide pressure support. In the following collapse of the star, the density increases and the free electrons and protons are forced to form neutrons via inverse beta decay. A neutron star forms in the core, with a density which equals that of the nuclear matter. The in-falling material of outer layers is reflected from the nuclear core and a shock wave propagates outwards heated by neutrino emission from the neutron star. The energy outfall from a supernova explosion (Sect. 12.10) is simply evaluated as the released gravitational binding energy, which is about  $(2-4) \times 10^{53}$  erg per explosion. A large fraction (99%) of this energy is emitted as neutrinos, and only 1% (thus,

about  $10^{51}$  erg is transferred into kinetic energy of the expelled material forming the shock wave. The energy emitted as electromagnetic radiation is even less, about 1% of the kinetic energy.

The acceleration mechanism due to the supernova explosions is consistent with the following points:

- **The energy balance.** In a successful core-collapse supernova (SN) around  $10 M_{\odot}$  are ejected with a velocity  $U \sim 5 \times 10^8$  cm/s, see (6.33). Assuming 3 SNs per century in the Galaxy, the average output in kinetic energy from galactic supernovae is  $P_{\text{SN}}^{\text{kin}} \sim 3 \times 10^{42}$  erg/s. This value is one or two order of magnitude larger than the luminosity  $P_{\text{CR}} \sim 5 \times 10^{40}$  erg/s requested to maintain a steady cosmic ray energy density  $\rho_{\text{CR}} \sim 1$  eV/cm<sup>3</sup> (see Sect. 2.10).
- **The efficiency of the acceleration process.** To fulfill the energy balance requirement, the CR acceleration mechanism should convert part of the kinetic energy of material ejected by the SN to high energy particles:  $P_{\text{CR}} = \zeta P_{\text{SN}}^{\text{kin}}$ , with efficiency  $\zeta = 0.01\text{--}0.1$ . According to (6.23a), the particle gain in the first order Fermi mechanism is proportional to  $\eta = 4/3(U/c)$ . We will derive in Sect. 6.2.2 that  $U/c \simeq \text{few } \%$ . Thus, the efficiency  $\eta$  is the order of the needed value for  $\zeta$ , as first suggested by Ginzburg and Syrovatskii.
- **The chemical abundances.** The composition of cosmic rays as measured by direct experiments (Sect. 3.6), when the effects of propagation in the Galaxy are considered, is very similar to the abundances of the elements in the Solar System. The chemical composition of the Solar System is similar to that produced by core-collapse supernovae (Sect. 3.6.1). It follows that the CRs acceleration sites are close (in this model, coincident) to regions where the abundance of the chemical elements is determined by a supernova explosion.
- **The maximum energy.** The supernova model provides CRs with energy up to the knee. The knee (in this model) is due to the different maximum energy given to nuclei with different charge,  $E^{\text{max}}(Z) \simeq 300 \cdot Z$  TeV, see Sect. 6.3. A prediction of this model is that the chemical composition of CRs becomes heavier as the energy increases from values below to above the knee.
- **The spectral index of the power-law energy spectrum.** A power-law energy spectrum for all types of charged particles is observed (protons, nuclei and electrons). The energy spectrum of cosmic rays and the electron energy spectrum from nonthermal sources have the form  $\Phi(E) \propto E^{-\alpha_S}$ , where the exponent  $\alpha_S$  is typically  $\sim 2$ . We derive this result in Sect. 6.4.

### 6.2.2 Relevant Quantities in a Supernova Explosion

The average energy emitted as kinetic energy  $K$  by a  $10 M_{\odot}$  supernova is roughly 1% of the total binding energy, i.e., for:

$$M = 10M_{\odot} = 2 \times 10^{34} \text{ g} \quad (6.32a)$$

we obtain

$$\text{Gravitational Energy} \sim 2 \times 10^{53} \text{ erg} \quad (6.32b)$$

$$K \sim 2 \times 10^{51} \text{ erg}. \quad (6.32c)$$

The velocity of the ejected mass (the *shock wave*) is of the order of:

$$U \simeq \sqrt{\frac{2K}{M}} = \sqrt{\frac{4 \times 10^{51}}{2 \times 10^{34}}} \simeq 5 \times 10^8 \text{ cm/s} \rightarrow \frac{U}{c} \simeq 2 \times 10^{-2}. \quad (6.33)$$

Density, velocity and temperature of the matter behind and ahead of the shock are determined by thermodynamical considerations in Sect. 6.4.2.

According to (6.33), a *shock wave* originated by a supernova explosion has typically  $U/c \simeq 10^{-2}$ , which corresponds to a *nonrelativistic velocity* but *much larger* than typical *velocities* of the *interstellar materials*. More *refined models* [see Hillas (2005) for a recent review] assume that the velocity is higher for *outer layers* ( $U/c \simeq 10^{-1}$ ), while the *inner layers* expand more *slowly*. The range of values:

$$\frac{4U}{3c} \equiv \eta \simeq 10^{-2} - 10^{-1} \quad (6.34)$$

correspond to the needed *efficiency*  $\eta$  of the acceleration process defined in (6.23a), and required to explain the CRs acceleration by supernovae explosions.

The *shock front expands* (we assume with constant *velocity*  $U$  and with *spherical symmetry*) across the *interstellar matter* (ISM), which has *density*  $\rho_{ISM} \sim 1 \text{ proton cm}^{-3} \simeq 1.6 \times 10^{-24} \text{ g cm}^{-3}$  (Sect. 2.7.2). During the expansion, the *shock collects interstellar matter*. When the *mass of the swallowed material* becomes *comparable* to the *mass of the ejected shells* of the supernova, the *velocity of the shock decreases remarkably*. As the radius  $R_{SN}$  of the shock front increases, the matter density  $\rho_{SN} \sim \text{mass}/R_{SN}^3$  inside the shock volume decreases. We *assume* that the *shock becomes inefficient* when the  $\rho_{SN} \simeq \rho_{ISM}$ . The radius within which the shock wave is able to accelerate particles can be derived using the condition

$$\rho_{SN} = \frac{10M_{\odot}}{(4/3)\pi R_{SN}^3} = \rho_{ISM}. \quad (6.35)$$

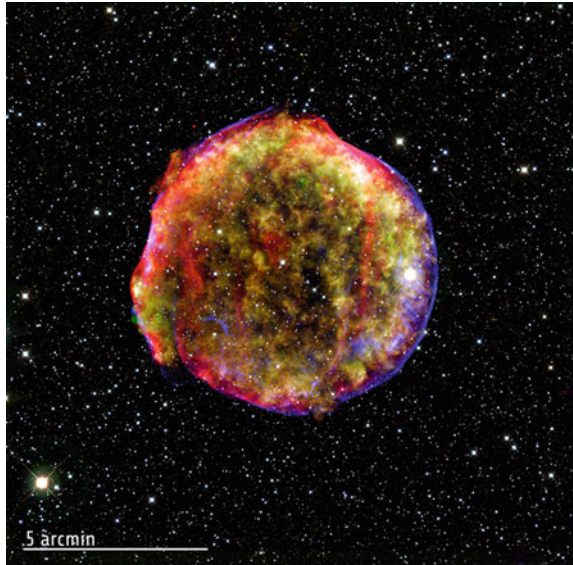
From this we obtain:

$$R_{SN} = \left( \frac{3 \times 10M_{\odot}}{4\pi\rho_{ISM}} \right)^{1/3} = \left( \frac{6 \times 10^{34}}{4\pi \cdot 1.6 \times 10^{-24}} \right)^{1/3} = 1.4 \times 10^{19} \text{ cm} = 5 \text{ pc}. \quad (6.36a)$$

The corresponding *time interval*  $T_{SN}$  during which particles are accelerated is:



**Fig. 6.6** This composite image of the Tycho Brahe SNR combines X-ray and infrared observations obtained with NASA's chandra X-ray observatory and spitzer space telescope, respectively, and the Calar Alto Observatory, Spain (<http://chandra.harvard.edu/photo/2009/tycho/>). It shows the scene more than four centuries after the brilliant star explosion witnessed by Tycho Brahe and other astronomers of that era. Credit: X-ray: NASA/CXC/SAO, Infrared: NASA/JPL-Caltech; Optical: MPIA, Calar Alto, O.Krause et al.



$$T_{\text{SN}} = \frac{R_{\text{SN}}}{U} = \frac{1.4 \times 10^{19} \text{ cm}}{3 \times 10^8 \text{ cm/s}} \simeq 3 \times 10^{10} \text{ s} \simeq \mathcal{O}(1000) \text{ y}. \quad (6.36b)$$

Figure 6.6 shows the SN 1572 (or Tycho's Supernova) as seen in different wavelengths from modern astronomers. It was a supernova of Type Ia in the Cassiopeia constellation, about  $D = 3 \text{ kpc}$  from Earth. SN 1572 is one of about eight supernovae visible to the naked eye in historical records. It appeared in early November 1572 and was independently discovered by many individuals, including the famous astronomer Tycho Brahe. He described the new star in the book *De nova et nullius aevi memoria prius visa stella* ("Concerning the Star, new and never before seen in the life or memory of anyone"), published in 1573, which contains his own observations and the analysis of many other observers. From the scale on the figure, we obtain an angular radius of  $\sim 4 \text{ arcmin}$ . Thus, the linear radius of the object visible from the figure is (we need to convert the arcmin to radians):

$$R_{\text{Tycho}} = D \Delta\theta = 3 \text{ kpc} \times \frac{2\pi}{360} \frac{4}{60} = 3 \text{ kpc} \times 0.0011 \simeq 3 \text{ pc} \quad (6.37)$$

in agreement with (6.36a) for a 450 old SN remnant.

A note of warning: the fact that protons or heavier nuclei are accelerated in the region shown in Fig. 6.6 is controversial (Sect. 9.7). Most of the detected nonthermal radiation, including that in the radio wavelength region, is almost certainly emitted by electrons.

Note that the timescale for particle acceleration is  $T_{\text{SN}} \sim \mathcal{O}(10^3) \text{ y}$ , while the timescale for CRs escape from our galaxy is  $\tau \sim \mathcal{O}(10^7) \text{ y}$ , as derived in Sect. 5.2.



A large number of supernova explosions, with a short acceleration time duration with respect to the CR escape time, contributes to fill the Galaxy with high energy particles. The CRs we detect could be accelerated by a number of supernovae as large as  $10^4$ !

All the young galactic supernova remnants in historical records (Sect. 12.10) are in the evolution phase when the swept-up mass is of the order of the mass of the ejected material and are entering in the so-called *Sedov phase*. This phase represents the situation when the shock has collected enough interstellar matter to initiate the slow-down period. An object as the Crab Nebula follows a different evolution scenario, since a continuous energy flux is originating from a central pulsar (Pulsar Wind Nebula). We will return on the Crab in Sect. 9.5.

Equation (6.36a) tells us that supernova explosions compress the inter-stellar material up to a few pc. This explains why the average distance between stars within galaxies (including our own) is of the order of the parsec. Also planetary systems cannot exist on smaller scales. It is believed that planetary systems (like our own) were formed from a cloud of gas and dust. If the cloud is hit by a shock wave generated by the explosion of a pre-existing, nearby star with a larger mass, the shock wave causes the compression of the gas and dust cloud. These matters, because of the gravitational attraction, begin to pull inward other material forming the star nebula. In the process of contraction, as a result of the gravitational attraction, pressure, magnetic fields and rotation, the nebula is flattened into a protoplanetary disk with a protostar at its center. In the protoplanetary disk, a certain number of planets were formed. If the protostar is too close to another massive star, the successive core-collapse restarts the process. The security distance within which long-lived stars (as the Sun, which has been shining since 5 Gy, and will last for other 5 Gy) are distributed is thus of the order of a few pc.

### 6.3 Maximum Energy Attainable in the Supernova Model

With simple arguments it is possible to derive the maximum energy that a charged particle can reach in the acceleration process due to the diffusive shock mechanism from a supernova explosion. Equation (6.23a) gives the energy gain for each iterative acceleration process. The rate of energy increase is given by the ratio between (6.23a) and the characteristic period  $T_{\text{cycle}}$  of the process, i.e. the time between two successive scattering processes:

$$\frac{dE}{dt} \sim \frac{\eta E}{T_{\text{cycle}}} \quad (6.38)$$

$T_{\text{cycle}}$  can be evaluated with the following considerations. When the accelerated particles pass through the shock front in either direction, their velocity distribution rapidly becomes isotropic in the reference frame of the moving fluid on either side of the shock. This occurs because they are scattered by streaming instabilities and

turbulent motions on either side of the shock wave and because they are trapped by the magnetic fields. The typical extension of the confinement region is given by the Larmor radius in the magnetic field  $B$  (2.5):

$$\lambda_{\text{cycle}} = r_L = \frac{E}{ZeB} \quad (6.39)$$

Referring to Fig. 6.5c, d, the typical time between successive encounters with the shock front moving at velocity  $U \simeq v_S$  is

$$T_{\text{cycle}} = \frac{\lambda_{\text{cycle}}}{U} = \frac{E}{ZeBU}. \quad (6.40)$$

Inserting (6.40) into (6.38), we obtain:

$$\frac{dE}{dt} \simeq \eta E \frac{ZeBU}{E} \quad (6.41)$$

where, using (6.31),  $\eta \simeq U/c$ . Thus, the rate of energy gain is independent of the particle energy  $E$ . This is relevant, because the model is not constrained from a particular mechanism of pre-acceleration of the charged particles.

The maximum energy that a charged particle could achieve is then simply the rate of energy gain, times the duration  $T_{\text{SN}}$  of the shock (6.36b):

$$E^{\text{max}} \simeq \frac{dE}{dt} \times T_{\text{SN}} = \eta ZeBR_{\text{SN}} \simeq \frac{ZeBR_{\text{SN}}U}{c} \quad (6.42)$$

Inserting the numerical values for the velocity  $U$  of the shock (6.33), the proton electric charge ( $e = 4.8 \times 10^{-10}$  e.s.u.), the maximum radius of the expansion  $R_{\text{SN}}$  (6.36a), and the typical value of the galactic magnetic field  $B \simeq 4 \times 10^{-6}$  Gauss, we obtain:

$$E^{\text{max}} = eB(U/c)R_{\text{SN}}Z \quad (6.43a)$$

$$= (4.8 \times 10^{-10}) \cdot (4 \times 10^{-6}) \cdot (2 \times 10^{-2}) \cdot (1.4 \times 10^{19}) \cdot Z$$

$$\simeq 500 \cdot Z \text{ erg} \simeq 300 \cdot Z \text{ TeV} \quad (6.43b)$$

The diffusive shock acceleration mechanism based on supernova explosions explains the spectrum of cosmic-ray protons up to few hundreds of TeV, i.e.  $\sim \text{few } 10^{14}$  eV, which corresponds to the energy region where the knee begins.

An important consequence of (6.43) is that  $E^{\text{max}}$  depends on the particle charge  $Z$ . It means that a fully ionized heavy nucleus of charge  $Z$  could achieve much higher total energy with respect to a single-charged proton. Thus, in this model, the knee is explained as a structure due to the different maximum energy reached by nuclei with different charge  $Z$  (see Fig. 6.7).

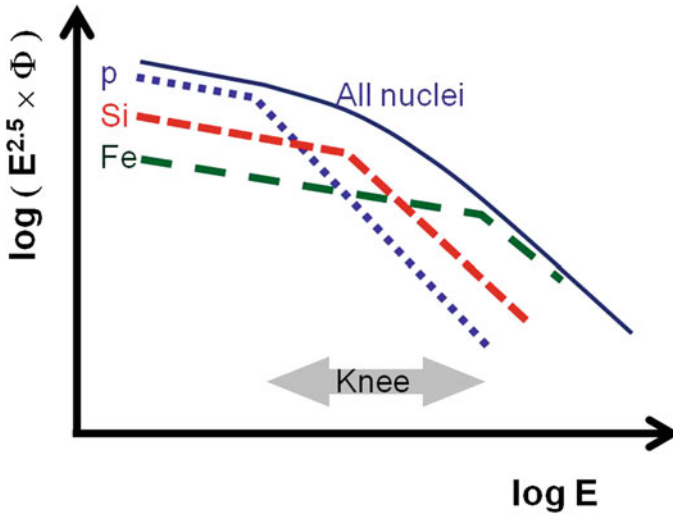


**Fig. 6.7** The interpretation of the CRs *knee* as due to the correlation between the maximum energy and the nuclear charge  $Z$ . The flux of each nuclear species sharply decreases after a given cut-off which depends on  $Z$  as  $E_Z^{\max} = E_p^{\max} \cdot Z$ , where  $E_p^{\max}$  is the maximum energy reached by protons. The behavior of hydrogen, silicon ( $Z = 14$ ) and iron ( $Z = 26$ ) nuclei are depicted in figure

As shown by (6.43), the diffusive shock acceleration model explains quite naturally the maximum rigidity (see Sect. 2.3.1) associated with acceleration effects. Models exist which attribute this effect also to the propagation, or to both propagation and acceleration. More exotic effects (connected with a change of the behavior of nuclear cross-sections at very high energies) seem ruled out. If cosmic rays are classified according to the energy per particle, as in the case of air shower measurements, then the spectrum should steepen first for protons, then for helium, then for the C, N, O group etc. The experimental evidence for the sequence of successive steepening for several groups of nuclei was discussed in Sect. 4.10.

## 6.4 The Spectral Index of the Energy Spectrum

The spectral index  $\alpha_S$  of the energy spectrum of accelerate particles in the framework of the diffusive shock acceleration model can be estimated following the procedure used in Longair (2011).

In Sect. 6.3 we have shown that the maximal energy  $E^{\max}$  for a particle accelerated at a specific source is determined by several factors. For a shock driven by a supernova explosion, a limited time  $T_{\text{SN}}$  is available for particle acceleration. This finite lifetime limits the maximum number  $k^{\max}$  of possible iteration cycles. In each cycle, the particle energy increases by a finite amount  $\mathcal{B}$  (6.31). In this simple model, all

particles will have the same final energy if they undergo the same number of cycles. An escape probability  $P_{\text{esc}}$  per encounter can be defined. Let  $P_{\text{esc}}$  represent the possibility that, after a collision, the particle escapes the acceleration region and it is lost for successive iterations. In regions where the acceleration mechanism is efficient,  $P_{\text{esc}}$  is small. Thus  $P = 1 - P_{\text{esc}}$  represents the probability that the particle remains inside the acceleration region after one collision process. Further assume that  $P_{\text{esc}}$  is constant all over  $T_{\text{SN}}$ .

The probability that a particle remains in the acceleration region after  $k$  encounters is  $(1 - P_{\text{esc}})^k$  and, if  $N_0$  is the initial number of particles and  $E_0$  their energy, after  $k$  cycles in the acceleration region there will be:

$$N = N_0 P^k \text{ particles with energy } \geq E = E_0 \mathcal{B}^k. \quad (6.44)$$

In fact, after the first encounter, there will be  $N_1 = N_0 P$  particles with energy  $E_1 = E_0 \mathcal{B}$ , with  $\mathcal{B}$  given in Eq. (6.31); after two encounters  $N_2 = N_1 P = N_0 P^2$  particles with energy  $E_2 = E_1 \mathcal{B} = E_0 \mathcal{B}^2$  and so on.

The unknown parameter  $k$  can be removed from both sides in (6.44) using the ratio:

$$\frac{\ln(N/N_0)}{\ln(E/E_0)} = \frac{\ln P}{\ln \mathcal{B}}. \quad (6.45)$$

If  $k$  is large, the discrete process is seen as a continuous process and hence:

$$\frac{N(\geq E)}{N_0} = \left( \frac{E}{E_0} \right)^{\ln P / \ln \mathcal{B}} \quad (6.46)$$

We explicitly write  $N(\geq E)$  because (as shown above in the discussion of the discrete case) it represents the number of particles having energy at least equal to  $E$ :

$$N(\geq E) = \int_E^{\infty} N(E') dE'.$$

The differential energy spectrum is thus given by the energy derivative of (6.46):

$$N(E) = \text{constant} \times E^{-1+\Lambda} \text{ where } \Lambda = \ln P / \ln \mathcal{B} \quad (6.47)$$

Again, as obtained in (6.30), we obtain a power-law spectrum. The numerical value of  $\Lambda$  in (6.47) is determined by the values of  $P$  and  $\mathcal{B}$ . The latter was already derived in (6.31).

### 6.4.1 The Escape Probability

To estimate the **escape probability  $P$** , we follow the argument due to Bell (1978) and reported also in Longair (2011). According to Sect. 2.4, if  $\Phi(> E)$  is the flux of particles with energy larger than  $E$ , the **flux  $\mathcal{F}$  from one hemisphere** through a planar surface is  $\pi\Phi(> E)$  (2.17b). The number density of relativistic ( $v \simeq c$ ) isotropic particles is given by (2.18a) as  $n = 4\pi\Phi(> E)/c$ . The **continuity equation** for mass (see Sect. 6.4.2) will **ensure** that the **fluxes of particles from left to right and from right to left** of the shock front are **equal**. Thus, the average flux of particles per square centimeter per second through the shock front is:

$$n = \frac{4\pi}{c}\Phi(> E) = \frac{4}{c}\mathcal{F} \quad \rightarrow \quad \mathcal{F} = \frac{nc}{4} \quad (6.48)$$

The **flux is the same in either direction** with respect to the shock front. **At each pass, the particle gains energy**. In the down-stream region, since the particle velocities are randomized by the collisions and are thus isotropic in that frame (Fig. 6.5b), there is a finite probability that the particle exits through boundary on the left. In this way, particles are removed from the shock region and lost. Referring to Fig. 6.5b, these **particles are moving with velocity  $v_2 = v_s/4$  towards the left boundary and are removed from the region of the shock at a rate:**

$$\mathcal{F}_{\text{esc}} = nv_2 = n\frac{v_s}{4} \quad (6.49)$$

Thus, the fraction of particles lost per unit time is the ratio between the two fluxes (6.49) and (6.48), and it represents the probability  $P_{\text{esc}}$  that a particle is removed from the shock region:

$$P_{\text{esc}} = \frac{\mathcal{F}_{\text{esc}}}{\mathcal{F}} = \frac{\frac{nv_s}{4}}{\frac{nc}{4}} = \frac{v_s}{c} \quad (6.50)$$

This is an important result: if the shock is nonrelativistic ( $v_s \ll c$ ), only a small fraction of the particles is lost per cycle. **The probability to remain in the acceleration region is thus:**

$$P = 1 - P_{\text{esc}} = 1 - \frac{v_s}{c}. \quad (6.51)$$

We are able now to obtain the unknown **spectral index  $\mathcal{A}$**  in (6.35) because:

$$\ln P = \ln\left(1 - \frac{v_s}{c}\right) \simeq -\frac{v_s}{c}; \quad \ln \mathcal{B} = \ln\left(1 + \frac{v_s}{c}\right) \simeq +\frac{v_s}{c} \quad (6.52)$$

and

$$\Lambda = \frac{\ln P}{\ln \mathcal{B}} = -1 \quad (6.53)$$

Thus, the exponent of the differential energy spectrum in (6.47) is:

$$\alpha_S = -1 + \Lambda = -2 \quad (6.54)$$

This represents **one of the principal results of the diffusive shock acceleration mechanism**: it provides a **power law spectrum** whose index is within the range of the experimental measurements. The **power law index of exactly 2** arises for the case of a strong nonrelativistic shock in an ideal gas and with constant escape probability  $P_{\text{esc}}$ . Inefficient situations in the shock conditions increase the spectral index between 2.0 and 2.4, as obtained using more refined computations (Hörandel 2007). Harder spectral indexes (1.5–1.8) are obtained in models with shock-amplified magnetic fields, Sect. 6.5.

### 6.4.2 A Shock Front in a Mono-Atomic Gas<sup>3</sup>

We will use here **thermodynamical arguments** to derive the relations between the **velocity** and **density** of **up- and down-stream materials**, and in particular the **compression factor  $R$**  introduced in Sect. 6.2. These considerations are **valid in the reference frame in which the shock front is at rest** (see Fig. 6.5b). **Particles in the reference frame of an outside observer**, having **density  $\rho_1$  up-stream** of the shock, have velocities  **$v_1 \simeq 0$**  much smaller than the shock velocity  $v_s$  (Fig. 6.5a). The material **down-stream has density  $\rho_2$** . The **gas behind the discontinuity** moves at the **velocity  $v_2$**  which depends on the shock front velocity.

The conditions of a material subjected to a shock are described by the ideal fluid equations. The three basic equations are the **conservation of mass**, of **momentum**, and the **Poisson equation**:

$$\frac{\partial \rho}{\partial t} + \nabla \cdot (\rho \mathbf{v}) = 0 \quad (6.55a)$$

$$\rho \frac{\partial \mathbf{v}}{\partial t} + \rho \mathbf{v} \cdot (\nabla \mathbf{v}) = \mathbf{F} - \nabla P \quad (6.55b)$$

$$\Delta \Phi = 4\pi G \rho \quad (6.55c)$$

**The left side of (6.55b) is Euler's equation**, which measures the velocity change  **$d\mathbf{v}/dt$**  of a **fluid element**, including both the time variation at a fixed coordinate ( $\partial \mathbf{v}/\partial t$ ), and the change due to the movement of the fluid element. The right side of the same equation includes the external **force  $\mathbf{F}$**  and the force due to the **pressure gradient  $\nabla P$** .

<sup>3</sup> This section can be skipped in the early reading steps.

The Poisson equation (6.55c) connects the mass density  $\rho$  with the gravitational potential  $\Phi$ .  $G$  is the gravitational constant.

In addition to the conservation laws for mass (6.55a) and momentum (6.55b) we can consider also the conservation law for energy:

$$\frac{\partial}{\partial t} \left( \frac{\rho v^2}{2} + \rho U + \rho \Phi \right) + \nabla \cdot \left[ \rho \mathbf{v} \left( \frac{v^2}{2} + U + \frac{P}{\rho} + \Phi \right) \right] = 0 \quad (6.56)$$

In (6.56) the term in the first brackets accounts for the change of kinetic, internal  $U$  and potential  $\Phi$  energy with time; this variation has to be balanced by the energy flux through the boundary of the considered volume (the term in the second bracket).

We will consider now shock waves in a perfect gas. Sound waves propagate in most circumstances adiabatically, i.e. without production of entropy,  $dS = 0$ . We specialize the situation for a mono-atomic gas, as the case of most interstellar matter. A mono-atomic gas is characterized by the adiabatic index<sup>4</sup>  $\gamma = c_P/c_V = 5/3$ . The sound velocity is:

$$c_{\text{sound}} = \left( \frac{\gamma P}{\rho} \right)^{1/2} \quad (6.57)$$

where  $P$  and  $\rho$  are the gas pressure and density, respectively.

We need to derive relations between the average gas velocity and that of the shock front,  $v_s$ . The shock front represents an abrupt discontinuity between two regions of gas. In the undisturbed region ahead of the shock wave, the gas is at rest with pressure  $P_1$ , density  $\rho_1$  and temperature  $T_1$ , and the speed of sound is  $c_1$ . Behind the shock wave, the gas moves supersonically at a speed  $> c_1$  and its pressure, density and temperature are  $P_2$ ,  $\rho_2$  and  $T_2$ , respectively (Fig. 6.5a). It is convenient to transform to a reference frame moving at velocity  $v_s$  in which the shock wave is stationary (Fig. 6.5b). In this reference frame, the undisturbed gas flows towards the discontinuity at velocity  $v_1 = |v_s|$  and, when it passes through it, its velocity becomes  $v_2$  away from the discontinuity.

We will consider for simplicity only the properties of a one-dimensional, steady shock in its rest frame and assume that magnetic and gravitational fields can be neglected. Then the continuity equation for mass (6.55a) becomes simply

$$\frac{d}{dx}(\rho v) = 0. \quad (6.58)$$

The Euler equation simplifies using the same assumptions and taking into account (6.58) to

$$\frac{d}{dx}(P + \rho v^2) = 0. \quad (6.59)$$

<sup>4</sup> In this section, as usual in thermodynamics, the symbol  $\gamma$  always refers to the adiabatic index of gases.

Eq. (6.56) for a stationary flow (i.e. time independent) with no external potential ( $\Phi = 0$ ) gives:

$$\frac{d}{dx} \left( \frac{\rho v^3}{2} + (U + P)v \right) = 0. \quad (6.60)$$

We can now integrate these equations over the discontinuity of the shock front:

$$\left[ \rho v \right]_1^2 = \text{const.} \quad (6.61a)$$

This means that the product of density and speed in region 1 is equal to that in region 2. Analogously:

$$\left[ P + \rho v^2 \right]_1^2 = \text{const} \quad (6.61b)$$

$$\left[ \frac{\rho v^3}{2} + \frac{\gamma}{\gamma - 1} P v \right]_1^2 = \text{const} \quad (6.61c)$$

where in (6.61c) we used the relation between internal energy and pressure:  $U = P/(\gamma - 1)$ . Since we assume a steady flow, these boundary conditions have to be evaluated in the shock rest frame, (cf. Fig 6.5b). Otherwise, time-derivatives should be included.

Inserting first the condition obtained from (6.61a):  $\rho_2 = (v_1/v_2)\rho_1$  into (6.61b), we obtain  $P_2 = P_1 + \rho_1 v_1 (v_1 - v_2)$ . The two relations above are used to eliminate  $\rho_2$  and  $P_2$  from (6.61c). Reordering the resulting equation according to powers of  $v_2$ :

$$\left( \frac{\gamma + 1}{\gamma - 1} \right) v_2^2 - \frac{2\gamma}{\gamma - 1} \left( \frac{P_1 + \rho_1 v_1^2}{\rho_1 v_1} \right) v_2 + \left( v_1^2 + \frac{2\gamma}{\gamma - 1} \frac{P_1}{\rho_1} \right) = 0 \quad (6.62)$$

We can now use the fact that the pressure  $P_1$  is related with the sound velocity  $c_1$  by Eq. (6.57), and thus  $P_1 = \rho_1 c_1^2 / \gamma$ . We use this relation to replace  $P_1$  in (6.62) and we divide also by  $v_1^2$  to obtain the quadratic relation:

$$\left( \frac{\gamma + 1}{\gamma - 1} \right) x^2 - \frac{2\gamma}{\gamma - 1} \left( \frac{1}{\gamma} \frac{c_1^2}{v_1^2} + 1 \right) x + \left( 1 + \frac{2}{\gamma - 1} \frac{c_1^2}{v_1^2} \right) = 0 \quad (6.63)$$

where  $x = v_2/v_1$ . The ratio  $v_1/c_1$  is defined as the Mach number  $\mathcal{M}$ . Since we are interested in fast flows, and  $\mathbf{v}_1 = -\mathbf{v}_s$ , we have also that  $v_1 \gg c_1$  and we can neglect the two terms quadratic in  $c_1/v_1$ . We obtain:



$$\left(\frac{\gamma+1}{\gamma-1}\right)x^2 - \frac{2\gamma}{\gamma-1}x + 1 = 0 \quad (6.64)$$

It is easily verified that the two solutions are

$$x = 1 \quad \longrightarrow \quad v_1 = v_2, \quad (6.65a)$$

$$x = \frac{\gamma-1}{\gamma+1} \equiv \frac{1}{R} \quad \longrightarrow \quad Rv_2 = v_1. \quad (6.65b)$$

The first solution is trivial (no shock), while the second one is the strong shock solution. The compression ratio  $R$  indicates how the density, the velocity and pressure in the up- and down-stream regions differ in the shock front reference frame. Remembering that  $v_1 = |v_s|$ , and that for a mono-atomic gas  $\gamma = 5/3$  and thus  $R = 4$ , we can write:

$$v_2 = v_s/R = v_s/4, \quad (6.66a)$$

$$\rho_2 = R\rho_1 = 4\rho_1, \quad (6.66b)$$

$$P_2 = 3/4\rho_1v_2^2. \quad (6.66c)$$

As a consequence of this model, no matter how strong a shock is, it can compress a mono-atomic gas only by a factor of four, and the velocity of the down-stream material after the transit of the shock front is  $v_s/4$ .

The ratio of the up- and down-stream velocities is independent of the particle nature (charge, mass, ...) and valid for any strong shock in different astrophysical environments. This fact has the consequence that the same energy spectral index is obtained for any kind of accelerated particles.

## 6.5 Success and Limits of the Standard Model of Cosmic Ray Acceleration

The arguments presented in the previous sections on acceleration mechanisms have a number of key features which show why the diffusive shock acceleration is considered the most reliable among all those that try to explain the origin of galactic CRs [see Drury (2012) for a recent review]. First, it is very natural and depends only on rather robust and simple physics arguments. Second, it produces power-law spectra without any unnatural fine-tuning; the exponent of the power-law is fixed entirely by the compression ratio  $R = 4$  of the shock and the simple theory predicts a universal energy spectrum at relativistic energies of the form  $\Phi(E) \sim E^{-2}$ , close to what is inferred for the cosmic ray source spectra (Sect. 5.6). Third, it does not require a separate pre-acceleration phase to produce seed particles for further acceleration; the

process appears capable to accelerate particles directly from the thermal population up to the highest energies allowed by the “scale” of the shock.

The “scale” of the shock refers to a number of important constraints on the acceleration process which act to limit the maximum attainable energy. The first and simplest is that in any accelerator where particles are magnetically confined while being accelerated, the Larmor radius  $r_L$  of the particles has to be smaller than the size of the system. In the diffusive shock acceleration, this corresponds to the requirement that the diffusion length-scale of the particles is small compared to the shock radius. In addition there are limitations from the finite age of the system, as worked out in Sect. 6.2.2. If we take fairly standard values for a SNR shock, the maximum particle rigidity reach about  $10^{14}$  V. According to (6.34), higher efficiencies  $\eta$  could be attained. In this case, following Eq. (6.43), the maximum particle rigidity will be a factor of  $\sim 10$  higher than the above value.

In the region of direct measurements, all nuclei up to uranium have been detected in CRs in proportions that are generally close to what one would obtain from a well-mixed sample of the local Galaxy (Sect. 3.6). This observation rules out some exotic models for CR origin, such for instance the iron-nickel rich composition one would expect from a neutron star crust (this excludes some models based on thermoionic emission from pulsars).

In general, direct production exclusively in one particular subclass of supernova is ruled out. The CR composition, like the general composition of the Galaxy, requires the mixing of a variety of elements produced by stellar nucleosynthesis in different sites. There are however very interesting recent measurements (Sect. 3.7) which suggest that there are slight, but significant, differences between the proton and helium energy spectra, and that heavier nuclei behave like helium. More refined models should consider the slight energy dependence of the composition. One of the suggested explanations for the difference between the spectral index of proton and helium nuclei is that they could be accelerated from different types of sources or acceleration sites. For example, most protons might come predominantly from the supernova explosion of low mass stars directly into the interstellar medium. Helium and heavier nuclei might come mainly from the explosion of more massive stars into the atmosphere swept out by the progenitor star rather than directly into the general interstellar medium (Biermann et al. 2010). Another reason could be the randomness in the spatial and temporal distribution of SNRs (Blasi and Amato 2012).

In addition to those induced by the fragmentation during propagation, there are other significant differences in the chemical composition of CRs and of the cosmic abundances. Some significant differences from Solar System abundances have been reported for elements heavier than Fe by the CRIS experiment as well as from the Trans-Iron Galactic Element Recorder (TIGER) balloon instrument (Rauch et al. 2009), see Table 3.3. These observations add support to the concept that the bulk of CR acceleration takes place in supernovae. Some of the parent stars of the supernova (see Sect. 12.12) are massive Wolf-Rayet stars, which form in loosely organized groups called *OB associations*. The abundances observed are consistent with a CR source mixture of about 20% ejecta of massive stars mixed with 80% material of solar system composition. According to some authors, the enhancements of these

elements appear to correlate with their first ionization potential (FIP).<sup>5</sup> Since a similar effect is known to operate on high-energy particles originated in the Sun, this effect on CRs was long interpreted as a FIP-based bias. However no satisfactory physical model for the FIP-effect exists for cosmic rays up to now and thus the result should be seen as an empirical correlation (Webber 1997).

Alternative models to that presented in Sect. 6.3 concerning the origin of the knee exist. More recent estimates (Hörandel 2007) give a maximum energy up to one order of magnitude larger than obtained in the previous section for some types of supernovae (Berezhko 1996; Kobayakawa et al. 2002; Sveshnikova et al. 2003). The effective field strength at the shock may in fact be substantially larger than the standard values, and in this way particles in galactic shocks can be accelerated up to substantially higher energies [models with a *shock-amplified magnetic field* (Drury 2012)]. Also the exponent of the differential energy spectrum could be significantly smaller than the value in (6.54), as for instance  $\alpha_S = 1.5$  or  $1.8$ . At an early stage of the SNR when the power of shocks is maximum and there is still significant field amplification, the maximum particle rigidity may extend up to  $10^{17}$  eV. These shocks are however unable to tap the full power of the explosion because the ejecta have only interacted with a small amount of matter surrounding the star. As the shocks continue to expand and slow down, the maximum rigidity drops as the field amplification becomes less and less effective. On this picture the steepening of the all-particle energy spectrum at the knee is due to the relative lack of power in the very fast early shocks responsible for the highest energy particles combined with the decrease in abundance as one moves to heavier elements.

Cosmic rays of energies well above the knee have in any case been observed. The onset of extragalactic sources is expected at energies above the ankle. Thus, in addition or in alternative to the models characterized by a shock-amplified magnetic field, some models with additional galactic sources should provide CRs between the knee and the ankle. In the next section, we describe some possible galactic candidates.

## 6.6 White Dwarfs and Neutron Stars

In order to overcome the rigidity-dependent limit (6.43) the possibility has been proposed that, under particular conditions, cosmic rays suffer additional acceleration by variable magnetic fields in the acceleration region. According to this mechanism, a neutron star (the remnant of the final stages of a massive star) or a powerful binary systems can accelerate CRs up to a maximum energy of  $10^{19}$  eV.

We start with the description of *white dwarfs* (although they are not involved in cosmic ray acceleration) as most of the physics needed to describe neutron stars can more easily be understood. Stars with mass a few times that of our Sun will, at the

---

<sup>5</sup> The first ionization energy is the amount of energy it takes to detach one electron from a neutral atom.

end of their life, become white dwarfs. A small fraction of stars in our Galaxy (only  $\sim 3\%$ ) are massive enough to become neutron stars.

### 6.6.1 White Dwarfs

A white dwarf is a small star made of electron-degenerate matter in which the gravitational pressure is counterbalanced by the pressure due to the electron degeneracy. The material in a white dwarf no longer undergoes fusion reactions, so the star has no source of energy, nor is it supported by the heat generated by fusion against gravitational collapse.

Let us evaluate the gravitational potential energy of a sphere having mass  $M$  and radius  $R$ . For our calculation it is enough to remind that the gravitational potential energy of a system consisting of a sphere having radius  $r < R$  and a thin spherical layer surrounding it, having thickness  $dr$ , both of density  $\rho$ , is given by  $dU_{\text{grav}} = G_N \rho^2 \frac{16}{3} \pi^2 r^4 dr$ . Integrating this expression over  $r$ , between  $r = 0$  and  $r = R$ , we obtain:

$$|U_{\text{grav}}| = \frac{3}{5} \frac{G_N}{R} M^2. \quad (6.67)$$

During the permanence of a star in the *main sequence*, thermonuclear reactions provide energy against the gravitational collapse. A white dwarf is supported only by electron degeneracy pressure, causing it to be extremely dense.

The Pauli exclusion principle disallows fermions from occupying the same quantum state. If one has a potential well (such as the one that in first approximation holds particles to form the star), fermions start filling up the quantum levels. The highest energy level filled by nuclei or electrons is called the *Fermi energy*. Degenerate states occur when the Fermi energy is larger than the typical thermal energy.

Let us consider first the case in which the degeneracy in a star is due to the atomic electrons. The degeneracy energy can be estimated using Heisenberg's uncertainty principle

$$\Delta x \cdot \Delta p \sim d \cdot p \sim \hbar.$$

If the number density is  $n$  [ $\text{cm}^{-3}$ ], then each fermion is essentially confined to a cube of size  $d^3 \sim 1/n$ . This implies that the momentum of an electron is  $p \sim \hbar/d \sim \hbar n^{1/3}$ . The energy of an electron is therefore:

$$E \sim \frac{p^2}{2m_e} \sim \frac{\hbar^2 n^{2/3}}{2m_e} \quad \text{in the nonrelativistic case} \quad (6.68a)$$

$$E \sim pc \sim \hbar n^{1/3} c \quad \text{in the relativistic case.} \quad (6.68b)$$

If the collapsing star has  $N_e$  electrons, the total degeneracy energy of the star is  $E_{\text{deg}} = EN_e$ .

Let us consider only the relativistic case (6.68b). This limit is reached when the relative distance  $\Delta x = d$  between electrons decreases and the energy increases up to the value  $pc = m_e c^2$ . Thus, from Heisenberg's principle, one can write:

$$d(pc) \sim \hbar c \quad \rightarrow \quad d \sim \frac{\hbar}{m_e c}$$

$$\rho_{ec} = \frac{\mu}{d^3} = \frac{\mu}{(\hbar/m_e c)^3} \sim 3 \times 10^{13} \text{ g cm}^{-3} \quad (6.69)$$

where  $\rho_{ec}$  is the critical density of matter for degenerate atomic electrons, and  $\mu = m_p + m_e$ . When the density  $\rho$  of the collapsing star is below  $\rho_{ec}$ , we are below the relativistic limit, and (6.68a) holds.

The total number of electrons in a star with mass  $M_*$  and radius  $R_*$  is

$$N_e = M_* Z / A \mu = M_* \eta / \mu \quad (6.70)$$

where  $A$  is the atomic mass,  $Z$  the number of electrons per atom and  $\eta = Z/A$ . The total degeneracy energy of the star in the relativistic case (when the density reaches  $\rho_{ec}$ ) is obtained using (6.68b):

$$E_{\text{deg}} = EN_e = \hbar n^{1/3} c N_e \sim \frac{\hbar c M_*^{4/3} \eta^{4/3}}{R_* m_p^{4/3}} \quad (6.71)$$

having used  $n = N_e / V \sim N_e / R_*^3$ .

Finally, we can use energy equipartition to estimate the equilibrium. This is done assuming that the gravitational binding energy  $|U|$  (6.67) is of the order of the degeneracy energy. Hence:

$$E_{\text{deg}} \sim |U_{\text{grav}}| \quad \rightarrow \quad \frac{\hbar c M_*^{4/3} \eta^{4/3}}{R_* m_p^{4/3}} \sim \frac{3}{5} \frac{G_N M_*^2}{R_*} \quad (6.72)$$

Note that *the radius of the star cancels out!* As the mass  $M_*$  increases, the radius decreases and once white dwarfs become compact enough for the electrons to be relativistic, there is a solution with only one mass (which we indicate as the Chandrasekhar mass limit), irrespective of the radius.<sup>6</sup>

The final (universal) value of the mass from (6.72) is (neglecting the 3/5 factor as we done for the factor  $4\pi/3$  in the expression of the volume):

<sup>6</sup> We leave for the student to work out the radius-mass relation for the nonrelativistic case. When the density in a white dwarf is below  $\rho_{ec}$ , as its mass increases, its radius becomes smaller and smaller, scaling as  $M_*^{-1/3}$ . As the white dwarf approaches the mass limit  $M_{\text{Ch}}$ , the electrons become relativistic, and the dependence on mass becomes sharper than  $-1/3$  as  $M_* \rightarrow M_{\text{Ch}}$ .

$$M_* \sim \left( \frac{\hbar c \eta^{4/3}}{G_N \mu^{4/3}} \right)^{3/2} = \left( \frac{\hbar c \eta^{4/3}}{G_N \mu^2} \right)^{3/2} \mu. \tag{6.73}$$

In the last equality, as  $M_*$  and  $\mu$  have the same dimension (mass), the quantity in the bracket is adimensional. If we consider hydrogen,  $\mu \sim m_p$  and  $\eta = 1$ . The term  $\left( \frac{\hbar c}{G_N m_p^2} \right)$  (Braubant et al. 2011) corresponds to the inverse of the gravitational coupling constant,  $\alpha_G$ . Thus, Eq. (6.73) can be written as:

$$M_{Ch} \sim \frac{m_p}{\alpha_G^{3/2}} = \frac{1.6 \times 10^{-24} \text{ g}}{(5.9 \times 10^{-39})^{3/2}} = 3.5 \times 10^{33} \text{ g} = 1.4 M_\odot. \tag{6.74}$$

Eq. (6.73) shows that  $\hbar$  appears in the Chandrasekhar mass limit  $M_{Ch}$ ; the Planck constant not only determines the interaction of elementary particles, but also the mass scale and the inner structure of stars. The evolution and structure of cosmic objects is determined by known physics laws and by the values of fundamental constants.

The typical radius of a white dwarf can be worked out from the ratio between the mass  $M_{Ch}$  and its density  $\rho_{ec}$ . Note that in (6.69), the quantity  $\hbar/m_e c$  corresponds to the electron Compton wavelength  $\lambda_e = 3.8 \times 10^{-13} \text{ m}$ , and  $\rho_{ec} = m_p/\lambda_e^3$ . Thus, one can write:

$$R_{WD} \sim \left( \frac{M_{Ch}}{\rho_{ec}} \right)^{1/3} = \left( \frac{m_p \lambda_e^3}{\alpha_G^{3/2} m_p} \right)^{1/3} = \frac{\lambda_e}{\alpha_G^{1/2}} = \frac{3.8 \times 10^{-13}}{(5.9 \times 10^{-39})^{1/2}} \simeq 5 \times 10^6 \text{ m}. \tag{6.75}$$

The radius of a white dwarf is a few thousand kilometers, and depends on the electron Compton wavelength.

### 6.6.2 Neutron Stars and Pulsars

A neutron star is a type of stellar remnant that can result from the gravitational collapse of a massive star ( $M > 8 M_\odot$ ). As the core of a massive star is compressed during a supernova event, increases in the electron Fermi energy allow the reaction (with threshold 1.36 MeV):



The weak interacting neutrinos escape, the matter cools down, the density increases and nuclei in the center of the star become neutron-enriched. At some point, the nuclei break into their components and enough neutrons are created so that they become degenerate. The neutron degeneracy pressure immediately stops the collapse and an equilibrium state is established. The transition from collapse to equilibrium is very sudden, and the infalling material experiences a bounce against the degenerate core.

which creates an outward-propagating shock wave (the *supernova*). The shock wave is further boosted by the neutrino pressure from the core (Herant et al. 1997), as more extensively described in Sect. 12.11.

From the mathematical point of view, the description of the equilibrium state in a neutron star is similar to that provided above in the case of the white dwarf. The degenerated fermions are now the neutrons, and the critical density is obtained from (6.69) with the exchange  $m_e \rightarrow m_n \sim \mu$ , where  $m_n$  is the neutron mass. Thus, neutrons become relativistic when the density reaches the value:

$$\rho_{nC} = \frac{m_n}{(\hbar/m_n c)^3} = \frac{m_n}{\lambda_n^3} \sim 10^{17} \text{ g cm}^{-3}. \quad (6.76)$$

The total degeneracy energy has the same value as that given in Eq. (6.71)! The only change is the replacement of the number of electrons  $N_e = M_* \eta / \mu$  with the number of neutrons:  $N_n = M_* / m_n$ , which corresponds to  $\eta = 1$ . In this condition, the same equality (6.72) between the degeneracy energy and binding energy  $|U_{\text{grav}}|$  holds, and the mass limit for a neutron star assumes the same value of the Chandrasekhar mass limit (6.74). The upper limit for a neutron star mass is the same as that of a white dwarf. As  $\rho_{nC} \sim 10^3 \rho_{eC}$  the neutron star radius is much smaller than  $R_{\text{WD}}$  and from (6.75):

$$R_{\text{NS}} \sim \left( \frac{M_{\text{Ch}}}{\rho_{nC}} \right)^{1/3} = \left( \frac{m_p \lambda_n^3}{\alpha_G^{3/2} m_p} \right)^{1/3} = \frac{\lambda_n}{\alpha_G^{1/2}} = \frac{2.1 \times 10^{-16}}{(5.9 \times 10^{-39})^{1/2}} = 3 \times 10^3 \text{ m}. \quad (6.77)$$

The radius of a neutron star, an object with a mass  $M_{\text{NS}} \sim 1.4 M_{\odot}$ , is  $\sim$  few km.

A *pulsar* is a rotating neutron star that emits a beam of electromagnetic radiation, typically in directions along its magnetic axis. The radiation can only be observed when the emitted radiation is pointing towards the Earth. The rotation period and thus the interval between observed pulses is very regular, and the periods of their pulses range from 1.4 milliseconds to 8.5 s. This rotation slows down over time as electromagnetic radiation is emitted.

The millisecond rotating period for young pulsars can be estimated using basic physics arguments. A star like our Sun has a radius  $R \sim 7 \times 10^5 \text{ km}$  and rotates at 1 revolution per 30 days, so that the angular velocity is  $\omega \sim 2.5 \times 10^{-6} \text{ rad/s}$ . After the collapse, the neutron star has a radius  $R_{\text{NS}} \sim 10 \text{ km}$ . From angular momentum conservation, one can write:

$$MR^2 \omega = M R_{\text{NS}}^2 \omega_{\text{NS}} \\ \omega_{\text{NS}} = \left( \frac{R}{R_{\text{NS}}} \right)^2 \times \omega = \left( \frac{7 \times 10^5}{10} \right)^2 \times 2.5 \times 10^{-6} = 12,500 \text{ rad/s} \quad (6.78)$$

so that  $T_{\text{NS}} = \frac{2\pi}{\omega_{\text{NS}}} = 0.5 \times 10^{-3} \text{ s}$ .

The gravitational collapse amplifies the stellar magnetic field. As a result, the magnetic field  $B_{NS}$  near the NS surface is extremely high. To obtain an estimate of its magnitude, let us use the *conservation of the magnetic flux* during the *contraction*:

$$\oint \mathbf{B}_{star} \cdot d\mathbf{A}_{star} = \oint \mathbf{B}_{NS} \cdot d\mathbf{A}_{NS} \tag{6.79}$$

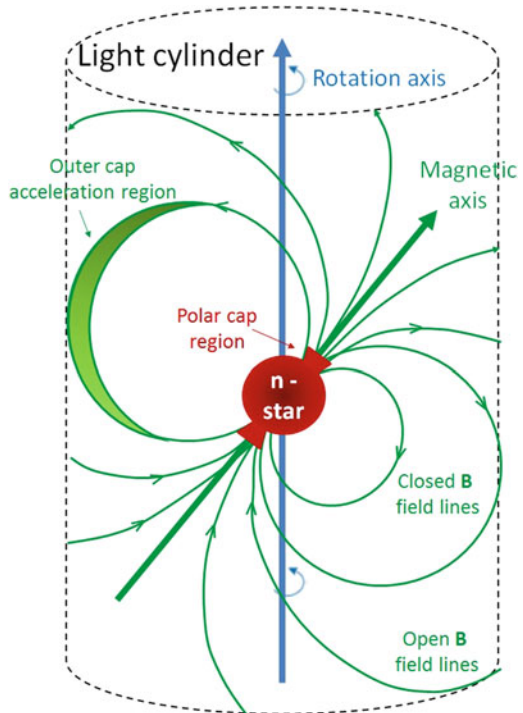
and, assuming the magnetic field constant and the elements of surface  $\mathbf{A}_{NS}$ ,  $\mathbf{A}_{star}$  that of two spheres of radius  $R_{NS}$  and  $R$  respectively, we obtain

$$4\pi B_{star} R^2 = 4\pi B_{NS} R_{NS}^2 \quad \rightarrow \quad B_{NS} = B_{star} \frac{R^2}{R_{NS}^2} \tag{6.80}$$

For typical values  $B_{star} = 1,000$  Gauss the magnetic fields on the NS surface becomes of the order of  $\sim 10^{12}$  Gauss. This expectation has been experimentally confirmed by measuring quantized energy levels of free electrons in pulsar strong magnetic fields.

Pulsars were discovered in the radio band by Hewish and Bell in 1967 and soon identified with isolated, rotating, magnetized neutron stars (Fig. 6.8). The key observations were the very stable, short periods of the pulses and the observation of

**Fig. 6.8** A schematic model of a pulsar as a magnetized rotating neutron star in which the magnetic and rotation axes are misaligned. The radio pulses are assumed to be due to beams of radio emission from the poles of the magnetic field distribution





polarized radio emission. The figure shows the details of the rotating magnetosphere inside the light cylinder centered on the pulsar and aligned with the rotation axis. The radius of the cylinder corresponds to the distance at which the co-rotating speed equals the speed of light.

The pulse periods of pulsars  $P$  as well as the rate at which the pulse period changes with time,  $dP/dt$ , can be measured with very high accuracy. Normal radio pulsars are slowing down and  $dP/dt$  is proportional to the rate of loss of rotational energy mainly due to magnetic braking. If the rotational energy of the pulsar is  $E_{\text{rot}} = I\omega_{\text{NS}}^2$ , where  $I \propto MR_{\text{NS}}^2$  is the inertial momentum, the rotational energy loss is

$$-\frac{dE_{\text{rot}}}{dt} = 2I\omega_{\text{NS}} \frac{d\omega_{\text{NS}}}{dt} = 8\pi^2 I \frac{dP/dt}{P^3} \quad (6.81)$$

The typical lifetime for normal pulsars can be estimated as

$$\tau_P = \frac{P}{2(dP/dt)} \quad (6.82)$$

and typical values are  $\tau_P \sim 10^5 - 10^8$  years.

The pulsar loses energy by electromagnetic radiation, which is extracted from the rotational energy of the neutron star. The pulsed radiation observed at a large distance is due to the fact that the pulsar magnetic dipole is oriented at an angle with respect to the rotation axis. The detected beamed radiation is associated with the beam sweeping the line of sight to the observer.

Pulsars are known to emit radiation at all wavelengths (Lorimer and Kramer 2005). Because the neutron star is a spinning magnetic dipole, it acts as a unipolar generator, where charged particles are subject to the total Lorentz force  $\mathbf{F} = q(\mathbf{E} + \frac{1}{c} \mathbf{v} \times \mathbf{B})$ . Electric charges in the magnetic equatorial region redistribute themselves by moving along closed field lines until they build up an electrostatic field large enough to cancel the magnetic force and give  $\mathbf{F} = 0$  in the so-called vacuum gaps regions. This induced high voltages where electrons and protons can be accelerated up to very high energies, Sect. 6.7. Vacuum regions occur (Fig. 6.8) at the polar cap, very close to the neutron star surface, in a thin layer along the boundary of the closed magnetosphere (slot gap), and in the outer region close to the light cylinder (outer gap).

If the co-rotating field lines emerging from the vacuum gaps cross the light cylinder, these field lines cannot close. Charged particles in the polar cap are magnetically accelerated to very high energies along the open but curved field lines (Aliu et al. 2008). The acceleration resulting from the curvature causes them to emit synchrotron radiation that is strongly polarized in the plane of curvature. Photons can reach energies up to the TeV region by the mechanisms described in (Sect. 9.4).

## 6.7 Possible Galactic Sources of Cosmic Rays Above the Knee

Let us use dimensional arguments to obtain the **maximum attainable energy** of a particle near an astrophysical object with a strong, rotating magnetic field. Small decreases of the energy associated with the magnetic field power the detected emission of high-energy electromagnetic radiation, particularly X-rays and  $\gamma$ -rays.

Let us start with some energy considerations for the cosmic ray spectrum **starting from energies around the knee,  $E_0 \sim 10^{14}$  eV = 100 TeV** and below the ankle, repeating those discussed in Sect. 2.11 for the energy region below the knee. Because of the steeply falling primary CR spectrum, the **power** needed to maintain a stationary presence of CRs above  $E_0$  in our galaxy

$$P(> E_0) = \frac{\rho_{\text{CR}}(> E_0) \cdot V_G}{\tau_{\text{esc}}(> E_0)} \quad (6.83)$$

is much smaller than the total power requirement (2.39). Here,  $\rho_{\text{CR}}(> E_0)$  is the energy density of CRs of energy above  $E_0$ .

The quantity  $\rho_{\text{CR}}(> E_0)$  is determined from the indirect measurement of the CR spectrum, using the integral spectrum above  $10^{16}$  eV given by Eq. (4.53). The **number density** is as usual given by  $(4\pi/c)\Phi(>E)$  and the **energy density** as  $(4\pi/c) \int \Phi(>E)dE$ . Note that at 100 TeV the number density is about 10 order of magnitudes smaller than (2.32a) for the whole range of energies above 3 GeV.

The value of the **escape time  $\tau_{\text{esc}}(> E_0)$**  in (6.83) **is much more difficult to estimate.** We follow the arguments discussed in (Gaisser 1991). Simple extrapolations of the escape time obtained using the direct measurements reported in Sect. 5.5 are not valid, as the direct measurements reach  $\sim 1$  TeV only. The simple  $E^{-0.6}$  power-law does not fit well the data in the high energy tail (Fig. 5.4). For instance, extrapolating this dependence of  $\tau_{\text{esc}}$  up to 100 TeV we would obtain  $\tau_{\text{esc}}(> 100 \text{ TeV}) \sim 1000$  y. With such a small value, we expect a huge migration of  $> 100$  TeV cosmic rays out of the galactic disk. This will correspond to a large anisotropy of these CRs: the number of particles arriving from the galactic plane should be much larger than of those arriving from outside the galactic plane. Such a strong anisotropy has not been observed by experiments, Sect. 5.7.

To obtain an order of magnitude estimate, from (5.47) and (5.49) we have

$$\tau \simeq T = \frac{L}{\bar{v}} = \frac{L}{\delta c / (\alpha + 2)} \simeq 10^6 \text{ year} \quad (6.84)$$

having used  $\delta \simeq 10^{-3}$  for  $E_0 = 10^{15} \text{ eV} = 10^3 \text{ TeV} = 1 \text{ PeV}$  (below the upper limit in Fig. 5.5) and for the **galactic half thickness  $L \simeq 100 \text{ pc} = 0.3 \times 10^{21} \text{ cm}$** . The following estimates of the escape times as a function of the threshold energy  $E_0$

$$\tau \simeq 2.5 \times 10^5 \cdot \left( \frac{E}{1 \text{ TeV}} \right)^{-0.13} \text{ year} \quad \text{for } 1 < E < 5 \times 10^3 \text{ TeV} \quad (6.85a)$$

$$\sim 0.8 \times 10^5 \cdot \left( \frac{E}{5 \text{ PeV}} \right)^{-0.53} \text{ year} \quad \text{for } E > 5 \text{ PeV} \quad (6.85b)$$

can be found in Gaisser (1991). Using now (4.52) and (6.85) in (6.83), with the galactic volume ( $V_G \sim 6 \times 10^{66} \text{ cm}^3$ ), we obtain:

$$P(> E_0) \simeq 2 \times 10^{39} \text{ erg/s for } E > 100 \text{ TeV}, \quad (6.86a)$$

$$\simeq 2 \times 10^{38} \text{ erg/s for } E > 1 \text{ PeV}, \quad (6.86b)$$

$$\simeq 5 \times 10^{37} \text{ erg/s for } E > 10 \text{ PeV}. \quad (6.86c)$$

The power needed to accelerate CRs above the knee is three orders of magnitude smaller than that required for the whole CR spectrum. Even one or two galactic powerful point sources could be important. Do sources exist in the Galaxy which can deliver such a quantity of energy per second?

### 6.7.1 A Simple Model Involving Pulsars

The rotation axis of pulsars usually does not coincide with the direction of the magnetic field. As an effect, the vector of these high magnetic fields spinning around the nonaligned axis of rotation will produce strong electric fields  $\mathcal{E}$  through Faraday's law (6.1). This may in turn accelerate particles. From dimensional arguments, if  $L \sim R_{\text{NS}}$  is the length of the region over which the magnetic field changes:

$$\frac{\mathcal{E}}{L} = \frac{1}{c} \frac{dB}{dt}, \quad (6.87)$$

the maximum energy  $E_{\text{max}}$  gained from a particle over the length  $L \sim R_{\text{NS}}$  is:

$$E^{\text{max}} = \int Ze\mathcal{E}dx = \int Ze \frac{L}{c} \frac{dB}{dt} dx = \int Ze \frac{L}{c} dB \frac{dx}{dt} = Ze R_{\text{NS}} B \frac{\omega_{\text{NS}} R_{\text{NS}}}{c} \quad (6.88)$$

where  $\omega_{\text{NS}}$  is the pulsar angular velocity.

As derived from the conservation of the flux of the magnetic field (6.80),  $B_{\text{NS}} \sim 10^{11} - 10^{12}$  Gauss on the surface of a neutron star. By inserting the numerical values in (6.88), for protons near a neutron star ( $R_{\text{NS}} = 10 \text{ km}$ ), one obtains (c.g.s. units):

$$\begin{aligned} E^{\text{max}} &= Ze R_{\text{NS}} B \frac{\omega_{\text{NS}} R_{\text{NS}}}{c} = 4.8 \times 10^{-10} [\text{statC}] \times 10^6 [\text{cm}] \times 10^{11} [\text{Gauss}] \times 0.1 \\ &\simeq 5 \times 10^6 \text{ erg} \simeq 3 \times 10^{18} \text{ eV} \end{aligned}$$

where the conversion factor  $1 \text{ eV} = 1.6 \times 10^{-12} \text{ erg}$  has been used in the last equality. For the angular velocity, we used the value  $\omega_{\text{NS}} \simeq 60\pi \text{ s}^{-1}$  which holds for the Crab

**Nebula**, Sect. 9.5. In this case,  $\frac{\omega_{\text{NS}} R_{\text{NS}}}{c} \simeq 0.1$ . Thus, some galactic accelerators could explain the presence of cosmic rays with energies up to few  $10^{18}$  eV. The validity of Eq. (6.88) will be made more general in Sect. 7.4.

**Pulsars** possess a **rotational energy** of about:

$$E_{\text{rot}} = \frac{1}{2} I \omega_{\text{NS}}^2 = \frac{1}{5} M_{\text{NS}} R_{\text{NS}}^2 \omega_{\text{NS}} \sim 10^{61 \div 62} \text{ eV}$$

using the values given above for  $M_{\text{NS}}$ ,  $R_{\text{NS}}$ ,  $\omega_{\text{NS}}$ . A very small fraction of this energy is sufficient to maintain the CR flux above  $E_0$  from just one single object in the Galaxy (Berezinsky et al. 1990). However, the theoretical details of the mechanism that should work inside a pulsar, allowing to transform a small fraction of its rotational and magnetic field energy into particle acceleration, is not known.

### 6.7.2 A Simple Model Involving Binary Systems

**Binary systems** are **very often found** in astrophysical environments. As candidate sites of CRs acceleration, we are interested in particular binary systems consisting of a **compact object** (a pulsar, a neutron star or a black hole) **and a normal star**. Sources of electromagnetic radiation (electrons) and probably also **high energy hadrons** are **produced** by **matter falling** from one component, called the **donor** (usually a relatively normal star) to the other compact component, called the “**accretor**”. The infalling matter releases gravitational potential energy. Due to these enormous motions of ionized matter, **very strong electromagnetic fields are produced** in the **vicinity of the compact object**, and charged particles can be accelerated to high energies.

A particular class of binary systems are the **microquasars**. Microquasars are **galactic X-ray binary systems**, which exhibit **relativistic radio jets**, observed in the radio band. The name is due to the fact that they result morphologically similar to the AGN, Sect. 9.9, since the presence of jets makes them **similar to small quasars** (Fig. 6.9). In **quasars**, the **accretion object** is a **supermassive** (millions of solar masses) **black hole**; in **microquasars**, the mass of the **compact object** is only a **few solar masses**. This resemblance could be more than morphological: the **physical processes** that govern the formation of the accretion disk and the plasma ejection in microquasars **are probably the same** ones as in large AGN. Microquasars have been proposed as galactic acceleration sites of charged particles up to  $E \sim 10^{16 \div 18}$  eV. This hypothesis was strengthened by the discovery of the presence of relativistic nuclei in microquasars jets like those of SS 433. This was inferred from the observation of iron X-ray lines. A part of the radio emission comes from relativistic jets, often showing apparent superluminal motion. Two microquasars, LS I +61 303 and LS 5039, have been detected as  $\gamma$ -ray sources above 100 MeV.

Also in the case of binary systems, we can work out the **maximum energy** gain by using dimensional arguments. The rotating magnetic field of the neutron star which is perpendicular to the accretion disk will produce a **strong electric field**  $\mathcal{E} = (\mathbf{v} \times \mathbf{B})/c$ .

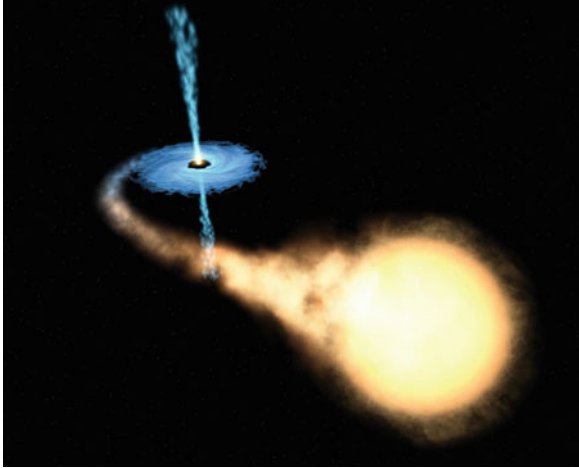


**Fig. 6.9** Artist’s impression of the microquasar GRO J1655-40. This microquasar (in blue) is the second discovered in our Galaxy. Microquasars are *black holes* of about the same mass as a star. They behave as scaled-down versions of much more massive *black holes* that are at the cores of extremely active galaxies, called *quasar*. Different microquasars have been found with masses ranging from 3.5 to approximately 15 times the mass of our sun. The companion star had apparently survived the original supernova explosion that created the *black hole*. Credits: NASA/ESA

A particle with charge  $e$ , moving with velocity  $\mathbf{v}$  in the accretion disk plane, will gain energy during the infall towards the compact object. The energy  $E$  will be:

$$E = \int e\mathcal{E} \cdot ds \simeq evB\Delta s \tag{6.89}$$

Under plausible assumptions ( $v \simeq c, B = 10^{10}$  Gauss,  $\Delta s = 10^7$  cm) particle energies up to  $10^{19}$  eV are possible. Due to the similarity between microquasars and quasars, we expect larger energies from the accretion disks which form around black holes or the compact nuclei of active galaxies.

## References

E. Aliu et al., Observation of pulsed gamma-rays above 25 GeV from the crab pulsar with MAGIC. *Science* **322**, 1221 (2008)  
 W.I. Axford, E. Leer, G. Skadron. The acceleration of cosmic rays by shock waves, in *Proceedings of the 15th International Cosmic Ray Conference*, vol 11 (1977) pp. 132–135  
 A.R. Bell, The acceleration of cosmic rays in shock fronts. *Mon. Not. R. Astron. Soc.* **182**, 147–156 (1978)  
 E. Berezhko, Maximum energy of cosmic rays accelerated by supernova shocks. *Astropart. Phys.* **5**, 367–378 (1996)  
 V.S. Berezhinsky et al., *Astrophysics of Cosmic Rays* (North Holland, Amsterdam, 1990)

- P.L. Biermann et al., The origin of cosmic rays: explosions of massive stars with magnetic winds and their supernova mechanism. *Astrophys. J.* **725**, 184–187 (2010)
- R.D. Blandford, J.P. Ostriker, Particle acceleration by astrophysical shocks. *Astrophys. J.* **221**, L29–L32 (1978)
- P. Blasi, E. Amato, Diffusive propagation of CRs from supernova remnants in the galaxy. I: spectrum and chemical composition. *J. Cosmol. Astropart. Phys.* **01**, 010 (2012)
- S. Braibant, G. Giacomelli, M. Spurio, *Particle and fundamental interactions*. Springer (2011). ISBN 978-9400724631
- F.F. Chen, *Introduction to Plasma Physics and Controlled Fusion*. Springer (1984) ISBN: 978-1-4419-3201-3
- L.C. Drury, Origin of cosmic rays. *Astropart. Phys.* **39–40**, 52–60 (2012)
- L.C. Drury, An introduction to the theory of diffusive shock acceleration of energetic particles in tenuous plasmas. *Rep. Prog. Phys.* **46**, 973–1027 (1983)
- E. Fermi, On the origin of the cosmic radiation. *Phys. Rev.* **75**, 1169–1174 (1949)
- E. Fermi, Galactic magnetic fields and the origin of cosmic radiation. *Astrophys. J.* **119**, 1–6 (1954)
- T.K. Gaisser, *Cosmic Rays and Particle Physics* (Cambridge University Press, Cambridge, 1991)
- M. Herant, S.A. Colgate, W. Benz, C. Fryer. Neutrinos and Supernovae. Los Alamos Science, No. 25 1997. <http://la-science.lanl.gov/lascience25.shtml>
- A.M. Hillas, Can diffusive shock acceleration in supernova remnants account for high-energy galactic cosmic rays? *J. Phys. G: Nucl. Part. Phys.* **31**, 39 (2005)
- J. Hörandel, Cosmic rays from the knee to the second knee:  $10^{14}$  to  $10^{18}$  eV. *Modern Phys. Lett. A* **22**, 1533–1552 (2007)
- J.R. Jokipii, Rate of energy gain and maximum energy in diffusive shock acceleration. *Astrophys. J.* **313**, 842–846 (1987)
- F.C. Jones, D.C. Ellison, The plasma physics of shock acceleration. *Space Sci. Rev.* **58**, 259 (1991)
- K. Kobayakawa et al., Acceleration by oblique shocks at supernova remnants and cosmic ray spectra around the knee region. *Phys. Rev. D* **66**, 083004 (2002)
- G.F. Krymsky, A regular mechanism for the acceleration of charged particles on the front of a shock wave. *Dokl. Akad. Nauk SSSR* **234**, 1306–1308 (1977)
- M.S. Longair, *High Energy Astrophysics*, 3rd edn. (Cambridge University Press, Cambridge, 2011). ISBN 978-0521756181
- D.R. Lorimer, M. Kramer, *Handbook of Pulsar Astronomy*. Cambridge University Press, 2005. ISBN: 978-0521828239
- B.F. Rauch et al., Cosmic ray origin in OB associations and preferential acceleration of refractory elements: evidence from abundances of elements  $^{26}\text{Fe}$  through  $^{34}\text{Se}$ . *Astrophys. J.* **697**, 2083–2088 (2009)
- L. Sveshnikova et al., The knee in galactic cosmic ray spectrum and variety in supernovae. *Astron. & Astroph.* **409**, 799–808 (2003)
- W.R. Webber, New experimental data and what it tells us about the sources and acceleration of cosmic rays. *Space Sci. Rev.* **81**, 107 (1997)

# Chapter 7

## Ultra High Energy Cosmic Rays

In the previous chapters we derived that through the diffusive shock acceleration model about 10 % of the energy emitted by galactic supernova explosions can provide the power needed to account for the observed CRs up to  $\sim 10^{15}$ – $10^{16}$  eV. Under particular conditions, already accelerated particles could gain additional energy through very high electric fields generated by rapidly rotating compact magnetized objects, such as young neutron stars. This represents a possible mechanism for the production of CRs up to the ankle.

CRs with energies above  $10^{18}$  eV will be denoted as Ultra High Energy Cosmic Rays (UHECRs). Their Larmor radius is so large—in particular for proton primaries—that their arrival direction could correlate with the position of the source, if their origin is galactic. As UHECRs are likely produced in extragalactic objects, in Sects. 7.1 and 7.2 we extend our field of view outside our Galaxy. An additional reason for this hypothesis is that no class of galactic sources seems to be energetic enough for the production of particles at energies above few  $10^{19}$  eV. Moreover, the non-observation of anisotropies even at the highest energies strengthens the extragalactic origin conjecture (Sect. 7.4). The interactions of UHECRs with the cosmic microwave background (CMB) radiation during their propagation and the effect of the extragalactic magnetic fields are discussed in Sect. 7.5.

The detection of UHECRs is based on the use of the Earth's atmosphere as a target (Sect. 7.6). Arrays of particle detectors at ground level reconstruct the energy, direction, and some parameters related to their nuclear mass by observing the density and pattern of the showers (Sect. 7.7). Arrays of optical telescopes detect the longitudinal development of the showers by observing the so-called fluorescence emission from atmospheric nitrogen, deriving an essentially calorimetric measurement of the energy and the longitudinal profiles.

The current generation of UHECR detectors, the Pierre Auger Observatory in Argentina and the Telescope Array experiment in Utah (Sect. 7.8) are hybrids, with both surface detector arrays and fluorescence detectors observing at the same site. Research and development efforts are under way for novel methods of air shower detection and measurement. The goal of these very large experiments is: (i) to measure accurately the flux of UHECRs (Sect. 7.9), in particular above  $3 \times 10^{18}$  eV

where the hardening of the spectrum is suggestive of an extragalactic component; (ii) to understand the nature (protons or heavier nuclei) of UHECRs (Sect. 7.10); (iii) to provide evidence of correlations of arrival directions at the highest energies with the large-scale distribution of matter in the near-by Universe (Sect. 7.11). These information are crucial in order to elucidate the physical mechanisms acting at the acceleration sites.

## 7.1 The Observational Cosmology and the Universe

Observational cosmology consists of the study of the structure, the evolution and the origin of the Universe through experimental measurements. Up to a few years ago, cosmology was a speculative science based on a very limited number of observations. The dispute between the supporters of the steady state and the promoters of Big Bang cosmology is an example of the scientific debate before the advent of observational cosmology.

The beginning of modern cosmology starts with the Hubble's observations, and thus from the correlation between the distance to galaxies and their recessional velocities, measured through the Doppler shift of the emission wavelengths. This shift can be measured because the emission and absorption spectra for atoms and molecules are distinctive and well known. Redshift (and blueshift) may be characterized by the relative difference between the observed ( $\lambda_{\text{obs}}$ ) and emitted ( $\lambda_{\text{emit}}$ ) wavelengths of the radiation emitted by an astrophysical object. In astronomy, it is customary to refer to this wavelength shift using the dimensionless quantity

$$z = \frac{\lambda_{\text{obs}} - \lambda_{\text{emit}}}{\lambda_{\text{emit}}} \quad (7.1)$$

When the shift of various absorption and emission lines from a single astronomical object is measured,  $z$  is found to be remarkably constant.

The discovery of a linear relationship between the redshift and the proper distance  $D$  (measured in Mpc) of a Galaxy, coupled with the assumption of a linear relation between recessional velocity  $v$  (in km/s) and redshift, yields a straightforward mathematical expression for the so-called *Hubble's Law*:

$$v = H_0 \cdot D \quad (7.2)$$

where the Hubble's constant,  $H_0$ , has physical dimensions of  $[\text{time}^{-1}]$ . The Hubble's constant is most frequently quoted in  $[\text{km s}^{-1} \text{Mpc}^{-1}]$ , thus giving the speed in km/s of a galaxy 1 Mpc away. The reciprocal of  $H_0$  is the Hubble time. The value of the Hubble time in the standard cosmological model corresponds to  $\tau_{H_0} = 1/H_0 \sim 13.7 \text{ Gy}$ . We will return to the standard cosmological model in Sect. 13.1.



**The Cosmic Microwave Background Radiation.** A second fundamental step in modern cosmology was the discovery of the cosmic microwave background (CMB) radiation, predicted in 1948 by G. Gamow and R. Alpher as a consequence of a hot origin of the Universe. In 1965, A. Penzias and R. W. Wilson (Nobel Prize in 1978) with a radiometer that they intended to use for radio astronomy and satellite communication discovered an excess of signal equivalent to a 3.5 K antenna temperature, which they could not account for. This antenna temperature was indeed due to the cosmic microwave background.

The CMB radiation is well explained as radiation left over from an early stage in the development of the Universe. The first nuclei were formed about three minutes after the Big Bang, through a process called *nucleosynthesis*. It was then that hydrogen and helium (and traces of heavier Li, Be and B) nuclei formed. The key parameter necessary to calculate the effects of Big Bang nucleosynthesis is the ratio  $n_{\gamma}/p$  of photons to baryon.

After nucleosynthesis, the energy of particles and radiation was so high that neutral atoms could not be formed. Charged particles were in a plasma state. As the Universe expanded, both the plasma and the radiation cooled. When the energy of the photons in the radiation field was not sufficient to ionize atoms, a transition phase occurred and nuclei and electrons combined to form neutral atoms (the so-called *recombination epoch*). These atoms could no longer absorb the thermal radiation, and consequently the Universe became transparent. Photons started to travel freely through space rather than constantly being scattered by electrons and protons (the *photon decoupling* transition phase). These photons have been propagating ever since becoming less and less energetic as the expansion of the Universe caused their wavelength to increase.

The birth of observational cosmology conventionally starts with the accurate measurement of the CMB radiation by the NASA Cosmic Background Explorer (COBE) satellite that orbited in 1989–1996. This experiment first detected and quantified the large-scale anisotropies at the limit of its detection capabilities. Inspired by the COBE results of an extremely isotropic and homogeneous CMB, different ground- and balloon-based experiments quantified the anisotropies on smaller angular scales. COBE found that the CMB has a thermal black body spectrum (shown in Fig. 7.1) at a temperature of  $2.7255 \pm 0.0006$  K. The spectral density in the Planck law  $dE_{\lambda}/d\lambda$  peaks in the microwave range, at a wavelength of 1.06 mm corresponding to a frequency  $\bar{\nu}$  of 283 GHz. Using this value, the average energy of the CMB is

$$E_{\text{cmb}} = h\bar{\nu} \simeq 1.2 \times 10^{-3} \text{ eV}. \quad (7.3)$$

The average number density of CMB photons is given by the integral of the Planck spectrum, divided by the average energy  $E_{\text{cmb}}$  and corresponds to

$$n_{\gamma\text{cmb}} \simeq 400 \text{ cm}^{-3}. \quad (7.4)$$

In June 2001, NASA launched a second space mission dedicated to cosmological measurements, the Wilkinson Microwave Anisotropy Probe (WMAP) satellite and a third space mission, Planck, was launched by the European Space Agency (ESA) in

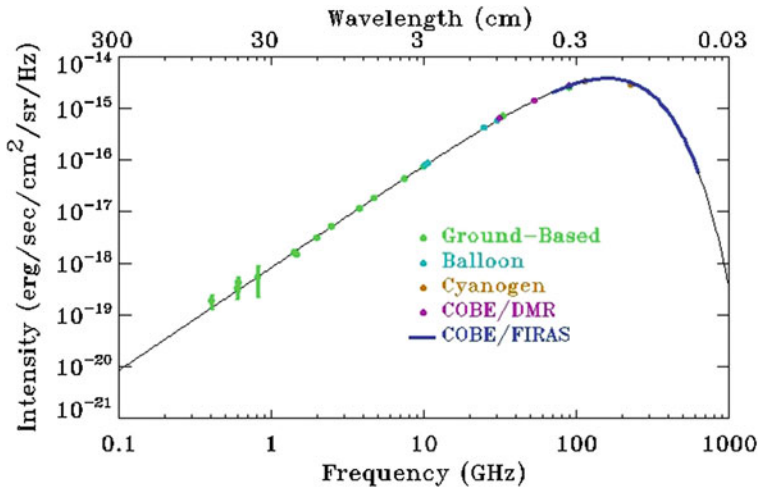


**Fig. 7.1** Cosmic microwave background spectrum measured by the FIRAS instrument on the COBE (blue points) as a function of frequency (bottom  $x$ -axis) and wavelength (upper  $x$ -axis). This corresponds to the most-precisely measured black body spectrum in nature. The error bars are too small to be seen even in an enlarged image, and it is impossible to distinguish the observed data from the theoretical curve. Other ground-based and balloon-based results at higher wavelengths than those measured by the FIRAS instrument are also shown ([http://asd.gsfc.nasa.gov/archive/arcade/cmb\\_spectrum.html](http://asd.gsfc.nasa.gov/archive/arcade/cmb_spectrum.html))

collaboration with NASA in May 2009. It has been measuring the CMB anisotropies at a higher resolution than WMAP. The measurements from these experiments played a key role in establishing the current Standard Model of Cosmology, Sect. 13.1.

## 7.2 The Large-Scale Structure of the Universe

The observable Universe consists of galaxies and other matter that can be observed from Earth an interesting web site designed to give an idea of what our universe actually looks like, created by R. Powell is: <http://www.atlasoftheuniverse.com/>. The interpretation of observations must take into account that light (or other particles) from those objects has had time to reach the Earth since the beginning of the cosmological expansion. Assuming the Universe to be isotropic, light can arrive in every direction from a distance  $L = \tau_{H_0} c$  that corresponds to the observable Universe. The crucial point that removes every anthropomorphic hypothesis is that every place in the Universe is in the center of its own observable horizon, with the same extension  $L$  as the one centered on Earth.

Sky surveys and mappings in different wavelengths have yielded much information on the contents and structure of the Universe. The estimated number of stars is between  $10^{22}$  and  $10^{24}$ . Stars are organized into about  $10^{11}$  galaxies, which in

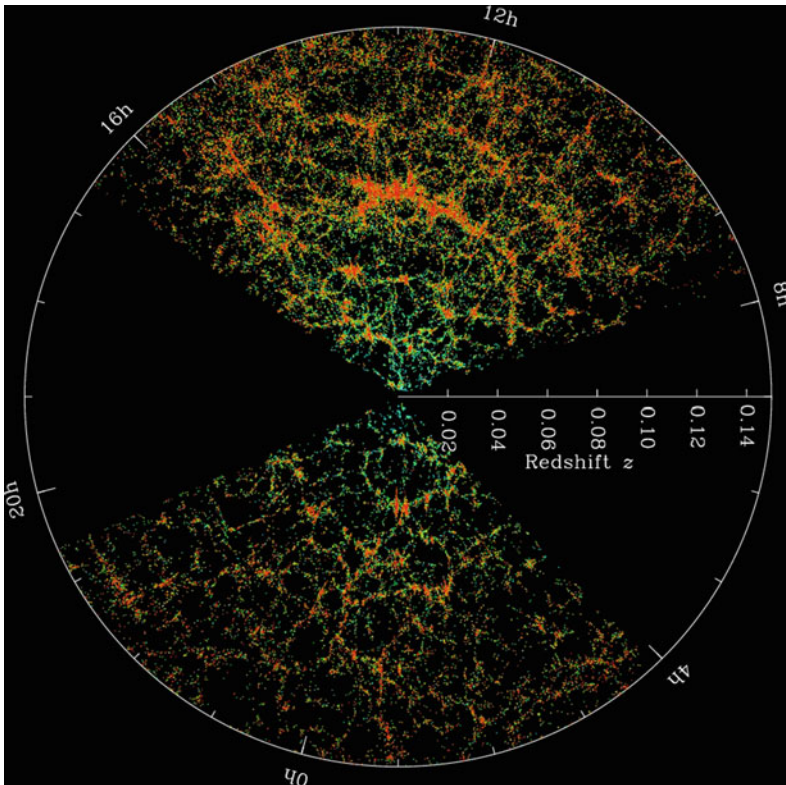


**Fig. 7.2** Slices through the 3-dimensional map of the distribution of galaxies from the Sloan Digital Sky Survey (SDSS). The Earth is at the *center*, and each point represents a galaxy, typically containing about  $10^{11}$  stars. The position of that point indicates its location on the sky, and the distance from the *center* of the image indicates its distance from the Earth. Galaxies are colored according to the ages of their stars, with the redder, more strongly clustered points showing galaxies that are made of older stars. The *outer circle* is at a distance of about  $2 \times 10^9$  light years. The region between the wedges was not mapped by the SDSS because dust in our own Galaxy obscures the view of the distant Universe in these directions. The *lower* part of the figure is thinner than the *upper*, so it contains fewer galaxies. Another group completed a similar survey of the galaxies in the Universe called the 2dF Redshift Survey. Credit: M. Blanton and the SDSS ([https://www.sdss3.org/science/gallery\\_sdss\\_pie2.php](https://www.sdss3.org/science/gallery_sdss_pie2.php))

turn form clusters of galaxies and superclusters that are separated by immense voids, creating a vast foam-like structure sometimes called the “cosmic web”. The organization of this structure appears to follow a hierarchical model with a classification in groups, clusters, superclusters, sheets, filaments, and walls (see Fig. 7.2).

Our Galaxy (sometimes called the *Milky Way*) belongs to a galaxy supercluster, which also contains the *Virgo Cluster* near its center, and for this reason, it is called the *Virgo Supercluster*. It is thought to contain over 47,000 galaxies and its dimension is about 35 Mpc.

A galaxy is a gravitationally bound system consisting of stars, stellar remnants and an interstellar medium of gas and dust. These objects emit or adsorb and re-emit electromagnetic radiation. An additional component due to the unknown form of dark matter seems to largely contribute to the gravitational bound, Sect. 13.4. The dimensions range from dwarf galaxies with as few as  $10^7$  stars to giant galaxies with  $10^{14}$  stars, each orbiting their galaxy's own center of mass. Observational data suggest that supermassive black holes may exist at the center of many, if not all, galaxies. Also our own galaxy appears to have a  $(2-3) \times 10^6$  solar masses black hole in its center.

Galaxies are usually classified based upon morphological visual observations in three main types: elliptical, spiral, and irregular. Most elliptical galaxies are composed of older, low mass stars, with a sparse interstellar medium and minimal star formation activity. They are preferentially found close to the centers of galaxy clusters. Elliptical galaxies make approximately 10–15 % of galaxies visible in the Virgo Supercluster, and they are not the dominant type of galaxy in the whole Universe. Spiral galaxies (as our own Milky Way) consist of a rotating disk of stars and interstellar medium, along with a central bulge of generally older stars. See also Sect. 2.7. This classification may miss certain important characteristics of galaxies such as star formation rate and activity in the core.

Active galaxies are galaxies with an abnormal emission of electromagnetic radiation. The emission is mostly due to a small active core embedded in an otherwise typical galaxy, which may be highly variable and very bright compared to the rest of the galaxy. Galaxies having abnormal activity in the central region are called Active Galactic Nuclei (AGN). AGN (as described in Sect. 9.9) range from nearby galaxies emitting about  $10^{40}$  erg s<sup>-1</sup> to distant point-like objects (named quasars) emitting more than  $10^{47}$  erg s<sup>-1</sup> (Woo and Megan Urry 2002).

AGN are UHECRs source candidates and are observed to emit also  $\gamma$ -rays up to energies of tens of TeV (Sect. 9.10) and probably neutrinos (Sect. 10.4.2).

### 7.3 Anisotropy of UHECRs: The Extragalactic Magnetic Fields

Magnetic fields affect the propagation of CRs because charged particles are deflected, emitting synchrotron radiation. For protons, synchrotron losses are negligible except in the strong magnetic fields present close to sources. Above  $10^{19}$  eV the galactic magnetic field would not trap very effectively even iron nuclei. The Larmor radius (2.5) of a particle with energy  $E$  and electric charge  $Ze$  in a magnetic field  $B$  can be expressed as

$$r_L = 110 (\text{kpc}) Z^{-1} \left( \frac{\mu\text{G}}{B} \right) \left( \frac{E}{10^{20} \text{eV}} \right), \quad (7.5)$$

which for UHECRs is much larger than the thickness of the galactic disk.

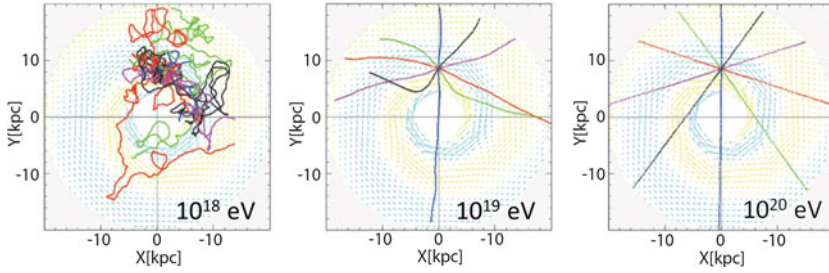


**Fig. 7.3** Simulated trajectory of charged particles in the galactic magnetic field. Low-energy charged particles are bent and wound by magnetic fields, but those above  $10^{20}$  eV travel along almost straight trajectories with little influence from magnetic fields, thereby retaining the original directional information. Credit: prof. T. Ebisuzaki (<http://www.asi.riken.jp/en/laboratories/chiefabs/astro/index.html>)

In intergalactic space where the magnetic field intensities are expected to be much lower than in the Galaxy, the Larmor radius of UHECRs becomes extremely large. The possibility of charged particle astronomy, in the sense of the possibility to connect the arrival direction of UHECRs to the coordinates of extragalactic objects is still an open question. This possibility depends on the magnitude of the poorly known extragalactic magnetic fields.

The deflection angle of a particle of energy  $E$  moving in a direction perpendicular to a uniform magnetic field  $B$  after travelling the distance  $d$  is

$$\theta \sim \frac{d}{r_L} \sim 0.5^\circ Z \left( \frac{E}{10^{20} \text{ eV}} \right)^{-1} \left( \frac{d}{\text{kpc}} \right) \left( \frac{B}{\mu\text{G}} \right) \quad (7.6)$$

A proton of energy  $5 \times 10^{19}$  eV will be deflected by  $1^\circ - 5^\circ$  in the galactic magnetic field depending upon the direction and length of the trajectory. Each panel of Fig. 7.3 shows the simulated trajectories of 10 CR protons originating in a fixed position in the galactic plane. The galactic disk lies in the  $xy$  plane and the structure of the magnetic field is similar to that of Fig. 2.10. The energies are  $10^{18}$ ,  $10^{19}$  and  $10^{20}$  eV as shown in the figure. The galactic magnetic field has little influence at energies  $> 10^{19}$  eV, and a galactic source of CRs with that energy would produce a clear anisotropy on Earth measurements, that is not observed. The confinement mechanism in the Galaxy is not maintained at the highest energies, motivating the search for extragalactic sources of CRs.

Magnetic fields beyond the galactic disk are poorly known. In few clusters of galaxies they have been estimated by observing the synchrotron radiation halos or performing Faraday rotation measurements. The two methods give somewhat different results for the field strength, with  $B \sim 0.1 - 1 \mu\text{G}$  and  $B \sim 1 - 10 \mu\text{G}$ , respectively. These regions enclose a small fraction of the Universe (less than  $10^{-6}$ ) and only upper limits on the extragalactic magnetic field exist for regions outside

galaxy clusters:  $B < 10^{-9} \text{ G}$  with coherent length of the field  $l_c \sim 1 \text{ Mpc}$ . The value of  $l_c$  corresponds to the average distance between galaxies.

## 7.4 The Quest for Extragalactic Sources of UHECRs

Following the arguments used for galactic CR sources, the extragalactic acceleration mechanisms must satisfy the following criteria: they must provide enough energy to reach the largest observed energies, and the accelerated population should have an injection energy spectrum that would fit the observed UHECR spectrum after propagation.

The diffusive shock acceleration mechanism (Sect. 6.2) is based on the repeated scattering of charged particles on magnetic irregularities back and forth across a shock front. For non-relativistic shocks the energy gain at each crossing is  $\Delta E \propto \eta E \simeq \beta E$ , see Sect. 6.1.3. As discussed in Chap. 6, the presence of plasmas in any real astrophysical condition destroys large-scale electric fields. Magnetic fields are instead almost omnipresent in astrophysical objects. Their space/time variations imply the existence of transient electric fields through the Faraday law that can supply a consequent amount of energy to charged particles (unipolar inductors, Sect. 6.7.1). The maximum energy (6.88) of a CR nucleus of charge  $Ze$  accelerated in a region where the magnetic field  $B$  changes in a spatial region of size  $L$  can be written as

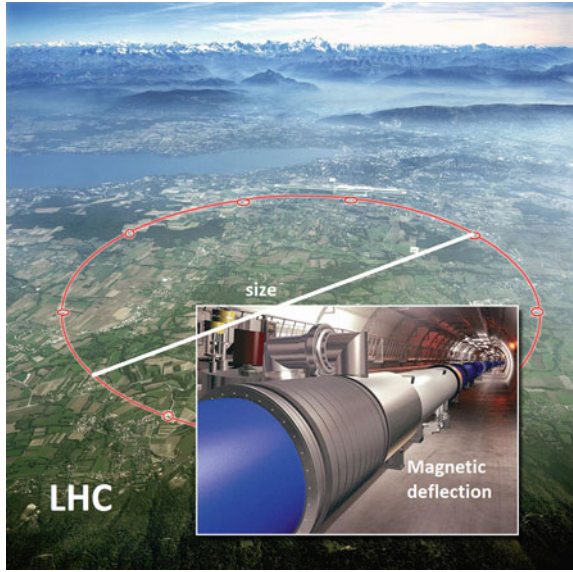
$$\frac{E^{\max}}{Ze\beta} = LB. \quad (7.7)$$

To reach energies above  $10^{18} \text{ eV} = 1 \text{ EeV}$ , the acceleration should occur with a necessary combination of scale  $L$  and magnetic field  $B$ : if the scale is small, the magnetic field must be huge, and viceversa.

Also in man-made accelerators the size  $L$  is related to the maximum energy obtainable. In the case of a collider, as the Large Hadron Collider (LHC) at CERN, the maximum energy is a function of the radius of the machine and the strength of the dipole magnetic field. This field keeps particles in their orbits, see Fig. 7.4. The LHC uses the 27 km circumference tunnel that was built for the previous lepton accelerator, LEP. In an accelerator, particles circulate in a vacuum tube. The accelerating cavities are electromagnetic resonators that accelerate particles and then keep them at a constant energy by compensating for energy losses. Particles are constrained using electromagnetic devices: *dipole magnets* keep the particles in their nearly circular orbits, *quadrupole magnets* focus the beam acting in a way analogous to converging lenses in optics. Heavy particles such as protons have a much lower energy loss per turn through synchrotron radiation than electrons. The LHC uses some of the most powerful existing dipoles and radio-frequency cavities. The size of the tunnel, magnets, cavities and other essential elements of the machine, represent the main constraints that determine the design energy of 7 TeV per proton beam.



**Fig. 7.4** In a man-made accelerator the maximum energy is a function of the radius of the machine and the strength of the dipole magnetic field that keeps particles in their orbits. An accelerator of size of the Mercury planet orbit would be needed to reach  $10^{20}$  eV (=100 EeV) with the LHC technology. Adapted from CERN pictures



The largest observed CR energy (about  $2 \times 10^{20}$  eV) corresponds to a macroscopic amount of the order of 20J. The basic problem of the origin of the highest energy CRs is how an astrophysical source can transfer efficiently this enormous quantity of energy to a single particle. To work out some hypothesis, we rewrite (7.7) in more appropriate units as

$$E^{\max} = Z\beta(4.8 \times 10^{-10}) \cdot (10^{-6}) \left(\frac{B}{1 \mu\text{G}}\right) \cdot (3.1 \times 10^{21}) \left(\frac{L}{1\text{kpc}}\right) [\text{erg}]. \quad (7.8)$$

Using the conversion  $1 \text{ eV} = 1.6 \times 10^{-12} \text{ erg}$  and  $1 \text{ EeV} = 1.6 \times 10^6 \text{ erg}$  we finally obtain:

$$E^{\max} \simeq Z\beta \cdot \left(\frac{B}{\mu\text{G}}\right) \cdot \left(\frac{L}{\text{kpc}}\right) [\text{EeV}]. \quad (7.9)$$

Equation (7.9) contains the factor  $\beta \equiv U/c$ , where  $U$  is the characteristic velocity of magnetic scattering centers and the above relation is usually called the Hillas criterion.

In the case of one-shot acceleration scenarios (when the particle escapes the accelerating region after the first iteration) the maximum reachable energy has a quite similar expression to the shock acceleration case. We already discussed the case of a pulsar (Sect. 6.7.1), where the quantity  $\beta$  in Eq. (7.9) is replaced by  $\omega_{\text{NS}} R_{\text{NS}}/c$ . In addition to the pulsar magnetospheres, other astrophysical candidate regions are gamma-ray bursts, active galactic nuclei and radio jets.

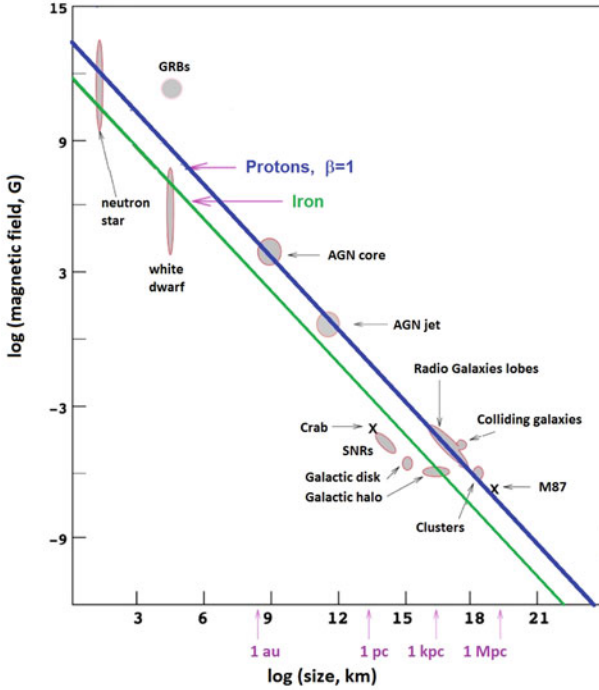


**Fig. 7.5** Example of the **diagram** first produced by **Hillas**. Acceleration of cosmic rays up to a given energy requires magnetic fields and sizes above the respective line. The **blue (green) line** corresponds to the condition for  $B, L$  to accelerate protons (iron) at  $10^{20}$  eV. Some source candidates are still controversial

In both the **shock acceleration** and **one-shot acceleration scenarios** a relationship analogous to (7.9) holds. The **maximum attainable energy** is, for a given nuclear charge  $Ze$ , approximately equal to the product of the magnetic field  $B$  and the size  $L$  of the acceleration/confinement region, Fig. 7.5. The **straight lines** shown correspond to values of  $E^{\max} = 10^{20}$  eV for **protons** and **iron nuclei**. Diagrams of this type were first proposed by Hillas in 1984, and in the figure several possible galactic and extragalactic acceleration sources are considered, see (Torres and Anchordoqui 2004) for details.

Let us consider the **blue line** that corresponds to **100 EeV protons**. If potential **sources lie to the left** of the line, **protons cannot be accelerated** to  $10^{20}$  eV by these objects. The diagram indicates that **there are potential sites** of particle acceleration in a wide range of high-energy astrophysical objects (Ostrowski 2002). Clearly, this **criterion is a necessary, but not sufficient condition**.

We will show in the next Chapter that **sources of CRs should emit also high-energy photons up to multi-TeV**. The  $\gamma$ -rays emission mechanism is naturally connected to the acceleration of electrons and/or protons in astrophysical sources. **The observed photon spectra allow also predicting neutrino fluxes**, since **photons** are the only



**Table 7.1** The values for typical electromagnetic emissions and the characteristic lifetimes for different galactic and extragalactic objects

Source class	Electromagnetic output erg/s	Lifetime	Energy range (eV)
<b>Galactic sources</b>			
Supernova remnants (SNR)	$10^{42}$	$10^3\text{--}10^4$ y	$10^{10}\text{--}10^{15}$
Wind-SNR	$10^{44}$	1,000 y	$10^{10}\text{--}10^{18}$
X-ray binaries	$10^{38}$	$10^5$ y	$10^{14}\text{--}10^{18}$
Pulsars	$10^{37}$	$10^6$ y	$10^{14}\text{--}10^{18}$
<b>Extragalactic sources</b>			
Galaxy clusters	$10^{44}$	$10^7$ y	$10^{18}\text{--}10^{21}$
AGN	$10^{44}\text{--}10^{47}$	$10^7$ y	$10^{18}\text{--}10^{21}$
GRBs	$10^{49}\text{--}10^{51}$	1–100 s	$10^{18}\text{--}10^{21}$

They estimates are based on the multiwavelength observations of objects in the electromagnetic emission. It should be noted that luminosity and lifetime distributions can scatter, and there are objects within the given classes that have values deviating from the given typical ones. In the case of GRBs, a lower limit is given; the actual value depends on whether or not GRB afterglow emission contributes to UHECRs

messengers giving direct evidence for the properties of their sources (Becker 2008). The observation of neutrinos from astrophysical objects would be the key ingredient to identify acceleration sources of CR protons and nuclei. Table 7.1 lists source classes with their intrinsic luminosity and possible contribution to the CR spectrum. The power measured in electromagnetic wavelengths should roughly correspond to the CR power at the source, since electromagnetic radiation originates from the emission processes of charged particles.

AGN are potential sites where UHECR acceleration might take place. They are (almost) steady sources of electromagnetic emission, although variability in the  $\gamma$ -ray emission is observed. The jets have transverse dimensions of the order of a fraction of a parsec and the magnetic field necessary to explain the synchrotron radiation from such objects of the order of a few Gauss. Using the Hillas condition (7.9) the maximum energy for protons in a region with magnetic field intensity of the order of  $1\ \mu\text{G}$  and  $L = 0.1\ \text{pc}$  would be  $\sim 10^{20}$  eV. The  $E^{\text{max}}$  attainable to protons in the AGN core, where  $B \sim 10^3\ \text{G}$  in a size of  $L \sim 10^{-5}\ \text{pc}$ , is almost the same.

One criticism of this model is that under realistic conditions, the quoted  $E^{\text{max}}$  is unlikely to be achieved. In fact the realistically attainable maximum energy should decrease because of energy loss mechanisms of charged particles, their synchrotron radiation in the magnetic field, and the interaction of high energy protons with the photons of the radiation field surrounding the central engine of AGN. The situation is worse for nuclei, which will photodisintegrate even faster in the photon field. This problem can be bypassed if we assume that energies up to the highest observed values can be reached when the final acceleration site is away from the active center. This should correspond to regions with a lower radiation density, as for instance the terminal shock sites of jets.

**Gamma Ray Bursts (GRBs)** are the **most energetic transient eruptions** observed in the Universe, see Sect. 8.9. The transient nature of **GRBs could possibly explain the lack of correlation between the arrival direction of the highest energy CRs and astrophysical objects**. In this scenario, sources are not visible since the detected CRs come from various bursts and reach the Earth long after the gamma-ray burst itself has occurred.

Based on  $\gamma$ -ray observations, the mechanism that produces bursts is likely to be due to the dissipation of the kinetic energy of a relativistic expanding fireball. The value of the magnetic field at these shocks is estimated to be of order  $B \sim 10^6$  G on a scale length  $L \sim 10^{-6}$  pc from the center, fulfilling the **Hillas conditions** for an energy of  $\sim 10^{20}$  eV. Consider that parameters can take different values at different times of the GRB explosion. The observation that the **flux of  $\gamma$ -rays reaching the Earth from GRBs is generally comparable to the observed flux of UHECRs**, implying a tight energetic connection, strengthens the hypothesis that GRBs are a part at least of UHECRs acceleration sources.

**Magnetars.** Like other neutron stars (Sect. 6.6.2), magnetars are around 20 km in diameter. Magnetars are **different from other neutron stars** by having even **stronger magnetic fields (up to  $10^{15}$  G, three orders of magnitude larger than normal neutron stars)**. The rotation period is comparatively slow, with most magnetars completing a rotation once every one to ten seconds. **The magnetic field gives rise to very strong and characteristic bursts of X-rays and  $\gamma$ -rays**. The active life of a magnetar is short. According to some models, UHECRs could be accelerated through unipolar induction in the relativistic winds for rapidly rotating magnetars. **The maximum energy** reached by particles injected by these objects **could reach  $10^{20}$  eV** and only 5% of the extragalactic magnetar population needs to be fast-rotators to account for the observed UHECR energetics. **Finally, magnetars, as well as GRBs, are transient sources and could not be associated with the detection of UHECRs.**

The **nature (protons or heavier nuclei)** of the highest energy CRs plays an **essential role** in the **understanding** of **acceleration mechanisms**. **If UHECRs are iron nuclei**, energies of  $10^{20}$  eV can be attained even in shock regions with  $\beta$  significantly less than one, or in regions with smaller size/smaller magnetic field as shown by the **green line** in Fig. 7.5. **If instead UHECRs are protons**, an origin in **AGN** or in **GRBs** seems the **most natural explanation**, given their **isotropy**. The magnetar option is very promising if the UHECRs are heavy nuclei. In fact, the possibility of injecting large proportions of heavy nuclei into an acceleration region may be more easily fulfilled by young neutron stars than alternative sources, due to their iron-rich surface. See (Kotera and Olinto 2011) for additional information on models.

**The discrimination between different scenarios is the goal of present and future generations of experiments.**

## 7.5 Propagation of UHECRs

There are **three main energy loss** processes for protons (or heavier nuclei) propagating over cosmological distances: **adiabatic energy loss**, **pion-production** on photons of the cosmic microwave background (CMB), and **electron-positron pair-production** always on the CMB (Kotera and Olinto 2011). We can **define the energy loss length**  $\ell$  as:

$$\ell^{-1} \equiv \frac{1}{E} \frac{dE}{dx} \quad (7.10)$$

### 7.5.1 The Adiabatic Energy Loss

The **adiabatic loss** of a cosmic ray with energy  $E$  is a general mechanism that affects particles and radiation and is **due to the expansion of the Universe**. The energy loss formula is similar to that valid for the electromagnetic radiation and depends on the Hubble constant

$$-\frac{1}{E} \frac{dE}{dt} = H_0. \quad (7.11)$$

The corresponding energy loss length is thus:

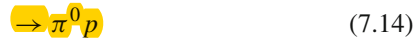
$$\ell_{\text{adia}} = \frac{c}{H_0} \simeq 4 \text{ Gpc} \quad (7.12)$$

where  $c$  is the light velocity and  $1/H_0 \sim 13.7 \text{ Gy}$ . Noticeably, the energy loss length does not depend on the CR energy.

### 7.5.2 The Propagation in the CMB: The GZK Cut-Off

The **propagation of UHECRs in** the newly discovered **CMB** was independently studied in 1966 by K. **Greisen**, V. **Kuzmin**, and G. **Zatsepin**. They foresaw that the flux of CRs originating at cosmological distances would **greatly be attenuated above a threshold energy**  $E_{\text{GZK}} \simeq 5 \times 10^{19} \text{ eV}$ . This is the so-called **Greisen-Zatsepin-Kuzmin (GZK) cut-off**: the **proton** component of the **CR flux** from sources at cosmological distances **drops sharply above the threshold energy**  $E_{\text{GZK}}$ . As we can easily derive from the considerations below, **a nucleus with mass  $A$  starts to be attenuated at an energy**  $A \cdot E_{\text{GZK}}$ .

During propagation, **protons** would **interact** with the **cosmic microwave background photons** ( $\gamma_{\text{cmb}}$ ) if the **proton energy is large enough** to reach in the **centre-of-mass system** the resonant **production** of the  $\Delta^+$  **hadron**. The  $\Delta^+$  **resonance** immediately **decays**



Neutral pions decay in two photons while the  $\pi^+$  decays into  $\mu^+ \nu_\mu$ . The produced neutrons also decay into  $pe^- \bar{\nu}_e$ . As a proton is always present in the final state, the final effect of the interaction is that the energy of the CR proton above threshold is reduced and high-energy photons and neutrinos are produced.

According to (3.1) the interaction length (in cm) is inversely proportional to the target number density ( $\text{cm}^{-3}$ ) and the particle cross-section ( $\text{cm}^2$ ). The energy loss length  $\ell_{p\gamma}$  in (7.10) in this case corresponds to:

$$\ell_{p\gamma}^{-1} = \langle \gamma \sigma_{p\gamma} n_\gamma \rangle \rightarrow \ell_{p\gamma} \equiv \frac{1}{\langle \gamma \sigma_{p\gamma} n_\gamma \rangle} \quad (7.15)$$

where  $y = (E - E')/E$  is the fraction of energy lost per interaction. Usually, the radiation field is due to the CMB radiation, where  $n_\gamma = n_{\gamma_{\text{cmb}}}$  is the corresponding photon number density (7.4). The brackets  $\langle \dots \rangle$  remind that we should integrate the differential cross-section over the momentum distribution of the target photons. In our following estimates, we avoid this complication by considering only reactions well above the threshold energy when essentially all photons participate in the reaction, and using average values for the cross-section and photon momentum.

We derive now the threshold energy for protons to induce this reaction and their mean free path.

The  $\Delta^+$  resonance has mass  $m_\Delta = 1,232 \text{ MeV}$  (we use natural units with  $c = 1$ ). The threshold for reaction (7.13) corresponds to the production of the  $\Delta^+$  resonance at rest. The condition is dictated by the center-of-mass invariant  $\sqrt{s} = m_\Delta$  [see Sect. 3.1 of Braibant et al. (2011)]. If  $p_p = (E_p, \mathbf{p}_p)$ ,  $p_\gamma = (E_\gamma, \mathbf{p}_\gamma)$  are the four-momenta of the proton and of the CMB photon, the resonance is produced when

$$s = (p_p + p_\gamma)^2 = m_\Delta^2 \rightarrow m_p^2 + 2E_\gamma E_p - 2\mathbf{p}_p \mathbf{p}_\gamma = m_\Delta^2. \quad (7.16)$$

For a photon,  $|\mathbf{p}_\gamma| = E_\gamma$  and at high energy  $E_p \simeq p_p$ . In this case (7.16) becomes

$$2E_p(E_\gamma - E_\gamma \cos \theta) = m_\Delta^2 - m_p^2$$

and using the values  $m_\Delta = 1.232 \text{ GeV}$ ,  $m_p = 0.938 \text{ GeV}$  we obtain

$$E_p = \frac{m_\Delta^2 - m_p^2}{2E_\gamma(1 - \cos \theta)} = \frac{0.32 \text{ GeV}^2}{E_\gamma(1 - \cos \theta)}. \quad (7.17)$$

The minimum value for  $E_p$  occurs when  $\theta = \pi$  (the directions of the photon and of the proton are opposite). In this case for collision with the CMB with average energy  $E_\gamma = 1.2 \cdot 10^{-3} \text{ eV}$  the threshold energy is

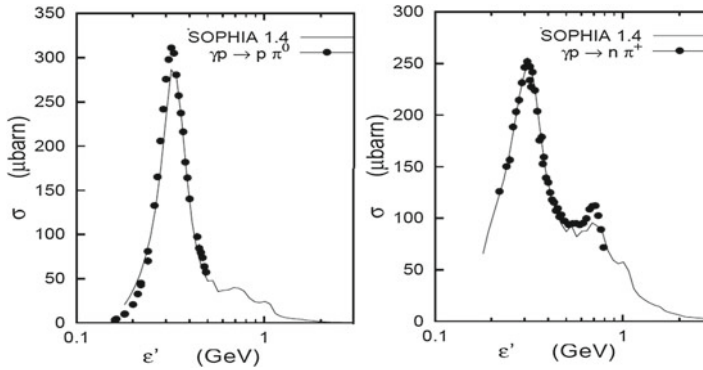


**Fig. 7.6** Total cross-section of  $\gamma p \rightarrow \pi^0 p$  (left) and  $\gamma p \rightarrow \pi^+ n$  (right) as a function of the photon energy  $\epsilon'$  in the laboratory frame. In this case, energetic photons interact with protons at rest and the resonance occurs at the energy  $\epsilon' = m_\Delta - m_p$ . The lines represent an analytical approximation of the data

$$E_p = \frac{m_\Delta^2 - m_p^2}{4E_\gamma} = 1.2 \times 10^{20} \text{ eV}. \quad (7.18)$$

The threshold decreases when the interaction occurs with CMB photons in the high-energy tail of the spectrum. The effect starts to become significant for protons with  $E_p \simeq 5 \cdot 10^{19} \text{ eV}$ .

The cross-section of the processes  $\gamma p \rightarrow \pi^0 p$  and  $\gamma p \rightarrow \pi^+ n$  were studied in laboratory (using high-energy photons and protons at rest), as a function of the photon energy in the laboratory frame. The cross-section for these two processes at resonance is  $\sigma_{p\gamma} \simeq 250 \mu\text{b}$ . The experimental results as well as the prediction from an analytic parameterization used in CR propagation (Muecke et al. 2000) are presented in Fig. 7.6.

The energy loss per interaction is relatively small and can be qualitatively estimated considering that in the final state of the process a proton and a pion are present and then

$$y = \frac{\Delta E_p}{E_p} \simeq \frac{m_\pi}{m_p} \simeq 0.1 \quad (7.19)$$

In each process around 10% of the proton energy is lost. This means that within few successive interactions, the proton energy decreases to a value below the threshold for the reaction. With the above quantities, from (7.15) the energy loss length  $\ell_{p\gamma}$  of a proton in the CMB for this process is

$$\ell_{p\gamma} = \frac{1}{y \cdot \sigma_{p\gamma} \cdot n_{\gamma\text{cmb}}} = \frac{1}{0.1 \cdot 250 \times 10^{-30} \cdot 400} = 10^{26} \text{ cm} = 30 \text{ Mpc}. \quad (7.20)$$

All protons originating at distances larger than  $\sim 30 \text{ Mpc}^1$  from us arrive on Earth with energy below  $\sim 10^{20} \text{ eV}$ . This horizon is small in terms of the dimensions of the Universe. Thus the energy loss length of a  $\sim 10^{20} \text{ eV}$  proton is comparable to the distance of the closest galaxy cluster (the Virgo). The mean free path of protons in the Universe above  $5 \times 10^{19} \text{ eV}$  becomes small on a cosmological scale. The eventual detection of CR protons with energy exceeding that value corresponds to protons produced in “local sources”.

For a heavier nucleus with mass  $A$  and energy  $E$ , the resonant reaction must occur through the interaction of one of the nucleons in the nucleus, which has energy  $E/A$ . In the nucleus center-of-mass each nucleon can in fact be considered as free with respect to a photon with energy  $\sim 300 \text{ MeV}$ . The threshold energy  $E_{\text{GZK}}$  for heavier nuclei is consequently higher by a factor  $A$ .

### 7.5.3 $e^\pm$ Pair Production by Protons on the CMB

During the propagation in the CMB, electron-positron pairs can be produced in the process



Also this process has a threshold which can be determined as in the case of the pion photoproduction, by the condition

$$s = (p_p + p_\gamma)^2 \geq (m_p + 2m_e)^2 \quad \longrightarrow \quad E_p \geq \frac{m_e m_p}{E_\gamma} \approx 2 \times 10^{18} \text{ eV} \quad (7.22)$$

where  $E_\gamma$  is the average energy of the CMB photon.

The cross-section for this electromagnetic reaction is

$$\sigma_{p\gamma} = (\alpha/32)\sigma_T \cdot f(s) \quad (7.23)$$

where  $\sigma_T$  is the Thomson cross-section (5.57),  $\alpha \approx 1/137$  is the fine structure constant and  $f(s)$  a function that depends on the center-of-mass energy of the proton-photon system. Below production threshold,  $f(s) = 0$ ; at the resonant energy,  $f(s) = 1$ . This cross-section is a factor  $\sim 10^{-4} \sigma_T \sim 0.1 \text{ mb}$ , which is thus comparable with that of the production of the  $\Delta^+$  resonance, Fig. 7.6. For comparison, Compton scattering (which is relevant in many astrophysical processes) has a cross-section which is proportional to  $\sigma_T$ .

As in the final state there is always a proton, Eq. (7.21) corresponds to an effective energy loss of the proton. The energy loss per interaction is relatively small and the

<sup>1</sup> Given the Hubble constant and the fact that  $z \approx v/c$ , it is straightforward to derive that  $30 \text{ Mpc}$  corresponds to  $z \approx 0.007$ . Compare this value with the scale of Fig. 7.2.

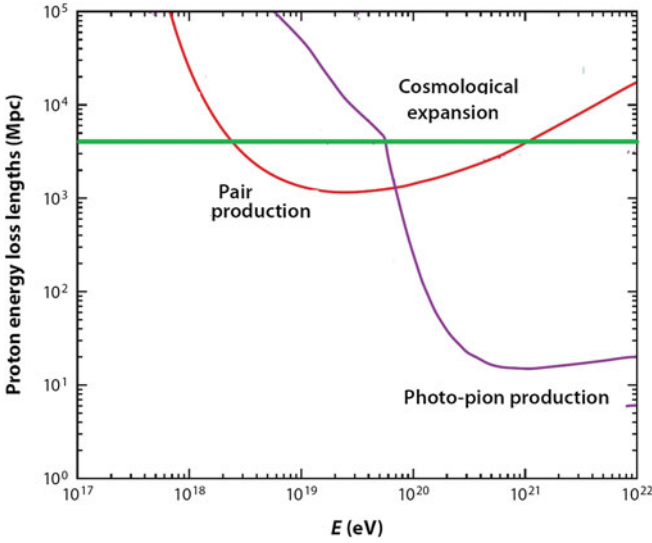


**Fig. 7.7** The energy loss lengths (7.15) for a high-energy proton propagating through the CMB radiation field. Pair creation (7.21), pion production (7.13), and energy loss through cosmological expansion (7.12) are shown

**fraction of energy loss** can be qualitatively estimated as

$$y = \frac{\Delta E_p}{E_p} \sim \frac{2m_e}{m_p} \approx 10^{-3} \tag{7.24}$$

The energy loss lengths for this process can be computed similarly to Eq. (7.20); the target is the same and the cross-section has a similar value. The quantity  $y$  has a value about two orders of magnitude smaller. Figure 7.7 compares the relative energy loss lengths of a proton due to pion-production and to  $e^+e^-$  pair-production on CMB photons, as well as that due to the redshift. One clearly recognizes that the  $e^+e^-$  pair-production process has a lower threshold energy compared to pion photoproduction, and an average path length about two orders of magnitude larger.

### 7.5.4 Propagation in the Extragalactic Magnetic Field

Upper limits on the extragalactic magnetic field are of the order of  $B < 10^{-9}$  G over scale dimension  $l_c$ , Sect. 7.3. Even such small fields can affect the propagation of UHECR. If we neglect energy loss processes, then the root mean square deflection angle  $\theta_{\text{rms}} = \langle \theta^2 \rangle^{1/2}$  for charged particles travelling over distances  $d \gg l_c$  is (Kachelriess 2008)

$$\theta_{\text{rms}} \sim \frac{(2dl_c/9)^{1/2}}{r_L} \approx 0.8^\circ Z \left( \frac{E}{10^{20} \text{ eV}} \right)^{-1} \left( \frac{d}{10 \text{ Mpc}} \right)^{1/2} \left( \frac{l_c}{1 \text{ Mpc}} \right)^{1/2} \left( \frac{B}{10^{-9} \text{ G}} \right). \quad (7.25)$$

The deflection  $\theta_{\text{rms}}$  can be estimated using observational data or reliable theoretical predictions both for the magnitude and the structure of extragalactic magnetic fields. At present, no single theory for the generation of magnetic fields in the extragalactic space has become widely accepted. The combination of poor observational data and of a missing consistent theoretical picture prevents at present a reliable estimate of the influence of extragalactic magnetic fields on the propagation of UHECRs.

The random walk due to the extragalactic magnetic fields causes an increase of the CR propagation path length from their sources that causes a corresponding time delay. If UHECRs are generated in a gamma-ray burst, or in an active transient state of an AGN, we may not be able to correlate the observed X- or  $\gamma$ - rays with the resulting incoming direction of CRs. The observation of correlation between the arrival direction of UHECR and the position of extragalactic sources would solve the mystery of the origin of UHECR and place strong constraints on the particle acceleration mechanism in its extreme manifestations. On the other hand, if we could know the origin of (at least a set of) UHECRs, we could use the arriving particles as messengers probing the intervening unknown extragalactic magnetic fields, by studying the deflections they suffered along their journey to the Earth (Aharonian et al. 2012).

## 7.6 The Fluorescence Light and Fluorescence Detectors<sup>2</sup>

Two detection techniques are principally employed to detect UHECRs. The first extends the use of extensive air shower arrays (Chap. 4) for energies above  $10^{18}$  eV. The second method exploits the excitation of nitrogen molecules by the particles in the shower and the associated fluorescence emission of light. The light is detected by photomultipliers and the profile of the shower in the atmosphere can be inferred rather directly.

Fluorescence detectors are based on the effect that high-energy particles present in a cosmic ray air shower, colliding with nitrogen molecules or nitrogen ions in the atmosphere, excite them to higher energy levels. The excited molecules undergo a very fast (10–50 ns) radiative decay, with emission of photons in the wavelength region between 300 and 440 nm, from the visible to the near ultraviolet. In dry air, the color of light produced by lightning is dominated by the emission lines of ionized nitrogen, yielding the primarily blue color observed. The fluorescence yield of an electron in the air shower is  $\sim 4$  photons per meter at ground level pressure (Arqueros et al. 2008).

As the shower advances, new nitrogen molecules are, in rapid succession, excited and decay and new photons are emitted. It worth noticing from the outset that the

<sup>2</sup> This section is largely due to V. Flaminio.



emission is *isotropic*, implying that in fluorescence detectors the air showers can be observed from all directions, from the sides as well. This is important because it allows to follow in detail the space development of the shower and to evaluate the variable  $X_{\max}$ . This makes fluorescence detectors conceptually and physically different from Cherenkov ones. If we could record with a kind of movie camera the photons emitted while the shower advances, we would have a perfect reconstruction of the space-time features and, if we could at the same time measure the number of photons emitted along the path of the shower, obtain even the energy of individual showers and an evaluation of  $X_{\max}$ .

A further advantage of this technique is related to the very good atmospheric transparency (at least in good weather conditions) to photons in this wavelength range. A drawback comes instead from the fact that the number of photons produced is relatively small, which makes the technique efficient mainly at the highest energies, where the number of particles in the shower is large.

Before going into a discussion of further advantages and disadvantages, it is important to clarify the way in which it is actually possible to follow, from ground, the shower development (the movie camera recording mentioned above). Assume that we have a single, small, light detector (a photomultiplier—PMT) pointing towards the sky, and that we have chosen a PMT of small angular acceptance (of the order of one squared degree). If the PMT happens to be pointing in the right direction it will record fluorescence photons coming from the small region of the sky falling within its angular acceptance. As the shower advances, new particles will be passing through that small region and the PMT will record the progress in time of the shower through that region.

Of course, if we want to record the space development of the shower, we must have many PMTs of this type, pointing in different but adjacent regions. This can be done using many PMTs, closely packed together next to each other, pointing in nearby directions, as shown in the toy example of Fig. 7.8.

Here we have only sketched, in an oversimplified two-dimensional arrangement, 5 different PMTs. We see that when the shower passes through position #1 it will fall

**Fig. 7.8** The arrangement of the PMTs in the two-dimensional oversimplified arrangement described in the text

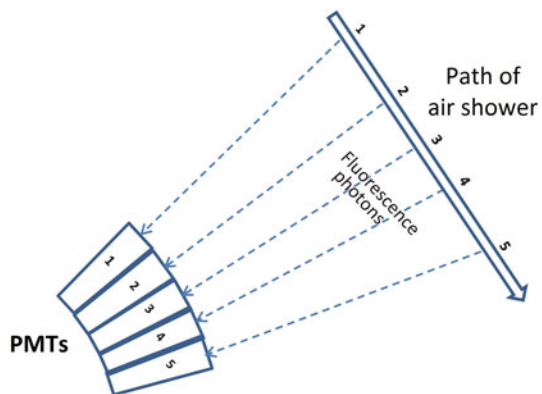
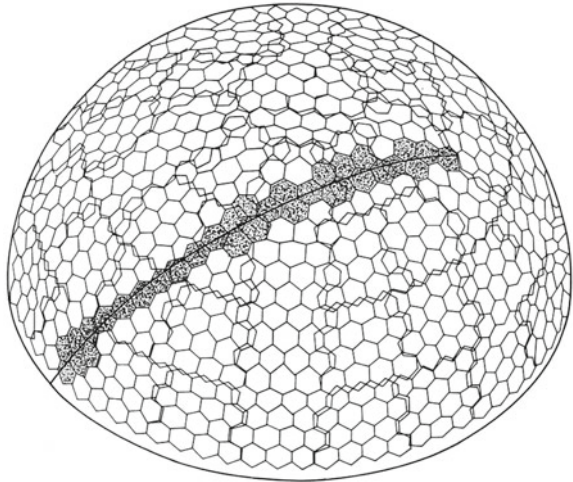


**Fig. 7.9** The arrangement of the PMTs in the Fly's Eye experiment. Credit: prof. P. Sokolsky



within the angular acceptance of PMT #1; it will fall within the angular acceptance of PMT #2 when, a few microseconds later, it passes through position #2, and so on. Since the shower can occur anywhere in the sky and moreover it will in general have a finite width, the **oversimplified 2-D** picture we have sketched must, in real life, be replaced by a **3-D arrangement** like the one shown in **Fig. 7.9**. The type of detector shown in the figure reminds us of the **eye of a fly**, from which the name given to the early detector of this type built, the University of Utah **Fly's Eye** detectors. This experiment was located in the western desert of Utah, USA, at Dugway Proving ground. It took data with different configuration from 1981 to 1992, paving the way for the **High Resolution Fly's Eye detector (HiRes)**, Sect. 7.7, which took data on the same site from 1997 until 2006. It is worth noticing that in a detector of this type the **shower** appears as a **bright spot, moving across the sky** at the **speed of light**.

Modern fluorescence detectors use **large spherical mirrors** to improve light collection. The light is then focused on an array of small PMTs, arranged in a very similar way to the one we have described. The latest (and largest) implementation of this technique, in the **Pierre Auger Observatory**, will be described later in Sect. 7.8. An illustrative example of such telescope is shown in **Fig. 7.10**.

A **fluorescence telescope** is enclosed in **its own building**, to protect it from weather conditions, and in addition a special **large optical filter** is placed **in front of it**, to remove undesired ambient light. The idea of an **optical filter** is to transmit most of the fluorescence signal in the **near-UV** while blocking other night sky background to which the PMTs are sensitive.

A **limitation** of this type of detectors is related to the fact that they may **only operate in clear, moonless nights**. Any spurious source of light would be a problem for the PMTs. Another limitation comes from the fact that a shower, travelling for a long distance in the sky, can move from regions of high air density to regions where the air density is low. These regions are characterized by different numbers

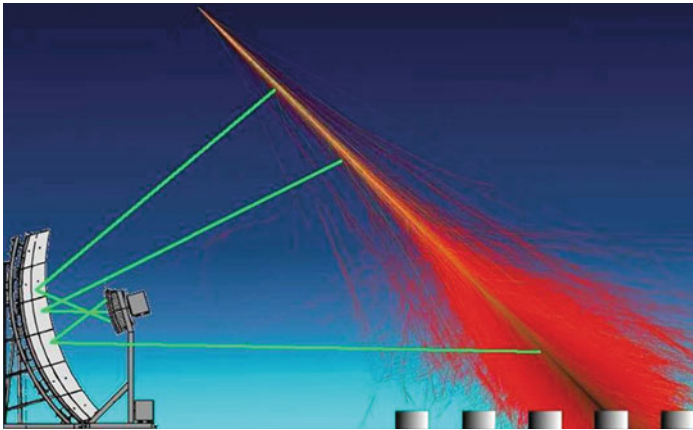


**Fig. 7.10** An artist’s impression of an air shower seen by a fluorescence detector. The fluorescence light is focused by the spherical mirror onto the matrix of PMTs analogous to that shown in Fig. 7.9. Courtesy of the Auger Observatory (<http://www.auger.org/>)

of nitrogen molecules/ions per unit path length and therefore different numbers of emitted photons. However, this effect finds a partial compensation in the fact that in regions of higher density, excited nitrogen molecules/ions undergo more frequent collisions, which cause de-excitation without emission of light.

Fluorescence detectors can observe showers developing even several km away, with a very large field of view. Because of the large distance between shower and detector and of the weak intensity of fluorescence light, aerosols and dust, that may cause absorption and scattering must be kept under careful control.

Cherenkov radiation has the property of emitting a much larger number of photons than fluorescence. However, the former radiation is strongly beamed in the very forward direction and does not constitute an important source of background noise.

It is easy to show (Kuempel et al. 2008) how the geometrical details of the shower (distance from telescope, direction in the sky) can be derived from observations made even with a single “eye”, like the one shown in Fig. 7.9. Those pixels that have recorded a signal define, with their space orientation, a plane. This is known in the literature as the shower-detector-plane and clearly the shower lies in such plane, as shown in Fig. 7.11. In this figure  $R_p$  is the distance of closest approach of the shower to the detector,  $t_0$  is the time of transit of the shower by this point,  $t_i$  is the time when pixel # $i$  has received light emitted at the corresponding position,  $\chi_i$  the angle that pixel # $i$  forms with the horizontal in the shower-detector-plane,  $\chi_0$  the angle between the shower and the horizontal plane (still measured in the shower-detector-plane). It can easily be seen that the following relationship between the measured quantities  $t_i$ ,  $\chi_i$  and the needed variables  $\chi_0$ ,  $R_p$ ,  $t_0$  hold:

$$t_i = t_0 + \frac{R_p}{c} \tan\left[\frac{\chi_0 - \chi_i}{2}\right] \tag{7.26}$$

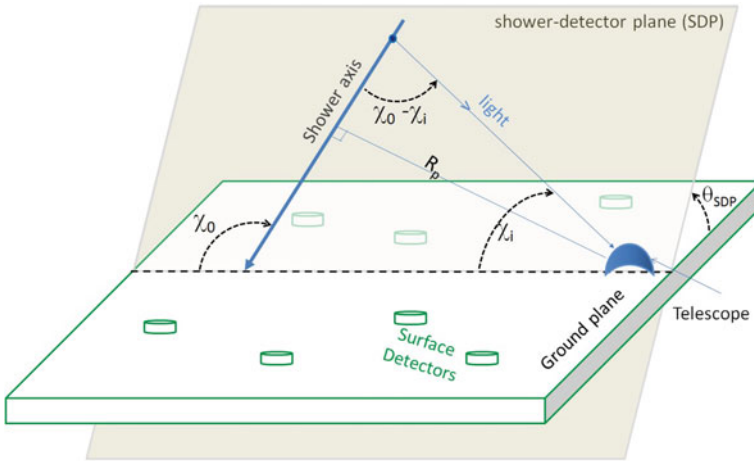


**Fig. 7.11** Geometry of the detection of an air shower by a fluorescence telescope

Fitting all the data for a given shower to this expression provides the desired geometrical values of the shower parameters.

It may happen that the fit fails or provides ambiguous solutions. If more than one telescope is available, the solution may be found by using the fact that each telescope provides its own shower-detector plane and the combined use of both planes provides easily the solution and constrains the geometry of the shower axis to within a fraction of a degree. This technique, used first by the HiRes experiment and more recently by the Pierre Auger Observatory, is known as *stereo reconstruction*. The other possibility is to complement the fluorescence detector with a surface shower detector. This provides independently the position of the impact point of the shower on ground and of the  $t_0$  parameter. This, known as the *hybrid technique*, has been used by both the Pierre Auger and the Telescope Array experiments.

When the shower geometry is determined, the fluorescence yield is proportional to the number of charged particles in the cascade at different depths  $X$  in the atmosphere. The total energy of the shower (dependent on the energy of the incident CR) is proportional to the sum of the light measured along the longitudinal development of the cascade. The depth in the atmosphere of the shower maximum,  $X_{\max}$ , is directly determined. Despite this fact, the identification of the parent primary nucleus originating the cascade cannot be done on a shower-by-shower basis because of intrinsic fluctuations (see Fig. 4.9). Even at the highest energies, the measured fluorescence profile can give information on the CRs chemical composition only through statistical methods.

## 7.7 UHECR Measurements with a Single Technique

Different experiment measured the CR flux above  $10^{18}$  eV. The pioneering **Volcano Ranch**, which took data from 1959 to 1963, and the **Yakutsk** array were already mentioned in Sect. 4.6. The **Sydney University Giant Air shower Recorder (SUGAR)** was the only operational in the Southern hemisphere, from 1968 to 1979. The **Haverah Park** array was operational in United Kingdom from 1968 to 1987. A detailed description of these array experiments and of early fluorescence detectors, as well as their results, can be found in Nagano and Watson (2000) and Sokolsky (2004).

The **Akeno Giant Air Shower Array (AGASA)** was the largest air-shower array before the advent of the Pierre Auger and Telescope Array detectors and it took data between 1984 and 2003. It consisted of 111 scintillation counters each having an area of  $2.2 \text{ m}^2$  and placed at a distance of  $\sim 1 \text{ km}$  from each other. Initially, AGASA was divided in four branches that operated individually. The four branches were unified in a single detector through an improved data acquisition system in 1995. This increased the effective detector area by a factor of 1.7 to reach  $100 \text{ km}^2$  of effective covered surface. 27 of the detector stations were equipped to detect also muons.

Each scintillator counter was viewed by a 125 mm diameter photomultiplier and serviced by a local module called the Detector Control Unit (DCU). The DCU had the function to record the arrival time and density of every incident shower and to monitor the performance of the detector (pulse-height distribution, voltage, counting rate, temperature, etc.). Several DCUs were connected in series to a common communication string consisting of two optical fibers. One of the two was used to send commands and the clock synchronization to the DCUs, the other to transmit triggers, shower data, and monitor data. In the Southeast corner of AGASA was the densely packed  $1 \text{ km}^2$  array Akeno, which studied the CR spectrum from below  $3 \times 10^{18}$  eV. The signal in the AGASA scintillator counters was produced by the electromagnetic component of the cascade with a small contribution from the shower muons. They used the methods described in Sect. 4.9 to estimate the primary CR energy, namely the particle density ( $\rho_{600}$ ) as measured 600 m from the shower axis.

The **HiRes observatory** improved the pioneering Fly's Eye. Two air fluorescence detectors (HiRes-I working from 1997; HiRes-II completed at the end of 1999) were located on two hills separated by 12.6 Km at an atmospheric depth of  $870 \text{ g cm}^{-2}$ . They operated on clear moonless nights with the typical fluorescence detectors duty cycle of about 10 %.

HiRes-I consisted of 21 telescope units with  $360^\circ$  view in azimuth. Each telescope was equipped with a  $5 \text{ m}^2$  spherical mirror and 256 phototube pixels at its focal plane. At the focus of each mirror a camera composed of 256 hexagonal photomultiplier tubes with 40 mm diameter was present, each tube viewing a  $\sim 1^\circ$  diameter section of the sky. Each telescope covered the elevation range between  $3$  and  $17^\circ$ . The phototubes were equipped with *sample and hold* electronics<sup>3</sup> which integrated the

<sup>3</sup> A sample and hold electronic circuit is an analog device that grabs (samples) the voltage of a continuously varying analog signal and stores (holds) its value at a constant level for a specified

fluorescence signal within a  $5.6 \mu\text{s}$  window, long enough to detect the whole signal from the shower.

Detectors on the HiRes-II site were similar to those of HiRes-I, but with twice as many mirrors organized in two rings covering an elevation from  $3$  to  $31^\circ$ . In addition, the HiRes-II phototubes were equipped with fast analog-to-digital converter electronics, which sampled the shower signal every  $100 \text{ ns}$ . This allowed the reconstruction of the shower geometry from timing alone with a precision of about  $5^\circ$ .

Although HiRes-I and HiRes-II could trigger and reconstruct events independently, an important fraction of events was measured stereoscopically, allowing the reconstruction of the shower geometry with a precision of  $0.4^\circ$ . HiRes-I and HiRes-II took data until April 2006 for an accumulated exposure in stereoscopic mode of  $3460 \text{ h}$ . The “monocular” mode had better statistics and covered a much wider energy range.

The parameter equivalent to the detector effective area for fluorescence detectors is the aperture (units:  $[\text{cm}^2 \text{ sr}]$ ). This parameter is dependent on the energy and mass number of the incoming CR. The HiRes Collaboration made extensive and detailed simulation of both the atmospheric cascade and their detector to study the aperture in the monocular and stereo modes and the systematic uncertainty in the estimations. The precision in the evaluation of the primary CR energy in monocular mode was better than  $20\%$  at energies above  $3 \times 10^{19} \text{ eV}$ .

To correctly evaluate the shower energy, an accurate measurement and monitoring of the environmental conditions and of the absolute gain of the telescopes was performed. Fluorescent light is in fact attenuated by molecular diffusion and aerosol scattering. While the former is approximately constant, the aerosol concentration varies rapidly. To monitor the aerosol content, nightly relative calibrations were performed with a laser connected to two mirrors and measuring the quantity of scattered light. In addition, monthly absolute calibrations were carried using a stable and standard light source.

The shower size on events measured by HiRes-I or HiRes-II was obtained by conversion of the photoelectron count at each atmospheric depth, using the known geometry of the shower, after correction for atmospheric attenuation. The sum of the counts over the atmospheric depth is proportional to the visible shower energy and thus to the primary CR energy. A correction factor (about  $10\%$ ) took into account the energy carried by particles that do not produce light, as the neutrinos.

### 7.7.1 Results from HiRes and AGASA

Globally, the number of UHECR events before the advent of the Pierre Auger Observatory (PAO) was too small, and the low statistics and large systematic uncertainties plagued a number of analyses based on this data set.

---

(Footnote 3 continued)

minimal period of time. Sample and hold circuits are typically used in analog-to-digital (ADC) converters.



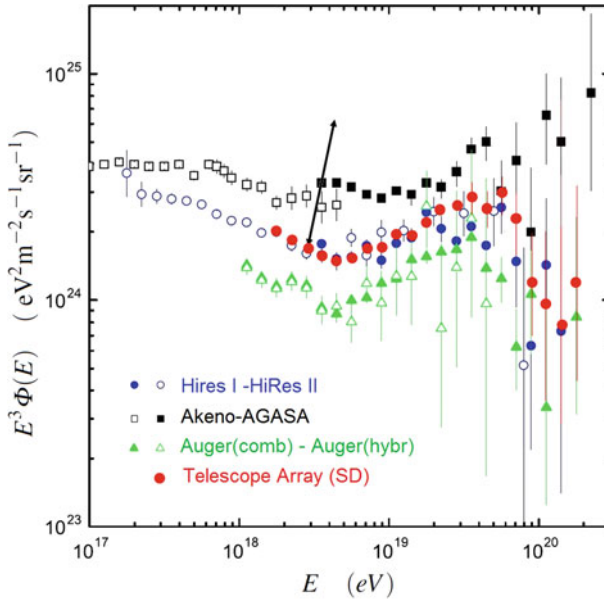


**Fig. 7.12** Flux of UHECRs multiplied by  $E^3$  as measured with Akeno-AGASA, HiRes, Telescope Array and the Pierre Auger Observatory. The values as published by the Collaborations using the nominal calibration of the detectors are reported. The end of the arrow on the first point of AGASA indicates the position of the point with a  $\pm 25\%$  shift in the energy scale

The HiRes energy spectrum was based on monocular observations with HiRes-I and HiRes-II (Abbasi et al. 2008) indicated by the blue bullets in Fig. 7.12. Most of the highest energy events were observed with HiRes-I. The CR spectrum measured by HiRes has two features: one at an energy of  $4 \times 10^{18}$  eV (the ankle) and another at  $5.6 \times 10^{19}$  eV. The second one corresponds to the expected feature from the GZK cut-off. Without the suppression, assuming a primary spectrum that continues as a power law with the same spectral index seen at lower energies, 43 events were expected above  $6 \times 10^{19}$  eV while only 13 events were observed. Using Poisson statistics, the number of observed events is 5.3 standard deviations away from that expected in absence of the UHECR suppression.

During its lifetime, AGASA has observed 11 events above  $10^{20}$  eV and zenith angle smaller than  $45^\circ$ . Differently from HiRes, the AGASA results (full squares in Fig. 7.12) seemed to indicate that the energy spectrum continues without a visible discontinuity beyond  $5 \times 10^{19}$ , in violation of the GZK effect (Takeda et al. 2003).

The discrepancy between the results of the two experiments was largely discussed before the advent of the PAO results. In fact, the HiRes spectrum was compatible with the existence of a UHECR suppression, while the AGASA spectrum did not. The ultrahigh energy events published by AGASA motivated the exotic top-down models of particle acceleration (see Sect. 7.12).

One possible explanation of the discrepancy between the two experiments is a possible bias on the energy assignment of the parent CR from one (or both) of the two methods. The energy in AGASA is estimated from the electromagnetic component of the shower with a small contribution from muons. In HiRes is determined from the observed development of the shower, with the critical parameter of the detector aperture.

One of the main objectives of a hybrid detector as the PAO was to disentangle these contradictory results. If one assumed wrong the AGASA result, the simplest interpretation of the HiRes result was that UHECRs are protons generated outside the local Superclusters of Galaxies (35 Mpc) where no reasonable accelerators seem to be present. The flux of protons above  $10^{20}$  eV is then attenuated by the GZK cut-off. On the other hand, if one assumed wrong the HiRes result, the non-evidence of a UHECR suppression could be due to heavier nuclei, or to their exotic production.

**Beware of the plots.** It is common to present the CR flux multiplied by  $E^\kappa$  to enhance deviations from a  $dN/dE \propto E^{-\alpha}$  power law. The proper choice is  $\kappa \simeq \alpha$  and for the UHECRs usually  $\kappa = 3$ , as in Fig. 7.12. In this representation, characteristic features such the ankle at  $\sim 10^{18.5}$  eV are more evident. However, it should be emphasized that scaling the flux with energy to some power could induce a bias on the interpretation of the results from the visual inspection of the figure. All experiments quote in fact a systematic uncertainty  $\Delta E$  on the estimated energy  $E$ . This means that points referring to a given experiment can be shifted along the  $x$ -axis by  $\pm \Delta E$ . Consequently, also points along the  $y$ -axis must be shifted by a quantity  $(1 \pm \Delta E/E)^3$ . As an example, if we assume that the AGASA points suffer from a 25% systematic overestimation of the energy, all points should be shifted left by a factor  $0.75 E$  along  $x$  and pushed down by  $(0.75)^3 = 42\%$  along  $y$  with respect to the nominal value. The arrow in Fig. 7.12 indicates such a shift for the first of the AGASA experimental points.

## 7.8 Large Hybrid Observatories of UHECRs

The Pierre Auger Observatory (PAO) is at present the largest operating CR observatory ever built. It was completed in 2008 and has been taking reliable data since 2004. The observatory is located in the southern hemisphere, in Argentina (province of Mendoza) at an average altitude of 1,400 m above sea level. It is based on the hybrid concept where both fluorescence and surface array detection techniques are used in order to combine and enhance the single detector capabilities and provide an accurate cross-check of systematic uncertainties of the two detection methods. The current layout of the PAO is shown in Fig. 7.13.

**The surface detector.** The surface detector (SD) array consists of 1,600 water Cherenkov detectors spaced by  $\sim 1.5$  km on a grid covering a total area of  $3,000 \text{ km}^2$ . 60 additional tanks were inserted inside the regular array with a smaller spacing



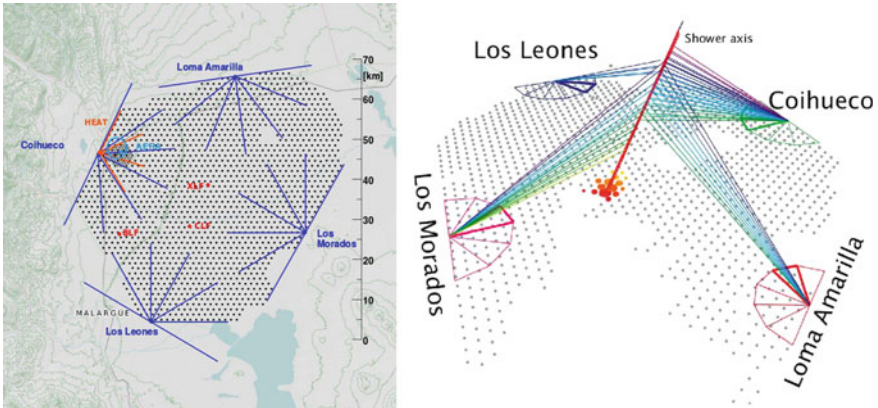


**Fig. 7.13** The Pierre Auger Observatory. On the *left*, the position and field of view of the fluorescence detector (FD) eyes surrounding the array is displayed. The *dots* mark the positions of the 1,600 surface detector (SD) tanks. On the *right* an event detected by the four FD eyes in coincidence with the SD array. Courtesy of the Auger Observatory (<http://www.auger.org/>)

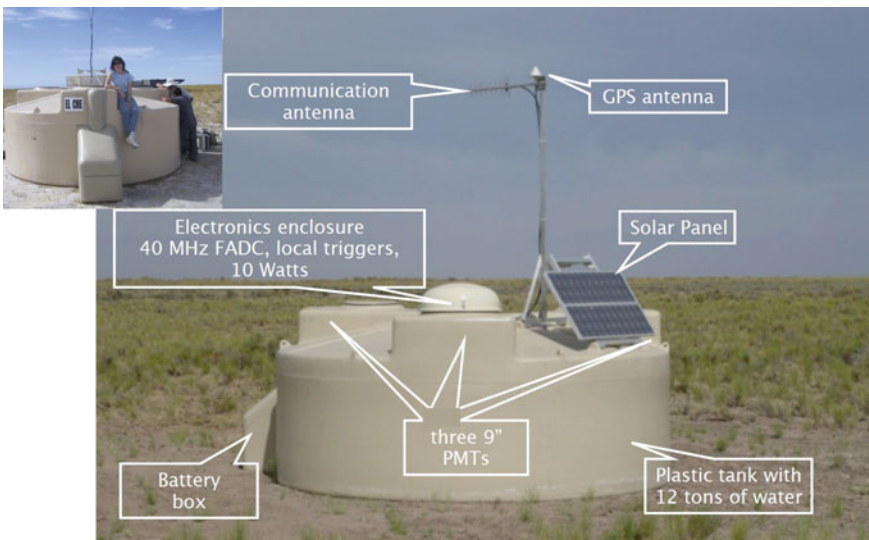


**Fig. 7.14** One of the SD water Cherenkov tanks. The inset gives an idea of the size of a tank. Courtesy of the Auger Observatory and of Dr. A. Castellina

(750 m) to extend the energy range to lower energies (down to  $3 \times 10^{17}$  eV). This denser array is coupled to the HEAT FD extension (see below).

Each tank of the SD array (Fig. 7.14) has a  $10\text{ m}^2$  surface and  $1.2\text{ m}$  depth of purified water. Each station is equipped with three PMTs to measure the Cherenkov light produced in the water, Flash Analog to Digital Converters (FADC), a data

acquisition and front-end electronic cards for control and trigger, a solar panel and two batteries for power, a Global Positioning System (GPS) receiver for the time tagging, and a custom radio emitter and receiver for trigger and data transfer. The station is connected with the **Central Data Acquisition System** in the Observatory building via a radio link to the nearest communication tower. The **SD** has a **100% duty cycle** and the height of the individual SD tanks allows to detect muons and to have excellent sensitivity to horizontal showers.

The **SD tanks** are **sensitive** to **muons, electrons, positrons, and photons**. A **vertical muon** in the tank **deposits** about **240 MeV** (the **muon energy loss in water is  $\sim 2 \text{ MeV/cm}$** ) while is on average only of **few tens of MeV** for **electrons**. The recorded signal in each detector is expressed in **vertical equivalent muon (VEM)** units. One VEM is the average of the signals produced in the 3 PMTs by a vertical muon that passes centrally through it. The atmospheric muon rate provides an in situ calibration of the PMT gains. Local triggers are sent to the Central Data Acquisition System where space-time coincidences of at least three tanks are required to trigger the apparatus and allow the permanent storage of the event.

The **position of the shower core** and the **lateral distribution function** are inferred with the techniques described in Sect. 4.8, see also Fig. 7.15. The **energy** of the primary particle is **correlated** with the signal at a fixed distance (1,000 m) from the core of the extensive shower. The signal at 1,000 m from the axis,  **$S(1,000)$** , corrected for the attenuation in the atmosphere, is used as an energy estimator. For a given energy, the value of  $S(1,000)$  decreases with the zenith angle of the incoming primary CR due to the attenuation of the shower particles and geometrical effects.

**The fluorescence detector.** The **fluorescence detector (FD)** uses the same detection method of HiRes and consists of **four eyes** (Fig. 7.13) each equipped with **6 telescopes** with a **field of view of  $\sim 30^\circ \times 30^\circ$**  in elevation and azimuth; they are observing

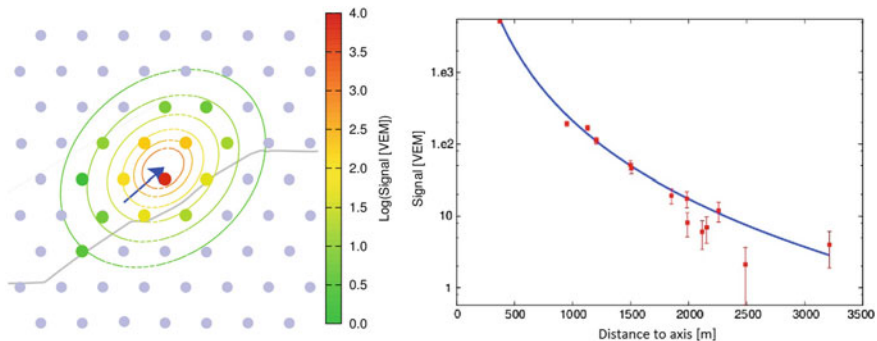


**Fig. 7.15** *Left* zoomed view of the Pierre Auger Observatory surface detector interested by a cascade. The quantity are expressed in terms of a vertical equivalent muon (VEM) crossing a tank. The *concentric lines* represent the distance from the axis shower with equal number of particles, obtained after reconstruction. *Right* fit of the event using the Auger Lateral Distribution Function. On the *y*-axis, the signal in units of VEM is proportional to the signal density  $\rho = \text{particles/cm}^2$  as a function of the distance from the axis shower. Courtesy of the Auger Observatory

the atmosphere above the ground array. This geometrical arrangement ensures full detection efficiency for showers originated by primaries with  $E > 10^{19}$  eV over the entire surface of the array.

The optical system consists of a diaphragm with an aperture of  $3.8 \text{ m}^2$  and a spherical mirror, which has an area of  $12 \text{ m}^2$  and a radius of curvature of 3.4 m. A camera consisting of 440 hexagonal PMTs arranged in a matrix is installed in the focal plane of the mirror. Each PMT forms a pixel of the camera and has a field of view of  $1.5^\circ \times 1.5^\circ$ .

The High Elevation Auger Telescopes (HEAT) consist of three tiltable fluorescence telescopes which represent a low energy enhancement of the FD system of the PAO. The installation of HEAT was finished in 2009 and data have been taken continuously since September 2009. By lowering the energy threshold by approximately one order of magnitude down to a primary energy of  $10^{17}$  eV, HEAT provides the possibility to study the CR energy spectrum and mass composition where the transition from galactic to extragalactic cosmic rays could probably occur.

As in HiRes, each fluorescence detector measures the total number of photons generated by an air shower from the fraction of the detected light. Calibrations are needed to accurately derive the fluorescence yield along the shower track taking into account the light scattering on aerosols in the atmosphere. An absolute calibration is done 3-4 times per year. A relative calibration is done every night of operation before and after data taking. Atmospheric properties are extensively monitored, also with a program of weather balloon launches.

The presence of surface and fluorescence detectors permits the measurement of the development profile of the air shower with the hybrid technique. The first step is the geometrical determination of the shower axis using directions and timing information from the FD pixels, coupled with the arrival time of the shower at the SD station with the highest signal.

The primary CR energy is determined by the FD in a calorimetric way using the reconstructed energy deposited along the shower profile. A correction factor of  $\sim 9\%$  includes the energy carried by high energy muons and neutrinos (invisible energy). The sub-sample of extensive air shower that are recorded by both the FD and the SD, called golden hybrid events, is used to relate the energy reconstructed with the FD,  $E_{\text{FD}}$ , to  $S(1,000)$  (see Fig. 7.16). The energy scale inferred from this data sample is applied to all showers detected by the SD array. The angular and energy resolution of hybrid measurements at 1 EeV is better than  $0.5^\circ$  and  $6\%$ , respectively, compared with about  $2.5^\circ$  and  $20\%$  for the surface detector alone.

The Telescope Array (TA) Observatory has been collecting data in the high desert in Millard County, Utah, USA since 2007 observing CRs with energies above  $10^{19}$  eV. It is a hybrid detector, mixing the information from both fluorescence detectors (FD) and surface detectors (SD) as in the case of PAO. The cosmic rays are observed at three fluorescence sites (FD) and with 507 surface detectors (SD) consisting of  $3 \text{ m}^2$  double layer scintillators powered by a solar panel. The SDs are located on a  $1.2 \text{ km}$  square grid covering a total area of  $762 \text{ km}^2$ . The array is divided into three parts that communicate with three control towers where information is digitized. A trigger is produced when the signals of three adjacent stations coincide

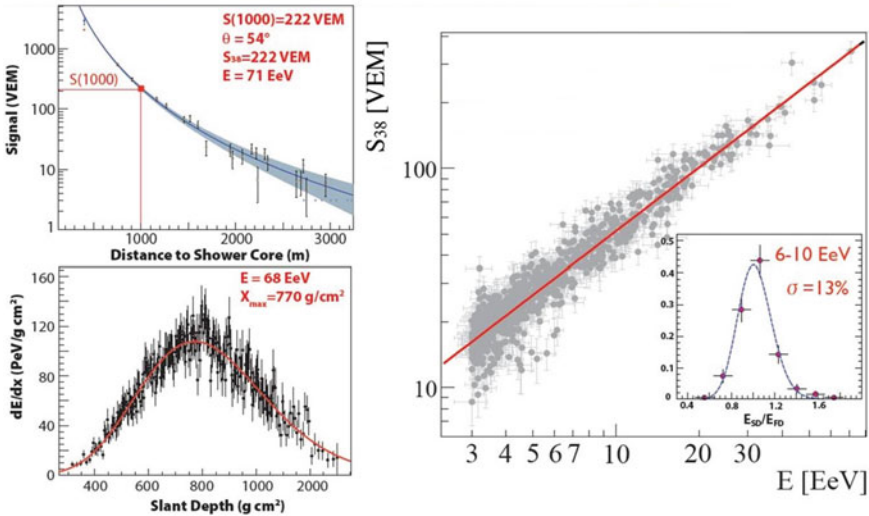


**Fig. 7.16** The *left side* shows one golden hybrid event from PAO. *Upper panel* the signal in the SD (in VEM units) as a function of the distance from the axis shower. The fit with the lateral distribution is also indicated with a line with error band. The SD information provide also the zenith angle of the incoming primary (in this case  $54^\circ$ ). The interpolated signal at 1,000 m is used to estimate the energy (71 EeV). The *left bottom panel* shows the energy loss as a function of the atmospheric slant depth as measured by the FD. The maximum of the shower occur at  $\sim 770 \text{ g cm}^{-2}$  and the estimated primary energy is 68 EeV. The *right panel* show the correlation between the energy reconstructed in golden hybrid events as presented at the ICRC conference in 2011. The energy from the FD is along the  $x$ -axis and that from the SD along the  $y$ -axis. The inset shows the distribution of the ratio between the two reconstructed energies and the estimated resolution. Courtesy of the Auger Observatory (<http://www.auger.org/>)

within  $8 \mu\text{s}$ . The SD reaches a full efficiency at  $5 \times 10^{18} \text{ eV}$  for showers having a zenith angle smaller than  $45^\circ$ . This corresponds to a SD acceptance of  $1,600 \text{ km}^2 \text{ sr}$ . The fluorescence sites are about thirty kilometers apart from one another, forming an approximately equilateral triangle. Two of them are new and consist of 12 telescopes viewing elevations from  $3^\circ$  to  $31^\circ$  and  $108^\circ$  in the horizontal field of view. Each telescope has a camera consisting of 256 PMTs with field of view of  $1^\circ \times 1^\circ$ . The signals are digitized by a 40 MHz sampling fast ADC converter and the waveforms are recorded when signals are found in 5 adjacent PMTs. The third station has 14 telescopes that use cameras and electronics from HiRes-I and mirrors from HiRes-II.

Currently, a low energy extension to the Telescope Array is under construction. TALE (the Telescope Array Low Energy extension) will allow the observation of CRs with energies as low as  $3 \times 10^{16} \text{ eV}$ . This is accomplished by adding 10 new high elevation angle telescopes, viewing up to  $72^\circ$ , to one of the telescope stations and adding a graded infill array of scintillator surface detectors.

## 7.9 The Flux of UHECRs

Almost at the same time as the final HiRes results, the first 3.5 years (2004–2007) of scientific data taking from PAO (Abraham et al. 2008) confirmed the existence of the UHECR suppression. The used data set had approximately four times the exposure of AGASA and 69 events above  $4 \times 10^{19}$  eV were measured while  $167 \pm 3$  were expected from an extrapolation of the power law measured at lower energies. Only 1 event above  $10^{20}$  eV was found, instead of 35 expected. Since then, the statistical sample has increased, confirming the early result.

As well as HiRes, PAO observes the shower profile with its fluorescence detectors, which have a 13% duty cycle compared to that of the surface detector. Using the correlation described on the right panel of Fig. 7.16, the energy derived from the fluorescence observations is correlated to the shower signal at 1,000m from the shower core measured with the SD, which is the least sensitive to the cosmic ray composition. In Fig. 7.12 the flux measured in the hybrid mode is shown by empty triangles. The result based on data from the surface detector array, with an energy calibration provided by the fluorescence detector, is shown by full triangles.

Recently, the Telescope Array collaboration has measured (Abu-Zayyad et al. 2013) the energy spectrum of UHECRs with energies above  $1.6 \times 10^{18}$  eV using four years of observation by the surface detectors. The spectrum shows a dip at an energy of  $4.6 \times 10^{18}$  eV and a steepening at  $5.4 \times 10^{19}$  eV, Fig. 7.12. To have an idea of the approximation involved in CR simulations, the energy scale of the SD determined from simulations can be reconciled with the calorimetric scale of fluorescence detectors by a renormalization of 27%. This result is in excellent agreement with that of the HiRes experiment.

Figure 7.17 shows a summary of all experimental results on the flux of UHECRs. In Fig. 7.12 the experimental points are plotted as they were presented in the original publications. Here, an (arbitrary) energy shift compatible with the quoted systematic error has been applied to all the experiments (Blümer et al. 2009). The figure demonstrates the importance of the systematic uncertainty on the experimental energy scale discussed above. Although the procedure is only motivated by a theoretical model and the value of the shift for each experiment is discretionary, after the shift a good overall agreement for almost all the different measurements is obtained.

The softening of the spectrum above  $\sim 5 \times 10^{19}$  eV is consistent with the GZK effect, but it does not necessarily represent an unambiguous proof that the cut-off has been discovered. The GZK cut-off at  $\sim 10^{20}$  eV necessarily implies that UHECRs are protons and not heavier nuclei. The discussion on the chemical composition of UHECRs given in the next section plays an important role. The softening of the spectrum can also be explained as an intrinsic feature of the source spectra themselves, indicating a maximum energy for the acceleration process.

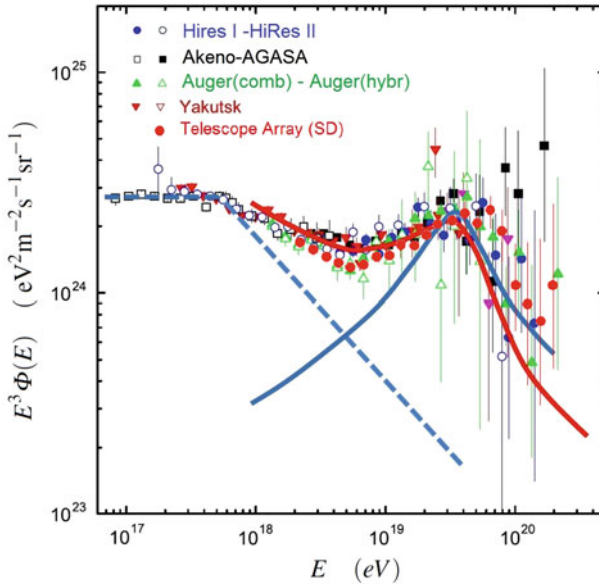


**Fig. 7.17** The same data as in Fig. 7.12 (with the inclusion of the Yakutsk experiment) after re-scaling the energy of the experiments to obtain a common position of the dip at  $\sim 5 \cdot 10^{18}$  eV. The underlying theoretical assumption is that the dip is due to the reaction  $p + \gamma_{\text{cmb}} \rightarrow pe^+e^-$  (Aloisio et al. 2012). The nominal energy scales of the experiments have been multiplied by 1.2 (Auger), 1.0 (HiRes), 0.75 (AGASA), 0.95 (TA) and 0.625 (Yakutsk) Superimposed, the prediction from two theoretical models [adapted from Letessier-Selvon and Stanev (2011)]. The red line represents the dip model due to extragalactic protons. The blue line the superposition model of a galactic (dashed line) plus an extragalactic component (full line)

## 7.10 The Chemical Composition of UHECRs

The determination of the charge (or mass) of the incoming primary UHECRs is difficult. Shower-to-shower fluctuations, which are larger for protons, prevent the individual measurement of the primary CR mass number. The general features of a cascade initiated by heavy nuclei are (Sect. 4.4.4): (i) the showers reach their maximum development higher in the atmosphere and (ii) they generate more muons than showers induced by a proton primary of equivalent energy. For this reason, at least two independent quantities must be measured to estimate the energy and mass of the primary cosmic ray that initiated the shower. This is usually achieved by observing either the longitudinal development of a shower (total number of photons and depth in atmosphere of the maximum) or by the simultaneous determination of the electromagnetic and muonic component of air shower at ground level.

The first analysis of the  $X_{\text{max}}$  energy dependence with fluorescence detector data was done with the Fly's Eye. The HiRes Collaboration published in 2005 an analysis of the UHECR composition above  $10^{18}$  eV with the same method. The depth of



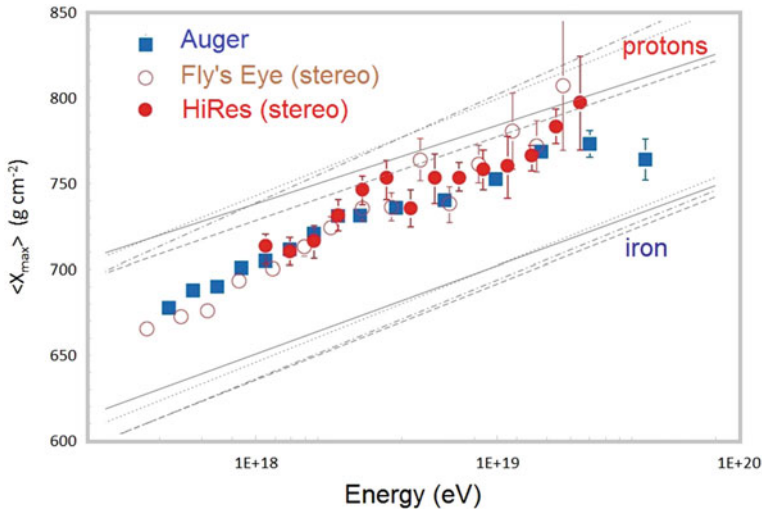


**Fig. 7.18** Position of the shower maximum  $X_{\max}$  versus energy. The measurements with fluorescence detectors HiRes, Pierre Auger Observatory and Fly's Eye compared to air shower simulations obtained using different hadronic interaction models: QGSJET-II (*solid line*), Sibyll2.1 (*dashed line*), QGSJET-I (*dotted line*), and EPOS 1.6 (*dashed-dotted line*). The Telescope Array data (missing in this compilation) are very close to those of HiRes

shower maximum as a function of the estimated energy of the incoming primary is shown in Fig. 7.18 that represents the high-energy section of Fig. 4.20. The HiRes result suggested a quick transition from heavy to light cosmic ray composition above few  $10^{18}$  eV. The Telescope Array measurement of the  $X_{\max}$  position is fully consistent with that of HiRes. Unfortunately this technique can be used only in clear, moonless nights and suffers from the lack of statistics at the highest energies.

The Pierre Auger Observatory published results based on hybrid events in 2010. Their results are somewhat in disagreement with those of HiRes. In their data, the cosmic ray composition becomes lighter up to  $2 \times 10^{18}$  eV and then consistently heavier up to the highest energy measured. This interpretation is confirmed by the analysis of the width of the  $X_{\max}$  distributions,  $\sigma(X_{\max})$ . As shown in Sect. 4.4.4, a wider  $\sigma(X_{\max})$  distribution for light primaries with respect to heavier ones is expected. In the PAO data while the  $\sigma(X_{\max})$  values from  $0.7 \times 10^{18}$  eV to  $5 \times 10^{18}$  eV look consistent with a light composition, at higher energies (up to the last point at  $4 \times 10^{19}$  eV) they are more consistent with a heavier composition. Note that data in Fig. 7.18 terminate before the region where the GZK effect starts to be effective. The chemical composition of CR above  $5 \times 10^{19}$  eV is completely unknown.

To improve the analysis, the Auger Collaboration is attempting to use the surface detectors (improved with fast electronic read-out) to study the muon composition of the shower (Sect. 4.8). The possibility to use also dedicated muon detectors in addition to the surface detectors is under study.

The interpretation of the  $X_{\max}$  and  $\sigma(X_{\max})$  data in terms of CR composition suffers from the fact that the experimental uncertainties are still too large. In addition, as mentioned in Sect. 4.5, hadronic interaction models play also an important role. The current models do not disagree with each other in the energy range studied by accelerators, and the incoming LHC results will improve the models used in the analyses.

The HiRes and Telescope Array results support the hypothesis that most of the CRs above  $10^{19}$  eV are likely protons of extragalactic origin and that the strong decline of the cosmic ray flux above  $\sim 5 \times 10^{19}$  eV is due to the interaction of primary protons with the CMB radiation background (the GZK cut-off). On the other hand, the PAO data seems to indicate a significant percentage of heavy elements in the UHECR composition. If confirmed, it might suggest that the structure above  $\sim 5 \times 10^{19}$  eV is caused by the presence of a limit on the acceleration (a maximum energy) at the CR sources, instead of propagation effects.

One related question is the origin of the dip at around  $5 \times 10^{18}$  eV, evident in Fig. 7.17. Most probably, the dip is at the intersection of the rise of the extragalactic component and the decline of the galactic one. In these superposition models, the extragalactic CRs have a flat spectrum (from  $\sim E^{-2}$  to  $\sim E^{-2.5}$ ) and the galactic ones have a steep (about  $\sim E^{-3.5}$ ) spectrum. Galactic cosmic rays, although in a minor way, contribute also above  $10^{19}$  eV (dashed line in Fig. 7.17).

A second hypothesis (the dip model) foresees that the dip is caused by  $e^+e^-$  pair-production by the extragalactic protons with the CMB (Sect. 7.5.3). The transition from galactic to extragalactic cosmic rays would, in this model, take place below  $10^{18}$  eV. The extragalactic CR had to be almost exclusively protons to allow  $e^\pm$  pair-production, and their injection spectrum be as steep as  $E^{-2.7}$ .

In both the above scenarios, the cosmological evolution of the Universe would not affect much the predicted spectra, because the observed UHECR have to be produced in a relatively small region of the visible Universe. This property seems to be common also to other, more complex, models (Allard 2012; Letessier-Selvon and Stanev 2011). The nature of UHECRs is an open research field; the lack of statistics and the large systematic uncertainties require long and detailed future studies.

## 7.11 Correlation of UHECRs with Astrophysical Objects

The study of the arrival direction distribution of the UHECRs has been used to search for possible identification of the sources. This possibility depends on the type of particle (protons or heavier nuclei) and on the intensity of the extragalactic magnetic fields. To date, no discrete source of ultrahigh-energy cosmic rays has been positively identified, and the arrival direction distribution of cosmic rays appears isotropic up to the highest energies.

Attempts to identify the sources of cosmic rays can be divided into three general categories: (i) searches for excesses from individual astrophysical objects or regions, for example the galactic center; (ii) searches for statistically significant correlations



of CR arrival directions with catalogs of astrophysical objects; (iii) searches for anisotropies in the CR arrival direction distribution itself, independent of any catalogs. These include searches for large-scale anisotropies or small-scale clustering.

Before the advent of HiRes, PAO and Telescope Array, some fine-tuning of the data set and the small number of events have led to a number of claims of anisotropies with marginal statistical significance. These early hypotheses have failed when tested with data from experiments with larger exposure and superior resolution, which ruled out several long-standing claims. See (Beatty and Westerhoff 2009; Letessier-Selvon and Stanev 2011) for a summary.

The statistics of high energy CRs increased significantly when the PAO started operations. The first study (Abraham et al. 2007) of arrival direction of UHECRs, based on data taken during the first years of operation, raised the attention of the scientific community. The PAO analysis links the arrival direction of CRs with energies above  $5.6 \times 10^{19}$  eV to AGN with redshift  $z < 0.018$  (corresponding to a distance of about 75 Mpc) from the twelfth edition of the catalog by Véron-Cetty & Véron. The maximum angular separation that defines a correlation is  $3.1^\circ$ . The thresholds on quoted values (energy, redshift and angular separation) were defined with a blind analysis (i.e. using Monte Carlo events and a small subset of data that was not used in the result) that maximized the discovery potential.

The statistical test on the null hypothesis (no correlation between arrival direction and the AGN catalog) had about 1% probability. It seemed to be the first indication for a correlation between CRs and sources. The same analysis was repeated with an exposure more than doubled with 27 selected high-energy events. Twenty of these events were within  $3.1^\circ$  of the AGN from the Véron-Cetty & Véron catalog when only 7.4 were expected for isotropic sources. The chance probability for this happening was  $\sim 2 \times 10^{-3}$ . An additional intriguing indication from the PAO data is that 13 events (in the 2011 data set) are coming from less than  $18^\circ$  from Centaurus A (Cen A), which is the nearest AGN at a distance of only about 3.8 Mpc, and two events very close to it.

The picture that emerged was that UHECRs are produced by nearby extragalactic sources; in addition the angular scale of the correlation, approximately  $3^\circ$ , indicates that deflections in magnetic fields are small.

Since its first publication, the PAO study on AGN correlation has been the subject of intense discussions. Some observations arise from the fact that the Véron-Cetty & Véron optical catalog includes many low power objects that are not likely to accelerate particles to such high energies. In addition, the PAO claim for a heavy chemical composition of UHECRs is contradictory with the correlation also with relatively near extragalactic sources. Nuclei with high  $Z_e$  suffer large angular deflections also for very small extragalactic magnetic fields. The PAO paper did not claim that the AGN from the used catalog are the sources of observed UHECRs, they only emphasized that sources may have a sky distribution similar to that of the correlating AGN.

A similar study in the northern sky with HiRes stereo data did not show significant correlations. However, the HiRes field of view is only partially overlapping with that of PAO and the Véron-Cetty & Véron catalog has different coverage of the corresponding fields of view.

The **excitation** about this **initial result** has **decreased** with time, because the **statistical significance** has **not increased** with the **increased PAO data sample**. At the 2013 ICRC the correlation has been marginally mentioned in the PAO report.

As a summary, it seems that the **following three results** suggested by the Pierre Auger Observatory data **cannot all be correct**: (1) There is genuine **anisotropy** (AGN correlation or excess in the Cen A region) **above 55 EeV**; (2) the anisotropic cosmic rays above 55 EeV are **dominated by heavy nuclei**; (3) the **energy spectra at sources** are **not** remarkably **hard**, and the CR **suppression** above  $\sim 10^{20}$  eV is due to the **GZK cut-off**.

## 7.12 Constraints on Top-Down Models

The results of **AGASA** about the **non-evidence of a change** of the **CR energy spectrum** above  $10^{20}$  eV **stimulated** many **theoretical ideas** about non-standard acceleration mechanisms. One very attractive scenario (at least for particle physicists) was the mere suppression of the astrophysics accelerators themselves. In these **top-down models**, UHECRs are **not accelerated** as such, but directly produced, via the **decay** of some **supermassive relic of the Big Bang**, or by the **collapse of topological defects**. These models necessarily imply the existence of **exotic particles** with **energies or masses largely exceeding  $10^{20}$  eV**. The disadvantage of top-down models is the replacement of the acceleration problem with the question of the nature and existence of such particles.

Parallel **implications** of top-down models are the **non-existence of a CR suppression** and the **prediction** of a **large flux** of **UHE  $\gamma$ -rays** and **neutrinos**. Around 2005, the UHECR suppression was observed by HiRes and PAO experiments, while the large flux of  $\gamma$ -rays and neutrinos was not. These **observational facts** have **strongly reduced the interest in the top-down models**.

Let us describe how it is possible to distinguish photon and neutrino showers from those induced by primary hadrons. For a **primary  $\gamma$ -ray** of energy  $\sim 10^{19}$  eV, the **average depth of shower maximum** is  $\sim 1,000 \text{ g cm}^{-2}$ , roughly  $200 \text{ g cm}^{-2}$  larger than for proton primaries. In addition, the corresponding **particle density** at a fixed distance is **smaller**. You can work-out these results using the arguments reported in Chap. 4.

The **Pierre Auger Observatory** has **set limits** on the presence of **primary photons** in the CR flux using the characteristics of both the surface (SD) and fluorescence (FD) detectors. A significant presence of photon primaries in the CR flux would in fact introduce a considerable bias in the energy determination based on the number of particles at a given distance from the impact point, i.e., the parameter  $S(1,000)$  used by the surface detectors. In addition, the **SD measures** the **radius of curvature** and the **spread of the arrival time** of the **shower front** at a fixed distance to the core, other quantities which behave differently for primary photons and hadrons. The **fluorescence detector** limit is based on the **direct measurement of  $X_{\max}$** . The result

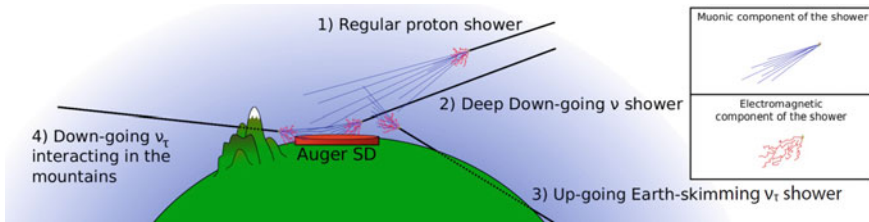


**Fig. 7.19** Near-horizontal or upward-going Earth-skimming showers are distinguished by the PAO by measuring the electromagnetic and muonic component of the shower using the surface detector array. Near *horizontal* proton cascades are depleted in the EM component, which is dominant for the  $\nu$ -induced cascades. Courtesy Auger Observatory (Guardincerri 2011)

is that a significant presence of UHECR photons as required by top-down models is excluded.

Also ultra-high energy neutrinos could be produced by top-down models. Since the neutrino cross-section grows with energy, PeV ( $= 10^{15}$  eV) and higher energy neutrinos cannot cross the Earth (see Sect. 10.5). The detection of a UHE neutrino is only possible if it interacts in close proximity to the detector and produces a cascade.

Based on searches for near-horizontal or upward-going Earth-skimming showers, upper limits on the electron neutrino flux have been published by the HiRes collaboration, and limits on the  $\nu_\tau$  flux by PAO using the SD array. If a nearly horizontal  $\nu_\tau$  with energy above  $10^{18}$  eV interacts in the mountains or the ground near the Observatory (see Fig. 7.19), the produced  $\tau$  lepton travels tens of kilometers before decaying and producing an air shower. Showers initiated by primary protons and nuclei from the horizontal direction reach ground level at a very large slant depth, so the electromagnetic component is nearly extinguished and only the muonic component survives. The shower signal is sampled with the Flash ADC system of the PAO SD and the analysis of its time structure allows identifying the presence of an electromagnetic component.

No candidates for Earth-skimming  $\nu_\tau$  event are seen up to now, and a 90% confidence level upper limit excludes also in this case most top-down models.

## 7.13 Summary and Discussion of the Results

The detection of the highest energies CRs (above a few tens of EeV) needs large, expensive arrays and a long lifetime of the experiments. At present, the lack of large statistics on two important observables, the chemical composition and the arrival direction, is the main problem. Both the composition and the anisotropies will tell us about the UHECRs sources and their distribution as well as about the involved acceleration mechanisms. The indetermination of the chemical composition also affects the interpretation of the change in slope of the cosmic ray energy spectrum at  $\sim 5 \times 10^{19}$  eV.

While the existence of the spectral softening is no longer questioned, its interpretation depends on the nature of primary UHECRs. The HiRes and Telescope Array measurements of air shower maximum development are compatible with protons. The PAO measurements up to  $3 \times 10^{19}$  eV, however, suggest a gradual change to a heavy composition. If the UHECR flux is dominated by protons, the most likely explanation of the slope change is the GZK cut-off. If the composition is increasingly heavier to the highest energies, the structure could be the result of the maximum acceleration rigidity having been reached at the sources.

The other salient feature of the UHE energy spectrum is the so-called ankle near  $4 \times 10^{18}$  eV, whose concavity (Fig. 7.17) is that expected for a simple transition between two power-law spectra. As such, it may correspond to the energy at which extragalactic cosmic rays become more abundant than cosmic rays originated within the Galaxy. Despite their enormous Larmor radius, the arrival directions of CRs at the ankle do not favor the galactic center region or the galactic plane. An alternative explanation for the structure is that UHE protons suffer gradual energy loss to  $e^\pm$  pair production by background microwave photons. The flux of extragalactic protons should exhibit a dip due to this propagation effect in the energy region of  $\sim 6 \times 10^{18}$  eV. The  $e^\pm$  dip occurs only in the case of extragalactic protons. Even a modest admixture of other nuclei or protons of galactic origin would preclude the salient feature being due to this particular energy loss mechanism.

We have also to mention that there is tentative evidence of a second knee in the energy spectrum below  $10^{18}$  eV, i.e., a softening of the spectrum before the hardening at the ankle, see Fig. 2.8. The Auger Observatory and Telescope Array are both attempting to make definitive measurements of the energy spectrum across that energy range, and the results can have implications for the interpretation of the ankle.

In conclusion, the available data from PAO on one hand, and Telescope Array and HiRes on the other, appear partially contradictory, and no model is able to explain in a coherent way all the observations (Sommers 2012). In particular, larger statistics is needed to confirm if the PAO excess on Cen A is really due to the first possible source candidate that may have been seen. The experimental effort needs to be pursued along at least three lines: (i) increasing the statistics by instrumenting larger surface arrays; (ii) improving the measurements by adding new detector components, i.e., muon detectors in the PAO surface detectors; (iii) covering the whole sky. To make definite progress, the next generation of detectors should be able to measure independently, and possibly redundantly, all shower components.

The expansion of the PAO and Telescope Array techniques to larger exposures seems unreachable without a significant budget increase. New experiments such as the proposed JEM-EUSO in space should be a great step forward by providing detailed sky maps at energies where the statistics are currently extremely low (<http://jemeuso.riken.jp/>).

## References

- R. Abbasi et al., (HiRes Coll.) First observation of the Greisen-Zatsepin-Kuzmin suppression. *Phys. Rev. Lett.* **100**, 101101 (2008)
- J. Abraham et al., (P. Auger Coll.) Correlation of the highest energy cosmic rays with nearby extragalactic objects. *Science* **318**, 938 (2007)
- J. Abraham et al., (P. Auger Coll.) Observation of the suppression of the flux of cosmic rays above  $4 \times 10^{19}$  eV. *Phys. Rev. Lett.* **101**, 061101 (2008)
- T. Abu-Zayyad et al., The CR energy spectrum observed with the surface detector of the telescope array experiment. *Astrophys J. Lett.* **768**, L1 (2013)
- F. Aharonian, A. Bykov, E. Parizot, V. Ptuskin, A. Watson, Cosmic rays in galactic and extragalactic magnetic fields. *Space Sci. Rev.* **166**, 97–132 (2012)
- D. Allard, Extragalactic propagation of ultrahigh energy cosmic-rays. *Astropart. Phys.* **39–40**, 33–43 (2012)
- R. Aloisio, V. Berezhinsky, A. Gazizov, Transition from galactic to extragalactic cosmic rays. *Astropart. Phys.* **39–40**, 129–143 (2012)
- F. Arqueros, J.R. Hoerandel, B. Keilhauer, Air fluorescence relevant for cosmic-ray detection-Review of pioneering measurements. *Nucl. Instrum. Methods Phys. Res. Sect. A* **597**, 23 (2008)
- J.J. Beatty, S. Westerhoff, The highest-energy cosmic rays. *Annu. Rev. Nucl. Part. Sci.* **59**, 319–345 (2009)
- J. Becker, High-energy neutrinos in the context of multimessenger astrophysics. *Phys. Rep.* **458**, 173–246 (2008)
- J. Blümer, R. Engel, J.R. Hörandel, Cosmic rays from the knee to the highest energies. *Prog. Part. Nucl. Phys.* **63**, 293338 (2009)
- S. Braibant, G. Giacomelli, M. Spurio, Particle and fundamental interactions. Springer, Berlin (2011). ISBN 978-9400724631
- Y. Guardincerri, The Pierre Auger observatory and ultra-high energy neutrinos: upper limits to the diffuse and point source fluxes. Contributions to the 32nd ICRC, Beijing, China (2011). [arXiv:1107.4805](https://arxiv.org/abs/1107.4805)
- M. Kachelriess, Lecture Notes on High Energy Cosmic Rays (2008). [arXiv:0801.4376](https://arxiv.org/abs/0801.4376)
- K. Kotera, A.V. Olinto, The astrophysics of ultrahigh-energy cosmic rays. *Annu. Rev. Astron. Astrophys.* **49**, 119–153 (2011)
- D. Kuempel et al., Geometry reconstruction of fluorescence detectors revisited. *Astropart. Phys.* **30**, 167 (2008)
- A. Letessier-Selvon, T. Stanev, Ultrahigh energy cosmic rays. *Rev. Mod. Phys.* **83**, 907 (2011)
- A. Muecke et al., Monte-Carlo simulations of photohadronic processes in astrophysics. *Comput. Phys. Commun.* **124**, 290–314 (2000). Also [arXiv:astro-ph/9903478](https://arxiv.org/abs/astro-ph/9903478)
- M. Nagano, A.A. Watson, Observations and implications of the ultrahigh-energy cosmic rays. *Rev. Mod. Phys.* **72**(3), 689–732 (2000)
- M. Ostrowski, Mechanisms and sites of ultra high energy cosmic ray origin. *Astrop. Phys.* **18**, 229–236 (2002)
- P. Sokolsky, Introduction to Ultrahigh Energy Cosmic Ray Physics. Westview Press, Boulder (2004). ISBN: 978-0813342122
- P. Sommers, Ultra-high energy cosmic rays: observational results. *Astropart. Phys.* **39–40**, 88–94 (2012)
- M. Takeda et al., Energy determination in the Akeno Giant air shower array experiment. *Astropart. Phys.* **19**, 447 (2003)
- D.F. Torres, L.A. Anchordoqui, Astrophysical origins of ultrahigh energy cosmic rays. *Rep. Prog. Phys.* **67**, 1663–1730 (2004)
- J.-H. Woo, C. Megan Urry, AGN black hole masses and bolometric luminosities. *Astrophys. Jour.* **579**, 530–544 (2002)

## Chapter 8

# The Sky Seen in $\gamma$ -rays

The presence of galactic magnetic fields makes it impossible to localize CR sources using charged particles. The only way to have information about their acceleration sites is by observing the neutral particles ( $\gamma$ -rays and neutrinos) generated by their interactions during acceleration. For this reason, this and the following two chapters are strictly related with the problem of the origin of the cosmic radiation.

In recent years, a new window has been opened on the observation of the electromagnetic component (the  $\gamma$ -rays) of the cosmic radiation up to the highest energies, Sect. 8.1. The development has been made possible by the availability of new detectors coming from technologies typical of experimental particle physics.

Gamma-rays are produced by a large variety of energetic astrophysical phenomena, including the interaction of CRs near the acceleration sites, Sect. 8.2. Astrophysical candidates for  $\gamma$ -ray production (Sect. 8.3) include supernova remnants, pulsars, and quasars. In most cases, electromagnetic radiation processes involving relativistic electrons (in the so-called *leptonic model*, Sect. 8.4) could explain the photon flux up to the highest energies, which presents a nonthermal emission with a characteristic double peaks distribution.

After a pioneering period [for a review of early experiments, see Thompson (2008); Thompson et al. (2012)], a real breakthrough for  $\gamma$ -ray astronomy was the launch in 1991 of the Compton Gamma Ray Observatory, Sect. 8.5, with different instruments on board. Nowadays, the scenario is dominated by few satellites, as Swift (launched in 2004), AGILE (2007) and, up to the highest energies detectable on space, by the Fermi-LAT (launched in 2008), Sect. 8.6. Unlike the sky at visible wavelengths, the  $\gamma$ -ray sky is dominated by a diffuse radiation originating in our Galaxy, Sect. 8.7, due to the propagation of CRs in the interstellar medium. In most cases, galactic and extragalactic sources appear as point-like objects, i.e., with angular dimensions much smaller than the resolution of the detectors, over the diffuse  $\gamma$ -ray background, Sect. 8.8.

In addition to these steady sources (although some of them present time variability in their intensity), flashes of  $\gamma$ -rays were discovered serendipitously as early as the beginning of the 1970. These Gamma Ray-Bursts (GRBs) are the brightest explosions in the Universe, observed at a rate of about 1/day. Their origin, classification, total

energy output and the  $\gamma$ -ray differential flux have been experimentally investigated only recently, Sect. 8.9. These objects are possible candidates as sources of ultra-high energy cosmic rays, as mentioned in the previous chapter.

Space experiments cover a very broad  $\gamma$ -ray energy region, extending from a few MeV to tens of GeV. However, beyond few hundreds of GeV the  $\gamma$ -ray fluxes are so small that the effective detection area of space-based experiments cannot provide adequate statistics, Sect. 8.10. The astrophysics studies of  $\gamma$ -rays at the highest energies rely on ground-based Imaging Cherenkov detectors, described in the next Chapter.

As almost standard, we use the definition “high energy” (HE) or “GeV” astronomy for the energy range from  $\sim 30$  MeV to  $\sim 100$  GeV, typically covered by space-based experiments. We will refer to “very high energy” (VHE), or “TeV” astronomy, for the range from 100 GeV to 100 TeV, covered by ground-based experiments.

## 8.1 The Spectral Energy Distribution (SED) and Multiwavelength Observations

A key role for the understanding of underlying physics processes in high-energy sources is played by the simultaneous observation of the same object using different experimental techniques, from radio to  $\gamma$ -rays. The electromagnetic emission is detected as incoming radiation over a wide range of photon energies (in the radio, microwave, infrared, visible, ...). At the highest energies that we are dealing with ( $\gamma$ -rays) individual photons are detected, and their energy estimated. It is convenient that the quantity of energy emitted by the source in a given region of the electromagnetic spectrum be represented in a unified way. Multiwavelength (or multifrequency) astrophysics gathers and interprets astronomical data collected using different instruments and detectors in many frequencies and/or energy bands. The *spectral flux density*

$$F(\nu) \text{ in units: } \text{erg cm}^{-2} \text{s}^{-1} \text{Hz}^{-1} \quad (8.1)$$

is the quantity that describes the rate at which energy is transferred by electromagnetic radiation through a real or virtual surface, per unit surface area and at a given frequency  $\nu$ . Always remember that frequency gives the corresponding energy, once multiplied by the Planck constant  $h$ .

When the electromagnetic energy at a given frequency  $\nu$  is measured as incoming radiation, the spectral flux density is determined using an appropriate detector of a given cross-sectional area  $A$  [ $\text{cm}^2$ ], pointing directly towards the source. If the detector is sensitive to a wide range of frequencies, a narrow band-pass filter placed in front of the detector is necessary to select only that radiation whose frequency lies within a very narrow range  $\Delta\nu$  centered on  $\nu$  and to measure the rate (erg/s) of the incoming electromagnetic energy. The measured rate is then divided by  $A\Delta\nu$  to obtain the spectral flux density (8.1).



When the electromagnetic emission from a source is measured through the detection of individual photons (the high-energy case), the energy  $E_\gamma$  of incoming photons must be determined. In most cases, the detector has an intrinsic efficiency  $\epsilon(E_\gamma)$  to detect photons of different energies. In this case, a quantity called effective area,  $A(E_\gamma)$ , is defined. The effective area is the geometrical area multiplied by the detection efficiency  $\epsilon(E_\gamma)$ . As these detectors measure the number of incoming photons in a given energy interval,  $\frac{\Delta n_\gamma}{\Delta E_\gamma}$  and in a given time interval  $T$ , the quantity equivalent to the spectral flux density (8.1) corresponds to

$$E_\gamma \frac{1}{A(E_\gamma) \cdot T} \frac{\Delta n_\gamma}{\Delta E_\gamma} = E_\gamma \frac{dN_\gamma}{dE_\gamma}, \quad \text{where } N_\gamma = n_\gamma / (T \cdot A). \quad (8.2)$$

The amount of power radiated through a given area in the given frequency interval  $\Delta\nu = \nu_2 - \nu_1$  or energy  $\Delta E_\gamma = E_2 - E_1$  in the form of electromagnetic radiation or individual photons, respectively, is the flux density

$$J(\nu) = \int_{\nu_1}^{\nu_2} F(\nu) d\nu; \quad J(E_\gamma) = \int_{E_1}^{E_2} E_\gamma \cdot \frac{dN_\gamma}{dE_\gamma} dE_\gamma \quad (\text{units: erg cm}^{-2}\text{s}^{-1}). \quad (8.3)$$

The flux density is the quantity that can be used to compare the electromagnetic energy emission in different regions of the electromagnetic spectrum as detected by different instruments. It is independent from the corpuscular or wavelike detection of the incoming radiation. Note that in most cases the  $F(\nu)$  and the  $(dN_\gamma/dE_\gamma)$  distributions can be represented by power-law functions, at least in a limited range of frequency or energy. In this case, the flux density in the considered frequency/energy range is given by

$$J(\nu) = \nu F(\nu); \quad J(E_\gamma) = E_\gamma^2 \cdot \frac{N_\gamma}{dE_\gamma} \quad (\text{units: erg cm}^{-2}\text{s}^{-1}) \quad (8.4)$$

The spectral energy distribution (SED) is a plot of the flux density  $J(\nu)$  versus frequency and/or  $J(E_\gamma)$  versus energy of the radiation. In some cases, the detected emission from a source starts in the radio frequency and ends in the TeV  $\gamma$ -rays. In this case, the SED for the source includes both measurement methods, and it can be plotted either as a function of frequency  $\nu$  or energy  $E_\gamma = h\nu$ . The radiative flux or radiation flux, is the amount of power radiated through a given area over the whole frequency/energy spectrum, also measured in  $(\text{erg cm}^{-2}\text{s}^{-1})$ .

The SED is used in many branches of astrophysics to characterize sources, as shown in the following sections and chapters.

## 8.2 Astrophysical $\gamma$ -rays: The Hadronic Model

A **direct signature** of the **presence** in astrophysical environments of accelerated **protons** is provided by the **presence** of **neutrinos** and of  **$\gamma$ -rays**. They are mainly generated in the **decay of charged and neutral pions**, respectively; these mesons are produced in **proton-proton collisions** via



where  $\dots$  represent the presence of higher mass mesons and baryons. Because the similarity with the process of production of secondary hadrons in a fixed-target accelerator experiment, process (8.5) is usually referred as the **astrophysical beam dump mechanism**. The **cross section** for (8.5) corresponds to **about 40–50 mb** [see Chap. 7 of Braibant et al. (2011)], and it is **dominated by inelastic processes** with **particles emitted with small transverse momentum** (*soft* or *low- $p_t$*  processes).

A **second process** which produces secondary mesons is due to **high-energy protons** interacting with **low-energy photons** in the surroundings of sources. The process (also called **photoproduction**) is similar to that discussed in Sect. 7.5.2 for **CR protons** interacting on **CMB photons**. **Around astrophysical sources** there is usually a **high density** of **radio, infrared, visible, and ultraviolet photons** (the **ambient photons**, denoted in the following as  $\gamma_e$ ). As discussed in the following, most ambient photons are produced by accelerated electrons in regions where high magnetic fields are present. The **photoproduction** occurs through the  **$\Delta^+$  resonance**:



and **cross section** (shown in Fig. 7.6) at the resonance of  **$\sim 0.250$  mb**. Although this cross section  $\sigma_{\gamma p}$  is **two orders of magnitude smaller** than the cross section  $\sigma_{pp}$  of the beam-dump process (8.5), in some astrophysical environments the probability that secondary mesons are produced by reaction (8.6) is much higher than the probability due to (8.5). This, because the **number density of ambient photons,  $n_\gamma$ , could be much larger** than that of **environmental matter number density,  $n$** , and the **event rate** for the latter process is  $\sigma_{pp} \cdot n \cdot c$ , while for the former is  $\sigma_{\gamma p} \cdot n_\gamma \cdot c$ . The fact that charged and neutral mesons are produced in beam-dump or in photoproduction processes, is dependent on the particular model of the considered astrophysical source.

**Secondary protons** may **remain trapped** because of **high magnetic fields**, while **neutrons** and the decay products of neutral and charged pions **escape**. **Neutrons** are not confined by magnetic fields, can escape the acceleration region and **turn into protons** through the weak interaction decay



Neutral pions decay into  $\gamma$ -rays, via the process:

$$\pi^0 \rightarrow \gamma\gamma \quad (8.8)$$

while the  $\pi^+$  mesons undergo the decay chain:

$$\begin{aligned} \pi^+ &\rightarrow \nu_\mu + \mu^+ \\ &\hookrightarrow \mu^+ \rightarrow \bar{\nu}_\mu + \nu_e + e^+ \end{aligned} \quad (8.9)$$

The energy escaping from the source is therefore shared among high-energy protons (=CRs),  $\gamma$ -rays and neutrinos produced by the decay of neutrons,  $\pi^0$  and  $\pi^+$  ( $\pi^-$ ), respectively.

To be observed, this energy partition between CRs,  $\gamma$ -rays and neutrinos requires the source to be transparent enough. A transparent source is defined as a source of a much larger size than the proton mean free path, but smaller than the meson interaction length. For these sources, protons have a large probability of interacting once, and most secondary mesons can decay.

Under these conditions, the mechanisms that produce CRs produce also neutrinos, Eq. (8.9) and high-energy photons, Eq. (8.8), and the candidate neutrino sources are in general also  $\gamma$ -ray sources. In this hadronic model there is a strong relationship between the spectral index of the CR energy spectrum  $\Phi_{\text{CR}}(E) \propto E^{-\alpha_{\text{CR}}}$ , and that of  $\gamma$ -rays and neutrinos. As derived in Sect. 11.2, the spectral index of secondary mesons (when their interaction processes can be neglected) is identical to that of the parent primary CRs. The same holds for the pion daughters ( $\gamma$ -rays and neutrinos) and thus:

$$\alpha_{\text{CR}} \sim \alpha_\nu \sim \alpha_\gamma \quad (8.10)$$

Hence  $\gamma$ -ray measurements give crucial information on primary CRs, and they constrain the expected neutrino flux.

### 8.2.1 Energy Spectrum of $\gamma$ -rays from $\pi^0$ Decay

While neutrinos will be discussed in Chap. 10, here we are interested in  $\gamma$ -rays produced by the decay of neutral pions, whose rest mass is  $m_\pi$ . Each photon has energy  $E_\gamma^* = m_\pi c^2/2 = 67.5 \text{ MeV}$  and momentum opposite to each other in the rest frame of the neutral pion. In the following, masses, momenta and energies are measured in the same units (GeV) using natural units ( $c = 1$ ). As the  $\pi^0$  has spin 0, the angular distribution of the emitted photons in pion rest-frame (or c.m. system) is isotropic, since there is no preferential direction and  $\frac{dN}{d\Omega^*} = \frac{1}{4\pi}$ , where  $d\Omega^*$  is the infinitesimal solid angle in the  $\pi^0$  c.m. system. In the laboratory system, the pion has a relative Lorentz boost with  $\beta = \frac{p_\pi}{E_\pi}$  and  $\Gamma = \frac{E_\pi}{m_\pi}$ .

For a given  $\beta$ ,  $\Gamma$ , the photon energy can be determined in the laboratory system (remembering that this system is seen by the pion with a negative velocity) using the Lorentz transformation:

$$E_\gamma = \Gamma E_\gamma^* + \beta \Gamma p_\gamma^* \cdot \cos \theta^* \quad (8.11)$$

from which one derives:

$$E_\gamma = \frac{E_\pi m_\pi}{m_\pi} \frac{1}{2} (1 + \beta \cos \theta^*) \quad \longrightarrow \quad E_\gamma = \frac{E_\pi}{2} (1 + \beta \cos \theta^*) \quad (8.12)$$

having used the relation  $p_\gamma^* = E_\gamma^*$  valid in the high-energy limit. Depending on the angle of emission in the c.m., the photon energy in the laboratory ranges between:

$$E_\gamma^{\min} = \frac{E_\pi}{2} (1 - \beta) \quad ; \quad E_\gamma^{\max} = \frac{E_\pi}{2} (1 + \beta). \quad (8.13)$$

For very high energy pions ( $\beta \approx 1$ ) these are very close to 0 and  $E_\pi$ , respectively. The shape of the energy spectrum of emitted photons in the laboratory frame,  $dN/dE_\gamma$ , is obtained by differentiating Eq. (8.11) with respect to the variable  $\cos \theta^*$ :

$$dE_\gamma = \beta \Gamma p_\gamma^* \cdot d \cos \theta^* \quad \longrightarrow \quad \frac{d \cos \theta^*}{dE_\gamma} = \frac{1}{\beta \Gamma E_\gamma^*} \quad (8.14)$$

from which one finds:

$$\frac{dN}{dE_\gamma} = \frac{dN}{d \cos \theta^*} \frac{d \cos \theta^*}{dE_\gamma} = \frac{1}{2} \frac{1}{\beta \Gamma p_\gamma^*}. \quad (8.15)$$

All quantities in (8.15) are constant for a given pion energy: that means that the probability to emit a photon of energy  $E_\gamma$  is constant over the range  $[E_\gamma^{\min}, E_\gamma^{\max}]$ . For many decaying  $\pi^0$ 's, the distribution of the number of photons is constant over the same energy range.

When a  $E^{-2}$  energy spectrum of accelerated protons at the source is considered, the  $\pi^0$ -decay spectrum for an observer in the laboratory frame in the  $E_\gamma^2 \frac{dN}{dE_\gamma}$  representation rises steeply below  $\sim 200$  MeV and approximately traces the energy distribution of parent protons at energies greater than a few GeV. This characteristic spectral feature is shown in Fig. 8.1 (green line), which shows the spectral energy distribution of photons emitted by different mechanisms. It is often referred to as the *pion-decay bump* and uniquely identifies the presence of  $\gamma$ -rays originated by  $\pi^0$ -decays. The discovery of the bump originated by the  $\pi^0$  decay in the source would identify the presence of high-energy protons, allowing a measurement of the spectrum of CRs directly at the source. In the figure, it is assumed that primary protons are accelerated up to  $\sim 1$  PeV, and that secondary  $\gamma$ -rays carry a few percent of the primary energy.

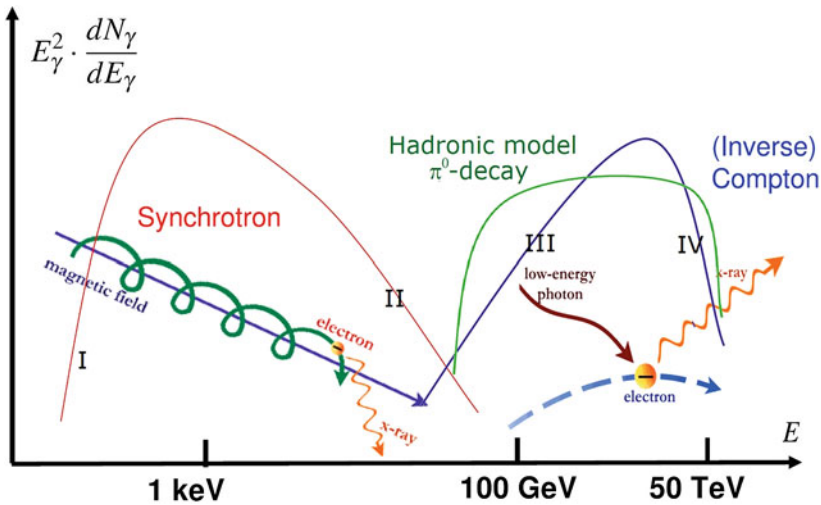


**Fig. 8.1** Spectral energy distribution of photons produced in leptonic/hadronic models. Synchrotron radiation is caused by relativistic electrons accelerated in a magnetic field. Photons from synchrotron emission represent also the target for inverse Compton scattering of the parent electrons. When hadrons interact with matter or ambient photons, a distribution of  $\gamma$ -rays from  $\pi^0$  decays as indicated by the *green* curve could be obtained. Superimposition of  $\gamma$ -rays from both leptonic and hadronic mechanisms is assumed in case of mixed models

### 8.3 Galactic Sources and $\gamma$ -rays

As widely discussed in Chap. 6, **Supernova Remnants (SNRs)** have long been thought to be the **main sources of galactic CRs** through the **diffusive shock acceleration** process. **The observation of  $\gamma$ -rays and neutrinos from SNRs is the most promising method of addressing the SNR paradigm for the origin of CRs.** The **detection of cosmic neutrinos is still problematic** (see Chap. 10), and the objective of **GeV–TeV  $\gamma$ -ray astronomy** is to identify the sources where protons (and nuclei) are accelerated, through the measurement of the  $\pi^0$ -decay into  $\gamma$ 's. The presence of  $\pi^0$ 's is the signature of the presence of accelerated hadrons interacting with the surrounding material or radiation fields.

There are **two epochs** in the evolution of a **supernova** when  **$\gamma$ -ray** and **neutrino emissions** are expected. The first is **shortly after the supernova explosion** and lasts about **2–10 years**. During this period, the density of the expanding supernova envelope is very high and the number **density of the surrounding matter** is **large enough** to allow **hadronic interactions**. The production of secondary particles will last for a long time, **until the supernova reaches the Sedov phase**, when most of accelerated **particles start escaping the acceleration region** and **enter the Galaxy as CRs**. Since **this phase lasts for more than 1,000 years**, there should be some **SuperNova Remnant (SNR)** that acts as  $\gamma$ -ray source.

### 8.3.1 A Simple Estimate of the $\gamma$ -ray Flux from a Galactic Source

We can estimate the expected  $\gamma$ -ray flux from hadronic production using a very simple approach. Let us assume that the energy density of CRs energetic enough to produce  $\gamma$ -rays corresponds to 10% of (2.33a), i.e.,  $\rho_{CR \rightarrow \gamma} = 0.1 \text{ eV/cm}^3$ . Consequently, the power of cosmic accelerators for this subsample of CRs is also one order of magnitude lower than (2.39), i.e.,  $P_{CR \rightarrow \gamma} \simeq 0.3 \times 10^{40} \text{ erg/s}$ . This rate of energy is provided by the sum of all cosmic accelerators occurred in our Galaxy in the last  $\tau_{\text{esc}} \sim 10^7 \text{ y}$ , which corresponds to the escape time (Sect. 5.1) of galactic CRs. If SNRs represent the accelerators, as their occurrence is of the order of one every  $t_{\text{SN}} = 100 \text{ year}$  then

$$N_{\text{acc}} = \tau_{\text{esc}} / t_{\text{SN}} \sim 10^5 \quad (8.16)$$

is the estimated number of explosions during the last ten million years. The power emitted as CRs by one individual explosion is

$$p_{CR \rightarrow \gamma} = \frac{P_{CR \rightarrow \gamma}}{N_{\text{acc}}} \simeq 3 \times 10^{34} \text{ erg/s}. \quad (8.17)$$

If sufficient target material is present around the accelerating source, a fraction  $\epsilon_{CR \rightarrow \gamma}$  of the CR energy is transferred to secondary particles by  $pp$  interactions (8.5). The appropriate estimate of  $\epsilon_{CR \rightarrow \gamma}$  depends crucially from the number density,  $n$ , of matter surrounding the source. For the interstellar medium,  $n$  is of the order of  $1 \text{ cm}^{-3}$  (Sect. 2.7.2). A reasonable guess for this unknown fraction could be  $\epsilon_{CR \rightarrow \gamma} \simeq 0.1$ . Under these assumptions, the power emitted by one source in the form of  $\gamma$ -rays is

$$L_{\gamma} = \frac{1}{3} \times \epsilon_{CR \rightarrow \gamma} \times p_{CR \rightarrow \gamma} \simeq 1 \times 10^{33} \text{ erg/s}. \quad (8.18)$$

The factor (1/3) takes into account the fact that only  $\sim 1/3$  of secondary particles in the hadronic shower are neutral mesons (mainly  $\pi^0$ ). If we consider a SNR at distance  $D = 1 \text{ kpc} = 3 \times 10^{21} \text{ cm}$ , the flux of energy arriving on Earth as  $\gamma$ -rays is

$$\frac{L_{\gamma}}{4\pi D^2} \simeq 0.9 \times 10^{-11} \text{ erg/(s cm}^2\text{)} \quad (8.19)$$

For a Fermi-like mechanism at sources, we expect an energy spectrum of the  $E^{-2}$ -type. In the hadronic mechanism of  $\gamma$ -ray production the energy spectrum of secondary particles follows that of the parent CRs. This is a consequence of the Feynman scaling discussed in Sect. 11.1. Therefore, we expect the number of arriving  $\gamma$ -rays  $dN_{\gamma}/dE_{\gamma}$  to decrease as  $E^{-2}$  and the quantity (8.19) corresponds to the  $E^2 dN_{\gamma}/dE_{\gamma}$ , for our hypothetic source. Hence, remembering that  $1 \text{ erg} = 1.6 \text{ TeV}$ , our estimated spectral energy distribution for a galactic SNR is

$$E_\gamma^2 \frac{dN_\gamma}{dE_\gamma} \simeq 1.4 \times 10^{-11} \text{ TeV}/(\text{s cm}^2) \quad \text{for } D=1 \text{ kpc}. \quad (8.20)$$

Detailed computations exist of the flux of TeV  $\gamma$ -rays from a hadronic model of particle acceleration in SNRs. The derived flux depends on explosion and acceleration parameters, on the properties of the ambient medium, and on the distance of the SNR. A noticeable model is due to Drury, Aharonian and Volk (Drury et al. 1994); they calculate that the expected integral flux of VHE  $\gamma$ -rays from SNRs generated from hadronic CR interactions above a given energy threshold  $E$  is

$$E_\gamma^{2.1} \frac{dN_\gamma}{dE_\gamma} \simeq 9 \times 10^{-11} \cdot \eta^{-2} \left( \frac{E_{\text{SN}}}{10^{51} \text{ erg}} \right) \cdot \left( \frac{D}{1 \text{ kpc}} \right) \cdot \left( \frac{n}{1 \text{ cm}^{-3}} \right) \text{ TeV}/(\text{s cm}^2). \quad (8.21)$$

where  $\eta$  is the efficiency of the particle acceleration (it has the role of  $\epsilon_{CR \rightarrow \gamma}$  in our computation),  $E_{\text{SN}}$  the total kinetic energy released during the supernova explosion,  $D$  the distance to the SNR and  $n$  the density of the interstellar medium surrounding the SNR. Here, the authors obtain a power law with a spectral index of 2.1 instead of 2. For the typical values used in the paper ( $\eta = 0.1$ ,  $E_{\text{SN}} = 10^{51} \text{ erg}$  and  $n = 1 \text{ cm}^{-3}$ ) the result of Drury et al. (1994) is remarkably in agreement with (8.20).

The number of such accelerators in the Galaxy which can be detected is not large. As SNRs can efficiently accelerate CRs for  $10^3$  y at most, the  $\gamma$ -rays are produced in a limited time interval. Taking into account their frequency ( $1/t_{\text{SN}}$ ), there could be order of tens of SNRs able to produce  $\gamma$ -rays in the whole Galaxy detectable in our epoch.

The discovery of a convincing case of a hadronic accelerator through the identification of  $\gamma$ -rays produced by  $\pi^0$ -decays is extremely difficult due to the additional  $\gamma$ -ray production mechanisms from relativistic electrons (Sect. 8.4). Gamma-rays originated from leptons can outnumber those produced by hadrons by a large amount. In particular, if the matter number density around the acceleration region is too low, no  $\gamma$ -rays from proton interactions are expected at all. A large effort is underway by the present generation of space- and ground-based experiments to identify the hadronic component of the  $\gamma$ -ray emission in SNRs, as we will see in the following chapter.

## 8.4 Astrophysical $\gamma$ -rays: The Leptonic Model

The basic interpretation for the production of high-energy photons in the *astrophysical leptonic model* is the so-called Self-Synchrotron Compton (SSC) mechanism. Synchrotron emission from electrons moving in a magnetic field generates photons with an energy spectrum peaked in a region ranging from the infrared to X-rays. Such photons in turn constitute a target for their own parent electron population. The process in which low-energy photons gain energy by collisions with high-energy electrons is the inverse Compton (IC) scattering. This mechanism



has the effect of increasing the photon energy, and is important in regions where accelerated electrons coexist with a high energy density of soft-photons. Since electrons in some astrophysical environments are ultra-relativistic with a Lorentz factor up to  $\Gamma = E/(m_e c^2) \sim 10^9$ , the energy of the scattered photon gets boosted by a factor  $\lesssim \Gamma$ . The energy distribution of  $\gamma$ -rays produced through the inverse Compton mechanism starting from an infrared/X-ray photon population can peak at GeV-TeV energies.

An astrophysical accelerator provides a continuous distribution of electron energies. As we know from Chap. 6, the energy spectra of cosmic rays and cosmic ray electrons can be approximated by power-law distributions. In the following, we assume the distribution of electron energies as

$$\frac{dN}{dE} dE = \kappa E^{-\alpha_e} dE, \quad (8.22)$$

where  $(dN/dE)dE$  is the number density of electrons in the energy interval  $E$  to  $E + dE$ . Concerning the units, the CRs power law intensity  $dN/dE$  is here measured in  $(\text{GeV cm}^2 \text{s})^{-1}$ . We consider fully isotropic emission, removing the dependence from the solid angle which usually explicitly appears in  $dN/dE$ . The constant provided by the integration over the solid angle is included in the coefficient  $\kappa$ .

Figure 8.1 shows the spectral energy distribution expected from high-energy electrons moving in a magnetic field. The resulting energy spectrum has two peaks. The first distribution is produced by the synchrotron emission of decelerated electrons; the second from the inverse Compton scattering of the same electrons with the produced radiation field. The high-energy part of the synchrotron radiation spectrum can be described by a power law with spectral index depending on the electron spectral index  $\alpha_e$ . The features of the distribution produced by the inverse Compton mechanism also depend on the synchrotron radiation spectrum and on  $\alpha_e$ .

In the following, we work out the behavior of the four branches indicated with I, II, III, IV in Fig. 8.1 using simply arguments. Fully detailed computations can be found in Longair (2011). The remaining part of this section can be skipped in a first reading.

### 8.4.1 The Synchrotron Radiation from a Power-Law Spectrum

The power emitted as synchrotron radiation from a relativistic electron of energy  $E$  moving perpendicularly in a region with magnetic field of intensity  $B$  was obtained in Sect. 5.8.1. Let us now work out the synchrotron emission spectrum for a power-law distribution of electron energies given by (8.22). We use the fact that the spectrum of synchrotron radiation is sharply peaked near the critical frequency  $\nu_c$  and that  $\Delta\nu$  is much narrower than the breadth of the power-law electron energy spectrum. In our simple approximation, the electron of energy  $E$  produces electromagnetic radiation

at the critical frequency  $\nu_c$ , which can be approximated using (5.66) by:

$$\nu_c = \Gamma^2 \nu_g = \left( \frac{E}{m_e c^2} \right)^2 \nu_g; \quad \text{with} \quad \nu_g = \left( \frac{eB}{2\pi m_e c} \right) \quad (8.23)$$

The flux density  $J(\nu)$  can be attributed to electrons with energies in the range  $E$  to  $E + dE$ , therefore:

$$J(\nu)d\nu = - \left( \frac{dE}{dt} \right) \left( \frac{dN}{dE} dE \right) = - \left( \frac{dE}{dt} \right) \kappa E^{-\alpha_e} dE. \quad (8.24)$$

$N(E)$  is measured in units  $(\text{cm}^2 \text{ s})^{-1}$  according to (8.22),  $\frac{dE}{dt}$  in (erg/s) and  $d\nu$  in  $\text{s}^{-1}$ . Thus, the quantity  $J(\nu)$  has units  $(\text{erg cm}^{-2} \text{ s}^{-1})$  as in (8.3).

Let us now consider the quantities on the right hand side of (8.24), remembering that the power loss  $-dE/dt$  was derived in Eq. (5.60):

$$E = \Gamma m_e c^2 = \left( \frac{\nu}{\nu_g} \right)^{1/2} m_e c^2, \quad (8.25a)$$

$$dE = \frac{m_e c^2}{2\nu_g^{1/2}} \nu^{-1/2} d\nu, \quad (8.25b)$$

$$-\frac{dE}{dt} = \frac{4}{3} \sigma_T c \left( \frac{E}{m_e c^2} \right)^2 \frac{B^2}{8\pi}. \quad (8.25c)$$

Inserting the numerical values into (8.25c) we have

$$-\frac{dE}{dt} = 0.4 \times 10^{-20} \left( \frac{E}{\text{GeV}} \right)^2 \left( \frac{B}{\mu\text{G}} \right)^2. \quad (8.25d)$$

The above quantities must be inserted into (8.24). Using the definition of  $\nu_g$  given in Eq. (8.23) and after some algebra, the flux density as a function of the frequency  $\nu$  is expressed in terms of the normalization constant  $\kappa$ , the magnetic field intensity  $B$  and of fundamental constants:

$$J(\nu) = (\text{constants}) \cdot \kappa \cdot B^{(\alpha_e+1)/2} \cdot \nu^{-(\alpha_e-1)/2}. \quad (8.26)$$

The quantity  $J(\nu)$  has a correspondence to the energy distribution (8.4) when  $E_\gamma = h\nu$  and

$$E_\gamma^2 \frac{dN_\gamma}{dE_\gamma} \propto E_\gamma^{-a} \quad \text{where} \quad a = (\alpha_e - 1)/2. \quad (8.27)$$

The SED for the synchrotron radiation also depends upon the magnetic field as

$$E_\gamma^2 \frac{dN_\gamma}{dE_\gamma} \propto B^{(\alpha_e+1)/2} = B^{a+1}. \quad (8.28)$$

The relation (8.27) accounts for the branch II in Fig. 8.1. If the electron spectrum is described by  $\alpha_e \simeq 2$ , it is  $a \simeq 1/2$  and the synchrotron spectrum behaves as  $\propto E_\gamma^{-1/2}$ . The spectrum decreases with increasing photon frequency/energy. However, this distribution has odd behavior for  $E_\gamma \rightarrow 0$ .

### 8.4.2 Synchrotron Self-Absorption

The above infrared divergence can be corrected by statistical thermodynamics considerations. The synchrotron emission is nonthermal, but the presence of matter in the region where the magnetic field is present modifies the emission spectrum. Matter is able to absorb part of the radiation, reaching at equilibrium a given effective temperature, as explained below.

According to the principle of detailed balance, for every emission process there is a corresponding absorption mechanism. In the case under consideration, to synchrotron radiation corresponds synchrotron self-absorption. Let us give a simple order-of-magnitude calculation of the basic physics of the process. If the source of synchrotron radiation has a power-law spectrum  $J(\nu)$  its flux density  $S(\nu) \propto J(\nu) \propto \nu^{-a}$ . We can define the brightness temperature,

$$T_b = (\lambda^2/2k)(S_\nu/\Omega) \propto \nu^{-(2+a)}, \quad (8.29)$$

where  $\Omega$  is the solid angle the source subtends at the observer. We recall that the brightness temperature  $T_b$  is defined using the expression for the intensity  $I_\nu$  of black-body radiation

$$I_\nu = \frac{S_\nu}{\Omega} = \frac{2h\nu^3}{c^2} \frac{1}{e^{(h\nu/kT_b)-1}} \simeq \frac{2kT_b}{\lambda^2} \quad (8.30)$$

where the last equality holds in the Rayleigh–Jeans limit. The accelerated electrons follow a power-law energy distribution and are not in thermal equilibrium. However, we can associate a temperature  $T_e$  with electrons of a given energy through the relativistic formula relating electron energy to temperature

$$\Gamma m_e c^2 = 3kT_e \quad (8.31)$$

where  $k$  is the Boltzmann constant. As a result, the effective temperature  $T_e$  of the electrons now becomes a function of their energy. Since  $\Gamma \propto (v/v_g)^{1/2}$  then

$$T_e \sim (m_e c^2/3k)(v/v_g)^{1/2}. \quad (8.32)$$

For a source with self-absorption processes, the brightness temperature of the radiation must be equal to the effective kinetic temperature of the emitting electrons,  $T_b = T_e$ , and therefore, in the Rayleigh–Jeans limit

$$S_\nu = \frac{2kT_e}{\lambda^2} \Omega = \frac{2m_e}{3v_g^{1/2}} \Omega v^{5/2} \propto v^{5/2} \cdot B^{1/2}. \tag{8.33}$$

This computation shows the physical origin of the suppression at low-frequency of the expected spectrum in sources in which synchrotron self-absorption is important. As  $J(\nu) \propto S_\nu \simeq \nu^{5/2}$ , in terms of the photon energy distribution

$$E_\gamma^2 \frac{dN_\gamma}{dE_\gamma} \propto E_\gamma^{5/2} \tag{8.34}$$

At low energies (branch I of Fig. 8.1) the SED of the synchrotron emission is not anymore divergent. Note also that the spectral form  $J(\nu) \propto \nu^{5/2}$  is independent of the spectrum of the emitting electrons, if the magnetic field is uniform.

The synchrotron spectra are observed in different astrophysical environments, in our Galaxy, in nuclei of active galaxies and quasars. An important aspect of these observations (from radio to the X-rays) is that they provide unambiguous evidence for the presence of relativistic electrons in the source regions.

Inserting the numerical values in the expression for the critical frequency  $\nu_c$ , we obtain

$$\nu_c = \Gamma^2 \frac{eB}{2\pi m_e c} = 2.8 \times 10^6 \Gamma^2 B \text{ Hz} \tag{8.35}$$

when  $B$  is measured in Gauss. It is easy to work out that for a magnetic field of  $B \sim 100 \mu\text{G}$  (as that estimated for the Crab pulsar, Sect. 9.5), and for 1 TeV electrons ( $\Gamma \sim 10^6$ ), the critical frequency corresponds to photon energies  $E_\gamma = h\nu_c$  of the order of a fraction of eV.

### 8.4.3 Inverse Compton Scattering and SSC

The inverse Compton (IC) scattering is the process in which ultra-relativistic electrons scatter low energy photons so that the photons gain energy at the expense of the kinetic energy of the electrons. The Feynman diagram of this process is similar to that of the Compton effect and the corresponding computation of the transition probabilities are similar. The interaction occurs with photons of a radiation field  $u_{\text{rad}}$  (in the rest of frame of the Galaxy and thus of the observer). The energy radiated by an electron is proportional to the total intensity of target radiation field and

$$- \left( \frac{dE}{dt} \right) = \sigma_T c u'_{\text{rad}} [\text{cm}^2][\text{cm/s}][\text{erg cm}^{-3}] \tag{8.36}$$

(in square brackets the units) where  $u'_{\text{rad}}$  is the energy density of radiation in the rest frame of the moving electron, with Lorentz boost  $\Gamma$ . The energy  $\epsilon'$  of the interacting photon is much less than  $m_e c^2$  and consequently the Thomson scattering cross section can be used to describe the photon-electron interaction. We must consider the relativistic effects between  $u'_{\text{rad}}$  and  $u_{\text{rad}}$ . The energy density of target photons in the laboratory frame is simply  $u_{\text{rad}} = n(\omega) \cdot \hbar\omega = n(E) \cdot E$ . The quantity  $n(E)$  is the number density of particles with energy between  $E$  and  $E + dE$ . Thus, the number of photons in the differential three-volume  $dN(E) = n(E) \cdot dx dy dz$  is a relativistic invariant. Because the four-volume element  $dt dx dy dz$  is also a relativistic invariant, the quantity  $n(E)$  behaves as the time-like component of a four-vector (it has the same Lorentz transformation as the time variable). Also the energy  $E$  is the time-like component of a four-vector. For this reason,  $E' = \Gamma E$  and  $n'(E') = \Gamma n(E)$ . Thus

$$u'_{\text{rad}} = n'(E') \cdot E' = \Gamma n(E) \cdot \Gamma E = \Gamma^2 u_{\text{rad}}. \tag{8.37}$$

By inserting this result into (8.36) we obtain

$$- \left( \frac{dE}{dt} \right) \simeq \frac{4}{3} \sigma_T c \Gamma^2 u_{\text{rad}}, \tag{8.38}$$

where the factor  $4/3$  arises from averaging over the possible directions between the electrons and the photons. This result holds until  $\Gamma \epsilon \ll m_e c^2$ .

Notice the remarkable similarity of the result (8.38) to the expression (5.60) for the energy loss rate of the ultra-relativistic electrons by synchrotron radiation. The reason for this is that the energy loss rate depends on the electron acceleration in its rest frame. It does not matter if the acceleration is produced by the electric field  $\mathbf{v} \times \mathbf{B}$  due to motion of the electron through the magnetic field (as in the synchrotron radiation) or by the electric fields of the electromagnetic waves incident upon the electron (as in the inverse Compton scattering).

The derivation of the spectrum of the scattered radiation is outside the scope of this book, and can be found in Longair (2011). The flux density  $J(\nu)$  for an electron incident on a region where an isotropic and monochromatic field of photons of frequency  $\nu_0$  is present may be written as

$$J(\nu) \simeq \frac{3\sigma_T c}{16\Gamma^4} \frac{N(\nu_0)}{\nu_0^2} \cdot \nu \tag{8.39}$$

where  $N(\nu_0)$  is the number density of photons in the laboratory frame. At low frequencies, the scattered radiation has a spectrum of the form  $J(\nu) \propto \nu$  or  $E_\gamma^2 (dN_\gamma/dE_\gamma) \propto E_\gamma$ , and this behavior is represented by branch III of Fig. 8.1.

The maximum energy that a photon can acquire corresponds to a head-on collision, in which the photon is scattered back along its original path, and can be determined using the kinematics of the Compton effect. Assuming an initial energy  $\epsilon$ , after the collision the maximum energy is

$$(E_\gamma)_{\max} = \epsilon \Gamma^2 (1 + v/c)^2 \simeq 4\Gamma^2 \epsilon \quad (8.40)$$

It is easy to work out that, averaging over all relative photon-electron directions, the average energy of the scattered photons is

$$\overline{E}_\gamma = \frac{4}{3} \epsilon \Gamma^2 \quad \text{for } \Gamma \epsilon \ll m_e c^2 \quad (8.41)$$

This result is valid when the electron-photon interaction can be described using the Thomson cross section, i.e., until the condition  $\epsilon \cdot \Gamma \ll m_e c^2$  holds. For highly relativistic electrons, when this condition is no more satisfied, the Klein-Nishina cross section for photon-electron scattering must be used. In the ultra-relativistic limit, the Klein-Nishina cross section is

$$\sigma_{KN} = \frac{\pi^2 r_e^2}{h\nu} \left( \ln 2h\nu + \frac{1}{2} \right). \quad (8.42)$$

The Klein-Nishina cross section decreases as  $\propto (h\nu)^{-1}$  at high energies. Consequently, high energy scatterings result in significantly reduced luminosities as compared with the nonrelativistic calculation. In this high-energy limit, the average energy of the scattered photons replacing (8.41) is

$$\overline{E}_\gamma = \frac{1}{2} E_e \quad \text{for } \Gamma \epsilon \gg m_e c^2 \quad (8.43)$$

The general result (8.41) that the frequency/energy of photons scattered by ultra-relativistic electrons with Lorentz factor  $\Gamma = E/(m_e c^2)$  is increased by  $\Gamma^2$  (in the Thomson regime) is of profound importance in high energy astrophysics. Different classes of astrophysical sources can provide accelerated electrons observed in the cosmic radiation, at least up to the TeV scale (see Sect. 3.9). This corresponds to  $\Gamma = 10^6$ . More frequent are situations in which  $\Gamma = 10^2 - 10^3$ .

Radio, infrared and optical photons scattered by electrons with  $\Gamma = 1,000$  have then average frequency (or energy) roughly  $10^6$  times that of the incoming photons. In all situations, the condition  $\Gamma \epsilon \ll m_e c^2$  holds. Radio photons with  $\nu_0 = 10^9$  Hz become ultraviolet photons with  $\nu = 10^{15}$  Hz (eV-scale photons); scattering on far-infrared photons with  $\nu_0 \simeq 10^{12}$  Hz, typical of the photons seen in galaxies which are powerful far-infrared emitters, produce X-rays with keV energies; optical photons with  $\nu_0 = 4 \times 10^{14}$  Hz become  $\gamma$ -rays of the MeV energy-scale. The inverse Compton scattering process is an effective means of creating very high energy photons. On the other hand, the process is highly efficient to reduce the energy of high energy electrons whenever large fluxes of photons and relativistic electrons occupy the same volume.

The similarity of the synchrotron and inverse Compton scattering processes noticed by the similarity between (8.38) and (5.60) for the mean energy loss rate means that we can use the results of Sect. 8.4.1 to work out the spectrum of radiation

produced by a power-law distribution of electron energies. We assume that  $\alpha_e$  is the spectral index of the electron energy spectrum incident on the radiation field with photon energy  $\epsilon$ . The corresponding spectral index of the scattered radiation becomes  $a = (\alpha_e - 1)/2$  in the Thomson limit. Thus, for electron energies in the Thomson regime, the spectral energy distribution:

$$E_\gamma^2 \frac{dN_\gamma}{dE_\gamma} \propto E_\gamma^{-\frac{\alpha_e-1}{2}} \quad \text{for } \Gamma\epsilon \ll m_e c^2 \quad (8.44a)$$

In the ultra-relativistic Klein–Nishina regime, the corresponding relation becomes:

$$E_\gamma^2 \frac{dN_\gamma}{dE_\gamma} \propto E_\gamma^{-\alpha_e} \ln(E_\gamma) \quad \text{for } \Gamma\epsilon \gg m_e c^2 \quad (8.44b)$$

Note that in the ultra-relativistic limit (corresponding certainly to TeV photons), the spectral index of the SED is almost exactly that of the accelerated parent electrons.

In the SSC mechanism, the processes of synchrotron radiation and inverse Compton are strongly correlated. An increase of the first increases also the number density of target photons. At equilibrium, we can assume that the ratio between the rates of energy loss of an ultra-relativistic electron by synchrotron and inverse Compton radiation in the presence of a photon energy density  $u_{\text{rad}}$  and a magnetic field of intensity  $B$  is constant:

$$\frac{(dE/dt)_{\text{IC}}}{(dE/dt)_{\text{sync}}} = \frac{u_{\text{rad}}}{B^2/8\pi} \quad (8.45)$$

having used the relations (8.38) and (5.60). Estimates of the magnetic field intensity can be obtained by the observations of the synchrotron spectrum from the radio band up to the X-rays. With high magnetic fields, the inverse Compton component is largely suppressed, as most of the electron energy is lost in the synchrotron emission.

Models of synchrotron self-Compton sources are worked out numerically and are strongly dependent upon the input assumptions. These computations assume that the source of radiation is stationary. Detailed predictions of the photon flux for both mechanisms (synchrotron and IC) can be derived, as we show for the case of the Crab nebula (Sect. 9.5). Many  $\gamma$ -ray sources are variable over short time-scales and display the features expected from synchrotron self-Compton radiation, but they must also involve relativistic bulk motions of the source regions to account for their extreme properties. As a consequence, the predictions are somewhat model-dependent.

In addition to synchrotron self-Compton, the external synchrotron radiation foresees electron scattering on radiation fields not produced by the primary electrons itself. The cosmic microwave background radiation can represent a target for high energy electrons. In the case of external synchrotron radiation, the constraints derived from relation (8.45) do not hold.



## 8.5 The Compton Gamma Ray Observatory Legacy

Following the Hubble space telescope, the **Compton Gamma-Ray Observatory (CGRO)** was the second of NASA's great observatories to cover the widest interval of the electromagnetic radiation. It was launched using the Space Shuttle Atlantis on April 5, 1991 and operated successfully until it was de-orbited on June 4, 2000. A listing of the observations, along with other information about CGRO, can be found at the **CGRO Science Support Center Web site** <http://cossc.gsfc.nasa.gov/docs/cgro/index.html>. The Hubble and the CGRO observatories have been followed (delayed in time) by the launches of the NASA's Advanced **X-ray** Astrophysics Facility (**Chandra**) and the **Spitzer** Space Telescope (**Infrared**) when the CGRO mission was essentially complete.

The **CGRO** carried **four instruments** for  **$\gamma$ -ray astronomy**, each with its own energy range, detection technique, and scientific goals, **covering energies** from less than **15 keV** to more than **30 GeV**, **over six orders of magnitude** in the **electromagnetic spectrum**. The four instruments were:

- The **Burst and Transient Source Experiment (BATSE)**. BATSE was the smallest of the CGRO instruments, consisting of **eight modules** located one on each corner of the spacecraft. Each unit included a large flat **NaI(Tl) scintillator** and a **smaller thicker scintillator** for spectral measurements, combined to cover an **energy range** from **15 keV** to over **1 MeV**.
- **Oriented Scintillation Spectrometer Experiment (OSSE)**. It used **four large, collimated scintillator detectors** to study  $\gamma$ -rays in the range from **60 keV** to **10 MeV**. OSSE **mapped the 0.5 MeV line from positron annihilation** and provided detailed **measurements of many hard X-ray/soft  $\gamma$ -ray sources**.
- The **Compton Telescope (COMPTEL)** detected, **for medium energy  $\gamma$ -rays** between **0.8 and 30 MeV**, used a Compton scattering technique. Among its results, COMPTEL **mapped the distribution of radioactive Aluminum-26 in the Galaxy**, showing the locations of newly formed material.
- The **Energetic Gamma Ray Experiment Telescope (EGRET)** was the high-energy instrument on CGRO, covering the energy range from **20 MeV** to **30 GeV**.

### 8.5.1 The EGRET $\gamma$ -ray Sky

In the energy range **above 10 MeV**, the **principal** interaction **process** for  $\gamma$ -rays is **pair production**. Gamma rays cannot be reflected or refracted and a high-energy  $\gamma$ -ray telescope detects  $e^\pm$  with a precision converter-tracker section followed by a calorimeter.

The operational concept of **EGRET**, similar in most respects to the designs of other high-energy  $\gamma$ -ray telescopes, is shown in Fig. 8.2. The **two key challenges** for any such telescope are: (1) the **identification of a  $\gamma$ -ray interaction among** the huge

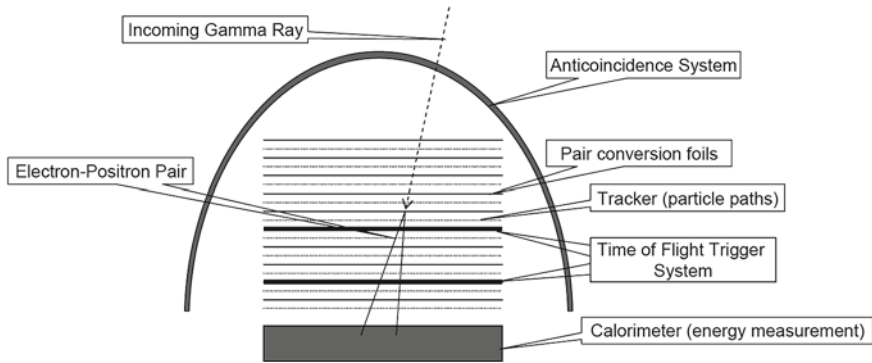


**Fig. 8.2** Schematic diagram of a telescope which use the conversion of a  $\gamma$ -ray into a  $e^{\pm}$  pair (pair-conversion telescope), reproducing the features of the EGRET experiment. The Fermi-LAT is similar, with an improved tracker device which avoids the use of a Time of Flight trigger system. Courtesy EGRET collaboration

background of CRs; (2) the measurement of the  $\gamma$ -ray energy, arrival time and arrival direction.

In EGRET, these objectives were obtained as follows:

- (i) The charged particles were vetoed through the Anticoincidence System (AS). The presence of a signal in the AS vetoed the tracking system electronics. A  $\gamma$ -ray candidate entered the detector without producing a signal in the Anticoincidence. The AS rejected nearly all unwanted signals produced by charged CRs. The AS consisted of a single dome of plastic scintillator, read out by 24 PMTs mounted around the bottom.
- (ii) The  $\gamma$ -rays interacted in one of 28 thin sheets of high-Z material (tantalum) converting via pair production into an electron/positron pair.
- (iii) A Tracker device, consisting of 36 wire grid spark chambers and interleaved with converter plates, was used to record the paths of the electron and positron, to reconstruct the conversion point and the arrival direction of the  $\gamma$ -ray. The spark chambers were gas detectors and their performance slightly deteriorated with time due to gas aging.
- (iv) The electron and positron passed through two scintillator detectors. These fast-devices triggered the readout of the spark chambers and provided the time-of-flight (TOF) measurement (used to confirm the direction of the particles).
- (v) The electron and positron entered the Calorimeter, producing an electromagnetic shower. Using standard methods derived from particle physics, the energies of the particles were measured and, therefore, the energy of the parent  $\gamma$ -ray determined. The calorimeter was made of 36 NaI crystals read out by 16 PMTs.

The angular resolution in the measurement of a single photon depends on the point spread function (PSF). The PSF is the quantity which characterizes the direction resolution of a detector. It is used to obtain also the angle containing 68% of the  $\gamma$ -rays emitted by an ideal point-like source. Usually, the PSF depends on the energy.

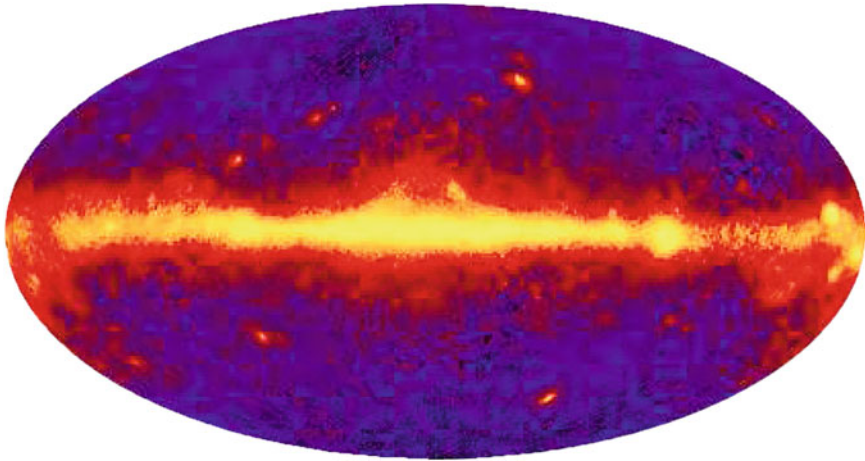


**Fig. 8.3** The  $\gamma$ -ray sky seen by EGRET, shown in galactic coordinates. In this false color image, the galactic center lies in the middle of the image. Courtesy of EGRET Collaboration

The EGRET angular resolution was  $\approx 6^\circ$  at an energy of 100 MeV and sources were localized with resolution of about 15 arcmin. The telescope has a field of view of about  $\sim 0.5$  sr. During its 9 years lifetime, EGRET detected over  $1.5 \times 10^6$   $\gamma$ -rays allowing to build up the first picture of the entire high-energy  $\gamma$ -ray sky. Figure 8.3 shows the summed photon map above 100 MeV, in galactic coordinates. The Milky Way runs horizontally across the figure, with the galactic center in the middle. One of the key features of this image, which provides a striking contrast to the sky at visible wavelengths, is the presence of a huge background of diffuse photons, particularly in the galactic plane. Over the diffuse background, some persistent sources are evident. In the galactic plane the brightest sources were identified with pulsars. Many of the bright sources away from the galactic plane are blazars (a class of Active Galactic Nuclei, Sect. 9.9).

**Gamma-ray sources: the third EGRET catalog.** A  $\gamma$ -ray source appears as an excess of photon counts above the diffuse emission, obtained from the map of Fig. 8.3. The last EGRET analysis of the sky produced the third catalog (Hartman et al. 1999), which contains 271 objects. A characteristic of the  $\gamma$ -ray sky is that it is highly variable, therefore not all sources were seen at all times.<sup>1</sup> As mentioned, the angular resolution of EGRET cannot be compared with that reached in other wavelengths of astronomical observations. In some cases, the 271  $\gamma$ -ray EGRET sources have been associated with known astrophysical objects. The association is much easier far from the galactic plane. In particular, a part the Large Magellanic Cloud which

<sup>1</sup> The Aristotle's view of the eternal and immutable heavens depicted in *De Caelo* had an enormous influence on the medieval view of the Universe, who modified it to correspond with Christian theology. A completely different history would have occurred if  $\gamma$ -ray sensors had been available to Aristotle.

was detected as an extended  $\gamma$ -ray source and one bright enough solar flare. 94 sources show a probable or possible association with blazars and five sources are known galactic pulsars. The remaining 170 sources, almost 60 % of the total, had no identification with known astrophysical objects.

After EGRET, the situation of the GeV  $\gamma$ -ray astronomy had a breakthrough in 2008 with the launch of the Fermi satellite.

## 8.6 Fermi-LAT and Other Experiments for $\gamma$ -ray Astronomy

### 8.6.1 The Fermi-LAT

*A revolution is underway in our understanding of the high energy sky.* This is the introductory sentence of the Fermi-LAT technical paper (Atwood et al. 2009). In fact, immediately after its launch, on June 11 2008, an overwhelming amount of data has significantly improved our knowledge of high energy astrophysics. The Large Area Telescope (LAT) is a telescope for  $\gamma$ -rays in the energy range from 20 MeV to more than 300 GeV, detected over the large background of energetic charged particles at the 565 Km altitude orbit of the Fermi satellite. For each  $\gamma$ -ray, the LAT measures its arrival time, direction, and energy.

The key improvements of this experiment have been obtained because of the newer technologies, principally in particle detection and in electronics, available since the construction of EGRET. These improvements provide a larger effective area over a much larger field-of-view; a better particle tracking which produces an improved angular resolution and background rejection, and a fast, flexible, multilevel trigger and data acquisition system. Fundamental is the rejection capability to discriminate between electromagnetic and hadronic showers, based on the different event topology in the three subsystems (the tracker, the calorimeter and the anticoincidence as in Fig. 8.2). The LAT therefore is a pair-conversion telescope with a precision converter-tracker section followed by a calorimeter. These two subsystems each consist of a  $4 \times 4$  array of 16 modules (see Fig. 8.4). The large field-of-view results from the low aspect ratio (height/width) of the LAT made possible by the choice of particle tracking technology (i.e., silicon-strip detectors) that allowed elimination of the time-of-flight triggering system used in EGRET.

For each  $\gamma$ -ray the arrival time, direction, and energy are measured. The effective collecting area is  $\sim 6,500 \text{ cm}^2$  at 1 GeV with a wide field of view ( $\sim 2 \text{ sr}$ ). The observing efficiency is very high, limited primarily by interruptions of data taking (13 % of the livetime) when Fermi passes through regions where charged particles are trapped by the Earth magnetic field (Sect. 2.9) and the trigger dead time fraction (9 %). As in EGRET, the angular resolution is strongly dependent on the photon energy; the 68 % containment radius is about  $0.8^\circ$  at 1 GeV (averaged over the acceptance of the LAT) and varies with energy approximately as  $E^{-0.8}$ , approaching asymptotically  $0.2^\circ$  at the highest energies.

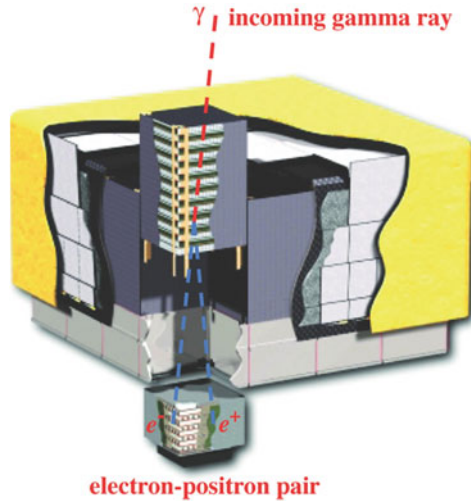


**Fig. 8.4** Schematic diagram of the LAT. The telescope's dimensions are  $1.8 \times 1.8 \times 0.72$  m. The power required and the mass are 650 W and 2789 kg, respectively. The upper part is the tracker, the lower part the calorimeter and the surrounding region (in yellow) the veto. Courtesy of Fermi-LAT Collaboration

The tracking section of the LAT has 36 layers of silicon strip detectors to record the tracks of charged particles, interleaved with 16 layers of tungsten foil. There are 12 thin layers, 0.03 radiation lengths each, at the top (or Front) of the instrument, followed by 4 thick layers, 0.18 radiation lengths, in the Back section to promote  $\gamma$ -rays pair conversion. Unlike EGRET, the LAT basically triggers on all the charged particles crossing the active volume, with no built in hardware trigger for photon selection which can induce inefficiencies. This drastic change of approach is largely due to the use of silicon detectors, allowing precise tracking with essentially no detector-induced dead time.

Beneath the tracker is a calorimeter comprising an 8-layer array of CsI crystals ( $1.08 X_0$  per layer) to determine the  $e^+$ ,  $e^-$  energy. The calorimeter allows imaging of the shower development and thereby corrections of the energy estimate for the shower leakage fluctuations out of the calorimeter. The total thickness of the tracker and calorimeter is approximately 10 radiation lengths at normal incidence.

The tracker is surrounded by segmented charged-particle anticoincidence detectors (ACD) made of plastic scintillators with photomultiplier tubes, to reject CR background events. A programmable trigger and data acquisition system uses prompt signals available from the tracker, calorimeter, and ACD to form a trigger that initiates readout of these three subsystems. The onboard trigger is optimized for rejecting events triggered by CR background particles while maximizing the number of events triggered by  $\gamma$ -rays, which are transmitted to ground for further processing. Additional information about Fermi-LAT can be found on <http://fermi.gsfc.nasa.gov/>.

The Fermi satellite carries also the **Gamma-ray Burst Monitor (GBM)** which complements the LAT for observations of high-energy transients. The GBM is sensitive to X-rays and  $\gamma$ -rays with energies between 8 keV and 40 MeV.

### 8.6.2 AGILE and Swift

The Fermi satellite was anticipated by the smaller-scale telescope **Astro-rivelatore Gamma a Immagini Leggero (AGILE)**. AGILE is a project of the Italian Space Agency (ASI) and was launched in April 2007. It is devoted to  $\gamma$ -ray observations in the 30 MeV–50 GeV energy range, with simultaneous hard X-ray imaging in the 18–60 keV band, and optimal timing capabilities for the study of transient phenomena. The AGILE instrument (Tavani et al. 2008) consists of the Silicon Tracker, the X-ray detector SuperAGILE, the CsI(Tl) Mini-Calorimeter and an anti-coincidence system. The combination of these instruments forms the Gamma-Ray Imaging Detector (GRID). The very large field of view (2.5 sr) of the  $\gamma$ -ray imager coupled with the hard X-ray monitoring capability makes AGILE well suited to study galactic and extragalactic sources, as well as GRBs and other fast transients. AGILE reaches its optimal performance near 100 MeV with good imaging and sensitivity. Gamma-ray and hard X-ray sources can be monitored 14 times a day, and an extensive database has been obtained for a variety of sources.

The **Swift space observatory** (Gehrels et al. 2004) is a multi-frequency, rapid response observatory that was launched on November 20, 2004. To fulfill its purposes Swift carries three instruments on board: the Burst Alert Telescope (BAT) sensitive in the 15–150 keV band, the X-Ray Telescope (XRT) sensitive in the 0.3–10.0 keV band, and the UV and Optical Telescope (170–600 nm) (UVOT). The primary objective of the Swift scientific program is the discovery and rapid follow up of GRBs, Sect. 8.9. However, as these elusive sources explode at random times and their frequency of occurrence is subject to large statistical fluctuations, there are periods when Swift is not engaged with GRB observations and the observatory can be used for different scientific purposes. The sources observed through this secondary science program are usually called Swift fill-in targets. The very wide spectral range covered by these three instruments is of crucial importance for the study of AGN as it covers the energy region where the transition between the synchrotron and inverse Compton emission usually occurs. Since the beginning of its activities Swift has observed hundreds of blazars as part of the fill-in program.

## 8.7 Diffuse $\gamma$ -rays in the Galactic Plane

Unlike the sky at visible wavelengths, the  $\gamma$ -ray sky is dominated by a diffuse radiation originating in our Galaxy, Fig. 8.3, and diffuse radiation is seen at all galactic latitudes. This diffuse  $\gamma$ -ray radiation is largely produced by galactic CR hadrons and electrons



interacting with the interstellar gas and photon fields. The spatial distribution of this high-energy radiation traces galactic structures as determined from radio and other measurements. These basic features were already discovered by the SAS-2 and COS-B spacecrafts.

The physical processes that produce the observed  $\gamma$ -rays are due to:

- Inelastic collisions of CR protons and nuclei with the interstellar gas during their propagation. In the interaction secondary particles are produced, particularly charged and neutral  $\pi$  mesons. The  $\pi^0 \rightarrow \gamma\gamma$  decay has the features described in Sect. 8.2, and the expected  $\gamma$ -rays distribution has a broad energy range.
- CR electrons colliding with low-energy photons. The inverse Compton scattering boost some low-energy photons into the  $\gamma$ -ray band. The principal targets are the optical and infrared photons found throughout the Galaxy.
- High-energy electrons interacting with the interstellar gas, producing  $\gamma$ -rays through bremsstrahlung.

The first detailed information on the galactic diffuse  $\gamma$ -ray radiation was provided by EGRET in the 30 MeV–40 GeV range. The spectrum was compared with a detailed modeling of the measured CR intensities combined with a three-dimensional model of the distribution of galactic photons and gas. The model reproduced most features of the observed gamma radiation, but for one unexpected feature: the flux above 1 GeV exceeded the model prediction by a significant amount. This discrepancy was known for some years as the “EGRET GeV excess”.

Using the first 5 months of the science phase of the mission, Fermi-LAT was able to measure the diffuse flux for the galactic latitude range  $10^\circ \leq |b| \leq 20^\circ$  (Abdo et al. 2009a). Figure 8.5 shows the spectral energy distribution (SED) of this radiation in the considered region of the sky, along with the estimated contribution from the three mentioned mechanisms due to the CR propagation (red line) and electron interactions (green and magenta lines).

The modeling necessary to produce the theoretical lines shown in Fig. 8.5 is not simple. It requires a good knowledge of the spatial distribution of CR protons and electrons and of all the radiation and matter distributions with which the CRs interact. The matter distribution was derived with the techniques described in Sect. 2.7.2. The most advanced models include the GALPROP code which was discussed in Sect. 5.4 and which is used to compare the data in the figure.

The Fermi-LAT measurements are in agreement with the hypothesis that CRs fill the whole Galaxy. According to the modeling, most  $\gamma$ -rays with energies between 100 MeV and 50 GeV originate from the decay of  $\pi^0$  produced in hadronic collisions when CR protons with energies from 0.5 to  $10^3$  GeV interact with InterStellar Matter (ISM) nuclei. The Fermi-LAT results do not confirm the unexpected excess in the few GeV energy range measured by EGRET. This excess could probably be explained by an incorrect energy assignment of the high-energy photons in EGRET.

As described in Sect. 9.12, extragalactic sources of  $\gamma$ -rays are probably objects characterized by jet activities, as in the case of *blazars*. It is interesting to note that some galaxies (as for instance the Large and the Small Magellanic Clouds and some



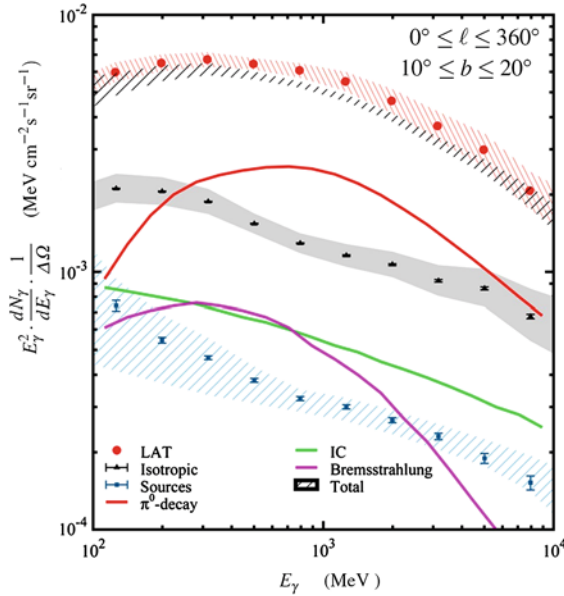


**Fig. 8.5** Spectral energy distribution divided by the observed solid angle ( $SED/\Delta\Omega$ ) of diffuse  $\gamma$ -rays as measured by Fermi-LAT. The SED is normalized to the solid angle region with galactic latitude  $10^\circ \leq b \leq 20^\circ$  and longitude  $0^\circ \leq \ell \leq 360^\circ$ . Overlaid are the expected SEDs for the physical processes which produce the diffuse emission. The lines represent the contribution from: the dominant  $\pi^0$  decay (red); bremsstrahlung (magenta); inverse Compton (IC, green). The unidentified isotropic background is represented by the gray shaded region. The blue/hatched distribution shows the unresolved contribution from sources. The black/hatched is the total theoretical prediction, in good agreement with data (red points with error band). Courtesy of Fermi-LAT Collaboration

starburst galaxies,<sup>2</sup> such as M82 and NGC 253) which do not exhibit apparent jet activities are also seen by Fermi-LAT as  $\gamma$ -ray sources. This observation provides information on the existence of CRs beyond our own Galaxy. In fact, GeV  $\gamma$ -rays in these galaxies come primarily from the interactions of hadrons and electrons produced by mechanisms similar to those providing our CRs, with interstellar matter and photon fields in that Galaxy. As a confirmation of this hypothesis, the luminosities of these normal and starburst galaxies show an approximately linear relationship with the product of the supernova rate and the total mass of gas in the galaxies (Thompson et al. 2012).

<sup>2</sup> In starburst galaxies an exceptionally high rate of star formation, as compared to the star formation rate observed in most other galaxies, is observed.

### 8.7.1 An Estimate of the Diffuse $\gamma$ -ray Flux

Let us work out an order of magnitude estimate of the diffuse  $\gamma$ -ray flux due to the propagation of CRs in the galactic ISM. The ingredients of our computation are the following.

1. **Cross section.** We assume that both CRs and target materials are protons, with inelastic cross section  $\sigma_{pp} \simeq 40 \text{ mb} = 4 \times 10^{-26} \text{ cm}^2$ .
2. **Number density of target material  $n$ .** According to the discussion in Sect. 2.10 its average value can range from  $n = n_{ISM} = 0.3$  to  $1 \text{ cm}^{-3}$ , see also Eq. (5.16).
3. **CRs energy density.** As in Sect. 8.3 we assume that the energy density of CRs producing the  $\gamma$ -rays observed by the Fermi-LAT corresponds to  $\rho_{CR \rightarrow \gamma} \simeq 0.1 \text{ eV/cm}^3$ .
4. **Energy transferred to  $\gamma$ -rays.** In the process  $pp \rightarrow \text{hadrons}$ , about 1/3 of the secondary particles are neutral pions. Thus, only 1/3 of the energy of primary interaction protons is converted into  $\gamma$ -rays.

Using the above assumptions, the interaction rate of one relativistic CR (moving at the speed of light  $c$ ) with target protons of the ISM corresponds to

$$R_{\text{coll}} = \sigma_{pp} \cdot n \cdot c = 4 \times 10^{-26} \times n \times 3 \times 10^{10} = 1.2 \times 10^{-15} \times n \quad [\text{s}^{-1}]. \quad (8.46)$$

This relation is important to verify the connection between the total energy of a source with the photon luminosity.

As the  $\sigma_{pp}$  cross section is assumed independent from the energy  $E$  of the CR, the energy emitted isotropically as  $\gamma$ -rays per unit of solid angle per cubic centimeter of the Galaxy per second corresponds to

$$L_{\gamma}^{\text{diff}} = \frac{1}{3} \cdot \frac{1}{4\pi} \cdot R_{\text{coll}} \cdot \rho_{CR \rightarrow \gamma} \quad \text{units: } [\text{sr}]^{-1} [\text{s}]^{-1} [\text{eV cm}^{-3}]. \quad (8.47)$$

The factor 1/3 takes into account the fraction of  $\pi^0$  in the secondary hadrons mentioned above. Inserting the numerical values

$$\begin{aligned} L_{\gamma}^{\text{diff}} &= 1/3 \cdot (1.2 \times 10^{-15}) \times n \cdot (0.1) = (4n \times 10^{-17}) \text{ eV cm}^{-3} \text{ s}^{-1} \text{ sr}^{-1} \\ &= (4n \times 10^{-23}) \text{ MeV cm}^{-3} \text{ s}^{-1} \text{ sr}^{-1}. \end{aligned} \quad (8.48)$$

The photon flux at the detector depends on the linear distance  $D$  from which photons can arrive from the galactic plane

$$N_{\gamma} = L_{\gamma}^{\text{diff}} \times D = 4 \times 10^{-23} \times (nD) \text{ MeV cm}^{-2} \text{ s}^{-1} \text{ sr}^{-1}. \quad (8.49)$$

The quantity  $(nD)$  represents the column density of material responsible for the photons seen by the experiment. To compare our order-of-magnitude estimate with Fermi-LAT data, we need to know the average column density of materials in the

region observed by the experiment. Column densities of atomic hydrogen gas were estimated by the Fermi-LAT collaboration from existing radio surveys of the 21 cm line of HI. The estimated average value is  $n \cdot D \sim 10^{20} \text{ cm}^{-2}$ . Inserting this value into (8.49) we obtain

$$N_{\gamma} = L_{\gamma}^{\text{diff}} \times D = 4 \times 10^{-23} \times 10^{20} = 4 \times 10^{-3} \text{ MeV cm}^{-2} \text{ s}^{-1} \text{ sr}^{-1}. \quad (8.50)$$

We compare our result with Fig. 8.5. Our estimate is in agreement with the Fermi-LAT measurement of the diffuse  $\gamma$ -ray flux in the 100 MeV–1 GeV range and within a factor of two with the expectation from  $\pi^0$  decay (the red line). Another prediction of our simple computation is the linear correlation between  $N_{\gamma}$  and the column density of matter,  $n \cdot D$ , which was effectively observed (Abdo et al. 2009b).

This diffuse component of the  $\gamma$ -rays is the most direct evidence that CRs are filling our Galaxy with an energy density which is the same as that measured on Earth.

## 8.8 The Fermi-LAT Catalogs

The Fermi-LAT (LAT, in this section) collaboration is producing a large number of scientific results. Additional analyses of LAT data are in progress also from scientist external to the collaboration due to the policy of data diffusion. During the first year the release of LAT data was restricted to allow the LAT team to calibrate the instrument and carry out their proposed sky survey. After the first year data are not proprietary any longer, and are made freely available on web. The LAT team has released data on transient sources and light curves for more than 20 regularly monitored sources, and continuously adds more sources to the list as they show significant brightening. Since the beginning of the second year of operations, all LAT science data is released as soon as possible.

At the time of writing this Chapter (Spring 2014), the LAT operations are still in progress. Different source catalogs are continuously produced and updated by the LAT collaboration. The following information are extracted from the official second catalog of high-energy  $\gamma$ -ray sources (2FGL) detected by LAT and derived from data taken during the first two years of the science phase of the mission. The 2FGL catalog contains 1,873 sources detected and characterized in the 100 MeV–100 GeV range of which 127 are considered as being firmly identified and 1,171 as being reliably associated with counterparts of known or likely  $\gamma$ -ray source classes.

The LAT 2-year Point Source Catalog is currently available in a file format to be used for data analysis within the Fermi Science Tools, and as a readable table. Supporting tools and documentation have been provided and available at: <http://fermi.gsfc.nasa.gov/ssc/data/access/>.

As in the case of EGRET, the sources are obtained from the photon counting map. LAT collects about 150 million  $\gamma$ -rays per year (compared with the 1.5 million detected by EGRET in 9 years). Figure 8.6 shows the LAT photon map in galactic coordinates. This plot should be compared with that produced by EGRET, shown

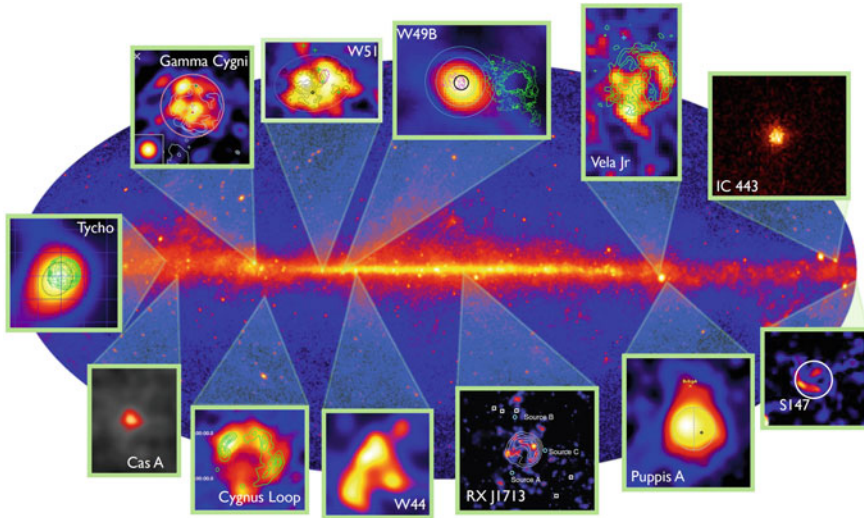


**Fig. 8.6** Fermi-LAT sky map in galactic coordinates. Superimposed, the position of the principal supernova remnants in the LAT  $\gamma$ -ray sky. From Tibaldo (2013)

in Fig. 8.3. The diffuse galactic emission is a foreground for the identification of point-sources, and hence affects the determination of their positions and fluxes. It is also a foreground for the much fainter extragalactic component, which is the sum of contributions from unresolved sources and truly diffuse extragalactic emission. The knowledge of the diffuse component, presented in Sect. 8.7, is a necessary first step as the sources are found after subtraction of the diffuse component from the photon counting map.

The basic analysis steps used to construct the 2FGL catalog are source detection, localization, and significance estimation. Once the final source list is determined, the flux in 5 energy bands (corresponding to the SED between 100 and 300 MeV; 300 MeV–1 GeV; 1–3 GeV; 3–10 GeV; 10–100 GeV) and the flux history (light curve of the integrated flux) for each source is produced. The minimum flux from a source that LAT can discriminate from the background corresponds to  $5 \times 10^{-12} \text{ erg cm}^{-2} \text{ s}^{-1}$  (Nolan et al. 2012). Compare this value to that of Eq. (8.19).

The 2FGL catalog is primarily a catalog of point-like sources detected in the first 24-months. A point-like object is spatially unresolved within the point spread function of the detector. The analysis and catalog also include a number of LAT sources that are known to be spatially extended. These extended sources are of particular importance and include seven supernova remnants (SNRs), two pulsar wind nebulae (PWNe), the Large Magellanic Cloud (LMC) and the Small Magellanic Cloud (SMC), and the radio galaxy Centaurus A. Also the Sun is a bright, extended source, due to CR interactions in its outer atmosphere and to IC scattering of CR electrons on the solar radiation field, which produces an extended  $\gamma$ -ray halo around our Star. The Moon is comparably bright as the Sun in  $\gamma$ -rays. Except for the diffuse

**Table 8.1** Number of objects cataloged in the 2FLG

Description	Designator	Identified	Associated
<b>Galactic sources</b>			
Pulsar, identified by pulsations	PSR	83	–
Pulsar, no pulsations seen in LAT yet	–	–	25
Pulsar wind nebula	PWN	3	0
Supernova remnant	SNR	6	4
Supernova remnant/ Pulsar wind nebula	snr/pwn	–	58
Globular cluster	GLC	0	11
High-mass binary	HMB	4	0
Nova	NOV	1	0
<b>Extragalactic sources</b>			
BL Lac type of blazar	BZB	7	429
FSRQ type of blazar	BZQ	17	353
Nonblazar active galaxy	AGN	1	10
Radio galaxy	RDG	2	10
Seyfert galaxy	SEY	1	5
Active galaxy of uncertain type	AGU	0	257
Normal galaxy (or part)	GAL	2	4
Starburst galaxy	SBG	0	4
<b>Class uncertain</b>			1
<b>Unassociated</b>			575
<b>Total</b>		127	1746

The first section refers to galactic objects; the second to extragalactic sources; the third to objects with uncertain classification. Identified (associated) objects are indicated with capital (lower case) designators. In the case of AGN, many of the associations have high confidence

emission and the sources explicitly considered as spatially extended, all remaining objects in the catalog are assumed to be point-like.

**Source Association and Identification.** The designations of the classes that are used to categorize the 2FGL sources are listed in Table 8.1 along with the number of sources assigned to each class. Each source can be either associated or identified, with associations depending primarily on close positional correspondence. The identification, shown in the catalog by capitals in the designator column in Table 8.1, is based on one of three criteria:

- (i) **Period variability.** Temporal variability is relatively common in  $\gamma$ -ray sources and provides a powerful tool to associate them definitively with objects known at other wavelengths and to study the physical processes powering them. The method is mainly used to associate known pulsars.
- (ii) **Spatial morphology,** which is used to identify spatially extended sources whose morphology can be related to that seen at other wavelengths. The method is used to identify SNR, PWNe, and galaxies.

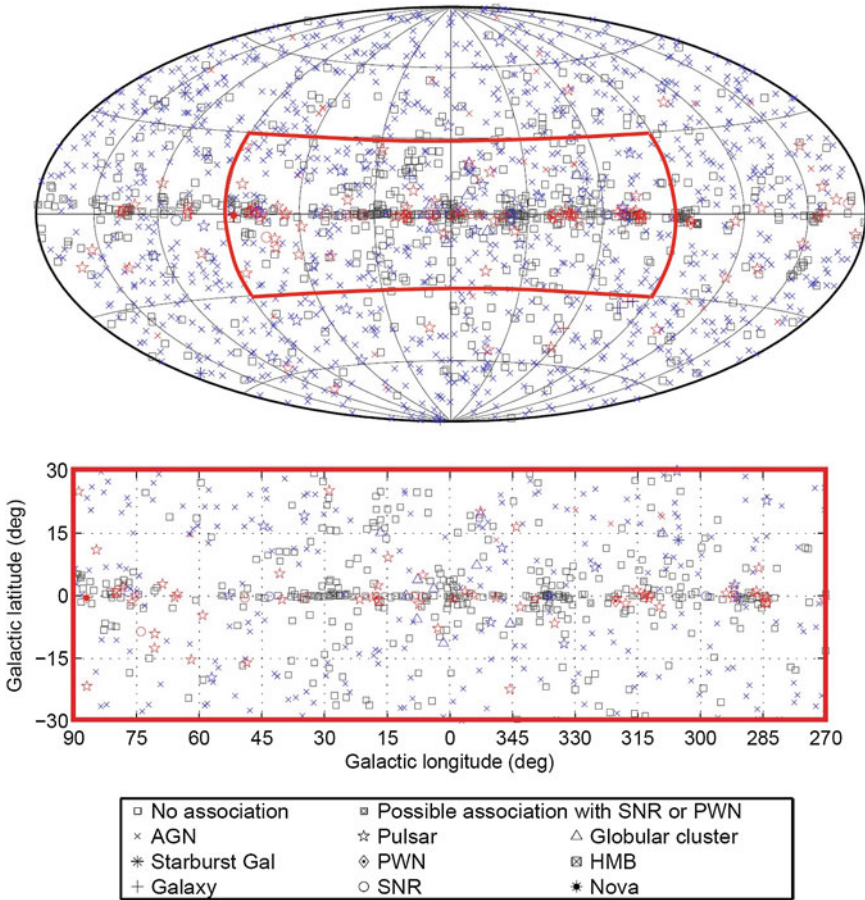


**Fig. 8.7** Full sky map (*top*) and blow-up of the inner galactic region (*bottom*) showing sources by source class (refers to Table 8.1). Identified sources are shown with a *red* symbol, associated sources in *blue*. Courtesy of Fermi-LAT Collaboration

- (iii) **Correlated variability.** Variable sources, primarily AGN, whose  $\gamma$ -ray variations can be matched to variability seen at one or more other wavelengths, are considered to be firm identifications.

In total, 127 out of the 1,873 2FGL sources are firmly identified (see table). The list of astronomical catalogs used for the identification/association is reported in Nolan et al. (2012). Sources associated with SNRs are often also associated with PWNe and pulsars, and the SNRs themselves are often not point-like. Figure 8.7 illustrates where the different sources are located in the sky.

**Source spectral shapes.** As the LAT measures the number of arriving photons as a function of their energy, the so-called *spectral shape* (photon flux as a function of the energy) can be constructed for each individual source. In most cases, a simple



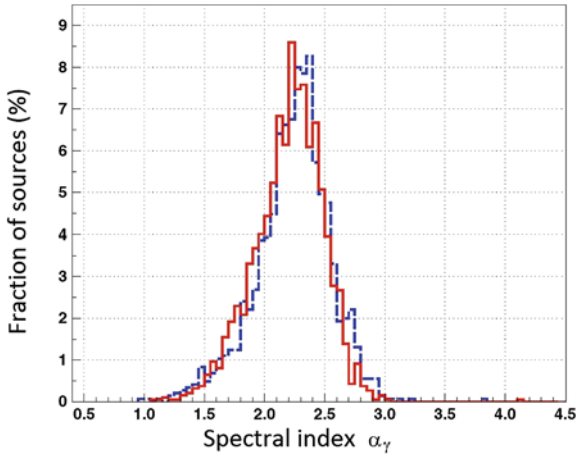


**Fig. 8.8** Distributions of the spectral index  $\alpha_\gamma$  for the 2FGL (1,873 sources, *red solid line*) catalog. The same distribution for the 1,451 sources of the first LAT catalog (1FGL) is also indicated (*dashed line*). Courtesy of Fermi-LAT Collaboration

power-law  $dN/dE = K(E/E_0)^{-\alpha_\gamma}$  can be considered. Frequently, the flux show a cut-off at high energy and the spectral shape is represented by exponentially cutoff power-laws

$$\frac{dN}{dE} = K \left( \frac{E}{E_0} \right)^{-\alpha_\gamma} \exp \left( - \frac{E - E_0}{E_c} \right)^b. \tag{8.51}$$

This is just the product of a power-law and an exponential. The fit parameters are  $K$ ,  $\alpha_\gamma$  (as in the power-law) and the cutoff energy  $E_c$ . The parameter  $b$  is fixed to 1 by the Fermi-LAT collaboration.  $E_0$  is a reference energy that is chosen freely for each source. This functional representation of the spectral shape is particularly suited for pulsars.

Other bright sources (mainly AGN) are also not very well represented by power-law spectra. The LAT collaboration uses a functional form called *LogParabola* which adds only one parameter to the power-law:

$$\frac{dN}{dE} = K \left( \frac{E}{E_0} \right)^{-\alpha - \beta \log(E/E_0)} \tag{8.52}$$

Figure 8.8 shows the distribution of the power-law index of all of the sources. Its average value is  $\alpha_\gamma = 2.21 \pm 0.01$  is very close to that expected for a Fermi mechanism for the acceleration of parent charged particles,  $\alpha_{CR} \sim 2$ .



## 8.9 Gamma Ray Bursts

Gamma-Ray Bursts (GRBs) are extremely intense and relatively short bursts of gamma radiation that occur a few times per day in the detectable Universe. Their emission exceeds the gamma emission of any other source. For instance, the GRB 080319B<sup>3</sup> was detected by the Swift (Gehrels 2004) satellite at 06:12 UTC on March 19, 2008 and was the brightest event ever observed in the known sky. The explosion set a new record for the most distant object that could be seen with the naked eye, it had a peak apparent magnitude<sup>4</sup> of 5.8 and remained visible to the human eye for approximately 30 s (Racusin et al. 2008).

Present knowledge suggests that GRBs occur in random directions in the sky and at cosmological distances. The time integrated fluxes, or the fluencies, range from  $\sim 10^{-7}$  to  $\sim 10^{-4}$  erg cm<sup>-2</sup>. The observed fluencies, combined with the distances determined from detections of the host galaxies for which optical redshift distances are obtained, show that GRBs are the brightest explosions in the Universe. If they were emitting isotropically, the  $\gamma$ -ray energy output would on average amount to a solar rest-mass energy,  $M_{\odot}c^2 \sim 10^{54}$  erg, emitted in a few seconds.

In fact, there is evidence that the emission is anisotropic or jet-like, with a typical jet opening angle  $\theta$  of a few degrees, corresponding to a solid angle  $\Delta\Omega \sim \pi\theta^2$ . This introduces for a double jet configuration an angular correction factor in the total energy emitted which is on average  $2\Delta\Omega/4\pi \sim 10^{-3}$ . Thus the actual average jet energy in  $\gamma$ -rays is  $\sim 10^{51}$  erg emitted in a few seconds. This is to be compared with the isotropic kinetic energy content of a supernova explosion,  $E_{\text{SN}} \sim 10^{51}$  erg, of which only  $\sim 1\%$  emerges as visible photons over periods of months to years (Sect. 12.11).

In astronomy many transient sources have generally rather simple time structures, which help to understand the underlying physics of the objects. GRBs are very peculiar from this point of view, as their light curves vary significantly one to another. There are no two identical GRBs: the duration, the number of peaks, the maximum brightness, in fact every parameter can be different. See Fig. 8.9 as an example of the light curves for two GRBs.

**History of the GRBs discovery.** GRBs were discovered accidentally. In the 1960s, both the United States and the former Soviet Union launched military satellites to monitor adherence to the nuclear test-ban treaty. These satellites were  $\gamma$ -ray detectors, as the signature of a nuclear detonation is a brief, but intense, pulse of  $\gamma$ -rays. While most satellites orbited at about 800 km above the Earth's surface, the U.S. Vela satellites orbited at an altitude of more than 100,000 km, above the Van Allen radiation belts, reducing the noise in the sensors. The extra height also meant that the satellites could detect explosions behind the Moon, a location where the U.S. government suspected the U.S.S.R would try to conceal nuclear weapon tests.

<sup>3</sup> GRBs are named according to the date *yymmdd* they have been detected; if more than one burst per day is present, there is the extension A for the first, B for the second and so on.

<sup>4</sup> The apparent magnitude of an object is a logarithmic measure of its brightness as seen from the Earth. For comparison, the value 0 is assigned to the star Vega.

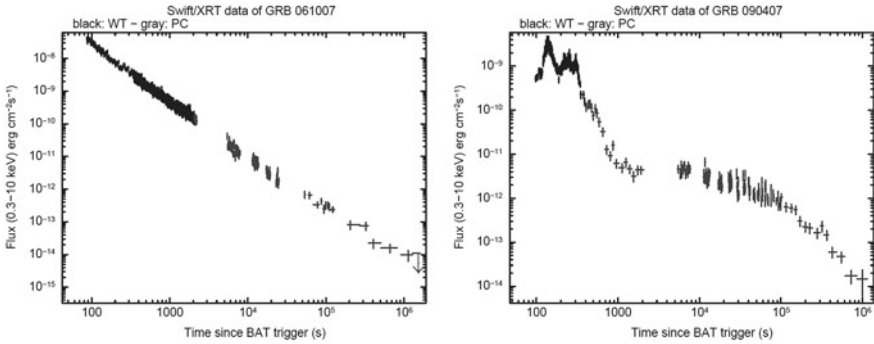


**Fig. 8.9** Light curves for two GRBs measured by the X-Ray Telescope (XRT) in the Swift satellite. For details of how these light curves were produced, see Evans et al. (2007)

On July 2, 1967 the U.S. Vela satellites indeed detected a  $\gamma$ -ray signal, but it had neither the intense initial flash nor the gradual fading that characterize nuclear weapon explosions. Instead there were two distinct peaks in the light curve. It was only in 1973 that the observations were published, identifying a cosmic origin for the previously unexplained observations of  $\gamma$ -rays.

Another milestone in the history of GRBs was the launch of the BATSE experiment on the CGRO satellite, Sect. 8.5. The main result achieved by the BATSE detector is the conclusive proof that GRBs occur isotropically in the sky. In addition, it revealed that the GRBs can be split in two families: short and long duration GRBs, which have correspondingly different spectra. Thanks to the BATSE data it has also been possible to measure the typical fluence (the flux integrated over time) of GRBs.

The emission spectra of the GRBs show a peculiar nonthermal behavior, peaking at around a few hundred keV and extending up to several GeV. The spectrum, that is the number of photons per unit energy, is generally of the form of a broken power law (Fig. 8.10) called Band Spectrum (Briggs et al. 1999) given by

$$\begin{aligned}
 N(E) \equiv \frac{dN_\gamma}{dE} &\propto E^{-\alpha} && \text{with } \alpha \simeq 1 \text{ for } E < E_b \\
 &\propto E^{-\beta} && \text{with } \beta \simeq 2 \text{ for } E > E_b
 \end{aligned}
 \tag{8.53}$$

The change of spectral slope occurs at a break energy  $E_b$  which, for the majority of observed bursts, is in the range of 0.1–1 MeV. The bottom plot of Fig. 8.10 shows also the spectral energy distribution of the considered GRB.

Due to their short duration, GRBs were very difficult to localize precisely. In this respect the real breakthrough was made by the Italian-Dutch satellite BeppoSAX, launched in April 1996. Its Wide Field Camera, sensitive to the medium-hard X-ray energy range between 2–25 keV, allowed for the first time to measure the position of the GRBs with uncertainties of only few arcminutes. The satellite could then observe the pinpointed region with the Narrow Field Instrument, covering the

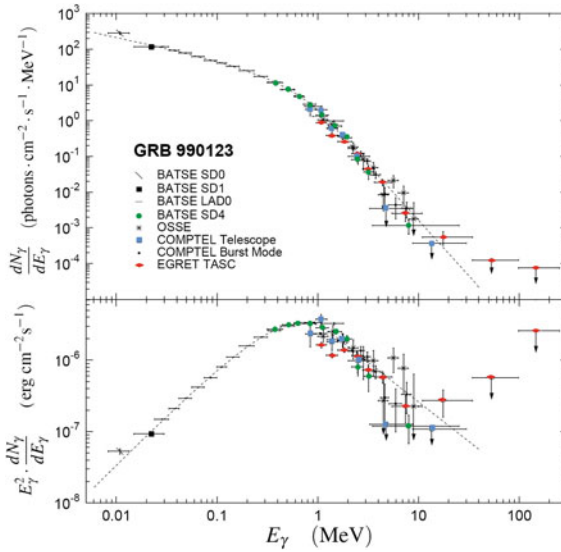


**Fig. 8.10** Example of the spectrum for one GRB (GRB 990123) measured from all experiments on board the CGRO, showing a band-type broken power law component. The upper panel shows the photon number spectrum  $N_E = dN/dE$ . The corresponding energy spectral energy distribution  $E^2 dN/dE$  is in the lower panel

0.1–10 keV range. It was then possible to detect a newly discovered feature: the X-ray afterglow of the GRB. In the meantime, a Gamma-ray burst Coordinates Network (the GCN system) that transmits a GRB alert to a network of selected instruments was set. The combination of BeppoSAX with the wide field camera trigger and the GCN system allowed for all ground based telescopes to point in the direction of the detected GRB and detect optical, IR and radio afterglows.

The observation of these afterglows, in different wavelengths, allowed the characterization of GRBs using additional information to that provided by the  $\gamma$ -ray data. For example, it was possible to measure the redshift (and thus the distance) of several GRBs. Knowing the redshift of a GRB, therefore, one has additional information extremely useful for the classification and study of each GRB. Determining the host galaxy of a GRB has been historically very challenging, as in most cases there were several relatively bright galaxies contained within the position uncertainty of the GRB.

Optical observations after the GRB were extremely important because they showed that the long GRBs came from not very bright galaxies, and that the location of the source is never very far from the center of its host galaxy. This information is useful to infer that long GRBs are generally associated with massive and short lived progenitors.

The Swift satellite succeeded BeppoSAX. The sensitivity of its Burst Alert Detector (BAT) is in the range 20–150 keV was higher than the previous instruments. The

speed with which the higher angular resolution X-ray and UV-optical detectors can turn toward the burst is less than 100s from the occurrence of the trigger. These two advantages significantly improved the measurement capabilities for GRBs, especially the ones shorter than two seconds (short GRBs).

The latest milestone was the launch of the Fermi satellite which allows the investigation the very high energy regime. Roughly one GRB per week is detected with the GBM between 8 keV–30 MeV, and roughly one a month is detected with the Fermi-LAT, 20 MeV–300 GeV. Several bursts have been detected by the Fermi-LAT at energies above 1 GeV (11 GRBs from August 2008 to January 2010), improving considerably our knowledge of high energy  $\gamma$ -ray emission. The most distant GRB is GRB 090423 (observed by Swift), with  $z \sim 8.1$ , hence being produced only 600 million years after the Big Bang.

### 8.9.1 Classification of GRBs

Observations from BATSE led to the separation of  $\gamma$ -ray bursts into two families. The main classification is “long GRBs” and “short GRBs”, where the long population has an average duration of about 30 s, while the short lasts on average 0.3 seconds. As shown in Fig. 8.11 there is a clear separation between two families of GRBs. It has been noticed that the short bursts spectrum is significantly harder (with more high energy photons) than the long bursts. Long GRBs are the most frequently observed and, therefore, also the best understood. Each family of GRBs is associated with a different progenitor.

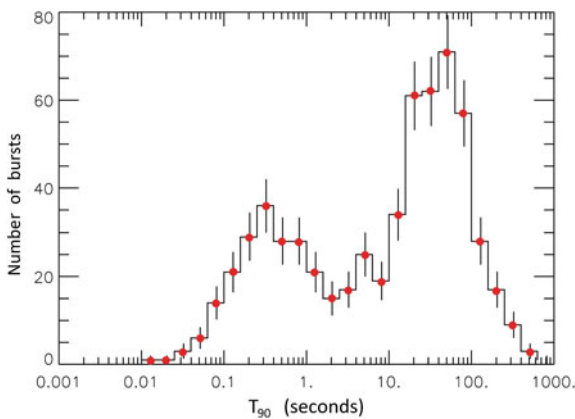


**Fig. 8.11** Distribution of GRBs that occurred in 2008–2009 as a function of the log of the T90 in seconds. Usually the duration of the GRB is expressed as the time during which 90% of the counts are detected, and denoted as T90. It is possible to see how the GRBs are split in two groups depending on their duration. “Long GRBs” last more than two seconds, the remaining ones are “short GRBs”. Figure from <http://f64.nsstc.nasa.gov/batse/>

**Progenitors of Long GRBs.** Observations show that host galaxies of long GRB are active star forming galaxies. In several cases it has been proved that long GRBs happen in correlation with supernovae, linking them unambiguously with the death of a massive star. Core-collapse supernovae are the explosive deaths of massive stars that occur when their iron cores collapse to neutron stars or black holes (Sect. 12.11). The connection between supernovae and GRBs is given by the total emitted kinetic energy. The observation of GRB 980425 in conjunction with SN 1998bw showed this connection unambiguously. These two events were coincident both in time and space, and the energetic coincidence left few doubts about the connection. The connection of GRBs with the *hypernova* model is discussed in Sect. 12.11.1.

**Progenitors of Short GRBs.** Models on the origin of the short GRBs had to wait for the detection of a large sample of afterglows by Swift. Observation of afterglows allowed the identification of host galaxies where short GRBs occurred. It was found that short GRBs are distributed uniformly among galaxies that contain a considerable quantity of old stars. In these galaxies there is no evidence of significant star formation, and such an old population is compatible with the presence of neutron star binary systems. The estimated total kinetic energy emitted by short GRBs exceeds that of long GRBs by many orders of magnitude. The current hypothesis attributes the origin of short GRBs to the merging of two compact objects. Possible candidates for such a process are mergers of neutron star binaries or neutron star-black hole binaries, which lose angular momentum and undergo a merger. Neutron star-neutron star binaries are observed in our galaxy, and the existence of neutron star-black hole binaries is plausible. Such structures lose energy due to gravitational radiation, as predicted by General Relativity, and the two objects will spiral closer and closer until tidal forces will disintegrate the neutron star and will free an enormous quantity of energy before merging to form a single black hole. This process is thought to be extremely fast and to last no more than a few seconds, in agreement with the observation of short GRBs. Furthermore, the lack of connection with a supernova observation supports the model of a merger.

**Mechanism of GRBs.** It is important to notice that although the two families of GRBs are known to have different progenitors, the acceleration mechanism that gives rise to the  $\gamma$ -rays themselves (and probably to the production of neutrinos) is most likely independent of the progenitor of the event. The *fireball model* is the most widely used theoretical framework to describe the physics of the GRBs. Independently of the details of the central engine, and based only on the release of the large amounts of energy ( $10^{51}$  erg on timescales of tens of seconds or less) the observed emission of  $\gamma$ -rays and the afterglow must arise from an emission region moving at relativistic velocities. The energy release in such short times in such compact regions produces a luminosity which exceeds the Eddington luminosity (see *Extras #4*), above which radiation pressure overwhelms gravity. The inner engine is attributed to a compact object, either the collapsing core of a massive star or the merger of two compact objects.

This inner engine causes an explosion that originates the relativistic blast waves moving through the star at relativistic speeds (the *fireball*). Two opposite jets form at

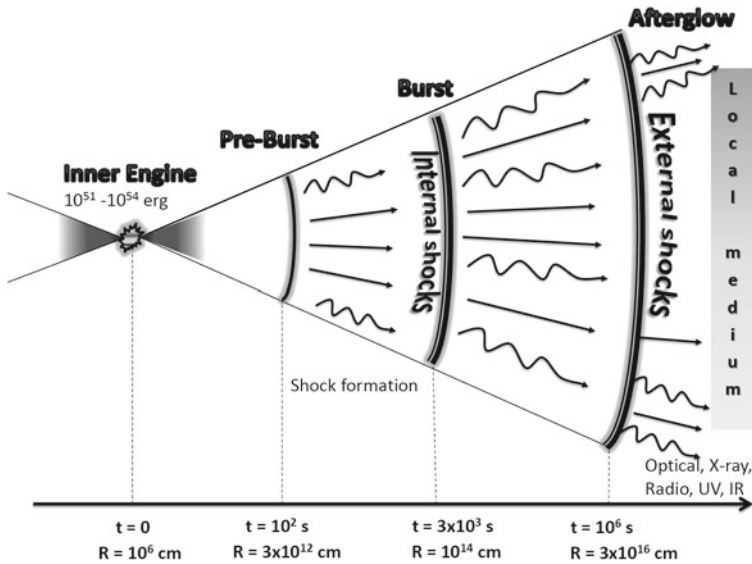


**Fig. 8.12** Sketch of the internal-external fireball shocks model. A compact source produces a relativistic outflow. Internal shocks within the outflow produce the prompt  $\gamma$ -ray emission while external shocks with the surrounding matter produce the lower energy and longer lasting afterglow. Courtesy of Dr. Presani (Presani 2011)

the two poles of the accretion disk and during the acceleration of matter in the jets, newly formed material accelerates faster and forms consecutive shells with different speeds. The fireball is expected to accelerate until it reaches a terminal bulk Lorentz factor  $\Gamma$ , which is estimated to be about  $\sim 300$ . Interactions of shells with the external medium or collisions between shells reconvert the kinetic energy into internal energy, ready to be radiated in the form of  $\gamma$ -rays or transferred to baryons via baryon-photon coupling. Shocks between shells are responsible for the emission of  $\gamma$ -rays.

Behind the shock, the blast wave pushes the stellar material through the star surface and sweeps through space at nearly the speed of light, colliding with external gas and dust, producing additional emission of photons. These emissions are the afterglow. Figure 8.12 shows a schematic of this fireball shock model. Although this scenario is widely accepted, the discussion is still open regarding the form in which the energy is carried out. In some models, the energy outflow is carried out in the form of kinetic energy of baryons, while in other models the flow is of electromagnetic nature. Measurements of neutrinos from a GRB (Sect. 10.4.3.) would then provide evidence for the presence of accelerated baryons.

For detailed reviews on the subject, refer to Piran (2004), Mészáros (2006).

## 8.10 Limits of $\gamma$ -ray Observations from Space

Despite the recent great achievements of high energy  $\gamma$ -ray astronomy, there are obvious limits to the performance of satellite-borne instruments. The photon flux threshold for which the Fermi-LAT can resolve a  $\gamma$ -ray source in the range between 1 and 100 GeV over the background corresponds to  $N_{\text{thr}} = 4 \times 10^{-10}$  photons  $\text{cm}^{-2} \text{s}^{-1}$  (Nolan et al. 2012). Sources with a lower photon flux cannot be resolved. Because the Fermi-LAT effective collecting area is  $A \sim 6,500 \text{ cm}^2$  at 1 GeV in a large field of view of  $\sim 2 \text{ sr}$ , the corresponding number of events  $n_{\text{thr}}$  per year from a source with a flux equal to the threshold one and assuming no dead-time is

$$n_{\text{thr}}(> 1 \text{ GeV}) = N_{\text{thr}} \cdot A \cdot \left( \frac{2 \text{ sr}}{4\pi \text{ sr}} \right) \cdot T = 12 \text{ y}^{-1}. \quad (8.54)$$

$T = 3.15 \times 10^7$  corresponds to the number of seconds/y. Because many sources are simultaneously monitored within the large and homogeneous field of view, this is an adequate sensitivity for studying persistent  $\gamma$ -ray sources in the multi-GeV range. The details on the temporal and spectral characteristics of highly variable sources like blazars or GRBs is instead limited by the small effective area of the detector.

Due to the constraints on the maximum size and weight of an instrument that can be delivered into space, the effective detection area of any satellite experiments (using current launch vehicles) is limited to the order of a few  $\text{m}^2$ . Assuming a constant SED for the sources also at higher energies, the photon flux decreases linearly with increasing energy. Thus to detect the same number of events the detector aperture  $A \cdot T$  must increase by a factor of 100. Even with a mission livetime of 10 years, this results in a practical limit for space-based observations of astrophysical sources at energies larger than few hundreds of GeV. Instruments with an effective area smaller than  $\sim 100 \text{ m}^2$  cannot detect the expected astrophysical flux in the TeV energy region. Even with the advent of new larger launch vehicles, the prospects for a space telescope with an area significantly larger than  $\sim 10 \text{ m}^2$  are highly uncertain.

Apparently, after Fermi-LAT and AMS-02 (Sect. 3.5) space-based experiments for GeV  $\gamma$ -ray astronomy and for direct CR measurements, respectively, have achieved a point where any further progress appears extremely difficult. However, in the near future, different projects have been envisaged to perform researches on space using particle identification, calorimetric and tracking devices. These are necessary to discriminate between charged particles (electrons/positrons, protons/antiprotons) and  $\gamma$ -rays. They will be devoted to search for dark matter signals, (Sect. 13.9), to extend the direct measurement of CRs in order to test theories of their origin, to investigate cosmic  $\gamma$ -ray emission, and to search for and study gamma-ray bursts.

CALET (<http://calet.phys.lsu.edu/>) is a Japanese led international mission, with US and Italy. The detector will be launched probably in 2015 and will be installed on the International Space Station. It is planned to detect electrons and  $\gamma$ -rays up to 10 TeV. GAMMA-400 (<http://gamma400.lebedev.ru/>) is a Russian project for a satellite experiment that will extend the Fermi-LAT energy range up to 3 TeV with a better angular resolution. The launch is foreseen around 2018. The HERD facility



(<http://herd.ihep.ac.cn/>) is one of the Cosmic Lighthouse Program onboard China's Space Station, planned to be launched and assembled starting in 2020. The main constraints imposed on HERD are a total weight less than around 2 tons and total power consumption less than around 2 kw. HERD must have the capability of accurate electron and  $\gamma$ -ray energy and direction measurement (tens of GeV–10 TeV) and an adequate CR energy measurement with charge determination up to PeV energies.

Any further effort to improve significantly the sensitivities of space-based experiments will be probably hard and expensive. A possibility is to use the Moon as a possible platform for the installation of a very large aperture  $\gamma$ -ray and CR telescope.

## References

- A.A. Abdo et al., Fermi large area telescope measurements of the diffuse gamma-ray emission at intermediate galactic latitudes. *Phys. Rev. Lett.* **103**, 251101 (2009a)
- A.A. Abdo et al., FERMI LAT observation of diffuse gamma rays produced through interactions between local interstellar matter and high-energy cosmic rays. *Astrophys. J.* **703**, 1249–1256 (2009b)
- W.B. Atwood et al., The large area telescope on the Fermi mission. *Astrophys. J.* **697**, 1071–1102 (2009)
- S. Braibant, G. Giacomelli, M. Spurio, *Particle and Fundamental Interactions* (Springer, Heidelberg, 2011). ISBN 978-9400724631
- M.S. Briggs et al., Observations of GRB 990123 by the compton gamma-ray observatory. *Astrophys. J.* **524**, 82–91 (1999). [arXiv:astro-ph/9903247v1](https://arxiv.org/abs/astro-ph/9903247v1)
- L.O. Drury, F.A. Aharonian, H.J. Volk, The gamma-ray visibility of supernova remnants: a test of cosmic ray origin. *Astron. Astrophys.* **287**, 959–971 (1994)
- P.A. Evans et al., An online repository of Swift/XRT light curves of  $\gamma$ -ray bursts. *Astron. Astrophys.* **469** 379–385 (2007). This work made use of data supplied by the UK Swift Science Data Centre at the University of Leicester
- N. Gehrels et al., The swift gamma-ray burst mission. *Astrophys. J.* **611**, 1005–1020 (2004)
- N. Gehrels, The swift  $\gamma$ -ray burst mission. *New Astron. Rev.* **48**, 431–435 (2004)
- R.C. Hartman et al., The third EGRET catalog of high-energy gamma-ray sources *astrophys. J. Supp.* **123**, 79 (1999)
- M.S. Longair, *High Energy Astrophysics*, 3rd edn. (Cambridge University Press, Cambridge, 2011). ISBN 978-0521756181
- P. Mészáros, Gamma-ray bursts. *Rep. Prog. Phys.* **69**, 2259–2321 (2006)
- P.L. Nolan et al., FERMI large area telescope second source catalog. *Astrophys. J. Suppl. Ser.* **199**, 31 (2012)
- T. Piran, The physics of GRBs. *Rev. Mod. Phys.* **76**, 1143–1210 (2004)
- E. Presani, Neutrino induced showers from Gamma-ray Bursts. PhD thesis Univ. of Amsterdam, 2011. <http://inspirehep.net/record/916768/files/>
- J.L. Racusin et al., Broadband observations of the naked-eye  $\gamma$ -ray burst GRB 080319B. *Nature* **455**, 183–188 (2008)
- M. Tavani, G. Barbiellini, A. Argan et al., The AGILE space mission. *Nucl. Instr. Meth. Phys. Res. A* **588**, 52–62 (2008)
- D.J. Thompson, Gamma ray astrophysics: the EGRET results. *Rep. Prog. Phys.* **71**, 116901 (2008). [arXiv:0811.0738](https://arxiv.org/abs/0811.0738)
- D.J. Thompson, L. Baldini, Y. Uchiyama, Cosmic ray studies with the Fermi gamma-ray space telescope large area telescope. *Astropart. Phys.* **39–40**, 22–32 (2012)
- L. Tibaldo, A tale of cosmic rays narrated in gamma rays by Fermi. Highlight Talk on the 33rd ICRC, Rio de Janeiro (2013)

## Chapter 9

# The TeV Sky and Multiwavelength Astrophysics

TeV  $\gamma$ -ray astronomy is outside the possibility of space-based experiments and can be at present studied only through ground-based experiments. However, because of the high background induced by CR showers, the large collection areas alone cannot provide adequate sensitivities for effective studies of cosmic  $\gamma$ -rays. The capability to suppress the events induced by charged CRs was made possible with the advent of the Imaging Air Cherenkov Technique (IACT), Sect. 9.1 and with some dedicated air shower particle arrays, Sect. 9.2.

Principally thanks to the successful realization of the stereoscopic technique adopted by recent IACT experiments, TeV astronomy rapidly evolved from an underdeveloped branch of CR studies to a truly astronomical discipline. The online source catalog contains now almost 150 galactic and extragalactic TeV sources, Sect. 9.3. For an historical review and details on early experiments, see (Aharonian et al. 2008; Holder 2012; Hinton and Hofmann 2009). The high sensitivity and the relatively large field of view (about  $4^\circ$ ) of IACT arrays allow not only the study of targeted sources, but also all-sky surveys at least of part of the sky, as the galactic plane.

The remarkable achievements of IACTs now include the study of morphology, energy spectrum, and time variability of several galactic and extragalactic source populations. The largest class of galactic TeV emitting sources corresponds to that of pulsars with a wind nebula (Sect. 9.4) among which the Crab is the most studied representative (Sect. 9.5). The open problem of the identification of galactic CR sources, Sect. 9.6, is connected with the identification of  $\gamma$ -rays originating from the hadronic mechanism. Shell-type supernova remnants represent the major candidates as galactic sources of CRs, and the status of the present GeV–TeV  $\gamma$ -ray observations is presented in Sect. 9.7.

Outside the galactic plane, it was discovered that the emission of radiation from jet dominated AGN (Sect. 9.9) covers a large interval of the electromagnetic spectrum and is extremely variable. Space- and ground-based  $\gamma$ -ray experiments allow now a sensitive coverage also of the MeV/GeV/TeV energy range, in addition to the band from radio to X-rays. The coordinated efforts from the community are crucial for a detailed and unbiased study of AGN and other extragalactic objects, Sect. 9.10. Multiwavelength searches are becoming more and more important in attempts to

obtain a complete picture of nonthermal processes in the Universe, as demonstrated by the campaigns made to measure the spectral energy distributions of some blazars, Sect. 9.11. Blazars, among the AGN, present some particular features, as for example strong and rapid variability and a jet orientation toward the observer (Sect. 9.12). As these objects are among the furthest observed objects in the Universe, their observation through TeV photons can constraint estimates of the presence of extragalactic background light, which is relevant also for cosmological models, Sect. 9.13.

Despite the substantial progress of GeV and TeV  $\gamma$ -ray observations, finding a convincing case of  $\gamma$ -rays due to  $\pi^0$ -decay remained extremely difficult, in particular in the PeV region. Only the detection of neutrinos could unambiguously solve the problem of the origin of the highest energy CRs, as discussed in Chap. 10.

## 9.1 The Imaging Cherenkov Technique

The Earth's atmosphere is opaque to high-energy  $\gamma$ -rays. As discussed in Sect. 4.3, their mean free path for pair production is almost the same as the electron radiation length,  $X_0 \simeq 37 \text{ g cm}^{-2}$  in air. Gamma-rays interact electromagnetically producing an electron/positron pair. These secondary particles yield a new generation of  $\gamma$ -rays through bremsstrahlung, starting the generation of an electromagnetic cascade. Any secondary charged particle in the shower produces Cherenkov light if its velocity exceeds the threshold  $\beta = v/c > n$  (Sect. 4.6.3). The light is emitted at the Cherenkov angle  $\theta$ , with  $\cos \theta = 1/\beta n$ . As the refraction index  $n$  of the atmosphere changes with atmospheric depth, the Cherenkov angle increases from  $0.66^\circ$  at a height of 10 km to  $0.74^\circ$  at 8 km. This results in a rough focusing of light onto the ground into a ring-like region with radius of  $R \simeq 10 \text{ km} \times 0.012 \text{ rad} = 120 \text{ m}$  for a typical  $\gamma$ -ray shower. The number of Cherenkov photons emitted per unit length is  $n_c \sim 0.1 \text{ photons cm}^{-1}$  at sea level. Multiplying  $n_c$  by the number of particles at maximum ( $N_{\text{max}}$ ) and by the path length of shower particles, the total number of Cherenkov photons turns out to be  $N_c \sim 10^6$  for 1 TeV  $\gamma$ -rays.  $N_c$  is proportional to  $E_\gamma$ .

Atmospheric Cherenkov detectors fall into two broad classes: sampling and imaging telescopes. Some sampling instruments used mainly for primary CR measurements have been described in Sect. 4.6. The imaging technique relies on the detection on ground of the images of the Cherenkov light distribution from these electromagnetic cascades. From the measurement, it is possible to determine both the longitudinal and lateral development of the electromagnetic showers, and the arrival direction and energy of the primary  $\gamma$ -rays.

Imaging Cherenkov are essentially wide-field optical telescopes consisting of a large reflector of about 10 m radius, reflecting the light (the image) into a high-speed multi-PMT camera in the focal plane. Short exposures (less than 30 ns) are required to detect the faint flashes of Cherenkov light against the Poisson fluctuation in the night-sky background.

An IACT array must be operated (as other telescopes) in almost total darkness, thus must be installed far from human environments. These telescopes operate usually on

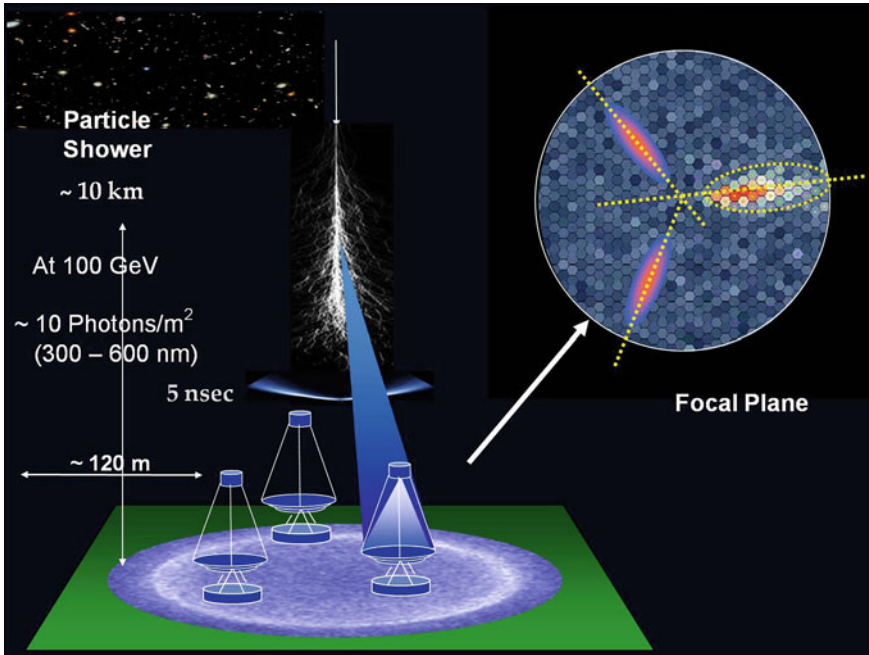


**Fig. 9.1** Sketch of the imaging atmospheric Cherenkov telescopes technique. A shower initiated by a  $\gamma$ -ray of energy  $\geq 100$  GeV is observed through the Cherenkov radiation emitted by charged particles with  $\sim 10$  m diameter reflectors positioned about 100 m away from each other. The Cherenkov light arrives on ground as a thin pancake, few ns wide. The fraction arriving at the reflector is focused into a high-speed PMT camera in the focal plane. The images at the focal plane of different telescopes (*upper right inset*) allow the determination of the shower direction and energy. Modified from an original drawing of W. Hofmann

moonless nights, thus limiting the duty cycle to 10–15%. High-speed detectors and electronics are required to minimize the integration time, the amount of time the chip spends “counting photons.” Ideally, the integration time should be reduced down to the shortest intrinsic timescale of the Cherenkov light wavefront, which corresponds to a few nanoseconds (Fig. 9.1). Longer integration time reduces the signal-to-noise.

The field of view (FoV) of IACTs is  $\sim 4^\circ$ , substantially larger than most optical telescopes. This FoV allows to obtain images of showers whose impact parameters on ground extend up to 120 m away. Thus, regions of the sky containing one or more source candidates are usually targeted for observations. Surveys can only be accomplished slowly, by tiling regions of the sky with overlapping FoVs. The energy interval from which the current generation of IACTs are sensitive ranges from 100 GeV to 100 TeV. Their angular resolution is of the order of  $0.1^\circ$ , the energy resolution around 15% and an integral energy flux sensitivity of few times  $10^{-13}$  erg  $\text{cm}^{-2}$   $\text{s}^{-1}$ . Their sensitivity is sufficient to detect the Crab nebula (Sect. 9.5) in

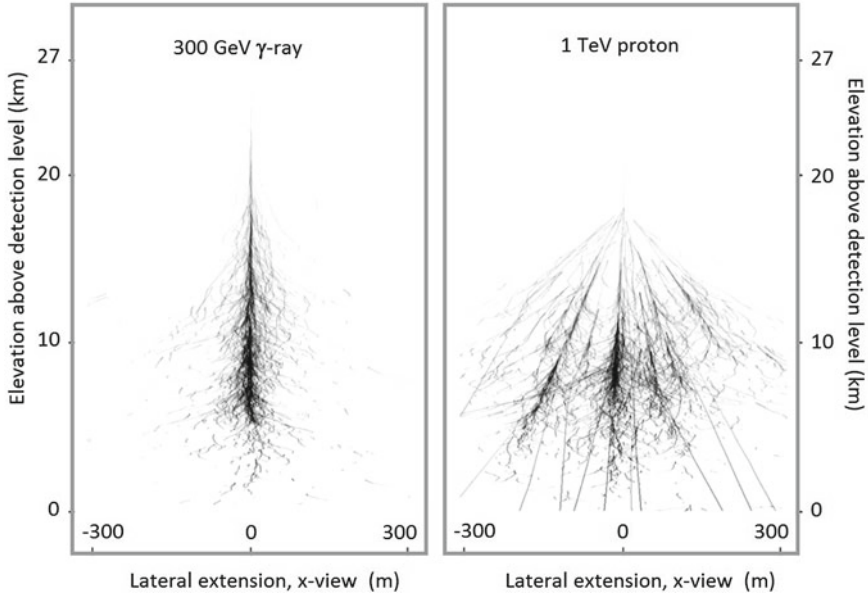


**Fig. 9.2** Comparison of a pure electromagnetic shower (from a 300 GeV  $\gamma$ -ray) and a shower initiated by a 1 TeV proton. The plot shows the projection of secondary particle trajectories onto a plane in which the ordinate corresponds to the elevation (courtesy of Dr. Konrad Bernloehr)

about one minute, and a source with 1% of the Crab flux in 25 h<sup>1</sup> As most very large optical telescopes, IACTs typically make use of an altitude-azimuth drive for tracking sources during large exposures. The angular resolution reached with the IACT technique allows to resolve important substructures of some sources.

Current telescopes are based on either simple parabolic reflectors (MAGIC) or many individual mirror segments having a radius of curvature equal to the focal length, placed on an optical support structure (HESS, VERITAS).

### 9.1.1 Gamma-Ray Versus Charged CR Discrimination

Pure electromagnetic showers, as those initiated by  $\gamma$ -rays, have different characteristics from those initiated by protons and nuclei, Fig. 9.2. Images of EAS initiated by  $\gamma$ -rays have a compact elliptic shape, and the major axis of the ellipse indicates the shower axis projected onto the image plane (see the focal plane inset in Fig. 9.1). In contrast, the images of EAS produced by protons or nuclei show a complex structure

<sup>1</sup> Note that a source with a flux equal to 1% of the Crab is not detected in 100 min. The statistical significance of a signal excess depends on the background level, and this increases linearly with the observation time.

due to electromagnetic sub-showers initiated by following generations of  $\pi^0$  decay and to the presence of penetrating muons originated by decays of charged pions. For this reason, the images of Cherenkov light observed by an individual IACT are typically analyzed to obtain a set of quantities that characterize the shape of the images. IACTs achieve good  $\gamma$ -ray/hadron separation using the information on the image shape at the trigger level.

To give an idea of the background level and of the intrinsic rejection power of IACTs, we can use the all-particle CR spectrum (2.20b) for primary energies larger than 100 GeV

$$\Phi(>100 \text{ GeV}) = 2 \times 10^{-3} \frac{\text{particles}}{\text{cm}^2 \text{ s sr}}. \quad (9.1)$$

The background event rate  $R_{CR}$  is obtained by multiplying (9.1) by the solid angle  $\Delta\Omega$  corresponding to the FoV of the telescope and by the pool area  $A$  covered by the telescope. The solid angle corresponding to a cone of aperture of  $4^\circ$  is  $\Delta\Omega \sim 3 \cdot 10^{-3}$  sr; the pool area  $A$  corresponds to a circle having a radius of about 100 m and therefore  $A \sim 3 \cdot 10^8 \text{ cm}^2$ . Hence the event rate on a single IACT due to charged CRs is

$$R_{CR} = \Phi(>100 \text{ GeV}) \cdot A \cdot \Delta\Omega \sim 2000 \text{ s}^{-1} = 2 \text{ kHz}. \quad (9.2)$$

As the trigger rate of a single telescope of HESS or VERITAS is of the order of 100–200 Hz, a single IACT can reject charged CRs at the trigger level by a factor of  $\sim 10$ .

As shown in Fig. 9.1, the projection of shower images on the focal plane results in ellipses with their major axes pointing in the direction of the source. Observation of individual showers with a system of multiple IACTs allows the reconstruction of the three-dimensional structure of  $\gamma$ -ray showers in the so-called *stereoscopic observation*. With stereo observations, background events are suppressed with higher efficiency (by about a factor 100) and the angular resolution reaches precisions of a few arcminutes. Such resolution enables the possibility of morphological studies of extended  $\gamma$ -ray sources, as the SNRs.

A single telescope is triggered when several pixels in the PMTs of the camera exceed the threshold, within some time coincidence window. For the current generation of IACT instruments, this window is typically between 3 and 25 ns and the pixel multiplicity ranges from 2 to 4. Stereo observations are enabled by an *array trigger*: the trigger signals from the individual telescopes are delayed and brought into coincidence within a coincidence window of  $\sim 40$ –100 ns.

### 9.1.2 HESS, VERITAS and MAGIC

There are currently three major imaging atmospheric Cherenkov telescope systems in operation, two in the Northern, and one in the Southern hemisphere.



The **High Energy Stereoscopic System (HESS) Observatory** is located in **Namibia** ( $-23^{\circ}\text{N}$ ,  $-16^{\circ}\text{W}$ , altitude 1,800 m), in the Southern Hemisphere. It is the **IACT** with the largest field of view and the only one in the Southern hemisphere with good observation conditions for the galactic plane. The initial **four HESS telescopes (Phase I, completed in 2004)** are arranged in the form of a square having a side length of 120 m, to provide multiple stereoscopic views of air showers. Each telescope of Phase I has a **diameter of 13 m**, with a total mirror area of  $108\text{ m}^2$  per telescope. **The cameras** which capture and record the Cherenkov images of air showers have a **large field of view ( $\sim 5^{\circ}$ )** to allow **observations** and **surveys** of **extended sources**. It has 960 photon detector elements (“pixels”) to resolve image details, and a triggering scheme which allows to identify the brief and compact Cherenkov images and to reject backgrounds. The complete electronics for image digitization, readout and triggering is integrated into the camera body.

In **Phase II** of the project, a **single huge dish with about  $600\text{ m}^2$**  mirror area was added at the center of the array, increasing the energy coverage, sensitivity and angular resolution of the instrument (see Fig. 9.3). This telescope started taking data in 2012. The **camera** of the new telescope follows the design of the others but it is **much larger**—it contains 2,048 pixels—and virtually every detail is improved.

The central trigger system receives trigger signals from the individual telescopes and searches for coincidences, properly accounting for the signal delays, and their dependence on telescope pointing. Coincident triggers result in the readout of telescope data; for noncoincident triggers, the telescope readout electronics is cleared after a few microseconds and is ready for the next event.

The **Very Energetic Radiation Imaging Telescope Array System (VERITAS)** (Fig. 9.4) is operating at the Fred Lawrence Whipple Observatory in southern **Arizona, USA** ( $32^{\circ}\text{N}$ ,  $111^{\circ}\text{W}$ , altitude 1,275 m). It is an array of **four 12 m optical reflectors** with **similar** characteristics of **HESS-Phase I**. Each reflector uses 499-pixel cameras, with a **field of view of  $3.5^{\circ}$** . The covered energy range is between **50 GeV and 50 TeV**. The four-telescope array was completed in January 2007.

The **Major Atmospheric Gamma-ray Imaging Cherenkov (MAGIC)** ( $28^{\circ}\text{N}$ ,  $17^{\circ}\text{W}$ , altitude 2,225 m) originally consisted of a single, **very large reflector ( $236\text{ m}^2$ )** installed on the **Canary island of La Palma**, with a  $3.5^{\circ}$  high-resolution camera com-



**Fig. 9.3** The HESS telescopes in Namibia. Credit: HESS collaboration (<http://www.mpi-hd.mpg.de/hfm/HESS/>)





**Fig. 9.4** The four IACT array VERITAS at Mt Hopkins, Arizona. Credit: VERITAS collaboration (<http://veritas.sao.arizona.edu/>)



**Fig. 9.5** The two large telescopes of the magic observatory. Credit: MAGIC collaboration (<https://magic.mpp.mpg.de/>)

posed of 576 ultra-sensitive PMTs. The first telescope was fully operational since 2004. In 2009, a second telescope of essentially the same characteristics was added; MAGIC-II was installed at a distance of 85 m from MAGIC-I, Fig. 9.5. MAGIC is characterized by the largest collection surface of any existing  $\gamma$ -ray telescope worldwide, an assembly of nearly 1,000 individual mirrors, together resulting in a parabolic dish with 17 m diameter; the diamond-grinding and polishing of the individual aluminum mirrors and their mounting (in altitude/azimuth controlled position) on a lightweight carbon fiber structure was a real technological challenge. The large

surface and the optimal light collection of the mirrors allow the detection of  $\gamma$ -rays with an energy threshold of  $\sim 25$  GeV.

A very fast (average time 40 s) repositioning of the telescope axis is one of the major characteristics of MAGIC with respect to other IACTs. This is achieved by minimizing the device weight and automating axis control. Repositioning in a matter of seconds is important when short-lived phenomena are signaled by other active devices, e.g., by satellite-based wide-angle detectors in the X-ray band, in particular for GRBs.

In addition to the above detectors, CANGAROO was a Japanese and Australian observatory placed in Australia. In its final design (operating from 2004 to 2011), it consisted of four 10 m diameter telescopes.

The Cherenkov Telescope Array (CTA) will be probably the future of observational  $\gamma$ -ray astronomy, at least for the next 10–20 years. The research objectives of the next generation of IACT arrays, and namely of CTA, are devoted to (i) a significant improvement (by an order of magnitude) of the flux sensitivities in the standard 0.1–10 TeV energy interval, and (ii) an expansion of the energy domain of IACT arrays in both directions—down to 10 GeV and well beyond 10 TeV. This ambitious research goal will be realized by increasing the number of telescopes with different sizes, from few very large 20 m diameter class telescopes to a large number of modest area (10–30 m<sup>2</sup>) reflectors. In this effort, all the three existing IACTs communities are involved (Rieger et al. 2013).

## 9.2 EAS Arrays for $\gamma$ -astronomy

The EAS technique, designed for the detection of CRs at PeV and EeV energies, can be adopted also for  $\gamma$ -ray astronomy. The mandatory requirement is that the energy threshold be reduced by two or three orders of magnitude, using dense particle arrays located at very high altitudes. The feasibility of the measurement at ground level of showers initiated by a  $\gamma$ -ray has been successfully demonstrated by the Milagro and ARGO collaborations.

The Milagro detector consisted of a large central water reservoir (60 × 80 m<sup>2</sup>) which operated between 2000 and 2008 in New Mexico (36°N, 107°W), at an altitude of 2,630 m. The reservoir was covered with a light-tight barrier, and instrumented with PMTs. In 2004, an array of 175 small tanks were added, irregularly spread over an area of 200 × 200 m<sup>2</sup> around the central reservoir. This configuration sampled with high-resolution the air shower over a relatively small area compared to the air shower footprint. Milagro developed analysis techniques for CR background discrimination that provided sufficient rejection for the first large-scale survey of the northern  $\gamma$ -ray sky in the TeV range. The strong TeV sources Crab Nebula (Sect. 9.5) and Markarian 421 (Sect. 9.11.2) were observed as well as three extended sources in the galactic plane, each with integrated fluxes comparable to the Crab nebula at 20 TeV.

**HAWC.** These Milagro results, as well as the potential for continuous monitoring a large fraction of the sky, have motivated the proposals of constructing larger EAS detectors like the **High-Altitude Water Cherenkov Observatory (HAWC)**. HAWC is located at an **altitude of 4,100 m** close to Sierra Negra, **Mexico** ( $19^\circ\text{N}$ ,  $97^\circ\text{W}$ ). The detector can **continuously monitor a solid angle of  $\sim 1$  sr** for  $\gamma$ -rays at **TeV energies**. HAWC in the final configuration will consist of **300 water tanks** of 7.3 m diameter and 4.5 m depth each viewed by 4 upward-facing PMTs, with an overall 15-fold increase in sensitivity with respect to Milagro. HAWC (<http://www.hawc-observatory.org/>) started data taking with about 1/3 of its final configuration in 2013.

**ARGO-YBJ.** A large plateau at a **very high altitude (4,300 m- $30^\circ\text{N}$ ,  $90^\circ\text{E}$ )** at Yangbajing in **Tibet** allows the installation of large surface array detectors. The **Astrophysical Radiation with Ground-based Observatory (ARGO)** experiment was in operation from 2001 until 2013 and consisted of a **single layer of resistive plate chambers completely covering an area of  $110 \times 100 \text{ m}^2$** . They observed the emission of  $\gamma$ -rays from the **Crab nebula, Markarian 421 and two Milagro sources**. The **Tibet Air Shower Experiment (AS $\gamma$ )** air shower array, also at Yangbajing, consists of  **$\sim 750$  closely spaced scintillation detectors covering an area of  $37 \times 10^3 \text{ m}^2$** .

At higher energies, recently a new project called **Large High Altitude Air Shower Observatory (LHAASO)** has been suggested, improving the features of ARGO. The proposed huge detector facility will consist of **several sub-arrays for the detection of the electromagnetic and muon components of air showers**. They will cover a huge area and can achieve an impressive sensitivity at energies of several tens of TeV.

### 9.2.1 Sensitivity of $\gamma$ -ray Experiments

**Fig. 9.6** shows the sensitivity as a function of the  $\gamma$ -ray energy of current and future ground-based detectors. Here, the **sensitivity** represents the minimum value for the **spectral energy distribution (SED)** of a source which can produce an observable **signal**. Sources with a SED smaller than the sensitivity will be completely overwhelmed by the background. We will return on this concept in Sect. 10.8.1. **The dashed line denoted as “Crab” represents the  $\gamma$ -ray flux from the Crab nebula**. Also **fluxes 1/10 and 1/100 of the “Crab”** are indicated. For comparison, also the sensitivities of AGILE and Fermi-LAT are reported. Satellite experiments as well Argo, Milagro, and HAWC have a much larger field of view with respect to the IACTs and can monitor simultaneously a large number of sources. **In the figure, 50 h of IACTs observations are considered, and 5 y of survey mode for large field of view detectors.**

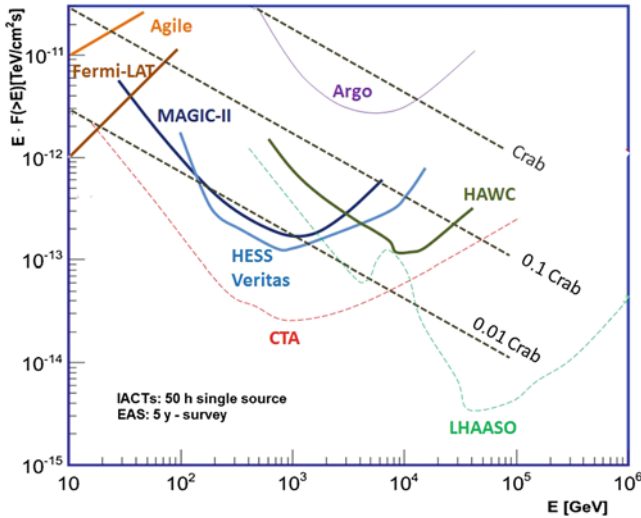


**Fig. 9.6** Sensitivity as a function of the  $\gamma$ -ray energy of current and future ground-based detectors. For EAS experiments (LHAASO, ARGO, HAWC) 5 y in survey mode have been assumed, while 1 y has been assumed for Fermi-LAT and AGILE. For the remaining IACTs, 50 h of observation on a single source are considered. Thin *dashed lines* represent future experiments

### 9.3 TeV Astronomy: The Catalog

Production of GeV (or HE) and TeV (or VHE)  $\gamma$ -rays are expected in astrophysical environments where acceleration of particles (protons, nuclei, and electrons) is accompanied by their intensive interactions with the surrounding gas and radiation fields. These interactions contribute significantly to high-energy emission from galactic objects such as young supernova remnants, star forming regions, pulsars, pulsars wind nebulae and compact binary systems. Gamma-ray emission is expected also from extragalactic objects as active galactic nuclei and radio galaxies.

In 2003, ten TeV-emitting sources were known, detected with the so-called first generation of IACTs: 7 blazars, 2 supernova remnants and the Crab. The second generation of IACTs (Sect. 9.1.2) started scientific operation in  $\sim 2004$  and in only a few years they brought data that transformed our view of the high-energy  $\gamma$ -ray sky. The 145 TeV-emitting sources known after the 2013 ICRC are shown in Fig. 9.7. Apart from four sources that were first detected by Milagro (MGRO J2019+37, MGRO J1908+06, Boomerang and Geminga), the sources were detected (and many of them later on characterized) by IACTs. As occurred in the GeV range, the number of known TeV sources has increased by one order of magnitude over the last decade, and new classes of emitting sources have been discovered, see Table 9.1. The fraction of unassociated TeV sources is  $\sim 20\%$ .

At TeV energies, the unidentified objects lie essentially on the galactic plane, differently from the GeV range objects. This could be due to an observational bias.

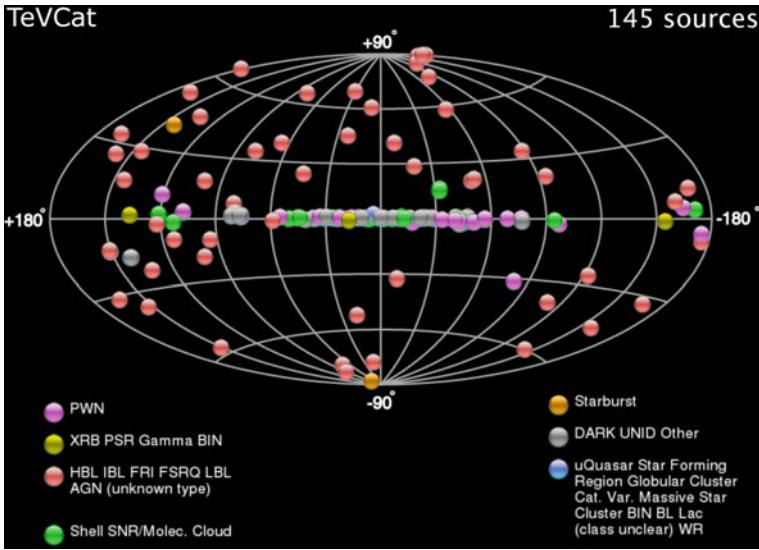


**Fig. 9.7** Map of TeV sources (Spring 2014) retrieved from the online TeV catalog (<http://tevcat.uchicago.edu/>), which displays with different color codes the position in galactic coordinates of the various  $\gamma$ -ray sources detected from ground. Most of the detections were performed by IACTs, which typically are sensitive to  $\gamma$ -rays well above 100 GeV

**Table 9.1** Number of objects cataloged in the TeVCat in winter 2013. From <http://tevcat.uchicago.edu/>

Type	Designator	Objects	Representatives
<b>Galactic sources</b>			
Pulsar wind nebula	PWN	31	Crab, Geminga, Vela X
Supernovaremnant with shell	Shell	11	See Table 9.2
Supernova remnant with mol. clouds	SNR/Mol. Cloud	8	W28, W51
Binary systems	Binary	5	LS 5039, LSI +61 303
Massive star clusters, globular cl.	–	5	–
<b>Extragalactic sources</b>			
HBL Lac type of blazar	HBL	41	Mrk 421, Mrk 501
IBL Lac type of blazar	IBL	7	Bl Lac, W Comae
LBL Lac type of blazar	LBL	1	–
FSRQ type of blazar	FSRQ	3	3C 279
FRI type of blazar	FRI	3	Centaurus A, M87
Starburst galaxy	Starburst	2	
<b>Unidentified</b>	<b>UNID</b>	<b>28</b>	<b>–</b>
<b>Total</b>		<b>145</b>	



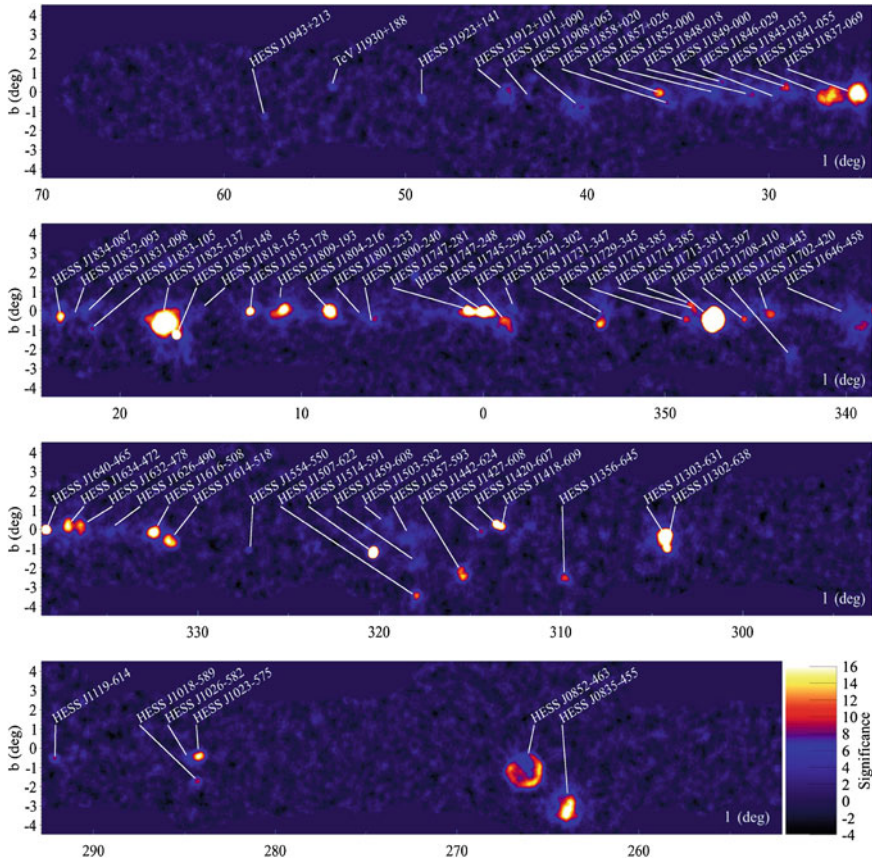


**Fig. 9.8** Significance map of  $\gamma$ -ray objects in the galactic plane as observed by HESS. Credit: HESS collaboration (Carrigan et al. 2013)

The wide field of view and the survey mode operation of the Fermi satellite allows the Fermi-LAT for a roughly (within a factor two) uniform exposure of the entire sky. The IACTs have very narrow effective fields of view and the galactic plane is the only large fraction of the sky that has been studied by HESS in detail. This dedicated survey of 2,800 hours has covered the range in galactic longitude between  $[-85^\circ, +60^\circ]$  and  $[-3.5^\circ, +3.5^\circ]$  in latitude. It has revealed more than fifty VHE  $\gamma$ -ray sources and the significance map of the discovered objects is shown in Fig. 9.8. A large fraction (more than half) corresponds to PWNe, located in the close vicinity of young and energetic pulsars (Paneque 2012).

In the next section, we describe pulsar and pulsar wind nebulae, which are the dominant galactic populations of identified objects emitting  $\gamma$ -rays at GeV and TeV energies. The efficiency of converting spin-down power into  $\gamma$ -rays is typically in the range of 1–10 %.

## 9.4 Gamma-Rays from Pulsars

Pulsars (PSR) are rotating neutron stars (Sect. 6.6.2), which have been traditionally a subject of radio astronomy, with about 1,800 pulsars found beaming radio waves. Some pulsars have an extended nebula emitting radiation. This constitutes the class of pulsar wind nebulae (PWNe). In some cases, PSR and PWNe are emitting also radiation at high energies. Since the launches of Fermi-LAT and AGILE, the number of  $\gamma$ -ray pulsars has increased from half a dozen to more than 150. Despite the high galactic background, the periodic  $\gamma$ -ray emission stands out due to the high fluxes, hard spectral index, and powerful timing identification. Due to the relatively poor angular resolution of space  $\gamma$ -ray telescopes, in most cases PWNe cannot be firmly distinguished by SNRs: the difference is the presence of an embedded pulsar in the nebula (see Table 8.1 for the Fermi-LAT survey). Concerning the TeV range, PWNe are the most abundant class of known emitters in the Galaxy, following the HESS survey of the galactic plane (see Table 9.1).

The continuous energy emission from the extended nebula requires a steady supply of high-energy particles, which must be provided by the inner pulsar with continuous injection of energy. In fact, a charged particle of energy  $E$  present in the nebula and with a characteristic energy loss ( $dE/dt$ ) (for instance due to synchrotron emission) produces radiation for a characteristic time  $\tau \simeq E/(dE/dt)$ . It can be worked out that  $\tau$  is much shorter than the age of the supernova remnant. For the considered production of GeV–TeV  $\gamma$ -rays, models that transfer a few percent of the rotational energy of pulsars to  $\gamma$ -rays exist.

**Models of  $\gamma$ -ray emission from a pulsar.** The regions of the magnetosphere where particle acceleration can occur are called vacuum gaps (Sect. 6.6.2). Also the pulsed, periodic  $\gamma$ -rays are thought to be originated in gaps regions. Models of particle acceleration differ, primarily, on the location of these gaps in the magnetosphere. The measured light curves and spectral energy distributions from space and ground-based experiments can help to disentangle the various models.

Most of the  $\gamma$ -ray energy spectra measured by Fermi-LAT (Nolan et al. 2012) are well fitted by a power-law function with an exponential cutoff, Eq. (8.5.1), with  $E_0$  ranging between 1 and 10 GeV and  $b \lesssim 1$ . If the production of  $\gamma$ -rays occurs in the polar cap regions (refer to Fig. 6.8), strong absorption effects are expected due to interaction of high-energy photons with the magnetic field as well as with the radiation field (production of  $e^\pm$  pairs). In this case, a super-exponential cutoff, i.e.,  $b > 1$  in (8.5.1), is expected and a strong suppression of the flux at relatively low energies (few GeV). The value  $b \lesssim 1$  is in general well explained by the mechanism of synchrotron radiation emission and gives a preference to models of  $\gamma$ -ray production in the outer gap regions.

**Pulsar Wind Nebulae (PWNe)** are objects in which a wind of energetic particles from a pulsar carries most of the rotational power into the surrounding medium. During the transport, accelerated leptons can lose energy in the magnetic fields. This originates nonthermal radiation, the “synchrotron nebula” around the pulsar, ranging



from the radio to the X-ray and, in some cases, to the MeV band. In the steady state, a second component is originated by the inverse Compton effect (IC) of electrons on low-energy radiations fields of synchrotron, thermal or microwave-background origins, as described in Sect. 8.4. The resulting extended nebula around the pulsar can be observed up to the VHE  $\gamma$ -rays (Aliu et al. 2008).

Observations with ground-based IACTs indicate that PWNe are the most effective galactic objects for the production of TeV gamma-rays, allowing the detection of such systems even in the neighboring LMC galaxy. Before 2004, only the Crab PWN was known as a source of steady TeV  $\gamma$ -rays. The development of the new sensitive IACTs has increased the number of likely PWNe detected, but the Crab still plays a fundamental role for the understanding of the physics involved in the pulsars, as shown in the next section.

## 9.5 The CRAB Pulsar and Nebula

The Crab nebula is the strongest TeV  $\gamma$ -ray source and it is used as a gauge for other sources (see Fig. 9.6). It is located at a distance of  $(2.0 \pm 0.2)$  kpc from the Earth and belongs to the class of supernova remnants with a pulsar in its center and without any detected shell component. It is associated with the supernova explosion reported by Chinese astronomers in 1054 AD. The Crab Pulsar at the center of the nebula is also known as PSR J0534+2200 and is one of the most energetic known pulsars. The rotational energy loss  $(6.81)$  of the Crab corresponds to  $dE_{\text{rot}}/dt \sim 5 \times 10^{38}$  erg/s. Estimation of its characteristic age using its rotation period ( $P = 33$  ms) and derivative ( $dP/dt = 4.2 \times 10^{-13}$  s/s) yields an age of 1,240 y, close to the elapsed time from the supernova of 1054.

The nebula and the inner pulsar are well studied in almost all wavelength bands of the electromagnetic spectrum from the radio ( $10^{-5}$  eV) to hundreds TeV  $\gamma$ -rays. A simple magneto-hydrodynamical model for the interaction of a high-energy electron-positron wind with the interstellar medium satisfactorily describes the main features of the nonthermal emission. Fig. 9.9 represents the observed  $E^2 \frac{dN}{dE}$  distribution from the Crab nebula, which extends over 21 decades of energies/frequencies. This spectral distribution is well explained by considering the SSC mechanism, Sect. 8.4 and details in Kennel and Coroniti (1984) and Aharonian et al. (2004). The contribution from hadronic interactions to the  $\gamma$ -ray production does not seem necessary.

The TeV emission from the Crab nebula was first established with very high significance by the Whipple group in 1989. This result demonstrated the power of the imaging atmospheric Cherenkov method. The Crab, well sampled from radio to TeV  $\gamma$ -rays, is used for the cross-calibration of ground-based detectors. The integral flux above 1 TeV corresponds to

$$\mathcal{F}_{\gamma}(> 1 \text{ TeV}) = (2.1 \pm 0.1) \times 10^{-11} \frac{\text{photons}}{\text{cm}^2 \text{ s}}. \quad (9.3)$$

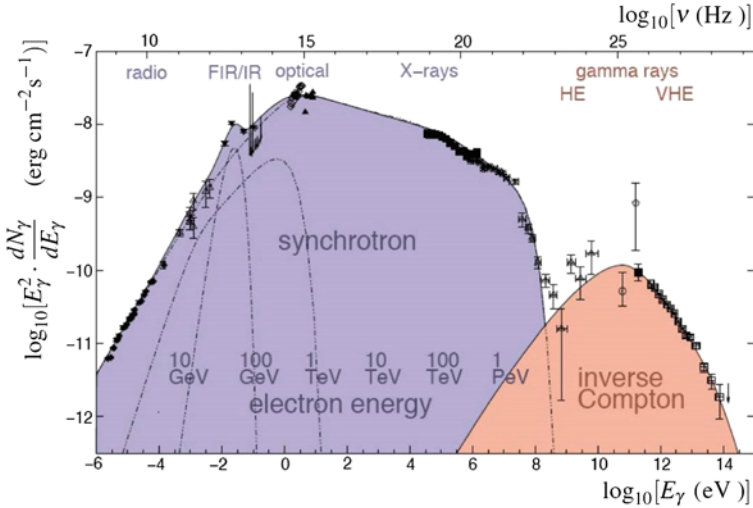


**Fig. 9.9** Multiwavelength observations of the crab nebula. The synchrotron emission is given by the superposition of the contributions of electrons with different energies. Mono-energetic electrons contribute with photons with spectrum peaked according to Eq. (8.35). For instance, 1 TeV electrons give photons in the visible wavelength. The synchrotron spectrum provides the target photons for the inverse Compton (IC) process (Funk 2011)

The Crab nebula was considered as a steady “standard candle”. Only recently,  $\gamma$ -ray flares have been detected by AGILE and Fermi-LAT and pulsed emission from the Crab pulsar up to beyond 100 GeV observed by MAGIC and VERITAS. The origins of these variations are still under investigation.

Although GeV–TeV  $\gamma$ -rays constitute only a small fraction of the luminosity of the nebula, they provide crucial information on the environmental conditions. The comparison of the X-ray and TeV  $\gamma$ -ray fluxes allows respectively the determination of the energy density of the magnetic field and that of the radiation energy density in (8.45). As the former exceeds by more than two orders of magnitude the latter, this has led to the estimate that the average nebular magnetic field is about  $100 \mu\text{G}$ , as expected from magneto-hydrodynamical models (Rieger et al. 2013). Thus, as evident from the two regions labeled *synchrotron* and *inverse Compton* in Fig. 9.9, the Crab nebula is very inefficient in producing  $\gamma$ -rays through inverse Compton scattering. Only its extremely high spin-down power allows the production of the observed flux (9.3).

Particularly interesting is the transition region between the falling edge of the *synchrotron* component and the rising edge of the *inverse Compton* component. Figure 9.10 shows in detail the results from high-energy experiments. The data collected by COMPTEL and EGRET carry information about the fading synchrotron part of the spectrum. The Fermi-LAT data reveal a sharp transition from the synchrotron to the IC component at around 1 GeV (Abdo et al. 2010b). The measurements with ground-based IACTs have almost approached 100 TeV. This is

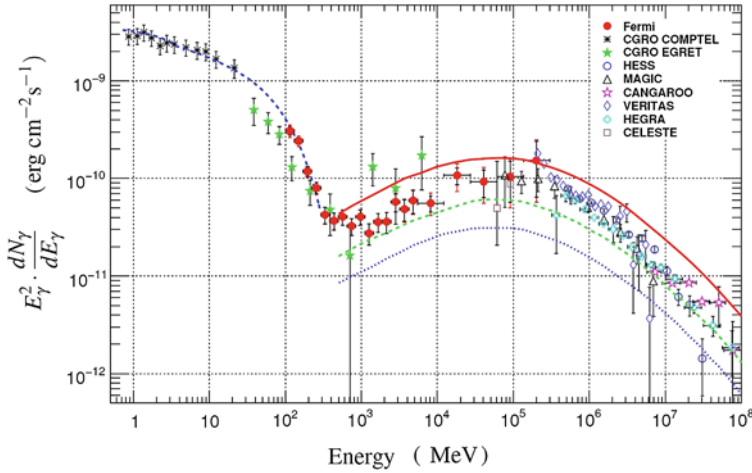


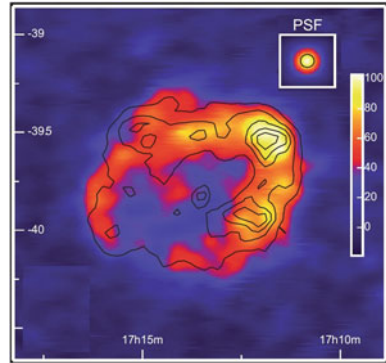
**Fig. 9.10** Spectral energy distribution of the crab nebula from soft to very high energy  $\gamma$ -rays. The fit of the synchrotron component, using COMPTEL and Fermi-LAT data (*dashed line* up to 300 MeV), is overlaid. The predicted inverse Compton spectra (from of 300 to 100 TeV) are overlaid for three different values of the mean magnetic field: 100 (*solid line*), 200 (*dashed line*), and 300  $\mu\text{G}$  (*dotted line*). Credit: Fermi-LAT collaboration

compatible with the fact that the IC component extends up to the maximum energy set by the maximum energy of the accelerated electrons, i.e., 1 PeV (see Fig. 9.9). At this energy, from Eq. (8.35), the critical energy for synchrotron emission corresponds to  $E_c = h\nu_c \sim 1$  MeV. The maximum of the inverse Compton curve occurs in correspondence of  $E_\gamma \simeq 60$  GeV. This is supported by both the Fermi-LAT and IACTs measurements, which agree remarkably with each other. This is one of the first cases in which measurements made by ground- and space-based experiments overlap in energy. Note that the predicted flux of  $\gamma$ -rays from IC decreases as the magnetic field increases. This is due to the fact that the synchrotron energy loss of electrons increases with the magnetic field  $B$ , Eq. (8.28). As a result, the high region part of the electron spectrum decreases as  $B$  increases.

## 9.6 The Problem of the Identification of Galactic CR Sources

The diffusive shock acceleration model predicts the production of accelerated particles in SNRs that can interact with ambient magnetic fields, with ambient photon fields, or with matter. The amount of relativistic particles present in the acceleration region increases with time as the SNR passes through its free expansion phase, and reaches a maximum in the early stages of the Sedov phase (Sect. 6.6.2). Correspondingly, the peak in  $\gamma$ -ray luminosity typically appears some  $\sim 10^3$ – $10^4$  years after the supernova explosion.

**Fig. 9.11** HESS map of  $\gamma$ -ray excess events for RX J1713.7-3946 - the first SNR shell to be resolved at TeV energies. The superimposed contours show the X-ray surface brightness as seen by ASCA in the 1–3 keV range. On the upper right side, the HESS point spread function (PSF). Credit: HESS collaboration



A straightforward test of the acceleration of CRs in SNRs up to PeV energies would be the detection of  $\gamma$ -rays produced through the hadronic mechanism directly from young remnants and/or from dense clouds overtaken by the expanding shells. The main challenge is to distinguish  $\gamma$ -rays emitted through hadronic ( $\pi^0$ -decay, Sect. 8.2) from those originating in leptonic processes, Sect. 8.4.

Multiwavelength observations of objects of different classes, as for the case of the Crab reported in Figs. 9.9 and 9.10, are fundamental in the quest for disentangling sources where leptonic or hadronic mechanisms are involved. The identification of galactic  $\gamma$ -ray emitters with astrophysical objects known at other wave bands is thus an important prerequisite in the study of the origin of cosmic rays.

The IACTs have been able to image SNRs in TeV  $\gamma$ -rays, probing the SNR-shell acceleration of either electrons or hadrons up to at least 100 TeV (in case of leptonic emission) or a few hundred TeV (for hadronic acceleration). Thanks in particular to the HESS survey of the galactic plane, we know that these acceleration sites are spatially superimposed with regions of nonthermal X-ray emission. This coincidence has strengthened the hypothesis that galactic CRs up to the knee are accelerated in SNRs. Fig. 9.11 shows the morphological structure of one SNR, namely RX J1713.7-3946 (Aharonian et al. 2007b). This image has revealed a good correlation of the TeV emission sites with the nonthermal emission detected in X-rays.

However, even if radio and X-ray data suggest that SNRs are indeed the sources of CR electrons, no compelling evidence for the acceleration of protons in SNRs up to the PeV energies has been found up to now, and it is not clear whether proton and electron accelerators are of different nature. We illustrate the reason in the following sections.

## 9.7 Extended Supernova Remnants

In radio, optical, and X-ray wavelengths detailed observations of supernova remnants (SNRs) have been performed. Several of them have been discovered as sources of TeV  $\gamma$ -rays, in particular by the HESS survey of the galactic plane.

The Green catalog on radio observations of known galactic SNRs contains 274 objects (<https://www.mrao.cam.ac.uk/projects/surveys/snrs/>), and is based on results published in the literature up to the end of 2008. The basic summary data for each SNR include its designation, position, angular size, type, flux density at 1 GHz, spectral index, and any other names by which it is known.

The second Fermi-LAT catalog (2FGL, Sect. 8.8), lists in addition to 6 identified SNRs, 58  $\gamma$ -ray sources associated with SNRs or PWNe, including such important objects as Cassiopeia A, Tycho's SNR, the Cygnus Loop, W51C, W44, and IC 443, and the TeV-bright SNRs RX J1713.7-3946 and RX J0852.0-4622 (Vela Junior), see Fig. 8.6.

The SNRs observed by Fermi-LAT allow potential associations of these objects with the Green radio catalog. Two main classes have been identified: young SNRs and those that are interacting, often with molecular clouds. If radio and GeV emission arise from the same particle population(s), e.g., leptons and/or hadrons accelerated at the SNR shock front, the indices of the energy spectra measured in GeV and radio bands should be correlated. The study of the correlation shows that several of the known, young SNRs are more consistent with a lepton-dominated emission via IC in the GeV regime. In other SNRs, the emission seems consistent with a production by a combination of leptonic and hadronic mechanisms.

Today, 11 shell-type SNRs have been firmly identified as  $\gamma$ -ray emitters at TeV energies (see Table 9.1). For these objects, their name, distance, size, age, luminosity (in units of the Crab), and spectral index in the TeV  $\gamma$ -ray emission are presented in Table 9.2. Their  $\gamma$ -ray luminosities (derived from flux and distance) are about  $(0.1-10) \times 10^{33}$  erg/s and have enabled the detection of these objects up to distances of  $\sim 3.5$  kpc with current instrument sensitivities. The source 0FGL J1954.4+2838

**Table 9.2** Shell-like SNRs firmly detected at TeV energies. The table shows the distance  $D$ , the size  $d$ , the estimated age since the explosion, the flux in Crab units (9.3), and the spectral index of the power-law energy spectrum. From <http://tevcat.uchicago.edu/>

Name	$D$ (kpc)	Size $d$ (pc)	Age (ky)	Flux (Crab u.)	$\alpha_\gamma$
RX J1713.7-3946	1	12	1.6	0.66	2.2
IC 443	1.5	4	3-30	0.03	3.0
RXJ0852-4622 (Vela Jr)	0.2	3.5	$\sim 1$	1	2.2
RCW 86	2.5	20	1.8	0.1	2.54
SN 1006	2.2	19	1	0.01	2.29
CTB 37B	2.2	14	$\sim 1$	0.02	2.65
Cassiopeia A	3.4	2.5	0.35	0.03	2.3
Tycho	3.5	6	0.44	0.01	1.95
0FGL J1954.4 + 2838	9.2	–	–	0.23	–
G106.3 + 2.7 (Boomerang)	0.8	3.5	4	0.05	2.29
SNR G353.6-0.7	3.2	8	2.5-14	0.01	2.32

at larger distance was discovered by Milagro. The relatively large sizes of several of these shell-like SNRs ( $>0.1^\circ$ ) have allowed to resolve them for morphological studies. The angular size (in radians) of each object can be obtained from the ratio  $\theta \sim d/D$  (see Table).

This small number of detected shell SNRs is in agreement with our simple considerations in Sect. 8.3, related to the acceleration mechanism in SNRs. The diffusive shock acceleration, Sect. 6.3, foresees that shock waves in SNRs may be able to accelerate CRs up to PeV energies (PeVatrons) in the first  $\sim 1,000$  y while later the high-energy hadrons escape from the system. The phase in which the maximum attainable energy is reached (from the model, up to some  $10^{15}$  eV=1 PeV) can last less than several hundred years, largely reducing the number of SNRs emitting as PeVatrons that can be observed.

However,  $\gamma$ -rays produced by protons and nuclei could be still observed in the period when CRs diffuse away from the acceleration regions and start to get integrated in the galactic volume, if certain conditions in the surrounding environment are fulfilled. In particular, the presence of massive molecular clouds relatively nearby the acceleration regions is probably necessary. This seems the case of supernova remnants relatively near to molecular clouds; eight such objects are present in Table 9.1. These dense matter regions trap those running-away CRs allowing them to have a significant probability for hadronic interactions.

### 9.7.1 The SED of Some Peculiar SNRs

The spectral energy distribution of young SNRs observed in  $\gamma$ -rays by space- and ground-based experiments extends over almost five decades. These simultaneous observations have improved our understanding of the origin of the  $\gamma$ -rays, but also evidenced a more complicated scenario in which different regions can contribute to the total emission.

One consideration, which seems to favor a hadronic scenario in some SNRs, is the presence of regions with high magnetic field amplification. These regions were discovered through the observation of synchrotron X-ray filaments. These high magnetic fields favor efficient confinement and acceleration of hadrons and prevent in principle a large inverse Compton contribution from leptons. In cases like RX J1713.7-3946 (see Fig. 9.11), Tycho or Cas A, the magnetic field has been estimated from multiwavelength observations to be  $>100 \mu\text{G}$ , restricting the contribution of the IC emission and in principle favoring a hadronic origin of the TeV emission.

SNR RX J1713.7-3946 is one of the powerful remnants and has long been the best candidate for  $\gamma$ -ray emission originated by hadronic interactions, although this claim has been extremely controversial. In fact, while the derived high magnetic field disfavors the leptonic acceleration mechanism, on the other hand the apparent low gas density ( $n \sim 0.1 \text{ cm}^{-3}$ ) in the shell of RX J1713.7-3946 poses troubles to standard hadronic scenarios.



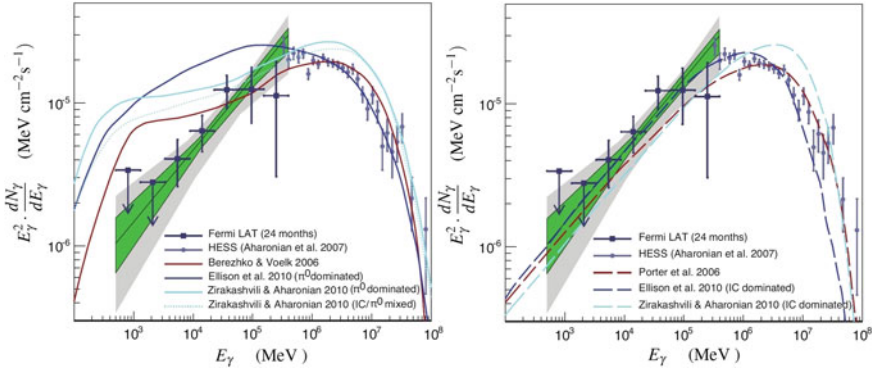


**Fig. 9.12** SED of  $\gamma$ -rays from RX J1713.7-3946 observed by Fermi-LAT and HESS. In the *left panel*, the lines represent the predictions derived before the Fermi-LAT measurements from different hadronic mechanisms. In the *right panel*, those derived assuming leptonic models. For details see Abdo et al. (2011). These observations suggest a leptonic origin of the emission, although hadronic models with a very hard proton spectrum cannot be ruled out. Credit: Fermi-LAT collaboration

The combined SED derived from observations by Fermi-LAT and HESS, Fig. 9.12, seems to be more in agreement with that expected from a leptonic scenario (Abdo et al. 2011). This does not exclude that CRs protons and nuclei are accelerated in the source. As discussed in Sect. 8.7, the  $\gamma$ -ray luminosity is  $L_\gamma \propto \rho_{CR} \cdot \sigma_{pp} \cdot n$ , where  $\rho_{CR}$  is the density of accelerated CRs and  $n$  the target number density. CR protons (or heavier nuclei) might not have enough ambient target nuclei (i.e., low number density  $n$ ) to yield a flux of  $\gamma$ -rays comparable with that produced by the leptonic mechanism.

The leptonic interpretation of  $\gamma$ -ray production by RX J1713.7-3946 is questioned using extensions of the standard diffusive shock acceleration models, Sect. 6.5. An increased acceleration efficiency could be reached if enhanced magnetic field regions were present in the expanding shells. These regions are particularly efficient in the acceleration mechanisms and they could produce an exponent of the differential energy spectrum  $\alpha_{CR} \simeq 1.5-1.8$  instead of the standard value 2.0. Under these assumptions, the model can reproduce a  $\gamma$ -ray flux resembling that obtained in the leptonic model and could therefore fit the Fermi-LAT and HESS data as well as the leptonic model does.

**Tycho SNR.** The composite image of the Tycho Brahe supernova remnant as seen by different instruments has been presented in Fig. 6.6. In the  $\gamma$ -ray energy range, the Tycho SNR has been detected both by Fermi-LAT and VERITAS. As evident from Table 9.2, this source is much fainter than RX J1713.7-3946. The SED modeling including GeV and TeV data shown in Fig. 9.13 seems to disfavor the leptonic model (Giordano et al. 2012). No cutoff is found in the VERITAS data. Taking into account the SNR age, the expected maximum proton energy would be  $\sim 300$  TeV, suggesting maximum acceleration below the CR knee. The hadronic interpretation is not completely compelling, however, given the large statistical errors in the measurements,



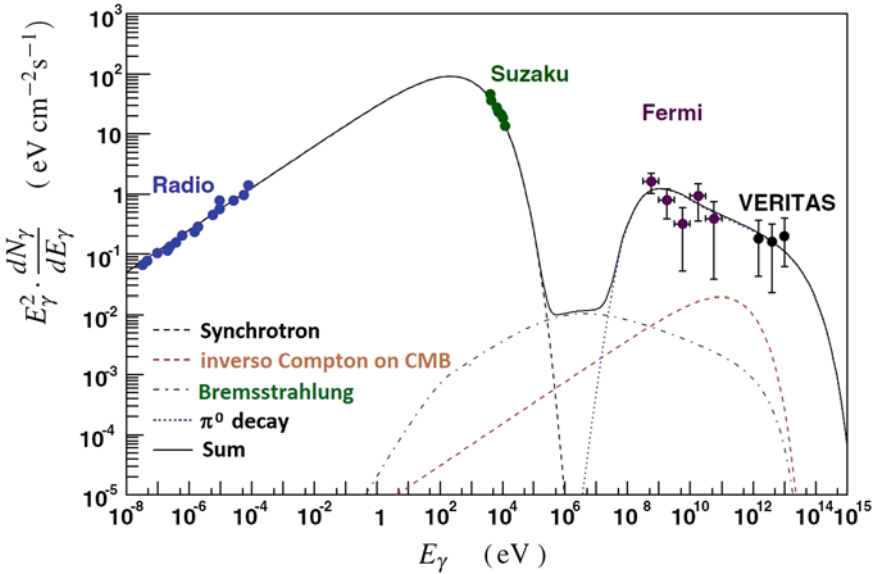


**Fig. 9.13** Broadband **SED** data (in **radio, X- and  $\gamma$ -rays**) and corresponding emission model of **Tycho's SNR**. Note that the shapes of the curves (synchrotron, Inverse Compton and  $\pi^0$ -decay) resemble that of Fig. 8.1, only with different relative weights. The hadronic contribution to  $\gamma$ -rays seems to be the dominant one. Credit: Fermi-LAT collaboration

the impact of **various unknown parameters** such as the SNR **distance**, and a possible **enhancement** of the  $\gamma$ -ray flux **due** to a nearby **molecular cloud**. Future measurements of the spectrum below 500 MeV, and better measurements at TeV energies, will further test the different interpretations.

**SNRs interacting with molecular clouds.** The **brightest  $\gamma$ -ray sources** associated with **SNRs** seen in the **GeV** region are **middle-aged remnants** that are **interacting with molecular clouds**. The SNRs detected by Fermi-LAT are generally also radio-bright objects. The **luminosity** in the **1–10 GeV band** is typically  $L_\gamma \approx (0.8–9) \times 10^{35} \text{ erg s}^{-1}$ , **larger** than that of young SNRs like **Cas A and RX J1713.7-3946**. The corresponding **luminosity** in the **TeV range** on the contrary is **much fainter**.

The **predominance of this class** in the SNRs detected by the Fermi-LAT and their high  $\gamma$ -ray luminosity **indicate** that the **emission** should be **enhanced** by the **presence of matter**. One model considers the  $\gamma$ -ray emission as due to the interaction of runaway CRs, escaping from their acceleration sites, with nearby molecular clouds. Another scenario is the so-called **crushed cloud model** that invokes a shocked molecular cloud into which a radiative shock is driven by the **impact of the SNR's blastwave**. In all models,  **$\gamma$ -ray emission from  $\pi^0$ -decay is enhanced** because of **more frequent  $pp$  interactions in the interstellar medium** (Thompson et al. 2012).

Probably the **best evidence** of **interactions** between **CRs** accelerated by a SNR and **dense clouds** are the cases of the remnants **IC 443** and **W44**. These objects are

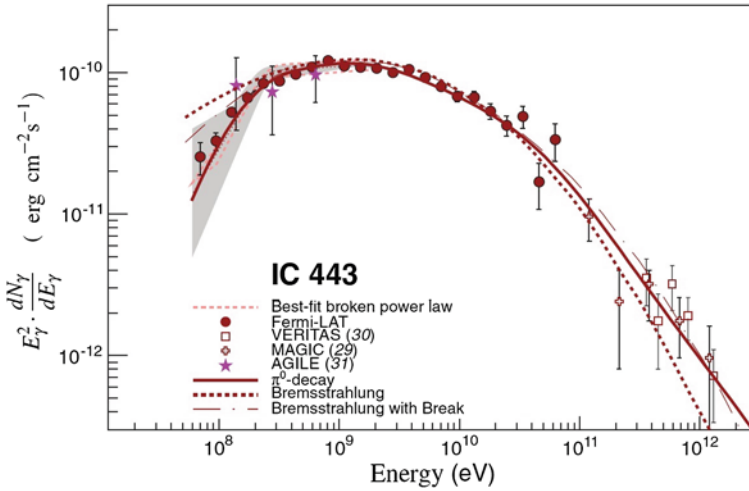


**Fig. 9.14** SED in the  $\gamma$ -ray region of IC 443. In the 0.1–60 GeV range, measurements of AGILE and Fermi-LAT are reported. The gray-shaded band shows the Fermi-LAT systematic errors below 2 GeV due mainly to the uncertainties on background subtraction of the galactic diffuse emission. In the TeV domain, the points came from MAGIC and VERITAS. The solid line denotes the best-fit  $\gamma$ -ray spectrum assuming a hadronic mechanism, the dashed line the best-fit bremsstrahlung spectrum, and the dash-dotted line denotes the best-fit bremsstrahlung spectrum when including an ad hoc low-energy break at 300 MeV/c in the electron spectrum. Credit: Fermi-LAT collaboration

the two highest-significance SNRs in the second Fermi-LAT catalog (2FGL). IC 443 and W44 are located at distances to the Earth of 1.5 kpc and 2.9 kpc, respectively. The age of both remnants is estimated to be  $10^4$  years. The SED measured by Fermi-LAT, Agile, MAGIC and VERITAS for the SNR IC 443 is presented in Fig. 9.14, together with the theoretical predictions for hadronic and leptonic models of  $\gamma$ -ray production (Ackermann et al. 2013).

The  $\gamma$ -rays from  $\pi^0$ -decay are likely emitted through interactions between “crushed cloud” gas and relativistic protons. Filamentary structures of synchrotron radiation seen in a high-resolution radio map support this picture. The mass of gas is large enough to explain the observed  $\gamma$ -ray luminosity with an average matter density of  $n = 20 \text{ cm}^{-3}$  in the case of IC 443.

The fact that the spectral measurements down to 60 MeV has enabled the identification of the  $\pi^0$ -decay feature in the case of IC 443 and W44 mid-aged SNRs, providing the first evidence for the acceleration of protons in SNRs, is largely stressed in Ackermann et al. (2013). However, these two objects are far from being able to accelerate CRs up to PeV energies, and the spectral index for the  $\gamma$ -ray energy spectrum is much greater than 2. The quest for PeVatron galactic accelerators is still open. In addition, the Fermi-LAT measurement is particularly difficult because of the presence of the background from diffuse emission (that must be subtracted to obtain the signal) and the uncertainties on the effective area of the detector at the lowest energies.

Other examples of observed enhancement of hadronic production due to the interactions of cosmic rays with dense gaseous complexes are W51, studied by MAGIC and HESS up to 5 TeV and the  $10^4$  y-old SNR W28. In this last case, a clear correlation between the TeV emission and near massive molecular clouds emitting in CO has been observed. More details and reference to the experiments in Holder (2012) and Rieger et al. (2013).

## 9.8 Summary of the Study of Galactic Accelerators

The importance of multiwavelength astrophysics is compelling: the combination of  $\gamma$ -ray with radio and X-ray data observations suggests that SNRs are indeed the sources of either CR electrons or hadrons. The first evidence of hadronic acceleration up to  $\sim 10$  TeV in some mid-aged SNRs interacting with molecular clouds are growing with Fermi-LAT data combined with observations from MAGIC, VERITAS, and HESS. However, the relative contributions of accelerated protons and electrons to  $\gamma$ -ray production in most objects still remain largely unknown and it is not clear whether proton and electron accelerators are of different nature.

As a general conclusion, if the magnetic field intensity near the acceleration region is low (i.e., smaller than  $\sim 10 \mu\text{G}$ ) the accelerated electrons lose a significant fraction of energy in IC  $\gamma$ -rays through interaction with the self-produced synchrotron radiation field. Thus, the observed VHE  $\gamma$ -ray spectrum is probably dominated by accelerated leptons. The contribution of the IC component will dominate over the  $\pi^0 \rightarrow \gamma\gamma$  also if the fraction of accelerated leptons at the same energy as the protons is very small, for instance  $e/p = 10^{-3}$ . The contribution of the hadronic component is expected to be dominant if the magnetic field in the shell significantly exceeds  $10 \mu\text{G}$  and if the ambient matter density  $n \gg 1 \text{ cm}^{-3}$ .

The detailed morphological studies possible with IACTs at the level of  $\sim 0.1^\circ$  show that the acceleration sites are spatially coincident with the sites of nonthermal X-ray emission, strengthening the hypothesis that primary galactic CRs up to the knee are accelerated in SNRs. The identification of these objects is still an open field. Probably, only neutrino telescopes (Chap. 10) can solve the problem.

The fact that a relatively small number of SNRs has been detected at TeV energies has a possible explanation in the evolution of SNRs, which may only be able to accelerate CRs to PeV energies for a few hundred years, while later the high-energy hadrons escape from the system before undergoing further acceleration. The intensity of  $\gamma$ -ray emission from hadronic interactions depends upon the flux of high-energy nuclei, and upon the density of target material. The production of  $\gamma$ -rays via  $pp$ -interactions in dense gas condensations (e.g., molecular clouds with densities  $> 100 \text{ cm}^{-3}$ ) embedded in low-density shells represents an interesting scenario for hadron acceleration sites.

Future imaging experiments as CTA will allow a precise measurement of the energy spectrum below 1 TeV (down to tens of GeV), and above 10 TeV (up to 100 TeV). In addition, the improved angular resolution could provide indepen-

dent and complementary information about the radiation mechanisms through morphological studies.

In the absence of neutrino detections, a proof of the origin of CRs up to the knee region in SNRs would be the detection of  $\gamma$ -rays of extremely high energies, in the PeV region. Synchrotron losses typically prevent the acceleration of electrons to energies beyond 100 TeV. In addition, at such high energies IC emission is suppressed because the Klein–Nishina cross-section replace the Thomson one (Sect. 8.4.3). Because of these two effects, the contribution of inverse Compton  $\gamma$ -rays to the radiation above 10 TeV is expected to gradually fade out. Thus, the detection of  $\gamma$ -rays up to 100 TeV would establish a hadronic origin of the radiation.

## 9.9 Active Galaxies

The terminology of active galaxies is often confusing, since the distinction between different types of AGN sometimes reflect historical differences in how the objects were discovered or initially classified, rather than real physical differences. Three main criteria used to classify active galaxies are as follows: (i) The emission of the source at radio wavelengths yields a division into radio loud and radio weak objects; (ii) The optical luminosity of the object. Radio weak sources are subdivided into optically strong and optically weak sources, while radio loud sources are subdivided into low luminosity and high luminosity. (iii) The orientation of the AGN toward the observer. The emission contribution from the jet(s) and the lobes that they inflate dominates the luminosity of the radio-loud AGN. The jet and jet-related emission can be neglected in the radio-quiet objects.

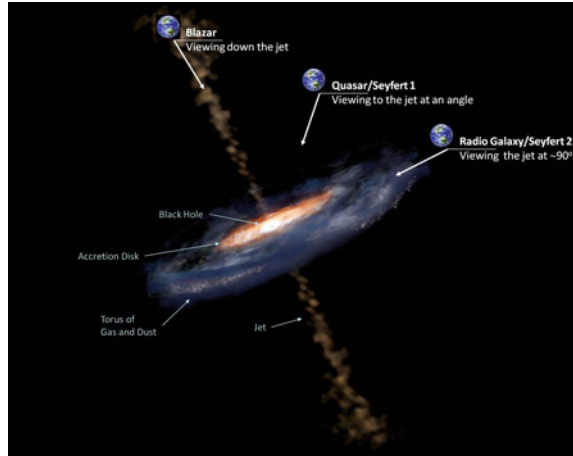
The radiation emitted by an AGN is usually attributed to one (or both) of the two following processes:

- *Thermal radiation* originating from in-falling matter strongly heated in the inner parts of an accretion disk close to the central black hole. Accelerated electrons can produce inverse Compton effect on the photons of the hot corona. The radiation produced in these processes ranges mostly in the optical, UV and X-ray bands. The AGN that are energetically dominated by thermal radiation can be classified as *thermal dominated*, or *disk dominated AGN*.
- *Nonthermal emission* emitted in a magnetic field by highly energetic particles that have been accelerated in a jet of material ejected from the nucleus at relativistic speed. The radiation produced through this mechanism encompasses the entire electromagnetic spectrum, from the radio to  $\gamma$ -rays. These represent the *jet dominated AGN*.

The *disk dominated AGN* are objects usually called *Seyferts galaxies* (or *quasi-stellar objects-QSOs*).<sup>2</sup> They are radio weak objects which show continuum emission

<sup>2</sup> Quasar is also the contraction of *quasi-stellar object* because in optical images they have optical luminosities greater than that of their host galaxy. Some astronomers use the term quasi-stellar object (QSO) to indicate radio-quiet quasars, reserving that of quasars for radio-loud objects.

**Fig. 9.15** This illustration shows the different features of an active galactic nucleus (AGN), and how our viewing angle determines what type of AGN we observe. The extreme luminosity of an AGN is powered by a supermassive *black hole* at the center



in the **optical range** from the central region. They present also narrow and occasionally broad emission lines, occasionally strong X-ray emission and sometimes a weak small-scale radio jet. The host galaxies of Seyferts are usually spiral or irregular galaxies. There is a correlation between the QSO's luminosity and the mass of its host galaxy, as the most luminous objects are located in the core of the most massive galaxies. Although thermal-dominated AGN are the large majority (~90%), none of the sources have been detected so far in the HE and VHE  $\gamma$ -rays.

Unified models exist supporting the hypothesis that different observational classes of AGN are really a single type of physical object observed under different conditions (Urry and Padovani 1995). The favored unified model foresees that the apparent differences arise simply because of their **different orientations to the observer**, see Fig. 9.15. If the jet is not pointing toward the observer, whose line of sight toward the core intercepts the significant amount of dusty disk of material, which lies in the plane of the galaxy, the **typical emission from Seyferts galaxies is expected**.

The class of **jet dominated AGN** corresponds mostly to **radio loud AGN**. These can be **subdivided** into **blazars** and **nonaligned blazars** depending on the orientation of their jets with respect to the line of sight.

- **Blazars.** The **strong and rapid variability** (including superluminal motion, Sect. 9.12) are the observational indicators that these objects **point their jet in a direction that is closely aligned to our line of sight**. Because of this very special perspective, their emission is modified by relativistic effects (see Sect. 9.12.1). Blazars are divided into three main subclasses depending on their optical spectral properties.
  - **FSRQs** or **Blazars of the QSO** type, or **BZQ**. These are blazars showing broad emission lines in their optical spectrum just like normal quasi-stellar objects. This category includes objects normally referred to as **flat spectrum radio quasars (FSRQs)** and **broad-line radio galaxies**.

- **BL Lacs** or **Blazars** of the **BL Lac** type or **BZB**. These are objects normally called BL Lacs or **BL Lacertae** objects. Their **radio compactness** and **broadband SED** are very similar to that of strong lined blazars but they have **no strong and broad lines in their optical spectrum**. In the literature, BL Lac objects are often **subdivided** into **three subclasses** depending on their **SEDs** (see Sect. 9.11). If the frequency  $\nu_s$  of the **synchrotron emission** is **peaked in the far IR or IR** ( $\nu_s < 10^{14}$  Hz), they are classified as **low-energy BL Lac (LBL)**; they are **intermediate energy BL Lac (IBL)** if the peak is between  $10^{14} < \nu_s < 10^{15}$  Hz. Otherwise, if the **synchrotron radiation peaks at higher energies** ( $\nu_s > 10^{15}$  Hz), they are called **high-energy BL Lac (HBL)**.
- **Blazars of the unknown type (BZU)** are objects that show many of the hallmarks of blazars but do not have optical spectra of sufficient quality to safely determine the presence of broad emission lines or to accurately measure their equivalent width.
- **Nonaligned blazars**. These sources are radio loud AGN with **jets pointing at large or intermediate ( $\sim 15\text{--}40^\circ$ ) angles** with respect to our line of sight. This category includes:
  - **Radio galaxies**. AGN with no broad emission lines. Often they **show extended, double-sided radio jets/lobes pointing in opposite directions** with respect to the galactic plane and with a very large angle with respect to the line of sight. The nuclear emission is similar to that of blazars but is usually fainter.
  - **Steep Spectrum Radio Quasars (SSRQ)**. AGN with broad emission lines. The orientation of the jet in these sources is thought to be **intermediate between that of blazars and radio galaxies**.

Approximately 1% of all galaxies hosts an active nucleus. Around 10% of these AGN exhibit relativistic jets powered by accretion onto a supermassive black hole. Despite the fact that AGN have been studied for several decades, the knowledge of the emission characteristics up to highest photon energies is mandatory to understand these extreme particle accelerators.

One of the big achievements of the **last decade** is the **large increase in the number of AGN** that have been **detected at  $\gamma$ -ray energies**, allowing to better understand some of their physical properties. In the GeV energy range, the **Fermi-LAT** collaboration reported in the **2FGL** catalog **about 1,000 AGN** while **at TeV energies** the **number of detected AGN is more than 50**, Table 9.1. There are however still **many open questions** regarding AGN: (a) the **location** and **structure** of their **dominant emission zones**; (b) the **content** of their **jets**; (c) the **origin** of their **variability**, observed on timescales from years down to minutes in different wavelengths; (d) the **role of external photon fields in the mechanism that involves the inverse Compton effect to produce the observed  $\gamma$ -ray spectra**; (e) the **energy distribution and the dominant acceleration mechanism** for the underlying radiating particles.

The other important experimental achievement is the organization and scientific interpretation of a large number of **multi-instrument observing programs** which

provide simultaneous observations from radio to  $\gamma$ -ray energies. Given the variability and the broadband nature of the jet emission, these coordinated efforts from the community are crucial for a detailed and unbiased study of AGN.

## 9.10 The Extragalactic $\gamma$ -ray Sky

The extragalactic sky is that observed at galactic latitudes  $|b| > 10^\circ$ . The presence of  $\gamma$ -ray sources outside the galactic disk is evident both in Fig. 8.6 for the GeV sky and in Fig. 9.7 for the TeV sky. Most of the observed objects at HE and VHE energies are blazars. The presence in blazars of a jet oriented toward the observer is of particular interest because the emission is dominated by relativistic beaming effects, which boost the observed photon energies and luminosity.

**The GeV range.** The large number of AGN in the Fermi-LAT catalog (Table 8.1) coupled with the all-sky monitoring of time varying processes has given a tremendous boost to the study of the extragalactic  $\gamma$ -ray sky. Among the detected extragalactic objects, the collaboration has detailed studied 116 sources associated with high confidence at  $|b| > 10^\circ$  with AGN extracted from the 2FLG catalog, producing the *LAT Bright AGN Sample* (Abdo et al. 2010a). About 90% of the considered sources have been associated with AGN listed in radio catalogs, thus implying that the bright extragalactic  $\gamma$ -ray sky is dominated by the class of radio-loud AGN, namely FSRQs, BL Lacs, and radio galaxies. Only about one-third of the bright Fermi-LAT AGN was also detected by EGRET. This is a likely consequence of the larger Fermi-LAT effective area and of the strong variability and duty cycle of GeV blazars. In addition, the fraction of different AGN classes is different between the two experiments, and is probably due to a selection effect induced by the different energy response of the EGRET and Fermi-LAT instruments. Finally, the Fermi-LAT observations provide important criteria for the scheduling of observations with the rather narrow field of view TeV instruments at ground.

At GeV energies, a significant number of AGN of uncertain type is present and relatively few non-AGN objects have been discovered. Among non-AGN objects, there are several local-group galaxies (LMC, SMC, M31) as well as other star-forming galaxies (NGC 4945, NGC 1068, NGC 253, and M82). As in our own galaxy, in each galaxy CRs should be accelerated by SNRs or other objects that are related to star-formation activity. These detections seem to confirm the relation between star-formation rate and  $\gamma$ -ray luminosity.

**The TeV range.** At TeV energies, the extragalactic  $\gamma$ -ray sky is completely dominated by AGN. At present, more than 50 objects have been discovered and are listed in the online TeV Catalog, Table 9.1. The two most massive close-by starburst galaxies NGC 253 and M82 are the only non-AGN sources detected at TeV energies through the emission of  $\gamma$ -rays from their own CR propagation. The majority of them (90%) are sources with the jet pointing along the line-of-sight (high-frequency BL LACs,



HBL). Only 3 radio galaxies (FRI) have been detected at TeV energies (Centaurus A, M87 and NGC 1275).

The observed VHE spectra can be described as usual by a power law  $dN/dE \propto E^{-\alpha}$ . For the HBL sources, inferred photon indices range in the interval from 2.3 to 4.5, with some indications for spectral hardening with increasing activity. Emission beyond 10 TeV has been established, for instance in Mrk 501 and Mrk 421 where measured photon energies reach 20 TeV. Non-HBL sources are usually detected during high states only, with low states expected to fall below current sensitivities.

As  $\gamma$ -ray objects are in most cases associated with sources known in other wavelengths, most AGN distances have been estimated by redshift measurements. It is found that the objects in the Seyferts class (FRI) are much closer to us than quasars or blazars (FSRQ, HBL). Blazars of the QSO type up to redshift  $z \sim 0.6$  (i.e., 3C 279 at  $z = 0.536$ ) have been detected at VHE energies. Most of them have  $z < 0.2$ . Blazar population studies at radio to X-ray frequencies indicate a redshift distribution for BL Lacs objects that seems to peak at  $z \sim 0.3$ , with only few sources beyond  $z \sim 0.8$ , while the FSRQ population is characterized by a rather broad maximum between  $z \sim 0.6-1.5$ .

Observed VHE flux levels for extragalactic objects typically range from 1% of the Crab nebula steady flux (for the average/steady states) up to 10 times as much when the AGN are in high activity phases. Because TeV instruments are now able to detect sources at the level of 1% of the Crab, the variability down to few-minute scale of the near and bright TeV-emitting blazars (Mrk 421 and Mrk 501) can be studied in detail. Another consequence of the sensitivity of IACTs instruments is that more than one extragalactic object could be visible in the same field of view. With respect to the early phase of the first decade of this century, the TeV instruments are now shifting their observation strategies to move toward higher-quality data sets of individual sources rather than trying to simply increase the number of sources.

## 9.11 The Spectral Energy Distributions of Blazars

The study and classification of AGN and their acceleration mechanisms require observations from different instruments. The spectral energy distributions (SEDs) of blazars can span almost 20 orders of magnitude in energy, making simultaneous multiwavelength observations a particular important diagnostic tool to disentangle the underlying nonthermal processes. Usually, SEDs of different objects were obtained using data not taken at the same time. Only very recently it was strengthened the necessity of strictly contemporaneous (or at least as contemporaneous as possible) and broadband sampling of SEDs. This effort is particularly relevant for time-varying sources where changes in overall brightness are often accompanied by changes in the energy spectra.

As an example of these efforts, we describe in Sect. 9.11.1 the result of a quasi-simultaneous study of the SEDs of 48 blazars based on the Fermi-LAT Bright AGN Sample (Abdo et al. 2010a), presented by the Fermi-LAT collaboration.

Quasi-simultaneous means that the Fermi data have been collected continuously over a period of three months while all other data over much shorter periods (typically less than a few hours) and are not necessarily simultaneous among themselves. In Sect. 9.11.2, the results are shown from the 4.5-month-long multiwavelength observations on Mrk 421 (Abdo et al. 2011). This campaign included the Fermi-LAT, VLBA, Swift, RXTE, MAGIC, and other collaborations and instruments that provided excellent temporal and energy coverage of the source throughout the year 2009. During this campaign, Mrk 421 showed a low activity at all wavebands. The extensive multi-instrument (radio to TeV) data set provides an unprecedented, complete look at the quiescent SED for this source.

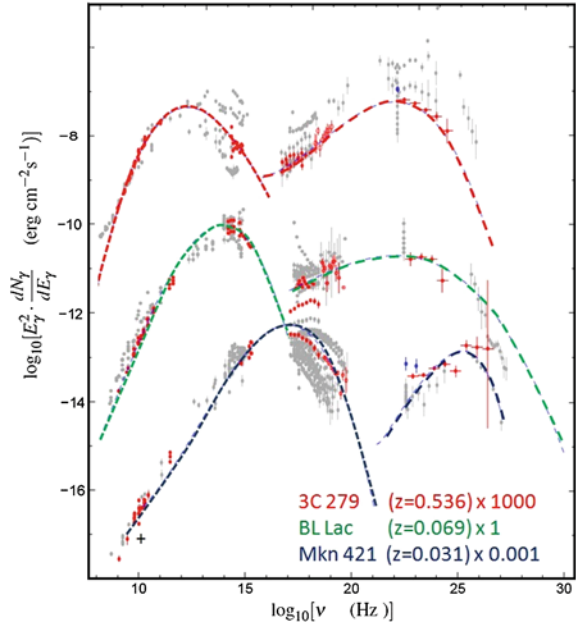
### 9.11.1 Quasi-Simultaneous SEDs of Fermi-LAT Blazars

The SEDs of 48 blazars selected by Fermi-LAT were constructed using:

- The Swift (Sect. 8.6.2) database, based on information from the three instruments measuring at different frequencies (UVOT, XRT, and BAT);
- the AGILE data (Sect. 8.6.2) for energies greater than 100 MeV;
- The available TeV data from MAGIC, HESS, and VERITAS;
- Radio surveys from: the broadband monitoring program, covering the frequency range 2.6–42 GHz, of the Effelsberg 100 m radio telescope of the Max Planck Institute for Radio Astronomy; the 15 GHz observations made using the Owens Valley Radio Observatory (OVRO) 40 m telescope; the 1–22 GHz instantaneous radio spectra provided by the 600 m ring radio telescope RATAN-600 of the Special Astrophysical Observatory, Russian Academy of Sciences;
- The information from radio, mm, near infrared and optical frequency range from a dedicated program to support the Fermi-LAT and AGILE scientific programs (<http://www.oato.inaf.it/blazars/web/>);
- Mid-infrared observations carried out using VISIR, the ESO/VLT mid-infrared imager and spectrograph, composed of an imager and a long-slit spectrometer;
- Additional nonsimultaneous observations from the Spitzer Space Telescope. It provides images and spectra in the range between 3 and 180  $\mu\text{m}$  through three instruments on board: the InfraRed Array Camera, the Multiband Imaging Photometer for Spitzer and the InfraRed Spectrograph.
- Nonsimultaneous multiwavelength archival measurements (included to illustrate the historical range of variability) at different frequencies from the NED (NASA/IPAC Extragalactic Database) and ASDC (ASI Science Data Center) online services.

Since HE  $\gamma$ -ray data have been accumulated over the relatively long period of three months, they likely represent the average of different intensity states. This is clearly a limitation as flux and spectral variability in blazars often takes place on shorter timescales.

**Fig. 9.16** The SED of three different AGN at different distance from the Earth and belonging to different subclasses. To improve the visibility of the spectra, the contents of the farthest (3C 279) have been multiplied by a factor  $10^3$ , while that of the nearest (Mrk 421) by a factor  $10^{-3}$ . The *dashed lines* represent the best fit to the data assuming leptonic production



In all cases, the overall shape of the SEDs exhibit the typical broad double hump distribution, as shown in Fig. 9.16 for three AGN at different distances. The SEDs of all considered AGN show that there are considerable differences in the position of the peaks of the two components and in their relative intensities.

According to current models, the low-energy bump is interpreted as due to synchrotron emission from highly relativistic electrons, and the high-energy bump is related to inverse Compton emission of various underlying radiation fields. UV photons generated by the accretion disk surrounding the black hole, or IR photons provided by the dusty torus can also contribute as seed photons to the IC process. Large variability is also present, especially at optical/UV and X-ray frequencies. In the GeV range, the  $\gamma$ -ray variability cannot be evaluated as the Fermi data are averaged over the entire data taking period.

The studies on different blazar populations seem to suggest that there is a continuous spectral trend from FSRQ  $\rightarrow$  LBL  $\rightarrow$  IBL  $\rightarrow$  HBL, often called the “blazar sequence”. The sequence is characterized by a decreasing source luminosity, increasing synchrotron peak frequency and a decreasing ratio of high- to low-energy component. This sentence must be considered with some caveats due to selection effects and unknown redshifts of considered objects.

In Fig. 9.16, 3C 279 is a very far ( $z = 0.536$ ) FSRQ low-frequency peaked. The BL Lacertae is a relatively near ( $z = 0.069$ ) blazar that gives the name to the subclass of BL Lac objects, and is of LBL type. Finally, Mrk 421 is the closest AGN ( $z = 0.031$ ) of the HBL type. Note that in the figure the SEDs of the three objects are shifted for better visibility by different factors as explained in the caption of the figure. The

luminosities of the sources ( $L_\gamma$ , [erg/s]) scale almost as  $1/z^2$  (for relatively small  $z$ , the redshift is proportional to the distance). When the effect of distances is considered, the luminosity in correspondence of the synchrotron peak decreases from  $\sim 5 \times 10^{47}$  erg/s for FSRQ to  $\sim 5 \times 10^{44}$  erg/s for HBL.<sup>3</sup>

In the models of  $\gamma$ -ray emission, all high-frequency BL LACs (HBLs) seem to be well described by homogeneous (*one-zone*) leptonic SSC model. In the so-called one-zone SSC model the emission, from radio through X-rays, is produced by synchrotron radiation from electrons in a homogeneous, randomly oriented magnetic field. The  $\gamma$ -rays are produced by inverse Compton scattering of the synchrotron photons by the same electrons which produce them. For IBLs, a combination of SSC plus inverse Compton on some additional external photons fields seems to be needed to fit the data. For FSRQs, the situation is rather complicated and probably leptonic plus hadronic models are necessary to fully explain the data (Funk 2012; Rieger et al. 2013). The dashed lines in Fig. 9.16 represent the fits using a leptonic model, as given in Abdo et al. (2010a).

### 9.11.2 Simultaneous SED Campaigns and Mrk 421

All the TeV IACTs are involved in massive, targeted, multiwavelength campaigns. Particularly important have been the large-scale multi-instrument efforts on Mrk 421 and on Mrk 501. Fig. 9.17 reports the most complete simultaneous SEDs collected for the BL Lac AGN Mrk 421 to date. The combination of the spectral observations from the  $\gamma$ -ray instruments Fermi-LAT and MAGIC have allowed to characterize, for the first time, the entire bump due to the inverse Compton over five orders of magnitude in energy and without gaps. Similar broadband studies have been made for other AGN sources.

The SED of Mrk 421 looks similar to that of the Crab (Fig. 9.9): the same physical processes are providing the emission spectrum. The broadband SED has been modeled in Abdo et al. (2011) with two different scenarios: a leptonic (one-zone SSC) model and a hadronic model. Both leptonic and hadronic frameworks are able to describe reasonably well the average SED, implying comparable powers for the jet emission, which constitutes only a small fraction ( $10^{-3}$ – $10^{-2}$ ) of the Eddington luminosity (see *Extras # 4*) of the source.

However, hadronic and leptonic models differ on the predicted environment for the blazar emission: the leptonic scenario constrains the size to be  $R \leq 10^4 R_g$ , the magnetic field to be  $B \sim 0.05$  G and electrons to have energies up to  $\sim 5 \times 10^{13}$  eV.  $R_g$  is the gravitational radius (or Schwarzschild radius) of the central massive black hole, defined in (9.5). For the hadronic model, and assuming the same power-law index of the injected electron and proton distributions  $\alpha_e = \alpha_{CR}$ , this implies a size

<sup>3</sup> As an exercise, try to estimate the peak luminosity for the three considered objects using the redshift-distance relation.

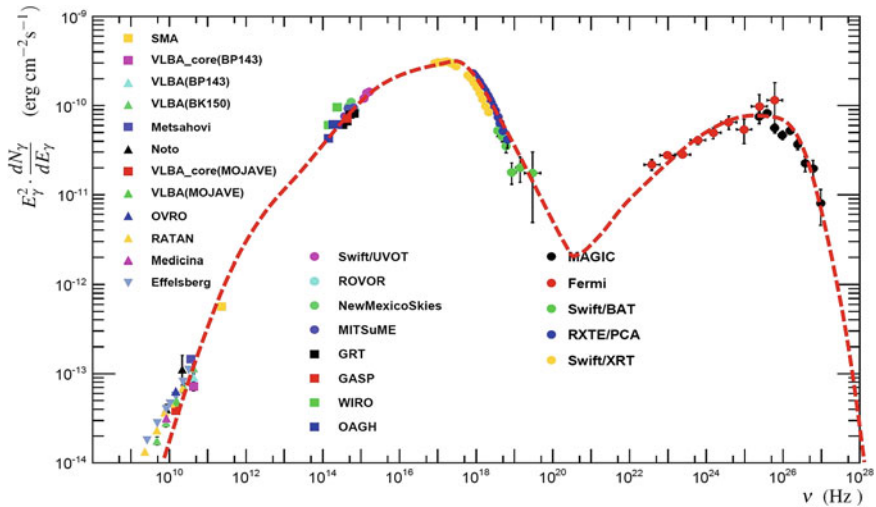


**Fig. 9.17** Extensive multiwavelength measurements showing the spectral energy distribution of Markarian 421 from observations made in 2009. The legend reports the correspondence between the instruments and the measured fluxes. The *dashed line* is a fit of the data with a leptonic model. See Abdo et al. (2011) for the references to the data

of the emitting region of a few  $R_g$ , a magnetic field  $B \sim 50$  G and particles (protons) with energies up to few  $10^{18}$  eV.

The hadronic mechanism in AGN jets could explain the production of UHECRs in the Universe. In this case, also neutrinos could be produced by the decay of charged mesons, as the  $\gamma$ -rays arise from the decay of the neutral ones. Larger maximum energies can be reached by other classes of blazars. In the particular case of Mrk 421, the hadronic mechanism seems to require extreme conditions for particle acceleration and confinement.

On the other hand, the observed variability of the blazar seems to be better explained by a leptonic production model of  $\gamma$ -rays. We derive in Sect. 9.12.1 how the source variability is connected with the size  $R$  of the emitting source. In the case of Mrk 421, it was observed that X-rays are significantly more variable than  $\gamma$ -rays, with timescales ranging from 1 hour to 1 day. No significant correlations between variations in X- and  $\gamma$ -rays have been observed so far. In addition, within the X-ray and  $\gamma$ -ray energy bands, the variability increased with photon energy. The physical interpretation of this result within the context of the one-zone SSC model is that the flux variability increases with the energy of the electrons that produce them.

Another relevant multi-year campaign is that on M87 that involved all the IACTs (VERITAS, MAGIC, HESS for 80 hours in total), the Fermi-LAT, the X-ray satellite Chandra, the Hubble space telescope, and various other instruments all the way down to radio measurements at 1.7 GHz from VLBA. Some flaring episodes detected in these observations provide a rich data set to study rise-and decay-times and spectral properties of flares in this close-by non-blazar AGN (Funk 2012).

### 9.12 Jets in Astrophysics

Powerful relativistic outflows and jets, with speeds approaching that of light, have been observed in different astrophysical sources, Fig. 9.18. This includes extragalactic objects (AGN), and galactic objects as pulsars and microquasars. If these outflows point toward us, as in blazars, relativistic effects can significantly change their appearance. The dynamics of nonthermal processes in these outflows are important fields of research. The jet compositions and their production mechanisms are in fact not completely understood. Up to now, observations cannot provide enough evidence to support one of the various theoretical models among the many that exist. In the case of AGN, the leading model foresees that the matter in the disk falls into the black hole, converting a large fraction of the gravitational potential into kinetic energy. In some cases, the jet of particles moves outwards with relativistic bulk velocity (measured in the radio wavelength) up to Lorentz factors  $\Gamma \simeq 50$  and with an extension that goes from fractions of kilo-parscs up to hundreds of kpc.

The blazar emission zone is unresolved by all instruments (a part interferometer radio telescopes using mm-waves), and the measurements of time variability are the only way of probing its structure. Additional information on the structure and the dynamics of the jet arises from the study of the polarization at radio and optical frequencies.

Radio interferometric observations of blazar jets have revealed significant apparent superluminal motion ( $\beta_a = v_a/c > 1$ ) of individual jet components on parsec-scale propagating away from the core. This superluminal motion is not in contradiction with special relativity. The situation is similar to that of a laser beam illuminating high clouds. It can result in the appearance of a spot on the clouds moving faster than the speed of light if the laser is rotated fast enough. This apparent motion is the source's pattern speed. One of the first examples of such superluminal motions was observed as early as the beginning of 1980 in the quasar 3C 273 in which a source component moved away from the nucleus at a speed of roughly eight times the speed

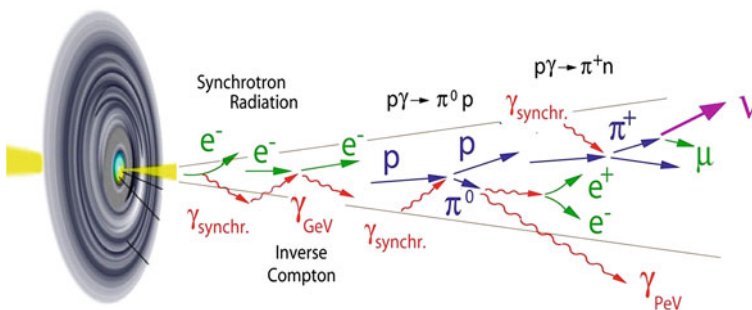


**Fig. 9.18** A sketch of a jet. Charged particles are accelerated and could emit  $\gamma$ -rays and neutrinos through different processes

of light. The kinematics of this motion is known, and it is related to the bulk velocity of the jet material. We refer to Longair (2011) for additional information.

### 9.12.1 Time Variability in Jets

The leptonic or hadronic origin of the  $\gamma$ -ray emission in the AGN jets, as well as the location of the  $\gamma$ -ray emission along the jets, are still open important questions. This last problem can be faced on by studying the time variability in the photon flux.

Despite the limited temporal coverage of the current IACTs to each single source, more than half of the AGN detected in the TeV domain have shown variability, albeit often weak. For the majority of them, variability timescales above one month have been found. In about a quarter of them there is clear evidence for short-term TeV variability.  $\Delta t_{TeV}$ , on observed timescales of less than one hour. In particular for the HBL class,  $\Delta t_{TeV} \simeq 3$  min have been measured for Mrk 501 and PKS 2155-304,  $\simeq 10$  min for PSK 1222+21 and Mrk 412. Also the representative of the BL Lac class, the BL Lacertae, shows variability of  $\simeq 15$  min. Fig. 9.19 shows the measured flux versus time for PSK 1222+21.

The TeV variations observed in blazars with evidence for sub-hour variability are the fastest observed in any other waveband so far, and already imply a compact size of the  $\gamma$ -ray emitting region. The observation of time variability  $\Delta t_{TeV}$  in a jet of particles, moving outwards with a relativistic bulk velocity characterized by the

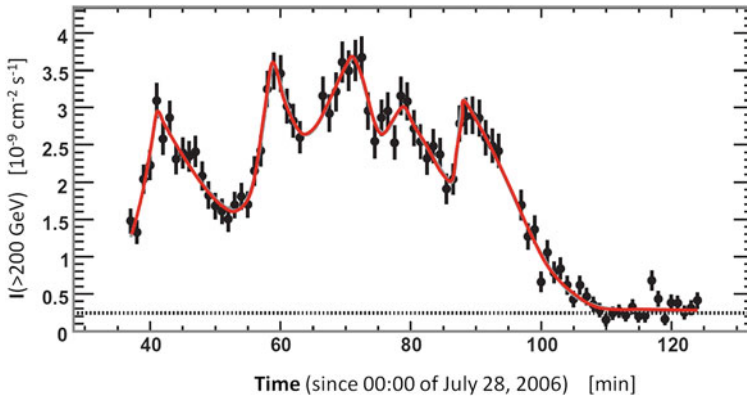


**Fig. 9.19** Integrated flux  $I(>200 \text{ GeV})$  versus time as observed by HESS for PKS 2155-304 starting from midnight of 28 July, 2006. The data are binned in 1 min intervals, and the horizontal *dashed line* shows for comparison the steady flux from the crab nebula (Aharonian et al. 2007a). Courtesy of Prof. F. Aharonian



Lorentz factor  $\Gamma$ , implies a restriction on the size  $R$  of the source given by

$$R < \frac{\Gamma \cdot c \cdot \Delta t_{TeV}}{(1+z)} \approx 10^{15} \cdot \left(\frac{\Gamma}{10}\right) \cdot \left(\frac{\Delta t_{TeV}}{1 \text{ h}}\right) \text{ cm} \tag{9.4}$$

where the factor  $(1+z)$  includes the general relativity effect of the Universe expansion. For the relatively near AGN observed in the TeV range, this factor can be neglected.

The sizes of massive compact objects  $M$  are ruled by general relativity, and the source size  $R$  could be compared with the Schwarzschild radius, defined as

$$R_g = 2 \frac{GM}{c^2} \tag{9.5}$$

Equation (9.4) for sources with  $\Gamma \sim 10$  and time variability  $\Delta t_{TeV} \sim 1 \text{ h}$  provides values of  $R$  comparable to the Schwarzschild radius of a very massive black hole in the AGN core:  $R_g = 3 \times 10^{14} \text{ cm}$  for  $M = 10^9 M_\odot$ . This led to believe that the  $\gamma$ -rays are produced close to the central engine of the blazars.

However, some recent results (see Paneque (2012) for a review) have shown a clear correlation of some  $\gamma$ -ray outbursts with optical polarization changes and/or with the passage of radio knots through the core structure in the mm-wave radio-interferometer images. The radio knots are believed to be a standing shock situated several pc away from the central engine. Therefore, at least for some sources and detected outbursts, the blazar emission has been pinpointed to be far away (1–10 pc) from the supermassive black hole.

A variety of leptonic and hadronic emission models have been discussed in the literature (Böttcher 2010) to explain the SEDs of AGN. The short-term variability seems to favor a leptonic synchrotron-Compton interpretation. On the other hand, the detected “orphan TeV flares” (flares observed at TeV energies and not in the lower energy wavebands) are much more difficult to account for in the leptonic scenario.

As in the case of galactic sources, probably only the detection of neutrinos can demonstrate the presence of the hadronic mechanism at work. Viceversa, the nonobservation of neutrinos does not exclude hadronic acceleration mechanisms, because a necessary ingredient is the presence of enough matter or radiation fields with which accelerated hadrons can interact.

### 9.13 The Extragalactic Background Light

The detection of very far  $\gamma$ -ray emitting blazars has started providing information useful for observational cosmology as well. In this section, we will derive how the Universe is opaque to  $\gamma$ -rays whenever the energy-dependent photon mean free path is smaller than distance of the source. The dominant process for the absorption of

VHE photons of energy  $E$  produced by astrophysical sources is pair-creation

$$\gamma_E + \gamma_\varepsilon \rightarrow e^+ e^- \quad (9.6)$$

on low-energy extragalactic background photons of energy  $\varepsilon$ . These photons extend from the CMB to the near-ultraviolet (UV) wavelengths. The UV/optical/infrared background radiation is called the *extragalactic background light* (EBL). The cross-section for the pair-production process is described by the Bethe-Heitler formula

$$\sigma(E, \varepsilon) \simeq 1.25 \times 10^{-25} (1 - \zeta^2) \text{ cm}^2 \quad (9.7)$$

where  $\zeta = \sqrt{1 - \frac{(m_e c^2)^2}{E \cdot \varepsilon}}$ . The cross-section in (9.7) is maximized when

$$\varepsilon = 2 \frac{(m_e c^2)^2}{E} \simeq \frac{520 \text{ GeV}}{E} \text{ eV} \quad (9.8)$$

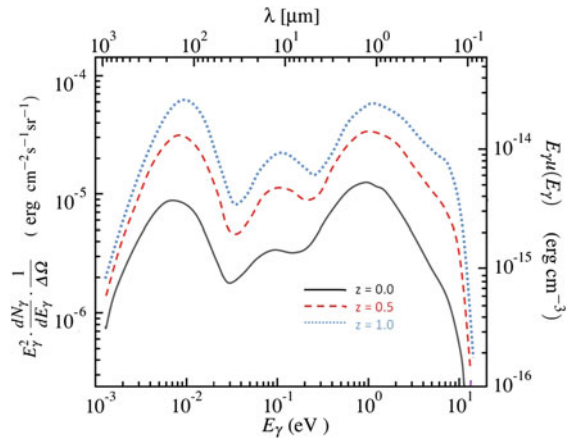
and the threshold energy is a factor of two lower. For energies above 100 TeV, the process (9.8) is important on the cosmic microwave background. For instance, if  $E = 400 \text{ TeV}$  the interaction cross-section is maximal if  $\varepsilon \sim 1.3 \times 10^{-3} \text{ eV}$ , corresponding to the average energy of the CMB photons, Eq. (7.3). For photons in the TeV range, the dominant process is on infrared/optical photons. At  $E = 1 \text{ TeV}$ ,  $\varepsilon = 0.5 \text{ eV}$  which corresponds to the near infrared.

The EBL is the totality of light emitted by stars, galaxies, and AGN over the lifetime of the Universe. Today, this pervasive photon background consists of light emitted at all epochs, modified by the redshift due to the expansion of the Universe. Therefore, in principle, the EBL contains information about the evolution of the baryonic components of galaxies and the structure of the Universe.

The bulk of the EBL falls in the range from  $\sim 10^{-3} \text{ eV}$  to  $10 \text{ eV}$ , corresponding to wavelengths from the far-infrared to the near-ultraviolet ( $\sim 1,000\text{--}0.1 \mu\text{m}$ ). Figure 9.20 shows the estimated spectral energy distribution (SED) normalized for the considered solid angle of the background photons as a function of photon energy or wavelength [the curves are obtained for the model C in Finke et al. (2010)]. The quantity in the ordinate (left scale) is the same  $\text{SED}/\Delta\Omega$  shown in Fig. 8.5 for the galactic  $\gamma$ -rays. To compare numerically the two figures, remember that  $1 \text{ MeV} = 1.6 \cdot 10^{-6} \text{ erg}$ . On the right-side scale, the energy density (in  $\text{erg cm}^{-3}$ ) of the EBL has been obtained by multiplying the  $\text{SED}/\Delta\Omega$  by  $4\pi/c$ . In the UV, optical and near-IR most of the EBL is due to direct starlight, as well as a subdominant contribution from AGN. From the mid-IR to submillimetric wavelengths, the EBL consists of re-emitted light from dust particles, including both continuum thermal radiation and line emission from molecules. The background at longer wavelengths (not shown in the figure) is dominated by the cosmic microwave background.<sup>4</sup> The

<sup>4</sup> As an exercise, demonstrate that the CMB contribution in Fig. 9.20 would be represented by a parabola with negative concavity and vertex at about  $5 \times 10^{-13} \text{ erg cm}^{-3}$  at  $E_\gamma \sim 10^{-3} \text{ eV}$ .

**Fig. 9.20** *Left scale* SED per unit of solid angle for the extragalactic background light (EBL) energy density as a function of proper photon energy (*bottom scale*) of wavelength (*upper scale*) for three values of redshifts. *Right scale* the energy density of the EBL



different lines in the figure represent the EBL background at three different epochs (redshifts) of the Universe.

Direct measurement of the EBL is difficult due to contamination from near objects and from galactic light. Due to different modeling approaches and uncertainties in underlying model parameters, the intensity and shape of the EBL spectrum remains controversial and a wide range of EBL models have been developed, see for instance Finke et al. (2010) and Gilmore et al. (2012).

Once the energy density of the EBL has been assumed from a particular model, the optical depth  $\tau_{\gamma\gamma}(E, z)$  for a photon of observed energy  $E$  produced in a source at redshift  $z$  can be calculated. The probability for the  $\gamma$ -ray of energy  $E$  to survive absorption along its path from the source at redshift  $z$  to the observer plays the role of an attenuation factor for the radiation flux, and it is usually expressed in the form

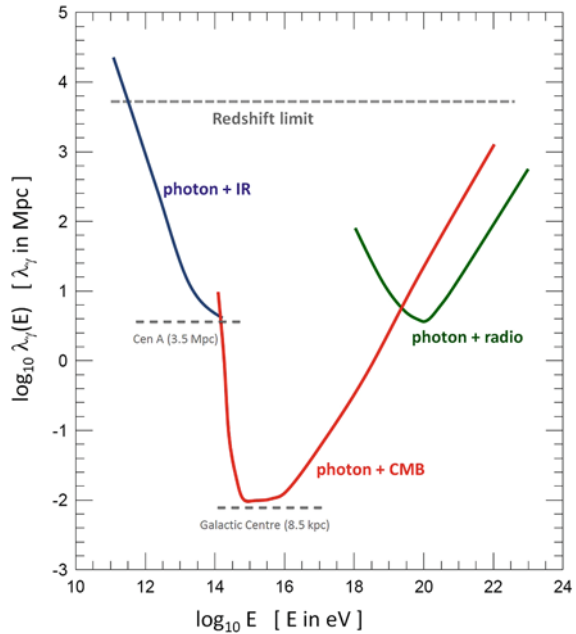
$$I(E, z) = I_0 e^{-\tau_{\gamma\gamma}(E, z)} \tag{9.9}$$

where  $I_0$  is the flux at source. This equation defines the optical depth  $\tau_{\gamma\gamma}$ , which is thus a dimensionless quantity. The computation accounts for the EBL photon number density and the cross-section (9.7), integrating over the distance and the energy of the background photons (De Angelis et al. 2008). Notice that QED, relativity and cosmology arguments are involved in the relation (9.9).

The energy dependence of  $\tau_{\gamma\gamma}$  leads to appreciable modifications of the observed source spectrum with respect to the spectrum at emission, due to the exponential dependence in (9.9). As  $\tau_{\gamma\gamma}$  increases with energy, the observed flux results more attenuated at higher energies, resulting in an effective mean free path of photons propagating in the Universe  $\lambda_\gamma(E)$ . Figure 9.21 shows the mean free path (in Mpc) of photons as a function of the photon energy. As a result, also for galactic sources of photons with energy of  $\sim 100$  TeV start being attenuated by the presence of the background photons. Photons from the nearby Universe (below some tens of Mpc) start to be attenuated above  $\sim 10$  TeV by the presence of the CMB.

**Fig. 9.21** Mean free path (Mpc) of photons as a function of the photon energy.

The contribution of the scattering (9.6) on IR, CMB and radio background photons are considered separately. The position of the galactic center and of the closest AGN are also shown



Absorption represents a drawback for  $\gamma$ -ray astronomy. On the other hand, the identification of absorption features in the spectra of GeV–TeV  $\gamma$ -rays should allow us to derive unique information about the poorly known EBL. This procedure requires precise measurements of the  $\gamma$ -ray flux from a large number of extragalactic objects located at different redshifts  $z$ , and, more importantly, a good understanding of the intrinsic  $\gamma$ -ray spectra at the sources, i.e., the quantity  $I_0$  in (9.9).

At present, the HESS collaboration has reported an upper limit on the EBL at near and mid-infrared wavelengths using measurements of  $\gamma$ -rays from blazars with redshifts between  $z \sim 0.1$ – $0.2$ . The inferred upper limit is very close to the lower limit given by the measured integrated light of resolved galaxies (galaxy counts). A similar result has been reported by the Fermi-LAT collaboration for the EBL at optical and UV bands (Rieger et al. 2013). Although the derived upper limits agree with most of the theoretical/phenomenological predictions for the EBL, they are not free of model assumptions. It is believed that future measurements by next-generation detectors, in particular by CTA, based on a much larger sample of AGN should significantly increase the source statistics and improve the quality of data, and consequently reveal details of the EBL.

## References

- A. Abdo et al., (FERMI Coll.) The spectral energy distribution of fermi bright blazars. *The Astrophys. J.* **716**, 30–70 (2010a)
- A.A. Abdo et al., FERMI Large area telescope observations of the Crab pulsar and nebula. *The Astrophys. J.* **708**, 1254–1267 (2010b)
- A.A. Abdo et al., Fermi large area telescope observations of Markarian 421: the missing piece of its spectral energy distribution. *The Astrophys. J.* **736**, 131 (2011)
- A.A. Abdo et al., (Fermi-LAT collaboration), Observations of the young supernova remnant RX J1713.7-3946 with the Fermi Large Area Telescope. *The Astrophys. J.* **734**, 28 (2011)
- M. Ackermann et al., Detection of the characteristic pion-decay signature in supernova remnants. *Science* **339**, 807 (2013)
- F. Aharonian et al., The Crab nebula and Pulsar between 500 GeV and 80 TeV: observations with the HEGRA Stereoscopic air Cerenkov telescopes. *The Astrophys. J.* **614**, 897–913 (2004)
- F. Aharonian et al., An exceptional very high energy gamma-ray flare of PKS 2155–304. *The Astrophys. J.* **664**, L71–L74 (2007a)
- F. Aharonian et al., Primary particle acceleration above 100 TeV in the shell-type supernova remnant RX J1713.7-3946 with deep HESS observations. *Astron. Astrophys.* **464**, 235–243 (2007b)
- F. Aharonian, J. Buckley, T. Kifune, G. Sinnis, High energy astrophysics with ground-based gamma ray detectors. *Rep. Prog. Phys.* **71**, 096901 (2008)
- E. Aliu et al., Observation of pulsed gamma-rays above 25 GeV from the crab pulsar with MAGIC. *Science* **322**, 1221 (2008)
- A. De Angelis, O. Mansutti, M. Persic, Very-high-energy gamma astrophysics. *Riv. del Nuovo Cimento* **31**, 187 (2008). doi:[10.1393/ncr/i2008-10032-2](https://doi.org/10.1393/ncr/i2008-10032-2)
- M. Böttcher, Models for the spectral energy distributions and variability of blazars. in: *Fermi Meets Jansky - AGN at Radio and Gamma-Rays*, Eds. T. Savolainen, E. Ros, R.W. Porcas, J. A. Zensus, p. 41 (2010). Also [arXiv:1006.5048](https://arxiv.org/abs/1006.5048)
- S. Carrigan et al., *The H.E.S.S. Galactic Plane Survey—maps, source catalog and source population* (2013). [arXiv:1307.4690v3](https://arxiv.org/abs/1307.4690v3)
- J.D. Finke, S. Razzaque, C.D. Dermer, Modeling the extragalactic background light from stars and dust. *The Astrophys. J.* **712**, 238–249 (2010)
- S. Funk, OG2 Rapporteurs talk at ICRC (2011)
- S. Funk, *The status of gamma-ray astronomy* (2012). [arXiv:1204.4529v1](https://arxiv.org/abs/1204.4529v1) [astro-ph.HE]
- R.C. Gilmore et al., Semi-analytic modelling of the extragalactic background light and consequences for extragalactic gamma-ray spectra. *Mon. Not. R. Astron. Soc.* **422**, 3189–3207 (2012)
- F. Giordano et al., Fermi large area telescope detection of the young supernova remnant tycho. *The Astrophys. J. Lett.* **744**, L2 (2012)
- J.A. Hinton, W. Hofmann, Teraelectronvolt astronomy. *Annu. Rev. Astron. Astrophys.* **47**, 523 (2009)
- J. Holder, TeV gamma-ray astronomy: a summary. *Astropart. Phys.* **39–40**, 61–75 (2012)
- C.F. Kennel, F.V. Coroniti, Confinement of the Crab pulsar’s wind by its supernova remnant. *The Astrophys. J.* **283**, 694–709 (1984)
- M.S. Longair, *High Energy Astrophysics*, 3rd edn. (Cambridge University Press, Cambridge, 2011)
- P.L. Nolan et al., FERMI Large area telescope second source catalog. *The Astrophys. J. Suppl. Ser.* **199**, 31 (2012)
- D. Paneque, Experimental gamma-ray astronomy. *J. Phys.: Conf. Ser.* **375**, 052020 (2012)
- F. M. Rieger, E. de Ona-Wilhelmi, Felix A. Aharonian. *TeV Astronomy* (2013). [arXiv:1302.5603](https://arxiv.org/abs/1302.5603)
- D.J. Thompson, L. Baldini, Y. Uchiyama, Cosmic ray studies with the fermi gamma-ray space telescope large area telescope. *Astropart. Phys.* **39–40**, 22–32 (2012)
- M. Urry, P. Padovani, Unified Schemes for Radio-Loud Active Galactic Nuclei. *Publ. Astron. Soc. Pac.* 107 (1995) 803. Also [arXiv:astro-ph/9506063](https://arxiv.org/abs/astro-ph/9506063)

# Chapter 10

## High-Energy Neutrino Astrophysics

Neutrino astronomy shares with  $\gamma$ -ray astronomy the objective of understanding the sources and mechanisms of CR acceleration. Due to their much larger interaction cross section,  $\gamma$ -rays are easier to detect than neutrinos, and  $\gamma$ -ray astronomy is having a fundamental importance on several topical areas of modern astrophysics and cosmology. The existence of CR sources seems to guarantee the existence of high-energy neutrino sources, in addition to those of  $\gamma$ -rays. While  $\gamma$ -rays can be produced both by hadronic (through  $\pi^0$  decay) or leptonic processes (inverse Compton, bremsstrahlung), neutrinos can only be produced by hadronic processes ( $\pi^\pm$  decay), Sect. 10.1.

As shown in the previous Chapter, the detailed modeling of the morphology and spectra of  $\gamma$ -ray sources seems to indicate a preference for their production through the leptonic mechanism in many source classes. At present, the hadronic mechanism seems more plausible for certain supernova remnants surrounded by molecular clouds. In most cases, however, it is generally possible to fit the  $\gamma$ -ray data with either leptonic or hadronic production models by varying the model assumptions (for instance, the intensity of magnetic fields or the environmental matter number density). No single source, either galactic or extragalactic, has been conclusively proven to accelerate CRs up to PeV energies. Neutrino astronomy is expected to be decisive in the quest of CR sources.

The idea of a large volume experiment for cosmic neutrinos based on the detection of the secondary particles produced in neutrino interactions was first formulated in the 1960s by M. Markov. He proposed: “to install detectors deep in a lake or in the sea and to determine the direction of the charged particles with the help of Cherenkov radiation”. A major challenge for these detectors is to separate the astrophysical signals from the large background of atmospheric neutrinos produced by CR interactions with atmospheric nuclei (Sects. 10.2 and 10.3).

The small neutrino interaction cross section allows them to come from far away. Moreover, neutrinos, being neutral, are not deflected by magnetic fields. There are many theoretical and experimental reasons to believe that high-energy neutrinos

are emitted in violent events taking place in many astrophysical objects, Sect. 10.4. Potential sources in our Galaxy are supernova remnants, pulsars and microquasars. Potential extragalactic sources are Gamma-Ray Bursts and AGN.

Starting from the Markov idea and from the present knowledge of TeV  $\gamma$ -rays sources, the challenge to detect galactic neutrinos is open for a multi kilometer-scale apparatus, Sect. 10.5, deployed in the Antarctic ice or in deep seawater, Sect. 10.6.

At present (Sect. 10.7) a  $\text{km}^3$  detector (IceCube) is operating in the ice of the South Pole and another smaller underwater telescope (ANTARES) is running in the Mediterranean Sea, waiting for the Mediterranean  $\text{km}^3$  telescope (KM3NeT). All of them use the Markov idea and are made by a grid of optical sensors (photomultipliers, PMTs) inside the so-called *instrumented volume*.

High-energy neutrino detectors are motivated by discovery and must be designed to detect neutrinos of all flavors over a wide energy range and with the best energy resolution. No astrophysical object is yet identified as high-energy neutrino source, and the status of the running experiments is discussed in Sect. 10.8. Lower energy neutrinos from the Sun and from core-collapse supernovae are discussed in Chap. 12. The recent first measurement of an astrophysical high-energy neutrino flux is reported in Sect. 10.9, opening the field of neutrino astronomy for the next decade.

## 10.1 The CRs, $\gamma$ -rays and Neutrino Connection

The astrophysical production of high-energy neutrinos occurs via the decay of charged pions in the *beam dump* of energetic protons in dense matter, or through photoproduction from CR protons interacting on ambient photons (Sect. 8.2).

In beam-dump processes, Eq. (8.5), almost the same number of  $\pi^0$ ,  $\pi^+$ ,  $\pi^-$  are produced. The  $\pi^0$  decays immediately in two  $\gamma$ -rays; the charged pions decay as  $\pi^- \rightarrow \mu^- \bar{\nu}_\mu$  and in turn there is the decay  $\mu^- \rightarrow e^- \bar{\nu}_e \nu_\mu$  (and the charge-conjugate reaction for the  $\pi^+$ ). Thus, there are three neutrinos for each pion, and six neutrinos every two  $\gamma$ -rays.

In photoproduction processes, Eq. (8.6), the neutrino energy from the  $\pi^+$  decay is related with the parent proton energy through the relation

$$E_\nu \simeq 0.05E_p \quad (10.1)$$

This arises because the average energy of the pion in (8.6) is  $f_{p\pi} \simeq 0.2$  that of the energy of the parent proton, and in the  $\pi^+$  decay chain four leptons are produced, each of which roughly carries 1/4 of the pion energy. Note also that, because of the isospin conservation (Chap. 7 of Braibant et al. (2011)), the branching ratio for the process (8.6a) is about twice as large as that for (8.6b), while the energy carried by the  $\pi^0$  is slightly smaller. Taking into account the fact that in the final state of (8.9) there are three neutrinos and one positron, the energy transferred to neutrinos is about  $(1/3) \times (3/4) = 1/4$ . The fraction of energy transferred to photons is



$(2/3) + (1/3) \times (1/4) = 3/4$  (because the positron annihilates producing additional photons). Following our simple arguments, the ratio of neutrino to photon luminosity in photoproduction processes is

$$\frac{L_\nu}{L_\gamma} = \frac{1}{3} \quad (10.2)$$

Here, and in the following, under the symbol  $\nu$ , we always consider the sum of neutrinos and antineutrinos.

The existence of neutrino sources not observed in  $\gamma$ -rays is not excluded. If a source is occulted by the presence of thick clouds or material along the line of sight to the Earth,  $\gamma$ -rays are absorbed while neutrinos survive.

### 10.1.1 Neutrino Detection Principle

The basic structure of a detector for cosmic neutrinos is a matrix of light detectors inside a transparent medium. This medium, such as ice or water at great depths:

- offers a large volume of free target nucleons for neutrino interactions;
- provides shielding against secondary particles produced by CRs;
- allows the propagation of Cherenkov photons emitted by relativistic particles produced by the neutrino interaction.

High energy neutrinos interact with a nucleon  $N$  of the nucleus, via either charged current (CC) weak interaction ( $l = e, \mu, \tau$ )

$$\nu_l + N \rightarrow l + X \quad (10.3)$$

or neutral current (NC) weak interactions

$$\nu_l + N \rightarrow \nu_l + X. \quad (10.4)$$

Figure 10.1 shows the  $\nu_\mu$  and  $\bar{\nu}_\mu$  cross sections as a function of the neutrino energy. The neutrino cross section is  $\sigma \propto E_\nu$  up to  $\sim 10^4$  GeV; at higher energies, the linear rise of the cross section starts flattening out. Outside the range measured with high precision at the HERA collider, no data constrain the quark and antiquark structure functions and the uncertainties on the total cross section increase.

An undoubtable advantage of  $\nu$ 's over  $\gamma$ 's as probes in astrophysical observations is related to their tiny cross section. While a 1 TeV  $\gamma$  has an interaction length (in water)  $\lambda \approx 42$  m, a  $\nu$  of the same energy has  $\lambda \approx 2 \times 10^9$  m. The increase of the  $\nu$  cross section with energy is such that at 1 PeV its interaction length becomes a thousand times smaller, or  $2 \times 10^6$  m. It may be seen that the  $\nu$  interaction length becomes equal to the diameter of the Earth at energies of the order of 200 TeV.

Charged particles produced by the neutrino interaction travel through the medium until they either decay or interact. The mean distance traveled by secondary charged particles is called the path length. It depends on their energy and energy loss in the

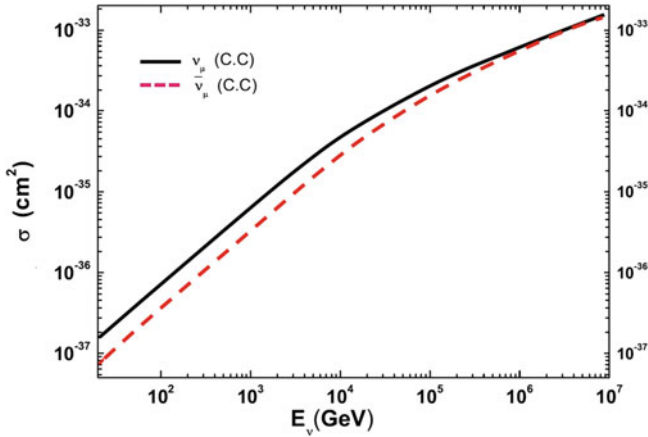


**Fig. 10.1** Cross section for  $\nu_\mu$  and  $\bar{\nu}_\mu$  as a function of their energy according to one particular parton distribution function (CTEQ6-DIS)

medium. Long tracks are produced by CC  $\nu_\mu$  interactions in or around the detector: the range of a 200 GeV muon corresponds to  $\approx 1$  km. In this case, usually the muon path length exceeds the spatial resolution of the detector, so that the trajectory of the particle can be resolved. Showers are induced by NC and by  $\nu_e, \nu_\tau$  CC interactions inside the instrumented volume of the detector, Sect. 10.3.

The detection principle of operating detectors for neutrinos in the TeV–PeV range is based on the collection of the optical photons produced by the Cherenkov effect of relativistic particles (Halzen 2006, Sapienza and Riccobene 2009, Chiarusi and Spurio 2010). The light is measured by a three-dimensional array of photomultiplier tubes (PMTs). The information provided by the number of photons detected and their arrival times are used to infer the neutrino flavor, direction and energy.

Cherenkov radiation is emitted by charged particles crossing an insulator medium with speed exceeding that of light in the medium. The coherent radiation is emitted along a cone with a characteristic angle  $\theta_C$  given by  $\cos \theta_C = \frac{1}{\beta n}$ , where  $n$  is the refracting index of the medium and  $\beta$  is the particle speed in units of  $c$ . For relativistic particles ( $\beta \simeq 1$ ) in seawater ( $n \simeq 1.364$ ) the Cherenkov angle is  $\theta_C \simeq 43^\circ$ .

The number of Cherenkov photons,  $N_C$ , emitted per unit wavelength interval,  $d\lambda$  and unit distance travelled,  $dx$ , by a charged particle of charge  $e$  is given by

$$\frac{d^2 N_C}{dx d\lambda} = \frac{2\pi}{137\lambda^2} \left( 1 - \frac{1}{n^2 \beta^2} \right) \tag{10.5}$$

where  $\lambda$  is the wavelength of the radiation. From this formula, it can be seen that shorter wavelengths contribute more significantly to Cherenkov radiation. The light absorption by water/ice will strongly suppress photons with wavelengths below 300 nm.

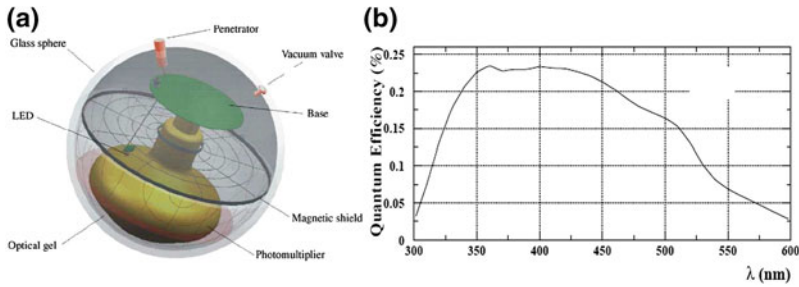


**Fig. 10.2** **a** Sketch of an ANTARES optical module (OM). Those used by the IceCube experiment are similar. A large *hemispherical* (10 in. in diameter) *photomultiplier* (PMT) is protected by a pressure-resistant *glass sphere*. The outer diameter of the *sphere* is 43.2 cm. A mu-metal cage protects the PMT from the Earth magnetic field. An internal *LED* is used for the calibration. **b** The quantum efficiency versus wavelength for PMTs commonly used in ice or water (from Hamamatsu)

**Figure 10.2** shows one typical optical module configuration (left side) used in ice and water experiments (Sect. 10.7). The PMT quantum efficiency (right side) is large in the wavelength range 300–600 nm, matching well the region in which ice and water are transparent to light. Typically the number of Cherenkov photons emitted per meter is about  $3.5 \times 10^4$ .

## 10.2 Background in Large Volume Neutrino Detectors

Atmospheric muons and neutrinos are produced by CR interacting with atmospheric nuclei, Chap. 11. Here, we will show that up to  $\approx 100$  TeV, muons and neutrinos are produced mainly by decays of charged pions and kaons in the cascade and their spectra are related by the kinematics of the  $\pi \rightarrow \mu\nu$  and  $K \rightarrow \mu\nu$  decays. Additional lower energy neutrinos are produced by muon decays. Before to discuss the possible cosmic signal, we need to understand the main background sources.

The atmospheric neutrino flux from charged pion and kaon decays is dominated by  $\nu_\mu$  (Sect. 11.3). This flux is usually referred to as the *conventional atmospheric neutrino flux* and measured in  $\text{cm}^{-2}\text{s}^{-1}\text{sr}^{-1}\text{GeV}^{-1}$ . At energies above 1 TeV and up to  $\approx 100$  TeV, the conventional atmospheric neutrino intensity can be expressed with a simple power-law spectrum:

$$\frac{d\Phi_\nu}{dE}(E) \propto E^{-\alpha_\nu^A}, \quad (10.6)$$

where  $\alpha_\nu^A \simeq \alpha + 1$ . The quantity  $\alpha \simeq 2.7$  corresponds to the measured spectral index for CRs below the knee, Sect. 2.6. The  $\nu_e$  flux at high energy is reduced by more than an order of magnitude with respect to the  $\nu_\mu$ .

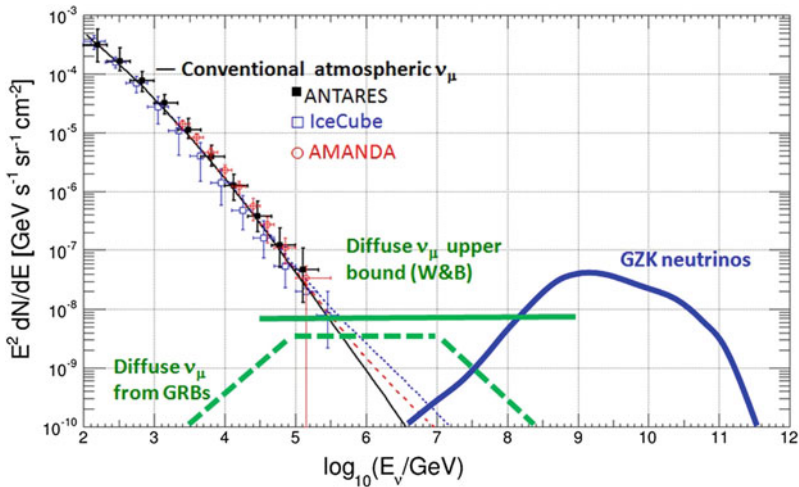


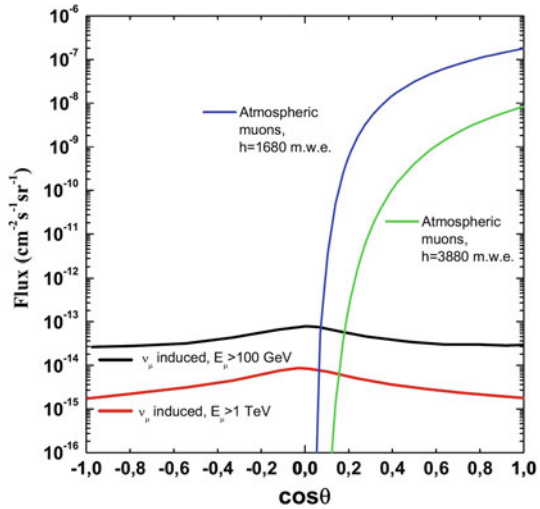
**Fig. 10.3** Expected neutrino fluxes from different diffuse cosmic models and the atmospheric neutrino background. The points represent the measurements of atmospheric  $\nu_\mu + \bar{\nu}_\mu$  flux as a function of the energy by three experiments. The *black line* is the expected conventional flux; the *dashed line* includes the contribution from two models of prompt neutrinos from charmed mesons decay. The *horizontal full green line* is the Waxman and Bahcall (W&B) upper bound from diffuse flux of neutrinos from extragalactic sources, Sect. 10.4.2. The *dashed green line* is the upper bound for  $\nu_\mu$  produced by GRBs, Sect. 10.4.3. The *blue line* indicated the possible contribution of cosmogenic neutrinos, Sect. 10.4.4

Interactions of primary CRs with atmospheric nuclei produce also charmed mesons. Their immediate decay yields a harder neutrino energy spectrum (*prompt neutrino flux*), Sect. 11.3.2, which is expected to exceed that of conventional neutrinos above  $\sim 100$  TeV.

Figure 10.3 shows the expected flux of atmospheric  $\nu_\mu$  as a function of the energy. The conventional flux is shown by the black line; the contribution from two different prompt models as dashed blue and red lines. Since the spectrum is steeply falling, we have, for better visibility, multiplied the flux by  $E^2$ . The different colored symbols represent the measurements from experiments in ice (AMANDA, IceCube) and in seawater (ANTARES) (Sect. 10.7). Atmospheric neutrinos represent an irreducible background in experiments aiming at the detection of cosmic neutrinos.

The atmospheric muons (Sect. 11.3) can penetrate the atmosphere and up to several kilometers of ice/water and represent the bulk of reconstructed events in any large volume neutrino detector. Neutrino detectors must be located deeply under a large amount of shielding in order to reduce the background. The flux of downgoing atmospheric muons exceeds the flux induced by atmospheric neutrino interactions by many orders of magnitude, decreasing with increasing detector depth, as shown in Fig. 10.4.

**Fig. 10.4** Flux as a function of the cosine of the zenith angle of: (i) atmospheric muons (Sect. 11.3) for two different depths; (ii) muons induced by CC interactions of atmospheric  $\nu_\mu$  (Sect. 11.7), for two different muon energy thresholds  $E_\mu$ . Upgoing (downgoing) events have  $\cos \theta < 0$  ( $>0$ )



Atmospheric muons can be used for a real-time monitoring of the detector status and for detector calibration. However, they represent a major background source: downward going particles wrongly reconstructed as upward going and simultaneous muons produced by different CR primaries could mimic high-energy neutrino interactions.

### 10.3 Neutrino Detectors and Neutrino Telescopes

To detect a cosmic signal, huge detectors are necessary. In a large volume neutrino detector, one can distinguish between two main event classes: events with a long track due to a passing muon, and events with a shower, without the presence of a muon. Schematic views of  $\nu_e$ ,  $\nu_\mu$  and  $\nu_\tau$  CC events and of a NC event are shown in Fig. 10.5. Neutrino and anti-neutrino reactions are not distinguishable; thus, no

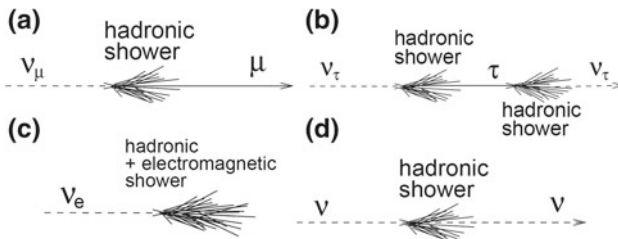


**Fig. 10.5** Some event signature topologies for different neutrino flavors and interactions: **a** CC interaction of a  $\nu_\mu$  produces a muon and a hadronic shower; **b** CC interaction of a  $\nu_\tau$  produces a  $\tau$  that decays into a  $\nu_\tau$ , tracing the double bang event signature. **c** CC interaction of  $\nu_e$  produces both an EM and a hadronic shower; **d** a NC interaction produces a hadronic shower. Particles and anti-particles cannot be distinguished in large volume neutrino detectors

separation between particles and anti-particles can be made. Showers occur in all event categories shown in Figure. However, for CC  $\nu_\mu$ , often only the muon track is detected, as the path length of a muon in water exceeds that of a shower by more than 3 orders of magnitude for energies above 2 TeV. Therefore, such an event might very well be detected even if the interaction has taken place several km outside the instrumented volume, in the Earth crust or in the surrounding transparent medium, provided that the muon traverses the detector. Property of showers (total visible energy, a rough estimate of the neutrino direction) are obtained if the interaction occur inside the instrumented volume.

Large volume neutrino detectors are able to identify the cosmic signal over the background using two methods:

1. For events with a track that can be accurately reconstructed, by the observation of an excess of events in a very small solid angle region  $\Delta\Omega$  over the expected background.
2. For all neutrino interaction candidates, by the observation of an excess of events above a given observed energy. The expected cosmic signal is harder than the atmospheric neutrino spectrum. The spectrum of the cosmic signal is expected to be  $d\Phi_\nu/dE \propto E^{-\alpha_\nu}$ , with  $\alpha_\nu \approx 2$  while  $\alpha_\nu^A \approx 3.7$  in (10.6) for the background;

This latter method relies on the calorimetric capabilities of the detector. It is usually more efficient for showering events, due to the fact that most of the neutrino energy is released inside the instrumented volume. Large volume neutrino detectors can identify neutrino candidates from all direction, using a part of the detector as a veto, see Sect. 10.8.

The first method requires that neutrino detectors have good tracking capabilities: usually, only the track produced by a  $\nu_\mu$  CC interaction can be reconstructed with precision much better than  $1^\circ$ . In this case, the  $\nu_\mu$  detector behaves as a “neutrino telescope”.

The sky of neutrino telescopes is reduced to the bottom hemisphere to avoid the contamination from the huge flux of atmospheric muons. The reason for looking for  $\nu$ 's coming from “underneath”, the ones that have crossed the Earth, stems from the need to avoid being swamped by the enormous background of atmospheric  $\mu$ 's. Neutrino telescopes, at the contrary of any other instrument devoted to astronomy, are “looking downward”.

Let us describe the different strategies for the detection of track and shower events.

### 10.3.1 Muon Neutrino Detection

A muon crossing the detector gives a clean experimental signal, which allows an accurate reconstruction of muon direction, closely correlated with the neutrino direction. Since neutrinos are not deflected by magnetic fields, it is possible to trace the muon back to the neutrino source. This is equivalent to traditional astronomy where photons point back to their sources. As an example, a muon with initial energy  $E_\mu = 10$  TeV

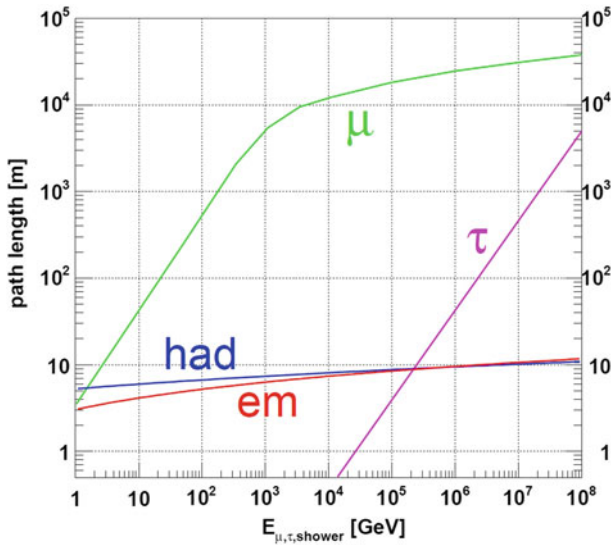


**Fig. 10.6** Path length of particles produced by neutrino interactions in water: muons ( $\mu$ ), taus ( $\tau$ ), electromagnetic (em) and hadronic (had) showers, versus their respective energy. The shower lengths are calculated using a shower profile parameterization

can travel  $\sim 5$  km in water keeping more than 1 TeV of residual energy. Figure 10.6 shows the path length of muons as a function of their energy. Muon energy losses and the muon range are the subject of *Extras # 5*.

The reconstruction ability for a muon track and the relation between neutrino and muon directions is essential for the concept of a neutrino telescope. The muon direction (and, optionally, muon energy) is determined by maximizing a likelihood which compares the time and position of fired PMTs with the expectation from the Cherenkov signal of a muon track. To do this, algorithms use functions which model the light propagation, giving the probability distribution function for a photon, radiated from a track with a given orientation, to reach a PMT at a given distance and orientation as a function of time. For this reason, photon scattering degrades the measurement of the muon direction.

Figure 10.7 shows the angular resolution estimated as the difference between the reconstructed and the true muon direction ( $\bar{\theta}_{\mu_r\mu}$ ) as a function of the neutrino energy. The angular resolution estimated as the difference between the reconstructed muon and the true neutrino direction ( $\bar{\theta}_{\mu_r\nu}$ ) is reported as well. The points are obtained with a pseudo-experiment with data produced by a Monte Carlo simulation of a detector in water similar to ANTARES (Sect. 10.7.2). The resolution  $\bar{\theta}_{\mu_r\nu}$  for the neutrino is worse than  $\sim 1^\circ$  for  $E_\nu \lesssim 0.5$  TeV because of kinematics. It decreases as  $\bar{\theta}_{\mu_r\nu} \propto E_\nu^{-1/2}$  at increasing energies, mainly depending on the reconstruction capabilities of the neutrino telescope and on the propagation medium. The maximum attainable precision is of the order of  $\sim 0.2^\circ$ . Multiple scattering affects the muon direction negligibly at these energies.



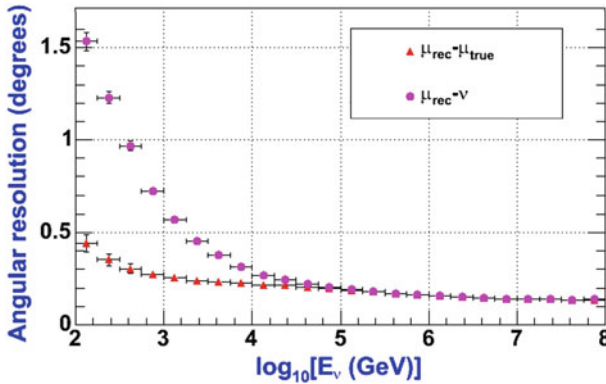


**Fig. 10.7** Angular resolution (evaluated with a Monte Carlo simulation) as a function of event energy for the underwater ANTARES detector. It is shown here the average differences between the true and reconstructed muon direction as well as the difference with respect to the neutrino direction

### 10.3.2 Showering Events

**Electron neutrinos.** A high-energy electron resulting from a charged current  $\nu_e$  interaction radiates a photon via bremsstrahlung after few tens of cm of water/ice (the radiation length in water is  $\sim 36$  cm); this process leads to the development of an electromagnetic (EM) cascade. The longitudinal extension of an EM shower is of the order of few meters and the lateral extension is negligible compared to the longitudinal one. The shower length, defined as the distance within which 95 % of the total shower energy has been deposited, slowly increases with the electron energy, Fig. 10.6. For instance, a 10 TeV electron induces a shower of length of  $\sim 8$  m. Such a shower is short compared to the spacing of the PMTs in any existing or proposed high-energy neutrino detector. EM showers represent, to a good approximation, a point source of Cherenkov photons that are emitted almost isotropically along the shower axis. For this reason, pointing accuracy for showering events is much inferior to that achieved in the  $\nu_\mu$  channel. Additional photons are produced by the hadronic system  $X$  in (10.3) at the  $\nu_e$  interaction vertex.

**NC and hadronic showers.** The NC channel gives the same signature for all neutrino flavors. In this channel, a fraction of the interaction energy is always carried away unobserved by the outgoing neutrino, and therefore the error on the reconstructed energy of the primary neutrino increases accordingly. Even though EM and hadronic showers are different from each other in principle, the  $\nu_e$  CC and the  $\nu_X$  NC channels are not distinguishable in large volume neutrino detectors. Hadronic cascades suffer event-to-event fluctuations that are much more important with respect to the EM ones. The dominant secondary particles in a hadronic shower are pions; kaons, protons or neutrons occur in variable fractions. Muons (from pion decay) can be present as well: as these usually leave the shower, they contribute significantly

to the fluctuations. Monte Carlo simulations show that the longitudinal profile of hadronic showers is very similarly to the EM one, Fig. 10.6.

**Tau neutrinos.** For  $\nu_\tau$  CC interactions, the produced  $\tau$ -lepton travels some distance (depending on its energy) before decaying and producing a second shower. The Cherenkov light emitted by the charged particles in the showers can be detected if both the  $\nu_\tau$  interaction and the  $\tau$  decay occur inside the instrumented volume of the detector. Below 1 PeV, also the  $\nu_\tau$  CC channels (except for the case where the  $\tau$  produces a muon) belong to the class of showering events, because the  $\tau$  track cannot be resolved.

The  $\tau$  lepton has a short lifetime, and in the energy range of interest it travels (depending on the Lorentz factor  $E_\tau/m_\tau c^2$ ) from a few meters up to a few kilometers before decaying (see Fig. 10.6). Most of the possible  $\tau$  decay modes include the generation of a hadronic or an electromagnetic cascade. Thus, if the track of the  $\tau$  is long enough to allow a separation of the primary interaction of the  $\nu_\tau$  from the decay of the tau (typically for  $\tau$  energies above 1 PeV, see Fig. 10.6), the expected signatures for the  $\nu_\tau$  CC events are those of a shower, plus a track, followed by a second shower. This signature is called *double bang event*, if the Cherenkov light emitted by the charged particles in the first shower can be detected and separated from the light emitted by the particles produced in the  $\tau$  decay.

## 10.4 Cosmic Neutrino Flux Estimates

The detection of neutrinos from a CR accelerator candidate would provide unambiguous (“smoking gun”) evidence that hadrons are accelerated. Gamma-ray telescopes give at present essential information to neutrino astronomy because they can tell where and/or when (in the case of transient sources or burst activities) to look for neutrinos. The specific characteristics (light curves and energy spectra) of each  $\gamma$ -ray source, either steady or transient as the GRBs, can be used to make specific predictions for neutrino signals under the hypothesis of hadronic  $\gamma$ -ray production and to optimize their searches. In this section, we present some theoretical predictions concerning galactic and extragalactic neutrino source candidates, based on observations and constraints from  $\gamma$ -ray observations or from the CR flux. The status of the experimental results is presented in Sect. 10.8.

### 10.4.1 A Reference Neutrino Flux from a Galactic Source

If the hadronic mechanism is at work in a galactic source (for instance, in a SNR accelerating CRs) a flux of neutrinos comparable to that of  $\gamma$ -rays could be expected. It is useful to define a sort of *reference neutrino flux* from a galactic source.

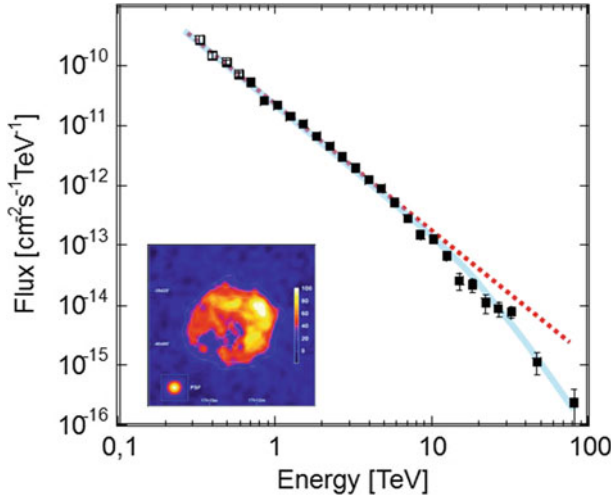


**Fig. 10.8** HESS Measurement of the  $\gamma$ -ray flux from RX J1713.7-3946. It corresponds to the high-energy tail of Fig. 9.12. The *blue line* represents the result of a fit using Eq. (10.7), while the *red curve* represents the fit without the exponential cutoff. The fits are used to compute the  $\nu_\mu$  flux in the case of hadronic mechanism

The SNR RX J1713.7-3946 has been the subject of large debates about the nature of the process (leptonic or hadronic) that originates its  $\gamma$ -ray spectrum, Sect. 9.7. This source has been observed with high statistics by the HESS telescope up to  $\sim 80$  TeV, with a spectrum that can be reasonably well described by a power law with an exponential cutoff

$$E^2 \frac{d\Phi_\gamma}{dE} = \Phi_\gamma^0 \exp[(-E/E_c)^{1/2}] \quad (10.7)$$

where  $\Phi_\gamma^0 = 1.8 \times 10^{-11} \text{ TeV s}^{-1} \text{ cm}^{-2}$  and the cutoff parameter  $E_c = 3.7 \text{ TeV}$ , Fig. 10.8.

Based on the measured HESS  $\gamma$ -ray flux, or starting from a primary proton population with an energy spectrum presenting an exponential cutoff, different models exist that give predictions on the neutrino flux. Several assumptions are usually made in the modeling of the neutrino spectra:

- no significant contribution of nonhadronic processes to the measured  $\gamma$ -rays;
- no  $\gamma$ -ray absorption within the source, i.e., radiation and matter densities are sufficiently low for most of the  $\gamma$ -ray photons to escape;
- $\pi^\pm$  decay before interacting (matter density is low) and also the  $\mu^\pm$  decay without significant energy loss (magnetic field is low);
- the size of the emitting region within each source is large enough that oscillations (Sect. 12.8) will produce a fully mixed neutrino signal at the Earth  $\nu_e : \nu_\mu : \nu_\tau = 1 : 1 : 1$  (see Sect. 12.8.1).

Grossly, the expected number of  $\nu_\mu$  is equal to that of  $\gamma$ -rays, as in proton-proton interactions the same number of  $\pi^0$ ,  $\pi^+$ ,  $\pi^-$  are produced. Two photons arise from the  $\pi^0$  decay, and six neutrinos from the decay chains of the two charged pions. At large distance from the source, two out of six arrive as  $\nu_\mu$  when neutrino oscillations are considered. However, the flux of high-energy neutrinos is about a factor of two lower with respect to the  $\gamma$ -rays of the same energy because of the kinematics. In the decay of charged pions, a larger fraction of kinetic energy is transferred to the muon: in the pion rest frame  $\sim 110$  MeV to the muon and  $\sim 30$  MeV to the neutrino (see Sect. 11.3.1). The results of the predictions agree on the fact that

$$\Phi_{\nu_\mu}(E) \simeq \frac{1}{2} \Phi_\gamma(E) \longrightarrow \frac{d\Phi_\nu}{dE_\nu} = \Phi_\nu^0 E_\nu^{-2} = 10^{-11} E_\nu^{-2} \text{ TeV s}^{-1} \text{ cm}^{-2}. \quad (10.8)$$

Detailed computations produce energy-dependent normalization factors in (10.8) (Vissani and Aharonian 2012, Stegmann et al. 2007).

Predictions of the neutrino flux are available for many galactic sources. As reference neutrino flux for our following considerations we use Eq. (10.8) derived from RX J1713.7-3946. Higher neutrino fluxes could be expected in the case of hidden  $\gamma$ -ray sources.

### 10.4.2 Extragalactic Diffuse Neutrino Flux

The prediction of extragalactic high energy neutrinos is a direct consequence of CR observations (Halzen 2006, Becker 2008). As for the origin of UHE Cosmic Rays, Active Galactic Nuclei (AGN) or  $\gamma$ -ray bursts (GRBs) are the principal candidates as extragalactic neutrino sources.

Different relations between the observed UHECR flux and the possible flux of diffuse neutrino exist. We consider here the simple approach to the problem due to Waxman and Bahcall (1998). The computation of the upper limit on the neutrino flux is based on the measured CR flux at  $10^{19}$  eV and an assumed flat  $E^{-2}$  injection spectrum at sources. W&B derived the emissivity of UHECR in the Universe,  $10^{44}$  erg/(Mpc<sup>3</sup> y) in the range  $10^{19}$ – $10^{21}$  eV, and with some assumptions about the interaction mechanism near sources they estimated a maximum neutrino flux.

With the information provided in the previous chapters, we can reproduce the W&B result. For a CR flux  $\Phi_{CR}(E)$ , Eq. (2.33a) gives the the corresponding energy density  $\rho(> E)$ . The energy density, neglecting the constant factors, can be expressed in terms of

$$\rho(> E) \propto \int E \Phi_{CR}(E) dE = E^2 \Phi_{CR}(E) \quad (10.9)$$

From Fig. 2.7 we obtain that the differential CR flux  $\Phi_{CR}(E)$  decreases by  $\sim 28$  order of magnitudes when the minimum energy  $E$  increases from  $\sim 10^9$  to  $10^{19}$  eV.

A more precise factor ( $1.4 \cdot 10^{-28}$ ) is obtained comparing Eq. (4.52) at an energy  $E_1 = 10^{19}$  eV with Eq. (2.20a) at  $E_0 = 10^9$  eV. Thus

$$\frac{\rho(> E_1)}{\rho(> E_0)} = \left(\frac{E_1}{E_0}\right)^2 \cdot \frac{\Phi_{CR}(E_1)}{\Phi_{CR}(E_0)}. \quad (10.10)$$

By inserting the numerical values

$$\rho_{19} \equiv \rho(> E_1) = 1 \frac{\text{eV}}{\text{cm}^3} \cdot (10^{10})^2 \cdot (1.4 \cdot 10^{-28}) \simeq 1.4 \cdot 10^{-8} \frac{\text{eV}}{\text{cm}^3}. \quad (10.11)$$

This quantity corresponds to  $\rho_{19} = 0.7 \times 10^{54}$  erg/Mpc<sup>3</sup>. Taking into account that the CR are generated all over the cosmic evolution during a time comparable to the Hubble time ( $t_H \sim 10^{10}$  y) then the emissivity of UHECR in the Universe corresponds to  $(\rho_{19}/t_H) \simeq 0.7 \times 10^{44}$  erg/(y Mpc<sup>3</sup>), in agreement with the W&B derivation.

The next observation is that a fraction of these CRs would undergo photoproduction interactions (8.6) at their sources and a fraction of their energy loss  $\epsilon < 1$  would be transferred to secondary  $\gamma$ -rays and neutrinos. According to (10.2), in photoproduction processes the photon luminosity is about a factor three larger than that of neutrinos, thus to the latter is transferred about (1/4) of the CR energy. As the muon neutrinos (as usual, we refer as muon neutrinos the sum of  $\nu_\mu + \bar{\nu}_\mu$ ) give a clear signature in a neutrino telescope, we specialize the calculation to this flavor, that corresponds to (2/3) of the emitted neutrinos in (8.9). We can define the maximum  $\nu_\mu$  flux  $[E^2 \Phi_{\nu_\mu}(E)]_{\text{max}}$  when  $\epsilon = 1$  as

$$[E^2 \Phi_{\nu_\mu}(E)]_{\text{max}} \simeq \left(\frac{2}{3}\right) \left(\frac{1}{4}\right) \left(\frac{c}{4\pi}\right) \rho_{19} = 0.6 \times 10^{-8} \frac{\text{GeV}}{\text{cm}^2 \text{ s sr}}. \quad (10.12)$$

The factor  $(c/4\pi)$  converts a number density into a flux, as explained in Eq. (2.18a).

The maximal neutrino flux (10.12) must be corrected for two effects: (1) the redshift energy loss of neutrinos produced at cosmic time  $t < t_H$  and the CR generation rate per unit of volume. These effects introduce a correction factor  $\xi_z = (1+z)^3$  which corresponds to a factor  $\xi_z \simeq 3$  when the cosmological evolution of the sources are considered (Waxman and Bahcall 1998). (2) Neutrino oscillations change the flavor of neutrinos during propagating, decreasing by a factor of two the number of cosmic muon neutrinos arriving on Earth, (Sect. 12.8). These two effects give a factor  $\xi_z/2$  and the upper bound on the flux of neutrinos of a given flavor is

$$[E^2 \Phi_{\nu_\mu}(E)]_{\text{max}} = 0.9 \times 10^{-8} \frac{\text{GeV}}{\text{cm}^2 \text{ s sr}}. \quad (10.13)$$

This upper limit is shown in Fig. 10.3 as a green line. The all-flavor upper limit (corresponding to the total  $\nu_e + \nu_\mu + \nu_\tau$  flux) is a factor of three larger. The result (10.13) is lower than that reported in the original paper (Waxman and Bahcall 1998);

the reason is that neutrino oscillation effects were not considered, and that the new measurements of the UHECRs from the PAO and TA experiments (Sect. 7.8) give a lower flux than considered in 1998.

The diffuse flux is expected to exceed the atmospheric neutrino one at energies above 100 TeV. This diffuse cosmic neutrino flux can be detected above the background using the calorimetric features of detectors, as mentioned in Sect. 10.2.

### 10.4.3 Neutrinos from GRBs

GRBs (Sect. 8.9) have been proposed as possible candidate sources for CRs above  $10^{18}$  eV (Waxman and Bahcall 1997). In the fireball model, the observed electromagnetic radiation is explained by highly relativistic outflows of material, most likely collimated in jets pointing towards the Earth. Shock fronts emerge in the outflows in which electrons are accelerated. Within the framework of the fireball model, protons can also be shock-accelerated yielding high-energy neutrinos accompanying the electromagnetic signal of the burst.

The neutrino fluence  $F_\nu$  (fluence measures the flux integrated over time in units  $\text{GeV}/\text{cm}^2$ ) can be obtained from theoretical models starting from the GRB luminosity by a convolution of the accelerated proton distribution with the photon energy density,  $U_\gamma$ . The predictions are strongly constrained by the observed average burst fluence  $F_\gamma \sim 3.6 \times 10^{-3} \text{ GeV}/\text{cm}^2$ . Assuming that the  $\gamma$ -rays are mostly produced by hadrons, from  $F_\gamma$  the average neutrino fluence is obtained

$$F_\nu \sim 1.2 \times 10^{-3} \text{ GeV}/\text{cm}^2 \quad (10.14)$$

using (10.2).

The maximum of this diffuse muon neutrino flux from GRBs can be obtained by the average fluence (10.14) with the GRB rate,  $r_{\text{GRB}} [\text{s}^{-1}]$ , which is estimated to be 667 per year over  $4\pi$  sr (Abbasi et al. 2011). Thus

$$E^2 [\Phi_{\nu_\mu}(E)]_{\text{max}}^{\text{GRB}} = \frac{F_{\nu_\mu} \times r_{\text{GRB}}}{4\pi} \simeq 1.5 \frac{1.2 \cdot 10^{-3} \times 667}{4\pi(3.15 \cdot 10^7)} = 3 \cdot 10^{-9} \frac{\text{GeV}}{\text{cm}^2 \text{ s sr}} \quad (10.15)$$

where the factor 1.5 includes the effects of neutrino oscillations and cosmic evolution as in Sect. 10.4.2.

The original computation of neutrino flux from GRBs (Waxman and Bahcall 1997) was based on the assumption of Fermi-accelerated protons in the relativistic ejecta of the burst interacting with the associated photon field to produce pions via Eq. (8.6). The subsequent decay of charged pions and muons leads to the emission of high-energy neutrinos. In the following, we work out the neutrino spectrum using simple approximations. According to the Band spectrum distribution (8.53), a doubly broken power-law spectrum for the neutrinos is obtained.

Because of the **beamed emission of GRBs**, both the accelerated protons and the photons are moving towards the observer collimated into a narrow cone of opening angle  $\theta$  along the jet axis. The  **$p\gamma$  collision are not head-on**, i.e.,  $\cos\theta = -1$  as in (7.17), but are grazing collisions **occurring at small angles**, which can be approximated with that of the **opening angle  $\theta$  of the jet**. The **resonance energy for reaction (8.6)** is given by (7.17):

$$(E_p^r E_\gamma^r) = \frac{m_\Delta^2 - m_p^2}{2(1 - \cos\theta)} \simeq \frac{0.64 \text{ GeV}^2}{\theta^2}. \quad (10.16)$$

Using **relativistic arguments**, in Sect. 5.8 was shown that the relation  **$\theta \propto 1/\Gamma$**  between the opening angle  $\theta$  of the beamed emission in the laboratory frame and its Lorentz factor  $\Gamma$  holds. Using this relation we can rewrite (10.16) as

$$E_p^r E_\gamma^r = 0.64 \Gamma^2 \text{ GeV}^2. \quad (10.17)$$

Note that we obtained again the same  $\Gamma^2$  factor derived in (8.40). This is a relativistic feature due to the change from the center-of-mass reference frame to the laboratory frame (the observer on our Earth). This  $\Gamma^2$  factor has important consequences on the neutrino spectrum, because **from electromagnetic observations  $\Gamma \sim \mathcal{O}(100)$** . As the  **$\gamma$ -ray spectrum (8.53)** has a **change of slope at  $\sim 1 \text{ MeV}$** , inserting  $E_\gamma^r = E_b = 1 \text{ MeV}$  we obtain:

$$E_p^r = \frac{0.6 \Gamma^2 \text{ GeV}^2}{E_b} \simeq 6 \cdot 10^{15} \text{ eV}. \quad (10.18)$$

Thus, considering the relation (10.1) between the neutrino and the proton energy in photoproduction processes we expect that a **break in the neutrino spectrum around**

$$E_\nu^b \simeq 0.05 E_p^r \simeq 10^{14} \text{ eV} \simeq 100 \text{ TeV} \quad (10.19)$$

is expected. The neutrino spectrum continues to higher energies and neutrinos in the PeV range are expected from the model.

The fluence  $F_\nu(E)$  as a function of the neutrino energy can be derived assuming a Fermi-like spectrum for the proton energy distribution,  $dN_p/dE_p \propto E_p^{-2}$ . The **photon energy distribution  $U_\gamma$  (in  $\text{GeV}/\text{cm}^3$ )** is related with the observed  $\gamma$ -ray spectral index distribution (8.53) by:

$$U_\gamma(E) = \frac{c}{4\pi} E^2 \frac{dN_\gamma}{dE} \propto E^2 \cdot E^{-\alpha} \quad \text{for } E < E_b \\ \propto E^2 \cdot E^{-\beta} \quad \text{for } E > E_b. \quad (10.20)$$

For a **GRB at a distance  $D$** ,  $F_{\nu_\mu}(E)$  can be obtained by the integration



$$F_{\nu_\mu}(E) \propto \frac{1}{4\pi D^2} \int \frac{dN_p}{dE_p} \cdot \sigma_{p\gamma} \cdot f_{p\pi} \cdot f_{\pi\nu} \cdot U_\gamma(E) \cdot dE_p \quad (10.21)$$

where, in addition to the already defined quantities,  $\sigma_{p\gamma}$  represents the photo-production cross section as given in Fig. 7.6,  $f_{p\pi}$  is the fraction of the proton energy transferred to pions, and  $f_{\pi\nu}$  that transferred from pions to  $\nu_\mu$ . With the simple approximation that  $(dN_p/dE_p)\sigma_{p\gamma} \sim 0$  outside the resonance region and  $(dN_p/dE_p)\sigma_{p\gamma} \sim \sigma_0/E_p^\alpha$  in a small range around the resonance energy  $E_p^r$ , the neutrino fluence is (considering only the energy dependence and including all the constants in the coefficient  $a = \frac{f_{p\pi}f_{\pi\nu}\sigma_0}{4\pi D^2 E_p^r}$ )

$$F_{\nu_\mu}(E) \propto aE^2 \cdot E^{-\alpha} \propto E^1 \quad \text{for } E < E_v^b \quad (10.22a)$$

$$\propto aE^2 \cdot E^{-\beta} \propto E^0 \quad \text{for } E_v^b < E < E_v^s \quad (10.22b)$$

$$\propto aE^2 \cdot E^{-\beta} \cdot E^{-1} \propto E^{-1} \quad \text{for } E > E_v^s. \quad (10.22c)$$

Pay attention to the last relation. At very high energies, the synchrotron radiation loss of secondary pions and muons prior to their decay also affects the neutrino spectrum. This energy loss becomes important when the synchrotron time scale is comparable to the pion lifetime. It can be computed that this occurs at energies  $E_p^s$  about 100 times larger than that of (10.18). Thus, for  $E > E_v^s \simeq 100 E_p^s \simeq 10^{16}$  eV, an energy loss term proportional to  $E^{-1}$  must be included.

The expected diffuse  $\nu_\mu$  spectrum from GRBs is thus given by

$$E^2[\Phi_{\nu_\mu}(E)]^{\text{GRB}} = \frac{F_{\nu_\mu}(E) \times r_{\text{GRB}}}{4\pi} \quad (10.23)$$

where the maximum given by (10.15) occurs in the energy interval between  $E_v^b = 100$  TeV and  $E_v^s = 10$  PeV. The fluence increases linearly with energy when  $E_v < E_v^b$ , and decreases linearly with energy when  $E_v > E_v^s$ , as given by (10.22a–10.22c) and as shown in Fig. 10.3 with a dashed line. Consistently with the assumption, the diffuse contribution from GRBs is below the upper limit derived in Sect. 10.4.2. It should be noted that from the experimental point of view the contribution of GRBs to the diffuse flux is much easier to detect, because neutrinos can be observed in spatial and temporal coincidence with the electromagnetic observation of a burst.

As the normalization parameters in (10.22a–10.22c) are quite general and based on average quantities, the prediction derived following (Waxman and Bahcall 1997) does not depend on the specific GRB. This of course cannot be completely true, and theoretical models exist able to calculate individual neutrino fluxes for the observed bursts (Guetta et al. 2004). Recently, the development of dedicated Monte Carlo algorithms with a more detailed treatment of the particle physics involved in the calculation of the neutrino spectra reduces the resulting neutrino flux predictions compared to the above description (Adrián-Martínez et al. 2013). These particle physics processes include an additional high-energy component from  $K$  decays, the

full energy-dependent photohadronic interaction cross section, the energy dependence of the mean free path of protons, individual treatment of secondary particles (including energy losses), the use of the real average photon energy instead of the peak energy of the photon distribution, and detailed neutrino mixing. The combination of all these effects gives rise to a prediction for the neutrino yield that is about one order of magnitude below the result derived above. This, without new assumptions on the nature of GRBs in general, but making use in greater detail of known physics, together with the paradigm of the fireball model.

#### 10.4.4 Cosmogenic Neutrinos

The prediction of a flux of cosmogenic neutrinos was first suggested by Berezhinsky and Zatsepin in the 1969 because of the GZK effect. These neutrinos are produced by UHECRs in photoproduction interactions with the CMB and other photon fields during propagation. The flux of cosmogenic  $\nu_\mu + \bar{\nu}_\mu$  peaks at about  $10^{18}$  eV and significantly decline at both lower and higher energy, as shown in Fig. 10.3.

The cosmogenic neutrino flux depends on the CR injection spectrum and composition, on the distribution of UHECR sources, and very strongly on the cosmological evolution of these sources. For a given total flux, a flatter UHECR injection spectrum would produce more photoproduction interactions and hence generate more neutrinos. The importance of considering the cosmological evolution is due to the fact that protons with  $E > 10^{20}$  eV reach us only from very low redshifts regions ( $z \ll 0.05$ ) due to the GZK effect. On the contrary, neutrinos can travel without energy loss (except adiabatic, due to the cosmic expansion) from the whole Universe. Finally, the influence of the CR composition on the cosmogenic neutrino flux is even stronger, although more difficult to evaluate. If only a percentage of UHECR are protons (as the PAO observations seems to indicate, Sect. 7.10), the neutrino flux should decrease accordingly. A measurement of the cosmogenic neutrino flux is an important and complementary measurement to that of the UHECR spectrum and composition and even the detection of a few events will considerably improve our knowledge of the UHECR features and origin (Allard 2012).

### 10.5 Why km<sup>3</sup>-Scale Telescopes

In this section, we use a simple calculation to work out why a detector having a volume of at least a cubic-kilometer is needed to detect cosmic neutrinos. In addition, we derive the minimum number of optical sensors in the instrumented volume required to track the events.

In the following, we consider the reference neutrino flux for a galactic source given by Eq. 10.8. The event rate can be obtained by defining the neutrino effective area.

We consider (Chiarusi and Spurio 2010)  $\nu_\mu$ 's interacting outside the instrumented volume of the telescope. The event rate during the observation time  $T$  can be expressed in terms of:

$$\frac{N_\nu}{T} = \int dE_\nu \cdot \frac{d\Phi_\nu}{dE_\nu}(E_\nu) \cdot A_\nu^{eff}(E_\nu) \tag{10.24}$$

where  $A_\nu^{eff}(E_\nu)$  (units: cm<sup>2</sup>) is called the *effective area* of the neutrino telescope. It corresponds to the quantity that, convoluted with the neutrino flux, gives the event rate, Fig. 10.9. All the “complications” of the neutrino detection are embedded in the definition of  $A_\nu^{eff}(E_\nu)$ . To detect the event:

1. the  $\nu_\mu$  must survive the Earth absorption and interact sufficiently near to the detector;
2. the daughter muon must reach the instrumented volume;
3. the muon must produce enough light to trigger the detector and to allow the track reconstruction.

Thus, the effective neutrino area corresponds to

$$A_\nu^{eff}(E_\nu) = A \cdot P_{\nu\mu}(E_\nu, E_{thr}^\mu) \cdot \epsilon \cdot e^{-\sigma(E_\nu)\rho N_A Z(\theta)} \tag{10.25}$$

Let consider all the terms of Eq. (10.25).

- $A$  [cm<sup>2</sup>] is the geometrical projected detector surface.
- The quantity  $P_{\nu\mu} \equiv P_{\nu\mu}(E_\nu, E_{thr}^\mu)$  represents the probability that a neutrino with energy  $E_\nu$  produces a muon arriving with a residual threshold energy  $E_{thr}^\mu$  at the detector.  $P_{\nu\mu}$  in turn can be expressed in terms of:

$$P_{\nu\mu} = N_A \int_0^{E_\nu} \frac{d\sigma_\nu}{dE_\mu}(E_\mu, E_\nu) \cdot R_{eff}(E_\mu, E_{thr}^\mu) dE_\mu \tag{10.26}$$

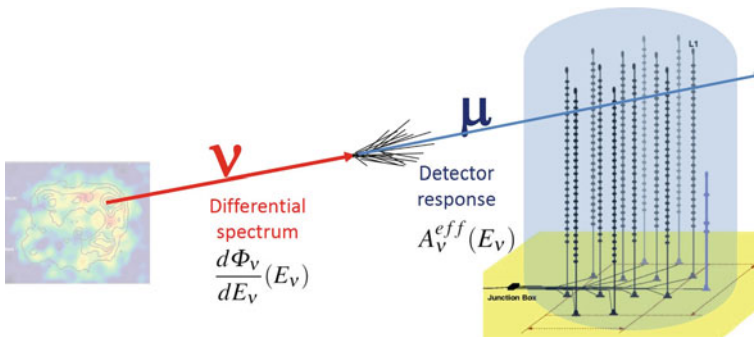


**Fig. 10.9** The number of observed events in a neutrino telescope is given by the convolution of the differential neutrino flux and the effective neutrino area of the detector

where  $N_A$  is Avogadro number,  $d\sigma_\nu/dE_\mu$  is the differential neutrino cross section for production of a muon of energy  $E_\mu$ , and  $R_{\text{eff}}(E_\mu, E_{\text{thr}}^\mu)$  is the muon range for a muon of energy  $E_\mu$  arriving at the detector with energy  $E_{\text{thr}}^\mu$ . These quantities can be obtained with analytical approximations or with full Monte Carlo simulations. For our purposes, the following approximation is adequate (Gaisser et al. 1996)

$$P_{\nu\mu} \simeq 1.3 \cdot 10^{-6} E_\nu^{2.2}, \quad \text{for } E_\nu = 10^{-3} - 1 \text{ TeV} \quad (10.27a)$$

$$\simeq 1.3 \cdot 10^{-6} E_\nu^{0.8}, \quad \text{for } E_\nu = 1 - 10^3 \text{ TeV} \quad (10.27b)$$

The dependence of  $P_{\nu\mu}$  in the two energy regimes reflects the energy dependence of the neutrino cross section,  $\sigma \propto E_\nu$ , and the effective muon range, which depends linearly on the muon energy up to  $\sim 1$  TeV. Above 1 TeV, muon radiative losses become dominant and the range is almost energy-independent. At higher energies, the cross section is not anymore linear as a function of energy and  $P_{\nu\mu} \propto E_\nu^{0.4}$ .

- The quantity  $\epsilon$  corresponds to the fraction of muons with energy  $E_{\text{thr}}^\mu$  that are detected. In general,  $\epsilon = \epsilon_t \cdot \epsilon_r \cdot \epsilon_c$ , where  $\epsilon_t$  represents the trigger efficiency (the muon must produce a sufficient number of photons to trigger the apparatus);  $\epsilon_r$  the reconstruction efficiency and  $\epsilon_c$  the probability to pass the analysis selection cuts. The quantity  $\epsilon$  can be derived for each experiment only by detailed Monte Carlo simulations which take into account all the features of the detector.
- The term  $e^{-\sigma(E_\nu)\rho N_A Z(\theta)}$ , where  $\sigma(E_\nu)$  is the total neutrino cross section, ( $\rho N_A$ ) the target nucleon density and  $\theta$  the neutrino direction with respect to the nadir, takes into account the absorption of neutrinos crossing along a path  $Z(\theta)$  in the Earth. From the nadir  $Z(0) = 6.4 \times 10^8$  cm, the absorption becomes not negligible for  $\sigma > 10^{-34}$  cm<sup>2</sup>, see Fig. 10.1, i.e., for  $E_\nu > 100$  TeV.

To solve analytically (10.24) in our simplified model, we assume that muons arriving at the detector with residual energy  $> 1$  TeV have constant probability  $\epsilon$  to produce enough light to be triggered, reconstructed and to pass the analysis selection criteria. With these approximations, the event rate for the reference neutrino flux

$$\frac{N_\nu}{T} = \int_{1 \text{ TeV}}^{10^3 \text{ TeV}} dE_\nu \cdot (\Phi_\nu^0 E_\nu^{-2}) \cdot A \cdot (P_\circ E_\nu^{0.8}) \cdot \epsilon = 0.5 \cdot 10^{-16} \cdot A \cdot \epsilon \text{ cm}^{-2} \text{ s}^{-1} \quad (10.28)$$

where  $P_\circ = 1.3 \cdot 10^{-6}$  as in (10.27b). Assuming a cross sectional area  $A = 1$  km<sup>2</sup> and  $\epsilon \simeq 0.1$ , roughly the effective area at  $E_\nu = 1$  TeV corresponds to  $A_\nu^{\text{eff}}(1 \text{ TeV}) \simeq 10^3$  cm<sup>2</sup> and the number of expected events is  $\sim 1.5$  year. This expected rate is in agreement with more detailed computations.

According to (10.28), a detector of the km<sup>3</sup>-size is required to detect few neutrino interactions/y from a galactic source, based on neutrino flux models constrained by the TeV  $\gamma$ -ray observations. The effect of the possible exponential cutoff, as in (10.7), is to decrease the event rate by a factor of 5–10.

This expected signal is not background-free. This means that when considering the events from a point-like source arriving from an angular cone of semi-aperture  $\psi$  from the source direction, events due to atmospheric neutrinos have to be considered. This irreducible background is described by a differential flux  $\frac{d^2\Phi_\nu^{\text{Atm}}}{dE_\nu d\Omega}$  (Chap. 11). The rate of background events is given by

$$\frac{N_B}{T} = \int \int dE_\nu \cdot \frac{d^2\Phi_\nu^{\text{Atm}}}{dE_\nu d\Omega}(E_\nu, \theta) \cdot A_\nu^{\text{eff}}(E_\nu) \cdot d\Omega \tag{10.29}$$

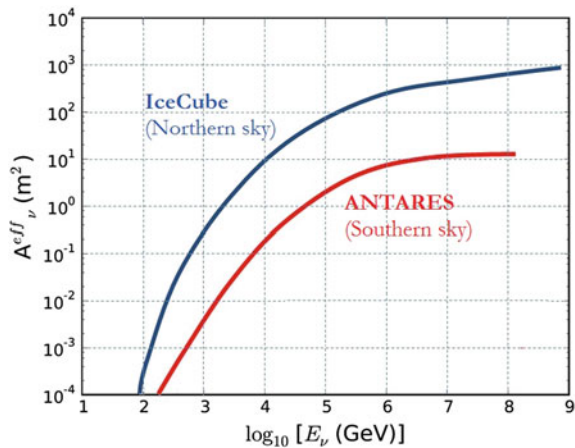
and it depends on the considered solid angle  $d\Omega$ . It is easy to derive that for small apertures  $d\Omega \propto \psi^2$ , and thus that also the background rate  $N_B/T \propto \psi^2$ . If the observational angle  $\psi$  is too large (i.e.,  $>0.5^\circ$ ), the background could dominate over the signal. A possibility to increase the signal-to-background ratio is to use the estimated energy of the events. As the signal behaves as  $d\Phi_\nu/dE_\nu \propto E^{-2}$  and the background as  $d\Phi_\nu^{\text{Atm}}/dE_\nu \propto E^{-3.7}$ , the background can be reduced by selecting high-energy events.

### 10.5.1 The Neutrino Effective Area of Real Detectors

The energy-dependent effective area  $A_\nu^{\text{eff}}(E_\nu)$  is obtained using Monte Carlo (MC) simulations for each experiment.  $A_\nu^{\text{eff}}(E_\nu)$  is in addition usually different for different analyses, as it depends on the selection criteria. This quantity is used also to compare the sensitivity of different experiments for similar physics studies.

Figure 10.10 shows the average effective areas computed for the IceCube and ANTARES detectors (Sect. 10.7) for point-sources searches of cosmic neutrinos. Since IceCube is located at the South Pole, the zenith angle  $\theta$  and declination angle  $\delta$  are simply related as  $\theta = \delta + 90^\circ$ . At a different location, due to the Earth’s motion,

**Fig. 10.10** Neutrino effective area as a function of the true simulated neutrino energy obtained for the events selected by the IceCube (Aartsen et al. 2013b) and ANTARES (Adrián-Martínez et al. 2012) detectors. A full Monte Carlo simulation is necessary to describe the triggering, tracking and selection efficiencies of the two detectors



the declination in the detector frame of a given source in the sky changes with daytime. The effective area must thus be computed for each source as a function of the declination by averaging over the local coordinates (zenith and azimuth angles). IceCube is sensitive to sources optically visible in the Northern sky, while ANTARES, located in the Mediterranean Sea, to sources visible in the Southern sky.

Using the published IceCube values of the effective area provided in a tabular form (Aartsen et al. 2013b) it is straightforward to compute the number of expected events with an electronic spreadsheet using Eq. (10.24). In the case of IceCube for a source located in the Northern sky with the reference neutrino flux (Sect. 10.4.1), 13 events/y are expected for no cutoff, and 2.7 events/y for  $E_c = 3.7 \text{ TeV}$ . Concerning the background of atmospheric neutrinos, IceCube detects 180  $\nu$ /days. Assuming a search cone of  $0.5^\circ$  centered on the source, the number of background events falling inside the cone is  $\sim 4$  events/y. The background depends on the declination of the source, and it can be reduced with a cut on the reconstructed energy.

RX J1713.7-3946 and other galactic SNRs are located near the galactic center and visible in the Southern sky. The sensitivity of the IceCube telescope for this region is substantially null for neutrino energies below 100 TeV, see Sect. 10.8.1. The galactic center region is studied in a better way with a detector in the Northern hemisphere, as ANTARES. However this detector has an effective area a factor of  $\sim 40$  smaller than IceCube and has marginal sensitivity to detect a source corresponding to the reference neutrino flux in an observation period of 10 year. A  $\text{km}^3$  detector in the Northern hemisphere is necessary for the detection of galactic sources.

### 10.5.2 Number of Optical Sensors in a Neutrino Telescope

A cubic kilometer instrumented volume is necessary to detect cosmic neutrinos. How many PMTs are needed to measure accurately a muon track? This is one of the major impact factors on the cost of an experiment.

To solve the problem, we assume that a signal in at least 10 different PMTs is needed to reconstruct a muon track. The reconstruction algorithm has to determine 5 degrees of freedom (the coordinate of the impact point on the detector surface and two angles). The larger the number of PMTs, the better the quality of the track reconstruction will be. In the case of a muon, many photons arrive on the same PMT during the integration window of the electronics (which is of the order of 20–50 ns). The exact number depends on the PMT distance and orientation with respect to the track. Assuming that on average 10 photoelectrons (p.e.) are detected per PMT, the minimum number of p.e. to accurately reconstruct a muon track is  $N_{p.e.} \sim 100$  p.e.

We assume that the telescope uses PMTs with 10" diameter (corresponding to detection area  $A_{\text{pmt}} \sim 0.05 \text{ m}^2$ ) and quantum efficiency  $\epsilon_{\text{pmt}} \sim 0.25$ , see Fig. 10.2b. Similar PMTs have the advantage to fit inside commercial pressure-resistant glass spheres (optical module, OM). This option has already been chosen by the IceCube and ANTARES collaborations. The overall efficiency of the PMT inside the OM is somewhat reduced, due to the presence of the glass, of the glue between the glass

and the PMT, and the mu-metal cage for magnetic shielding. We can assume that  $\epsilon_{\text{om}} \simeq 0.8 \cdot \epsilon_{\text{pmt}} \simeq 0.2$ .

Cherenkov photons emitted during the muon propagation do not produce any signal if they are not intercepted by the photocathode of the PMT. Let us assume that only a photon propagating inside the *effective PMT volume* can induce a photoelectron (p.e.) with a probability  $\epsilon_{\text{om}} \simeq 0.2$  when arriving at the photocathode. The effective PMT volume  $V_{\text{pmt}}$  is defined as a cylinder of ice/water with base area  $A_{\text{pmt}}$  and height  $\lambda_{\text{abs}}$ . The quantity  $\lambda_{\text{abs}}$  is the ice/water *absorption length*, introduced in the next section. For the following, we assume  $\lambda_{\text{abs}} = 50 \text{ m}$  in the wavelength interval where the PMT quantum efficiency is not null, Fig. 10.2b. Thus the effective PMT volume corresponds to  $V_{\text{pmt}} = A_{\text{pmt}} \times \lambda_{\text{abs}} \simeq 2.5 \text{ m}^3$ .

If  $N_{\text{pmt}}$  is the number of optical sensors inside the instrumented volume, the ratio  $R$  between the effective PMT volume of  $N_{\text{pmt}}$  and the instrumented volume ( $1 \text{ km}^3$ ) is:

$$R = \frac{V_{\text{pmt}} \times N_{\text{pmt}}}{10^9 \text{ m}^3} = 2.5 \times 10^{-9} N_{\text{pmt}}. \quad (10.30)$$

$N_{\text{pmt}}$  is the unknown number to be determined.

The total number of Cherenkov photons emitted by a 1 Km long muon track in the wavelength range of the PMTs sensitivity (Sect. 10.1.1) is  $N_C \simeq 3.5 \times 10^7$ . Only the small fraction falling inside the effective volume of one PMT can be converted with efficiency  $\epsilon_{\text{om}}$  into photoelectrons and the total number of p.e. produced by the muon track will be

$$\begin{aligned} N_{\text{p.e.}} &= N_C \times R \times \epsilon_{\text{om}} \simeq (3.5 \times 10^7) \cdot (2.5 \times 10^{-9} N_{\text{pmt}}) \cdot \epsilon_{\text{om}} \\ &= 1.8 \times 10^{-2} N_{\text{pmt}} \end{aligned} \quad (10.31)$$

By requiring that  $N_{\text{p.e.}} = 100$ , from (10.31) the minimum number of optical sensors in a neutrino detector is

$$N_{\text{pmt}} \simeq 100 / 1.8 \times 10^{-2} \simeq 5000. \quad (10.32)$$

As we will show in Sect. 10.7.1, the IceCube collaboration has buried in the ice 5160 OMs. ANTARES (which is smaller than IceCube) uses 885 PMTs. The option planned by the KM3NeT collaboration is to use a larger number of smaller PMTs (3" diameter) inside each OM.

## 10.6 Water and Ice Properties

The effects of the medium (water or ice) on light propagation are absorption and scattering of photons. These affect the reconstruction capabilities of the telescope. Water is transparent only to a narrow range of wavelengths ( $350 \text{ nm} \leq \lambda \leq 550 \text{ nm}$ ). The *absorption length* is the distance over which the light intensity has dropped to



$1/e$  of the initial intensity  $I_0$ . Thus, the light intensity in a homogeneous medium reduces to a factor  $I(x) = I_0 \exp(-x/\lambda_{\text{abs}})$  after traveling a distance  $x$ . For deep polar ice, the maximum value of  $\lambda_{\text{abs}} \sim 100$  m is assumed in the blue-UV region, while it is about 70 m for clear ocean waters. Absorption reduces the amplitude of the Cherenkov wavefront, i.e., the total amount of light arriving on PMTs. Scattering changes the direction of the Cherenkov photons and consequently delays their arrival time on the PMTs; this degrades the measurement of the direction of the incoming neutrino. *Direct photons* are those arriving on a PMT in the Cherenkov wavefront, without being scattered; the others are *indirect photons*.

Seawater has a smaller value of the absorption length with respect to deep ice, which is more transparent. The same instrumented volume of ice corresponds to a larger effective volume with respect to seawater. On the other hand, the effective scattering length for ice is smaller than water. This is a cause of a larger degradation of the angular resolution of detected neutrino-induced muons in ice with respect to water.

The South Pole ice has optical properties that vary significantly with depth and that need to be accurately modeled. Impurities trapped in the ice depend on the quality of the air present in the snows: Antarctica ice is laid down through a process of snowfall, hence trapping bubbles of air as it compacts itself. This happened over roughly the last  $10^5$  years. Because of variations in the long-term dust level in the atmosphere during this period, as well as occasional volcanic eruptions, impurity concentrations are depth dependent. The ice is almost background-free from radioactivity.

The background in seawater has two main natural contributions: the decay of radioactive elements dissolved in water, and the luminescence produced by organisms, the so-called bioluminescence. The  $^{40}\text{K}$  is by far the dominant of all radioactive isotopes present in natural seawater. The beta-decay of  $^{40}\text{K}$  is above the threshold for Cherenkov light production. Bioluminescence is ubiquitous in oceans and due to two main phenomena in deep sea: steady glow of bacteria and flashes produced by animals. These can give rise to an optical background which occasionally can reach a level of several orders of magnitude larger than that due to  $^{40}\text{K}$ .

Optical properties of water depend on many factors. Environmental parameters such as water temperature and salinity are indicators of the aggregation state of  $\text{H}_2\text{O}$  molecules, which biases the diffusion of light. Water absorption and scattering depend also on the density and the sizes of the floating particulate, which affects the telescope response also in terms of detector aging. Due to bio-fouling and sediments sticking on the optical modules, efficiency in photon detection can be reduced for long-term operations. In order to minimize the bias induced by external agents, the telescope sites must be far enough from continental shelf breaks and river estuaries, which can induce turbulent currents and spoil the purity of water. At the same time, the neutrino telescope should be close to scientific and logistic infrastructures on shore. With such requirements, the Mediterranean Sea offers optimal conditions on a worldwide scale.

## 10.7 Operating Neutrino Telescopes

The activities for the construction of a neutrino telescope started in the early 1970. This was initially mainly a joint Russian-American effort that, after the Soviet invasion of Afghanistan, forced the teams to take separate paths (the DUMAND project for the Americans, BAIKAL for the Russian). The DUMAND project was canceled in 1995 (the indispensable submarine technology was not advanced enough at that time) and the efforts of the two communities turned toward an experiment in a lake with iced surface and in the South Pole ice.

**The experiment in Lake Baikal.** Winter ice covers as a platform the Russian Lake Baikal (52°N, 104°E), and this has allowed the construction of a neutrino detector operating since 1993. Lake Baikal is the deepest in the world, reaching a depth of more than 1600 m. The ice layer can be used for assembly and deployment of instruments, instead of using ships and underwater remotely operating vehicles. The disadvantage of lake water is that the scattering length is much shorter than in seawater, with a consequent very poor determination of the neutrino direction. In 1984–1990 single-string arrays equipped with 12–36 PMTs were deployed and operated via a shore cable. The optical properties of the lake water at great depths have been established, and the detection of high-energy neutrinos has been demonstrated with the existing detector NT200/NT200+, with about 200 optical modules deployed 3.6 Km from shore at a depth of 1.1 km. This achievement represents a proof of concept for commissioning a new instrument, the so-called Gigaton Volume Detector (BAIKAL-GVD), with an effective size at or above the kilometer-scale.

**The AMANDA experiment at the South Pole.** An experiment at the South Pole, at the Amundsen-Scott station where the ice is about 2800 m deep, was pioneered by the Antarctic Muon And Neutrino Detector Array (AMANDA) collaboration. They drilled holes in the ice using a hot water drill, and lowered strings of optical sensors before the water in the holes could freeze again. The first AMANDA string was deployed in 1993, at a depth of 800–1,000 m. It was quickly found that at that depth the ice had a very short scattering length, >50 cm. In 1995–1996 AMANDA deployed 4 strings at depths between 1,500 and 2,000 m. These detectors worked as expected, and AMANDA detected its first atmospheric neutrinos. This success led to AMANDA-II, which consisted of 19 strings holding 677 optical sensors.

An exhaustive description of the history of neutrino telescopes is in Spiering (2012).

### 10.7.1 A Telescope in the Antarctic Ice

At present the only running km<sup>3</sup>-scale detector is the IceCube neutrino observatory (<http://icecube.wisc.edu/>) at the geographic South Pole, Fig. 10.11. The instrumented detector volume is a cubic kilometer of highly transparent Antarctic ice and it was built between 2005 and 2010. IceCube uses an array of 5,160 Digital Optical Modules

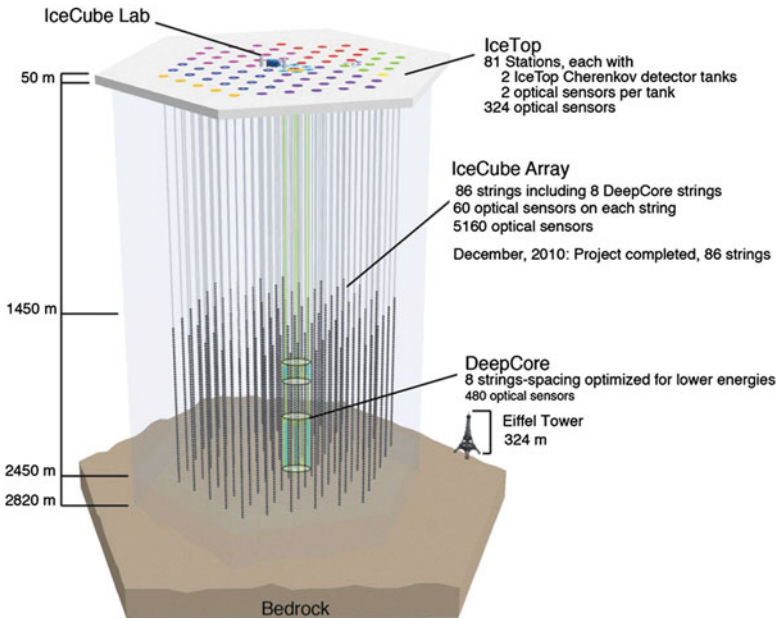


**Fig. 10.11** Side view of the **IceCube detector**, consisting of 86 buried InIce strings. The *IceTop* surface array and the DeepCore are also shown. Credit: IceCube/NSF

(DOMs) deployed on 86 strings at a depth of 1.5–2.5 km below the surface just above the bedrock in the clear, deep ice. Strings are arranged at the vertices of equilateral triangles that have sides of 125 m. The DOMs are spherical, pressure resistant glass housings containing each a 25 cm diameter photomultiplier tube (PMT) plus electronics for waveform digitization, and vertically spaced 17 m from each other along each string. High quantum efficiency PMTs are used in a denser sub-array located in the center of the detector. This sub-array, called DeepCore, enhances the sensitivity to low energy neutrinos. Finally, a surface CR detector, called IceTop, completes the IceCube Observatory. Data acquisition with the complete configuration started in May 2011.

Because of the Antarctic weather, high altitude and remote location of the South Pole, logistics is a key issue. The construction season lasted from November through mid-February (during the Austral summer). Everything needed was flown to the Pole on ski-equipped transports planes. The main task in the construction of IceCube consisted in the drilling of holes for the strings (see Fig. 10.12). This was done with a 5 MW hot-water drill, melting a hole through the ice. Drilling a 2,500 m deep, 60 cm diameter hole takes about 40 hours.

In the search for cosmic neutrinos (Aartsen et al. 2013b) the trigger consists of at least 8 DOMs recording a signal within a  $5 \mu\text{s}$  time window. Most of the events selected with this trigger are atmospheric muons (rate of  $\sim 2.2 \text{ kHz}$ ) entering the detector from above. Only about one in  $10^6$  recorded events is induced by an



**Fig. 10.12** The hot water hose and support cables disappear down one of the many boreholes drilled into the Antarctic ice to construct the IceCube Neutrino Observatory. Credit: Jim Haugen, IceCube/NSF

**atmospheric neutrino.** Key elements in the selection of the neutrino candidates are the reconstruction of the event direction and of the deposited energy. Only high quality reconstructed events are selected to suppress the background of downward going muons mis-reconstructed as upward going. The quality cuts depend on the likelihood of the fit, on the number of direct photons, on the length of the track, on “smoothness” criteria requiring a uniform distribution of photoelectrons along the length of the track, etc.

### 10.7.2 A Telescope in the Mediterranean Sea

The **ANTARES** detector (<http://antares.in2p3.fr>) is at present the largest neutrino observatory in the Northern hemisphere ( $42^\circ\text{N}$ ,  $6^\circ\text{E}$ ), which offers a privileged view of the most interesting areas of the sky, like the galactic center, where many neutrino source candidates are expected. The ANTARES detector was completed in 2008, after several years of site exploration and detector R&D. The detector is located at a **depth of 2475 m, in the Mediterranean Sea**, 40 km from the French town of Toulon. It comprises a three-dimensional array of **885 optical modules (OMs)** looking  $45^\circ$  downward and distributed along **12 vertical detection lines**, Fig. 10.13. An OM consists of a **10" PMT** housed in a pressure resistant glass sphere together with its base, a special gel for optical coupling and a  $\mu$ -metal cage for magnetic shielding, Fig. 10.2a. The OMs are grouped in 25 triplets (or storeys) on each line with a vertical spacing of 14.5 m between triplets. The total length of each line is 450 m; these are kept taut by a buoy located at the top of the line. The separation between the lines ranges from 60 to 75 m. Each line has been deployed by a ship and connected to a junction box by a remotely operated submarine vehicle. The junction

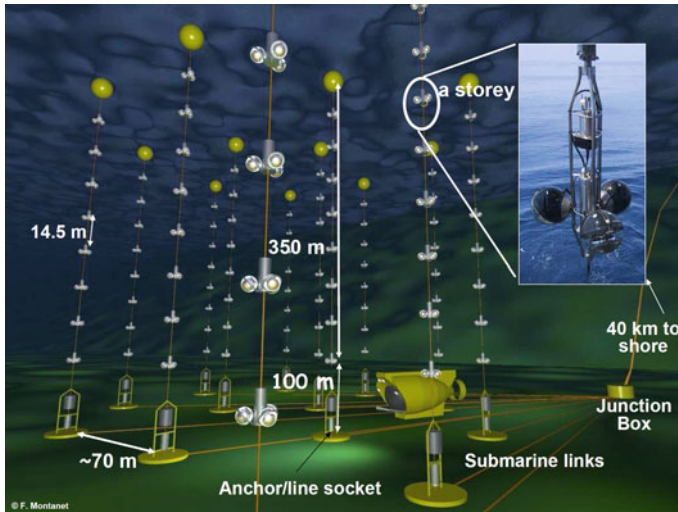


**Fig. 10.13** Schematic view of the Astronomy Neutrino Telescope and Abyss environmental RESEARCH (ANTARES) detector. The *inset* shows the details of one of the PMT triplets mentioned in the text. Credit: F. Montanet and the ANTARES Collaboration

box in turn is connected to shore via an electro-optical cable. Sea operations and sea technologies are of fundamental importance for the realization of underwater experiments.

The detector also includes several calibration systems. The lines slowly move due to the sea current (up to  $\sim 15$  m at the top of the line in case of currents of 20 cm/s). A set of acoustic devices together with tiltmeters and compasses along the lines are used to reconstruct the shape of the lines and orientation of the storeys every two minutes. The acoustic system provides the position of each optical module with a precision better than 15 cm.

The total ANTARES sky coverage is  $3.5\pi$  sr, with an instantaneous overlap of  $0.5\pi$  sr with that of the IceCube experiment. The galactic center is observed 67% of the time.

**KM3NeT** is a future deep-sea research infrastructure hosting a neutrino telescope with a volume of several cubic kilometers to be constructed in the Mediterranean Sea. The design, construction and operation of the KM3NeT neutrino telescope will be pursued by a consortium formed by numerous research institutes. Different solutions for the neutrino telescope have been studied. The chosen design relies on a three-dimensional array of OMs attached to vertical structures, the Detection Units (DUs), structured in strings. An array of DUs constitutes a detector building block. Several building blocks (located also in different sites in the Mediterranean Sea) will form the full detector of about 300 DUs. The OM in the DUs will consist of a 17'' pressure-resistant glass sphere housing 31 PMTs of 3'' diameter.

## 10.8 Results from Neutrino Telescopes

We discuss here some recent results obtained in the study of neutrino fluxes presented in Sect. 10.4. Each analysis is based on appropriate cuts depending on the magnitude of the background and on the purity required to isolate an eventual signal. Neutrino candidates are selected using criteria that have been determined in a “blind” manner before performing the data analysis, i.e., using only simulations and/or a small subsample of data. The blinding policy limits the use of data during the optimization steps of analyses to avoid that the selection procedure be inadvertently tuned towards a discovery. This procedure requires the simulation of a large number of pseudo-experiments, with the generation of both signal and background events. The background consists generally of atmospheric neutrinos and of wrongly-reconstructed atmospheric muons.

### 10.8.1 Point-Like Sources

The  $\nu_\mu$  charged current interaction produces a long muon track that can be correlated with the parent neutrino direction, Sect. 10.3.1. No neutrino cosmic source has been identified so far. Only upper limits on neutrino flux from cosmic objects have been set. The number of signal events  $N(s)$  from a given source in a given time  $T$  (10.24) depends on the effective area  $A_v^{\text{eff}}$ , Eq. (10.25), which in turns depends on the selection cuts of the analysis through the parameter  $\epsilon$ . The same is true for the number of background events,  $N(b)$ , which is usually dominated by atmospheric neutrinos and can be calculated using Eq. (10.29). The selection cuts are optimized using the pseudo-experiments, in order to maximize the number  $N(s + b)$  of signal events (which necessarily includes the irreducible background) over the number of background events. The procedure depends on the hypothesized energy spectrum from the source. Usually, an  $\propto E^{-2}$  dependence is assumed, as expected from Fermi acceleration mechanism. The number of signal and background events varies according to the angular aperture of the search cone, to the cut imposed on the track quality parameters, and on the quantities used as estimators of the energy of the event. This operation defines a set of optimal parameters, corresponding to an efficiency  $\epsilon^*$  which gives the best value  $A_v^{*,\text{eff}}$  for the considered analysis.

The selection criteria are chosen to optimize the so-called sensitivity or the discovery potential. These two quantities are generally used as figures of merit of the experiment and well-defined statistical methods exist to perform such optimization using pseudo-experiments. The discovery potential is defined as the flux  $d\Phi_\nu/dE_\nu$  in (10.24) needed to make a  $5\sigma$  discovery in 50% of the pseudo-experiments. The sensitivity is defined as the average upper limit on the flux  $d\Phi_\nu/dE_\nu$  using a detector with  $A_v^{*,\text{eff}}$  that would be obtained by an experiment with the expected background and no true signal,  $N(s + b) = N(b)$ .



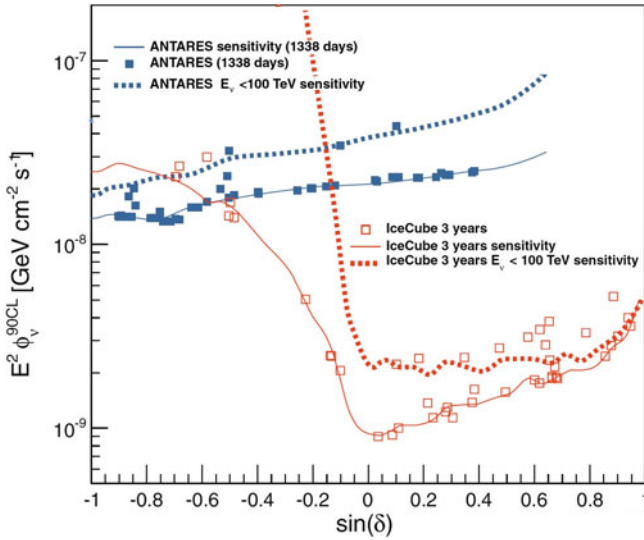


**Fig. 10.14** Upper limits and sensitivities for an  $E^{-2} \nu_{\mu} + \bar{\nu}_{\mu}$  spectrum from point sources as a function of  $\sin(\delta)$ . The *open (full) squares* represent the 90% C.L. flux upper limits for 44 (50) objects considered by IceCube (ANTARES). The *full lines* are the sensitivity (at 90% C.L.) for a point-source with an  $E^{-2}$  spectrum for three years of IceCube (Aartsen et al. 2013b) and for 3.7 years of ANTARES (Adrián-Martínez et al. 2014). The *dashed lines* represent the same sensitivity, but for neutrino energies lower than 100 TeV. The IceCube sensitivity for sources in the Southern hemisphere is mostly due to events of higher energy

Let us better define these quantities using the results of neutrino telescopes. Figure 10.14 shows as a function of the sine of the declination  $\delta$  the upper limits on selected IceCube and ANTARES point source candidates and the sensitivity of ANTARES and IceCube experiments (full lines).

IceCube searched for neutrino candidates coming from the direction of 44 objects selected a priori, according to observations in  $\gamma$ -rays or astrophysical models of neutrino emission. The results in Fig. 10.14 refer to almost three years of livetime, one each with a detector with 40, 59 and 79 strings respectively. The strength of the analysis cuts has been varied as a function of the declination. From the Northern hemisphere ( $\sin \delta > 0$ ) most of the sensitivity is for neutrinos with  $E_{\nu} > 100$  GeV. A different situation arises for sources located in the Southern hemisphere ( $\sin \delta < 0$ , that includes almost the whole galactic plane). Neutrino candidate events coming from negative declinations are observed as downward going events in IceCube. They have been selected with strong topological cuts, with the veto capability of the surface array IceTop and with a cut on the reconstructed energy to reject the huge contamination of downward going atmospheric muons. In fact, atmospheric muons are accompanied by extended air showers, which can produce early hits in the IceTop surface array. The corresponding sensitivity (red line) for sources located in the galactic center region is mostly for neutrinos with  $E_{\nu} > 100$  TeV. When pseudo-experiment



events with energy lower than 100 TeV are selected (red dashed line in figure), the IceCube sensitivity in the  $\sin \delta < 0$  region is substantially null.

A neutrino observatory able to monitor with higher efficiency the region of the sky with negative declinations is the one located in the Mediterranean Sea. The sensitivity of the ANTARES neutrino telescope shown in Fig. 10.14 as a blue line refers to 1339 days of livetime with the full 12 string detector and refers to neutrinos with  $E_\nu > 100$  GeV. ANTARES studied 50 selected sources, mainly in the galactic plane and assuming an  $E^{-2}$  energy spectrum.

The discovery potential corresponds to a curve almost parallel to the sensitivity and a factor 3-5 higher.

In both IceCube and ANTARES cases, after optimizing the cuts, the number of events in the search cone around each considered source was compared with the number of expected events. Three different possibilities can occur for source  $i$  at a given declination  $\delta_i$ : the number of events in the data  $\mathcal{N}_i$  is equal, larger or smaller than  $N_i(b)$ , the number of expected background events. In the case of  $\mathcal{N}_i = N_i(b)$ , the flux upper limit (the point in the figure) overlaps exactly the sensitivity value of the detector at declination  $\delta_i$ . The case of  $\mathcal{N}_i < N_i(b)$  is simply interpreted as an under-fluctuation of the background. The upper limit would lie below the sensitivity value but conventionally in the plot it matches the sensitivity as in the previous case. Finally, the number of data events could be larger than expected,  $\mathcal{N}_i > N_i(b)$ . This is attributed to a over-fluctuation of the background or to the presence of a real signal if  $\mathcal{N}_i - N_i(b)$  exceeds a value pre-defined by the discovery potential.

For all sources studied by IceCube and ANTARES, the excesses are compatible with an over-fluctuation of the background. The corresponding upper limit for a source at declination  $\delta_i$  lies above the corresponding sensitivity position. In Fig. 10.14 the positions of the 44 (50) upper limits obtained by IceCube (ANTARES) are indicated by the red (blue) points. The larger the distance of the point from the sensitivity line, the larger will be the difference between  $\mathcal{N}_i$  and  $N_i(b)$ . However, no source shows an excess of events incompatible with an over-fluctuation of the background.

In absence of signals, different sources at the same declination can have under- or over-fluctuations, the upper limits can be above or below the sensitivity. For this reason, it is sometimes said that the sensitivity corresponds to the average upper limit that would be obtained by an ensemble of experiments with the expected background and no signal.

The IceCube result indicates that none of the considered sources located in the Northern hemisphere of the equatorial coordinate system generates a  $\nu_\mu$  flux larger than  $E_\nu^2 \Phi_\nu \sim 0.5 \times 10^{-11}$  TeV/(cm<sup>2</sup> s). Note that this is below the value of our reference neutrino flux defined in Sect. 10.4.1. Concerning the limit from sources located in the Southern sky (the location of the galactic center is at  $\delta \sim -29^\circ$ ), IceCube has no sensitivity for  $E_\nu < 100$  TeV. Galactic sources are better constrained by ANTARES. Also in this case, no significant statistical fluctuations have been observed. For the area of the sky that is always visible (that with declination  $\delta < -48^\circ$ ), the sensitivity is  $E_\nu^2 \Phi_\nu \simeq 1.5 \times 10^{-11}$  TeV/(cm<sup>2</sup> s). The region with  $\delta > 42^\circ$  is never visible by a telescope in the Mediterranean sea. An experiment with

a larger volume in the Northern hemisphere is needed to study efficiently galactic neutrino source candidates.

It is interesting to compare the discovery potential of neutrino telescopes with that of space and ground  $\gamma$ -ray experiments shown in Fig. 9.6. Neutrino astronomy is approaching the level of sensitivity of  $\gamma$ -ray astronomy experiments, in spite of the incredibly small neutrino cross section and the consequent need for huge detectors.

### 10.8.2 Limits from GRBs and Unresolved Sources

The detection of neutrinos in spatial/temporal coincidence with GRBs would be an unambiguous proof of hadronic acceleration in cosmic sources, and could also serve to explain the origin of UHECRs. IceCube and ANTARES observe at least half the sky with a large duty cycle efficiency, and the requirement of temporal and spatial coincidence with a recorded GRB significantly reduces the number of expected background events. The observation of just one neutrino coincident within few seconds with a  $\gamma$ -ray burst would be statistically significant. It is left as an exercise to show that the present limits on the neutrino mass do not delay significantly the neutrino arrival time with respect to that of a photon.

No neutrino events in IceCube is associated with one of the 200 GRBs observed when the detector was in operation with 40 and 59 lines. In Abbasi et al. (2012), the absence of neutrinos associated with GRBs is interpreted either as the fact that GRBs are not the only sources of CRs with energies exceeding  $10^{18}$  eV or that the efficiency of neutrino production is much lower than predicted by the mechanism described in Sect. 10.4.3. Also ANTARES reported no observation of neutrinos from about 300 GRBs in coincidence with electromagnetic observations. Due to the smaller size, the derived limit is about one order of magnitude less stringent than that of IceCube.

These null results motivated the more detailed Monte Carlo simulation of neutrino production in the GRB jet, also discusses in Sect. 10.4.3. The new evaluation reduces the neutrino yield by an order of magnitude below that foreseen by analytic computations. With this reduced prediction, the IceCube limit still does not exclude that a large fraction of CRs with energies  $> 10^{18}$  eV are produced by GRBs.

No steady extragalactic individual object is expected to produce a neutrino flux detectable as a point source in the current generation of neutrino telescopes. It is nevertheless possible that many sources, isotropically distributed throughout the Universe, could combine to make a detectable signal, Sect. 10.4.2. A cosmic diffuse flux is searched as an excess of high energy events over the expected atmospheric neutrino background above a certain value of the energy (Fig. 10.3). The difficult task is the estimate of the neutrino energy using the calorimetric properties of neutrino telescopes. Two different channels can be studied: the  $\nu_{\mu}$ -induced muons and the showering events.

The average muon energy loss per meter ( $dE/dX$ ) is the observable correlated with the  $\nu_{\mu}$  energy. The energy loss  $dE/dX$  is estimated from the observed collection

of Cherenkov photoelectrons. The muon energy yields only a coarse proxy for the neutrino energy that, as already mentioned, is only partially transferred to the muon.

The interactions generating a shower provides little information about the neutrino direction. For diffuse flux measurements, the poor directional resolution is not a major draw-back, and the resolution on the shower energy (about 30%) is better than that obtained in the muon channel.

Different searches for a diffuse flux of cosmic neutrinos in both the  $\nu_\mu$  and the showering channels have been performed by the AMANDA, BAIKAL, and ANTARES experiments, all with negative results. All these detectors have an instrumented volume well below  $1 \text{ km}^3$ . The most stringent limit on the diffuse  $\nu_\mu$  flux arises from IceCube (Aartsen et al. 2014) and it corresponds to the full green line shown in Fig. 10.3. However, the most recent IceCube analysis studying a  $4\pi$  steradians sample of high-energy neutrino contained events shows a positive excess of neutrino with respect to the background, as presented in the following section.

## 10.9 The First Measurement of Cosmic Neutrinos

The interaction of neutrinos in the PeV range would induce a characteristic signal in a cubic kilometer apparatus, firing a large number of optical sensors. As the Earth reduces significantly the flux of PeV neutrinos, candidate events are searched also in the downward going sample. The first observation of an excess of high-energy astrophysical neutrinos over the expected background has been recently reported by IceCube (Aartsen et al. 2013a), using data collected with the full detector from May 2010 to May 2013 and with livetime of 988 days.

The high-energy neutrino candidates have been selected with the requirement that the interaction vertex is contained within the instrumented ice volume, without any signal on the PMTs located on the top or sides of the detector. In such a way, the edges of IceCube are used as a veto for downgoing atmospheric muons. The muon rejection efficiency of the veto has been measured in data by using one region of IceCube to tag muons and then measuring their detection rate in a separate layer of PMTs equivalent to the veto.

Atmospheric neutrinos are produced by the same parent mesons that generate the shower muons. A high-energy atmospheric neutrino has a large probability to be accompanied with a downgoing atmospheric muon produced in the same cascade. Thus, the veto provides also a partial reduction of the downgoing atmospheric neutrino background. To ensure a reliable trigger efficiency of the anticoincidence muon veto, an overall minimum number of 6,000 photoelectrons (p.e.) have been required. From the number of p.e., the deposited energy  $E_{dep}$  in the detector is derived and, in turns, the true energy  $E_\nu$  of the neutrino is estimated with the help on Monte Carlo simulation techniques. An event with 6,000 p.e. corresponds to a deposited energy of  $\sim 30 \text{ TeV}$ . This minimum energy requirement provides rejection of all but one part in  $10^5$  of the cosmic ray muon background.

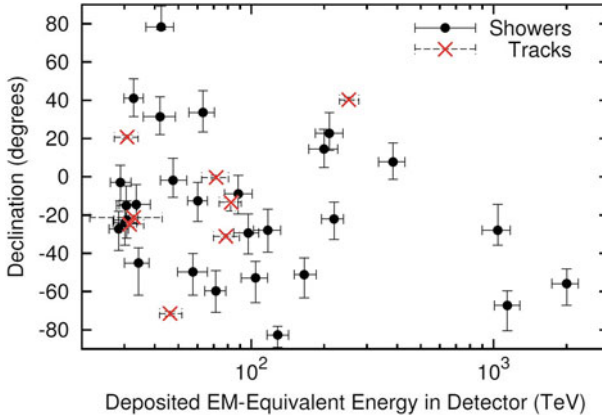


**Fig. 10.15** Arrival *declination angle* and deposited energies of the *high-energy neutrino candidate* sample of *IceCube*. At the South Pole, the declination  $\delta$  and the local *zenith angle*  $\theta$  are related by the simple condition  $\theta = \delta + 90^\circ$ . Courtesy of the IceCube collaboration

In the 3 years sample, *37 events* interacting within the IceCube fiducial volume, escaping the veto and with a number of p.e. 6, 000 have been observed, *nine accompanied with a visible muon track*, the remaining 28 with shower-like topologies. *Twenty-eight of the events arrived from the Southern hemisphere, containing most of the galactic plane*. The distribution of the declination and deposited energy for these events is shown in Fig. 10.15. The expected background is of  $8.4 \pm 4.2$  atmospheric muons escaping the veto and  $6.6^{+5.9}_{-1.6}$  atmospheric neutrinos, including that from charmed meson decay (prompt neutrinos, Sect. 11.3.2).

Referring to the two-dimensional distribution of events shown in Fig. 10.15, atmospheric muon background would appear as low-energy track events in the Southern sky (region with negative declination). Atmospheric neutrino backgrounds would appear primarily in the Northern sky (positive declination), also at low energies and predominantly as tracks. The attenuation of high-energy neutrinos due to the Earth absorption is clearly visible in the top right of the figure. The *nine events (crosses)* classified as *tracks correlate with the parent  $\nu_\mu$*  with an *angular resolution* of about  $1^\circ$ . The *shower-like events (filled circles)* correlate with the parent neutrino with an angular resolution of  $\sim 15^\circ$ .

Figure 10.16 shows the distribution of the data and of the expected backgrounds as a function of the deposited energy  $E_{dep}$ . *The measurement highlights a significant excess (about  $5.7\sigma$ ) with respect to the hypothesis that the data sample is due only to the atmospheric backgrounds*. The additional contribution in the data sample with respect to the background corresponds to the *astrophysical signal*, which is *parameterized as a diffuse flux* of the type  $E_\nu^2 \Phi_\nu^D(E) = (0.95 \pm 0.3) \cdot 10^{-8} \text{ GeV cm}^{-2} \text{ s}^{-1} \text{ sr}^{-1}$  per flavor, in the range 60 TeV–3 PeV.

The most probable indication of IceCube measurement is that data contain a *mixture of background* plus a  $\sim 1:1:1$  of neutrino flavors, as expected for a cosmic signal

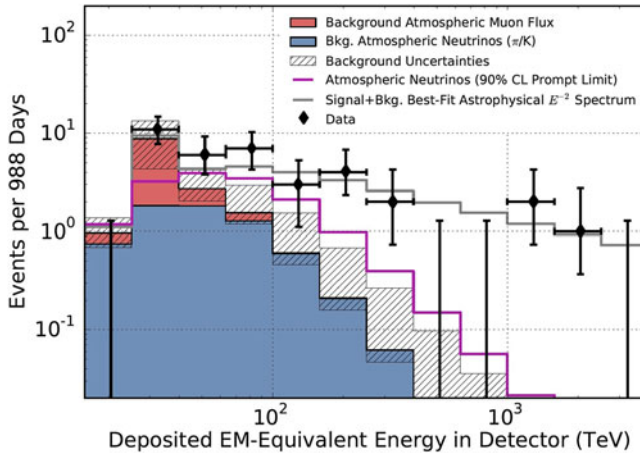


**Fig. 10.16** Deposited energies  $E_{dep}$  of observed IceCube events (crosses), compared with predictions. The hashed region shows uncertainties on the sum of all backgrounds, due to atmospheric muons and neutrinos. The contribution of an astrophysical ( $\nu + \bar{\nu}$ ) flux in the range  $60 \text{ TeV} < E_{dep} < 3 \text{ PeV}$  is also indicated, with a normalization of  $E_\nu^2 \Phi_\nu^D(E) = (0.95 \pm 0.3) \cdot 10^{-8} \text{ GeV cm}^{-2} \text{ s}^{-1} \text{ sr}^{-1}$  per flavor. A fit of data without the astrophysical contribution is disfavored at 5.7 standard deviations. Courtesy of the IceCube collaboration

(Sect. 12.8). Most of the signal originates primarily from the Southern hemisphere where neutrinos with  $E_\nu \gg 100 \text{ TeV}$  are not absorbed by Earth, and have a hard energy spectrum  $\propto E_\nu^{-2}$ , compatible with that expected from CR accelerators. However, an unbroken  $E_\nu^{-2}$  flux would produce 3.1 additional events above 2 PeV, that are not observed. This is interpreted, along with the slight excess in the lower energy bins, either due to a softer spectrum or due to a cutoff at high energies. The poor angular resolution ( $\sim 15^\circ$ ) of showering events prevent the possibility of accurate localization in the sky of the parent neutrino direction. To identify any bright neutrino sources in the data, usual maximum-likelihood clustering search has been used, as well as searches for directional correlations with TeV  $\gamma$ -ray sources. No hypothesis test yielded at present statistically significant evidence of clustering or correlations. Given the high galactic latitudes of many of the highest energy events, the data seem to suggest an extragalactic origin with a possible Galactic contribution, Fig. 10.17.

Further IceCube observations detector will improve the knowledge of physical properties of this high-energy sample. However, the main limitation due to the poor angular resolution for showering events will preclude the identification of sources in the galactic region (negative declination in Fig. 10.15).

The planned KM3NeT Mediterranean neutrino telescope, with an effective area much larger than ANTARES, will probably answer many questions about the nature of the unknown sources generating this astrophysical flux. To estimate the importance of a detector in the Northern sky, let for instance assume that the four events clustering near the center of the galactic plane in Fig. 10.17 come from a single galactic source.

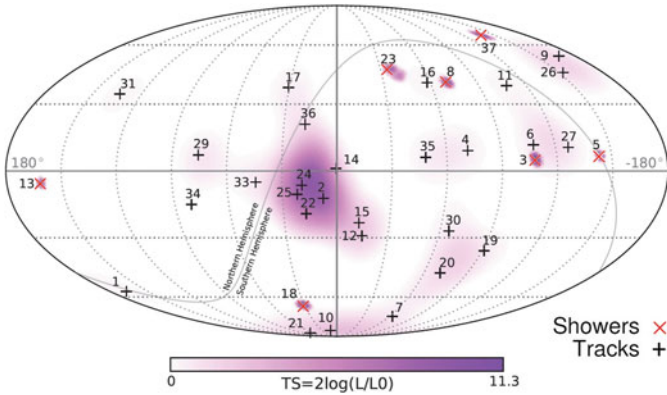


**Fig. 10.17** Arrival directions of the IceCube events in galactic coordinates. Shower-like events are marked with  $\times$  and those containing muon tracks with  $+$ . The gray line denotes the equatorial plane. The color map shows the test statistic for the point source clustering test at each location. A clustering of a fraction of the signal is present around the galactic center region, although statistically nonsignificant. Courtesy of the IceCube collaboration

After removing 15 background events to the 37 IceCube signal, assuming a diffuse neutrino flux per flavor of  $E_\nu^2 \Phi_\nu^D(E) = (0.95 \pm 0.3) \cdot 10^{-8} \text{ GeV cm}^{-2} \text{ s}^{-1} \text{ sr}^{-1}$ , the hypothetical muon neutrino flux from such a source would correspond to:

$$E_\nu^2 \frac{d\Phi_\nu}{dE_\nu} = \left( \frac{4}{37 - 15} \right) \times E_\nu^2 \Phi_\nu^D(E) \times (4\pi \text{ sr}) = 2 \times 10^{-8} \text{ GeV cm}^{-2} \text{ s}^{-1}. \quad (10.33)$$

We consider the  $\nu_\mu$  flux as the only able to produce a long track whose direction is strictly related with the parent neutrino direction. The above equation represents a simple and useful way to extract a point-like contribution from a diffuse flux measurement. By comparison with Fig. 10.14, the value (10.33) corresponds to the sensitivity of an experiment of the size of ANTARES, which has already excluded the presence of a single point source with a flux normalization as high as  $4 \times 10^{-8} \text{ GeV cm}^{-2} \text{ s}^{-1}$  anywhere in the galactic center region (Adrián-Martínez et al. 2014).

The mission to identify galactic sources, to measure the neutrino energy spectrum and flavor distribution of events coming from the galactic region is demanded to a neutrino telescope in the Northern sky. Such a detector will provide unique information about possible galactic accelerators. The flavor composition, in particular, will provide information on whether the flux is, as expected, coming from the decays of charged pions or from a different mechanism. Follow-up  $\gamma$ -ray, optical, and X-ray observations of the directions of individual high-energy neutrinos, which point to a sky region of angular size  $< 1^\circ$  may also be able to identify neutrino sources, and cosmic ray accelerators, even from those objects whose neutrino luminosity is too low to allow identification from neutrino measurements alone.



If the scientific community will be able in the next decade to successfully achieve this task, the detection of gravitational waves connected to high-energy astrophysics processes will be the last missing piece of multimessenger astrophysics.

## References

- M.G. Aartsen et al., Evidence for high-energy extraterrestrial neutrinos at the IceCube detector. *Science* **342** (2013a) 1242856–1. Updated in [arXiv:1405.5303](https://arxiv.org/abs/1405.5303)
- M.G. Aartsen et al., Search for time-independent neutrino emission from astrophysical sources with 3 years of IceCube data. *Astrophys. J.* **779**, 132 (2013b)
- M.G. Aartsen et al., Search for a diffuse flux of astrophysical muon neutrinos with the IceCube 59-string configuration. *Phys. Rev.* **D89**, 102001 (2014). Also [arXiv:1311.7048](https://arxiv.org/abs/1311.7048)
- R. Abbasi et al., Limits on neutrino emission from gamma-ray bursts with the 40 string IceCube detector. *Phys. Rev. Lett.* **106**, 141101 (2011)
- R. Abbasi et al., An absence of neutrinos associated with cosmic-ray acceleration in  $\gamma$ -ray bursts. *Nature* **484**, 351 (2012)
- S. Adrián-Martínez et al., Search for cosmic neutrino point sources with four years of data from the ANTARES telescope. *Astrophys. J.* **760**, 53 (2012)
- S. Adrián-Martínez et al. Search for muon neutrinos from gamma-ray bursts with the ANTARES neutrino telescope using 2008 to 2011 data. *Astronomy Astrophys.* **559** (2013) A9. Also [arXiv:1307.0304v1](https://arxiv.org/abs/1307.0304v1)
- S. Adrián-Martínez et al., Searches for point-like and extended neutrino sources close to the galactic center using the ANTARES neutrino telescope. *Astrophys. J. Lett.* **786**, L5 (2014)
- D. Allard, Extragalactic propagation of ultrahigh energy cosmic-rays. *Astropart. Phys.* **39–40**, 33–43 (2012)
- J. Becker, High-energy neutrinos in the context of multimessenger astrophysics. *Phys. Rep.* **458**, 173–246 (2008)
- S. Braibant, G. Giacomelli, M. Spurio. *Particle and Fundamental Interactions*. Springer (2011). ISBN 978-9400724631
- T. Chiarusi, M. Spurio, High-energy astrophysics with neutrino telescopes. *Eur. Phys. J.* **C65**, 649 (2010)
- T.K. Gaisser, F. Halzen, T. Stanev, Particle astrophysics, with high-energy neutrinos. *Phys. Rep.* **258**, 173–236. Erratum-ibid. **271**(1996), 355–356 (1995)
- D. Guetta et al., Neutrinos from individual gamma-ray bursts in the BATSE catalog. *Astropart. Phys.* **20**, 429–455 (2004)
- F. Halzen, Astroparticle physics with high energy neutrinos: from AMANDA to IceCube. *Eur. Phys. J. C* **46**, 669–687 (2006)
- P. Sapienza, G. Riccobene, High-energy neutrino astronomy. *Rivista del Nuovo Cimento* **32**(12), 591 (2009)
- C. Spiering. Towards high-energy neutrino astronomy: a historical review. *Eur. Phys. J.* **H37** 515–565 (2012). Also: [arXiv:1207.4952v1](https://arxiv.org/abs/1207.4952v1)
- C. Stegmann, A. Kappes, J. Hinton, F. Aharonian, Potential neutrino signals in a northern hemisphere neutrino telescope from galactic gamma-ray sources. *Astrophys. Sp. Sci.* **309**, 429 (2007)
- F. Vissani, F. Aharonian, Galactic sources of high-energy neutrinos: highlights. *Nucl. Instr. and Methods A* **692**, 5–12 (2012)
- E. Waxman, J. Bahcall, High energy neutrinos from cosmological gamma-ray burst fireballs. *Phys. Rev. Lett.* **78**, 2292–2295 (1997)
- E. Waxman, J. Bahcall, High energy neutrinos from astrophysical sources: an upper bound. *Phys. Rev.* **D59**, 023002–1 (1998)



# Chapter 11

## Atmospheric Muons and Neutrinos

Muons are the most abundant charged particles arriving at sea level and the only ones able to penetrate deep underground. The reason relies on their small energy loss (only  $\sim 2$  GeV across the whole atmosphere), the relatively long lifetime, and the fairly small interaction cross-section. The flux of muons with energy  $> 1$  GeV at sea level is of the order of 200 particles/(m<sup>2</sup> s). In this chapter, starting from the production of secondary nucleons (Sect. 11.1) and charged mesons (Sect. 11.2) by primary CRs interactions with atmospheric nuclei, we derive the energy spectra of atmospheric muons and atmospheric neutrinos, Sect. 11.3. The measurements of the muon flux and energy spectrum at sea level are presented in Sects. 11.4, 11.5.

Atmospheric muons can penetrate up to  $\sim 12$  km of water. As for high-energy cosmic neutrinos, for the study of low-energy astrophysical neutrinos, and in the search of rare events in the cosmic radiation presented in the following chapters, atmospheric muons represent the most dangerous background. The flux of underground muons as a function of depth, Sect. 11.6, is important to evaluate the background in searches of rare events. For instance, the simplest Grand Unified Theories (GUTs), the theories developed since the 1980s suggesting the unification of the electroweak interaction with the strong one, predicted proton lifetime values of  $\tau_p \sim 10^{30}$  years and the existence of massive magnetic monopoles. This motivated the searches with kton- and 1000 m<sup>2</sup>-scale detectors in underground laboratories. The first generation of underground experiments immediately realized that atmospheric neutrinos represent the irreducible background, Sect. 11.7. Because of the close relation between muon and neutrino production, the parameters characterizing the muon spectrum can provide important information on the atmospheric neutrino flux.

These early searches for rare phenomena predicted by GUT theories failed, but these experiments discovered an unexpected phenomenon: the disappearance of atmospheric  $\nu_\mu$ , explained by neutrino oscillations, Sect. 11.8. The high-precision measurements of the oscillation parameters of atmospheric  $\nu_\mu$  (Sect. 11.9) represent up to now the primary contribution of astroparticle experiments to particle physics, successively confirmed by accelerator experiments, Sect. 11.10. The flux of atmospheric neutrinos at higher energies, up to 100 TeV, was measured by neutrino telescopes, Sect. 11.11.

## 11.1 Nucleons in the Atmosphere

Air showers (Chap. 4) are described by a set of coupled cascade equations with boundary conditions at the top of the atmosphere to match the primary spectrum. Using transport equations, analytic expressions of the cascade can be constructed. The solutions of these equations allow computing the differential particle flux anywhere within the atmosphere. Concerning the muon component, some approximate analytic solutions are valid in the limit of high energies (Gaisser 1990, 2002; Lipari 1993). Numerical or Monte Carlo calculations are needed to account accurately for decay and energy loss processes, and for the energy dependence of the cross-sections.

We use here a simplified one-dimensional differential transport equation in the atmosphere following the approach of (Gaisser 1990). Neutrons are stable during the transit time in the atmosphere, and the effect of their decay is completely negligible. An important parameter to describe the interactions and the subsequent propagation of the particles is the vertical atmospheric depth  $X_v$  (Sect. 4.2). The nucleon mean free path in the atmosphere is given in Eq. (3.2). Some aspects of the mathematical developments are similar to those used in Sect. 5.1 for the propagation in the interstellar matter of  $\mathcal{M}$  and  $\mathcal{L}$  nuclei.

Let the quantity  $\mathcal{N}_N(E, X)dE$  represent the flux of nucleons (protons and neutrons) with energy in the interval  $E$  to  $E + dE$  at the slant depth  $X$  in the atmosphere. The attenuation of nucleons traversing a layer  $dX$  of atmosphere is,

$$\frac{\partial \mathcal{N}_N(E, X)}{\partial X} = -\frac{\mathcal{N}_N(E, X)}{\lambda_{I_N}} + \int_E^\infty \frac{\mathcal{N}_N(E', X)}{\lambda_{I_N}} F_{NN}(E, E') \frac{dE'}{E} \quad (11.1)$$

Note that, we assume constant the cross-sections of nucleons on atmospheric nuclei and correspondingly a nucleon mean free path  $\lambda_{I_N} = \lambda_{I_p} = 85 \text{ g cm}^{-2}$  as in (3.8a). The first term (with the  $-$  sign) in (11.1) is an attenuation term, indicating that the number of nucleons of a given energy  $E$  decreases as  $X$  increases. From baryon number conservation, it follows that the total number of nucleons is constant. The positive term takes into account the fact that an incident nucleon of energy  $E'$  can collide with an air nucleus and produce a nucleon with energy  $E$ . The quantity  $F_{ac}(E_c, E_a)$  represents, in general, the probability that the particle  $c$  with energy  $E_c$  be produced by the particle  $a$  with energy  $E_a > E_c$  during the process:

$$a + X \rightarrow c + Y \quad (11.2)$$

If  $a, c$  are hadrons, from the properties of hadronic interactions and namely from Feynman scaling (see *Extras # 3*), we have:

$$F_{ac}(E_c, E_a) = F_{ac}(x^*) \quad \text{where} \quad x^* = \frac{E_c}{E_a} \quad (11.3)$$

This *scaling* condition represents the fact that in hadronic interactions, the probability that a 10 GeV secondary particle be produced by a 100 GeV primary is the same as the probability of producing a 1 GeV secondary from a 10 GeV primary. Feynman scaling is violated in high-energy interactions.

Equation (11.1) has the boundary condition (2.20) at the top of the atmosphere:

$$\mathcal{N}_N(E, 0) = \Phi(E) = KE^{-\alpha} \quad (11.4)$$

Note from this equation that the units of  $\mathcal{N}_N$  are the same as those of  $\Phi(E)$ , namely ( $\text{cm}^{-2}\text{s}^{-1}\text{sr}^{-1}\text{GeV}^{-1}$ ). The same applies to the quantities  $\mathcal{N}_\pi, \mathcal{N}_\mu$  defined in the following. Using Feynman scaling (11.3), Eq. (11.1) can be written in terms of the adimensional quantity  $x^*$  as:

$$\frac{\partial \mathcal{N}_N(E, X)}{\partial X} = -\frac{\mathcal{N}_N(E, X)}{\lambda_{IN}} + \frac{1}{\lambda_{IN}} \int_0^1 \mathcal{N}_N\left(\frac{E}{x^*}, X\right) F_{NN}(x^*) \frac{dx^*}{x^{*2}} \quad (11.5)$$

where use has been made of the fact that  $x^* = E/E'$  and thus  $dx^* = \frac{E}{E'^2} dE' = x^{*2} \frac{dE'}{E}$  and finally  $\frac{dE'}{E} = \frac{dx^*}{x^{*2}}$ . We can solve the problem by assuming factorization as follows:

$$\mathcal{N}_N(E, X) = \Phi_N(E) \cdot H_N(X) \quad (11.6)$$

Then, Eq. (11.5) becomes:

$$\Phi_N \frac{dH_N}{dX} = -\frac{\Phi_N \cdot H_N}{\lambda_{IN}} + \frac{H_N}{\lambda_{IN}} \int_0^1 \Phi_N(E/x^*) \cdot F_{NN}(x^*) \cdot \frac{dx^*}{x^{*2}} \quad (11.7)$$

Dividing the two sides by  $\Phi_N \cdot H_N$ :

$$\frac{1}{H_N} \frac{dH_N}{dX} = -\left( \frac{1}{\lambda_{IN}} - \frac{1}{\Phi_N \lambda_{IN}} \int_0^1 \Phi_N(E/x^*) \cdot F_{NN}(x^*) \cdot \frac{dx^*}{x^{*2}} \right) \equiv -\left( \frac{1}{\Lambda_N} \right) \quad (11.8)$$

The solution of (Eq. 11.8) is:

$$H_N(X) = H_N(0) \cdot \exp\left(-\frac{X}{\Lambda_N}\right) \quad (11.9)$$

the flux of nucleons of a given energy is exponentially attenuated during propagation in the atmosphere with attenuation length  $\Lambda_N$ . At a given depth  $X$ , the form of the energy spectrum  $\Phi_N(E)$  at the top of the atmosphere is preserved. The quantity  $\Lambda_N$  has the dimension of an attenuation length as  $\lambda_{IN}$ . The second term in (11.8) increases the effective mean free path because of the regeneration of  $p, n$  with energy

$E$  from higher energy nucleons during propagation in the atmosphere.  $\Lambda_N$  depends on the energy spectrum  $\Phi_N(E)$  and on the  $F_{NN}$  function. In general, the  $F_{ac}$  functions are parameterized by phenomenological models of hadronic interactions using accelerator data.

A deeper insight into (11.8) can be obtained assuming that the solution  $\Phi_N(E)$  has the same dependence on energy as the boundary condition at  $X = 0$ , i.e.,

$$\Phi_N(E) = KE^{-\alpha}. \quad (11.10)$$

By replacing this trial solution in (11.8) we obtain:

$$\begin{aligned} \frac{1}{\Lambda_N} &= \frac{1}{\lambda_{IN}} \left( 1 - \frac{1}{E^{-\alpha}} \int_0^1 \left( \frac{E}{x^*} \right)^{-\alpha} \cdot F_{NN}(x^*) \cdot \frac{dx^*}{x^{*2}} \right) \\ &= \frac{1}{\lambda_{IN}} \left( 1 - \int_0^1 (x^*)^{\alpha-2} \cdot F_{NN}(x^*) \cdot dx^* \right) = \frac{1}{\lambda_{IN}} (1 - Z_{NN}) \end{aligned} \quad (11.11)$$

The quantities  $Z_{ac}$  depend on the hadronic interactions and are called *spectrum-weighted moments*. In general:

$$Z_{ac} \equiv \int_0^1 (x^*)^{\alpha-2} \cdot F_{ac}(x^*) \cdot dx^* \quad (11.12)$$

The quantity

$$\Lambda_a \equiv \frac{\lambda_{Ia}}{1 - Z_{aa}} \quad (11.13)$$

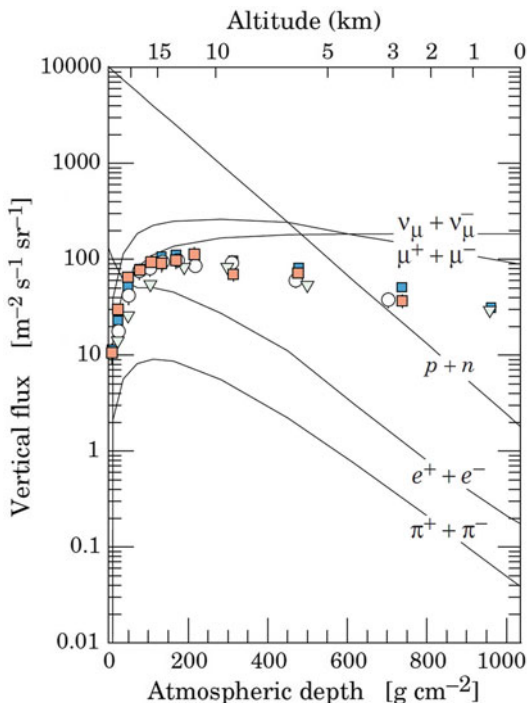
is the *equivalent attenuation length* of particle  $a$  when propagating in the atmosphere, under the effect of regeneration of higher energy particles of the same type. Table 11.1 shows the equivalent attenuation lengths for the main hadronic components of the atmospheric shower [from (Gaisser 1990)]. The values are about 20–30% higher than the corresponding values of  $\lambda_{Ia}$ .

Under the mentioned simplifications (and in particular under Feynman scaling), the elementary solution of the cascade equation preserves the power law energy spectrum. The quantity  $Z_{NN}$  in (11.11) is a constant that produces an increase of

**Table 11.1** Atmospheric equivalent attenuation lengths for nucleons, pions, and kaons from the definition (11.13)

$\Lambda_N$	$\Lambda_\pi$	$\Lambda_K$
120 g cm <sup>-2</sup>	160 g cm <sup>-2</sup>	180 g cm <sup>-2</sup>

**Fig. 11.1** Vertical fluxes as a function of the atmospheric depth  $X$  of different CR components with  $E > 1$  GeV. The estimates derive from the nucleon flux (2.20). The points show measurements of negative muons with  $E_\mu > 1$  GeV. Figure from Beringer et al. (2012)



the effective mean free path of nucleons in the atmosphere. The flux is attenuated as nucleons proceed in the atmosphere. The nucleons' flux in the atmosphere (11.6) using (11.9 and 11.10) is thus given by:

$$\mathcal{N}_N(E, X) = H_N(0) \cdot e^{-X/\Lambda_N} \cdot KE^{-\alpha} . \tag{11.14}$$

With the boundary condition (11.4),  $H_N(0) = 1$ . Figure 11.1 shows the vertical flux of different secondary CR components as a function of the atmospheric depth  $X$  and that of nucleons is indicated by  $p + n$ . We will show in the following that the flux of secondary particles in the atmosphere depends on their zenith angle  $\theta$ . For this reason usually the flux measured (or computed) in a small solid angle region centered on the vertical direction ( $\cos \theta = 1$ ) is reported. This is called the vertical flux.

## 11.2 Secondary Mesons in the Atmosphere

All hadrons can be produced by a primary CR interaction with an air nucleus. The full shower development can be described today using Monte Carlo simulations, Sect. 4.5. A look into analytical solutions is useful to understand the underlying processes. The two principal channels that produce atmospheric muons and neutrinos are the decays of charged pions and kaons. The development of  $\pi^\pm$  (as well as of kaons) can be described mimicking Eq. (11.5), with the difference that:

- Charged pions can either interact or decay with characteristics lengths  $\lambda_{I\pi}$  and  $d_\pi$ , respectively;
- Their mean free path  $\lambda_{I\pi} > \lambda_{IN}$  in atmosphere, see (3.8b);
- At a given energy, pions can be produced either by interactions of nucleons or of more energetic pions;
- Pions are not present as primary radiation: this corresponds the boundary condition  $\mathcal{N}_\pi(E, 0) = 0$ .

Including all these effects, the differential equation describing the pion propagation is, with obvious notation:

$$\frac{\partial \mathcal{N}_\pi(E, X)}{\partial X} = -\left(\frac{1}{\lambda_{I\pi}} + \frac{1}{d_\pi}\right) \mathcal{N}_\pi(E, X) \quad (11.15)$$

$$+ \int_0^1 \frac{\mathcal{N}_\pi\left(\frac{E}{x^*}, X\right)}{\lambda_{I\pi}} \cdot F_{\pi\pi}(x^*) \cdot \frac{dx^*}{x^{*2}} + \int_0^1 \frac{\mathcal{N}_N\left(\frac{E}{x^*}, X\right)}{\lambda_{IN}} \cdot F_{N\pi}(x^*) \cdot \frac{dx^*}{x^{*2}}$$

This equation has no simple solution, as the analogous of (11.6). The reason is that the quantity  $d_\pi$  depends on  $E$  and on  $X$ . The pion decay length  $d'_{\pi^\pm} = \Gamma c \tau_{\pi^\pm}$  was already introduced in Eq. (Eq. 4.27) (units: cm). The quantity in units of  $(\text{g cm}^{-2})$  is obtained by multiplying by the air density:  $d_\pi = \rho(X_\nu) d'_{\pi^\pm}$ . The complication arises from the fact that the air density depends on the atmospheric depth  $X_\nu$ . From (4.8), we have  $\rho(X) = X_\nu/h_0 \simeq \frac{X \cos \theta}{h_0}$  for zenith angles  $\theta \lesssim 60^\circ$ . Thus, using the fact that  $\Gamma = E/m_\pi c^2$ , we have:

$$\frac{1}{d_\pi} = \frac{1}{\Gamma c \tau_{\pi^\pm} \rho(X)} = \frac{m_\pi c^2 h_0}{E c \tau_{\pi^\pm} X \cos \theta} = \frac{\varepsilon_\pi}{E X \cos \theta} \quad (11.16)$$

The quantity

$$\varepsilon_\pi \equiv \frac{m_\pi c^2 h_0}{c \tau_{\pi^\pm}} \quad (11.17)$$

has the dimension of an energy and corresponds to the *characteristic pion decay constant*, see Table 11.2.

**Table 11.2** Lifetime  $\tau_i$  and decay constants  $\varepsilon_i = mc^2 h_0 / c \tau_0$  for secondary particles  $i$  produced by primary hadrons

Particles						
$i =$	$\mu^\pm$	$\pi^\pm$	$\pi^0$	$K^\pm$	$D^\pm$	$D^0$
$\tau_i$ (s)	$2.19 \times 10^{-6}$	$2.60 \times 10^{-8}$	$8.4 \times 10^{-17}$	$1.24 \times 10^{-8}$	$1.04 \times 10^{-12}$	$4.10 \times 10^{-13}$
$\varepsilon_i$ (GeV)	1.0	115	$3.5 \times 10^{10}$	850	$4.3 \times 10^7$	$9.2 \times 10^7$

Inserting explicitly (11.16) in (11.15) and using (11.14) for the nucleon flux, we obtain:

$$\begin{aligned} \frac{\partial \mathcal{N}_\pi(E, X)}{\partial X} = & - \left( \frac{1}{\lambda_{I_\pi}} + \frac{\varepsilon_\pi}{EX \cos \theta} \right) \mathcal{N}_\pi(E, X) \\ & + \int_0^1 \frac{\mathcal{N}_\pi\left(\frac{E}{x^*}, X\right)}{\lambda_{I_\pi}} \cdot F_{\pi\pi}(x^*) \cdot \frac{dx^*}{x^{*2}} + \frac{Z_{N\pi}}{\lambda_{I_N}} \mathcal{N}_N(E, 0) e^{-X/\Lambda_N} \end{aligned} \quad (11.18)$$

The term under the integral can be simplified assuming that the unknown  $\mathcal{N}_\pi(E, X)$  can be factorized as a product of  $E^{-\alpha}$  and a function of the depth. With this assumption, following (11.11):

$$\int_0^1 \frac{\mathcal{N}_\pi\left(\frac{E}{x^*}, X\right)}{\lambda_{I_\pi}} \cdot F_{\pi\pi}(x^*) \cdot \frac{dx^*}{x^{*2}} = \mathcal{N}_\pi(E, X) \cdot Z_{\pi\pi}$$

and thus, we can define the term:  $\frac{1}{\lambda_{I_\pi}}(1 - Z_{\pi\pi}) \equiv \frac{1}{\Lambda_\pi}$ . Finally, we can write (11.18) as:

$$\frac{\partial \mathcal{N}_\pi(E, X)}{\partial X} = -\mathcal{N}_\pi(E, X) \left( \frac{1}{\Lambda_\pi} + \frac{\varepsilon_\pi}{EX \cos \theta} \right) + \frac{Z_{N\pi}}{\lambda_{I_N}} \mathcal{N}_N(E, 0) e^{-X/\Lambda_N} \quad (11.19)$$

As the variables  $X, E$  are strongly coupled, we can easily solve (11.19) only under the additional approximations of low energy ( $E \ll \varepsilon_\pi$ ) or high energy ( $E \gg \varepsilon_\pi$ ).

An equivalent equation holds for charged kaons; in this case, the subscript  $\pi$  must be replaced with  $K$ .

**High-energy limit in pion production.** In the high-energy (*he*) limit ( $E \gg \varepsilon_\pi$ ), we neglect in (11.19) the energy-dependent decay term and:

$$\frac{\partial \mathcal{N}_\pi^{he}(E, X)}{\partial X} = + \frac{Z_{N\pi}}{\lambda_{I_N}} \mathcal{N}_N(E, 0) e^{-X/\Lambda_N} - \frac{\mathcal{N}_\pi^{he}(E, X)}{\Lambda_\pi}. \quad (11.20)$$

In this form, we recognize immediately the same equation (5.8) obtained for the  $\mathcal{L}$  nuclei in the propagation of CRs in Sect. 5.1.  $\mathcal{N}_\pi$  has the same boundary condition  $\mathcal{N}_\pi(E, 0) = 0$  as  $N_{\mathcal{L}}(0)$ . The equation  $\mathcal{N}_N$  describing nucleons has the same exponential behavior as  $N_{\mathcal{M}}$ . Thus, after replacing

$$\begin{aligned} P_{\mathcal{M}\mathcal{L}} & \rightarrow Z_{N\pi} \\ \lambda_{I_{\mathcal{M}}} & \rightarrow \Lambda_N = \lambda_{I_N}/(1 - Z_{NN}) \\ \lambda_{I_{\mathcal{L}}} & \rightarrow \Lambda_\pi \\ N_{\mathcal{M}}^0 & \rightarrow \mathcal{N}_N(E, 0) = KE^{-\alpha} \end{aligned} \quad (11.21)$$



we obtain the same solution as (5.11):

$$\mathcal{N}_\pi^{he}(E, X) = \left[ \frac{Z_{N\pi}}{1 - Z_{NN}} \cdot \frac{\Lambda_\pi}{\Lambda_\pi - \Lambda_N} (e^{-X/\Lambda_\pi} - e^{-X/\Lambda_N}) \right] \cdot KE^{-\alpha}. \quad (11.22)$$

The moments  $Z_{ab}$  are defined in (11.12) and  $\Lambda_N, \Lambda_\pi$  in Table 11.1.

In conclusion in the high-energy limit, the pion flux (11.22) can be factorized as a function  $H_\pi^{he}(X)$ —the quantity in the square bracket that depends only on the depth  $X$ —and a power law energy function with the same spectral index  $\alpha$  as that of primary nucleons:

$$\mathcal{N}_\pi^{he}(E, X) = H_\pi^{he}(X) \cdot KE^{-\alpha} \quad (11.23)$$

**Low-energy limit in pion production.** In the low-energy (*le*) limit, when  $E \cos \theta \ll \varepsilon_\pi$ , we can neglect the term  $\lambda_{I_\pi}$ . In the *le* limit, all pions are assumed to decay and (11.19) becomes

$$\frac{\partial \mathcal{N}_\pi^{le}(E, X)}{\partial X} = -\mathcal{N}_\pi^{le}(E, X) \left( \frac{\varepsilon_\pi}{EX \cos \theta} \right) + \frac{Z_{N\pi}}{\lambda_{I_N}} \mathcal{N}_N(E, 0) e^{-X/\Lambda_N}. \quad (11.24)$$

It is straightforward to see that if we replace the term  $\mathcal{N}_\pi^{le}$  on the right-hand side with:

$$\mathcal{N}_\pi^{le}(E, X) = \frac{Z_{N\pi}}{\lambda_{I_N}} \mathcal{N}_N(E, 0) e^{-X/\Lambda_N} \cdot \frac{XE \cos \theta}{\varepsilon_\pi} \quad (11.25)$$

we obtain  $\frac{\partial \mathcal{N}_\pi^{le}(E, X)}{\partial X} = 0$ . This condition represents the fact that the number of decayed pions are regenerated by the production of new pions in the atmosphere by pions and nucleons. Equation (11.25) has a maximum at  $X = \Lambda_N \simeq 120 \text{ g cm}^{-2}$  which corresponds to an altitude of 15 km. The correctness of the hypothesis leading to (11.25) is confirmed by Monte Carlo simulations. Using (11.14), the pion flux  $\mathcal{N}_\pi^{le}$  in the *le* limit can be factorized as:

$$\mathcal{N}_\pi^{le}(E, X) = \left[ \frac{Z_{N\pi}}{\lambda_{I_N}} \cdot e^{-X/\Lambda_N} \cdot X \right] \cdot \frac{E \cos \theta}{\varepsilon_\pi} \cdot KE^{-\alpha} = H_\pi^{le}(X) \frac{\cos \theta}{\varepsilon_\pi} \cdot KE^{-\alpha+1} \quad (11.26)$$

The quantities inside the square brackets define  $H_\pi^{le}(X)$ .

In Fig. 11.1, particles with energy above 1 GeV are considered, and the pion contribution is dominated by the *le* solution. The main features of the pion component in the atmosphere are evident in the curve labeled  $\pi^+ + \pi^-$ . The maximum number of pions is at depth  $\simeq 120 \text{ g cm}^{-2}$ . Using (11.26) and (11.14) the ratio between the pion and nucleon components as a function of  $X$  is:

$$\frac{\mathcal{N}_\pi^{le}(E, X)}{\mathcal{N}_N(E, X)} = \frac{Z_{N\pi} X}{\lambda_{I_N}} \cdot \frac{E}{\varepsilon_\pi} \cdot \cos \theta \quad (11.27)$$

Numerically, the quantity  $Z_{N\pi} \simeq 0.08$  (Gaisser 1990). For the energy threshold of 1 GeV considered in Fig. 11.1, the ratio is  $(E/\varepsilon_\pi) \sim 10^{-2}$ . Using  $\lambda_{IN} = 85 \text{ g cm}^{-2}$ ,  $Z_{N\pi} = 0.08$ , we obtain from (11.27) in the vertical direction a ratio  $\sim 2 \times 10^{-3}$  at the position  $X = \Lambda_N = 120 \text{ g cm}^{-2}$  where the number of pions in the shower has a maximum, and  $\sim 10^{-2}$  at sea level. Compare this result with Fig. 11.1.

### 11.3 Muons and Neutrinos from Charged Meson Decays

Muons and neutrinos are produced by the decay of charged mesons (mainly pions and kaons). The muon flux as a function of  $X$  and  $E$  can be deduced from (11.19) folding with the kinematics for the decays:

$$\pi^+(K^+) \rightarrow \nu_\mu + \mu^+ \quad (11.28a)$$

$$\hookrightarrow \mu^+ \rightarrow \bar{\nu}_\mu + \nu_e + e^+$$

$$\pi^-(K^-) \rightarrow \bar{\nu}_\mu + \mu^-$$

$$\hookrightarrow \mu^- \rightarrow \nu_\mu + \bar{\nu}_e + e^- . \quad (11.28b)$$

We derive the spectrum of atmospheric muons using the above *le* and *he* limits obtained for the pion flux.

The number of muons and neutrinos (as well as the ratio between particles and antiparticles) is strictly correlated. On the other hand, the energy distribution of muons and neutrinos differ because of their different masses. The loss of pions due to *decay* process in (11.15) is:

$$\frac{d\mathcal{N}_\pi}{dX} = -\frac{\mathcal{N}_\pi}{d_\pi} \quad (11.29)$$

with  $d_\pi$  defined in (11.16). The number of decaying charged pions in a layer  $dX$  of atmosphere is

$$d\mathcal{N}_\pi(E, X) = -\frac{\mathcal{N}_\pi(E, X) \cdot \varepsilon_\pi}{E \cdot X \cdot \cos \theta} \cdot dX \quad (11.30)$$

Equation (11.30) explains the meaning of the decay constant  $\varepsilon_\pi$ : if the particle energy is  $E \gg \varepsilon_\pi$  then the decay process is strongly suppressed with respect to the interaction. As 99.99% of pions decay into  $\mu\nu$ , the corresponding number of produced muons is:

$$d\mathcal{N}_\mu(E_\mu, X) = -d\mathcal{N}_\pi(E, X) \quad (11.31)$$

From this relation and (11.30), we obtain:

$$\frac{\partial \mathcal{N}_\mu}{\partial X}(E_\mu, X) = \mathcal{N}_\pi(E, X) \cdot \frac{\varepsilon_\pi}{E \cdot X \cdot \cos \theta} \quad (11.32)$$

We use now the  $le$  and  $he$  limits of the previous section. In the low-energy limit, we use (11.26) and:

$$\frac{\partial \mathcal{N}_\mu^{le}}{\partial X}(E_\mu, X) \simeq \left( H_\pi^{le} \frac{\cos \theta}{\varepsilon_\pi} \cdot KE_\mu^{-\alpha+1} \right) \cdot \frac{\varepsilon_\pi}{E_\mu \cdot X \cdot \cos \theta} = \frac{H_\pi^{le}}{X} \cdot KE_\mu^{-\alpha} \quad (11.33)$$

In the case of the high-energy limit, we use (11.23):

$$\frac{\partial \mathcal{N}_\mu^{he}}{\partial X}(E_\mu, X) \simeq H_\pi^{he}(X) \cdot \frac{\varepsilon_\pi}{E_\mu \cdot X \cdot \cos \theta} \cdot KE_\mu^{-\alpha} \quad (11.34)$$

Note here that the dependence on energy is of the type  $E_\mu^{-\alpha-1}$ .

The general solution can be obtained as the superposition of the low- and high-energy solutions:

$$\frac{\partial \mathcal{N}_\mu}{\partial X}(E_\mu, X) = KE_\mu^{-\alpha} \left( \frac{A(X)}{1 + \frac{B(X)E_\mu \cos \theta}{\varepsilon_\pi}} \right) \quad (11.35)$$

with  $A(X) = H_\pi^{le}(X)/X$  and  $A(X)/B(X) = H_\pi^{he}(X)/X$ .

The functional dependence on the atmospheric depth  $X$  it is not easy to obtain analytically also with the assumed simplifications on hadronic interactions. In general, the values assumed by  $H_\pi(X)$  are obtained from full Monte Carlo simulations, although some analytical approximations exist [see for instance Gaisser (1990)]. An equation similar to (11.35) holds for kaon decay.

The *differential muon intensity*  $\Phi_\mu(E_\mu)$  is normally given at sea level ( $X^{\text{sea}} = 1030 \text{ g cm}^{-2}$ ) and obtained by integration of (11.35) along the whole atmospheric depth. The units of  $\Phi_\mu(E_\mu)$  are  $\text{cm}^{-2}\text{s}^{-1}\text{sr}^{-1}\text{GeV}^{-1}$  as shown in (11.4). In Monte Carlo simulations, the muon energy loss in the atmosphere  $-dE_\mu/dX$  is also taken into account. The so-called atmospheric muon flux at sea level mimics Eq. (11.35) and holds for zenith angles  $\theta \lesssim 60^\circ$  including the contributions from decays of pions, kaons, and charmed mesons:

$$\Phi_\mu(E) = KE^{-\alpha} \left( \frac{A_\pi}{1 + \left( \frac{B_\pi E}{\varepsilon_\pi} \right) \cos \theta} + \frac{A_K}{1 + \left( \frac{B_K E}{\varepsilon_K} \right) \cos \theta} + \frac{A_c}{1 + \left( \frac{B_c E}{\varepsilon_c} \right) \cos \theta} \right). \quad (11.36)$$

The coefficients  $A_i$  with  $i = \pi, K, c$  depend on the ratio of muons produced by pions, kaons, and charmed hadrons. The  $A_i, B_i$  coefficients can be derived from Monte Carlo computations, numerical approximations or from experimental data. Usually, the term due to the charmed mesons can be neglected, because  $\varepsilon_c \gg \varepsilon_{\pi, K}$ .

Different estimates of the parameters that enter in (11.36) for the conventional atmospheric muons were published by several authors. For a review, see Lesparre et al. (2010). For the following, we will use the numbers reported in

Beringer et al. (2012) which assumes (11.36) to be valid when muon decays are negligible ( $E_\mu > 100/\cos\theta$  GeV) and when the curvature of the Earth can be neglected ( $\theta \lesssim 60^\circ$ ):

$$\begin{aligned} KA_\pi &= 0.14 \text{ cm}^{-2}\text{s}^{-1}\text{sr}^{-1}\text{GeV}^{-1} \\ A_K/A_\pi &= 0.054 ; B_\pi = B_K = 1.1 \end{aligned} \quad (11.37)$$

in addition to the already known values of  $\alpha = 2.7$  and  $\varepsilon_\pi = 115$  GeV,  $\varepsilon_K = 850$  GeV, as given in Table 11.2. The contribution from the decay of charmed hadrons is discussed below.

### 11.3.1 The Conventional Atmospheric Neutrino Flux

As indicated by Eq. (11.28), the production mechanisms of atmospheric muons and neutrinos are strongly correlated, see (Illana et al. 2011) for a recent review. However, due to the two-body kinematics, the energy spectra of the  $\mu$ 's and  $\nu_\mu$ 's from meson decays are different.<sup>1</sup> Let us consider for instance, the pion decay in the center of mass (c.m.) system ( $m_\pi = 139.6$  GeV;  $m_\mu = 105.7$  GeV). The c.m. muon energy is  $E_\mu^* = (m_\pi^2 + m_\mu^2)/2m_\pi = 109.8$  MeV. Similarly for the neutrino, considering that in the c.m. system  $E_\mu^* + E_\nu^* = m_\pi$ , one has:  $E_\nu^* = (m_\pi^2 - m_\mu^2)/2m_\pi = 29.8$  MeV. In the laboratory system, the energies are boosted by the Lorentz factor  $\Gamma = E_\pi/m_\pi c^2$ . In any case, muons carry a larger fraction of the meson energy than neutrinos. As consequence, the energy spectrum of atmospheric  $\nu_\mu$  is given by an equation similar to (11.36), with different coefficients  $A_i$ ,  $B_i$  in order to produce a distribution slightly shifted toward lower energies. This gives the so-called *conventional atmospheric neutrino flux*.

Additional  $\nu_\mu$  are produced by the in-flight decay of muons, together with a  $\nu_e$  and an electron/positron. Therefore, also the  $\nu_e$  flux depends on the decay chain of charged mesons and muons. As the muon decay probability in the atmosphere decreases with increasing  $E_\mu$ , the  $\nu_e$  spectrum is reduced with respect to that of  $\nu_\mu$  at high energy, see Sect. 11.7.

### 11.3.2 The Prompt Component in the Muon and Neutrino Flux

At sufficiently high energies, another muon (and neutrino) production mechanism is possible. The so-called *prompt* (or *direct*) atmospheric muons are produced in the semileptonic decays [see Sect. 8.11 of Braibant et al. (2012)] of charmed mesons, like  $D^\pm$ ,  $D^0$ , and baryons. As the lifetime of charmed particles is smaller than  $10^{-12}$  s

<sup>1</sup> In the following, when not explicitly stated, we use the symbol  $\nu_\mu$  or  $\nu_e$  to indicate both neutrinos and antineutrinos of the given flavor.

(*prompt decays*), prompt muons are produced before the parents lose energy in collisions and are, in general, highly energetic for kinematic reasons. Hence, for  $E_\mu < \varepsilon_c$ , the spectrum for the prompt flux more closely follows the CR spectrum ( $\Phi_{\text{prompt}} \propto E^{-\alpha}$ ) and is about one power harder than the *conventional* flux at high energy. Since the production cross-section of charmed mesons in proton–nucleon interactions is rather small,  $D$  decays contribute significantly only at very high energies. The prompt flux (both of muons and neutrinos) has not yet been measured, but is expected to be important above  $\sim 100$  TeV. As for the conventional flux, predictions for the prompt one are dependent upon uncertainties in the normalization and spectral distribution of the primary CR flux. Additional sources of uncertainty for the prompt muons and neutrinos include charm production cross-sections and fragmentation functions, which have not been measured at these energies in accelerator experiments.

## 11.4 The Particle Flux at Sea Level

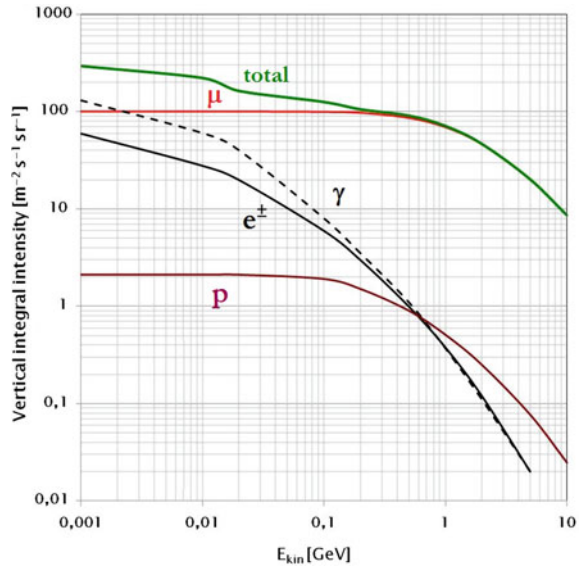
**Muons** are the dominant components of charged particles at sea level. As seen in the previous discussion, the bulk of the processes that yield muons are two-body decays with an associated  $\nu_\mu$  or  $\bar{\nu}_\mu$  to satisfy conservation laws. Below the few GeV energy range, the muon decay probability cannot be neglected. A 1 GeV muon has a Lorentz factor  $\Gamma = E_\mu/m_\mu c^2 \sim 10$  and has a mean decay length  $d_\mu = \Gamma \tau_\mu c \sim 6$  km. Since low-energy pions are typically produced at altitudes of 15 km and decay relatively fast (for  $\Gamma = 10$  the decay length is  $d_\pi \sim 78$  m, which is almost the same value as  $\lambda_{I_\pi}$ ), the daughter muons do not reach the sea level but rather decay themselves or are absorbed in the atmosphere.

The situation changes at higher energies. For 100 GeV pions ( $d_\pi \sim 5.6$  km, corresponding to a column density of  $160 \text{ g cm}^{-2}$  measured from the production altitude) the interaction probability starts to dominate over that of decay. Pions of these energies will therefore produce further tertiary pions in subsequent interactions, which will decay eventually into muons, typically of lower energy. Therefore, the muon spectrum at high energies is always steeper compared to the parent pion spectrum.

Resuming to the discussions of the previous sections, three different energy regions in the sea-level muon spectrum are distinguishable. The thresholds between different energy regimes are set by the values of the decay constants defined in Table 11.2:

- $E_\mu \leq \varepsilon_\mu \sim 1$  GeV. Muon decay and muon energy loss are important and must be taken into account. Only full Monte Carlo simulations give accurate predictions. The energy spectrum is almost flat, gradually reproducing the energy dependence of the primary CR spectrum above 10 GeV.
- $\varepsilon_\mu \leq E_\mu \leq \varepsilon_{\pi,K}$ . Above  $\sim 100$  GeV, the muon flux has the same power law of the parent mesons, and hence of the primary CRs. Below 100 GeV the effect of the muon energy loss in the atmosphere is still important, particularly approaching the horizontal direction.

**Fig. 11.2** Integral fluxes averaged over the 11 year solar cycles of  $\mu$ ,  $e$ ,  $p$  and photons (ph) arriving at geomagnetic latitudes  $\sim 40^\circ$  versus their kinetic energy. The lines include the contributions of both particles and antiparticles. From (Cecchini and Spurio 2012)



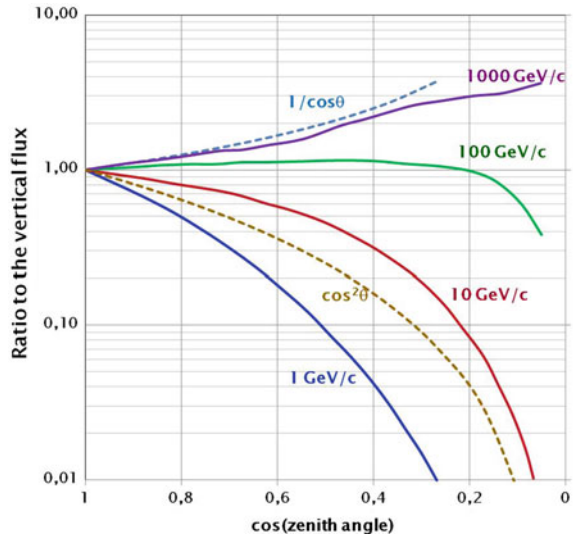
- $E_\mu \gg \varepsilon_{\pi,K}$ . The meson production spectrum has the same power law dependence as the primary CRs,  $\Phi_{\pi,K} \propto E^{-\alpha}$ , but the rate of their decay steepens by one power of  $E_\mu$  since the pion and kaon decay length  $d_{\pi,K} \propto 1/E$ . The thickness of the atmosphere is not large enough for most pions to decay, because of the high Lorentz factor.

Plots of the integral flux of muons arriving at geomagnetic latitudes  $\sim 40^\circ$  versus their kinetic energy are shown in Fig. 11.2. The muon intensity depends on the incoming direction, due to the  $\cos \theta$  dependence of (11.36). From the vertical direction and for  $E_\mu > 1 \text{ GeV}$ , the intensity corresponds to  $\sim 1$  particle per  $\text{cm}^2$  and per min:  $I_\nu(E_\mu > 1 \text{ GeV}) \sim 70 \text{ m}^{-2} \text{ s}^{-1} \text{ sr}^{-1}$  (Grieder 2010). The mean energy of muons at ground level is about 3-4 GeV (Beringer et al. 2012).

The muon intensity from the horizontal directions at low energies is naturally reduced because of muon decays and absorption effects in the thicker atmosphere at large zenith angles. At high energy, the parent particles of muons travel relatively long distances in rare parts of the atmosphere. As a consequence, their decay probability is increased compared to the interaction probability.

Figure 11.3 gives a quantitative description of this effect. Muons below the few GeV/c momentum range fade fairly quickly with increasing zenith angle, with a dependence  $\propto \cos^n \theta$ , with  $n \sim 2 \div 3$ . The flux of muons in the 100 GeV/c range is relatively flat up to  $\cos \theta \simeq 0.2$  and then quickly declines. At 1 TeV/c the flux monotonically increases with the zenith angle, approaching the  $1/\cos \theta$  dependence. The flux of TeV muons is particularly sensitive at large values of the zenith angle. When approaching the horizontal direction, a small difference in  $\cos \theta$  changes appreciably the thickness and the density profile of the atmosphere and the corresponding

**Fig. 11.3** Angular distribution of muons at ground level for different muon energies. The overall angular distribution of muons measured at sea level is  $\propto \cos^2 \theta$ , which is characteristic of muons with  $E_\mu \sim 3 \text{ GeV}$ . At high energies, the flux approaches the  $1/\cos \theta$  dependence as predicted by (11.36). The estimate of the angular distribution is based on a Monte Carlo simulations and accounts for the curvature of the Earth atmosphere



muon energy spectrum. For this reason, the measurements of almost horizontal muons are very difficult.

The **electromagnetic** component is made of electrons, positrons, and photons initiated by decays of neutral and charged mesons. At a variance from the case of the upper atmosphere, where the decay of neutral pions is the dominant component, muon decay  $\mu \rightarrow e\nu_e\nu_\mu$  is the dominant source of low-energy electrons at sea level. The integral vertical intensity of electrons plus positrons is very approximately 30, 6, and  $0.2 \text{ m}^{-2}\text{s}^{-1}\text{sr}^{-1}$  above 10, 100, and 1000 MeV, respectively (Grieder 2010). The exact numbers depend sensitively on altitude, on the solar epoch of the measurement and on geomagnetic latitude. Figure 11.2 shows the integral fluxes of the electromagnetic component (lines with label  $e^\pm$  for  $e^+$ ,  $e^-$  and  $\gamma$  for the photons). Because we include here secondary particles produced by sub-GeV primary CRs, the fluxes are averaged over the 11-year solar cycles. The angular dependence is complex because of the different altitude dependence of the muons decaying into electrons and the other different electron sources.

The **hadronic component** is made mainly of nucleons. The presence of other long lived hadrons, as the charged pions, is relatively small,  $O(10^{-2})$  with respect to the nucleons, as derived in Sect. 11.2. The contributions of other hadrons can be neglected. Nucleons with momentum  $>1 \text{ GeV}/c$  at ground level are degraded remnants of the primary cosmic radiation. The intensity is approximately given by (11.9) for  $\theta \lesssim 60^\circ$ . At sea level, about 1/3 of the nucleons in the vertical direction are neutrons (neutrons are about  $\sim 10\%$  at the top of the atmosphere). The integral intensity of vertical protons above  $1 \text{ GeV}/c$  at sea level is  $\sim 0.6 \text{ m}^{-2}\text{s}^{-1}\text{sr}^{-1}$  at the geomagnetic location of about  $40^\circ$  (see Fig. 11.2).



## 11.5 Measurements of Muons at Sea Level

The measurements of muons at ground level offer the advantage of a high stability, large collecting factor, and long exposure time due to relatively favorable experimental conditions. Sea level data offer the possibility to perform a robust check of the reliability of existing Monte Carlo codes.

Many of the experiments devoted to the measurement of the muon momentum spectra and intensity (vertical and inclined directions) have been carried out since the 1970s. Recently new instruments, mainly spectrometers designed for balloon experiments or used primarily in CERN LEP and LHC experiments and used also for CR studies, have added new valuable information.

The vertical muon intensity at sea level is a quantity that varies with the geomagnetic latitude, altitude, solar activity, and atmospheric conditions. The 11-year solar cycle modulates the CR flux up to energies of about 20 GeV. When comparing muon observations at such low energies, it is important to know the year and location where the measurements were made (Cecchini and Spurio 2012).

The *geomagnetic field* tends to prevent low-energy CRs from penetrating through the magnetosphere down to the Earth's atmosphere, Sect. 2.9. Primary nuclei having rigidity lower than the cutoff (2.31) are deflected by the action of the geomagnetic field and do not produce muons. The geomagnetic effects are important for sea level muons up to about  $E_\mu \sim 5$  GeV.

Different experimental methods have been used to measure the muon flux and energy spectrum. Muon telescopes are made of several planar detectors arranged horizontally parallel to each other. They are interlaid by one or more layers of absorbing material. In some experiments, the detector and absorber are in a rigid construction which could be rotated in zenith and azimuth, allowing the selection of muons from a given direction of the celestial hemisphere. The quantity of material (in  $\text{g cm}^{-2}$ ) crossed by muons in such a telescope is approximately constant and it sets the muon energy threshold.

Multidirectional muon telescopes generally consist of at least two layers of segmented muon detectors. The coincidence of signals between two counters in the upper and bottom layers determines the arrival direction of muons. The quantity of material crossed by the particle in such detectors increases with increasing zenith angle, so the threshold energy for multidirectional muon telescopes depends on  $\theta$ .

The muon energy spectrum has been extensively measured, mainly by iron magnet spectrometers. For these detectors, multiple scattering plays an important role in the momentum resolution, particularly at low energies. Recently, measurements have been performed using low-mass superconducting magnet spectrometers designed as a balloon-borne apparatus for cosmic ray studies, as for instance in the BESS experiment (Sect. 3.3).

The atmospheric muon flux and energy spectrum was also measured using the precise muon spectrometer of the L3 detector which was located at the LEP collider at CERN. This apparatus collected muons  $\sim 30$  m below a stratified rock overburden,

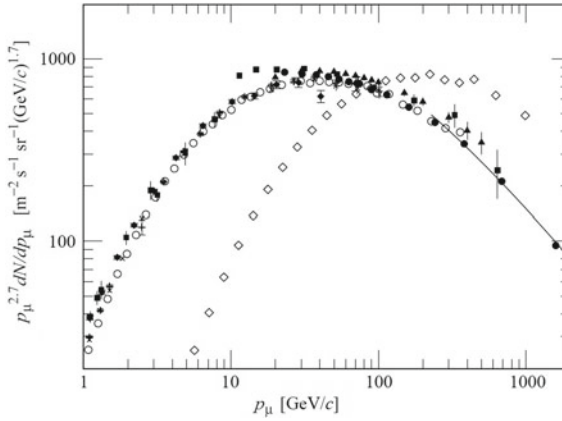


**Fig. 11.4** Differential muon intensity  $p_\mu^{2.7} dN_\mu/dE_\mu$  at sea level. The ordinate values have been multiplied by  $p_\mu^{2.7}$  in order to compress the plot and to emphasize the differences. In this energy range,  $p_\mu \simeq E_\mu$ . All data points correspond to the vertical ( $\theta = 0^\circ$ ), with the exception of the set with the symbol ( $\diamond$ ) corresponding to  $\theta = 75^\circ$ . The line for  $E_\mu > 200$  MeV shows the result from Eq. (11.36) for the vertical direction. From Beringer et al. (2012) and references therein

and with dimensions much larger than previous experiments (the volume of the 0.5 T magnetic field region was  $\sim 1000 \text{ m}^3$ ). Finally, information about the muon flux with momenta larger than few TeV have been extracted from underground measurements, see Sect. 11.6. A comprehensive review of various types of particle detectors used for muon detection at sea level can be found in (Dorman 2004).

The compilation of measurements of the momentum of vertical muons are presented in Fig. 11.4. The agreement between measurements is relatively good and the largest contribution to the deviations is the systematic error due to incorrect knowledge of the acceptance, efficiency of the counters, and corrections for multiple scattering. Measurements of the muon momentum spectra for  $p_\mu < 1$  TeV/c are particularly important for the comparison of nuclear cascade models with available data.

## 11.6 Underground Muons

Underground measurements offer the possibility to extend the energy range of the muon spectrum beyond 1 TeV. Deep underground detectors normally have large collecting areas and are not subject to the time restrictions of balloon experiments, hence they can measure the muon flux over long periods. The penetrating component of CRs underground depends on a complex convolution of different physics processes, such as muon production mechanisms and muon energy losses. Particularly important is the knowledge of the composition and of the thickness of the material overburden above the detector.

### 11.6.1 The Depth–Intensity Relation

The muon spectrum at energies above few TeV is deduced by underground measurements. The procedure used for this *indirect* measurement of the sea-level energy spectrum passes through the determination of the so-called *depth–intensity relation*  $I_\mu^0(h)$ . This quantity represents the muon intensity in the vertical direction as a function of the depth  $h$ . The number of muons reaching the depth  $h$  depends on their energy distribution at surface.  $I_\mu^0(h)$  is related with the muon intensity  $\Phi_\mu(E) = \frac{d^2\varphi_\mu}{dE_\mu d\Omega}$  at the surface. The relation between the measured function  $I_\mu^0(h)$  and the differential sea-level muon spectrum is expressed as:

$$I_\mu^0(h) = \int_0^\infty \frac{d^2\varphi_\mu}{dE_\mu d\Omega} \cdot P(E_\mu, h) dE_\mu \quad (11.38)$$

Here,  $P(E_\mu, h)$  is the muon survival function. It represents the probability that muons of energy  $E_\mu$  at the surface reach a given depth  $h$ , and is usually determined via Monte Carlo calculations. Assuming (11.36), from (11.38) it is possible to unfold the sea level muon spectrum from the measured vertical muon intensity (Cecchini and Spurio 2012).

As underground detectors are at a fixed depth, in principle only one point can be obtained. However, when measuring the muon intensity  $I_\mu(h, \theta)$  at different zenith angle  $\theta$ , the quantity of rock (or water) overburden changes. At high energy ( $E_\mu > 1$  TeV) and for  $\theta \lesssim 60^\circ$ , Eq. (11.36) provides a simple relationship between  $I_\mu^0(h)$  and  $I_\mu(h, \theta)$ :

$$I_\mu(h, \theta) = I_\mu^0(h) / \cos \theta . \quad (11.39)$$

Using this expression, measurements of the muon intensity at different values of  $\theta$  can be translated into an estimate of the vertical flux. Figure 11.5 shows the vertical muon intensity as a function of depth as measured by underground experiments. The figure shows also the contribution from neutrino-induced muons for depths larger than  $\sim 12$  km.w.e. Assuming a threshold energy of 2 GeV, the flux of  $\nu_\mu$  induced upgoing events is  $\sim 2 \times 10^{-13} \text{ cm}^{-2} \text{ s}^{-1} \text{ sr}^{-1}$ .

### 11.6.2 Characteristics of Underground/Underwater Muons

Figure 11.6 shows a multiple muon event detected by the MACRO experiment, Sect. 11.9.3. Multiple events are closely packed bundles of parallel muons, usually of high energy, originating from the same primary CR. These muons are expected to arrive almost at the same time in the plane perpendicular to the shower axis. MultimMuon events have been used to explore the properties of very high-energy

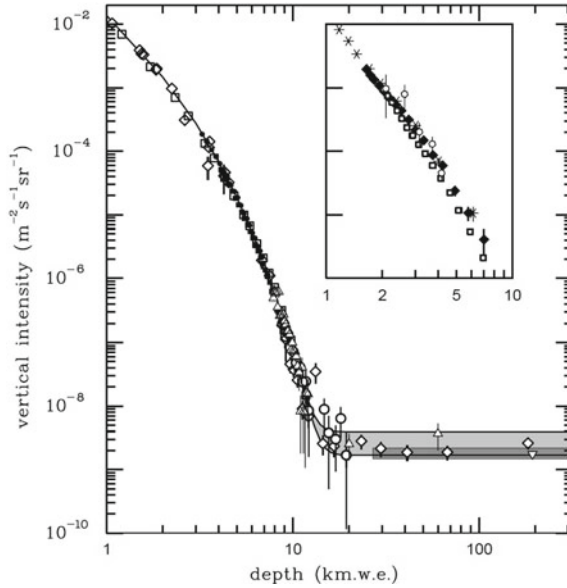


**Fig. 11.5** Vertical muon intensity versus depth. The quantity on the  $x$ -axis is the depth, expressed in km of water equivalent:  $1 \text{ km.w.e.} = 10^5 \text{ g cm}^{-2}$  of standard rock. The shaded area at large depths represents neutrino-induced muons of energy  $> 2 \text{ GeV}$ . The inset shows the vertical intensity curve measured under water and ice from neutrino telescopes (Chap. 10). From Beringer et al. (2012)

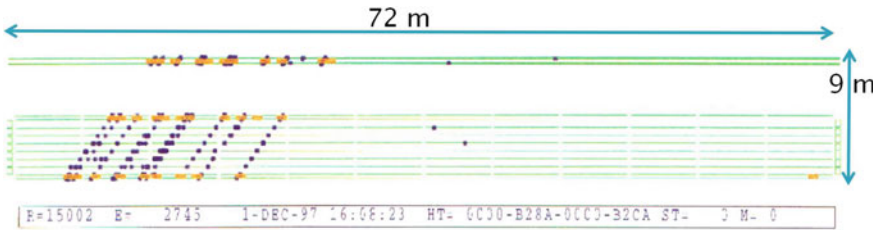


**Fig. 11.6** A bundle of muons seen in the MACRO experiment, at a depth of  $\sim 3500 \text{ m.w.e.}$  10 different tracks are identified

hadronic interactions and to study the longitudinal development of showers. The multiplicity of produced secondary particles increases with the energy of the initiating particle. The muon multiplicity is observable which is also correlated with the mass of the primary CR: at a given total energy, heavier nuclei produce more muons than a primary proton.

The interaction vertex of the particles which initiate the air showers is typically at an atmospheric altitude of 15 km. Since secondary particles in hadronic cascades have small transverse momenta  $p_t$  ( $\sim 300 \text{ MeV}/c$ ), high-energy muons are essentially collimated near the shower axis. Considering a primary nucleon producing mesons of

energy  $E_{\pi,K}$  with transverse momentum  $p_t$  at a height  $H_{\text{prod}}$ , the average separation of their daughter high-energy muons from the shower axis is given by

$$r \simeq \frac{p_t}{E_{\pi,K}} H_{\text{prod}} \quad (11.40)$$

For primary energies around  $10^{14}$  eV, lateral displacements of energetic muons ( $\sim 1$  TeV) of several meters are typically obtained underground. Displacements are almost exclusively caused by transferred transverse momenta in hadronic processes. Typical multiple scattering angles for muon energies around 100 GeV in thick layers of rock (50–100 m) are of the order of a few mrad.

The full characteristics of atmospheric muon bundles are particularly important for neutrino telescopes (Chap. 10) and other underground detectors. In fact, atmospheric muons usually represent the most abundant signal and can be used to calibrate the detectors and to check their expected response to charged particles. On the other side, atmospheric muons represent a dangerous background source. In neutrino telescopes, for instance, they can mimic high-energy neutrino interactions. The main features of muons reaching underground detectors can be reproduced with a full Monte Carlo simulation of atmospheric showers or with parametric formulae (Becherini et al. 2006). These parameterizations allow to evaluate not only the total muon flux, but also the total number of muon bundles in deep detectors starting from the primary CR flux, CR composition, and interaction model which reproduces the MACRO data.

## 11.7 Atmospheric Neutrinos

Starting from the 1980s, the search for proton decay, *Extras #7*, was the main reason for developing underground laboratories and large detectors. The simplest GUT model, SU(5), predicts a proton lifetime value of  $\tau_p \sim 10^{30}$  years for the process  $p \rightarrow e^+\pi^0$ . From the experimental point of view, the prediction corresponds to many proton decay events in a kiloton-scale detector. The atmospheric neutrinos represented the irreducible background, Fig. 11.7. The experiments started to measure the fluxes of  $\Phi_{\nu_\mu}$ ,  $\Phi_{\nu_e}$  in the GeV range and their theoretical estimate became a fundamental aspect in astroparticle physics.

The detailed calculation of the atmospheric neutrino fluxes is a nontrivial problem. It requires a description of the primary CRs and a model of hadronic interactions to compute the multiplicity, energy, and angular distributions of the final-state particles. The measurements of the atmospheric muons described in the previous sections help to constrain the neutrino estimates. Usually, a Monte Carlo is used to follow the shower development taking into account all relevant processes, like the energy losses of charged particles, the competition between interaction and decay for unstable hadrons, and the weak decays of mesons and muons, see (Gaisser and Honda 2002) for a review.

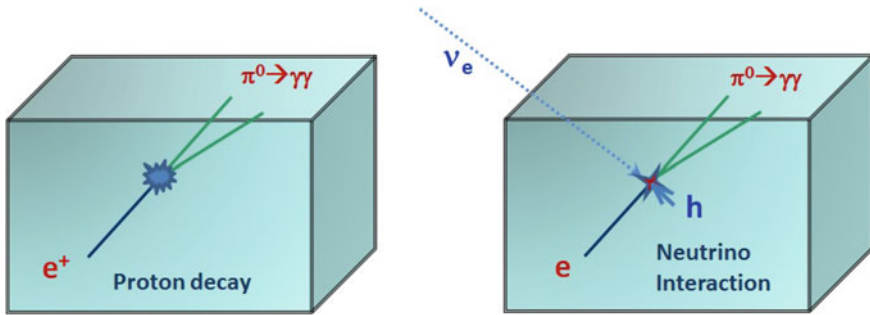


**Fig. 11.7** Example of the expected signal (*left*) for the decay mode  $p \rightarrow e^+\pi^0$  in a water Cherenkov detector or in a fine-grained calorimeter. Some interactions due to atmospheric neutrinos (*right*) are almost indistinguishable from the signal. The remaining hadronic system  $h$  could not emit Cherenkov radiation or could remain confined in the passive sectors of tracking experiments

The uncertainties in the calculation of atmospheric neutrino fluxes differ between high and low energies. In most cases, neutrinos of a given energy  $E_\nu$  are produced by primary CRs of energy at least a factor of 10 larger. For  $E_\nu \sim 1$  GeV, the primary fluxes of CR components are relatively well known. On the other hand, the low-energy CR flux is modulated by solar activity and affected by the geomagnetic field. As a consequence, the flux of low-energy neutrinos is higher for detectors located near the poles than for those near the equator. At higher energies ( $E_\nu > 100$  GeV), solar activity and the rigidity cutoff do not affect the primary CRs, but larger uncertainties exist on the primary flux, in particular on the chemical composition.

Independently from the details of the computation of  $\Phi_{\nu_\mu}(E)$ ,  $\Phi_{\nu_e}(E)$ , one can obtain two fundamental and very robust properties:

- At energies below few GeV, the flux of  $\nu_\mu$  is approximately twice as large as the flux of  $\nu_e$ , i.e.,  $\Phi_{\nu_\mu} \simeq 2\Phi_{\nu_e}$
- The fluxes of all neutrino species are up-down symmetric in the zenith angle  $\theta$ , i.e.,  $\Phi_{\nu_\alpha}(E_\nu, \theta) = \Phi_{\nu_\alpha}(E_\nu, \pi - \theta)$

These assumptions are valid if neutrinos do not change flavor during propagation from the production point to the detector. The condition  $\Phi_{\nu_\mu}(E)/\Phi_{\nu_e}(E) \simeq 2$  is a simple consequence of (11.28): after the completion of the chain decay, for each  $\pi^+$  there is one  $\nu_\mu$ , one  $\bar{\nu}_\mu$ , and one  $\nu_e$  (and the charge conjugates for the  $\pi^-$ ) that have approximately the same average energy, Fig. 11.8a). The ratio increases at high energy ( $E_\nu \gtrsim 3$  GeV for vertical neutrinos) when, because of relativistic effects, the muon decay length becomes longer than the thickness of the atmosphere, and muons reach ground level dissipating their energy by ionization without decaying. The prediction of the up-down symmetry is even more robust, and is a consequence of the (quasi-exact) spherical symmetry of the Earth and the isotropy of the primary CR flux, see Fig. 11.8b).

A remarkably physical effect, originally predicted by Bruno Pontecorvo (Pontecorvo 1968) is that of *neutrino flavor oscillations*. It is a quantum-mechanical

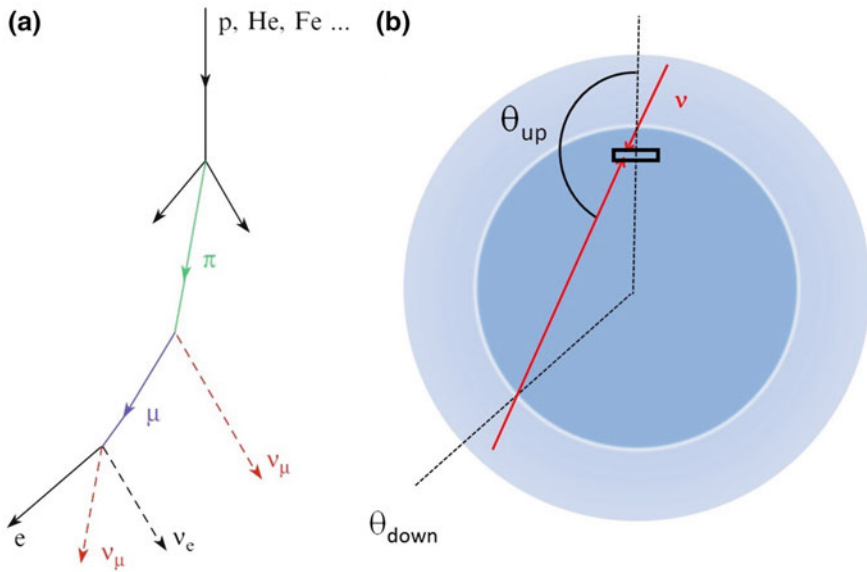


**Fig. 11.8** Right CR chain for atmospheric neutrino production. The neutrinos originate from an atmospheric layer of  $(10 \div 20)$  km thickness. Left up/down symmetry for atmospheric neutrinos

phenomenon connected with non-null neutrino masses. Both the above predictions for the atmospheric neutrino fluxes offer a gold-plated method to study flavor oscillations. As the Earth does not absorb neutrinos with energies below tens of TeV (see Sect. 10.5), the path lengths for upgoing and downgoing neutrinos are very different (by a factor up to  $10^3$  in the vertical direction). In the presence of oscillations, one expects that the  $\nu_\mu, \nu_e$  fluxes be modified in different ways. Therefore, if oscillations occur, the up-down symmetry will be broken and the effect can be easily observed measuring a difference in the rates of upgoing and downgoing events of different flavors.

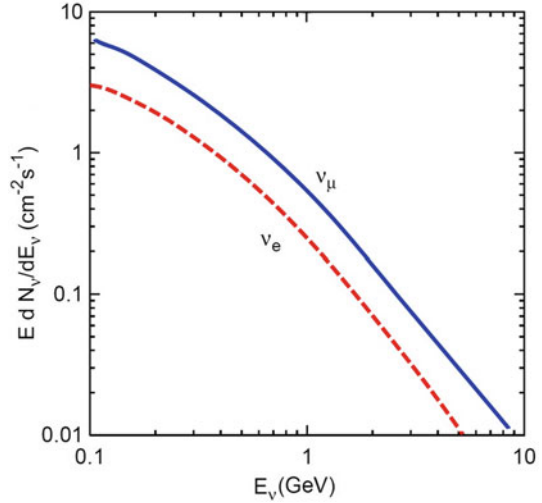
### 11.7.1 Early Experiments

Underground experiments of the kton scale, ready in the 1980s for searches of proton decay, started to measure atmospheric  $\nu_\mu$  and  $\nu_e$  charged current interactions. Two detection techniques were essentially utilized: tracking iron calorimeters with a segmentation of the order of 1 cm (such as Frejus, NUSEX and Soudan 2) and water Cherenkov detectors, such as Kamiokande and IMB. The flavor (electron or muon) of the charged lepton was identified through the different behavior of these two particles in the detector.

The expected event rate of atmospheric neutrinos can be obtained from the flux computed via Monte Carlo by different groups (Barr et al. 2004; Honda et al. 2007),



**Fig. 11.9** Integral flux of atmospheric neutrinos ( $= \nu + \bar{\nu}$ ) as a function of the threshold energy  $E_\nu$  up to  $\sim 10$  GeV. The flux is integrated over the whole solid angle. The  $\nu_\mu$  flavor (blue line) is about a factor of two higher than the  $\nu_e$  in the whole energy range. This computation is from the Bartol group (Barr et al. 2004)



as in Fig. 11.9. With a threshold of about 1 GeV (relevant for background evaluation in proton decay searches), the  $\Phi_{\nu_\mu} (>1 \text{ GeV})$  flux is  $\sim 0.65 \text{ cm}^{-2} \text{ s}^{-1}$ , and that of  $\Phi_{\nu_e} (>1 \text{ GeV})$  a factor of two lower. The neutrino must interact inside the detector to produce a visible event. The event rate for  $T = 1 \text{ y}$  and for the flavor  $i = \mu, e$  is given by

$$N_{\nu_i} = \Phi_{\nu_i}(>1\text{GeV}) \cdot \sigma_\nu \cdot N_T \cdot T \quad (11.41)$$

where  $\sigma_\nu = \sigma_0 E_\nu$  is the neutrino cross-section. After averaging over  $\nu$  and  $\bar{\nu}$ , we have  $\sigma_0 = 0.5(0.667 + 0.334) \cdot 10^{-38} = 0.5 \cdot 10^{-38} \text{ cm}^2/\text{GeV}$  [see Chap. 10 of Braibant et al. (2012)].  $N_T = 6 \times 10^{32}$  nucleons/ton is the number of target nucleons in 1 ton of material,  $T = 3.15 \cdot 10^7 \text{ s}$  is the number of seconds in 1 year. Thus, inserting the numerical values, we obtain

$$N_{\nu_\mu} = 66 \text{ kton/y} \quad ; \quad N_{\nu_e} = 34 \text{ kton/y} \quad (11.42)$$

As a first estimate, the total number of contained events is  $\sim 100$  events/(kton y).

The results of all the quoted experiments measuring atmospheric neutrinos were expressed in terms of the double ratio  $R' = R_{obs}/R_{MC}$  where  $R_{obs} = (N_{\nu_\mu}/N_{\nu_e})_{obs}$  is the ratio of observed contained  $\mu$  and  $e$  events and  $R_{MC} = (N_{\nu_\mu}/N_{\nu_e})_{MC}$  is the same ratio for Monte Carlo (MC) events. The  $R'$  double ratios from IMB and Kamiokande were smaller than expectations and pointed out to a deficit of  $\nu_\mu$ , while the NUSEX and Frejus  $R'$  agreed with expectations. See (Koshiba 1992) for a review.

The IMB and Kamiokande deficit of muon-like events was the first indication for atmospheric neutrino oscillations, discussed in the next section.

## 11.8 Oscillations of Atmospheric Neutrinos

The Standard Model of the microcosm includes three flavors of massless and left-handed neutrinos, denoted as  $\nu_e, \nu_\mu, \nu_\tau$ . Three degenerate massless particles are surprising and cannot explain the difference amongst themselves and the reason for the separate  $L_e, L_\mu, L_\tau$  lepton number conservation.

If the neutrinos have non-null and nondegenerate masses, neutrino mixing and oscillations as suggested by Pontecorvo can be formally treated in the same manner as for the quark sector [Chap. 12 of Braibant et al. (2012)]. The  $\nu_e, \nu_\mu, \nu_\tau$  states are defined as *weak flavor eigen states* which must be considered in particle decays (for example, in  $\pi^+ \rightarrow \mu^+ \nu_\mu$ ) and in particle interactions (e.g.,  $\nu_\mu n \rightarrow \mu^- p$ ). As far as the neutrino propagation is concerned, we shall consider the *mass eigenstates* denoted as  $\nu_1, \nu_2, \nu_3$ . It is thus not correct to speak of the  $\nu_\mu$  or of the  $\nu_e$  masses. According to quantum mechanics, the flavor eigen states,  $|v_f\rangle$  ( $f = e, \mu, \tau$ ), are linear combinations of the mass eigen states  $|v_j\rangle$  ( $j = 1, 2, 3$ ):

$$|v_f(t)\rangle = \sum_j U_{fj} |v_j(t)\rangle. \quad (11.43)$$

In vacuum, the mass eigen states  $|v_j\rangle$  propagate independently, that is,

$$|v_j(t)\rangle = e^{-E_j t} |v_j(0)\rangle. \quad (11.44)$$

For a given momentum, the eigen states  $|v_j\rangle$  propagate with different frequencies: in (11.44), the energies  $E_j = \sqrt{p^2 + m_j^2}$  (in natural units with  $c = 1$ ) of the mass eigen states are slightly different for  $\nu_1, \nu_2, \nu_3$  for nondegenerate massive neutrinos.

We will return on the full mixing formula (11.43) on Sect. 12.6. The first indications of neutrino oscillations from atmospheric neutrinos were discussed in terms of the simple approximation of only two neutrino flavors, for example, the pair  $\nu_\mu, \nu_\tau$ . Each state is a linear combination of the two mass eigen states, e.g.,  $\nu_2, \nu_3$ . The flavor and mass eigen states are related by a unitary transformation with one mixing angle  $\vartheta$ :

$$\begin{pmatrix} \nu_\mu \\ \nu_\tau \end{pmatrix} = \begin{pmatrix} \cos \vartheta & \sin \vartheta \\ -\sin \vartheta & \cos \vartheta \end{pmatrix} \begin{pmatrix} \nu_2 \\ \nu_3 \end{pmatrix}. \quad (11.45)$$

Using a simple algebra [see Sect. 12.6 of Braibant et al. (2012)] it is possible to evaluate the probability  $P(\nu_\mu \rightarrow \nu_\mu) \equiv |\langle \nu_\mu(t) | \nu_\mu(t) \rangle|$  that the  $\nu_\mu$  originated at  $t = 0$  remains a  $\nu_\mu$  at a given time  $t$ . On the other hand, the probability that the  $\nu_\mu$  transforms itself into a  $\nu_\tau$  is  $P(\nu_\mu \rightarrow \nu_\tau)$ . These two probabilities are

$$\begin{cases} P(\nu_\mu \rightarrow \nu_\mu) = 1 - \sin^2 2\vartheta \cdot \left[ \sin^2 \left( \frac{E_3 - E_2}{2} t \right) \right] = 1 - \sin^2 2\vartheta \cdot \sin^2 \left( \pi \frac{L}{L_{\text{osc}}} \right) \\ P(\nu_\mu \rightarrow \nu_\tau) = 1 - P(\nu_\mu \rightarrow \nu_\mu) = \sin^2 2\vartheta \cdot \sin^2 \left( \pi \frac{L}{L_{\text{osc}}} \right) \end{cases} \quad (11.46)$$

where

$$L_{\text{osc}} = \frac{4\pi p}{\Delta m^2} \simeq \frac{4\pi E}{\Delta m^2} = 2.48 \frac{E[\text{GeV}]}{\Delta m^2[\text{eV}]^2} [\text{km}] \quad (11.47)$$

is the *neutrino oscillation length*,  $\Delta m^2$  is expressed in  $\text{eV}^2$ ,  $L \simeq ct$  is the distance (in km) between the  $\nu_\mu$  production and the  $\nu_\mu$  (or equivalently the  $\nu_\tau$ ) observation points; the neutrino energy  $E$  is expressed in GeV. The factor 2.48 results from this choice of units. Thus in (11.46):

$$\left( \pi \frac{L}{L_{\text{osc}}} \right) = \left( 1.27 \frac{\Delta m^2[\text{eV}]^2 L[\text{km}]}{E[\text{GeV}]} \right). \quad (11.48)$$

To observe the largest  $\nu_\mu$  disappearance (or  $\nu_\tau$  appearance), the argument of the sine function must be equal to  $\pi/2$ . For  $E \simeq 1$  GeV,  $\Delta m \simeq 0.05$  eV, the distance between the observer and the neutrino production point must be  $L \simeq 10^3$  km. There are no theoretical estimates for  $\vartheta$ .

## 11.9 Measurement of Atmospheric $\nu_\mu$ Oscillations in Underground Experiments

In 1998, Super-Kamiokande (SK) (Fukuda et al. 1998), MACRO (Ambrosio et al. 1998), and Soudan 2 (Sanchez et al. 2003) in the same conference session in Japan presented new results with definitive indications for atmospheric neutrino oscillations. In all experiments, the zenith angle distributions of the  $\mu$ -like events (i.e., attributed to  $\nu_\mu$  charged current interactions) showed a clear deficit compared to the no-oscillation expectation. The number of  $e$ -like events (those induced by CC  $\nu_e$ ) was roughly in agreement with the prediction. None of the experimental techniques used by the detectors is able to measure the charge of the final-state leptons, and therefore, neutrino and antineutrino induced events cannot be discriminated (Kajita 2012).

### 11.9.1 Event Topologies in Super-Kamiokande

The Super-Kamiokande (SK) detector consists of a stainless steel tank filled with 50,000 tons of ultrapure water, Fig. 11.10. The construction started in 1991, the observation began on 1996. The detector is divided into two regions; in the inner region, 11,200 photomultipliers (PMTs), 20 inches (50.8 cm) in diameter, detect faint flashes of light produced by the Cherenkov effect from charged particles passing through. The external region offers a shielded volume for atmospheric muons and it is used for anticoincidence. SK is located 1000m underground in the Kamioka mine in Japan. Here, the flux of atmospheric muons is reduced by a factor of  $\sim 10^5$

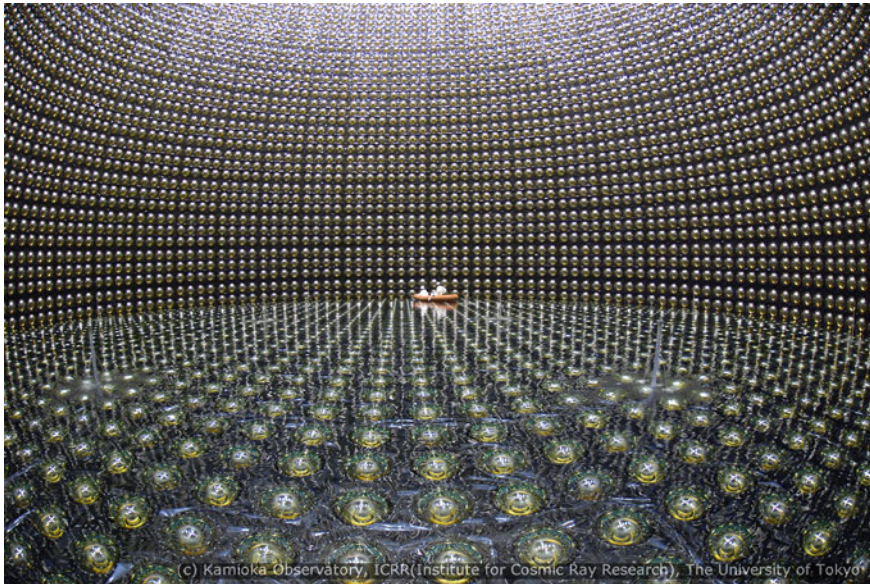


**Fig. 11.10** The Super-Kamiokande detector during the construction phase. The water tank is 39 m in diameter and 42 m tall. In the inner detector, the 20 inches PMTs are placed at intervals of 70 cm, covering more than 40% of the *cylinder* surface. The picture was taken during the water filling phase. *Credit* Kamioka Observatory, ICRR (Institute for Cosmic Ray Research), The University of Tokyo (<http://www-sk.icrr.u-tokyo.ac.jp/index-e.html>)

with respect to the one at sea level. The experiment also measures solar neutrinos (Sect. 12.3). In 2001, an accident destroyed more than half of the PMTs, ending SK-I phase (Apr. 1996–Jul. 2001). SK-II (Dec. 2002–Oct. 2005) came back into operation using about 5000 PMTs, with a slightly lower energy resolution. The full detector was restored for SK-III phase, from Jul. 2006 to Aug. 2008. SK-IV started in Sep. 2008 and is still taking data.

The flavor assignment and the energy estimate of the incoming neutrino plays a crucial role in this experiment. The flavor identification of the neutrino occurs through pattern recognition of the event. The range of muons in water corresponds to about 5 m per GeV of energy. Muons lose energy continuously and emit Cherenkov light until they reach the critical velocity, near the end of their range. This results in a “ring” of Cherenkov light at the surface of the detector. From the shape and “brightness” of the ring, it is possible to determine the neutrino interaction vertex and the muon direction and energy. On the other hand, electrons in water undergo bremsstrahlung and originate an electromagnetic shower, so that their energy is dissipated in the ionization of several  $e^+$ ,  $e^-$  particles. Each secondary particle generates a Cherenkov ring that overlaps in a single visible ring that is more “fuzzy” than that produced by muons, because low-energy electrons suffer considerable multiple Coulomb scattering in water. The difference between the sharp ( $\mu$ -like) and fuzzy ( $e$ -like) rings allows to determine the flavor of the charged lepton (see Fig. 11.11).

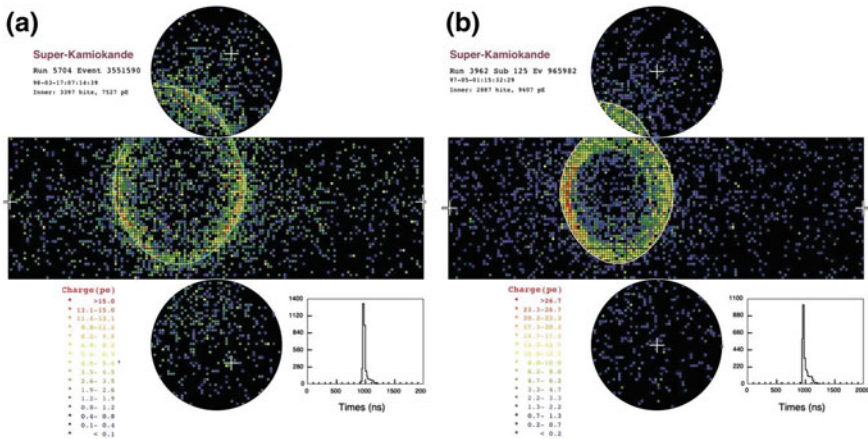


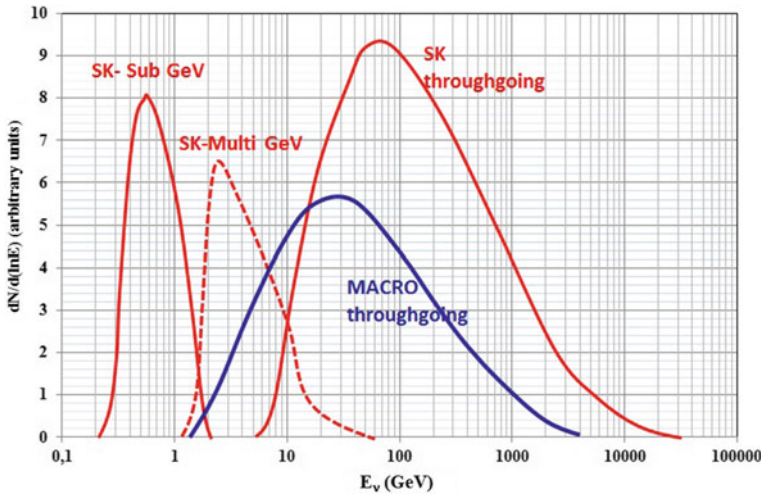
**Fig. 11.11** Event displays of two events in SK-I. Shown are unrolled views of a single-ring electron-like event (a) and a single-ring muon-like event (b). Colored points indicate the number of detected photoelectrons in each photomultiplier tube. Credit Kamioka Observatory, ICRR (Institute for Cosmic Ray Research), The University of Tokyo

The neutrino energy estimate is done through the classification of the events in different *event topologies*: fully contained (FC) events, partially contained (PC) events, and upward-going muons. The FC events are required to have no activity in the outer detector (veto). The neutrino interaction vertex for FC and PC events is required to be reconstructed within the *fiducial volume*, a region 2 m away from the detector walls with a *fiducial mass* of 22.5 ktons. The FC events are classified into “sub-GeV” (visible energy,  $E_{\text{vis}} < 1.33$  GeV) and “multi-GeV” ( $E_{\text{vis}} > 1.33$  GeV). These events are further separated into subsamples based on the number of observed Cherenkov rings. Single-ring events have only one charged lepton which radiates Cherenkov light in the final state, and particle identification ( $e^-$  or  $\mu^-$ -like) is particularly clean for single-ring FC events. All the PC events were assumed to be  $\mu^-$ -like: in simulated events, the PC events comprise a 98% pure charged current  $\nu_\mu$  sample.

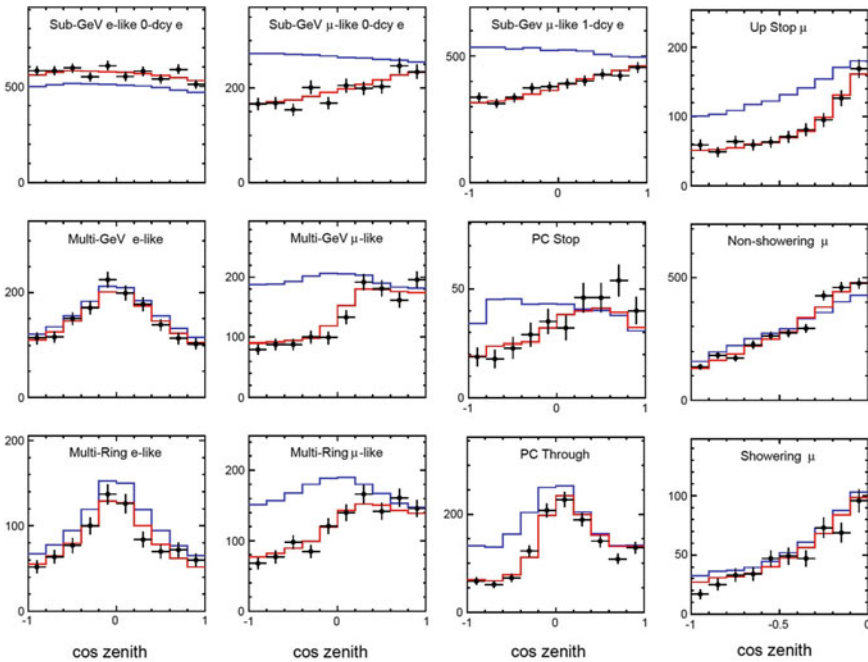
In addition to FC and PC events, higher energy neutrino events are observed as upward-going muons. Upward-going muons are classified into “upward throughgoing muons” if they pass through the detector, or into “upward stopping muons” if they come into and stop inside the detector. The upward throughgoing muons are further subdivided into “showering” and “nonshowering” based on whether their Cherenkov pattern is consistent with light emitted from an electromagnetic shower produced by a muon exceeding one TeV. The energy distributions of the parent neutrinos for different event topologies are shown in Fig. 11.12.

Figure 11.13 shows the zenith angle distributions of  $e^-$ -like and  $\mu^-$ -like events from SK for 12 different event topologies (Takeuchi 2012). The value  $\cos\theta = 1$  corresponds to the downward direction, while  $\cos\theta = -1$  corresponds to the upward direction. The three panels in first column show FC  $e^-$ -like events while the corresponding events classified as  $\mu^-$ -like are shown in the second. The third column shows





**Fig. 11.12** Event rates as a function of neutrino energy for sub-GeV, multi-GeV, and through going muons in Super-Kamiokande and for up throughgoing muons in MACRO



**Fig. 11.13** Zenith angle distributions observed in SK-I+II+III (2806 days livetime). The panels in the first column show three topologies of  $e$ -like events, the remaining are  $\mu$ -like.  $\cos \theta < 0$  ( $> 0$ ) are vertical upward (*downward*)-going events. The *black* markers represent the data points; the *blue* histograms show the Monte Carlo prediction without neutrino oscillations. The *red* histograms show the best fit for  $\nu_\mu \rightleftharpoons \nu_\tau$  using the best-fit parameters ( $\Delta m^2 = 2.11 \times 10^{-3} \text{ eV}^2$  and  $\sin^2 2\theta = 1$ ). The last column shows upgoing events induced by higher energy  $\nu_\mu$ . *Credit* Kamioka Observatory, ICRR (Institute for Cosmic Ray Research), The University of Tokyo

the zenith distributions for two topologies of PC events. The fourth column shows event topologies measured only for upward-going events. These latter topologies are due to  $\mu$ -like events. The average energy of parent neutrinos increases from top to bottom, namely as: sub-GeV < multi-GeV  $\sim$  Multi-Ring < Up Stop  $\sim$  PC stop < PC through < non showering < showering. With the exclusion of sub-GeV events, the final-state leptons have good directional correlation with the parent neutrinos.

The results of SK are shown in Fig. 11.13 together with the corresponding Monte Carlo expectations (blue histograms) (Honda et al. 2007). Several aspects appear clearly from an inspection of the figure, in particular the fact that the zenith angle distribution of the FC and PC  $\mu$ -like events shows a strong deviation from the expectation. The most spectacular effect is the 50% reduction of the detected upgoing events ( $\cos\theta < 0$ ) of the multi-GeV and of the Multi-Ring  $\mu$ -like events. Deviations from expectations are almost nonvisible in the highest energy topologies in the last column. On the other hand, the zenith angle distributions of the  $e$ -like events are consistent with the expectation and exhibit the predicted up-down symmetry.

These characteristic features may be interpreted assuming  $\nu_\mu \rightleftharpoons \nu_\tau$  oscillations. The oscillation probability (11.46) depends on the neutrino energy and path length  $L$ . Upgoing  $\nu_\mu$ , having traveled  $L \sim 10^4$  km, will have larger oscillation probabilities than downgoing ones, that have  $L$  ranging from a few to a few tens of km. Disappeared  $\nu_\mu$  should have oscillated into  $\nu_\tau$  neutrinos because there is no indication of electron neutrino appearance (the  $e$ -like events from  $\cos\theta < 0$  are consistent with those in the  $\cos\theta > 0$  region).

As shown in Fig. 11.12, the atmospheric neutrinos corresponding to different topologies in Fig. 11.13 have energies over a wide range. The median energies vary from a fraction of GeV to more than 1 TeV, depending on the topology.

The neutrino path length  $L$  is very strongly correlated with the zenith angle  $\cos\theta$  of the measured charged lepton. The outgoing charged lepton  $\ell$  and the incoming neutrino  $\nu$  directions are correlated by kinematic reasons, and the average angle  $\langle\theta_{\ell\nu}\rangle$  between  $\ell$  and  $\nu$  shrinks with increasing energy as approximately  $E_\ell^{-1}$ . For sub-GeV events SK evaluated  $\langle\theta_{\ell\nu}\rangle \sim 60^\circ$  and the correlation between the charged lepton and neutrino directions is rather poor. For multi-GeV events  $\langle\theta_{\ell\nu}\rangle \sim 10^\circ$ , and the correlation is much more stringent.

Atmospheric neutrinos are produced at a typical height  $h \sim 20$  km, with only a weak dependence on the energy, flavor, and zenith angle. Assuming that the neutrino direction is given by the observed charged lepton, the neutrino path length  $L$  is therefore given to a reasonable approximation by (Lipari 2001)

$$L \simeq -R_\oplus \cos\theta + \sqrt{(R_\oplus \cos\theta)^2 + 2R_\oplus h + h^2}. \quad (11.49)$$

This expression ranges from  $L \sim h \sim 20$  km for vertically downgoing neutrinos ( $\cos\theta = 1$ ) to  $L \simeq 2R_\oplus + h \sim 13000$  km for neutrinos crossing the Earth diameter  $2R_\oplus$  at  $\cos\theta = -1$ . For horizontal neutrinos, the path length is  $L \sim \sqrt{2R_\oplus h} \sim 500$  km.



For a first estimate of the oscillation parameters without the use of a full Monte Carlo simulation, we consider multi-GeV events that have traveled over a length  $L_{\text{osc}} \sim 10^4$  km. The energy of the events can be assumed as the median energy  $\bar{E}_\nu \sim 5$  GeV of the distribution. Thus, using (11.47),  $\Delta m^2 [\text{eV}]^2 \simeq 2.48 \frac{E[\text{GeV}]}{L_{\text{osc}}[\text{km}]} \simeq 10^{-3} \text{eV}^2$ . The  $E_\nu$  of the parent neutrinos in multi-GeV events ranges from  $\sim 1$  to  $\sim 100$  GeV. For a fixed value of  $L$  (i.e., for neutrino directions in a small interval of  $\cos \theta$ ) the argument of the function  $\sin^2(1.27 \Delta m^2 L/E)$  in (11.46) can assume values much larger than 1, and this produces fast oscillating probabilities. The observable quantity is simply the average  $\langle \sin^2(1.27 \Delta m^2 L/E) \rangle = 1/2$ . Thus, the oscillation probability takes the simple form:

$$P(\nu_\mu \rightarrow \nu_\mu) = 1 - \frac{\sin^2 2\vartheta}{2} \text{ for } E/L \gg \Delta m^2 \quad (11.50)$$

The observed 50% reduction for upgoing  $\nu_\mu$  suggests  $\sin^2 2\vartheta \sim 1$ .

In conclusion, SK data and predictions can be reconciled assuming the presence of  $\nu_\mu \leftrightarrow \nu_\tau$  oscillations and choosing appropriate values of  $\vartheta$  and  $\Delta m^2$ . A precise determination of the oscillation parameters can be obtained weighting the Monte Carlo predictions without the assumption of oscillations with the oscillation probability (11.46). The SK best fit in the framework of two neutrino oscillations to the data shown in Fig. 11.13 as red histograms gives  $\sin^2 2\vartheta = 1$  and  $\Delta m^2 = 2.11 \times 10^{-3} \text{eV}^2$ .

### 11.9.2 The Iron Calorimeter Soudan 2 Experiment

The Soudan 2 was an iron tracking calorimeter with 770 ton of fiducial mass which operated as a time projection chamber. The detector was active from 1989 to 2001 at a depth of 2070 m.w.e. at the Soudan Underground Mine State Park (USA). The active elements were 1 m long, 1.5 cm diameter drift tubes encased in a honeycomb matrix of 1.6 mm thick corrugated steel plates. Surrounding the tracking calorimeter on all sides but mounted on the cavern walls, there was a 1700 m<sup>2</sup> active shield array to veto the arrival of atmospheric muons.

Events were divided into two classes: fully contained events within the detector (FCE) and partially contained events, in which only the produced lepton exits the detector (PCE). The FCE data were further divided into topology classes to discriminate  $e$ -like (if the highest energy secondary produces a shower) or  $\mu$ -like (if the highest energy secondary is a nonscattering track) events, Fig. 11.14.

Differently from earlier experiments, probably because of the use of veto counters, Soudan 2 observed deviations from the no-oscillation hypothesis in an iron calorimeter (Sanchez et al. 2003). The  $e$ -like events behave as expected, while there is a deformation of the zenith angle distribution of the  $\mu$ -like sample, Fig. 11.15. The event detection and reconstruction properties of Soudan 2 were different, and in many cases superior, to those of SK but the exposure was much smaller. Also the geographical locations and backgrounds of the two experiments were different.

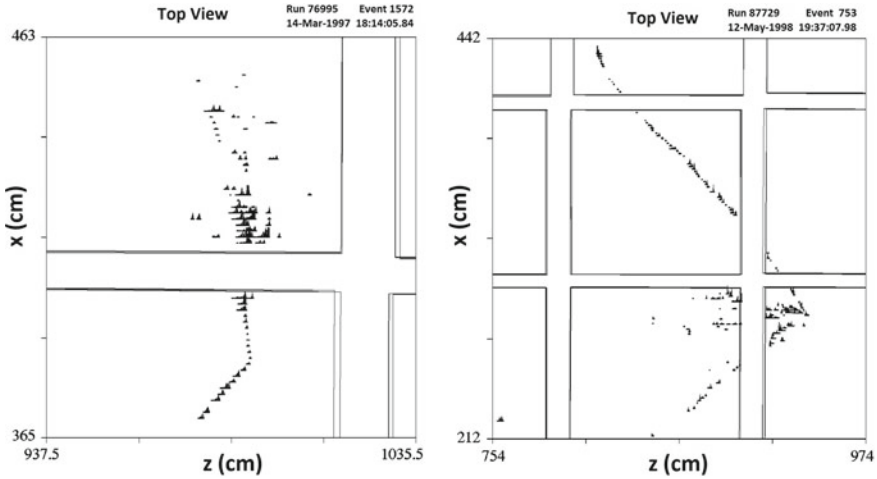


**Fig. 11.14** Two neutrino interactions in the Soudan 2 detector. The event on the left is a  $\nu_e + n \rightarrow p + e^-$  event. The electron travels about one radiation length before showering. The proton is easily recognizable by its heavy ionization (large symbols) and its lack of Coulomb scattering. The event on the right has a long noninteracting muon track, which shows typical Coulomb scattering, and a hadronic shower at the vertex

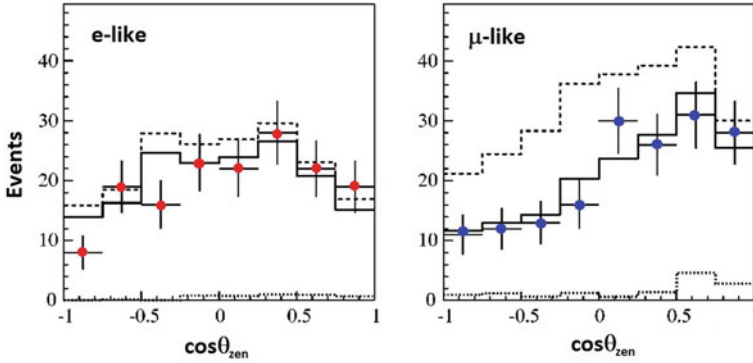


**Fig. 11.15** Angular distributions for  $e$ -like (left) and  $\mu$ -like events (right) in Soudan 2 as a function of the cosine of the zenith angle. The points with error bars are the data, the dashed histograms the predicted unoscillated neutrino distribution plus background; the solid histograms show the neutrino distribution weighted by the oscillation probability predicted by the best-fit parameters ( $\Delta m^2 = 5.2 \times 10^{-3} \text{ eV}^2$  and  $\sin^2 2\vartheta = 0.97$ )

### 11.9.3 Upward-Going Muons and MACRO

A different method for measuring the flux of atmospheric muon neutrinos (as usual,  $\nu_\mu + \bar{\nu}_\mu$ ) is through the observation of upward-going muons. In these events the neutrino interaction occurs in the rock around the detector. Because of the up-down

symmetry of the atmospheric neutrino fluxes one expects an equal number of upgoing and downgoing  $\nu_\mu$  induced events. However,  $\nu_\mu$ -induced downgoing events cannot be distinguished from atmospheric muons (Fig. 10.4) and therefore only upgoing events can be used to study the neutrino flux, as in neutrino telescopes. In standard rock, a muon travels about 1.7 m for each GeV of energy. In throughgoing events the muons arrive and cross the detector, while in stopping events the muons range out inside the detector volume. The average energy of observed events depends on the minimum track length which required at the trigger level. This depends on the experimental conditions.

MACRO was a large area apparatus ( $12 \times 9.3 \times 76.6$  m) in the Gran Sasso underground laboratory in Italy under a minimum rock overburden of 3150 m.w.e. It had a modular structure of six modules and took data from 1994 to 2000. The bottom part contained layers of limited streamer tubes interleaved with passive material plus two layers of liquid scintillator detectors and one plane of nuclear track detectors. The top part of the apparatus was empty and had a “roof” with four horizontal planes of limited streamer tubes and another liquid scintillator layer. Vertically, the apparatus was surrounded by a liquid scintillator plane and six lateral planes of limited streamer tubes. The tracking was performed using the hits in streamer tubes; the time information provided by scintillation counters allowed the determination of the direction by the time-of-flight (ToF) measurements. The MACRO detector measured three classes of atmospheric neutrino interactions, Fig. 11.16:

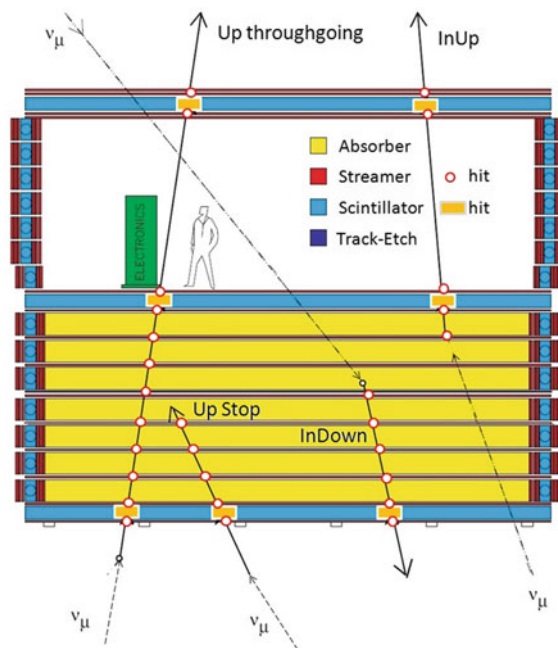


**Fig. 11.16** Cross-sectional sketch of the Monopoles And Cosmic Ray Observatory (MACRO) detector and the different topologies of detected atmospheric neutrinos. At least two scintillator hits were needed to measure the ToF. The streamer hits allowed a precise track reconstruction

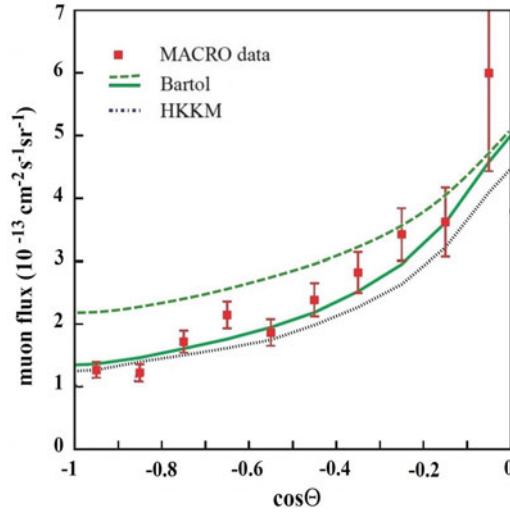


**Fig. 11.17** Measured angular distribution of throughgoing muons in MACRO (*full squares*). The *lines* shows the prediction assuming their best-fit values:  $\Delta m^2 = 2.5 \times 10^{-3} \text{ eV}^2$  and  $\sin^2 2\vartheta = 1$ , using as input the Bartol (Barr et al 2004) and HKKM (Honda et al 2007) fluxes. The *green dashed line* represents the Bartol expectation without oscillations

- The “Up throughgoing muons” with  $E_\mu > 1 \text{ GeV}$ . They were generated in the rock below the detector by  $\nu_\mu$  interactions with median energy of  $\bar{E}_\nu = 50 \text{ GeV}$ . The measured angular distribution was found to deviate from the expectation without neutrino oscillations, Fig. 11.17. In particular, the vertical flux was 50% of the expected value.
- The “Internal Upgoing” (InUp) muons arose from  $\nu_\mu$  interactions with  $\bar{E}_\nu \sim 4 \text{ GeV}$  inside the lower apparatus. Since two scintillation counters were intercepted, the ToF method was applied to identify upward-going events. A 50% reduction was measured, without any distortion in the shape of the angular distribution.
- The “Upgoing Stopping muons” (Up Stop) are due to  $\nu_\mu$  interactions in the rock below the detector yielding upgoing muon tracks. The “semicontained downgoing muons” (InDown) were due to  $\nu_\mu$  induced downgoing tracks with vertex in the lower part of MACRO. The events were found by means of topological criteria; the lack of at least two scintillator hits prevented a separation of the two subsamples. Without oscillations, an almost equal number of Up Stop and InDown events were expected. The measured ratio of (Up Stop + In down) was  $\sim 30\%$  smaller than expected.

For upgoing muon events the two methods most commonly used to reduce systematic uncertainties (the  $\mu/e$  ratio and the up/down comparison) available for contained events cannot be applied. The uncertainty in the prediction of the absolute rate of the fluxes is of order of 15–20%. In this case, a robust method to disentangle the presence of  $\nu_\mu \rightleftharpoons \nu_\tau$  oscillations uses the shape of the zenith angle distribution of the measured  $\nu_\mu$  flux, which has a  $1/\cos\theta$  dependence as given in (11.36).

In the presence of oscillations, vertical neutrinos with  $L \sim 10^4$  km undergo larger oscillations, and are more suppressed than horizontal ones. This distorts the expected shape of the up throughgoing muon flux, as shown in Fig. 11.17, with a best-fit point of  $\sin^2 2\vartheta = 1$  and  $\Delta m^2 = 2.5 \times 10^{-3} \text{ eV}^2$ .

Also the lower energies' topologies were consistent with the existence of  $\nu_\mu \rightleftharpoons \nu_\tau$  oscillations. In case of oscillations, a  $\sim 50\%$  reduction in the flux of the up stopping events (Up Stop) and of the semicontained upgoing muons (InUp) is expected due to averaged oscillations (11.50). No reduction is instead expected for the semicontained downgoing (InDown) events which come from neutrinos which traveled  $\sim 20$  km, in good agreement with the measured reductions.

## 11.10 Atmospheric $\nu_\mu$ Oscillations and Accelerator Confirmations

The simplest explanation of the  $\nu_\mu$  disappearance observed by the three quoted experiments is the conversion of  $\nu_\mu$  into  $\nu_\tau$ , whose interactions are (almost) not detectable. Charged current  $\nu_\tau$  interactions occur at energies above the threshold for the formation of a  $\tau$  lepton ( $m_\tau \sim 1.7 \text{ GeV}$ ). The  $\tau$  flavor identification is not a simple task, as discussed in Sect. 10.3, as most events look like a neutral current interaction with a shower. The hypothesis of  $\nu_\mu \rightleftharpoons \nu_\tau$  oscillation is strengthened by the fact that the behavior of the atmospheric  $\nu_e$  flavor is compatible with the no-oscillation hypothesis.

Starting from the expected neutrino flux and the disappearance probability  $P(\nu_\mu \rightarrow \nu_\mu)$  given in (11.46), information on  $\Delta m^2$  and on the mixing angle  $\vartheta$  were obtained in each experiment by a global fit of the zenith angle distribution of all event topologies. Each set of  $(\sin^2 2\vartheta; \Delta m^2)$  parameters for a given topology gives a reduction of  $\nu_\mu$  events that depends on the zenith angle. The set of values giving the best reduced  $\chi^2$  when using all the event topologies represents the best fit of the experiment; statistical methods were then used to define the region on the parameter phase space that gives the 90% confidence level (c.l.). Other methods to obtain the best parameters were also used, as for instance the fit of the number of events as a function of the observed  $L/E$ . The best-fit values for each experiment have been already quoted in the captions of Figs. 11.13, 11.15 and 11.17.

The remarkable result in 1998 of the study of atmospheric neutrino oscillations was that the high-significance result from SK had the same best-fit parameters obtained by MACRO. The two collaborations used different experimental techniques (water Cherenkov vs. tracking and scintillation) and measured neutrinos in different energy ranges. The simultaneous evidence for an unexpected process by two experiments is an important aspect in experimental physics.<sup>2</sup> Moreover, the successive Soudan 2 analysis was also compatible with the SK and MACRO results.

---

<sup>2</sup> In 2011 there was a huge emphasis on a high-statistical significance claim made by the OPERA collaboration that neutrinos travel with a speed exceeding that of light. Waiting for the confirmation from the MINOS experiment, few months later the collaboration discovered a problem in a hardware connection which invalidated the claim (Adam et al. 2014).

The discovery with atmospheric neutrinos of neutrino oscillations motivated a large efforts to have independent checks from accelerator experiments. Before 1998, two *short baseline experiments* were carried out at CERN: CHORUS and NOMAD. These two detectors were exposed to a high-energy  $\nu_\mu$  beam, and had  $L \sim 1$  km. Their goal was to search for neutrino oscillations with  $\Delta m^2 \sim 1$  eV, by performing disappearance and appearance measurements. The results were null, because they had been designed to explore a range of  $\Delta m^2$  values that Nature had not chosen.

Neutrino oscillations were then explored by accelerator-based long-baseline experiments with typically  $E_\nu \sim 1 - 10$  GeV and  $L \sim$  several hundred km. With a fixed baseline distance and a narrower, well understood neutrino spectrum, the value of  $\Delta m^2$  and, with higher statistics, also the mixing angle, are potentially better constrained in accelerator experiments.

The KEK to Kamioka (K2K) long-baseline neutrino oscillation experiment in Japan was the first accelerator-based experiment with a neutrino path length covering hundreds of kilometers. K2K aimed at confirmation of the neutrino oscillation in  $\nu_\mu$  disappearance in the  $\Delta m^2 > 2 \times 10^{-3}$  eV<sup>2</sup>. The wideband muon neutrino beam had an average  $L/E_\nu \sim 1.3$  GeV/250 km. The beam was produced from the KEK-PS accelerator and directed to the Super-Kamiokande detector from 1999 to 2004.

MINOS was the second long-baseline neutrino oscillation experiment, taking data from 2005 to 2012. Neutrinos were produced from the Fermilab Main Injector. MINOS comprised both a near and a far detector. The far detector was a 5.4 kton (total mass) iron-scintillator tracking calorimeter with a toroidal magnetic field, located underground in the Soudan mine. The baseline distance was 735 km. The near detector was also an iron-scintillator tracking calorimeter with a toroidal magnetic field, with a total mass of 0.98 kton. Both MINOS and K2K measured the neutrino-induced muon energy spectrum and confirmed a distortion consistent with what is expected assuming neutrino oscillations. MINOS provided the most accurate measurement of the allowed region of the  $(\sin^2 2\vartheta; \Delta m^2)$  parameters, with best fit  $\Delta m^2 = (2.32_{-0.08}^{+0.12}) \times 10^{-3}$  eV<sup>2</sup> and  $\sin^2 2\vartheta > 0.90$  at 90% c.l. These values are very close to those found by SK and MACRO.

Although the atmospheric neutrino oscillations and accelerator long-baseline  $\nu_\mu$  disappearance data are fully consistent with  $\nu_\mu \rightleftharpoons \nu_\tau$  oscillations, the appearance of  $\nu_\tau$  remained to be confirmed in order to definitively rule out other exotic explanations (Berlinger et al. 2012). For this purpose, an accelerator long-baseline experiment for studying the *appearance* of a  $\tau$  lepton in a  $\nu_\mu$  beam was realized.

The OPERA experiment at Gran Sasso Laboratory started data taking in 2008 and ended in 2012. The detector was a combination of nuclear emulsions and a magnetized spectrometer. The emulsion technique was used to identify short-lived  $\tau$  leptons event-by-event in a  $\nu_\mu$  beam produced at CERN, with the baseline distance of 730 km. Data analysis is still in progress and until now (May 2014) OPERA reported the observation of four  $\nu_\tau$  candidates, an excess of more than  $4\sigma$  with respect to the nonoscillation hypothesis. The OPERA experiment has confirmed in a definitive way the oscillation scenario opened in 1998 by underground experiments.

### 11.11 Atmospheric Neutrino Flux at Higher Energies

The leptonic or semileptonic decays of charged pions or kaons produce atmospheric  $\nu_\mu$  ( $\nu_e$ ) from a fraction of GeV up to about 100 (10) TeV (conventional neutrinos). Neutrinos from muon decay are important up to a few GeV. Oscillations modify the flux of different neutrino flavors in a relatively small energy range. Above  $\sim 100$  GeV, neutrino oscillation do not play any role on the scale of terrestrial path lengths,  $L \sim 10^4$  km corresponding to  $\cos \theta \sim -1$ . Figure 11.18 shows the  $\nu_\mu$  disappearance probability for three different neutrino energies as a function of the zenith angle  $\theta$ .

At sufficiently high energies, in addition to the conventional flux, another production mechanism is expected. The *prompt* atmospheric neutrino flux is originated by the semileptonic decays of charmed mesons and baryons with lifetimes of  $10^{-12}$  s, before losing energy in collisions. Hence, the spectrum for the prompt flux more closely follows the CR spectrum and is harder about one power than the conventional flux at high energy. The prompt flux could represent a dangerous background for cosmic neutrinos and has not yet been measured, but is expected to be important above  $\sim 100$  TeV.

The ANTARES and IceCube neutrino telescopes presented in Chap. 10 were able to observe the disappearance of the atmospheric  $\nu_\mu$  with energies as low as few tens of GeV. On the other hand, neutrino telescopes are the only devices large enough to detect a sizeable flux of atmospheric neutrinos above the TeV energy. Figure 11.19 shows the measurement of the  $\nu_\mu$  energy spectrum reported by the Frejus, AMANDA and IceCube experiments. IceCube (Aartsen et al. 2013) recently measured also the atmospheric  $\nu_e$  component up to 1 TeV. The only existing measurement was between  $\langle E_{\nu_e} \rangle \sim 0.4\text{--}14$  GeV by the Frejus underground experiment.

The data sets are consistent with current models of the atmospheric neutrino flux.

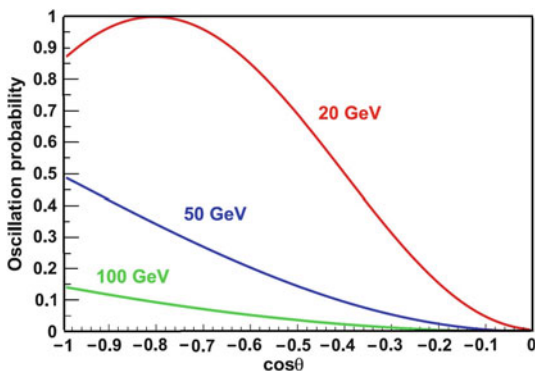


**Fig. 11.18**  $P(\nu_\mu \rightarrow \nu_\mu)$  disappearance probability as a function of the cosine of zenith angle  $\theta$  for atmospheric  $\nu_\mu$  with  $E_{\nu_\mu} = 20, 50$  and  $100$  GeV. The curves were produced using Eq. (11.46) assuming  $\Delta m^2 = 2.32 \times 10^{-3} \text{ eV}^2$  and  $\sin^2 2\vartheta = 1$



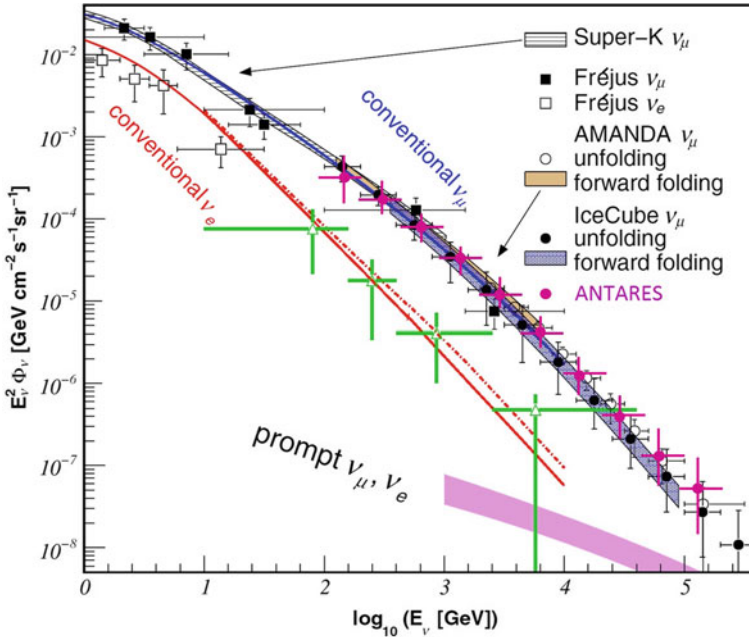


**Fig. 11.19** Measured flux of atmospheric  $\nu_\mu$  and  $\nu_e$  compared with expectations from the conventional flux of atmospheric neutrinos. The prompt component is at present too low to be measured. Courtesy of IceCube collaboration

## References

- M.G. Aartsen et al., Measurement of the atmospheric  $\nu_e$  flux in IceCube. *Phys. Rev. Lett.* **110**, 151105 (2013)
- T. Adam et al., Measurement of the neutrino velocity with the OPERA detector in the CNGS beam (2014). Compare [arXiv:1109.4897v1](https://arxiv.org/abs/1109.4897v1) with [arXiv:1109.4897v4](https://arxiv.org/abs/1109.4897v4)
- M. Ambrosio et al., Measurement of the atmospheric neutrino-induced upgoing muon flux using MACRO. *Phys. Lett.* **434**, 451 (1998). (MACRO Coll.)
- G.D. Barr, T.K. Gaisser, P. Lipari, S. Robbins, T. Stanev, Three-dimensional calculation of atmospheric neutrinos. *Phys. Rev. D* **70**, 023006 (2004)
- Y. Becherini, A. Margiotta, M. Sioli, M. Spurio, A Parameterisation of single and multiple muons in the deep water or ice. *Astropart. Phys.* **25**, 1 (2006)
- J. Beringer et al., (Particle Data Group). The review of particle physics. *Phys. Rev.* **D86**, 010001 (2012)
- S. Braibant, G. Giacomelli, M. Spurio, *Particles and Fundamental Interactions* (Springer, New York, 2012)
- S. Cecchini, M. Spurio. Atmospheric muons: experimental aspects. *Geosci. Instrum. Method. Data Syst.* **1** 185–196 (2012). [arXiv:1208.1171](https://arxiv.org/abs/1208.1171)
- L.I. Dorman, *Cosmic Rays in the Earth's Atmosphere and Underground* (Kluwer Academic Publisher, New York, 2004)
- Y. Fukuda et al., Evidence for oscillation of atmospheric neutrinos. *Phys. Rev. Lett.* **81**, 1562 (1998). (SuperKamiokande coll.)

- T.K. Gaisser, *Cosmic Rays and Particle Physics* (Cambridge University Press, Cambridge, 1990)
- T.K. Gaisser, Semi-analytic approximations for production of atmospheric muons and neutrinos. *Astropart. Phys.* **16**, 285 (2002)
- T.K. Gaisser, M. Honda, Flux of atmospheric neutrinos. *Annu. Rev. Nucl. Part. Sci.* **52**, 153–199 (2002)
- P.K.F. Grieder, *Extensive Air Showers* (Springer, Berlin, 2010)
- M. Honda, T. Kajita, K. Kasahara, S. Midorikawa, T. Sanuki, Calculation of atmospheric neutrino flux using the interaction model calibrated with atmospheric muon data. *Phys. Rev. D* **75**, 043006 (2007)
- J.I. Illana, P. Lipari, M. Masip, D. Meloni, Atmospheric lepton fluxes at very high energy. *Astropart. Phys.* **34**, 663–673 (2011). [arXiv:1010.5084](https://arxiv.org/abs/1010.5084).
- T. Kajita, Atmospheric neutrinos. *Adv. High Ener. Phys.* 504715 (2012). doi:[10.1155/2012/504715](https://doi.org/10.1155/2012/504715)
- M. Koshiba, Observational neutrino astrophysics. *Phys. Rep.* **220**, 229–381 (1992)
- N. Lesparre et al., Geophysical muon imaging: feasibility and limits. *Geophys. J. Int.* **183**, 1348 (2010)
- P. Lipari, Introduction to neutrino physics. 1st CERN-CLAF School of High-energy Physics, Itacuruca, Brazil (2001), <http://cds.cern.ch/record/677618/files/p115.pdf>
- P. Lipari, Lepton spectra in the earth's atmosphere. *Astropart. Phys.* **1**, 195 (1993)
- B. Pontecorvo, Neutrino experiments and the problem of conservation of leptonic charge. *Sov. Phys.* **26**, 984–988 (1968). (English translation of a paper in Russian in 1967)
- M. Sanchez et al., Measurement of the L/E distributions of atmospheric  $\nu$  in Soudan 2 and their interpretation as neutrino oscillations. *Phys. Rev.* **D68**, 113004 (2003). (Soudan 2 Coll.)
- Y. Takeuchi, Results from Super-Kamiokande. *Nucl. Phys. Proc. Supl.* **79–84**, 229–232 (2012) (Super-Kamiokande Collaboration)

## Chapter 12

# Connections Between Physics and Astrophysics of Neutrinos

Stellar evolution, the theory of how stars evolve, relies on observations on many stars with different masses, colors, ages, and chemical composition. Two of the principal successes of the stellar evolution theory are the prediction of the mass-luminosity relation in main sequence stars and the explanation of the Hertzsprung-Russell diagram. This is a scatter graph of absolute magnitude or luminosity of stars versus temperature (color). The energy of stars is provided by nuclear fusion reactions in their core, Sect. 12.1, and their evolution is strongly dependent upon their mass.

The Sun, through the Standard Solar Model (SSM), is the only star for which the stellar evolution theory can be deeply tested, Sect. 12.2. Probe useful to verify the theoretical predictions of the various thermonuclear processes occurring inside the Sun, are the neutrinos that in such processes are emitted. The experimental study of solar neutrinos (Sects. 12.3, 12.4 and 12.5) has given a fundamental contribution both to astroparticle and to elementary particle physics, offering an ideal test of solar models and providing at the same time fundamental indications on the physics of the neutrino sector.

In conjunction with those on atmospheric neutrinos (Chap. 11), the solar neutrino experiments have given compelling evidence for the existence of neutrino oscillations, Sect. 12.6, transitions in flight between the three neutrino flavors, caused by nonzero neutrino masses and neutrino mixing. This has a huge impact on particle physics at these days. It has also consequences on the prediction of the neutrino flavor composition from high energy neutrino sources, Sect. 12.8.

Neutrinos play a key role not only during the life of a star. When a massive star has exhausted hydrogen, it evolves by producing energy through the fusion of heavier elements up to the iron, Sect. 12.9. Neutrinos produced during such reactions escape unimpeded from the stellar material and more and more intense nuclear burning is needed to replace the huge amount of energy carried away. Once the inner region of a star becomes primarily iron, further compression of the core does not ignite nuclear fusion anymore; the star collapses to form a compact object such as a neutron star or a black hole, Sect. 12.10. A prominent prediction from theoretical models of the core-collapse of a massive star (Sect. 12.11) is that 99% of the gravitational binding energy of the resulting remnant is converted to neutrinos with energies of a few tens

of MeV over a timescale of 10 s. Neutrinos were observed from the celebrated 1987A supernova (SN1987A) in the Large Magellanic Cloud, 50 kpc away from the Earth, Sect. 12.13. Few neutrino events in coincidence with the explosion were sufficient to confirm the baseline model of core-collapse and to provide a very wide range of constraints on neutrino physics and astrophysics. Today, more advanced and larger experiments are ready to witness the next galactic core-collapse supernova.

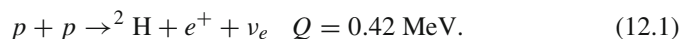
## 12.1 Stellar Evolution of Solar Mass Stars

The interplay between the gravitational, the electromagnetic and the nuclear forces determines the life evolution of stars. The force field that holds the nuclei in the star core is due to the gravitational pressure of matter present in the outer layers. A star is a system in equilibrium between pressure due to gravity and pressure due to radiation produced by fusion reactions in the core. The basic equations of stellar evolution and structure involve simple physics and can be found in Bachall (1989).

The stars shine through nuclear fusion reactions. As light elements (starting from hydrogen) are burned, stars slowly evolve. Their central temperature is adjusted so that the average thermal energy of a nucleus is small compared to the Coulomb repulsion from potential fusion partners. Nuclear fusion reactions are possible because of the *tunneling effect* through a potential barrier. This effect was first discussed by Gamow in connection with the  $\alpha$ -decay [see Chap. 14 of Braibant et al. (2011)]. For instance, in our Sun the temperature is  $T_{\odot} \simeq 1.5 \times 10^7$  K, corresponding to a proton kinetic energy of  $E_p = kT_{\odot} \simeq 1.3$  keV. The large Coulomb repulsion, which corresponds to few MeV, slows the nuclear reaction rates to long time scales, and the energy dependence of the fusion cross section represents one of the main input factors for the theory of stellar evolution. Uncertainties on cross sections reflect into uncertainties on stellar parameters.

Approximately 80% of observed stars (called *main sequence stars*) lie along a path in the Hertzsprung-Russell diagram characterized by energy generation through proton burning. Main sequence stars fuse protons to produce energy contrasting the gravitational collapse via the proton-proton (pp) or the carbon-nitrogen-oxygen (CNO) cycles, two distinct reaction chains. The Sun provides a unique opportunity to test the theory of how stars evolve, as we can compare model predictions to solar properties that are precisely known.

The luminosity of a main sequence star is determined by the atomic opacity, the chemical composition, and the balance of gravitational and pressure forces. Stellar nucleosynthesis is responsible for the abundances of elements up to iron nuclei. The first reaction of the proton-proton cycle occurs through the weak interactions, that is,



The cross section for this low energy process is extremely small,  $\sigma \sim 10^{-55} \text{ cm}^2$ . The reported  $Q$  value represents the sum of the  $e^+$  kinetic energy and the neutrino

energy. In the following it includes also the total thermal energy released.  ${}^2\text{H}$  can be also formed though the so-called pep reaction which occurs at a very small rate (0.24 %) with respect to (12.1)

$$p + e^- + p \rightarrow {}^2\text{H} + \nu_e \quad Q = 1.442 \text{ MeV.} \quad (12.2)$$

This reaction produces a monochromatic neutrino of energy equal to the Q-value.

The successive steps of the pp chain are shown in Fig. 12.1. The proton–proton cycle can be summarized as

$$4p \rightarrow {}^4\text{He} + 2e^+ + 2\nu_e \quad Q = 26.73 \text{ MeV} \quad (12.3)$$

of which 2 MeV are due to the annihilation of the two positrons. In the chain, there are two important channels that produce  ${}^4\text{He}$  with neutrinos as by-products. Neutrinos (each with average energy  $\bar{E} \sim 0.3 \text{ MeV}$ ) do not energetically contribute to stellar equilibrium because they have a low interaction probability and immediately escape. It is interesting to note that the isotopes of  ${}^2\text{H}$ ,  ${}^3\text{H}$ ,  ${}^7\text{Li}$ ,  ${}^4\text{Be}$ , and  ${}^8\text{B}$  are collaborating spectators whose local number densities do not change when the chain is in equilibrium.

Due to many other physical processes, the energy produced by fusion propagates to the surface of the star, the photosphere. The diffusion time of photons from the stellar core to the photosphere (taking into account the  $\gamma - p$  cross section) is of the order of  $10^5 - 10^6$  years.

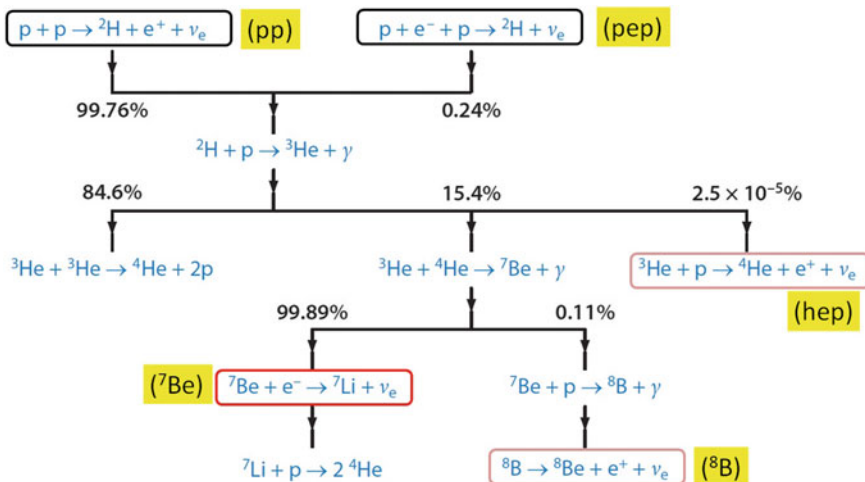


**Fig. 12.1** The diagram shows the principal cycles comprising the proton–proton ( $pp$ ) chain, and the associated neutrinos produced during the different branches. The  $pp$  processes occur in all stars of the main sequence. The probability of each branch reported in the figure is characteristic of our Sun at our epoch

**Table 12.1** The nuclear fusion reactions in the CNO cycle

Reaction	Q (MeV)
$p + {}^{12}\text{C} \rightarrow {}^{13}\text{N} + \gamma$	1.94
${}^{13}\text{N} \rightarrow {}^{13}\text{C} + e^+ + \nu_e$	1.20
$p + {}^{13}\text{C} \rightarrow {}^{14}\text{N} + \gamma$	7.55
$p + {}^{14}\text{N} \rightarrow {}^{15}\text{O} + \gamma$	7.29
${}^{15}\text{O} \rightarrow {}^{15}\text{N} + e^+ + \nu_e$	1.73
$p + {}^{15}\text{N} \rightarrow {}^{12}\text{C} + {}^4\text{He}$	4.96

A star with roughly the solar mass, when hydrogen is exhausted, tends to contract, and to increase its density; this happens because the radiation produced by the fusion reactions is no longer able to balance the gravitational pressure. During the contraction phase, gravitational energy is converted into kinetic energy of nuclei: the temperature increases and further fusion reactions may be ignited.

A critical point is the carbon formation. In a star composed mainly of  ${}^4\text{He}$  nuclei,  ${}^8\text{Be}$  is continuously formed.  ${}^8\text{Be}$  has a mass which is slightly larger than twice the  ${}^4\text{He}$  mass, that is,  ${}^4\text{He} + {}^4\text{He} \rightarrow {}^8\text{Be}$ ;  $Q = -0.09\text{ MeV}$ . Once  ${}^8\text{Be}$  is formed, it splits again into two  ${}^4\text{He}$  nuclei. When the  ${}^4\text{He}$  density is extremely high, a fusion reaction forming carbon nuclei in an excited state occurs with a resonant cross section:  ${}^4\text{He} + {}^8\text{Be} \rightarrow {}^{12}_6\text{C}^*$ . The excited state  $\text{C}^*$  immediately decays to the ground state. The carbon abundance in the Universe is relatively high, and it may also be present in stars that have not exhausted the proton cycle. In the presence of protons, the nucleus  ${}^{12}\text{C}$  acts as a *catalyst* for another cycle, similar to the proton–proton cycle, that produces energy transforming protons into helium nuclei: the CNO cycle (Table 12.1). At the end of the process, one has  ${}^{12}\text{C} + 4p \rightarrow {}^{12}\text{C} + {}^4\text{He} + 2e^+ + 3\gamma + 2\nu_e$  with a total energy released of about 26 MeV. The  ${}^{12}_6\text{C}$  nucleus is strongly bound and is the starting point for the formation in massive stars of heavier nuclei through fusion, Sect. 12.9.

## 12.2 The Standard Solar Model and Neutrinos

The Sun has been converting hydrogen into helium for roughly  $4.5 \times 10^9$  years. The value of the solar mass and of the emitted power indicate that the process will continue for about as many years. The process shown in Fig. 12.1 produces energy, Eq. (12.3), and two neutrinos which escape from the Sun, carrying away a fraction of the released energy. The kinetic energy of the other particles is the source of the thermal energy. The flux of solar neutrinos that reaches the Earth is then given by

$$\Phi_{\nu_e} \simeq \frac{1}{4\pi D_\odot^2} \frac{2L_\odot}{(Q - \langle E_\nu \rangle)} = 6 \times 10^{10} \text{ cm}^{-2} \text{ s}^{-1} \quad (12.4)$$

where  $L_{\odot} = 3.842 \times 10^{33}$  erg/s is the solar luminosity,  $D_{\odot} = 1.495 \times 10^{13}$  cm is the Sun-Earth distance, and  $\langle E_{\nu} \rangle \simeq 0.3$  MeV is the average energy of neutrinos produced in the fusion cycle.

Main sequence stars burn their hydrogen into helium following the pp cycle and/or the CNO cycle. The same energy output can be produced by the two cycles that result in different energy distributions of neutrinos. In order to compute the relative importance of the different fusion cycles, and to obtain a precise prediction for the  $\nu_e$  flux, it is necessary to compute in detail the structure of the Sun. This includes its density, temperature, composition profiles, and the rates of the different nuclear reactions, that also depend on the radial position inside the Sun. This is the task of the so-called Standard Solar Model (SSM) that uses well known physics and some approximations, notably spherical symmetry, and the absence of rotation, to compute the structure of the Sun and predict the neutrino fluxes. The SSM calculations have been developed starting from the pioneering work of Bahcall (1989) and his collaborators about 50 years ago. The SSM calculations have been rather frequently updated to match new input data. For this reasons, today slightly different versions of the SSM exist as a consequence of different interpretations of the best available physics and input data (Haxton 2009). The SSMs are based on the following assumptions (Bahcall 1989; Antonelli et al. 2013; Haxton et al. 2013):

- The Sun is in a state of hydrodynamic equilibrium, maintaining a local balance between the thermal pressure (outward) and the weight of the material above pressing downward (inward). To implement this condition, an equation of state is needed. Helioseismic information (see below) have provided important tests of the associated theory.
- The Sun produces its energy (12.3) by fusing protons into  ${}^4\text{He}$  via the pp chain and the CNO cycle. Nuclear cross sections of different processes are taken from experiments or from theory.
- The mechanisms for energy transport from the core to the photosphere are radiation and convection. The inner region of the Sun ( $\sim 70\%$  by radius) is radiative. In order to describe radiative transport, the *opacity* must be known as a function of temperature, density, and composition. The opacity for the emitted  $\gamma$ -rays includes: Thomson scattering on electrons; interactions with fully ionized hydrogen and helium nuclei; complex processes such as bound-free scattering on metals. In the Sun's outer envelope, where the radiative gradient is larger, convection dominates the energy transport.
- The initial condition of the problem is a total mass of material and an *initial* (or *presolar*) composition. The latter is estimated as equal to the present composition at the surface. The presolar composition is divided into hydrogen  $X_{\text{ini}}$ , helium  $Y_{\text{ini}}$ , and metals (=elements heavier than He)  $Z_{\text{ini}}$ , with  $X_{\text{ini}} + Y_{\text{ini}} + Z_{\text{ini}} = 1$ . Relative metal abundances can be determined from a combination of photospheric and meteoritic abundances and are generally assumed to have remained constant since the Sun formed. This observable is one of the key parameters of different versions of the SSM.



- The composition of the core evolves with time according to the rates of the nuclear reactions, and the structure slowly evolves according to these changes.
- Boundary conditions include the modern Sun's mass, age, radius  $R_\odot$ , and luminosity  $L_\odot$ .

The resulting solar models are dynamic and trace the evolution of the Sun to the present condition, thereby predicting contemporary solar properties such as the composition, temperature, pressure, sound-speed profiles, energy output, relative weight of pp and CNO cycles and the neutrino fluxes. The luminosity of the Sun has increased by  $\sim 40\%$  over the solar lifetime. The interaction rates of different reactions shown in Fig. 12.1 depend on the quantity  $\langle \sigma v \rangle$ , where  $v$  is the relative velocity between two colliding nuclei and  $\sigma$  the cross section. The  $\langle \dots \rangle$  denotes an average over the Maxwell-Boltzmann velocity distribution in the solar plasma. The energy  $E_G$  for which the probability of a solar reaction reaches a maximum corresponds to the so-called *Gamow peak*. At energies higher than  $E_G$  the number of particles able to induce the reaction becomes insignificant; at lower energies the tunneling through the Coulomb barrier makes the reaction improbable, Fig. 12.2.

The most important observable for tests of the nuclear reactions occurring in the Sun's core are the neutrinos. The predicted spectrum of  $\nu_e$  emitted by the Sun is shown in Fig. 12.3. Different experiments have different energy thresholds, and are sensitive to different regions of the neutrino spectrum. Referring to Fig. 12.1, the most abundant contribution comes from deuteron formation. The two reactions  $pep$  and  ${}^7\text{Be}$  induced by electron capture, produce line sources of neutrinos of energy  $E_\nu^{\text{max}}$  only broadened by thermal effects.

The possibility to compare model predictions to solar properties has inspired a great deal of laboratory work to reduce uncertainties in atomic opacities and nuclear

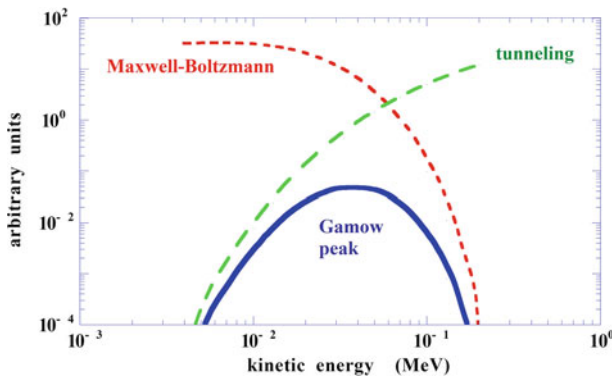


**Fig. 12.2** The Gamow peak is the convolution of the Maxwell-Boltzmann distribution with the tunneling probability of nuclei through their Coulomb barrier. This plot shows (in arbitrary units) the Maxwell-Boltzmann distribution of protons at  $T = 1.5 \times 10^7$  K (red distribution) and their tunneling probability through the Coulomb barrier (green line). The product between the two curves (blue line) gives the Gamow peak

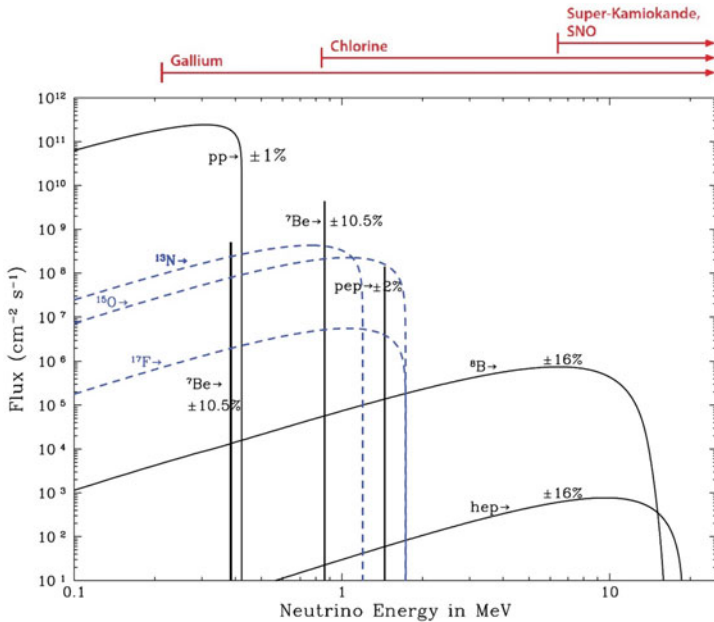


**Fig. 12.3** The energy spectrum of solar neutrinos arriving on Earth along with the standard solar model uncertainties. Flux densities are shown for continuous sources: one must integrate over  $E$  to obtain fluxes in the indicated units. The abbreviations refer to reactions indicated in Fig. 12.1. The *solid lines* indicate the neutrinos coming from the most important reactions of the  $pp$  cycle, the *dashed blue lines* indicate the neutrinos from the CNO cycle. The *red arrows* at the *top* represent the thresholds of the indicated experiments. The numbers associated with the neutrino sources show theoretical errors of the fluxes. Adapted from the late John Bahcall's web site (<http://www.sns.ias.edu/jnb/>)

crosssections (Broggini et al. 2010). The neutrino fluxes are a sensitive thermometer for the solar core, provided the associated nuclear physics is under control. Particularly important are input data from radiative opacities and from the determinations of solar abundances of heavy elements. Table 12.2 gives fluxes for two solar models which reflect the uncertainties on the metallicity in the Sun. There are significant differences between older composition models, with higher metallicity abundance (GS98) (Serenelli et al. 2011) and the newer ones, with lower heavy element abundances (AGSS09) (Asplund et al. 2009). The model labeled with GS98 uses abundances derived from simple assumptions of the solar interior based on current analyses of the photosphere, yielding a ratio between metal and hydrogen ( $Z/X$ ) = 0.0229. The model labeled as AGSS09 takes abundances derived from updated techniques, a three-dimensional hydrodynamic model of the Sun's atmosphere and improved atomic physics, yielding ( $Z/X$ ) = 0.0178.

The assumed percentage of metals in SSMs is an important parameter to evaluate the opacity. In the model with a low-metallicity ratio, the Sun's core is somewhat

**Table 12.2** Standard solar model (SSM) neutrino fluxes from the GS98 (Serenelli et al. 2011) and AGSS09 (Asplund et al. 2009), with associated uncertainties

Abbreviations	Reaction	$E_\nu^{\max}$ (MeV)	$\Phi_{\nu_e}$ (GS98) (high $Z/X$ ) $\text{cm}^{-2} \text{s}^{-1}$	$\Phi_{\nu_e}$ (AGSS09) (low $Z/X$ ) $\text{cm}^{-2} \text{s}^{-1}$
pp	$pp \rightarrow {}^2\text{H} e^+ \nu_e$	0.42	$(5.98 \pm 0.6\%) 10^{10}$	$(6.03 \pm 0.6\%) 10^{10}$
pep	$pe^- p \rightarrow {}^2\text{H} \nu_e$	1.44	$(1.44 \pm 1.2\%) 10^8$	$(1.47 \pm 1.2\%) 10^8$
${}^7\text{Be}$	${}^7\text{Be} e^- \rightarrow {}^7\text{Li} \nu_e$	0.86 (90%)	$(5.0 \pm 7\%) 10^9$	$(4.6 \pm 7\%) 10^9$
		0.38 (10%)		
${}^8\text{B}$	${}^8\text{B} \rightarrow {}^8\text{Be} e^+ \nu_e$	$\sim 15$	$(5.6 \pm 14\%) 10^6$	$(4.6 \pm 14\%) 10^6$
hep	${}^3\text{He} p \rightarrow {}^4\text{He} e^+ \nu_e$	18.77	$(8.0 \pm 30\%) 10^3$	$(8.3 \pm 30\%) 10^3$
${}^{13}\text{N}$	${}^{13}\text{N} \rightarrow {}^{13}\text{C} e^+ \nu_e$	1.20	$(3.0 \pm 14\%) 10^8$	$(2.2 \pm 14\%) 10^8$
${}^{15}\text{O}$	${}^{15}\text{O} \rightarrow {}^{15}\text{N} e^+ \nu_e$	1.73	$(2.2 \pm 15\%) 10^8$	$(1.6 \pm 15\%) 10^8$
${}^{17}\text{F}$	${}^{17}\text{F} \rightarrow {}^{17}\text{O} e^+ \nu_e$	1.74	$(5.5 \pm 17\%) 10^8$	$(3.4 \pm 16\%) 10^8$

cooler (by  $\sim 1\%$ ). A small variation of the central temperature induces large variations of high energy neutrinos, such as those from  ${}^8\text{B}$  decay, which are reduced by  $\sim 20\%$  with respect to the model with high-metallicity (see Table 12.2). The uncertainties associated with the  $\nu_e$  fluxes are linked with uncertainties assigned to approximately 20 model input parameters which include the solar age, present day luminosity, opacities, the diffusion constant, the cross sections for the pp chain and CNO cycle, and the abundances of different elements.

A unique tool to determine the structure of the solar interior is provided by the *helioseismology*, the study of the natural oscillations of the Sun. Measurements and analysis of Doppler shifts of photospheric absorption lines show that the Sun's surface oscillates with amplitudes  $\sim 30$  m and velocities  $\sim 0.1 \text{ m s}^{-1}$ , reflecting a variety of interior modes. The significant effort invested in helioseismological measurements and analysis has yielded a rather precise map of associated sound speed  $c(r)$  over the outer 90% of the Sun by radius. This function depends on the same quantity used in the SSM to derive the neutrino fluxes, namely the Sun quasi-static pressure, density, temperature, entropy, gravitational potential, and nuclear energy generation profiles that are all functions of the radial coordinate  $r$ .

The comparisons of results of the SSM with helioseismic data pose a still unresolved problem, named the *solar abundance problem*. In short, all helioseismic predictions of SSMs with low  $Z/X$  ratio as the AGSS09 are in disagreement with helioseismic observations. On the other hand the GS98, derived with simpler assumptions to model the solar interior and giving a higher  $Z/X$  ratio, is in better agreement with helioseismic data. The solar abundance problem represents thus the incompatibility between the model with the best description of the solar atmosphere and the helioseismologic description of the Sun's interior.

## 12.3 Solar Neutrino Detection

The detection of low-energy electron neutrinos is extremely challenging. Electron neutrino interactions considered in the previous Chapters occurred through the deep inelastic scattering process  $\nu_e N \rightarrow e^- X$ . Here,  $N$  is either a proton or a neutron, and  $X$  a hadronic system. This reaction occurs for neutrino energies much higher than the threshold for single pion production ( $\sim 140$  MeV). Lower energy neutrinos (including the MeV-scale solar  $\nu_e$ ) interact only via quasi-elastic scattering



or through elastic scattering (ES) on electrons, with a much smaller cross section. The problem of (12.5) is that free neutrons do not exist in nature. Only neutrons bound in nuclei can be used in reactions



By changing the number of protons,  $\nu_e$  capture transforms the nuclide into a new element. This requires an additional energy with respect to (12.5) due to the difference of the nuclear binding energies between the nucleus  ${}^A_Z X$  and  ${}^A_{Z+1} Y$ . Reaction (12.6) can be used to detect solar neutrinos only if the very few  $Y$  atoms produced by the weak-interaction process can be separated from the huge number of  $X$  target atoms of the detector using *chemical extraction* techniques. Only few elements  $X$  are thus suitable to be effectively used. The production rate of the  $Y$  atoms can be easily measured if the  ${}^A_{Z+1} Y$  isotope is *radioactive* and, moreover, if the lifetime is neither too short nor too long. In this case, when extracted, the decay rates can be counted. The combination of these techniques give rise to the so-called *radiochemical* experiments.

**The chlorine radiochemical experiment.** Radiochemical detection of neutrinos using  ${}^{37}\text{Cl}$  in (12.6) was suggested by Pontecorvo as early as 1946 and explored in more detail by Alvarez in 1949 (Lande 2009). It was Ray Davis (Nobel laureate in 2002) in 1955 at Brookhaven who started to develop practical detectors, using about a 4,000 l tank of perchloroethylene ( $\text{C}_2\text{Cl}_4$ ) placed few meters underground. The construction of an experiment with the scale necessary for solar neutrino detection (390,000 l of  $\text{C}_2\text{Cl}_4$ ) began on the Homestake mine (South Dakota) in 1965, at a depth of 4,000 m.w.e. The first results were announced in 1968 and the measurements continued until 2002, when the mine closed.

The ‘‘chlorine experiment’’ exploited the fortuitous properties of  ${}^{37}\text{Ar}$  nuclei. They are produced with a threshold energy of 0.814 MeV in the reaction



The average solar neutrino reaction rate in the tank was 0.48 counts/day, above an estimated background of 0.09 counts/day. Argon is a noble gas that does not interact chemically, and it can be extracted with high efficiency (estimated as  $\sim 95\%$ ) from large volumes of organic liquid. In addition, the  ${}^{37}\text{Ar}$  isotope has a half-life of 35 days,

long enough to allow to build up their concentrations in the tank over a saturation time of about two months.

After extraction of  $^{37}\text{Ar}$  nuclei from the tank, they decay via the capture of one orbital electron (usually from the K shell) returning to  $^{37}\text{Cl}$  via the inverse reaction of (12.7). The newly formed  $^{37}\text{Cl}$ , although still electrically neutral, is formed in an excited state with a missing electron in the inner shell. An outer shell electron will fill the empty inner level thereby dropping to a lower state. During this process, the transient electron will emit an X-ray of 2.82 keV. Davis developed miniaturized gas proportional counters for counting such decays.

The chlorine experiment counted  $\sim 25$  Ar nuclei per year. Taking into account detector efficiencies and losses due to  $^{37}\text{Ar}$  decaying in the tank, the counting rate can be converted to a capture rate that is the measurable quantity in the radiochemical experiments. It corresponds to the probability per unit time that a target nucleus captures a solar neutrino. The capture rate can be calculated as:

$$\langle \sigma \Phi \rangle \equiv \int dE \frac{d\Phi_{\nu_e}}{dE} \sigma(E) \quad [\text{s}^{-1}] \quad (12.8)$$

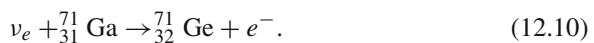
where  $d\Phi_{\nu_e}/dE$  is the differential flux of solar neutrinos and  $\sigma(E)$  is the cross-section for the reaction considered. It has become customary to use the unit 1 SNU  $\equiv$  1 Solar Neutrino Unit =  $10^{-36}$  captures per second. The final result obtained by Davis was

$$\langle \sigma \Phi \rangle_{Cl} = 2.56 \pm 0.16_{\text{stat}} \pm 0.16_{\text{sys}} \text{ SNU} \quad (12.9)$$

which is about a factor of three below the SSM best values: the GS98 predicts a rate of  $8.00 \pm 0.97$  SNU. This result represents the beginning of the *solar neutrino problem*, a major discrepancy between measurements of the numbers of neutrinos reaching the Earth and theoretical predictions, lasting from the early results of the chlorine experiment to about 2002. The discrepancy between data and expectation on solar neutrinos had three possible interpretations: (i) experimental errors; (ii) an astrophysical overestimate of the solar neutrino production; (iii) new physics in the neutrino sector. Over the years, the last interpretation of the measured deficit was found to be the correct one, as we show in the following.

As shown in Fig. 12.3, reaction (12.7) is mostly sensitive to the boron and beryllium neutrinos (above the threshold production of Ar), whose flux estimate had originally large uncertainties. These were connected with uncertainties on the central temperature of the Sun, on which the higher energy neutrino flux is primarily sensitive. For this reason the solution of the solar neutrino problem was not immediately apparent and many explanations were proposed to change the SSM in order to produce a somewhat cooler core.

**GALLEX/GNO, Sage.** Another possible element for reaction (12.6) is gallium through the reaction



The Soviet-American Gallium Experiment (SAGE) (Abdurashitov et al. 2009) and the Gallium Experiment (GALLEX) (Hempel et al. 1999) (successively: Gallium Neutrino Observatory (GNO) Altmann et al. 2005) began solar neutrino measurements in December 1989 and May 1991, respectively, exploiting the above reaction.

SAGE (still in operation) is located at the Baksan Neutrino Observatory in the Caucasus mountains in Russia and uses a target of 50 tons of Ga under the form of a molten metal at a temperature of 30 °C. It has reported results for 168 extractions through December 2007. GALLEX, which used 30 tons of Ga in the form of a GaCl<sub>3</sub> solution, ran between 1991 and 1997 at the Gran Sasso Laboratory (LNGS) in Italy. A number of improvements in Ge extraction procedures, electronics, counter efficiency calibrations, and radon event characterizations were incorporated into the follow-up experiment GNO, who continued through 2003.

As <sup>71</sup>Ge has a half-life of 11.4 days, a radiochemical experiment analogous to that done for chlorine is possible, although the chemistry of Ge recovery is considerably more complicated than that for Ar. GALLEX/GNO recovered Ge as GeCl<sub>4</sub> by bubbling nitrogen through the solution, and then scrubbing the gas. The Ge can be further concentrated and purified, converted into GeH<sub>4</sub>, and then counted in miniaturized gas proportional counters similar to those used in the chlorine experiment. The separation of <sup>71</sup>Ge atoms in the liquid Ga metal of SAGE is different and more complex.

Reaction (12.10) has a low threshold (233 keV) and a strong cross section for absorbing the low-energy pp neutrinos giving <sup>71</sup>Ge via Gamow-Teller transition. In this transition [Chap. 8 of Braibant et al. (2011)] the spin vectors of the initial and final nuclei change by one unit. Because of this lower threshold, reaction (12.10) occurs also for low energy  $\nu_e$  from the deuteron formation ( $pp$  in Table 12.2). Assuming steady-state luminosity of the Sun and the standard weak interaction physics, 79 SNU is foreseen from this reaction. The remaining channels in Table 12.2 give additional 48 SNU, mainly from <sup>7</sup>Be and <sup>8</sup>B.

A unique aspect of the Ga experiments was the use, in a limited time interval, of an external <sup>51</sup>Cr artificial source with intensities of  $\sim 0.5$  MCi. This radioactive isotope has half-life of 27.7 days for electron capture that produces a  $\nu_e$ . When inserted in a cavity of the detector, the external sources give an additional counting rate to the solar contribution, which can be evaluated from the source intensity. This additional event rate was correctly identified by the experiments. The procedure allowed thus an overall check of the experimental procedures: chemical extraction, counting, and analysis techniques.

After many years of operations, the weighted average of SAGE ( $65.4 \pm 5$  SNU), GALLEX ( $73.1 \pm 7$  SNU), and GNO ( $62.9 \pm 6$  SNU) results is

$$\langle \sigma \Phi \rangle_{Ga} = 66.1 \pm 3.1 \text{ SNU} \quad (12.11)$$

while the expected SSM (GS98) rate is  $126.6 \pm 4.2$  SNU.

**The real-time experiments (Kamiokande and SK).** A different detection strategy which confirmed the Cl and Ga deficit was used by the Kamiokande (Fukuda et al. 1996) experiment, and later on by Super-Kamiokande (SK), in Japan: neutrinos

interacting via elastic scattering on electrons

$$ES : \nu e^- \rightarrow \nu e^- \tag{12.12}$$

were detected in a large water tank. This reaction does not have an energy threshold, however it is detectable above the natural radioactivity background only when the final state electron has a sufficiently high energy. This method can only reveal the highest energy neutrinos coming from the  $^8\text{B}$  (Fig. 12.3).

The Kamiokande was an experiment led by M. Koshiba. It used a  $\sim 2.2$ kt tank filled with purified water and viewed by 948 20" photomultiplier, providing  $\sim 20\%$  surface coverage. The innermost 0.68 kt of the detector served as the fiducial volume for solar neutrino detection. The energy threshold varied from the initial 9MeV to 7MeV after subsequent detector improvements. The outer portion of the detector was instrumented with 123 PMTs to serve as a muon veto, and additional water was added to shield against  $\gamma$ -rays from the surrounding rock.

The electron scattering method is sensitive to all neutrino types; however, the cross section for  $\nu_e$  is approximately 6 times larger than for  $\nu_\mu$  or  $\nu_\tau$ . The reason is that reaction (12.12) occurs for all flavors through  $Z^0$  exchange, Fig. 12.4a, while for  $\nu_e$  also through  $W^\pm$  exchange, Fig. 12.4b. The final state electron is emitted in a direction correlated with that of the incoming neutrino. Thus, by relating event directions with the position of the Sun, one can remove a large background uncorrelated with the solar position to reveal solar neutrino events in a forward cone, Fig. 12.5.

The first result of Kamiokande was based on a livetime of 450 days through May 1988. The number of measured events was  $(46 \pm 15)\%$  with respect to the SSM prediction. The statistics increased with time until 1995, before it was succeeded by SK. Kamiokande was the first experiment to record solar neutrinos event by event, establish their solar origin through a correlation with the direction to the Sun, and to provide direct information on the  $^8\text{B}$  energy spectrum.

The most accurate measurement of solar  $\nu_e$  through reaction (12.12) is due to SK-III, which ran from August of 2006 through August of 2008 with a lower total energy threshold of 5 MeV (Abe et al. 2011). The Kamiokande and SK results were expressed in terms of neutrino flux from the  $^8\text{B}$  reaction. At present, the latest result from SK-III (Smy et al. 2013) is

$$\Phi_{\nu_e}(^8\text{B}) = (2.39 \pm 0.04_{\text{stat}} \pm 0.05_{\text{sys}}) \times 10^6 \text{ cm}^{-2} \text{ s}^{-1} \tag{12.13}$$

**Fig. 12.4** Feynman diagrams for **a** the  $\nu_e, \nu_\mu$  and  $\nu_\tau$  scattering on electrons through a neutral current weak interaction and **b** the charged current scattering of a  $\nu_e$  on electron

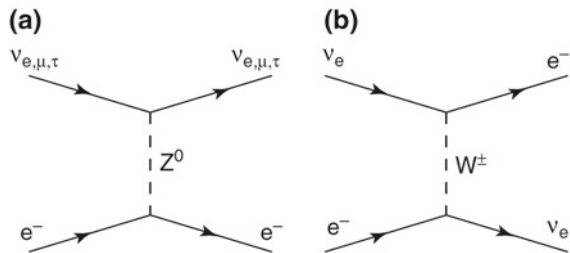
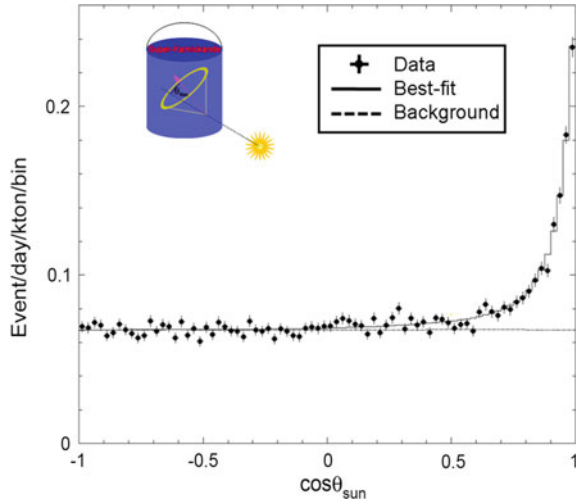




**Fig. 12.5** Angular distribution of solar neutrino event candidates detected by SK-III in the energy range between 5.0 and 20.0 MeV. The area under the *dotted line* is the contribution from remaining background events. The area between the *solid* and *dotted line* indicates the elastic scattering peak. The definition of the angle  $\theta_{\text{sun}}$  is in the inset. *Credit* Kamioka Observatory, ICRR (Institute for Cosmic Ray Research), The University of Tokyo



in agreement with the Kamiokande result of  $(2.80 \pm 0.19 \pm 0.33) \times 10^6 \text{ cm}^{-2}\text{s}^{-1}$ . The neutrino flux (12.13) is  $\sim 50\%$  smaller than expected from the SSM (compare with the predictions shown in Table 12.2).

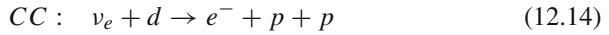
All the above results indicate that there are “missing” neutrinos from the Sun, when data are compared to the SSM. Because neutrino oscillations were already observed in atmospheric neutrinos, they represent a natural explanation for the problem. However, none of the above experiments was able to conclusively prove that the lack of solar electron neutrinos was not connected with a combination of experimental problems, or to shortcomings of the theory. They were all  $\nu_e$  *disappearance experiments*. Oscillations produce neutrino of different flavors but conserve the total number. Neutrino *appearance experiments* should be able to observe neutrinos of flavor different from  $\nu_e$ . The  $\nu_\mu$  (or  $\nu_\tau$ ) appearance through charged current (CC) interactions produces the corresponding charged lepton. Nevertheless, the muon (or tau) rest mass is much larger than the energy corresponding to solar neutrinos, and the CC reactions cannot occur. The problem was solved by the SNO experiment, which measured the fraction of  $\nu_\mu + \nu_\tau$  in the neutrino flux from the Sun using their neutral current (NC) interactions.

## 12.4 The SNO Measurement of the Total Neutrino Flux

The Sudbury Neutrino Observatory (SNO) in Canada recorded data from 1999 until 2006. It was able to detect Cherenkov light emitted by charged particles crossing the detector. The detector was a 12-m diameter spherical acrylic vessel viewed by an array of 9,500 20-cm PMTs, covering 56% of the spherical surface. It was filled with 1,000 tons of heavy water ( $\text{D}_2\text{O}$ ) contained in the inner volume, and surrounded by 1,500 tons of normal water used for screening purpose. Heavy water is essential to the operation of CANadian Deuterium Uranium (CANDU) nuclear power reactors.  $\text{D}_2\text{O}$

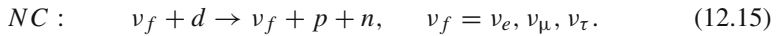
is used as both a moderator and a heat transfer agent. The heavy water is extracted from the lake Ontario water. The SNO experiment loaned heavy water from the Atomic Energy of Canada Limited. The reactions that occur in heavy water are:

- the elastic scattering (ES) on electron (12.12). As in the normal water, the ES is sensitive to neutrinos of any flavor, but the cross section for  $\nu_e$  is largely enhanced by  $W^\pm$  exchange:  $\sigma(\nu_e e \rightarrow \nu_e e) \simeq 6 \times \sigma(\nu_{\mu,\tau} e \rightarrow \nu_{\mu,\tau} e)$ .
- the  $\nu_e$  CC interaction on the proton of the deuteron  $d = (pn)$ :



which only occurs for  $\nu_e$  through a  $W^\pm$  exchange. With the CC reaction, the flux of higher energy  $\nu_e$  can be probed by detecting the produced electron. The deuterium breakup threshold is 1.44 MeV; the electrons carry off most of the energy and thus provide significant information on the incident neutrino spectrum. The electron is detected through its Cherenkov emission in water.

- the deuterium dissociation through a  $Z^0$  exchange:



A  $\sim 2.2$  MeV photon is emitted as a result of the  $d$  dissociation in  $p + n$ .

Operations were carried out in three phases (Jelley et al. 2009). The first phase of SNO (SNO-I, from November 1999 through May 2001) operated with pure heavy water (Ahmad et al. 2002). No charged particles above the Cherenkov threshold are present in reaction (12.15). However, the neutron produced in the NC reaction can be captured on deuterium, releasing a 6.25 MeV  $\gamma$ -ray. This  $\gamma$ -ray can produce a signal in the PMTs through a Compton scattering on electrons of the medium, yielding light for recoils above the Cherenkov threshold. The data contain events from all of the three above mentioned reactions (CC, NC, ES) plus a small background. The results of an analysis aimed at detecting events above an effective kinetic energy of 5 MeV is shown in Fig. 12.6a. The CC and ES reactions could be resolved through the use of the strong directional dependence of the ES reaction. The neutron capture efficiency was measured by deploying a  $^{252}\text{Cf}$  source at various positions throughout the heavy water volume.

In the second SNO phase (SNO-II) (Aharmim et al. 2005), two tons of purified NaCl were dissolved in the water, in order to increase the neutron capture rate and energy release through the reaction  $n + {}^{35}\text{Cl} \rightarrow {}^{35}\text{Cl}^* \rightarrow {}^{35}\text{Cl} + \gamma$ . Data were accumulated from July 2001 through August 2003. Detector calibrations completed in SNO I were repeated and extended in SNO II. The analysis, aimed to unfold from the data the solar  ${}^8\text{B}$  spectrum shape, was performed for a kinetic energy threshold of 5.5 MeV. The result of SNO-II are shown in Fig. 12.6b. In SNO-I and -II, the CC, ES, and NC rates were determined by a statistical analysis that decomposed the common signal, the Cherenkov light, into the three contributing components. The analysis made use of the angular correlations with respect to the Sun in ES events and of the energy differences in the CC-, ES-, and NC-associated light.

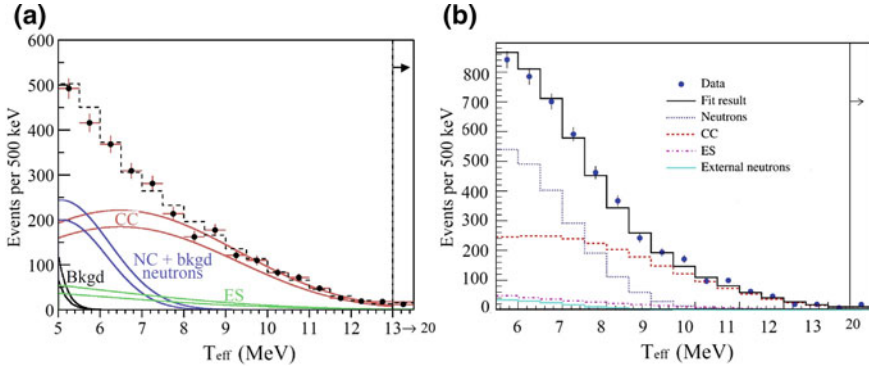


**Fig. 12.6** **a** Kinetic energy spectrum (*brown* data points) for events with measured energy  $T_{eff} \geq 5$  MeV occurring inside the fiducial region ( $R \leq 550$  cm) in the SNO-I. Also shown are the Monte Carlo predictions for charged-current (CC = *red lines*), elastic scattering (ES = *green lines*), and neutral current (NC) and background (bkgd) neutron events (*purple lines*). The simulations are scaled to fit the results. The *dashed line* represents the summed components, and the bands show the statistical uncertainties from the signal-extraction fit. **b** The same, for the salt phase SNO-II which increased the neutron (*dotted line*) capture rate. Courtesy of prof. Arthur B. McDonald and the SNO collaboration

In a third phase (SNO-III, from November 2004 to November 2006), the separation of the NC and CC/ES signals was accomplished by direct counting of NC neutrons. The salt introduced in SNO-II was removed and an array of a specially designed proportional counters was deployed in the heavy water for neutron detection. The 40 strings of proportional counters were anchored to the inner surface of the acrylic vessel, forming a lattice on a 1-m grid. The counters were filled with a 85:15 % mixture of  $^3\text{He}$  and  $\text{CF}_4$ , and the NC detection occurred through the reaction  $n + ^3\text{He} \rightarrow p + ^3\text{H}$ ; the final  $p^3\text{H}$  state has a total kinetic energy of 764 keV. The signals from each string were amplified and digitized. The neutron detection efficiency and the response of the arrays were determined with a variety of neutron calibration sources. Cherenkov light signals from CC, NC, and ES reactions were still recorded by the PMTs, though the rate of such NC events from reactions (12.15) was significantly suppressed due to neutron absorption in the  $^3\text{He}$  proportional counters.

The SNO-I/II and SNO-III results are in generally good agreement, and both separately and in combination established the following:

- The total flux of active neutrinos  $\nu_f = \nu_e + \nu_\mu + \nu_\tau$  from  $^8\text{B}$  decay measured through NC interactions corresponds to

$$\Phi_{SNO}^{NC} = \Phi_{\nu_f}({}^8\text{B}) = (5.25 \pm 0.16_{\text{stat}} \pm 0.13_{\text{sys}}) \times 10^6 \text{ cm}^{-2}\text{s}^{-1}. \quad (12.16)$$

in good agreement with SSM predictions, see Table 12.2.

- The flux of the  $\nu_e$  flavor producing CC interactions is (SNO-II)

$$\Phi_{SNO}^{CC} = \Phi_{\nu_e}({}^8\text{B}) = (1.68 \pm 0.06_{\text{stat}} \pm 0.09_{\text{sys}}) \times 10^6 \text{ cm}^{-2}\text{s}^{-1}. \quad (12.17)$$

- The flux of the ES interactions is (SNO-II)

$$\Phi_{SNO}^{ES} = (2.35 \pm 0.22_{\text{stat}} \pm 0.15_{\text{sys}}) \times 10^6 \text{ cm}^{-2} \text{ s}^{-1} \quad (12.18)$$

with  $\Phi^{ES} \simeq \Phi_{\nu_e} + (1/6)\Phi_{\nu_\mu + \nu_\tau}$  due to the relative weights on ES of different flavors.

- There is no statistically significant day-night effects (due to the passage of detected neutrinos through the Earth) or spectral distortions in the region of the  $^8\text{B}$  neutrino spectrum above 5 MeV.

This result clearly indicates that  $\Phi_{\nu_\mu + \nu_\tau} = \Phi_{\nu_f} - \Phi_{\nu_e}$  is nonzero, providing a definitive proof that 2/3 of the  $^8\text{B}$  solar electron neutrinos, on their way to the Earth, changed flavor. On the other hand, the *total* number of solar neutrinos as measured through the NC is in agreement with the SSM expectation.

## 12.5 Oscillations and Solar Neutrinos

The solution of the solar neutrino problem in terms of new physics in the neutrino sector was clearly given by a nonsolar neutrino experiment in 2002. This year is very often denoted as the “annus mirabilis” of solar neutrino physics: in April the first SNO result including NC showed that the total neutrino flux was compatible with the SSM; in October the Nobel prize was awarded to R. Davis and M. Koshiba for the detection of cosmic neutrinos; in December the first results of KamLAND offered the first clear terrestrial confirmation of the validity of the oscillation solution to the solar neutrino problem.

The **Kamiokande Liquid scintillator ANtineutrino Detector (KamLAND)** was a 1,000 ton ultra-pure liquid scintillator detector located at the old Kamiokande’s site in Japan. The primary goal was a long-baseline (flux-weighted average distance of  $\sim 180$  km) neutrino oscillation studies using  $\bar{\nu}_e$  emitted from a large number of nuclear reactors in the central region of Japan. Prior to the earthquake and tsunami of March 2011, Japan generated  $\sim 30\%$  of its electrical power from nuclear reactors (more than 60 GW). In commercial nuclear reactors the energy is released in neutron induced fissions with a nuclear fuel constituted by uranium enriched (to 2–5%) in the  $^{235}\text{U}$  isotope. The most important processes are of the type  $n + ^{235}\text{U} \rightarrow X_1 + X_2 + 2n$  and result in the production of typically two neutrons (that can therefore sustain a chain reaction), two fragments  $X_1$  and  $X_2$  and thermal energy. The fragments of the fission are too rich in neutrons (the  $^{235}\text{U}$  has 92 protons and 143 neutrons) and to reach stability they must undergo a succession of beta decays (on average a total of six), therefore emitting an average of 6  $\bar{\nu}_e$ . From a knowledge of nuclear physics it is possible to compute in detail the decay chains that are generated by the nuclear fissions, and from the knowledge of the reactor power it is possible to estimate the flux and energy spectrum of the emitted  $\bar{\nu}_e$ . They have energy below 10 MeV, with an average value  $E_{\bar{\nu}_e} \sim 3$  MeV.

As a  $\bar{\nu}_e$  disappearance experiment, KamLAND studied the flux and the energy spectrum of positrons produced in the inverse beta-decay reaction

$$\bar{\nu}_e + p \rightarrow e^+ + n. \quad (12.19)$$

The prompt positron annihilation and the delayed coincidence of a 2.2 MeV  $\gamma$ -ray from neutron capture on a proton was used to identify the  $\bar{\nu}_e$ . With a prompt-energy analysis threshold of 2.6 MeV, this experiment had a sensitivity for neutrino oscillations down to  $\Delta m^2 \sim 10^{-5} \text{ eV}^2$ . The result of this experiments is in relation to solar  $\nu_e$  disappearance through the  $CP$  theorem [Chap. 6 of Braibant et al. (2011)], which assumes that the properties of particles and antiparticles are strictly correlated and in particular that

$$P(\nu_\alpha \rightarrow \nu_\beta) = P(\bar{\nu}_\alpha \rightarrow \bar{\nu}_\beta), \quad (12.20)$$

where  $P$  represents the oscillation probability in vacuum. The search for the violating  $CP$  effects in the neutrino sector is a fascinating and very important topic in particle physics that will not be discussed in this book.

The first KamLAND result with a 162 ton·y exposure gave a ratio of observed to expected number events of  $(0.611 \pm 0.085_{\text{stat}} \pm 0.041_{\text{sys}})$ . With increased statistics, KamLAND observed not only the distortion of the  $\bar{\nu}_e$  spectrum, but also for the first time the oscillatory feature of the survival probability expected from neutrino oscillations, Fig. 12.7. The best fit for two-flavor oscillations using Eq. (11.46) gave

$$\Delta m_{12}^2 = (7.9 \pm 0.6) \cdot 10^{-5} \text{ eV}^2; \quad \tan^2 \theta_{12} = (0.40 \pm 0.10), \quad (12.21)$$

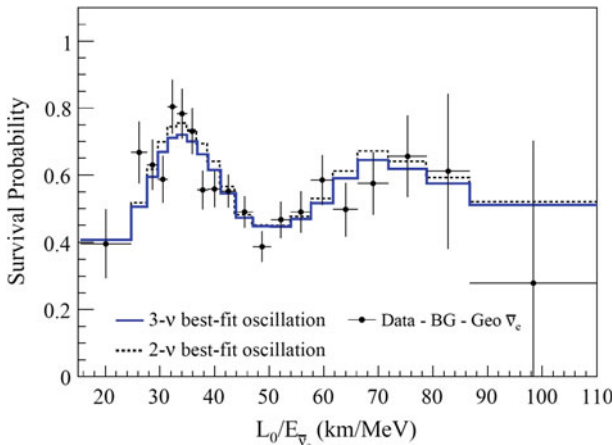


**Fig. 12.7** The ratio of the measured  $\bar{\nu}_e$  spectrum (after subtraction of the background) to the predicted one without oscillations as a function of  $L_0/E$ , where  $L_0 = 180 \text{ km}$ . The histogram represents the survival probability based on the best-fit parameter values from the two- and three-flavor neutrino oscillation analyses. *Credit* Particle Data Group (Beringer et al. 2012)

as shown by the dashed histogram in Fig. 12.7. Their results in terms of neutrino oscillation parameters (in this case, the  $\bar{\nu}_e$  oscillations occur in vacuum) are in good agreement with the results obtained using solar neutrinos when matter effects are included, as discussed in the following.

Note that the above parameters are different from those derived from atmospheric neutrino experiments and accelerator long-baseline  $\nu_\mu$  disappearance, Sect. 11.10. This arises from the fact that three neutrino families are known; the mixing among different flavors depends on two different squared mass differences and on a  $3 \times 3$  matrix with three mixing angles.

## 12.6 Oscillations Among Three Neutrino Families<sup>1</sup>

In the case of three flavors, the mixing between flavor and mass eigenstates is described by a  $3 \times 3$  unitary matrix, similarly to the Cabibbo-Kobayashi-Maskawa one describing the mixing among quarks (Braibant et al. 2011). The unitary matrix for neutrino mixing is called Pontecorvo-Maki-Nakagawa-Sakata (PMNS) matrix and it can be parameterized as ( $f = e, \mu, \tau; j = 1, 2, 3$ )

$$U_{fj} = \begin{pmatrix} c_{12}c_{13} & s_{12}c_{13} & s_{13}e^{-i\delta} \\ -s_{12}c_{23} - c_{12}s_{23}s_{13}e^{i\delta} & c_{12}c_{23} - s_{12}s_{23}s_{13}e^{i\delta} & s_{23}c_{13} \\ s_{12}c_{23} - c_{12}s_{23}s_{13}e^{i\delta} & -c_{12}s_{23} - s_{12}c_{23}s_{13}e^{i\delta} & +c_{23}c_{13} \end{pmatrix} \quad (12.22)$$

or, equivalently, as

$$U_{fj} = \begin{pmatrix} 1 & 0 & 0 \\ 0 & c_{23} & s_{23} \\ 0 & -s_{23} & c_{23} \end{pmatrix} \begin{pmatrix} c_{13} & 0 & s_{13}e^{-i\delta} \\ 0 & 1 & 0 \\ -s_{13}e^{i\delta} & 0 & c_{13} \end{pmatrix} \begin{pmatrix} c_{12} & s_{12} & 0 \\ -s_{12} & c_{12} & 0 \\ 0 & 0 & 1 \end{pmatrix} \quad (12.23)$$

(abbreviations, e.g.,  $s_{13} = \sin \theta_{13}$ , are used). The phase angle  $\delta$  would allow the  $CP$ -violation in the leptonic sector.

The limit of two-flavor oscillations was already discussed in Sect. 11.8, where the mixing angle was denoted as  $\vartheta$ . Extending the discussion to 3 flavors,  $\vartheta$  can indicate one of the above mixing angles  $\theta_{12}, \theta_{23}, \theta_{13}$  in (12.22). The numerical values of the matrix components and the differences between mass squared have been measured with atmospheric and solar experiments, and using reactors and accelerators, as summarized in Table 12.3. The measured values of the mixing angles are reported in Sect. 12.8.

The more general formulas for the probability of three flavor neutrino oscillations are rather complicated (Lipari 2001). They are obtained from Eq. (11.43) using the matrix  $U$  (12.22). The formulas can be greatly simplified if there is a *hierarchy*

<sup>1</sup> This section can be skipped in the early reading steps.

**Table 12.3** Summary of experiments studying neutrino oscillations

Source	Experiments	Neutrino Type	$\bar{E}$ (GeV)	$L$ (km)	$\Delta m_{\min}^2$ (eV <sup>2</sup> )
Reactors	Chooz, Daya Bay, Reno	$\bar{\nu}_e$	$10^{-3}$	1	$10^{-3}$
Reactors	KamLAND	$\bar{\nu}_e$	$10^{-3}$	100	$10^{-5}$
Accelerator	Chorus, Nomad	$\nu_\mu, \bar{\nu}_\mu$	1	1	$\sim 1$
Accelerator	K2K, MINOS, OPERA	$\nu_\mu, \bar{\nu}_\mu$	1	$300 \div 700$	$10^{-3}$
Atmospheric <sup>a</sup>	SK, Soudan	$\nu_{\mu,e}, \bar{\nu}_{\mu,e}$	1	$10 \div 10^4$	$10^{-1} \div 10^{-4}$
Atmospheric <sup>b</sup>	SK, MACRO	$\nu_\mu, \bar{\nu}_\mu$	10	$10^2 \div 10^4$	$10^{-1} \div 10^{-3}$
Sun	SK, SNO, GALLEX, ...	$\nu_e$	$10^{-3}$	$10^8$	$10^{-11}$

The columns report: the source of neutrinos; some of the most significant experiments; the neutrino flavor at the source; the mean path length from the source to the detector; the minimum value of  $\Delta m^2$  which can be tested with the formalism of two-flavor oscillations

<sup>a</sup> The neutrino flavor is detected from the contained event topology

<sup>b</sup> Measured by  $\nu_\mu$ -induced upgoing muons

between the neutrino masses, for example <sup>2</sup>

$$m_3 \gg m_2 > m_1 > 0, \quad (12.24)$$

yielding:

$$|\Delta m_{13}^2| \simeq |\Delta m_{23}^2| \gg |\Delta m_{12}^2| > 0. \quad (12.25)$$

This is exactly the situation depicted by measurements of atmospheric neutrinos on one hand (*atm*), and solar neutrinos and KamLAND on the other ( $\odot$ ), which demonstrated that  $\Delta m_{\text{atm}}^2 \gg \Delta m_{\odot}^2$ . The first mass difference approximates  $|\Delta m_{23}^2| \simeq |\Delta m_{13}^2|$  and the latter  $|\Delta m_{12}^2|$ , Sect. 12.8.

In this situation, there are basically two characteristic oscillation lengths given by Eq. (11.47), and that involving  $|\Delta m_{12}^2|$  ( $L_{12} \simeq E/\Delta m_{12}^2$ ) is longer. Then, there is a range of  $E$  and  $L$  values such that “short” fluctuations (i.e., those relating to  $|\Delta m_{23}^2|$ ) are active, while the “long” oscillations have not yet developed. The probability of short oscillation ( $\alpha \neq \beta$ ) can be approximated by

$$P(\nu_\alpha \rightarrow \nu_\beta) = 4|U_{\alpha 3}|^2|U_{\beta 3}|^2 \sin^2\left(\frac{\Delta m_{13}^2}{4E}L\right). \quad (12.26)$$

This formula is similar to that for two-flavor oscillations (11.46), and (for a given energy) the probability oscillates with a single frequency, related to the mass difference  $|\Delta m_{13}^2| \simeq |\Delta m_{23}^2|$ . For these “short” oscillations the probability amplitudes only depend on the elements of the third column of the mixing matrix  $U$  (12.22).

<sup>2</sup> This is usually called *normal ordering* or *Normal Hierarchy*. Another possible solution is the case with  $0 < m_3 \ll m_1 < m_2$ , which corresponds to an *inverted ordering* or *Inverted Hierarchy*. We do not consider these aspects of  $\nu$  physics.



Explicitly, one has

$$\begin{aligned} P(\nu_e \rightarrow \nu_\mu) &= 4|U_{e3}|^2|U_{\mu3}|^2 \sin^2\left(\frac{\Delta m_{13}^2 L}{4E}\right) \\ &= s_{23}^2 \sin^2 2\theta_{13} \sin^2\left(\frac{\Delta m_{13}^2 L}{4E}\right) \end{aligned} \quad (12.27a)$$

$$\begin{aligned} P(\nu_e \rightarrow \nu_\tau) &= 4|U_{e3}|^2|U_{\tau3}|^2 \sin^2\left(\frac{\Delta m_{13}^2 L}{4E}\right) \\ &= c_{23}^2 \sin^2 2\theta_{13} \sin^2\left(\frac{\Delta m_{13}^2 L}{4E}\right) \end{aligned} \quad (12.27b)$$

$$\begin{aligned} P(\nu_\mu \rightarrow \nu_\tau) &= 4|U_{\mu3}|^2|U_{\tau3}|^2 \sin^2\left(\frac{\Delta m_{13}^2 L}{4E}\right) \\ &= c_{13}^4 \sin^2 2\theta_{23} \sin^2\left(\frac{\Delta m_{13}^2 L}{4E}\right) \end{aligned} \quad (12.27c)$$

Because in atmospheric neutrinos only (12.27c) gives observable results and the electron neutrinos are practically not affected by oscillations,  $\sin^2 2\theta_{13}$  should be very small. The small  $\theta_{13}$  mixing angle was recently measured by dedicated experiments, Sect. 12.6.2.

The survival probability for diagonal transitions ( $\alpha = \beta$ ) takes also the simple form (for instance for  $\nu_e$ ):

$$\begin{aligned} P(\nu_e \rightarrow \nu_e) &= 1 - [1 - |U_{e3}|^2]|U_{e3}|^2 \sin^2\left(\frac{\Delta m_{13}^2 L}{4E}\right) \\ &= 1 - \sin^2 2\theta_{13} \sin^2\left(\frac{\Delta m_{13}^2 L}{4E}\right) \end{aligned} \quad (12.28)$$

It coincides with the  $\nu_e$  survival probability in the two-flavors case (11.46) with the substitutions:  $\Delta m^2 \rightarrow \Delta m_{13}^2$  and  $\vartheta \rightarrow \theta_{13}$ .

### 12.6.1 Three Flavor Oscillation and KamLAND

When the condition  $x = \frac{\Delta m_{13}^2 L}{4E} \gg 1$  holds, the “short” oscillations formulas (12.27a–12.27c) and (12.28) are averaged out and “long” oscillations are active. This corresponds to the other extreme case, the detection of  $\bar{\nu}_e$  from KamLAND and solar neutrinos. If the argument  $x$  of the  $\sin^2(x)$  function is rapidly oscillating, only its average value is important. Thus, long-type oscillations are observed, where the electron neutrino survival probability is given by

$$P(\nu_e \rightarrow \nu_e) \simeq c_{13}^4 P + s_{13}^4 \quad (12.29)$$

with

$$P = 1 - \sin^2 2\theta_{12} \sin^2 \left( \frac{\Delta m_{12}^2 L}{4E} \right). \quad (12.30)$$

Because of the small value of  $\theta_{13}$  in (12.29),  $c_{13}^4 \simeq 1$ ,  $s_{13}^4 \simeq 0$  and the electron neutrino oscillations can be described by a formula which looks like that used for two-flavor oscillations. The fact that the  $\theta_{13}$  mixing angle is small can be appreciated in Fig. 12.7 by comparing the fit using (12.29) (the full blue line) with that obtained in the limit of two-flavor oscillations assuming  $\theta_{13} = 0$  (dashed line).

The KamLAND observations are thus simply explained by vacuum oscillations. To interpret the results of solar neutrino experiments, we must consider (i) the numerical value of  $\theta_{13}$  (Sect. 12.6.2), recently measured; (ii) the propagation of neutrinos in matter from the core of the Sun to the surface and in vacuum, on their way to the Earth, Sect. 12.7.

### 12.6.2 Measurements of $\theta_{13}$

Reactor  $\bar{\nu}_e$  disappearance experiments with  $L \sim 1$  km,  $E \sim 3$  MeV are sensitive to  $\sim E/L \sim 3 \times 10^{-3} \text{ eV}^2 \sim |\Delta m_{\text{atm}}^2|$ . At this baseline distance, the reactor  $\bar{\nu}_e$  oscillations driven by  $\Delta m_{\odot}^2$  are negligible. Therefore, as can be seen from Eq. (12.28), the quantity  $\sin^2 2\theta_{13}$  can be directly measured from  $\nu_e$  disappearance.

A reactor neutrino oscillation experiment at the Chooz nuclear power station in France was the first experiment of this kind in the 1990s. The detector was located in an underground laboratory with 300 m.w.e. rock overburden, at about 1 km from the reactor. It consisted of a central 5 tons target filled with 0.09% gadolinium loaded liquid scintillator, surrounded by an intermediate 17 tons and outer 90 tons regions filled with undoped liquid scintillator. Reactor  $\bar{\nu}_e$ 's were detected via the reaction (12.19). Gadolinium-doping was chosen to maximize the neutron capture efficiency. The Chooz experiment found no evidence for  $\bar{\nu}_e$  disappearance and the 90% c.l. upper limit on the  $\theta_{13}$  mixing angle was  $\sin^2 2\theta_{13} < 0.15$ .

The mixing angle  $\theta_{13}$  can be measured also using the  $\nu_{\mu} \rightarrow \nu_e$  appearance method through Eq. (12.27a) using a conventional neutrino beam at an accelerator [see details on Chap. 8 of Braibant et al. (2011)]. The K2K was the first long-baseline experiment to search for the  $\nu_e$  appearance signal in a  $\nu_{\mu}$  beam. Also MINOS searched for a nonnull value of this mixing angle.

Only in 2011, experimental indications of  $\nu_{\mu} \rightarrow \nu_e$  oscillations and a nonzero  $\theta_{13}$  have been reported by the T2K experiment. The baseline distance is 295 km between the J-PARC in Tokai, Japan and Super-Kamiokande. The T2K experiment is the first off-axis long-baseline neutrino oscillation experiment [Chap. 12 of Braibant et al. (2012)]. A narrow-band  $\nu_{\mu}$  beam produced by 30 GeV protons from the J-PARC Main Ring is directed  $2.5^\circ$  off-axis to SK. In this configuration, the  $\nu_{\mu}$  beam is tuned to the energy corresponding to the first oscillation maximum. Before the earthquake

of March 2011, T2K observed six candidate  $\nu_e$  events having all the characteristics of being due to  $\nu_\mu \rightarrow \nu_e$  oscillations, while the expectation for  $\theta_{13} = 0$  was 1.5 events. In 2013, T2K announced the observation of 28  $\nu_e$  appearance events with 4.6 predicted background events for  $\theta_{13} = 0$ . This result means that  $\theta_{13} = 0$  is excluded with a significance of  $7.5\sigma$ , and  $\sin^2 2\theta_{13} = 0.140^{+0.038}_{-0.032}$ .

In 2012 three reactor neutrino experiments (Daya Bay, Double Chooz and RENO), much improved with respect to the old Chooz experiment, reported their first results on reactor  $\bar{\nu}_e$  disappearance. Daya Bay and RENO measured reactor  $\bar{\nu}_e$ s with near and far detectors. The first results of Double Chooz was obtained with only a far detector. The  $\bar{\nu}_e$  detectors of all the three experiments have similar structures; an antineutrino detector consisting of three layers and an optically independent outer veto detector. The innermost layer of the antineutrino detector is filled with Gd-doped liquid scintillator; it is surrounded by a  $\gamma$ -catcher layer of liquid scintillator and an outermost layer filled with mineral oil. The outer veto detector is filled with purified water (Daya Bay and RENO) or liquid scintillator (Double Chooz).

The Daya Bay experiment measured  $\bar{\nu}_e$ s from the Daya Bay nuclear power complex (six 2.9 GW reactors) in China with six functionally identical detectors deployed in two near (470 and 576 m of flux-weighted baselines) and one far (1,648 m) underground halls. With only 55 days of live time, Daya Bay reported evidence at a level of  $5.2\sigma$  for nonzero  $\theta_{13}$ . Data taking is still in progress, and the latest result reported in Beringer et al. (2012) is  $\sin^2 2\theta_{13} = 0.089 \pm 0.010_{\text{stat}} \pm 0.005_{\text{sys}}$ , and the no-oscillation hypothesis is excluded with a significance of  $7.7\sigma$ . The RENO experiment measured  $\bar{\nu}_e$ s from six 2.8 GW reactors at Yonggwang Nuclear Power Plant in Korea with two identical detectors located at 294 and 1,383 m from the reactor array center. The RENO measurements (March 2013) give  $\sin^2 2\theta_{13} = 0.100 \pm 0.010_{\text{stat}} \pm 0.015_{\text{sys}}$  from 402 live days of data taking. Finally, Double Chooz measured  $\bar{\nu}_e$ s from two 4.25 GW reactors with a far detector at 1,050 m from the two reactor cores, giving  $\sin^2 2\theta_{13} = 0.109 \pm 0.030_{\text{stat}} \pm 0.025_{\text{sys}}$  with 228 live days of running.

## 12.7 Matter Effect and Experimental Results

The presence of matter changes drastically the pattern of neutrino oscillations: neutrinos interact with protons, neutrons and electrons. In particular, the presence of electrons significantly affect the propagation of  $\nu_e$  due to charged current processes of Fig. 12.4b. This induce a situation analogous to the electromagnetic process leading to the refractive index of light in a medium. This means that neutrinos in matter have a different effective mass than neutrinos in vacuum, and since neutrino oscillations depend upon the squared mass difference of the neutrinos, neutrino oscillations are different in matter than they are in vacuum.

For a pedagogical and beautiful description of quantum-mechanical physics of neutrino oscillation in vacuum and matter, we refer to Lipari (2001). For the latest results, refer to the *Neutrino mass, Mixing, and Oscillations* section of <http://pdg.lbl.gov/>. We limit in *Extras # 6* to discussion to a two-neutrino flavors scheme. Here,

it is derived a resonant condition for the neutrino energy, usually referred to as the *resonance energy*:

$$E_{res} = \frac{\Delta m_{12}^2 \cos 2\theta_{12}}{2\sqrt{2}N_e G_F} \quad (12.31)$$

which depends the Fermi constant  $G_F$ , on neutrino physics properties ( $\Delta m_{12}^2$  and  $\cos 2\theta_{12}$ ) and on solar properties (the electron number density in the Sun,  $N_e$ ). In the Sun,  $N_e$  changes considerably along the neutrino path. In the core, the matter density is about  $\rho \sim 150 \text{ g/cm}^3$  and it decreases monotonically towards a small value at the surface.

As a general results, the electron neutrino survival probability is a function of the neutrino energy  $E$  and depends on solar and neutrino physical properties:

$$P_{ee}(E) \equiv P_{(\nu_e \rightarrow \nu_e)}(E) = f(N_e; \Delta m_{12}^2, \theta_{12}, \theta_{13}) \quad (12.32)$$

Using the best-fit values obtained by KamLAND (12.21) in (12.31) with the density of the Sun core, we obtain the minimum energy for which the resonance condition occurs, which is of the order of  $E_{res} \lesssim 1 \text{ MeV}$ . This means that below  $\sim 1 \text{ MeV}$  (corresponding to the lower-energy solar neutrinos, those of the pp reaction with  $E < 0.42 \text{ MeV}$ ) oscillations occur as in vacuum. Matter effect strongly affects neutrinos arising from the  ${}^8\text{B}$  transitions observed by SK and SNO experiments, with  $E \gtrsim 5 \text{ MeV}$ .

Different measurements of the ratio between data and SSM prediction by solar neutrino experiments tightly constrained the  $P_{ee}$  values in the high-energy (matter-dominated) region, in the low-energy (vacuum-dominated) region and in the transition region, between 1 and 3 MeV. The Borexino experiment has a particularly important role.

**Borexino** (Calaprice et al. 2012) measures the  $\nu_e e$  elastic scattering (ES) by using a liquid scintillator as active target. One fundamental Borexino characteristic consists in the reduction of the radioactivity of the scintillator itself. This has been achieved using several radio-purification techniques developed by the physicists, chemists and engineers of the collaboration. This allows to test the SSM using neutrinos of lower energy than those of the  ${}^8\text{B}$  branch. As evident in Table 12.2, the uncertainty on the  ${}^7\text{Be}$  flux is smaller than that on  ${}^8\text{B}$ . As usual, the measured ES rate would depend on all the neutrino flavors, although dominated by the  $\nu_e$  flavor.

Borexino consists of 278 tons of a high-purity liquid scintillator, it is located at the Gran Sasso Laboratory in Italy and the operation began in 2007. The scintillation light yield is a measure of the energy imparted to the electron of the ES but has no sensitivity to direction. The scintillation photons are detected with an array of 2,200 PMTs mounted on the inside surface of the stainless-steel sphere. With a light yield of 500 detected photons per MeV, the energy resolution is approximately 5%

**Table 12.4** Summary of the interaction rates (column 2) of the different neutrino species measured by Borexino and the ratios with respect to SSM (column 3)

$\nu$ React.	Interaction rate counts (day 100 ton) <sup>-1</sup>	$\left(\frac{Data}{SSM}\right)$ ratio	$\Phi_{\nu_e}(E)$ (10 <sup>8</sup> cm <sup>-2</sup> s <sup>-1</sup> )	$\left(\frac{Data}{SSM}\right)/P_{ee}$ ratio
<sup>7</sup> Be	46.0 ± 1.5 ± 1.6	0.51 ± 0.07	48.4 ± 2.4	0.97 ± 0.09
<i>pep</i>	3.1 ± 0.6 ± 0.3	0.62 ± 0.17	1.6 ± 0.3	1.1 ± 0.2
CNO	<7.9	–	<7.7	<1.5
<sup>8</sup> B	0.22 ± 0.04 ± 0.01	0.31 ± 0.15	0.05 ± 0.01	0.91 ± 0.23

The derived flux and the ratio with respect to SSM when data are corrected for neutrino oscillations are reported in columns 4 and 5

at 1 MeV, and the position resolution is ~10–15 cm. The 0.862 MeV <sup>7</sup>Be neutrinos produce a recoil electron spectrum with a distinctive cut-off edge at 665 keV.

The Borexino results are reported in Table 12.4. Borexino was the first experiment able of making spectrally resolved measurements of solar neutrino interactions below 3 MeV. The measured interaction rates for the different channels are shown in the second column. The ratio between the data and the SSM predictions (using the AGSS09 as reported in Table 12.2) is shown in the third column. The Borexino results, and those of all the previously described experiments, indicate that the reduction with respect to the SSM predictions ranges between 1/3 and 1/2, depending on energy.

Using the oscillation probability derived from the best-value parameters from a global fit of all available data (Beringer et al. 2012), one can compare the Borexino results reported in Table 12.4 to the SSM expectations. Once the energy-dependent oscillation probability  $P_{ee}(E)$  is considered, the observed  $\nu_e$  flux on Earth at a given energy,  $Data(E)$  is related with the flux originated in the center of the Sun,  $\Phi_{\nu_e}(E)$ , through the relation:

$$Data(E) = P_{ee}(E) \cdot \Phi_{\nu_e}(E). \quad (12.33)$$

The  $\nu_e$  fluxes in the core of the Sun from different reactions after the correction from oscillation effects are reported in column four of Table 12.4. Finally, the ratio between the measured neutrino flux corrected for the neutrino oscillation effects and the SSM prediction is shown in the last column.

Figure 12.8 shows, in addition to that of Borexino, the values of different  $Data/SSM$  as measured from the experiments described in Sects. 12.3, 12.4 and 12.5 as a function of energy. The gray band corresponds to the expected  $P_{ee}$  from three-flavor neutrino oscillations including the matter effect in the Sun. For the computation, the oscillation parameters reported in Table 12.5 are used. The band is due to the uncertainties on the parameters.

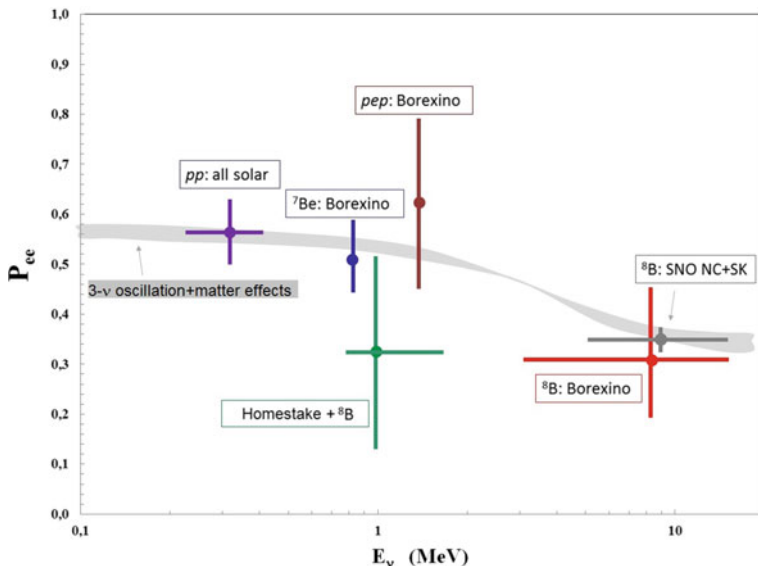


**Fig. 12.8** Electron neutrino survival probability  $P_{ee}$  as a function of energy measured by different experiments. With the exception of the  $^8\text{B}$  data,  $P_{ee}$  is determined by comparing measured fluxes with SSM predictions. The gray band represents the prediction of the SSM when neutrino oscillation in matter are considered

**Table 12.5** The best-fit values of the 3-neutrino oscillation parameters, derived from a global fit of the current neutrino oscillation results from Beringer et al. (2012)

Parameter	best-fit value ( $\pm 1\sigma$ )
$\Delta m_{\odot}^2$	$(7.58^{+0.22}_{-0.26}) \times 10^{-5} \text{ eV}^2$
$\Delta m_{\text{atm}}^2$	$(2.35^{+0.12}_{-0.09}) \times 10^{-3} \text{ eV}^2$
$\sin^2 \theta_{12}$	$0.306^{+0.018}_{-0.015}$
$\sin^2 \theta_{23}$	$0.42^{+0.08}_{-0.03}$
$\sin^2 \theta_{13}$	$0.0251 \pm 0.0034$

## 12.8 Summary of Experimental Results and Consequences for Neutrino Astrophysics

All existing compelling data on neutrino oscillations can be described assuming three-flavor neutrino mixing. In this case, there are only two independent neutrino mass squared differences. The numbering of massive neutrinos  $\nu_j$  is arbitrary. It proves convenient from the point of view of relating the mixing angles  $\theta_{12}$ ,  $\theta_{23}$  and  $\theta_{13}$  to observables, to identify  $|\Delta m_{21}^2|$  with the smaller of the two neutrino mass

squared differences. As it follows from the data, this mixing angle is responsible for the solar  $\nu_e$  and for the reactor  $\bar{\nu}_e$  oscillations observed by KamLAND. Then the larger neutrino mass square difference  $|\Delta m_{31}^2|$  or  $|\Delta m_{32}^2|$ , can be associated with the experimentally observed oscillations of the atmospheric neutrinos and accelerator long-baseline experiments (Sect. 11.9).

As  $\sin \theta_{13}$  is relatively small, it makes possible to identify the angles  $\theta_{12}$  and  $\theta_{23}$  with the neutrino mixing angles associated with the solar  $\nu_e$  and the dominant atmospheric  $\nu_\mu, \bar{\nu}_\mu$  oscillations, respectively. For this reason, the angles  $\theta_{12} = \theta_\odot$  and  $\theta_{23} = \theta_{\text{atm}}$  are often called *solar* and *atmospheric* neutrino mixing angles, while  $\Delta m_{21}^2 = \Delta_\odot$  and  $\Delta m_{31}^2 \simeq \Delta m_{32}^2 \simeq \Delta m_{\text{atm}}^2$  are often referred to as the *solar* and *atmospheric* neutrino mass squared differences.

As a summary, we present in Table 12.5 the best fit values of the PMNS matrix mixing parameters and mass squared differences derived from a global fit of the current neutrino oscillation data (Fogli et al. 2012; Beringer et al. 2012). The possibility of *CP*-violation in the leptonic sector depends on the phase parameter  $\delta$ , which presently is unknown.

### 12.8.1 Effects of Neutrino Mixing on Cosmic Neutrinos

Neutrino oscillations have effects on the flavor composition of astrophysical neutrinos arriving on Earth. High-energy neutrinos (Chap. 10) in galactic or extragalactic systems follow mainly from the production and decay of unstable hadrons, mainly charged pions. These hadrons may be produced when the accelerated protons in these environments interact with the ambient photon field in  $p\gamma$  and/or protons  $pp$  interactions, Sect. 8.2. The  $\nu_\tau, \bar{\nu}_\tau$  may also be produced by decay of heavy charmed mesons. However, the high energy threshold and low cross section for such reactions imply that the ratio of charmed meson to pion production is  $\sim 10^{-4}$  and the fraction of  $\nu_\tau/\nu_\mu$  another factor of ten smaller. Thus, in  $p\gamma$  and in  $pp$  collisions, typically one obtains the following ratio of intrinsic high-energy cosmic neutrinos in proximity of sources:

$$\Phi^0(\nu_e) : \Phi^0(\nu_\mu) : \Phi^0(\nu_\tau) = 1 : 2 : < 10^{-5} \simeq 1 : 2 : 0 \quad (12.34)$$

Vacuum neutrino mixing modify the observed ratios as described below, following the elegant method presented in Athar et al. (2000). As usual, we count both neutrinos and antineutrinos in the symbol for neutrinos. In most situation, the matter effect plays no role because high-energy cosmic neutrinos originate in regions of sufficient low densities around the sources. The presence of relatively dense objects between the distant high-energy neutrino sources and neutrino telescopes is unlikely. A different scenario arises when neutrinos are produced in dense environments, as in the core-collapse supernova, Sect. 12.11. In addition, when distant sources are involved, the change in the flavor composition of the high-energy cosmic neutrinos due to vacuum mixing is essentially energy independent over the entire energy range relevant for observations. This occurs because in the oscillation formulas (12.27a–12.27c) the



energy  $E$  appears as argument of an oscillating function  $[\sin^2(\Delta m^2 L/E)]$  whose effects are averaged out for large  $L$ .

The flavor oscillation probability in vacuum (12.26) and in the limit  $L \rightarrow \infty$  (after averaging the rapid oscillating  $\sin^2$  function) can be written as

$$P_{\alpha\beta} \equiv P(\nu_\alpha \rightarrow \nu_\beta) = \sum_j |U_{\alpha j}|^2 |U_{\beta j}|^2 \quad (12.35)$$

We can represent the oscillation probability as a symmetric matrix  $\mathcal{P}$ :

$$\mathcal{P} = \begin{pmatrix} P_{ee} & P_{e\mu} & P_{e\tau} \\ P_{e\mu} & P_{\mu\mu} & P_{\mu\tau} \\ P_{e\tau} & P_{\mu\tau} & P_{\tau\tau} \end{pmatrix} \equiv AA^T, \text{ with } A = \begin{pmatrix} |U_{e1}|^2 & |U_{e2}|^2 & |U_{e3}|^2 \\ |U_{\mu1}|^2 & |U_{\mu2}|^2 & |U_{\mu3}|^2 \\ |U_{\tau1}|^2 & |U_{\tau2}|^2 & |U_{\tau3}|^2 \end{pmatrix}. \quad (12.36)$$

Now, the neutrino flux from a far cosmic source can be expressed as a product of  $\mathcal{P}$  and the intrinsic flux  $\Phi^0(\nu_\alpha)$ ,  $\alpha = e, \mu, \tau$ :

$$\begin{pmatrix} \Phi(\nu_e) \\ \Phi(\nu_\mu) \\ \Phi(\nu_\tau) \end{pmatrix} = \mathcal{P} \begin{pmatrix} \Phi^0(\nu_e) \\ \Phi^0(\nu_\mu) \\ \Phi^0(\nu_\tau) \end{pmatrix} = AA^T \begin{pmatrix} \Phi^0(\nu_e) \\ \Phi^0(\nu_\mu) \\ \Phi^0(\nu_\tau) \end{pmatrix}. \quad (12.37)$$

We assume the standard ratio of the intrinsic cosmic neutrino flux (12.34) so that we obtain

$$A^T \begin{pmatrix} \Phi^0(\nu_e) \\ \Phi^0(\nu_\mu) \\ \Phi^0(\nu_\tau) \end{pmatrix} = \begin{pmatrix} |U_{e1}|^2 & |U_{\mu1}|^2 & |U_{\tau1}|^2 \\ |U_{e2}|^2 & |U_{\mu2}|^2 & |U_{\tau2}|^2 \\ |U_{e3}|^2 & |U_{\mu3}|^2 & |U_{\tau3}|^2 \end{pmatrix} \begin{pmatrix} 1 \\ 2 \\ 0 \end{pmatrix} \Phi^0(\nu_e) \quad (12.38)$$

$$= \begin{pmatrix} 1 \\ 1 \\ 1 \end{pmatrix} \Phi^0(\nu_e) + \begin{pmatrix} |U_{\mu1}|^2 - |U_{\tau1}|^2 \\ |U_{\mu2}|^2 - |U_{\tau2}|^2 \\ |U_{\mu3}|^2 - |U_{\tau3}|^2 \end{pmatrix} \Phi^0(\nu_e), \quad (12.39)$$

where we have used the unitarity condition, i.e.,  $\sum_j |U_{\alpha j}|^2 = 1$ . When  $|U_{e3}|^2 \ll 1$ , there is  $s_{13} \simeq 0$ ,  $c_{13} \simeq 1$  and  $|U_{\mu j}| \simeq |U_{\tau j}|$ . In fact, using the values reported in Table 12.5 it can be easily obtained that the numerical values of matrix elements in (12.22) are  $|U_{\mu1}| \simeq |U_{\tau1}| \simeq 0.4$ ,  $|U_{\mu2}| \simeq |U_{\tau2}| \simeq 0.6$ , and  $|U_{\mu3}| \simeq |U_{\tau3}| \simeq 0.7$ . For this reason, the second term in Eq.(12.39) is negligible. Hence with the constraints of the solar and atmospheric neutrino and the reactor data, we obtain from (12.39):

$$\begin{pmatrix} \Phi(\nu_e) \\ \Phi(\nu_\mu) \\ \Phi(\nu_\tau) \end{pmatrix} = A \begin{pmatrix} 1 \\ 1 \\ 1 \end{pmatrix} \Phi^0(\nu_e) \simeq \begin{pmatrix} 1 \\ 1 \\ 1 \end{pmatrix} \Phi^0(\nu_e). \quad (12.40)$$

where we have used the unitarity condition again. Therefore, we conclude that the ratio of the cosmic high-energy neutrino fluxes at far distances from us is (1:1:1). This only depends on the fact that the PMNS matrix elements in the second and third row are almost identical and on the flavor flux ratio (1:2:0) at the source.

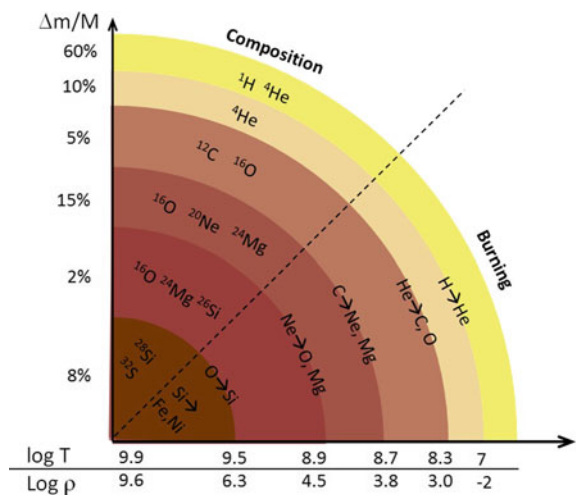
The message of this excursus in the neutrino oscillation formalism is clear. The observation of solar neutrinos contributed to the understanding of physics properties of these eluding particles. The neutrino oscillation effects must be considered when astrophysical properties are studied, as in the case of energy production in the Sun. Also high-energy neutrino from astrophysical sources, propagation effects changes the flavor composition ratio of neutrino arriving on Earth.

### 12.9 Formation of Heavy Elements in Massive Stars

Nucleosynthesis from nuclear fusion proceeds until the formation of nuclei with  $A \leq 60$ . Nuclei with  $A \sim 60$  (the *iron peak*) have the highest binding energy, Fig. 3.8. The luminosity of a main sequence star of mass  $M$  changes very little until it begins to move off the main sequence when the helium core has a mass about 10 % of  $M$ . The central temperature  $T$  is  $T \propto M$  and if  $M \geq 1.7 M_\odot$ , the CNO cycle dominates. In yet more massive stars, post-main sequence evolution proceeds by successive core and shell burning to produce nuclei with higher and higher binding energies.

For the most massive stars ( $M > 8 M_\odot$ ), the sequence continues with carbon and oxygen burning to produce silicon which can eventually be burned to create elements around the iron peak. It is therefore expected that in the final stages of evolution a very massive star will take up an “onion-skin” structure. The central core of iron peak

**Fig. 12.9** The onion-like structure in the final stage of a massive star ( $25 M_\odot$ ). The outermost envelope is composed of hydrogen and helium, and progressively heavier nuclei (up to iron) are layered, due to successive fusion reactions. Typical values of the mass, density  $\rho$  (in  $\text{g}/\text{cm}^3$ ) and temperature  $T$  (in K) of the different *shells* are indicated along the axes (Kippenhahn and Weigert 1990)



elements is surrounded by successive shells of silicon, carbon and oxygen, helium and hydrogen, Fig. 12.9.

As the nuclear reactions proceed through the sequence of carbon, neon, oxygen and silicon burning, the temperature in the core increases and consequently the time-scale for nuclear burning decreases. In particular, after helium burning, the time-scales are drastically reduced. The reason is due to the enormous neutrino luminosity that exceeds the optical luminosity of the star. As  $T \gtrsim 10^9$  K, thermal populations of  $e^+e^-$  pairs are created, which in turn can annihilate into  $\nu + \bar{\nu}$ . Neutrinos escape unimpeded from the stellar material and nuclear burning is needed to replace the huge amount of energy carried away. The time-scales for the silicon burning last only about tens of days.

Once the star inner region is made primarily of Fe, further compression of the core does not ignite nuclear fusion anymore; the star is unable to thermodynamically support its outer envelope made of concentric shells, Fig. 12.9. The rest of the star, without the support of the radiation, collapses, compressing the star nucleus, producing a *core-collapse supernova*.

## 12.10 Stellae Novae

At least as early as 185 AD, Chinese astronomers observed and recorded “guest stars”. These objects suddenly appeared in the sky, were visible for a certain length of time, and then faded away. The most brilliant guest star (or supernova in modern language) ever appeared was recorded on May, 1st 1006 by Chinese and Arab astronomers. The remnant of this explosion was first identified at radio wavelengths on the basis of historical evidence, and now observed with different instruments at different wavelengths up to TeV  $\gamma$ -rays (Acero et al. 2010). The most famous old supernova is that of 1054, also recorded by Chinese astronomers and not reported anywhere in Europe, although in the field of view. The appearance of a guest star was in contradiction with the Aristotle’s view of heavens mentioned in Chap. 8. The remnant of the 1054 supernova (SN) is the Crab Nebula, Sect. 9.5. At the center of the Crab there is a pulsar, which emits electromagnetic radiation. The remnants of the 185 and 1006 SN have no pulsars in the center.

Another historical SN occurred in 1572 and was recorded by Thyco Brahe, Sect. 6.2.2. Kepler, in October 1604, saw another *Stella Nova* (as the title of its book published in Prague in 1606), less bright than that of Tycho but remaining visible for a whole year. Another supernova, Cassiopeia A or Cas A, exploded in our galaxy between 1650 and 1680. Its remnant is a very strong radio source and observed at different wavelengths (Sect. 9.7), but it was not reported by contemporary observers. The advent of modern instruments and photographic plates allowed the observation of supernovae in other galaxies since 1885. See Bethe (1990) and Marschall (1988) for an introduction to SN.

A systematic study of supernovae was started around 1930 by Zwicky and Baade with newly developed Schmidt telescopes, which allowed photographing a large area of the sky. Since then astronomers have discovered between 10 and 30 SN each year,

and for most of them they measured the spectrum and the *light curve*, i.e., the optical luminosity as a function of time. SN are designated by the year of discovery and a capital letter.

Connected with the possibility of measuring the spectra of the discovered SNe, the astronomers found that there are at least two topologies. If the spectrum contains lines of hydrogen, the supernova is classified as *core-collapse* SN (or Type II). The remnants usually have a neutron star or a black hole at their center. Supernovae whose spectrum does not contain hydrogen lines are classified as *thermonuclear* or Type I supernovae. The inherent physical processes of the two SN topologies are completely different.

**Type I supernovae** play a fundamental role in cosmology. In fact, about 80% of Type I SNe (designated as Type Ia) have a characteristic light curve. The SNe of this subset are used as *standard candles* for determining the absolute magnitudes of galaxies, and hence their distance. There now appears to be agreement in theoretical models that Type Ia SN are due to the thermonuclear disruption of white dwarfs (WD, Sect. 6.6.1). A WD consists mainly of carbon and oxygen; if it accretes material from a companion star, carbon (or possibly helium) is ignited under highly degenerate conditions. Within a few seconds, a substantial fraction of the matter in the WD undergoes nuclear fusion, releasing enough energy ( $1 - 2 \times 10^{51}$  erg) to unbind the star in a supernova explosion (Hoeflich et al. 1993).

The end product of this nuclear burn is Fe, which is very abundant in the optical spectrum of Type I SNe. The total optical energy observed can be calculated from the assumption that most of the light is generated by the successive  $\beta^-$  decays of  $^{56}\text{Co} \rightarrow ^{56}\text{Ni} \rightarrow ^{56}\text{Fe}$  and that essentially all the mass of the star burns to these end products. Because the WD mass at the Chandrasekhar limit is fixed, the model explains why the light curves of all Type Ia SNe are similar. The absence of hydrogen lines is because the hydrogen accreted from the companion is quickly converted into helium, before the supernova explosion. However, some experimental aspects do not completely fit in the model and the mechanism of the burn is still unclear. In summary, the mechanism of Type I supernovae is less well understood than core-collapse (or Type II SNe).

## 12.11 Core-Collapse Supernovae (Type II)

A completely different physics mechanism is involved in Type II supernovae. Since the 1960s, it was generally accepted that the core of a massive star collapses at the end of its lifetime to something like a neutron star. After collapse, this incompressible core would bounce back the in-falling material and would start a shock, which would then propagate into the mantle and propel most of the star's mass to the interstellar medium. As for Type I SN, the total energy release observable with astronomical tools are of the order of  $10^{51}$  erg. However, this quantity represents in Type II SNe only  $\sim 1\%$  of the total estimated energy balance. About 99% of the energy must be emitted in a form not easily detectable: the neutrinos. This fundamental function in the supernova mechanism is much in contrast with the usual marginal position of neutrinos due to their weak interaction processes.

The kinetic energy of the matter emitted by the SN explosion can be estimated from the mass of the pre-collapsing star and the observed velocity of the ejecta ( $v \sim 10^{-2}c$ ). This gives typically  $\sim 10^{51}$  ergs for a  $M = 10 M_{\odot}$  star. The bolometric observations of electromagnetic radiation add a negligible contribution (about 1 %) to this energy balance. The final stage is a neutron star ( $M_{NS} = 1.4 M_{\odot}$ ,  $R_{NS} \simeq 10$  km, see Sect. 6.6.2) and the explosion destroys the remains of the star. Thus, the work  $U$  done by gravity in compressing the core represents a total energy of

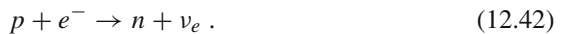
$$U = \left| \frac{3GM^2}{5R} - \frac{3GM_{NS}^2}{5R_{NS}} \right| \simeq \frac{3GM_{NS}^2}{5R_{NS}} \simeq 3 \times 10^{53} \text{ erg} \quad (12.41)$$

where  $G$  is the gravitational constant and  $R$  is the radius of the pre-collapsing star. This quantity is almost independent on the initial mass  $M$ , as  $R \gg R_{NS}$ . According to energy conservation, and based on the interaction theory among the constituents of the collapsing star, about 99 % of the gravitational energy must be converted into kinetic energy of massless particles different from the photons: the neutrinos.

The theoretical relationship between neutrinos and supernovae was experimentally confirmed in February 1987, when at least two underground detectors recorded a burst of neutrinos (Sect. 12.13) and a spectacular supernova was later observed by astronomers worldwide. That observation was a breakthrough in the long history of supernovae.

Analytic models and more and more sophisticated 1-D, 2-D and three-dimensional computer simulations of Type II SN have been developed to reproduce the observations. The first requirement is a good equation of state, both at densities below normal nuclear density  $\rho_N \sim 10^{14} \text{ g/cm}^3$  and above that density. The weak interaction processes involving neutrinos must be accurately modeled, namely CC capture and emission by nuclei; NC scattering by nuclei and nucleons; scattering by electrons; production of neutrino pairs from electron pairs; its inverse reaction, neutrino pair annihilation into  $e^+e^-$ . The results of these studies, still not definitive, are summarized below. For a detailed description, see Bethe (1990), Janka et al. (2007).

Near the end of its live, a massive star consists of concentric shells that are the relics of its previous burning phases, Fig. 12.9. Iron is the final stage of nuclear fusion, as the synthesis of any heavier element does not release energy. The dynamics of the collapse is very sensitive to the equation of state of the system, and in particular to the number of leptons per baryon,  $Y_e$ . In the early stage of the collapse,  $Y_e$  decreases through electron capture on protons bound inside Fe nuclei



This reaction is energetically favorable when the electrons have energies of a few MeV at the densities involved in the star center. Reaction (12.42) reduces the electron pressure, and produces nuclei in the core which are more neutron-rich. Consequently, some of the nuclei undergo  $\beta^-$ -decay producing  $\bar{\nu}_e$ . Iron-group nuclei can also suffer partial photodisintegration to  $\alpha$  particles. The above processes reduce the core energy

and its lepton density. The electron degeneracy pressure cannot longer stabilize the core and the star collapses (*core-collapse*).

An important change in the physics of the collapse occurs when the central density reaches  $\rho_t \approx 10^{12} \text{ g/cm}^3$ . Under these conditions, neutrinos produced by (12.42) are essentially trapped in the core, Fig. 12.10a. We can estimate the mean free path of  $\nu_e$  of energy  $E_\nu$  assuming that the scattering process is due to NC interactions on protons. The cross section of  $\nu_e p \rightarrow \nu_e p$  corresponds (Fig. 12.11)

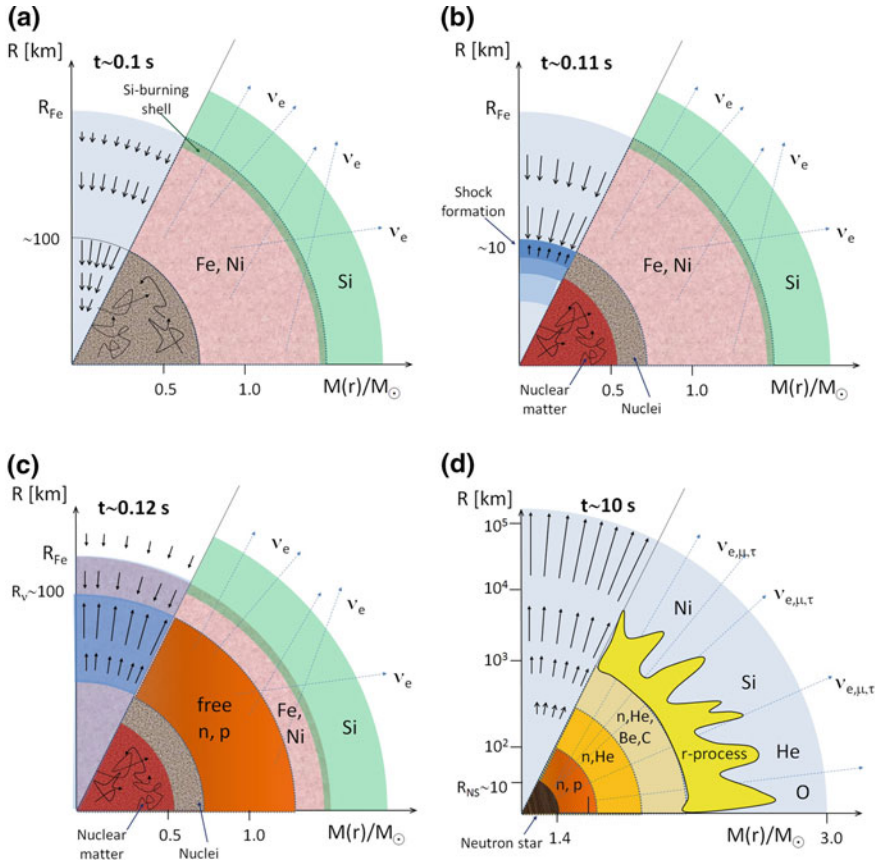


**Fig. 12.10** Schematic representation of the evolutionary stages of the core-collapse supernova. At  $t = 0$  the infall dynamics starts because the gravitational pressure is no longer supported by radiation pressure. Plot **a** shows the beginning of the neutrino trapping phase,  $t \simeq 0.1 \text{ s}$ ; **b** the bounce and shock formation,  $t \simeq 0.11 \text{ s}$ ; **c** the shock propagation and the neutronization  $\nu_e$  burst,  $t \simeq 0.12 \text{ s}$ ; **d** the neutrino-driven wind during the neutrino-cooling phase of the proto-neutron star,  $t \simeq 10 \text{ s}$ . Each *panel* displays the dynamical conditions on the *left*, with *arrows* representing velocity vectors. The nuclear composition as well as the nuclear and weak processes are indicated in the *lower half* of each *panel*. The *horizontal axis* gives mass information in units of the solar mass  $M_\odot$ . The *vertical axis* (not in scale) shows corresponding radii. The proto-neutron star has densities above that of nuclear matter  $\rho_\nu$

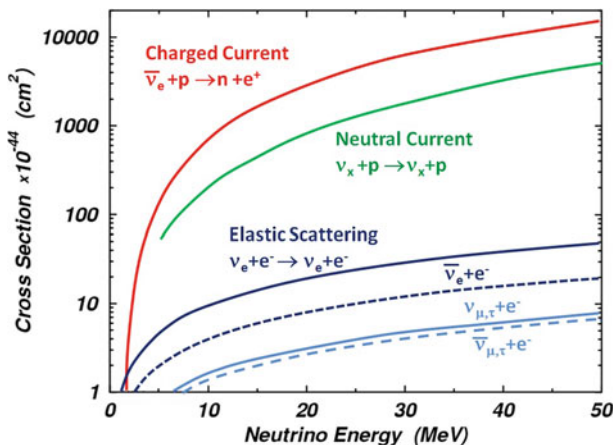


**Fig. 12.11** Cross section for different processes at energies of interest for SN neutrinos

to  $\sigma^{NC}(E) \simeq 2 \times 10^{-42} (E_\nu/10 \text{ MeV})^2 \text{ cm}^2$ . The interaction length (Sect. 3.2.3) of neutrinos is given by  $\lambda_\nu = 1/(\sigma^{NC} \cdot N_A \cdot \rho)$  [cm] where  $N_A$  is the Avogadro number and  $\rho$  the matter density. At a density  $\rho_t$  the  $\nu_e$  mean free path is given by

$$\begin{aligned} \lambda_\nu(E_\nu) &= \frac{1}{\sigma^{NC} \cdot N_A \cdot \rho_t} = \frac{1}{2 \cdot 10^{-42} \left(\frac{E_\nu}{10 \text{ MeV}}\right)^2 \cdot 6 \cdot 10^{23} \cdot 10^{12}} \\ &\simeq 10 \text{ km} \left(\frac{E_\nu}{10 \text{ MeV}}\right)^{-2}. \end{aligned} \quad (12.43)$$

This quantity is smaller than the radius of a sphere with density  $\rho_t$  and one solar mass; remember that the final state will be a 10 km neutron star with  $M = 1.4 M_\odot$ . This situation is called the *neutrino trapping phase*.

After this phase, the collapse proceeds essentially homogeneously, until nuclear densities ( $\rho_N \approx 10^{14} \text{ g/cm}^3$ ) are reached in the core. Since nuclear matter has a much lower compressibility, the core decelerates and the in-falling matter bounces in response to the increased nuclear matter pressure. This drives a shock wave into the outer core, i.e., the region of the iron core, which lies outside of the homologous core and in the meantime has continued to fall inwards at supersonic speed. The core bounce and the formation of a shock wave trigger the supernova explosion, Fig. 12.10b. The exact mechanism of the explosion and the crucial ingredients are still uncertain and controversial. A large fraction of the neutrinos produced in the neutronization phase by electron captures (12.42) leave the star quickly in the so-called *neutrino burst* at shock break-out. Energy is carried away with  $\nu_e$ s and the shock is weakened so much that it finally stalls and turns into an accretion shock at a radius between 100 and 200 km, because the matter downstream of the shock has velocities toward the center and continues falling inward, Fig. 12.10c. After the core bounce, a compact remnant forms at the center of the collapsing star, rapidly growing



by the accretion of in-falling stellar material. This nascent remnant will evolve to a neutron star or collapse to a black hole, depending on whether the progenitor star had a mass below or above  $\sim 25 M_{\odot}$ . The newly born neutron star is initially still proton-rich and contains a large number of degenerate electrons and trapped neutrinos. The region with matter density high enough to trap neutrinos is called the *neutrinosphere*.

The models of stellar collapse and subsequent explosion using computer simulations started at the end of 1960s. It was immediately recognized that the prompt shock following collapse alone is not sufficient to explain the SN explosion as the shock uses its energy in the outer core mostly by the dissociation of heavy nuclei into nucleons. The shock can be revived by absorption of the neutrinos emitted by the hot star that is formed at the center, the proto-neutron star. This *delayed shock* starts about half a second after the collapse.

In the delayed shock explosion scenario, the stalled shock wave can be revived by the neutrinos streaming off the neutrinosphere. Near the center, the temperature is very high,  $kT \sim 10\text{MeV}$  or more. In these conditions, electron pairs (which are plentiful already at lower temperature) transform rapidly into neutrino pairs of each flavor ( $f = e, \mu, \tau$ )

$$e^+ + e^- \rightarrow \bar{\nu}_f + \nu_f . \quad (12.44)$$

The rate of energy transfer by this process from electron to neutrino pairs has been calculated and found to be proportional to  $T^9$ . Therefore, during the infall, neutrino pair production is negligible. During the shock phase, it is only important in the inner part of the core, typically the inner solar mass or less. The production of neutrino pairs stops when the neutrino density has become high enough so that the inverse process to (12.44) reaches equilibrium. These neutrinos carry most of the energy set free in the gravitational collapse of the stellar core and deposit some of their energy in the layers between the nascent neutron star and the stalled shock front mainly by CC interactions on free nucleons

$$\nu_e + n \rightarrow e^- + p; \quad \bar{\nu}_e + p \rightarrow e^+ + n \quad (12.45)$$

and NC interaction of  $\nu_f$ . These processes increase the thermal energy of the stellar medium and the pressure behind the shock. At high matter density,  $\nu_f$  continue to be trapped. But as the heated layers begin to expand, the pressure increases and drives the shock outwards again. Thus, the density at its front decreases and finally it becomes smaller than the trapping density. At this point, neutrinos will be released: those close behind the shock escape immediately. Neutrinos from deep inside are free as they are able to make their way by diffusion. This delayed shock explosion scenario requires that a few percent of the radiated neutrino energy be converted to thermal energy of nucleons, leptons, and photons. This corresponds to the kinetic energy observed in the SN ejecta. The further cooling of the hot interior of the proto-neutron star then proceeds by neutrino-pair production and diffusive loss of neutrinos of all three lepton flavors, as depicted in Fig.12.10d. After several tens of seconds the compact remnant becomes transparent to neutrinos and the neutrino luminosity drops significantly.

### 12.11.1 GRB Supernovae

Some long-duration GRBs (Sect. 8.9) have been correlated with SN explosions, sometimes denoted as hypernovae (HNe). HNe have exceptional brightness, originated by high Ni production; they are now considered to be core-collapse with unusually high ejecta velocities and therefore high kinetic energies. In the HNe case, rapid stellar rotation is thought to be relevant.

GRBs are understood to be originated in ultrarelativistic, collimated jets. Some emission lines observed in many HNe suggest strong global asymmetry. Such events are interpreted as signatures of black hole-forming stellar collapses (*collapsars*). Matter around rapidly spinning black holes sets free energy in neutrinos, electromagnetic flux, and mass outflow with an efficiency of up to roughly 40% of the rest-mass energy of accreted material. A similar energy flux could be originated by fast rotating ( $P \simeq 1$  ms) neutron stars with a dynamo-generated magnetic field (*magnetars*). The jet and stellar explosion could be powered either by the rotational energy of the magnetar or by the gravitational and rotational energy of the collapsar.

Such requirements favor particular stars (as the so-called Wolf-Rayet stars) as progenitors, with special initial conditions as high angular momentum. In the present-day Universe HNe and GRB are rare (with a frequency of  $10^{-3}$  with respect to normal supernovae). Black hole forming core-collapse events and GRBs could be very common in the early Universe.

## 12.12 Neutrino Signal from a Core-Collapse SN

Despite enormous recent progress, the physics of core-collapse is not completely understood. The only experimental verification of the theoretical scenario depicted in the previous section occurred in 1987 (Sect. 12.13). Worldwide capabilities for supernova neutrino detection have increased by orders of magnitude since then. The next multi-messenger observation of a nearby core-collapse supernova will provide a great deal of information for both physics and astrophysics.

### 12.12.1 Supernova Rate and Location

The standard method to estimate the SN rate in our Galaxy is to scale optical observations from external galaxies. Another classic approach is to extrapolate the five historical SNe of the past millennium to the entire Galaxy. A third estimate can be made using measurements of  $\gamma$ -rays emitted by  $^{26}\text{Al}$ , that traces explosions of massive stars. All these observations give about 1–3 core-collapse SNe per century in our Galaxy and in its satellites.

To estimate the typical distance for a galactic SN, it is considered that core-collapse mark the final evolution of massive stars and thus they must occur in regions

of active star formation, i.e., in the galactic spiral arms, Sect. 2.7. Active star formation regions in other galaxies or in our Galaxy show significant presence of pulsars, SN remnants, molecular and ionized hydrogen, and hot and massive stars (OB-stars). All of these observables are consistent with a deficit of SNe in the inner Galaxy and a maximum at 3.0–5.5 kpc from the galactic center. Detailed models indicate that the characteristic distance of a possible SN event in our Galaxy is about 10 kpc from Earth.

### 12.12.2 The Neutrino Signal

At the beginning of a collapse, one expects a short, bright neutronization or breakout burst dominated by  $\nu_e$  from electron capture (12.42), with a time duration  $\Delta t \sim \mathcal{O}(10$  ms). This burst is followed by an accretion phase,  $\Delta t \sim \mathcal{O}(100$  ms), with  $\nu_e, \bar{\nu}_e$  produced by reactions (12.45). Finally during the cooling,  $\Delta t \sim \mathcal{O}(10$  s), the core loses most of its gravitational potential energy by production of  $\nu_f \bar{\nu}_f$  pairs. About 90% of the energy is released during this phase and, as neutrinos escape, the temperatures gradually decrease. An overall feature of the neutrino flux is that the luminosity is roughly equally divided among the three flavors. The neutrinos have an expected energy distribution whose average energies follow the hierarchy  $\langle E_{\nu_e} \rangle < \langle E_{\bar{\nu}_e} \rangle < \langle E_{\nu_\mu, \nu_\tau} \rangle$ . This ordering reflects the strength of interaction with matter:  $\nu_e$  have more interactions than  $\bar{\nu}_e$  because of the excess of neutrons in the core; in turn  $\bar{\nu}_e$  have more interactions than  $\nu_\mu, \nu_\tau$ , which are restricted to neutral currents. These expected average energies are largely model-dependent, ranging between  $\sim 12$  and 20 MeV.

Figure 12.12 shows an example of a flux prediction (Gava et al. 2009). There may be significant variations in the expected flux from supernova to supernova due to

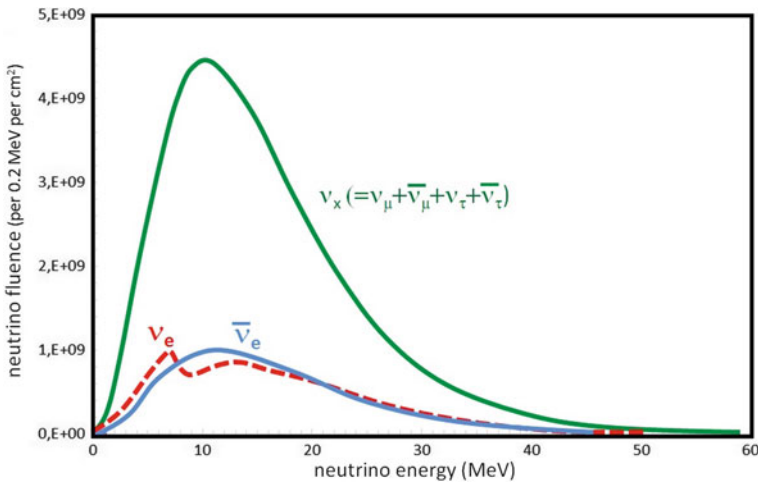


**Fig. 12.12** Example of supernova neutrino fluence (the time integrated neutrino flux) for the different flavor components. The prediction includes collective effects, which are responsible for the structure observed in the  $\nu_e$  dashed line

differences in the mass and composition of the progenitor, and possibly asymmetries, rotational effects, or magnetic field effects.

Matter oscillation effects modify the spectra as the neutrinos traverse dense matter, so the neutrino spectra arriving on Earth will depend both on supernova matter profiles and on neutrino oscillation parameters. Matter propagation affects differently neutrinos and antineutrinos (in particular  $\nu_e, \bar{\nu}_e$ ). Also the mass hierarchy (Sect. 12.5) plays a role: in the Normal Hierarchy there are two light and one heavy neutrino mass states; in the Inverted Hierarchy there are two heavy and one light neutrino mass states. The observation of neutrinos from a galactic SN would provide fundamental information on the neutrino physics (Raffelt 1999), improving the constraints obtained with SN1987A.

Supernova neutrinos have energies (10–20 MeV) intermediate between those of solar (1 MeV) and atmospheric neutrinos (>100 MeV), Fig. 1.5. In addition, the signal contains about equal amount of all neutrino flavors. However,  $\nu_\mu, \nu_\tau$  are below threshold for CC interactions. Thus, most of the signal produced by a supernova is provided by  $\bar{\nu}_e + p$  inverse beta decay reaction (12.19), as was in the case of SN1987A. Interaction on electrons and NC interactions of all neutrino flavors can add only a small contribution to the signal, as evident from the cross sections shown in Fig. 12.11.

Although the cross section is relatively small compared with that for interaction on nucleons, neutrino-electron elastic scattering could be important because of its directionality. As supernova neutrinos are more energetic than solar neutrinos, the electron is scattered closer to the direction of the incoming neutrino; ES events can be thus used to point to the supernova direction, although this represents a difficult experimental task.

Neutrinos also interact with nucleons in nuclei via CC and NC processes, although cross sections are typically somewhat smaller for bound than for free nucleons. The kinematic threshold depends on the binding energies of the initial and final nucleus. Neutrino interactions on nuclei in the tens-of-MeV range are not completely theoretically understood, see Scholberg (2012) for a review.

Relatively cheap detector materials such as water and hydrocarbon-based scintillators have many free protons. The neutrino energy threshold for the reaction (12.19) is 1.8 MeV and the positron's energy loss is usually observed. The neutron may also be captured on free protons, after thermalization and capture time of  $\sim 200 \mu\text{s}$ , producing MeV-scale  $\gamma$ -rays, as discussed for the KamLAND detector.

### 12.12.3 Detection of Supernova Neutrinos

Starting from the 1980s, different experiments have been or are sensitive to a supernova neutrino burst in our Galaxy. As derived below, typical event yields for current detectors are a few hundred events per kiloton of detector material for a core-collapse SN 10 kpc away from Earth. The expected number of events from a supernova should scale simply with distance to the supernova  $D$  as  $1/D^2$ . An ideal detector would

measure the flavor, energy, time, and direction of the neutrinos on an event-by-event basis and no background. A real detector would settle for imperfectly reconstructed events and inferred statistical information. To a good approximation for most technologies event rates scale linearly with detector mass.

The detection techniques use the fact that a high fraction of neutrinos from a SN burst exceeds 5–7 MeV, the typical energy threshold of real-time experiments used for solar neutrino studies. Liquid scintillator detectors (as Borexino, KamLAND, LVD, MACRO, Baksan) are composed of hydrocarbons, which have the approximate chemical formula  $C_nH_{2n}$ . The energy loss of charged particles is proportional to the light emitted from de-excitation of molecular energy levels. The interaction vertices may be reconstructed using the timing information of the photons. Because of the presence of free protons in scintillators, inverse beta decay (12.19) is largely dominant for a supernova burst signal. Elastic scattering on  $e^-$  will contribute a few percent to the total supernova burst event rate.

Water is an inexpensive medium with an abundance of free protons and detectors with large volumes are possible (Kamiokande, IMB, SK, future detectors). As for scintillators, interaction rates in water are dominated by the reaction (12.19). Secondary charged particles are detected via their Cherenkov light emission. The neutrino energy is estimated through particle energy loss, which is proportional to the number of detected photons.

Backgrounds for SN neutrino detection vary by detector type and location. Ambient radioactivity, from the environment or detector materials, produces irreducible signals whose decay products have rarely energies  $>10$  MeV. Nevertheless, radioactivity can be troublesome for measurements of the low-energy end of the signal, possibly at late times of SN burst, and for low-threshold detectors. Cosmic ray related backgrounds could be suppressed by constructing detectors deep underground. Nuclear fragments produced by spallation or capture processes of survived atmospheric muons can still be produced in the detector or in the surrounding materials. Muon spallation events can produce fake bursts over timescales of tens of seconds and represent a potential background. However, for current underground detectors, background rates should be very low for the duration of a galactic SN burst that typically lasts  $\mathcal{O}(10\text{ s})$ .

Expected event rates can be computed by folding a given supernova neutrino flux with the NC and CC interactions of different neutrino flavors on the different targets ( $p$ ,  $e^-$ , nuclei) in the detector, and taking into account the detector response. In the following, we present a first-order estimate of the expected number of signal events in a typical 1 kiloton detector using only  $\bar{\nu}_e$  and the dominant inverse beta decay reaction (12.19).

The energy released by a core-collapse SN is  $E_{SN} = 3 \cdot 10^{53}$  erg, Eq.(12.41). As average neutrino energy, we assume  $\langle E_\nu \rangle \sim 15\text{ MeV} \simeq 2.5 \times 10^{-5}\text{ erg}$ . The total number of neutrinos of all flavor,  $N_{\nu_f}$ , at the source in 10 s interval is

$$N_{\nu_f} = \frac{E_{SN}}{\langle E_\nu \rangle} = \frac{3 \times 10^{53}}{2.5 \times 10^{-5}} = 1.2 \times 10^{58} \quad \rightarrow \quad N_{\bar{\nu}_e} = \frac{N_{\nu_f}}{6} = 2 \times 10^{57}. \quad (12.46)$$

$N_{\bar{\nu}_e}$  represents the number of  $\bar{\nu}_e$ , producing most of the signal in a water Cherenkov detector. This is derived from  $N_{\nu_f}$  assuming equipartition of neutrino flavors during the cooling phase, Fig. 12.12.

The neutrino fluence  $F_{\bar{\nu}_e}$  on Earth depends on the distance  $D$  of the SN. For a typical distance  $D = 10 \text{ kpc} = 3 \times 10^{22} \text{ cm}$ :

$$F_{\bar{\nu}_e} = \frac{N_{\bar{\nu}_e}}{4\pi D^2} = 1.7 \times 10^{11} \text{ cm}^{-2}. \quad (12.47)$$

Note that the average neutrino flux (the fluence divided by the SN time of 10 s) is about a factor of 3 smaller than the flux of solar neutrinos, Eq. (12.4). SN neutrinos are however much easier to detect, due to their higher energy.

The expected number of events in a detector depends on the medium, on the  $\nu$  cross section  $\sigma(E_\nu)$  and critically on the detection efficiency  $\varepsilon(E_\nu)$ . Water, for instance, contains 2 free protons per molecule. The number of free protons in a kt of water is thus  $N_p = (2/18) \times 10^9 \text{ cm}^3 \times N_A \text{ cm}^{-3} = 7 \cdot 10^{31}$ . The cross section for the inverse beta decay (12.19) at 15 MeV corresponds to  $\sigma_0 = \sigma(15\text{MeV}) \simeq 2 \cdot 10^{-41} \text{ cm}^2$  (see Fig. 12.11). The expected number of interactions with a positron in the final state in one kt of water is thus given by (using average values):

$$\begin{aligned} N_{e^+} &= F_{\bar{\nu}_e} \times \sigma_0 \times N_p \times \bar{\varepsilon} = 1.7 \cdot 10^{11} \times 2 \cdot 10^{-41} \times 7 \cdot 10^{31} \\ &\times \bar{\varepsilon} \simeq 230 \bar{\varepsilon} \text{ events.} \end{aligned} \quad (12.48)$$

Indicatively, the number of expected events for some of the quoted experiments (some of them operated in the past) for a SN event 10 kpc away are (in parenthesis, the fiducial detector mass): 7,000 events in SK (32 kt); 300 events in LVD, MACRO, KamLAND ( $\sim 1$  kt); 100 events in Borexino (0.3 kt); 50 events in Baksan (0.33 kt). Some future proposed experiments can have hundreds kt of fiducial mass (Scholberg 2012), opening possibly the field of extra-galactic SN observations.

A prompt alert from a SN neutrino signal would give astronomers valuable time to catch the electromagnetic signal from the supernova and to study the environment immediately surrounding the progenitor star during the initial stages of the event. Advance warning could enable observation of ultraviolet and soft X-ray flashes, which are predicted at very early times. There could also be entirely unexpected effects at early times. A galactic supernova is rare enough that it will be critical to save all available information.

The SN1987A neutrino events described in the next section were recorded approximately 2.5 h before the inferred time of the supernova's first light. In reality (due to lack of on-line monitoring at that time), the experimentalists found the neutrino signal in their data only by a search triggered from the optical discovery. The situation will be different for the next nearby supernova event. The SuperNova Early Warning System (SNEWS) (Antonioli et al. 2004) is an international network of detectors that aims to provide an early alert to astronomers of a supernova's occurrence.

### 12.13 The SN1987A

SN1987A was the first supernova since 1604 visible with the naked eye. The progenitor was Sanduleak-69202, a main-sequence star of mass  $M = 16 - 22 M_{\odot}$ . It was located in the Large Magellanic Cloud (LMC), a small galaxy satellite of our Milky Way at a distance of about  $50 \pm 5$  kpc from the Earth. The gamma line emission successively observed from SN1987A gave confirmation that heavy elements up to iron, cobalt, and nickel were synthesized by the exploded star, in agreement with predictions of the core-collapse supernova model. SN1987A also was the first (and unique, up to May 2014) supernova from which neutrinos were observed, in fact the first extraterrestrial identified neutrino source other than the Sun.

Two water Cherenkov detectors, Kamiokande-II and the Irvine Michigan Brookhaven experiment (IMB) experiment observed 12 and 8 neutrino interaction events respectively, over a 13 s interval. This time interval is consistent with the estimated duration of a core-collapse. The IMB detector was a 5 kt underground detector located at a depth of 1,570 m.w.e. It was bigger than Kamiokande (2.2 kt, energy threshold of 7–8 MeV) but used smaller PMTs (8-inch) with an overall detection threshold of about 20 MeV. For this reason, IMB was not suited for solar neutrinos. The signals of the two experiments were almost simultaneous, although in 1987 the technology of time dissemination through the GPS was not available. The relative time precision between the signals in the two experiments was about 1 min (according to the Kamiokande synchronization procedure). Nearly all the SN1987A events were consistent with  $\bar{\nu}_e$  interactions (Koshiba 1992; Bethe 1990).

Two smaller scintillator detectors, Baksan and LSD, also reported observations. Baksan reported five counts, but the first came 25 s after IMB. The LSD report was controversial because the events were recorded several hours early (Bethe 1990).

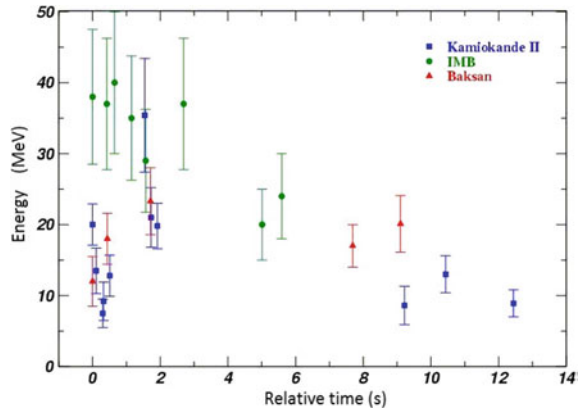
Although the Kamiokande and IMB experiments collected a small sample of neutrino events from the SN1987A, they were sufficient to give an exact time for the start of the explosion to which the light curve can be normalized and to confirm the baseline model of core-collapse. In particular, referring to Fig. 12.13:

- the time distribution of the observed events is in reasonable agreement with theoretical predictions of a  $\sim 10$  s burst;
- their energy distribution gives a measure of the temperature of the neutrinosphere  $T \sim 4.2$  MeV. The average energies of detected neutrinos is  $\sim 15$  MeV;
- the number of the observed events is in agreement with the expected  $3 \times 10^{53}$  erg luminosity of a core-collapse burst.

This last point is the crucial one. By scaling the number of expected events for a 10 kpc SN, Eq. (12.48), to the LMC distance, the number of expected events for a 100% efficient detector is  $N_{e^+}^{LMC} = (10/50)^2 N_{e^+} = 9$  events/kt. Kamiokande had a mass of 2.2 kt, and about 20 events were thus expected. The experiment had a threshold of about 7–8 MeV for the emitted positron; thus the detection efficiency  $\bar{\epsilon}$  averaged over the neutrino energy spectrum is large (of the order of  $\sim 0.5$ ). This is in agreement with the 11 observed events (one event was estimated as due to



**Fig. 12.13** Relative time and energy of SN1987A neutrino events observed by Kamiokande, IMB and Baksan. The time of the first event was arbitrarily set as  $t = 0$



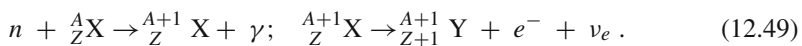
background), assuming that 99% of the SN energy is carried away by neutrinos. IMB had a mass about  $\times 2$  larger, but higher detection energy threshold and average detection efficiency about  $\times 1/4$  that of Kamiokande.

SN1987A allowed also investigations on particle physics that were hitherto inaccessible to laboratories. The neutrino arrival time distribution sets an upper limit on the neutrino mass of  $m_\nu \lesssim 10 \text{ eV}$  [see Chap. 13 of Braibant et al. (2012)], magnetic moment  $\mu_\nu < 10^{-12} \mu_B$ , where  $\mu_B$  is the Bohr magneton and a lower limit on its lifetime. A limit on the neutrino velocity  $v_\nu$  was also imposed, as deviations from light speed was  $\frac{|v_\nu - c|}{c} < 2 \times 10^{-9}$ .

## 12.14 Stellar Nucleosynthesis of Trans-Fe Elements

During the supernova explosion the outer shells of the star are ejected. Core-collapse supernovae are the main contributors of the heavy elements ( $A \geq 12$ ) in galaxies, and the elements that have been produced during the various stellar burning stages are mixed into the interstellar medium. For a review of stellar nucleosynthesis, see Woosley et al. (2002).

During the late stages of the life of main-sequence stars, before the formation of a white dwarf, free neutrons are produced. They are plentiful enough to produce heavy elements via *slow* neutron capture



In this way, relatively heavy elements are produced. A slow neutron capture process (or *s-process*) occurs when the characteristic time for neutron capture  $\tau_n$  for the formation of the instable nucleus  $\frac{A+1}{Z}\text{X}$  is  $\tau_n \gg \tau_\beta$ . The newly formed nucleus has enough time to undergo  $\beta^-$  decay with lifetime  $\tau_\beta$  and the nucleus tends to stabilize along the nuclear stability valley.

Another process by which heavier nuclei are produced is via proton capture (or *p-process*). Coulomb repulsion ensures that proton capture is a much rarer event than neutron capture and the process only takes place at very high temperatures ( $>2 \times 10^9$  K) in very massive stars ( $\sim 25M_{\odot}$ ) during supernova explosions.

The passage of the huge flux of neutrinos through a star experiencing core-collapse would cause interesting transmutation of the elements, even in the relatively cool outer regions. However, because of the small  $\nu$  cross section, production of new elements in this *\nu-process* is restricted to rare species made from abundant target elements.

The last and probably more important process for the formation of stable elements up to uranium is the so-called *r-process*, which involves neutron capture as in reaction (12.49). However, here the neutron capture time is much smaller than the nucleus decay time,  $\tau_n \ll \tau_{\beta}$ , due to the high neutron density. The newly formed nucleus does not decay immediately; after subsequent captures, the isotopes move away from the stability valley ( ${}^A_Z X \rightarrow {}^{A+1}_Z X \rightarrow {}^{A+2}_Z X \rightarrow \dots$ ). The number of neutrons increases and thus the instability favoring  $\beta^-$  decay. Since the probability of neutron capture is large and the reactions occur at a high rate, these are called *r-processes* (*r* = rapid). However, there are large uncertainties in the site where reactions occur, Fig. 12.10d. Although the environment around core-collapse SN is the most plausible candidate, alternative models exist. These involve a neutrino powered wind of a young neutron star, or a very asymmetric explosion and jetlike outflows, as the explosion producing a gamma-ray burst. Whether *r*-process synthesis would occur in common supernovae or some particularly energetic subset (those with a GRB) is not clear, and the details of the synthesis vary from model to model. There is little doubt however that nuclei above the iron peak are mostly produced during different processes involving supernova explosions.

## References

- J.N. Abdurashitov et al., Measurement of the solar neutrino capture rate with gallium metal. III. Results for the 2002–2007 data-taking period. *Phys. Rev. C* **80**, 015807 (2009)
- K. Abe et al., Solar neutrino results in Super-Kamiokande-III. *Phys. Rev. D* **83**, 052010 (2011)
- F. Acero et al. (HESS Collab.), First detection of VHE gamma-rays from SN1006 by H.E.S.S. *Astron. Astrophys.* **516**, A62 (2010)
- B. Aharmim et al., Electron energy spectra, fluxes, and day-night asymmetries of 8B solar neutrinos from the 391-day salt phase SNO data set. *Phys. Rev. C* **72**, 055502 (2005)
- Q.R. Ahmad et al., Direct evidence for neutrino flavor transformation from neutral-current interactions in the Sudbury Neutrino Observatory. *Phys. Rev. Lett.* **89**, 011301 (2002)
- M. Altmann et al., Complete results for five years of GNO solar neutrino observations. *Phys. Lett. B* **616**, 174 (2005)
- V. Antonelli, L. Miramonti, C. Peña Garay, A. Serenelli, Solar neutrinos. *Adv. High Energ. Phys.* (2013) Article ID 351926. doi:10.1155/2013/351926
- P. Antonioli et al., SNEWS: the SuperNova Early Warning System. *New. J. Phys.* **6**, 114 (2004)
- M. Asplund, N. Grevesse, A.J. Sauval, P. Scott, The chemical composition of the Sun. *Annu. Rev. Astron. Astrophys.* **47**, 481 (2009)

- H. Athar, M. Jezabek, O. Yasuda, Effects of neutrino mixing on high-energy cosmic neutrino flux. *Phys. Rev.* **D62**, 103007 (2000)
- J.N. Bahcall, *Neutrino Astrophysics* (Cambridge University Press, Cambridge, 1989). ISBN: 978-0521379755. The Solar Standard Model is also described on the website: <http://www.sns.ias.edu/jnb/>
- J. Beringer et al., (Particle Data Group). The review of particle physics. Section: 13. Neutrino mass, mixing, and oscillations. *Phys. Rev.* **D86**, 010001 (2012)
- H.A. Bethe, Supernova mechanisms. *Rev. Mod. Phys.* **62**, 801 (1990)
- S. Braibant, G. Giacomelli, M. Spurio, *Particle and fundamental interactions* (Springer, Berlin, 2011). ISBN 978-9400724631.
- S. Braibant, G. Giacomelli, M. Spurio, *Particles and Fundamental Interactions: Supplements, Problems and Solutions* (Springer, Dordrecht, 2012)
- C. Brogгинi, D. Bemmerer, A. Guglielmetti, R. Menegazzo, LUNA: nuclear astrophysics deep underground. *Annu. Rev. Nucl. Part. Sci.* **60**, 53–73 (2010)
- F. Calaprice, C. Galbiati, A. Wright, A. Ianni, Results from the Borexino solar neutrino experiment. *Annu. Rev. Nucl. Part. Sci.* **62**, 315–336 (2012)
- G.L. Fogli et al., Global analysis of neutrino masses, mixings and phases: entering the era of leptonic CP violation searches. *Phys. Rev.* **D86**, 013012 (2012)
- Y. Fukuda et al., Solar neutrino data covering solar cycle 22. *Phys. Rev. Lett.* **77**, 1683 (1996)
- J. Gava, J. Kneller, C. Volpe, G.C. McLaughlin, A dynamical collective calculation of supernova neutrino signals. *Phys. Rev. Lett.* **103**, 071101 (2009)
- W. Hampel et al., GALLEX solar neutrino observations: results for GALLEX IV. *Phys. Lett. B* **447**, 127 (1999)
- W. Haxton, The scientific life of John Bahcall. *Annu. Rev. Nucl. Part. Sci.* **59**, 1–20 (2009)
- W.C. Haxton, R.G. Hamish Robertson, A.M. Serenelli, Solar neutrinos: status and prospects. *Annu. Rev. Astron. Astrophys.* **51**, 21–61 (2013)
- A. Hoefflich, E. Mueller, P. Hoefflich, Light curves of type IA supernova models with different explosion mechanisms. *Astron. Astrophys.* **270**, 223–248 (1993)
- H.Th. Janka et al., Theory of core-collapse Supernovae. *Phys. Rept.* **442**, 38 (2007)
- N. Jelley, A.B. McDonald, R.G.H. Robertson, The sudbury neutrino observatory. *Annu. Rev. Nucl. Part. Sci.* **59**, 431–465 (2009)
- R. Kippenhahn, A. Weigert, *Stellar Structure and Evolution* (Springer, Berlin, 1990)
- M. Koshiya, Observational neutrino astrophysics. *Phys. Rep.* **220**, 229–381 (1992)
- K. Lande, The life of Raymond Davis, Jr. and the beginning of neutrino astronomy. *Annu. Rev. Nucl. Part. Sci.* **59**, 21–39 (2009)
- P. Lipari, Introduction to neutrino physics. 1st CERN—CLAF School of High-energy Physics, Itacuruca, Brazil, (2001), <http://cds.cern.ch/record/677618/files/p115.pdf>
- L.A. Marschall, *The Supernova Story*. Princeton Science Library 1988. ISBN: 978-0691036335
- G. Raffelt, Particle Physics from Stars. *Annu. Rev. Nucl. Part. Sci.* **49**, 163 (1999)
- K. Scholberg, Supernova neutrino detection. *Annu. Rev. Nucl. Part. Sci.* **62**, 81 (2012)
- A.M. Serenelli, W.C. Haxton, C. Pena-Garay, Solar models with accretion. I. Application to the solar abundance problem. *Astrophys. J.* **743**, 24 (2011)
- M.B. Smy et al. (SK Collab.), Super-Kamiokande's solar  $\nu$ . *Nucl. Phys. B Proc. Suppl.* **49**, 235–236 (2013)
- S.E. Woosley, A. Heger, T.A. Weaver, The evolution and explosion of massive stars. *Rev. Mod. Phys.* **74**, 1015 (2002)

## Chapter 13

# Microcosm and Macrocosm

Particles with their fundamental interactions, astrophysics, and cosmology have become closely related fields. The submicroscopic phenomena allow us to better understand the cosmic evolution, Sect. 13.1, and vice versa. When the Universe was very small, it could be considered as a hot gas of highly energetic particles. As it expanded (in four dimensions), it cooled down (the average energy of its constituents decreased) and passed through several phase transitions where the nature of the particles involved in the “gas of the Universe” changed.

The theory of the electromagnetic, weak, and strong interactions, which mediate the dynamics of the known subatomic particles, is called the *Standard Model (SM) of particle physics*. The predictions of the SM have been verified with great precision, particularly at LEP and LHC experiments. The SM explains the weak and electromagnetic unification at the electroweak energy scale,  $\mathcal{O}(100 \text{ GeV})$ . The gauge structure of the SM suggests the existence of a Grand Unified Theory (GUT) of strong and electroweak interactions at an energy scale of roughly  $10^{16} \text{ GeV}$ , Sect. 13.2. Are really all interactions (excluding eventually the gravitation) unified at high energies? Which symmetry governs this unification? No answer can probably be provided by accelerator experiments, while some experimental tests of GUTs predictions, such as the searches for baryon number nonconservation and the existence of relic particles from the Big Bang are performed in underground laboratories.

The subject within which particle physics, astrophysics, and cosmology are more strictly correlated is that connected with dark matter (DM), Sects. 13.3, 13.4. The combination of many observations, including galactic rotation curves, gravitational lensing, the cosmic microwave background (CMB), and primordial light element abundances, cannot be explained without new, non-SM objects, that may annihilate or decay to ordinary particles detectable far from their source, or that may be scattered by ordinary matter. Although there are other motivations for physics beyond the Standard Model, astrophysics, and cosmology give direct evidence for new physics, thus making the search for signatures of DM particles an especially compelling area of research.

Supersymmetric (SUSY) theories, Sect. 13.5, provide perhaps the most promising candidates to solve the DM enigma, based on a common paradigm for particle physics and cosmology. Although speculative, supersymmetric DM is very well motivated and based on a simple physical principle. This “coincidence” between cosmological observations and new physics at the electroweak scale is highly suggestive and has stimulated a large experimental effort over the last 20 years on the search of a weakly interacting, stable, and massive particle (the WIMP).

The two processes that can underline the presence of DM in the Universe are annihilation of WIMP pairs and their elastic scattering with ordinary matter, Sect. 13.6. Based on the WIMP-matter cross section, Sect. 13.7, dedicated experimental searches have been developed in the so-called *direct detection methods*, Sect. 13.8, or *indirect detection methods*, Sect. 13.9. No conclusive results have been obtained so far from these experiments, as well as for signals of physics beyond the Standard Model at accelerators. The next few years will be probably decisive for the solution of this joint astroparticle physics-cosmology problem, Sect. 13.10.

### 13.1 The Standard Model of the Microcosm: The Big Bang

The fundamental scenario which describes the Universe as a system evolving from a highly compressed state is the so-called *Big Bang model*. The expansion of the Universe originated around  $10^{10}$  years ago from a primordial event, the “Big Bang”, from a space-time singularity of very high density and temperature. Starting from the Big Bang, the Universe can be considered as a gas of particles rapidly expanding. Three fundamental ingredients are needed to build a cosmological model: (1) the equations relating the geometry of the Universe with its matter and energy content. They are provided by the Einstein field equations. (2) The metrics, describing the symmetries of the problem. The properties of statistical homogeneity and isotropy of the Universe greatly simplifies the mathematical analysis. (3) The equation of state, specifying the physical properties of the matter and energy content. Particle physics enters in this last aspect. The theory of fundamental interactions (the Standard Model of particle physics) and its possible extensions have been applied to describe the evolution of the Universe immediately following the Big Bang.

Einstein initially introduced a cosmological constant term  $\Lambda$ , to obtain a stationary solution. The term  $\Lambda$  represents a “vacuum energy” associated with space-time itself, rather than its matter content, that is a source of gravitational field even in the absence of matter. Einstein removed the  $\Lambda$  term when the expansion of the Universe was discovered.

Assuming that the matter content can be treated as a perfect fluid, the Einstein field equations simplify to the Friedmann-Lemaître equations, that closely connect the evolution and the curvature of the Universe with its matter density. The matter density is defined in terms of the *critical density of the Universe*,  $\rho_c$ :

$$\rho_c \equiv \frac{3H^2}{8\pi G_N} = 1.88 \cdot 10^{-29} h^2 [\text{g cm}^{-3}] = 1.05 \cdot 10^{-5} h^2 [\text{GeV cm}^{-3}] \quad (13.1)$$

where the scaled Hubble parameter,  $h \sim 0.7$ , is defined in terms of the Hubble constant  $H \equiv 100h \text{ km s}^{-1} \text{ Mpc}^{-1}$ , Sect. 7.1. The complete state of the homogeneous Universe can be described by giving the current values of all the density parameters  $\Omega_i \equiv \rho_i/\rho_c$  for the various matter species, and reintroducing a term  $\Omega_\Lambda$  for the cosmological constant. Thus, the Friedmann equation describing the time evolution of a scalar quantity representing the size of the Universe,  $R = R(t)$ , can be written as:

$$\sum_i \Omega_i + \Omega_\Lambda - 1 = \frac{k}{R^2 H^2}. \quad (13.2)$$

Its ultimate evolution is determined by the constant  $k$  (called the *curvature constant*) that in turns depends on  $\Omega = \sum_i \Omega_i + \Omega_\Lambda$ . For  $k = +1$  ( $\Omega > 1$ ), the Universe will recollapse in a finite time, whereas for  $k = 0, -1$  ( $\Omega = 1$  or  $< 1$ , respectively), the Universe will expand indefinitely. Typically, contributions to  $\Omega$  arise from baryons ( $\Omega_b$ ), photons ( $\Omega_\gamma$ ), neutrinos ( $\Omega_\nu$ ), and cold dark matter ( $\Omega_c$ ).

The knowledge of these parameters also allows us to track the history of the Universe back in time, at least until an epoch where interactions allow interchanges between the densities of the different species. This interchange is believed to have happened until the neutrino-decoupling epoch, shortly before Big Bang Nucleosynthesis. To look further back into the history of the Universe is only a matter of guesses at present.

The goal of observational cosmology is to make use of astrophysical information to derive cosmological parameters, Sect. 7.1. Starting from 1998, two astrophysicist teams began to study the distance-redshift relation by observing Type Ia SNe, Sect. 12.10. Although not perfect standard candles, their luminosity at maximum brightness (after some corrections depending on the light curve shape and color) have a very small dispersion with respect to a central value. Thus, the peak luminosity of Type Ia SNe is used as an efficient distance indicator. The two teams found that very far galaxies are moving away from us more slowly than expected from the Hubble law. Saul Perlmutter, Brian P. Schmidt and Adam G. Riess were awarded the Nobel Prize in 2011 following this discovery.

In the Big Bang model, the attraction due to gravity slows down the motion of bodies that are moving away from each other. Therefore young “objects” should move faster away from us than older ones. The results from Type Ia SNe indicate the opposite, namely, that the Universe is now expanding faster than in the past. This is an outstanding result, which has forced the reintroduction of something similar to the “vacuum energy” term in the Einstein equations. The origins of this vacuum energy contribution are not understood in the Standard Models of the microcosm and macrocosm.

One of the major achievements of experimental cosmology is the series of precision measurements of the cosmic microwave background (CMB). In 1992, the COBE satellite measured the black body spectrum (at a temperature of 2.725 K) of

the CMB. The measurements confirmed that any deviation from a Planck curve was smaller than  $1/10,000$ , as expected (Mather and Smoot, Nobel laureates in 2006). The deviations from a perfect black body spectrum were first measured with experiments placed on balloons (BOOMERanG, MAXIMA).

Recently, the WMAP and Planck satellite experiments measured the temperature differences in the CMB radiation with high precision. When the temperature of the Universe was  $\sim 3000$  K, electrons and protons combined to form neutral hydrogen (the so-called *recombination* process). Before this epoch, free electrons acted as glue between photons and baryons through Thomson and Coulomb scattering, so the cosmological plasma was a tightly coupled photon-lepton-baryon fluid. The “initial conditions”, the energy contents of the Universe before recombination, can be studied using basic fluid mechanics equations, which express the temperature  $T$  as a function of two angular variables,  $T = T(\theta, \phi)$ , (Hu and Dodelson 2002). The precise observation of the CMB radiation in different directions  $(\theta, \phi)$  in the sky provides a map which allows to determine temperature anisotropies. These are used to estimate the Universe’s geometry, content, and evolution; to test the Big Bang model and the cosmic inflation theory.

The Planck satellite has released in 2013 (Ade et al. 2014) the most accurate results to date on the CMB spectrum, with a measurement of the temperature power spectrum corresponding to a precision on the angular size smaller than  $0.1^\circ$ . In combination with other data [see Sects. 21: Big-Bang cosmology, 22: Big-Bang nucleosynthesis, 23: Cosmological parameters of Beringer et al. (2012)] Planck and WMAP observations are consistent with spatial flatness, corresponding to  $k = 0$  in Eq. (13.2), or, equivalently, to  $\Omega = 1$ . They also provide a precise measurement of the age of the Universe, which is about 13.7 billion years old (with a 1% error margin). This experimental scenario is well reproduced by inflation models of the Universe evolution, which automatically generate negligible spatial curvature with  $k = 0$ .

The combination of cosmological observations of CMB data gives a baryon density  $\Omega_b \sim 5\%$  of the critical density. This value is consistent with that coming from Big Bang Nucleosynthesis. The observed baryon-to-photon ratio is equal to  $\eta = n_B/n_\gamma \simeq 10^{-9}-10^{-10}$ . The photons in the Universe are mainly the photons of the CMB radiation, with average energy of  $\sim 10^{-4}$  eV. Thus,  $\Omega_\gamma \lesssim 10^{-4}\Omega_b$ . The density parameter in neutrinos is predicted to be  $\Omega_\nu h^2 = \sum m_\nu/93$  eV. Different upper limits on the sum of the mass of *active neutrinos* exist. Active neutrinos are those interacting through standard weak interactions. These limits give  $\sum m_\nu \ll 1$  eV, and thus  $\Omega_\nu \ll 1$ . Active neutrinos contribute negligibly to  $\Omega$ .

From these observations, the best scenario for the Universe composition is the so-called  $\Lambda$  with Cold Dark Matter ( $\Lambda$ CDM) model. The Universe evolution depends mainly on the cosmological constant and nonrelativistic (cold) dark matter, with a density term denoted  $\Omega_c$ . The approximate values of some of the key parameters are [see Sect. 23: Cosmological parameters of Beringer et al. (2012) for more details and different combination of experimental data]:

$$\Omega_b \sim 0.05; \quad \Omega_c \sim 0.25; \quad \Omega_\Lambda \sim 0.70, \quad (13.3)$$



and a scaled Hubble constant  $h \sim 0.70$ . The spatial geometry is very close to be flat (and usually assumed to be precisely flat). The nature of the dark energy remains a mystery.

## 13.2 The Standard Model of Particle Physics and Beyond

The “*Standard Model*” (SM) of the microcosm is a gauge theory in which the fundamental fermions are leptons and quarks. The SM provides an excellent description of the phenomena of the microcosm (at least until  $\sqrt{s} \simeq \text{few TeV}$ ), with the triumph of the recently-discovered Higgs boson.

There are many reasons, however, to believe that the SM is incomplete and represents a valid theory at relatively low energies only, Sect. 1.1. For these reasons, models that contain the SM in the low energy limit were sought. Of particular interest are the models based on complete symmetries, as those attempting a true unification between leptons and quarks in terms of a single symmetry group (*Grand Unified Theories*, *GUTs*) and those attempting unification between fermions and bosons, such as the *supersymmetry*. Finally, some models are even trying to include gravity (*supergravity*, *SUGRA*).

In the Standard Model structure, quarks and leptons are placed in separate multiplets. In the first family, there are two quarks [the ( $u$ ,  $d$ )] and two leptons [ $(\nu_e$ ,  $e$ )]. Baryon number conservation forbids proton decay. However, there is no known gauge symmetry which generates baryon number conservation. Therefore, the validity of baryon number conservation must be considered as an experimental question. On the other hand, Grand Unified Theories place quarks and leptons in the same multiplets; we may think that quarks and leptons are, at the low energies of our laboratories, different manifestations of a single particle. At very high energies, therefore, quark  $\leftrightarrow$  lepton transitions are possible.

Starting from the 1980s, the search for proton decay was the main reason for developing large detectors and underground laboratories (Perkins 1984). As shown in *Extras # 7*, no proton decay events have been observed so far. Despite its beauty, the simplest GUT model is rejected.

Theories beyond the SM of fundamental interactions have been applied to describe the evolution of the Universe after the Big Bang. This model predicts that the huge initial temperature decreased as the Universe expanded (see Fig. 1.1) with an evolution of the interactions among particles. Collisions at LEP have reproduced situations that were typical some  $10^{-10}$ – $10^{-9}$  s after the Big Bang, while the collisions studied at the LHC ( $\sqrt{s} = 14$  TeV) correspond to typical situations of about  $10^{-12}$ – $10^{-11}$  s after the Big Bang. For subnuclear physicists, the first moments of the Universe represent the equivalent of a limitless energy accelerator!

Researches related to supersymmetric particles refer to the TeV scale, which are probably accessible at the LHC and/or in astroparticle experiments, as discussed in this Chapter. Energies associated with the GUT theories cannot be reached with accelerators on Earth. GUTs foresee that electroweak and strong interactions were

unified from  $\sim 10^{-44}$  to  $\sim 10^{-35}$  s after Big Bang, in a highly symmetric Universe. As the temperature decreased, some phase transitions took place. A situation similar to that occurring to a magnetic substance happened: at a high temperature, there is no preferred direction; when the temperature decreases below the Curie point, the material loses its rotational symmetry. Magnetic domains appear: this corresponds to a more ordered phase, but with a lower degree of symmetry. Many important events probably occurred in the Universe evolution at  $t = 10^{-35}$  s, corresponding to a temperature of  $10^{15}$  GeV ( $\simeq 10^{28}$  K).

GUT theories require the existence of supermassive *magnetic monopoles* (MMs), (Giacomelli 1984). They could be created as point-like topological defects at the time of the Grand Unification symmetry breaking into subgroups at  $10^{15}$  GeV. These MM should have a mass  $m_M$  equal to the mass of the massive  $X, Y$  bosons, divided by the unified coupling constant  $\alpha$  at  $10^{15}$  GeV,  $m_M \simeq m_X/\alpha \sim 10^{15}/0.03 \sim 3 \times 10^{16}$  GeV/ $c^2$ .

Many different experimental searches for magnetic monopoles have been performed. The largest apparatus constructed to detect GUTs MM was the MACRO experiment (Sect. 11.9). No MM candidate was observed (see *Extras # 7*) and MM are excluded as a significant component of *dark matter* in the Universe.

### 13.3 Gravitational Evidence of Dark Matter

Most of the information about our Galaxy, as well as the rest of the Universe, mainly comes from the electromagnetic emission: not only in the optical band, but also in the radio, infrared, X-rays and  $\gamma$ -rays bands. The existence of matter in the Universe that does not emit electromagnetic radiation, the dark matter, was indirectly highlighted through its gravitational interaction with ordinary matter, which emits electromagnetic radiation.

Deviations from trajectories expected from Newton's gravitation law have proved very effective in deepening our understanding of the Universe. Observed anomalies in the past were regarded as an indication of the existence of unseen ("dark") objects, as the anomalous motion of the planet Uranus, which led to the discovery of Neptune. In other situations, they induced deep revisions of the theory, as in the case of the attempt to explain the anomalies in the motion of Mercury as due to the existence of a new planet. This interpretation failed, and the final solution had to wait for the advent of Einstein's theory of general relativity.

The modern problem of dark matter is conceptually very similar to the old problem of unseen planets. We observe in large astrophysical systems, with sizes ranging from galactic to cosmological scales, some "anomalies" that can only be explained either by assuming the existence of a large amount of unseen dark matter, or by assuming a deviation from the known laws of gravitation and general relativity.

The first hints for the presence of dark matter (in the modern sense) was inferred in 1933 by Zwicky from measurements of the velocity dispersion of the galaxies in the Coma cluster. He derived a mass-to-light ratio of around 400 solar masses per

unit of solar luminosity. This ratio exceeds that observed in the solar neighborhood by two orders of magnitude. Today, the mass of a galaxy cluster can be determined via several methods, including application of the virial theorem to the observed distribution of radial velocities, by gravitational lensing, and by studying the profile of X-ray emission that traces the distribution of hot emitting gas in rich clusters.

The most robust evidence for dark matter emerges from the analysis of the revolution speeds of stars and gas clouds in the galactic halo as a function of the distance from the center of the galaxy (Trimble 1987). Spiral galaxies, like our own Galaxy, contain  $\sim 10^{11}$  stars, arranged in the form of a central nucleus and a flattened rotating disk. The revolution speed of a mass  $m$  star around the center of the galaxy is determined by the condition of stable orbits, resulting from the equality of the gravitational and centrifugal force, that is,

$$\frac{G_N m M_r}{r^2} = \frac{mv^2}{r} \quad (13.4)$$

from which:

$$v(r) = \sqrt{\frac{G_N M_r}{r}}. \quad (13.5)$$

$M_r$  is the total mass of stars and interstellar material within the distance  $r$  from the center of the galaxy. Most of the stars of a spiral galaxy are located in the central spherical bulge with radius  $r_s$ . If  $\bar{\rho}$  is the average density of stars in the bulge, we have  $M_r = \bar{\rho} \cdot \frac{4}{3}\pi r^3$  for  $r < r_s$ ; it follows that

$$v(r) = \sqrt{\frac{4}{3}G_N \bar{\rho} \cdot r} \propto r \quad \text{for } r < r_s. \quad (13.6a)$$

If all the galaxy mass is assumed to lie inside the bulge, then  $M_r \simeq \text{constant}$  for  $r > r_s$ , and

$$v(r) \propto 1/\sqrt{r} \quad \text{for } r > r_s. \quad (13.6b)$$

Using the neutral hydrogen 21-cm emission line, the circular velocities of clouds of neutral hydrogen can be measured as a function of  $r$ . In almost all cases, after a rise near  $r = 0$ , the velocities remain constant as far as can be measured, as shown in Fig. 13.1 for the spiral galaxy NGC3198 (Begeman 1989). The luminous disk extends no further than about 5 kpc from the center of the galaxy. Observations of tracers other than neutral hydrogen give similar results, leading to an expected revolution speed of the stars as shown by the dashed line. The figure also shows the contribution of a possible dark matter halo. The experimental data obtained using the Doppler effect are indicated with black dots. From the figure it is evident that at high  $r$ , the measured velocities  $v \simeq 200 \text{ km s}^{-1}$  are larger than those obtained using (13.5), also including the additional contribution of stars in the disk. There must be a contribution from a halo of dark matter. Similar results are obtained by measuring the speed of stars in other spiral galaxies and in elliptical galaxies.

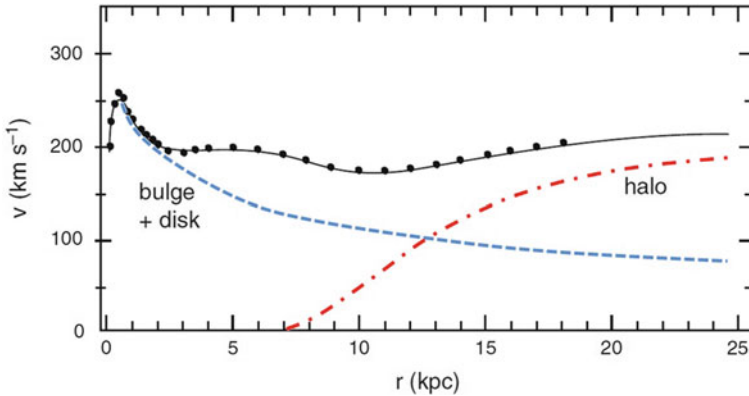


**Fig. 13.1** The *points* indicate the measured rotation speeds of stars in the spiral galaxy NGC3198, versus their distance  $r$  from the galactic center. The *dashed line* represents the expected contribution based on the visible matter in the galactic nucleus (*bulge*) and in the galactic disk; the *dotted-dashed line* includes the contribution of a halo of dark matter. The *solid line* is a fit to experimental data assuming visible matter in the bulge and disk and dark matter in the halo

The evidence for dark matter in the Universe from the dynamics of objects is compelling at all observed astrophysical scales, from galaxies to galaxy clusters.

## 13.4 Dark Matter

The  $\Lambda$ CDM model, whose predictions are given in Eq. (13.3), is largely accepted by cosmologists as the best description of the present data. Leaving for the moment the problem of dark energy, in the following we describe one of the major issues of astroparticle physics: *what is dark matter made of?*

Several categorization schemes have been defined in the past to organize the DM candidates and to suggest possible searches. The first is the *baryonic* versus *nonbaryonic* distinction. Although Big Bang Nucleosynthesis rules out that baryonic objects contribute to the nonobserved DM, searches for baryonic DM candidates have performed. The baryonic fraction of DM could be due to astrophysical bodies in their terminal phase (*remnants*) as white dwarfs, neutron stars and black holes. They could also be smaller objects, with insufficient mass to become stars (Jupiter-like planets). The search in galactic halos (via effects like *gravitational lensing*) indicates that such objects with  $m \lesssim 0.1M_{\odot}$  exist, but that their total mass is much smaller than that of the dark matter halo, confirming that dark baryonic objects contribute negligibly to  $\Omega$ .

Among the nonbaryonic candidates, an important distinction is between “hot” versus “cold” objects. A dark-matter candidate is called “hot” if relativistic at the time when galaxies started to form. It is called “cold” if its motion was nonrelativistic at

that time. This classification has important consequences for structure formation, and studies of galaxy formation has provided clues as to whether dark matter is hot or cold. In fact, N-body computer simulations of structure formation in a universe dominated by hot dark matter do not reproduce the observed structure. Relativistic particles smooth out (moving from high to low density regions) fluctuations preventing the formation of larger structures from smaller ones. The N-body simulations require that the mass of thermal relics be above  $\sim 1$  keV.

The nonbaryonic cold dark-matter candidates are elementary massive particles that have not yet been discovered. There is no shortage of candidates [see Feng (2010) for a recent review], and the leading nonbaryonic cold-dark-matter candidates are sterile neutrinos, axions, Kaluza-Klein states, superheavy particles and Weakly Interacting Massive Particle (WIMP).

A possible DM candidate is a “sterile” **neutrino**, an hypothetical particle that does not interact via weak interactions. The term “sterile” neutrino usually refers to neutrinos with right handed chirality, which may be added to the Standard Model, to distinguish them from the known “active” neutrinos that couple with the  $Z^0$  and  $W^\pm$  bosons. The existence of right-handed neutrinos is theoretically well motivated, as all other known fermions have been observed with left and right chirality, and they can explain the small value of active neutrino masses in a natural way. In some models, the introduction of a sterile neutrino solves also the matter/antimatter asymmetry in the baryogenesis. The number of sterile neutrino types is unknown and their mass could have any value between 1 eV and  $10^{15}$  GeV. Searches for sterile neutrinos are in progress, and most experimental techniques rely on the mixing between active and sterile neutrinos that would produce particular oscillation patterns in active neutrinos.

The hypothesis that **axions** are the main DM component would represent also a possible solution to the so-called strong- $CP$  problem. The strong  $CP$  problem [for the definition of the parity,  $P$ , and charge conjugation,  $C$ , operators see Chap. 6 of Braibant et al. (2011)] is the puzzling question why quantum chromodynamics (QCD) does not seem to break the  $CP$ -symmetry. There are in fact natural terms in the QCD Lagrangian that are able to break the  $CP$ -symmetry in the strong interactions. However, there is no experimentally known violation of the  $CP$ -symmetry in strong interactions. One of the solutions of this “fine tuning” problem, involves the existence of a new scalar particle, the axion. See the Section on Axions on Beringer et al. (2012) for further details.

The **Kaluza-Klein states** rely on the concept of extra dimensions. This idea received great attention after the attempt of Kaluza, in 1921, to unify electromagnetism with gravity. Although our world appears to consist of 3+1 (three space and one time) dimensions, it is possible that other dimensions exist and appear at higher energy scales. Motivations for the study of theories with extra dimensions come from string theory, searching for a consistent theory of quantum gravity and a unified description of all interactions. It appears that such theories may require the presence of six or even more extra-dimensions. A general feature of extra-dimensional theories is that upon “compactification” of the extra dimensions, a set of modes, called Kaluza-Klein (KK) states, appears. From our point of view in the four-dimensional

world, these KK states appear as a series of states with definite masses. Each of these new states has the same quantum numbers, such as charge, color, etc.

Some **superheavy particles**, as the GUT magnetic monopoles, have already been excluded as a major component of DM. In the recent past a common motivation for superheavy dark matter candidates comes from the claim of a large excess of UHECRs in the AGASA data above the GZK cutoff, Sect. 7.5.2. As discussed, this originated top-down models in which the UHECRs are the decay product of superheavy particles. These models are ruled out by the Auger Observatory and Telescope Array results, Sect. 7.12.

The **WIMPs** represent the most investigated class of cold-dark-matter candidates. WIMPs are stable particles that arise in extensions of the Standard Model of particle physics. They are colorless (no strong interactions) and electrically neutral (no electromagnetic interactions). They interact with ordinary matter with the coupling characteristic of weak interactions, in addition to gravity. A well-motivated WIMP candidate is the Lightest Supersymmetric Particle (LSP). Predicted WIMP masses are typically in the range from  $10 \text{ GeV}/c^2$  to few  $\text{TeV}/c^2$ .

Due to the importance of this DM candidate, we introduce in the next section how supersymmetric extensions of the Standard Model justify the most promising WIMP candidate, the so-called *neutralino*.

## 13.5 Supersymmetry

*Super SYmmetry (SUSY)* is a proposed extension of spacetime symmetry that relates bosons and fermions. Each particle from one group is associated with a particle from the other, called its superpartner (or *sparticle*), whose spin differs by a half-integer. If supersymmetric transformations were to exist, they would imply that bosons and fermions are different manifestations of a unified state. A supersymmetric operation changes by  $1/2$  the spin of particles, leaving the electric and color charges unchanged. Supersymmetry has a cultural interest in itself; it also addresses some of the difficulties of Grand Unified theories. Without supersymmetry, it is indeed difficult to understand why the known fundamental particles are so light with respect to the Grand Unification scale at  $\sim 10^{15} \text{ GeV}$ .

An example of this last type of problems is the *gauge hierarchy problem*, connected with the reason why the Higgs boson mass  $m_h$  is so small. From the known fundamental constants, one combination could be obtained with dimensions of mass, called the Planck mass

$$M_{Pl} = \sqrt{\frac{\hbar c}{G_N}} \simeq 1.2 \times 10^{19} \text{ GeV}/c^2 . \quad (13.7)$$

We therefore expect parameters connected with a mass to have values of either 0, if enforced by a symmetry, or of the order of  $M_{Pl}$ . In the SM, electroweak symmetry is broken, and the Higgs boson mass is nonzero. The gauge hierarchy problem is the

question of why  $m_h \simeq 126 \text{ GeV}/c^2 \ll M_{Pl}$ . The problem could possibly be solved by considering higher order corrections to Feynman diagrams. If an energy scale  $\Lambda$  exists at which the SM is no longer a valid description of nature, the gauge hierarchy problem may be eliminated if  $\Lambda < 1 \text{ TeV}$ , implying new physics at the weak scale  $m_{\text{weak}} \sim 10 \text{ GeV} - 1 \text{ TeV}$ . Supersymmetric models offer a natural solution and with the right energy scale for this problem.

Because in the Standard Model there is no connection between fundamental bosons and fermions, the sparticles must be new objects. Since no sparticle has been observed up to now, a new quantum number, *R-parity*, was introduced in order to provide the supersymmetric particles with some properties that make them (currently) inaccessible. *R-parity* is equal to  $R = (-1)^{3(B-L)+2S}$ , where  $B$  is the baryon number,  $L$  the lepton number, and  $S$  the spin. This means that  $R = 1$  for ordinary particles and  $R = -1$  for their superpartners. Supersymmetric particles are expected to be heavier than any known particle. We consider SUSY models where the lightest *R*-odd particle will be absolutely stable. The models predict the existence of a stable supersymmetric particle with a minimum mass (the “Lightest Supersymmetric Particle,” LSP).

### 13.5.1 Minimal Standard Supersymmetric Model

Among SUSY models, the Minimal Standard Supersymmetric Model (MSSM) represents the simplest one. The MSSM is minimal in the sense that it contains the smallest possible object content necessary to give rise to all the particles of the Standard Model. The MSSM requires at least two complex doublets of Higgs bosons to generate the masses of quarks and of charged leptons. Supersymmetric neutral states should mix themselves, similarly to neutrinos. The four neutral supersymmetric fermions (the sparticles of the photon, of the  $Z^0$  and of the two neutral Higgs bosons) are not mass eigenstates. These states mix into four Majorana fermionic mass eigenstates, called *neutralinos*. A Majorana particle is equivalent to its own antiparticle. These neutralinos are indicated with  $\tilde{\chi}_1^0, \tilde{\chi}_2^0, \tilde{\chi}_3^0, \tilde{\chi}_4^0$ , in order of increasing mass. In the following we will refer to  $\tilde{\chi}_1^0$ , i.e., the lightest of the four neutralinos, as the *neutralino*.

Neutralinos are expected to be extremely nonrelativistic in the present epoch. The neutralino interactions relevant for the purposes of dark matter detection are self-annihilation and elastic scattering off nucleons. Calculations in the MSSM use the same Feynman rules of the Standard Model, adding the contribution of diagrams in which particles are replaced by their supersymmetric partners. Since in the MSSM model *R-parity* is a conserved quantum number, all vertices include supersymmetric partner pairs. This implies that SUSY partners are produced in pairs from normal particles and that there is always a SUSY particle in the decay products of a SUSY particle. It is usually assumed that the LSP is the neutralino,  $\tilde{\chi}_1^0$ , which is neutral both



in terms of electric and color charges. This is the reason that made the neutralino an important DM candidate. As the Standard Model, supersymmetric theories cannot predict the values of the particle masses.

Although relatively simple in many respects, the MSSM has a huge number of free parameters. Most of these parameters represent masses and mixing angles, as in the case of the Standard Model. To allow a practical phenomenological study of the MSSM, the number of parameters that are considered must be reduced. This is done with theoretically well-motivated assumptions, which reduce the free parameters from more than 100 to a more tractable quantity. In many cases, experimental results can be interpreted in terms of some widely considered supersymmetric scenarios, as mSUGRA (often called the constrained MSSM) or a phenomenologically simplified MSSM (called the phenomenological, or, pMSSM). In all models, however, the coupling of neutralinos with ordinary matter is a free and unknown parameter.

### 13.5.2 Cosmological Constraints and WIMP

The stable LSP<sup>1</sup> could have a significant cosmological abundance today. The basic idea is simple. If it exists, such a particle must have been in thermal equilibrium in the early Universe, when the temperature  $T$  exceeded the mass of the particle,  $kT > m_\chi$ . The equilibrium abundance was maintained by annihilation of the sparticle with its anti-sparticle  $\bar{\chi}$  into lighter particles  $\ell$  ( $\chi\bar{\chi} \rightarrow \ell\bar{\ell}$ ) and vice versa ( $\ell\bar{\ell} \rightarrow \chi\bar{\chi}$ ). If the LSP is a Majorana object, then  $\chi = \bar{\chi}$ . When at a given time  $t^*$  the Universe cooled to a temperature such that  $kT < m_\chi c^2$ , the rate  $\Gamma$  for the annihilation reaction falls below the Universe expansion rate  $H(t^*)$  when expressed in units of [ $s^{-1}$ ]. The rate  $\Gamma = \sigma_\chi \cdot v \cdot n_\chi$  depends on the annihilation cross section  $\sigma_\chi$ , on the relative velocity  $v$  between the two WIMPs and their number density  $n_\chi$ . At the given time  $t^*$  the interactions which maintained thermal equilibrium came to an end and a relic cosmological abundance of WIMPs froze in. This condition can be expressed as:

$$H(t^*) = \Gamma = \langle \sigma_\chi v \rangle n_\chi \quad [\text{cm}^2][\text{cm/s}][\text{cm}^{-3}] \quad (13.8)$$

where  $\langle \sigma_\chi v \rangle$  represents the convolution of the  $\chi\bar{\chi}$  annihilation cross-section times the relative velocity  $v$  over their thermal distribution spectrum. When condition (13.8) was reached, the  $\chi$ 's ceased to annihilate, fell out of equilibrium, and their total number in the Universe no longer changed significantly. Freezing out happened at a temperature  $kT \sim m_\chi/20$  almost independently of the properties of the WIMP. Assuming this kinetic energy, the corresponding velocity is  $v_{dec} \sim 0.3c$ . This means that WIMPs were already nonrelativistic when they decoupled from the thermal plasma. Because of Eq. (13.8), the abundance today is inversely proportional to the WIMP annihilation cross section  $\sigma_\chi$ .

<sup>1</sup> The LSP is also denoted as  $\chi$ . However, some of the following related discussions can be extended also to other no-SUSY WIMP candidates.

The present density of a generic  $\chi$  particles can be derived by applying Eq. (13.8) using a Maxwell–Boltzmann distribution of the particle velocities. One can find the standard calculation for instance in (Jungman et al. 1996). Following this computation, if such a stable particle of mass  $m_\chi$  exists, its *relic abundance* (that is, the present mass density in units of the critical density  $\rho_c$ , Eq. 13.1), is given by:

$$\Omega_\chi h^2 \equiv \frac{m_\chi n_\chi}{\rho_c} = \frac{3 \times 10^{-27} \text{cm}^3 \text{s}^{-1}}{\langle \sigma_\chi v \rangle}. \quad (13.9)$$

The above constraint on  $\Omega_\chi$  is only derived from cosmological conditions.

To reproduce the observed DM density of our Universe, Eq. (13.3), the condition  $\Omega_\chi \equiv \Omega_c$  is required and thus  $\Omega_\chi h^2 \sim 0.1$ . To obtain an order of magnitude estimate of the annihilation cross section in (13.9), we assume  $\langle \sigma_\chi v \rangle \sim \sigma_\chi v_{\text{dec}}$  where  $v_{\text{dec}} \sim c/3 = 10^{10}$  cm/s is the average velocity of the WIMPs at the time of decoupling. Thus, the annihilation cross section of our hypothetical  $\chi$  particle should be of the order of

$$\sigma_\chi \sim \frac{3 \times 10^{-27} \text{cm}^3 \text{s}^{-1}}{0.1 \cdot v_{\text{dec}}} \simeq 3 \times 10^{-36} \text{cm}^2 \quad (13.10)$$

From the particle physics side, let us assume that a new, not yet detected, neutral particle with weak-scale interaction exists. The reasonable mass for this particle is that of the electro-weak symmetry breaking, i.e.,  $m_{EW} \sim 100 \text{GeV}/c^2$ . The annihilation cross section for such a particle has the same behavior as that of the  $e^+e^-$  annihilation in two fermions  $f\bar{f}$  [for instance, the process  $e^+e^- \rightarrow \mu^+\mu^-$ , Chap. 9 of Braibant et al. (2011)]:

$$\sigma(e^+e^- \rightarrow f^+f^-) \simeq \frac{\alpha_{EM}^2 (\hbar c)^2}{s} \simeq \frac{100}{s[\text{GeV}^2]} [\text{nb}] \quad (13.11)$$

where  $\alpha_{EM} \sim 1/137$  is the electromagnetic coupling constant and  $s$  is the square of the center-of-mass energy. One may worry about the assumptions in (13.11): we are estimating the annihilation cross section assuming *charged* particles and using the *electromagnetic* coupling constant  $\alpha_{EM}$ ! However, at energies above the  $Z^0$  pole ( $\sim 90 \text{GeV}$ ), the electromagnetic and weak coupling constants are unified,  $\alpha_W \sim \alpha_{EM}$ . The symmetry below that energy is broken while above it the annihilation proceeds through a  $Z^0$  exchange with almost the same probability as an electromagnetic process. At the energy  $\sqrt{s} = m_\chi$  our hypothetical neutral, heavy and weakly interacting particles annihilate behaving almost as  $e^+e^-$  pairs and (13.11) yields

$$\sigma(\chi\bar{\chi} \rightarrow \ell^+\ell^-) \simeq \frac{\alpha_W^2 (\hbar c)^2}{s} \simeq \frac{100[\text{nb}]}{100^2} \simeq 10^{-35} [\text{cm}^2] \quad (13.12)$$

The cross section of such a particle is remarkably close to the value required to account for the dark matter in the Universe, Eq. (13.10). There is no a priori

reason for a particle with a weak-scale interaction to have anything to do with closure density, a cosmological requirement that produces the condition (13.10). This striking coincidence suggests that if there is a stable particle associated with new physics at the electroweak scale, that WIMP would likely represent the main component of dark matter. *Se non é vero, é ben trovato.*

### 13.6 Interactions of WIMPs with Ordinary Matter

WIMPs must have some unknown, small but finite coupling to ordinary matter. This requirement follows from the fact that otherwise WIMPs would not have annihilated in the early Universe and they would be unacceptably overabundant today. They can annihilate yielding *normal* particles into the final state, which are accessible to so-called *indirect experiments*, Sect. 13.9. By crossing symmetry, the amplitude for WIMPs annihilation into quarks is related to the amplitude for elastic scattering of WIMPs from quarks. Although unknown in strength, the WIMP-matter coupling has motivated different experimental strategies to search for such relic objects. These strategies rely on the small, but nonzero, coupling of WIMPs to nuclei in a detector that would provide a finite (albeit small) event rate in the so-called *direct experiments*, Sect. 13.7.

The key ingredients for an estimate of the signal rate in detection experiments are the density and the velocity distributions of WIMPs in the solar neighborhood, the WIMP-nucleon scattering cross section, and the annihilation cross section into different “normal” particle pairs.

There are numerous arguments which lead to believe that our Galaxy, like most other spiral galaxies, is embedded in a DM halo which exceeds the luminous component by about a factor of ten. The crucial quantities for experimentalists are the DM density in the region of our solar system, or the *local density*  $\rho_0$ , and the distribution of DM particle velocities. These quantities are determined by observing the rotation curves of the Galaxy with some difficulties due to the location of the Sun within it. N-body simulations suggest the existence of a universal DM density profile, with the same shape for all masses, epochs and input power spectra (Navarro et al. 1996).

The velocity is usually assumed to have a Maxwellian distribution, corresponding to an isothermal and spherical model of the DM halo. In the following, we will use its average value,  $\bar{v} = \langle v^2 \rangle^{1/2}$ . As canonical values for the local density and average speed [see Sect. 24. Dark Matter of Beringer et al. (2012)] we shall use:

$$\rho_0 = (0.39 \pm 0.03) \text{ GeV cm}^{-3} \quad \text{and} \quad \bar{v} = 220 \text{ km/s} \quad (13.13)$$

although there is considerable uncertainty and model dependence in these numbers.

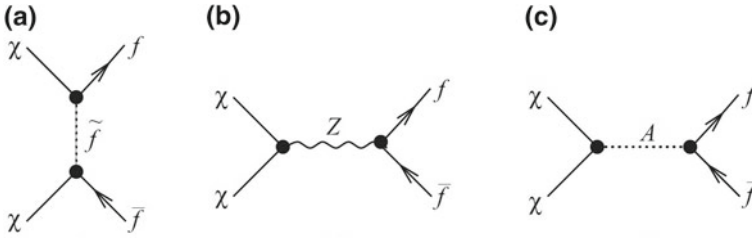


**Fig. 13.2** Tree level diagrams for neutralino annihilation into fermion pairs, ( $\chi\chi \rightarrow f\bar{f}$ ). **a** Annihilation through the  $t$ -channel, with the exchange of a sfermion, **b**  $s$ -channel exchange of a  $Z^0$  boson, and **c** of a pseudoscalar Higgs boson

### 13.6.1 WIMPs Annihilation

The annihilation cross section  $\sigma_\chi$  is the relevant quantity related to the relic abundance of cosmological DM. In the assumption of a weakly interacting massive particle, the cross section should correspond to that given in (13.10). This assumption could not hold in different DM scenarios (KK, axions, ...).

WIMPs can annihilate into numerous final states. The most studied ones are those referring to the neutralino, the LSP. For a more general discussion and extension to other DM candidates, see Cirelli et al. (2011). The dominant annihilation processes are those at the lowest order in perturbation theory, with two vertices (the so-called “tree” level). All these processes are characterized by two-body final states: fermion-antifermion pairs ( $f\bar{f}$ ),  $W^+W^-$ ,  $Z^0Z^0$ , two Higgs bosons, one ordinary gauge boson and a Higgs boson, see (Jungman et al. 1996; Bertone et al. 2005). Several Feynman diagrams contribute to each process, so the computation of the total annihilation cross section is a difficult task. All the terms computed at the tree level (as well as those computed at higher orders) contain unknown supersymmetric parameters.

The annihilation of neutralinos to a fermion-antifermion pair, Fig. 13.2, has several important features. The neutralino mass is expected to be of the order or greater than  $10 \text{ GeV}/c^2$ . Thus, the annihilation channel into light fermions will always be accessible. For many interesting neutralino masses, other channels will be forbidden or suppressed, so that  $f\bar{f}$  final states are often the only open channels. One important feature of this channel is the helicity constraint. Neutralinos are Majorana fermions, and in the limit of zero relative velocity, they are in a relative  $s$ -wave (i.e., null relative orbital angular momentum). Consequently, by Fermi statistics, they must have spins oppositely directed, and the total angular momentum is null. Therefore, the two fermions  $f\bar{f}$  in the final state must have spins oppositely directed as well. This configuration introduces a helicity factor in the probability decay into  $f\bar{f}$  which is proportional to the mass of the fermion  $m_f$ . The situation is analogous to the decay of a spinless particle as the charged pion, as presented in Sect. 8.10 of (Braibant et al. 2011). Thus, neutralinos prevalently decay into the highest mass accessible fermions: annihilation into light quarks (i.e.,  $u$ ,  $d$ ,  $s$ , and  $c$ ) and leptons ( $e$  and  $\mu$ ) is negligible in comparison with annihilation into heavy quarks (i.e.,  $b$ , and  $t$ ) and into

the  $\tau$  lepton. Direct decay into massless particles is forbidden (and that into neutrino thus completely negligible). If the neutralino is heavy enough to annihilate into a top quark ( $m_\chi > m_t = 173 \text{ GeV}/c^2$ ), then annihilation occurs essentially entirely into  $t\bar{t}$  pairs in most models usually considered.

### 13.6.2 WIMPs Elastic Scattering

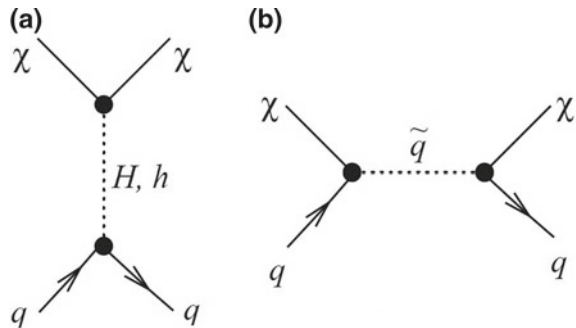
The elastic scattering of a WIMP with a nucleus in a detector can be seen as the interaction of the WIMP with a nucleus as a whole, causing it to recoil. The energy of the recoil nucleus can be measured, if large enough. The WIMP-nucleus elastic scattering cross section is the quantity studied in direct experiments. This cross section determines also the rate at which particles from the Galactic halo accrete onto the Sun (or other massive objects), and contributes to the signal yield in the indirect detection experiments.

The cross section for WIMP-proton or WIMP-neutron elastic scattering (in the following always denoted as  $\sigma_0 \equiv \sigma_{\chi p} \sim \sigma_{\chi n}$ ) depends on the WIMP-quark interaction strength. The interaction of WIMPs with quarks and gluons (=partons) of the nucleon is quantified in the cross section using Feynman diagrams, as those shown in Fig. 13.3. For supersymmetric models, the effective interactions of neutralinos at the microscopic level depend on the masses of the exchanged particles and on other important SUSY parameters. Under general conditions, the elastic-scattering cross section  $\sigma_0$  is related to the WIMP annihilation cross section  $\sigma_\chi$  and

$$\sigma_0 \ll \sigma_\chi \simeq 10^{-36} \text{ cm}^2 = 1 \text{ pb} \tag{13.14}$$

Even in simplified SUSY versions, there are typically many possible values allowed. In MSSM, in a raster scan of the model parameters,  $\sigma_0 \sim 10^{-3} - 10^{-13} \sigma_\chi$ . In DM models different from SUSY, the relation between annihilation and interaction cross sections could be more complicated. Experimental results are thus used to infer limits on  $\sigma_0$ , under sometimes particular conditions.

**Fig. 13.3** Tree level Feynman diagrams for neutralino-quark scalar (spin-independent) elastic scattering. **a**  $t$ -channel exchange of a Higgs boson, **b**  $s$ -channel exchange of a squark



Important simplifications in the estimates of  $\sigma_0$  occur when the nonrelativistic limit holds. This is exactly the situation for local WIMPs, with average velocity given in (13.13). Only two general cases need to be considered: the spin-spin (or *spin-dependent*) interaction and the scalar (or *spin-independent*) interaction. In the case of the spin-spin interaction, the WIMP couples to the spin of the nucleus; in the case of the scalar interaction, the WIMP couples to the mass of the nucleus.

**Spin-independent interactions.** In the nonrelativistic limit, the spin-independent (SI) term of the WIMP cross section on a proton or a neutron (we assume here  $m_p = m_n$ ) can be parameterized as

$$\sigma_0^{SI} = \frac{4m_\chi^2 m_p^2}{\pi(m_\chi + m_p)^2} f_{p,n}^2 = \frac{4m_{r_p}^2}{\pi} f_{p,n}^2 \quad (13.15)$$

where  $m_{r_p} \equiv (m_p m_\chi)/(m_p + m_\chi)$  is the reduced mass of the WIMP-proton system ( $m_{r_p} \simeq m_p$  for  $m_\chi \gtrsim 10 \text{ GeV}/c^2$ ). The quantity  $f_{p,n}$  represents the WIMP spin-independent coupling to protons or neutrons, as derived from Feynman diagrams on the partons constituents. In general, as in SUSY models, this quantity depends on the coupling of the WIMP with quarks and gluons. Equation (13.15) is called *spin-independent*, SI, or *scalar* cross section.

Usually, the interaction of a WIMP with a nucleus  $A$  is experimentally studied. Thus, the cross sections  $\sigma_{\chi A}$  must be related to  $\sigma_0$ , taking into account the distribution of quarks in the nucleon and the distribution of nucleons in the nucleus. To relate  $\sigma_{\chi A}$  to  $\sigma_0$  we need to consider the de Broglie wavelength of the scattering system. For reasonable values of the WIMP mass ( $m_\chi = 10 \text{ GeV}/c^2$  to few  $\text{TeV}/c^2$ ) the average momentum transferred to a nucleus of mass  $m_A \sim Am_p$  is  $p = m_{r_A} \bar{v}$ , where  $m_{r_A}$  is the reduced mass of the WIMP-nucleus system and  $\bar{v}$  their relative velocity given in (13.13).

Assuming nuclei in the range  $A = 10 - 100$ , the reduced mass is  $m_{r_A} \sim m_\chi$  when  $m_\chi \ll m_A$ , and  $m_{r_A} \sim m_A$  when  $m_\chi \gg m_A$ . Thus the transferred momentum  $p$  ranges between 10 and 50  $\text{MeV}/c$ . Hence, elastic scattering occurs in the extreme nonrelativistic limit. The de Broglie wavelength corresponding to a momentum transfer of  $p = 10 \text{ MeV}/c$  is:

$$\lambda = \frac{h}{p} = \frac{hc}{pc} = \frac{197 \text{ MeV fm}}{10 \text{ MeV}} = 20 \text{ fm} \quad (13.16)$$

which is larger than the radius of the nucleus  $r_A \sim 1.25A^{1/3} \text{ fm}$  [see Chap. 14 of Braibant et al. (2011)]. The extrapolation of the scattering amplitudes (13.15) to nuclei with  $Z$  protons and  $A - Z$  neutrons will then add coherently as:

$$\sigma_{\chi A}^{SI} = \frac{4m_{r_A}^2}{\pi} [Zf_p + (A - Z)f_n]^2 \simeq \left( \frac{m_{r_A}}{m_{r_p}} \right)^2 A^2 \sigma_0^{SI} . \quad (13.17)$$

The last equality holds if  $f_p - f_n$ . The main feature of the SI scattering is the increase with the squared mass number  $A$  of the target nuclei. Current experiments using heavy atoms as targets are typically dominated by spin-independent scattering.

**Spin-dependent interactions** Axial-vector interactions result from couplings of WIMP semi-integer spin to the spin content of a nucleon. The analogous of (13.15) for *spin-dependent*, SD, interactions on protons and neutrons is

$$\sigma_{\chi A}^{SD} = \frac{32m_r^2}{\pi} G_F^2 \frac{J+1}{J} [a_p \langle S_p \rangle + a_n \langle S_n \rangle]^2. \quad (13.18)$$

$G_F$  is the Fermi constant and  $a_p, a_n$  are the effective WIMP-couplings to proton,  $\langle S_p \rangle$ , and neutron,  $\langle S_n \rangle$ , expectation values of the spin operators. In general, the SD cross section is proportional to  $J(J+1)$ , where  $J$  is the total angular momentum of the nucleus. No relevant gain of the spin-dependent cross section is obtained using heavy target nuclei.

WIMPs **nonelastic interactions** include inelastic scattering, as the interaction with orbital electrons in the target, or the interactions with the target nuclei yielding an excited nuclear state. They are usually not considered because they give signatures that have to compete with huge backgrounds of natural radioactivity.

### 13.7 Direct Detection of Dark Matter: Event Rates

The idea that WIMPs can be detected by elastic scattering off nuclei in a terrestrial detector, Fig. 13.4a, dates back to 1985 (Goodman and Witten 1985). It was immediately extended to include the fact that the Earth's motion around the Sun would produce an annual modulation in the expected signals (Drukier et al. 1986).

When considering a nucleus of mass  $m_A \simeq Am_p$ , using nonrelativistic kinematic arguments, the energy that is transferred to the recoiling nucleus is:

$$E_R = \frac{p^2}{2m_A} = \frac{m_{rA}^2 v^2}{m_A} (1 - \cos \theta), \quad (13.19)$$

where  $p$  the transferred momentum,  $v$  the WIMP velocity and  $\theta$  the scattering angle. Numerically, assuming  $m_\chi = 100 \text{ GeV}/c^2$ ,  $v \simeq \bar{v} \simeq 10^{-3}c$  and a nucleus with  $A \sim 100$  such that  $m_A \sim m_\chi$  and  $m_{rA} = m_\chi/2$  we obtain at maximum ( $\cos \theta = -1$ )

$$\langle E_R \rangle = \frac{1}{2} m_\chi \bar{v}^2 \sim 50 \text{ keV} \quad (13.20)$$

Specialized detectors able to measure recoils of considerably lower energy, as low as few keV, and to distinguish them from background, may make such direct detection possible. The event rate in a detector depends on many input factors: (i) the nature



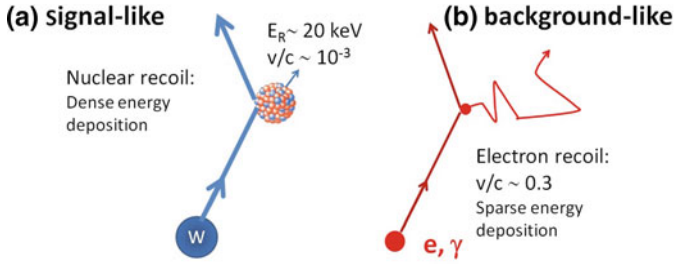


**Fig. 13.4** Sketch of the elastic WIMP scattering off a nucleus. The nucleus recoil (a) produces excitation/ionization of the medium, different from that produced by the background interaction (b) of electrons/photons on the electrons of the medium

of the interacting particle, related to the unknown scattering cross section  $\sigma_{\chi A}^{SD,SI}$ ; (ii) the nuclear form factors of the detection material; (iii) the astrophysical density distribution of WIMPs and their velocity distribution  $f(v)$  in the Galactic halo; (iv) the response of the detector as a function of the nucleus recoil energy.

If the halo of our Galaxy consists of WIMPs with the density and average velocity given in (13.13), their flux on Earth is given by:

$$\Phi_{\chi} = \frac{\rho_0 \cdot \bar{v}}{m_{\chi}} \simeq 7 \times 10^4 \left( \frac{100}{m_{\chi} [\text{GeV}/c^2]} \right) \text{cm}^{-2} \text{s}^{-1}. \quad (13.21)$$

Let us compute an order-of-magnitude of the event rate, which can be simply expressed as the product of (13.21) by the cross section on nuclei  $A$  of a homogeneous detector of mass  $M_T$ . The corresponding number of target nuclei is given by  $N_T = M_T N_A / (A m_p)$ , where  $N_A$  is Avogadro's number. The event rates are usually expressed for 1 kg detector, such as  $N_T = 6 \times 10^{26} / A \text{ kg}^{-1}$ . Assuming a spin-independent interaction, the WIMP-nucleus cross section is given by (13.17). Thus a first-order estimate of the event rate is:

$$R = N_T \cdot \frac{\rho_0 \cdot \bar{v}}{m_{\chi}} \cdot \sigma_{\chi A}^{SI} = \frac{6 \times 10^{26}}{A} \cdot \left( \frac{7 \times 10^4}{m_{\chi} [100 \text{ GeV}/c^2]} \right) \cdot \left( \frac{m_{rA}}{m_{r_p}} \right)^2 A^2 \sigma_0 \text{ kg}^{-1} \text{s}^{-1} \quad (13.22)$$

Assuming: a WIMP having mass  $m_{\chi} = 100 \text{ GeV}/c^2$ , cross section  $\sigma_0 = 10^{-9} \text{ pb} = 10^{-45} \text{ cm}^2$ , one day ( $=86400 \text{ s}$ ), and using the definition of reduced mass ( $m_{\chi} \gg m_p$ ) we obtain:

$$R = 3.6 \times 10^{-9} \left( \frac{A^{3/2} m_{\chi}}{A m_p + m_{\chi}} \right)^2 \left( \frac{\sigma_0}{10^{-45} \text{ cm}^2} \right) \text{ kg}^{-1} \text{d}^{-1} \quad (13.23)$$

For materials used in typical detectors, the factor depending on  $A$  in bracket is about  $4.0 \times 10^5$  for Xe ( $A = 131$ ),  $1.2 \times 10^5$  for Ge ( $A = 73$ ), and  $0.3 \times 10^5$  for Ar

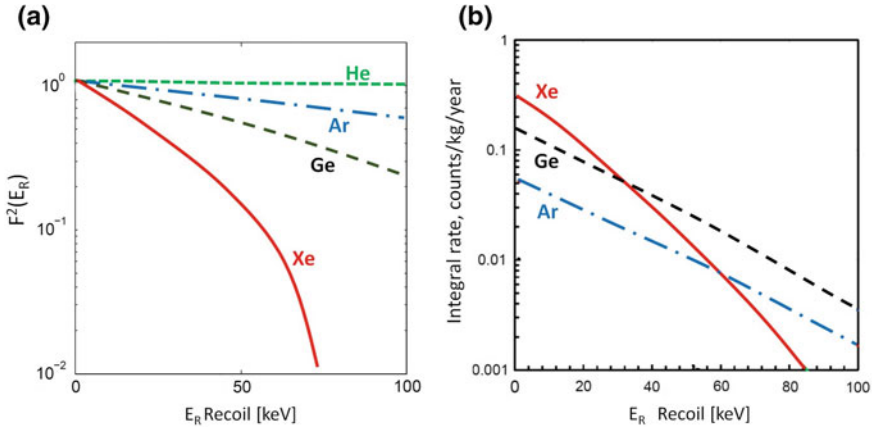


**Fig. 13.5** **a** Nuclear form factors  $F^2(E_R)$  for four different nuclei as a function of the nucleus recoil energy  $E_R$ . The more extended is the nuclear distribution, the stronger is the fall-off as a function of the recoil energy. **b** Integral energy spectrum of a spin-independent elastic scattering WIMP-nucleus for four different nuclei, assuming perfect energy resolution of the detector. The heavier nuclei show a higher interaction rate at low recoil energies. The assumptions are:  $m_\chi = 100 \text{ GeV}/c^2$ ,  $\sigma_0 = 10^{-45} \text{ cm}^2$  and the astrophysical conditions given by (13.13)

( $A = 40$ ). Thus from (13.23) the corresponding event rates are of the order of  $\sim 10^{-4} - 10^{-3} \text{ /kg/day}$  for argon and xenon, respectively.

Direct-detection experiments measure the number of signals equivalent to a given nuclear recoil  $E_R$  per day per kilogram of detector material as a function of deposited energy. It should be noted that many background sources can simulate events with a deposited energy equivalent to  $E_R$ , see Fig. 13.4b. For a real experiment, the detailed distribution of velocities  $f(v)$ , the nuclear form factor  $F^2(E_R)$  and the detector efficiency must be considered, decreasing significantly the number of signal events. The nuclear form factor term is about unit for light nuclei, while it suppresses high energy recoils for heavy nuclei, see Fig. 13.5a, reducing the number of observable events. The nuclear form factor depends on nuclear physics properties only. The integral event rate as a function of the nuclear recoil computed for some peculiar nuclei (expressed as events/kg/year) is shown in Fig. 13.5b. For a realistic 100 kg Xe detector (as XENON100), the number of expected events above a detection threshold of 5 (15) keV is 18 (8) events per year, assuming a cross section  $\sigma_0 = 10^{-45} \text{ cm}^2$  and a WIMP mass of  $m_\chi = 100 \text{ GeV}/c^2$ .

In the above example, the experimental observable (the event rate) depends on  $m_\chi$  and  $\sigma_0$ , according to (13.23). For this reason, the results of experimental searches are usually expressed as a contour in the plane of parameters of cross section vs. WIMP mass. A closed contour expresses the range of parameters that produce the observed signal compatible with errors (in case of a positive claim); a curve delimits the region of parameter values that are excluded, as shown in Sect. 13.8.4.

## 13.8 WIMPs Direct Detection

Direct detection experiments in astroparticle physics play a complementary role with respect to collider experiments. A new, massive, and long-lived particle eventually discovered at LHC cannot automatically be associated with a DM candidate. Accelerator detectors cannot record the cosmological abundance of an observed WIMP. On the other hand, the detection of dark matter particles in astroparticle physics experiments will not be sufficient to identify conclusively the nature of these particles.

To observe WIMPs, detectors with a low energy threshold, an ultra-low background noise and a large target mass are mandatory (Saab 2012). There is currently a continuous development of larger and more sophisticated detectors sensitive to WIMP-nucleus interactions yielding ionization and/or excitation. See (Gaitskell 2004) for a review of early experimental techniques.

In a detector, the kinetic energy of a nucleus after a WIMP elastic scattering is converted into a measurable signal: depending on experimental techniques, the signal corresponds to (1) *ionization*, (2) *scintillation light*; (3) *vibration quanta (phonons)*. The main experimental problem is to distinguish the genuine nuclear recoil induced by a WIMP from the huge background due to environmental radioactivity. All detectors have a threshold energy  $E_R^{th}$  above which they are sensitive, typically in the 5–40 keV range. The simultaneous detection of two observables strengthens the discrimination against background events.

Highly granular detectors and/or with good timing and position resolution are used to distinguish the WIMP localized energy depositions. Some experimental techniques are sensible to only a fraction of the recoil energy of the nucleus. The measured energy has thus to be converted into the true recoil energy through an energy-dependent factor called the *quenching factor*. The measured energy is often labeled in units of keVee (keV electron equivalent), while the nuclear recoil energy is often labeled with units of keV, keVr, or keVnr.

In the energy range of interest for WIMP detection (deposited energy below 100 keV) the main contributions to background are electromagnetic interactions originated from  $\alpha$ ,  $\beta$  and  $\gamma$ -decays of environmental radioactivity interacting with electrons of the medium, Fig. 13.4b. Radioactive isotopes are present in the material surrounding the detectors, in airborne contaminants that can be deposited on the surfaces, or within the detectors themselves. Neutron interactions, as genuine WIMP signals, scatter off nuclei. Sometimes, neutron sources are used to simulate the signal. Particularly dangerous are neutrons from natural radioactivity (the so-called radiogenic neutrons, with energies below 10 MeV), or induced by  $\alpha$  capture of a nucleus, or produced by secondary CRs. Regardless of the experimental technique, all the DM detectors are located at a deep underground site to reduce the flux of muon-induced energetic neutrons, Fig. 1.7.

Appropriate shielding with passive and/or active materials and sometimes the use of veto detectors around the experiment can significantly suppress the background event rate. Lead, copper, and other high- $Z$  materials are necessary to absorb electrons and  $\gamma$ -rays, whereas water, polyethylene, and other hydrogen-rich materials are well

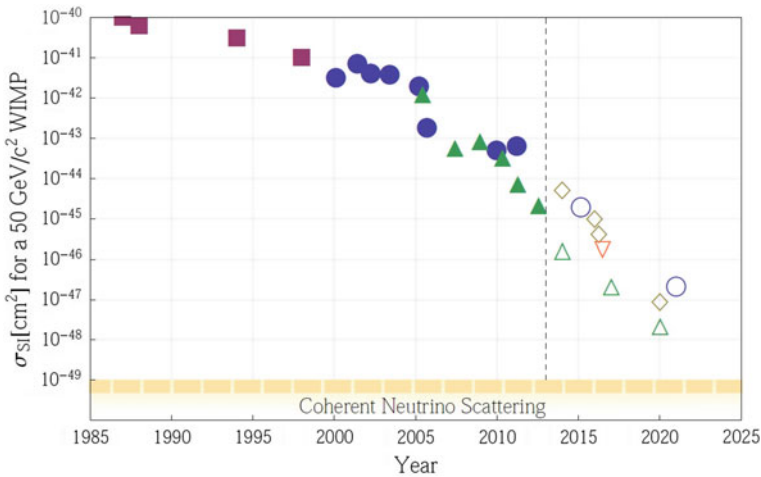


**Fig. 13.6** History and projected evolution with time of SI WIMP-nucleon cross-section limits for a 50 GeV WIMP. The symbols used denote the different technologies: cryogenic solid state (*blue circles*), crystal detectors (*purple squares*), liquid argon (*brown diamonds*), liquid xenon (*green triangles*), and threshold detectors (*orange inverted triangle*). Below the *yellow dashed line*, WIMP sensitivity is limited by coherent neutrino-nucleus scattering. From Bauer et al. (2014)

suit for moderating the neutron background. Appropriate selection, clean fabrication and operation procedures of the materials used for the detector and their support structures are mandatory to minimize the backgrounds from within the experiment itself. Direct detection experiments have made tremendous progress in the last three decades. Figure 13.6 shows the sensitivity reached on SI cross section as a function of year. This rapid progress has been driven by remarkable innovations in detector technologies that have provided extraordinary active rejection of backgrounds.

Solar (Sect. 12.2) and atmospheric neutrinos (Sect. 11.7) represent the ultimate, irreducible background. Nuclear recoils induced from coherent neutrino-nucleus scattering cannot be distinguished from a genuine WIMP-induced signal. This background could dominate the measured event rate if the WIMP-nucleon cross section is below  $10^{-49} \text{ cm}^2$  (Baudis 2012), see Fig. 13.6.

### 13.8.1 Solid-State Cryogenic Detectors

Cryogenic detectors operate at sub-Kelvin temperatures and allow to perform a calorimetric energy measurement down to very low energies ( $E_R < 10 \text{ keV}$ ), with unsurpassed energy resolution and the ability to differentiate nuclear from electron recoils on an event-by-event basis.

The operational principles rely on the fact that the heat capacity of a dielectric crystal depends on temperature as  $\sim T^3$ . A small energy deposition, such as that induced by a nuclear recoil, significantly changes the temperature of the absorber,

yielding collective excitations (phonons) of the lattice of the detector crystal. The phonon (or thermal) response of the detector determines the total recoil energy of an interaction. The signals induced by a nuclear recoil and by ionization from an electron (the two cases of Fig. 13.4) are different. For this reason, if a second detector response is available in addition to the thermal response, such as those dependent on scintillation or ionization for example, the background rejection is highly improved.

The leading cryogenic detectors are the CDMS, CRESST and EDELWEISS experiments, all operating underground. CRESST, in a run with  $730 \text{ kg} \times \text{days}$  exposure, has an event excess compatible with a DM signal, implying a WIMP mass of around  $20 \text{ GeV}/c^2$  and a cross section  $\sigma_0 \sim 10^{-42} \text{ cm}^2$ . In contrast, CDMS and EDELWEISS have reached sensitivities down to  $\sigma_0 \sim 3 \times 10^{-44} \text{ cm}^2$  in a combined analysis with an effective exposure of  $614 \text{ kg} \times \text{days}$ , not confirming the CRESST findings. See the corresponding allowed region and upper limits on Fig. 13.8.

The CoGeNT experiment uses as detection mechanism the ionization signal from high-purity, low-radioactivity germanium. As other germanium ionization detectors, it can reach sub-keV energy thresholds and low backgrounds, but it lacks the ability to distinguish nuclear recoils from the signals produced by ionization. Using data from a  $18.5 \text{ kg} \times \text{days}$  exposure, CoGeNT has claimed evidence for a  $7 \text{ GeV}/c^2$  WIMP with a cross section  $\sigma_0 \sim 10^{-40} \text{ cm}^2$ . This potential low-mass WIMP signal is excluded by other experiments, and it could be mostly caused by residual surface events.

### 13.8.2 Scintillating Crystals

A second technique uses scintillator crystals encased in a low-radioactivity enclosure and read out with photomultiplier tubes (PMTs). Electron and nuclear recoils induce signals in the PMTs with different pulse shapes, but normally this effect is too weak to exploit on an event-by-event basis. For this reason, some experiments are looking for a time-dependent modulation of a WIMP signal in their data. The *seasonal (or annual) modulation* effect is a discrimination method based on the expected annual variation in the WIMP event rates. The WIMPs are assumed stationary in the galactic frame. As the Earth moves around the Sun their flux, if any, should be maximum in June (when the revolution velocity of the Earth adds to the velocity of the solar system in the Galaxy) and minimum in December (when the two velocities have opposite directions), with an expected amplitude variation of a few percent. To produce an acceptable statistics, this method requires an experiment with large exposure and long data acquisition periods (many years).

The DAMA/LIBRA (and the former DAMA/NaI) is the first experiment using this detection strategy. The apparatus is made of 25 highly radio-pure NaI(Tl) crystals, each with a mass of 9.7 kg, arranged in a  $5 \times 5$  grid. Each detector is encapsulated in a pure copper housing with quartz light guides coupled to a PMT at two opposing faces of the crystal. The detector is placed in the center of a multilayer Cu/Pb/Cd-foils/polyethylene/paraffin structure for shielding at the Gran Sasso laboratory.

The latest DAMA/LIBRA result uses a total exposure of  $1.17 \text{ ton} \times \text{years}$  covering a period of 13 annual cycles, with an event rate of  $\sim 1 \text{ count/kg/keV/day}$  above an energy threshold of  $\sim 2 \text{ keV}$ . The experiment has detected with a high statistical significance an annual modulation of the event rate that is consistent with the phase, amplitude, and spectrum expected from a nonrotating WIMP halo. Although the WIMP-nucleon cross section calculated from this data is compatible with some MSSM, it is incompatible with the current upper-limits from other experiments (Fig. 13.8).

A number of possible explanations for this discrepancy have been proposed: effects due to non-MSSM dark matter candidates; variations in the dark matter halo model; unaccounted physical effects in the detectors; unaccounted background sources; issues with the data and/or its interpretation. At present, none of the proposed explanations seems to offer a satisfactory solution to the incompatibility of the various experimental results.

Future projects will also look for this seasonal effect using the same NaI(Tl) or different crystals, as the DM-Ice at the South Pole, a 250 kg experiment at a depth of 2,450 m in the Antarctic icecap.

### 13.8.3 Noble Liquid Detectors

Noble elements in liquid state such as argon ( $A = 40$ ) and xenon ( $A = 131$ ) offer excellent media for building nonsegmented, homogeneous, compact, and self-shielding detectors. Liquid xenon (LXe) and liquid argon (LAr) are good scintillators and ionizers in response to the passage of radiation. They can operate in single read-out mode as a scintillation only detector (similar to the scintillator crystals). Detectors can be also arranged in such a way as to allow on an event-by-event basis a strong rejection of electron recoils. The features of LXe and LAr, together with the relative facility of scaling-up to large masses, have contributed to make noble gases/liquids powerful targets for WIMP searches. An interaction in the liquid produces ionization and excitation of the target atoms. Using pulse-shape discrimination of the signal in the PMTs, the nuclear-recoil induced by a WIMP can be separated from a background electron-recoil. Example of these single-phase experiments are XMASS and miniCLEAN.

Two-phase time projection chambers (TPC) have also been developed for dark matter detection using xenon [see Aprile and Doke (2010)] and argon, and several large detectors are under commissioning or construction. All experiments have a common design/operation principle, which is shown schematically in Fig. 13.7. A low-radioactivity vessel is partially filled with liquid xenon (or argon), with the rest of the vessel containing xenon (argon) gas. Electric fields of  $\sim 1 \text{ keV/cm}$  and  $\sim 10 \text{ keV/cm}$  are established across the liquid and gas volumes respectively by applying a voltage bias to the electrodes (shown as dashed lines in the figure). An interaction in the LXe produces excitation and ionization processes. Photomultiplier tube arrays are present at the top (in the gas volume) and bottom (in the liquid). A first signal (called S1) after the interaction is due to the de-excitation processes, yielding prompt photons near

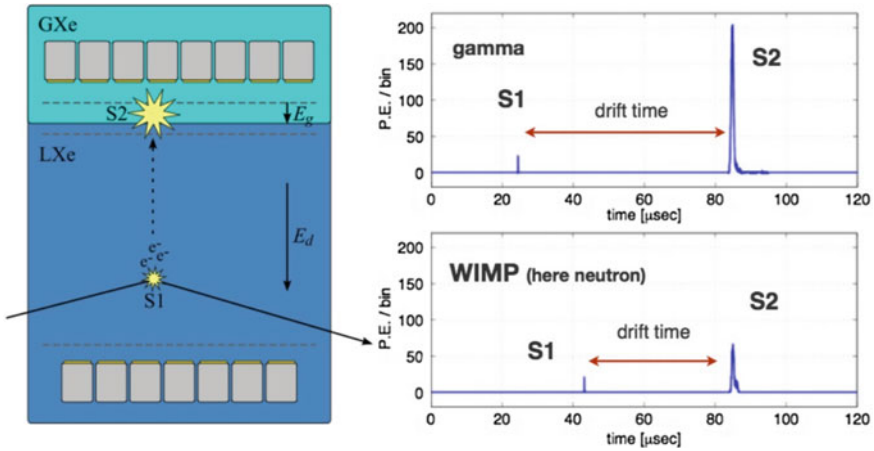


**Fig. 13.7** Schematic of a xenon two-phase time-projection chamber, showing the recorded signals for a  $\gamma$ -ray interaction and a WIMP (actually a neutron used for calibration). The ratio S2/S1 is used to discriminate between electron and nuclear recoils. Courtesy prof. T. Saab

the interaction vertex in the LXe. The associated electrons produced by ionization drift under the electric field; when they reach the liquid surface, they are extracted into the gas phase by the higher electric field. As electrons accelerate through the gas, their interactions produce a second scintillation signal (S2). The right side of Fig. 13.7 shows the S1 and S2 signals for two events: an electron recoil caused by a background event (here, a  $\gamma$ -ray interaction), and a nuclear recoil caused by a neutron interaction, simulating a genuine WIMP process. The ratio of the S2 and S1 signals is used as a discriminator between these types of events.

Neutron background cannot be removed using this procedure. The reconstruction of the interaction vertex inside a fiducial volume of the detector offers an additional tool to suppress the neutron contamination that piles up near the detector surface. The TPC configuration allows the measurement of the vertex position. The pattern of hits in the PMTs determines the  $(x; y)$  coordinates; the time difference between the S1 and S2 pulses measures the electron drift time, and thus determines the  $z$  position (that along the electric field). The low energy threshold of the experiment is determined by the smaller S1 signal, and is typically set at a few photons per event.

### 13.8.4 Present Experimental Results and the Future

WIMPs could have scalar,  $\sigma_0^{SI}$ , and/or spin-dependent,  $\sigma_0^{SD}$ , interactions with nuclei and experimental results are discussed in terms of either interaction type. Figure 13.8 illustrates the current best limits on WIMP spin-independent scattering cross sections as a function of the WIMP mass. The closed colored areas represent the allowed



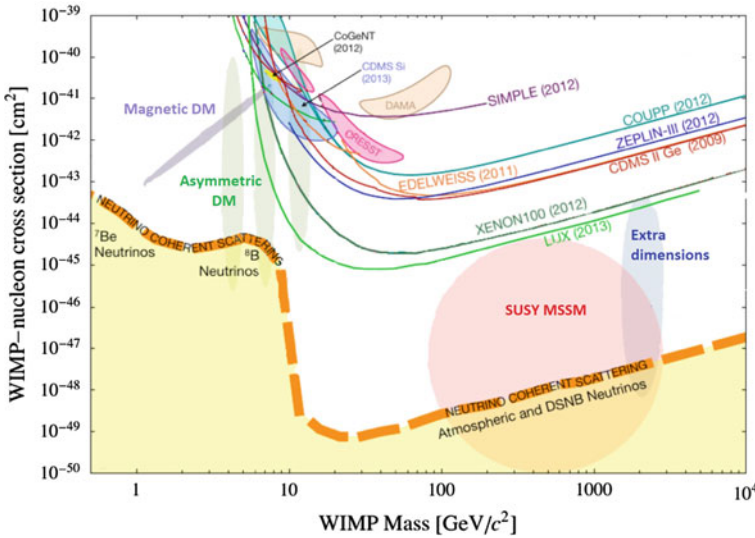


**Fig. 13.8** A compilation of WIMP-nucleon SI cross-section limits (*solid curves*) as a function of  $m_\chi$ . The regions of interest arising from different claims for a signal from DAMA/LIBRA, CREST II, CDMS-Si, and CoGeNT are represented by enclosed areas. An approximate band where coherent scattering of solar neutrinos, atmospheric neutrinos and diffuse supernova neutrinos with nuclei will begin to limit the sensitivity of direct detection experiments to WIMPs is also reported. Finally, a suite of theoretical model predictions is indicated by the *shaded* regions. Adapted from Bauer et al. (2014), which we refer to for the references to experiments and models

regions of the space parameters derived from positive claims. The results of experiments using different target nuclei are normalized to scattering on a single nucleon,  $\sigma_0$ , using Eq. (13.17).

The upper limits as a function of  $m_\chi$  derive from the above discussion on the event rate: the sensitivity is maximum for WIMP masses near the mass of the recoiling nucleus (50–100  $\text{GeV}/c^2$ ). At lower WIMP mass, the sensitivity drops because of effects connected with the energy threshold of detectors. At higher masses, the sensitivity worsens because the WIMP flux decreases as  $\propto 1/m_\chi$ .

The limits from direct detection are competitive with the limits obtained at accelerator experiments. At present (June 2014) the absence of any signal of physics beyond the SM at the LHC, as well as the discovery of a SM-like Higgs boson with the relatively high mass  $\sim 126 \text{ GeV}/c^2$ , constrains many well-motivated WIMP models towards large WIMP masses and low  $\sigma_0$ .

Several ton-scale direct detection experiments are in their construction phase, and will start taking science data well within this decade, using the same (or improved) detection techniques illustrated above (Baudis 2012). Those experiments can reach a discovery if the WIMP-nucleon cross section is larger than  $10^{-46} \text{ cm}^2$  in the mass range  $20 < m_\chi < 1000 \text{ GeV}/c^2$ .

Sensitivities down to  $\sigma_0 \sim 10^{-49} \text{ cm}^2$  are needed to probe nearly all of the MSSM parameter space at WIMP masses above  $10 \text{ GeV}/c^2$ . Below this limit, the irreducible neutrino-induced background would probably cover any DM signature. Such sensitivities will be reached with multi ton mass detectors with superb background discrimination capabilities. Such experiments [see Sect. 24. Dark Matter of Beringer et al. (2012)] are envisaged by the US project LZ (6 tons), the European consortium DARWIN, and the MAX project (a liquid Xe and Ar multiton project).

Alternative solutions to huge massive experiments are detectors able of measure the direction of the recoiling nucleus. This represents a signature that would unequivocally confirm the Galactic origin of a signal. Because of the correlation between the direction of the incoming WIMP and that of the recoiling nucleus, signal events should point in the direction of the WIMP wind. The relative directions of the laboratory frame and the WIMP wind has a 24-hour modulation, due to the Earth rotation around its axis. With an ideal detector able to reconstruct the tracks of individual nuclei, a challenging discrimination technique using this 24-hour modulation can be developed. Background events are not expected to exhibit anisotropies. Because nuclear recoils have a small energy, probably only gaseous detectors can measure precisely the very limited nuclear range. Several directional detectors are presently in the research and development phase.

## 13.9 Indirect WIMPs Detection

WIMPs annihilate into standard model particles with the cross section given in (13.10) to explain cosmological observations. This small value no longer affects the overall WIMP abundance after decoupling. However, WIMPs annihilation continues, and may be large enough to be observed indirectly if the end products include photons, neutrinos, electrons, protons, deuterium, and their corresponding antiparticles. As a consequence of this long particle list, there are many indirect detection methods being pursued. The relative sensitivities of indirect detection methods are highly dependent on which WIMP candidate is being considered. The difficulties in determining backgrounds and systematic uncertainties also vary greatly from one method to another. The most exploited methods refer to the detection of neutrinos from massive objects; the study of  $\gamma$ -rays; the searches for antimatter in cosmic rays.

### 13.9.1 Neutrinos from WIMP Annihilation in Massive Objects

Massive objects (as our Sun) act as amplifiers for DM annihilations by capturing DM particles as they lose energy through elastic scattering with nuclei. Once gravitationally captured, DM particles settle into the core, where their densities and annihilation rates are greatly enhanced. Most of their annihilation products are immediately absorbed, and only neutrinos escape these dense objects. The centers of massive

objects represent the natural places to look for a possible neutrino excess from DM annihilation using neutrino telescopes. In the following, we specialize the discussion to the case of the Sun ( $\odot$ ). The extension to other massive objects (the Earth core, the Galaxy center, nearby dwarf spheroidal galaxies) exists in the literature.

The DM capture rate  $C^\odot$  [ $\text{s}^{-1}$ ] can be written as:

$$C^\odot \simeq \Phi_\chi \cdot \left(\frac{M_\odot}{m_p}\right) \cdot \sigma_0 \quad (13.24)$$

where  $\Phi_\chi$  is the local DM flux (13.21), the ratio  $(M_\odot/m_p) \simeq 10^{57}$  is an estimate of the number of target nucleons in the Sun and  $\sigma_0$  represents as usual the WIMP-nucleon cross section. As discussed, this quantity could be spin-dependent, spin-independent or both. The current bounds from direct searches are  $\sigma_0^{SD} \lesssim 10^{-39} \text{ cm}^2$  and  $\sigma_0^{SI} \lesssim 10^{-45} \text{ cm}^2$  (see Fig. 13.8). Thus, inserting the relevant numbers in (13.24) and arbitrarily assuming a reference cross section of  $10^{-42} \text{ cm}^2$ , intermediate between the above two SI and SD limits, we obtain:

$$C^\odot \simeq \frac{3 \times 10^{20}}{[\text{s}]} \cdot \left(\frac{\rho_0}{0.3 \text{ GeV cm}^{-3}}\right) \cdot \left(\frac{\bar{v}}{220 \text{ km s}^{-1}}\right) \cdot \left(\frac{100 \text{ GeV}}{m_\chi}\right) \cdot \left(\frac{\sigma_0}{10^{-42} \text{ cm}^2}\right) \quad (13.25)$$

The number of DM particles present in the Sun depends on time: they are accumulating at a constant rate (13.25), but some of them undergo annihilation processes that depend on the annihilation cross section  $\sigma_\chi$ . Under reasonable assumptions, it is possible to show [follow the details of this exercise in Bertone et al. (2005) and Profumo (2014)] that an equilibrium solution is reached. At equilibrium, the annihilation rate  $\Gamma_{\text{ann}}$  of WIMP particles in the Sun is

$$\Gamma_{\text{ann}} = \frac{C^\odot}{2} [\text{s}^{-1}]. \quad (13.26)$$

The rate of energy release through this hypothetical process (not included in the Solar Standard Model) corresponds from (13.25) to  $\Gamma_{\text{ann}} \cdot 100 \text{ GeV} = 10^{19} \text{ erg/s}$  (for the assumed cross section of  $10^{-42} \text{ cm}^2$ ), which is negligible with respect to the solar luminosity  $L_\odot \simeq 3.8 \times 10^{33} \text{ erg/s}$ . The existence of DM does not perturb the energy balance due thermonuclear reactions in main sequence stars.

Neutrinos (of all flavors) could be produced in the Sun core by decays or interactions of standard model particles produced in the WIMPs scattering with matter and/or by their annihilation into  $\chi \bar{\chi} \rightarrow \ell \bar{\ell}; q \bar{q}; W^+ W^-; Z^0 Z^0; \gamma \gamma; hh$ . Here,  $\ell$  represents a charged lepton,  $q$  a quark,  $W^\pm, Z^0$  the gauge bosons,  $\gamma$  the photon and  $h$  the Higgs scalar boson. If the WIMP is not the neutralino or another Majorana particle, neutrinos could also be directly produced by  $\chi \bar{\chi} \rightarrow \nu_f \bar{\nu}_f$  annihilations.

The corresponding neutrino energy spectrum  $dN_\nu/dE_\nu$  ( $\text{GeV}^{-1}$ ) depends on the assumed DM candidate. These neutrinos have typically energies much larger than those of thermonuclear origin (MeV or fraction). There are no astrophysical processes in main sequence stars that produce GeV (or higher energies) neutrinos. The spectrum

$dN_\nu/dE_\nu$  depends on the capture rate  $C^\odot$ , mass  $m_\chi$  and, for a given candidate, on the main decay channel and annihilation cross section. Details can be found in Baratella et al. (2014). From the energy spectrum  $dN_\nu/dE_\nu$  at the Sun, the differential flux on Earth can be derived:

$$\frac{d\Phi_\nu}{dE_\nu} = \frac{\Gamma_{ann}}{4\pi d^2} \frac{dN_\nu}{dE_\nu} = \frac{C^\odot}{8\pi d^2} \frac{dN_\nu}{dE_\nu} \quad [\text{GeV}^{-1}\text{cm}^{-2}\text{s}^{-1}] \quad (13.27)$$

where  $d$  is the Sun-Earth distance.

The flux prediction (13.27) depends strongly on the assumed preferred WIMPs annihilation channel. Conventionally, two reference channels are used: the *hard channel* assumes that all WIMPs annihilations produce a  $W^+W^-$  pair (sometimes, the  $\tau^+\tau^-$  leptons). This assumption gives rise to a harder neutrino energy spectrum, with the largest fraction of high-energy neutrinos. The so-called *soft channel* assumes on the other hand 100% production of  $b\bar{b}$  pairs, giving rise to a softer neutrino energy spectrum. In SUSY models, they are exactly the preferred final states for the lightest neutralinos. The interpretation of the neutrino flux from the Sun in terms of WIMPs parameters depends on the assumed WIMP decay channel (if hard, soft or intermediate). The effective area of neutrino telescopes increases with  $E_\nu$  (Fig. 10.10): the hypothesis of a preferred hard spectrum for WIMP annihilations produces a larger event rate.

The number of events expected in neutrino telescopes (typically in the energy range  $E_\nu \gtrsim 100 \text{ GeV}$ ) as IceCube, ANTARES or the planned KM3NeT is given by inserting the predicted flux (13.27) into Eq. (10.24). A precise measurement of the neutrino direction (for events from the position of the Sun) can be achieved only for  $\nu_\mu$ , thus only the  $\nu_\mu$  fraction in the flux is considered. As usual, atmospheric neutrinos represent the irreducible background and a statistically significant signal excess over a flat background is searched for. At present, no excess of neutrino events from the direction of the Sun or other massive objects is reported.

For a given WIMP mass,  $m_\chi$ , a null result can be translated on a 90% C.L. upper limit on the WIMP-nucleon cross section, assuming a spin-independent,  $\sigma_0^{SI}$ , or spin-dependent,  $\sigma_0^{SD}$ , interaction. The limits are different depending on the assumption of a hard or soft WIMP decay channel. In general, the spin-independent limit obtained with this method is not competitive with that of direct experiments. In fact, the WIMP-nucleus cross section enters in the capture rate (13.24). The Sun is made of light elements (H and He) and there is no gain due to the  $A^2$  behavior of the SI cross section.

In Fig. 13.8, where limits from direct experiments are reported assuming a SI interaction, the actual best result from neutrino telescopes (Aartsen et al. 2013) would produce an upper limit (under the hypothesis of a hard channel) of  $\sigma_0^{SI} \sim 10^{-42} - 10^{-43} \text{ cm}^2$  in the energy range between 100 GeV and 1 TeV. The hypothesis of WIMP annihilations in a soft channel gives a limit two orders of magnitude worse.

On the other hand, indirect measurements using neutrinos provide the best result if the WIMP-nucleon interaction occurs through the spin-dependent coupling. The 90% C.L. upper limits obtained by the ANTARES and IceCube neutrino telescopes

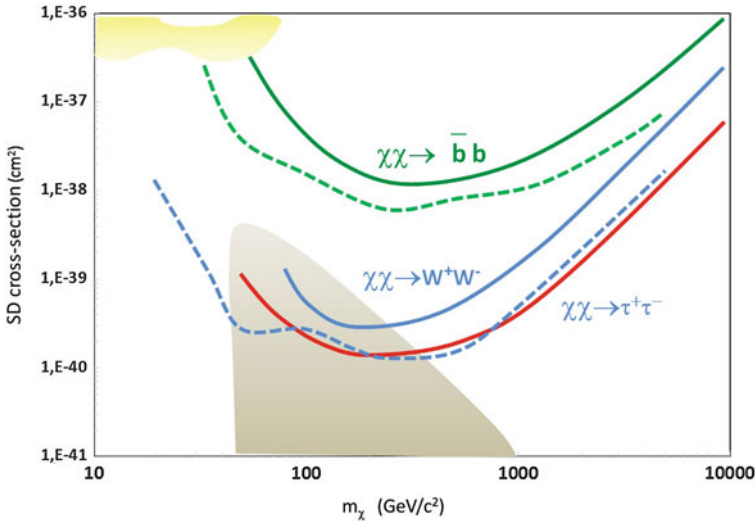


**Fig. 13.9** Upper limits (at 90% C.L.) on WIMP-nucleon cross sections versus the WIMP mass  $m_\chi$  under the assumption of a spin-dependent coupling and for the three self-annihilation channels. The limits are obtained by the ANTARES (*full lines*) (Adrián-Martínez et al. 2013) and IceCube (*dashed lines*) (Aartsen et al. 2013) neutrino telescopes searching for an excess of high-energy  $\nu_\mu$  from the direction of the Sun. The assumption of WIMPs annihilation into the *hard* channels  $\tau^+\tau^-$  (red line) or  $W^+W^-$  (blue line) provides the most stringent limits. The *soft*  $b\bar{b}$  channel (green lines) is less restrictive. As in Fig. 13.8, the *bottom* colored region represents the space of parameters allowed by MSSM and the *yellow* region at the *top left* the DAMA allowed region

under the SD assumption are shown in Fig. 13.9. Direct detection experiments (as COUPP, Simple, PICASSO) give less restrictive upper limits. Refer to Sect. 24—Dark Matter—of Beringer et al. (2012) for further information.

### 13.9.2 Gamma-Rays from WIMPs

Gamma rays eventually produced in DM annihilations or decays are not deflected by magnetic fields. If produced in transparent regions, they can travel to us from anywhere in the Galaxy and local Universe, effectively indicating the direction of their source. However, disentangling a possible DM signal from astrophysical backgrounds is not straightforward (Porter et al. 2011). Spectral information is the only method for distinguishing between a DM signal and that of astrophysical origin. It is in fact likely that DM annihilation or decay produces a  $\gamma$ -ray spectrum falling with increasing energy at a slower rate than that produced by a typical astrophysical source and with a bump (or edge) near the WIMP mass.

As shown in Sect. 8.7, the production and propagation of CR protons, nuclei, and electrons induce a diffuse nonthermal emission of photons from radio to  $\gamma$ -rays. For a while, the GeV excess seen by EGRET (the anomalous signal in the diffuse Galactic

emission observed at  $\gamma$ -ray energies  $\gtrsim 1$  GeV) received attention as a possible DM signature. The subsequent result of Fermi-LAT suggests that the EGRET GeV excess was likely the result of instrumental errors.

The cleanest and most convincing DM signal that could be measured would be annihilation into final states that include photons, such as  $\gamma\gamma$ ,  $\gamma Z^0$  or  $\gamma h$ . These processes can provide a mono-energetic feature giving a distinctive line in the  $\gamma$ -ray spectrum that is potentially distinguishable from otherwise challenging astrophysical backgrounds. However, DM models predict branching fractions into such states that are typically  $\sim 10^{-4} - 10^{-1}$  compared to the total annihilation or decay rate, placing them below the flux sensitivity of any existing instrument.

A search for  $\gamma$ -ray lines from the direction of the galactic center was done by EGRET in the range of 0.1–10 GeV, and from the Fermi-LAT in the energy range of 30–200 GeV. Another search for a  $\gamma$ -ray flux originating from DM candidates was made by Fermi-LAT from the directions of nearby dwarf spheroidal galaxies. They represent the most attractive candidate objects for DM searches, because the observations of these structures show very high mass-to-light ratios. All the above searches gave null results.

### 13.9.3 The Positron Excess: A WIMP Signature?

DM can annihilate into charged particles in the final state, which add to the cosmic radiation from astrophysical origin. This additional contribution to cosmic rays is, at best, subdominant to the observed CR energy density, much smaller than an  $\mathcal{O}(1\%)$  effect. Typical dark matter models are however democratic in producing as much matter as antimatter in the annihilation or decay final products. From the experimental point of view, the search for stable antiparticles (namely,  $\bar{p}$  and  $e^+$ ) in the cosmic radiation is a promising method to search for a possible DM signal. Antimatter is not abundant as primary radiation.

The antiproton flux (see Fig. 3.11) does not show any unexpected feature with respect to the hypothesis of pure secondary production of  $\bar{p}$ , Sect. 3.8. On the contrary, one of the most intriguing recent results is the excess of positrons in the CR spectrum, shown in Fig. 3.13, found by HEAT, PAMELA, Fermi-LAT and finally by AMS-02 experiments, Sect. 3.9. Particularly important is the measurement of the positron fraction in the energy range 5–350 GeV presented in 2013 by the AMS-02 collaboration. After this result, obtained with a large statistical sample, the likelihood that the excess is the result of experimental artifacts is negligible.

Most DM annihilation or decay models can naturally reproduce the observed rise of the positron fraction, and this has been a widely conjectured explanation of the  $e^+$  excess, as shown by the green curve in Fig. 3.13. However, models must also explain several unexpected characteristics of these data. In particular, the positron excess over that expected from CR propagation (the black full line in Fig. 3.13) requires, if due to DM annihilation, a cross section  $\sigma_\chi \sim 10^2 \div 10^3$  times larger than given by Eq. (13.10). In addition, the nonobservation of a similar antiproton excess requires the hypothesis that hadron production is suppressed: the DM must be “leptophilic”.

It is plausible that both the positron excess and the  $e^\pm$  spectrum (Fig. 3.12) can be explained by modifying the assumption usually made in models of CR propagation, as for instance in GALPROP, Sect. 5.4. This (as similar ones) computer code has proven very successful in describing a wide range of CR data in different sections of this book: antiprotons, Fig. 3.11, or other heavier antinuclei; stable secondary nuclei, Fig. 5.4; radioactive nuclei; diffuse  $\gamma$ -rays, Fig. 8.5. The only exception seems to correspond to the case of electrons and positrons, where a smooth spatial distribution of sources could not be completely adequate. For the  $e^\pm$  component, details of the discrete source distributions in the local Galaxy are probably important. In particular, the presence of a nearby pulsar seems to explain the positron excess (the red line in Fig. 3.13). However, no unique cosmic object has been identified able to explain the measured data. We can argue about what are the requirements on the age and distance of a pulsar that could contribute to the observed positron anomaly.

The rate of energy loss of an electron (or positron) in a region with a high magnetic field is given by Eq. (8.25d). Typical values of the magnetic field in the region surrounding a pulsar is about  $B \sim 100 \mu\text{G}$ , see Fig. 9.10 for the case of the Crab. For 100 GeV electrons, the dissipated power from (8.25d) is  $|dE/dt| = 0.4 \times 10^{-20} \cdot (10^2 \text{ GeV})^2 \cdot (100 \mu\text{G})^2 \sim 10^{-12} \text{ GeV/s}$ . Thus, the characteristic time  $\tau_{\text{loss}}$  for which a  $E = 100 \text{ GeV}$  electron loses its energy is

$$\tau_{\text{loss}} \simeq \frac{E}{|dE/dt|} \longrightarrow \tau_{\text{loss}} \simeq \frac{100 \text{ GeV}}{10^{-12} \text{ GeV/s}} = 10^{14} \text{ s} \sim 3\text{My} \quad (13.28)$$

Thus the pulsar age  $T_{\text{psr}}$  must be shorter than this characteristic time,  $T_{\text{psr}} < \tau_{\text{loss}}$ .

Cosmic electrons/positrons propagate in the interstellar matter in an analogous way as CR protons, following a diffusion process, Sect. 5.3.2. Using the diffusion coefficient  $D$  derived in Eq. (5.32) and the pulsar age  $T_{\text{psr}}$ , we can derive the characteristic length scale  $L$ . In this case, this corresponds to the distance  $L_{\text{psr}}$  from which electrons/positrons can arrive, i.e., the pulsar distance from the Earth:

$$L_{\text{psr}} = \sqrt{D \cdot T_{\text{psr}}} < \sqrt{D \cdot \tau_{\text{loss}}} = (3 \times 10^{27} \cdot 10^{14})^{1/2} \sim 10^{21} \text{ cm} = 0.3 \text{ kpc}. \quad (13.29)$$

The above condition gives a sufficient estimate for our following considerations, although it can be improved considering the energy-dependence of the diffusion coefficient  $D = D(E)$ . A possible candidate pulsar originating the positron excess is younger than about few My and closer than a kpc from us. Note that this result is in good agreement with that obtained in Sect. 5.8.2, Eq. (5.75).

Astrophysical models ensure that enough power can be injected under the form of accelerated  $e^\pm$  pairs. Some authors find a remarkable agreement between the data and the hypothesis that the positrons excess is originated from a single nearby pulsar, such as Geminga (a pulsar 0.25 kpc away and  $\sim 3 \times 10^5$  y old) or Monogem (also known as B0656+14, a  $\sim 10^5$  y old pulsar at 0.3 kpc), with the spectral index  $\Gamma_e \sim 2$ . The possibility that the positron excess is due to multiple known pulsars is also considered viable.



In the next years, AMS-02 will increase the energy range over which positrons and electrons are measured, as well as the total number of collected events. If the positron excess is originated from a single astrophysical source, as a nearby pulsar, it would probably give an anisotropy in the arrival direction of  $e^+$ ,  $e^-$  of the highest energy. If the origin is due to few nearby pulsars, the corresponding spectrum should have characteristic structures which can be observed with a large statistics data sample (Peng-Fei Yin et al. 2013). On the other hand, a sharp cut-off in the positron fraction would probably be the signature of a DM origin of the positron excess.

## 13.10 What's Next?

The decades-long quest to discover the Higgs boson was completed at the CERN LHC in 2012. In the SM scenario, the Higgs represented the last missing piece. Also after the 2013 Nobel Prize award for this discovery, the particle physics community is still feeling unsatisfied. There are deficiencies and open questions related to experimental data that the SM cannot explain (the neutrino mass problem), and to experimental data that can be explained, but only for seemingly unnatural choices of parameters (the strong CP, Sect. 13.4, and the gauge hierarchy, Sect. 13.5, problems). SUSY theories seem to offer a natural solution for the latter type of problems.

Supersymmetry offers some leading dark matter candidates and provide guidance for dark matter searches. For this reason, the hunt for signals beyond the SM at the LHC has an impressive priority now. The LHC is currently the highest-energy accelerator in the world. Starting from 2015, the machine will operate at 14 TeV, an energy roughly twice that at which the Higgs scalar boson was discovered.

In parallel to LHC operations, by 2017 we will have the first results of  $\sim 1$  ton direct experiment for WIMPs, that will cover the parameter phase space of Fig. 13.8 in the region of  $m_\chi \sim 50\text{--}100\text{ GeV}/c^2$  and cross section  $\sigma_0 \sim 10^{-46} \div 10^{-47}\text{ cm}^2$ . In conjunction with the LHC results, these experiment can confirm (or exclude) a discovery over a large region of the parameters allowed by SUSY models. This will open a new epoch for the search and study of massive SUSY-partners of SM particles.

What will occur if both, accelerator, and astroparticle experiments for WIMP searches, give null evidence of supersymmetric partners? Beyond the present phase of LHC operation improvements, the priority in the world strategy for particle physics is the exploitation of the full potential of the LHC including the high-luminosity upgrade of the machine and detectors. This will allow collecting ten times more data than in the initial design, by around 2030. The upgrades will cost around  $10^9$  euro, a nonnegligible fraction of the research budget of CERN member states.

The next step for direct matter experiments would be multi-ton experiments, or detectors able to point out the direction of the nuclear recoil. Those experiments would cover the parameter phase-space until the irreducible background induced by neutrinos is reached. Again, the cost would be in the range of the LHC upgrade.

Also if the searches for SUSY particles fail, the evidence for DM is so strong that non-SUSY models must be tested (Kaluza-Klein, massive neutrinos, axions, SuperWIMPs, ...) (Feng 2010). Some intriguing present results (the modulation in the DAMA event rate, the positron excess) must be investigated to confirm (or exclude) the possibilities that they are induced by DM candidates.

In the field of astroparticle physics, the beginning of this century has been characterized by many important discoveries and fast improvements in our understanding of the field: the observation of the suppression in the CR flux above  $3 \times 10^{19}$  eV; the measurement of the positron fraction up to 350 GeV, suggesting the existence of primary sources of positrons from astrophysical processes and/or dark matter interactions; the first detection of very high energy neutrinos from astrophysical sources; and confirmation that supernova remnant systems are a source of galactic CRs. These and other discoveries have been made by the current generation of experiments. The next decade will probably be remembered for the high precision measurement of the cosmic radiation up to the 10 TeV energy scale by the AMS-02 experiment, the opening of high-energy astrophysics with neutrino telescopes and for the observation (or for the nonobservation!) of gravitational waves with the improved laser interferometers.

The goals of future astroparticle physics experiments include astrophysics studies, such as: the searches for galactic PeVatrons; a better understanding of the origin of the highest energy particles in the Universe and of the acceleration processes at work; the discovery of a flux of extremely high-energy neutrinos from interactions of protons with the CMB, if UHECRs are protons. In the occurrence of a galactic core-collapse supernova, the details of the explosion mechanisms.

Some other studies are more related to arguments traditionally faced by particle physicists, such as: the possibility to measure the mass hierarchy of the neutrinos through experiments using atmospheric neutrinos crossing the Earth; the search for particles outside the Standard Model in the cosmic radiation; the measurement of particle cross sections at energies unattainable in Earth-bound accelerators; the search for baryon number violation.

Finally, some others are strictly related with cosmology, such as: the measurement of the extragalactic background light, using the attenuation of  $\gamma$ -rays, understanding the cosmic history of star formation; the search for hints on the origin of the matter-antimatter asymmetry of the Universe; the probe of the fundamental nature of spacetime.

From the particle physics point of view, the progress will depend upon either the detailed understanding of cosmic particle acceleration or the development of methods for controlling systematic errors introduced by our lack of understanding of these processes. To understand the nature of cosmic accelerators, the information arising from measurements of  $\gamma$ -rays with high-resolution instruments, those derived from high-statistics measurements of charged CRs and the new frontiers offered by neutrino telescopes must be combined. In the near future, probably also gravitational waves will enter into, in case of positive detection.

Any improvement in the performance of the present generation of detectors (Fermi-LAT for the GeV  $\gamma$ -rays; the IACTs for the TeV  $\gamma$ -rays; the P. Auger Observatory and Telescope Array for the UHECRs; the AMS-02 experiment on the ISS; the ANTARES and IceCube neutrino telescopes) would be extremely expensive and the community must adequately ponder the priorities.

## References

- M.G. Aartsen et al., (IceCube collaboration). Search for dark matter annihilations in the Sun with the 79-string IceCube detector. *Phys. Rev. Lett.* **110**, 131302 (2013)
- P.A.R. Ade et al. (Planck Collaboration). (2014), [arXiv:1303.5062v1](https://arxiv.org/abs/1303.5062v1)
- S. Adrián-Martínez et al., (ANTARES Coll.) First results on dark matter annihilation in the Sun using the ANTARES neutrino telescope. *JCAP11* (2013) 032. [arXiv:1302.6516](https://arxiv.org/abs/1302.6516)
- E. Aprile, T. Doke, Liquid xenon detectors for particle physics and astrophysics. *Rev. Mod. Phys.* **82**, 2053–2097 (2010)
- P. Baratella et al. PPPC 4 DM $\nu$ : A poor particle physicist cookbook for neutrinos from DM annihilations in the sun. (2014), [arXiv:1312.6408](https://arxiv.org/abs/1312.6408)
- L. Baudis, Direct dark matter detection: the next decade. *Dark Universe* **1**, 94–108 (2012)
- D. Bauer et al., Snowmass CF1 summary: WIMP dark matter direct detection. (2014), [arXiv:1310.8327v2](https://arxiv.org/abs/1310.8327v2)
- K.G. Begeman, HI rotation curves of spiral galaxies. I - NGC 3198. *Astron. Astrophys.* **223**, 47–60 (1989)
- J. Beringer et al. (Particle Data Group). The review of particle physics. *Phys. Rev. D* **86** (2012) 010001. See <http://pdg.lbl.gov/>
- G. Bertone, D. Hooper, J. Silk, Particle dark matter: evidence, candidates and constraints. *Phys. Rep.* **405**, 279–390 (2005)
- S. Braibant, G. Giacomelli, M. Spurio, *Particle and Fundamental Interactions* (Springer, Berlin, 2011). ISBN 978-9400724631
- S. Braibant, G. Giacomelli, M. Spurio, *Particles and Fundamental Interactions: Supplements, Problems and Solutions* (Springer, Berlin, 2012)
- M. Cirelli, et al. PPPC 4 DM ID: A poor particle physicist cookbook for dark matter indirect detection. *JCAP* **1103** (2011) 051.
- A. Drukier, K. Freese, D. Spergel, Detecting cold dark matter candidates. *Phys. Rev.* **D33**, 3495–3508 (1986)
- J. Einasto. Dark Matter. (2014), [arXiv:0901.0632](https://arxiv.org/abs/0901.0632)
- J.L. Feng, Dark matter candidates from particle physics and methods of detection. *Annu. Rev. Astron. Astrophys.* **48**, 495–545 (2010)
- R.J. Gaitskell, Direct detection of dark matter. *Annu. Rev. Nucl. Part. Sci.* **54**, 315–359 (2004)
- G. Giacomelli, Magnetic monopoles. *La Rivista del Nuovo Cimento* **7**(12), 1 (1984)
- M.W. Goodman, E. Witten, Detectability of certain dark matter candidates. *Phys. Rev.* **D31**, 3059 (1985)
- D. Hooper, E.A. Baltz, Strategies for determining the nature of dark matter. *Annu. Rev. Nucl. Part. Sci.* **58**, 293–314 (2008)
- W. Hu, S. Dodelson, Cosmic microwave background anisotropies. *Ann. Rev. Astron. Astrophys.* **40**, 171–216 (2002)
- G. Jungman, M. Kamionkowski, K. Griest, Supersymmetric dark matter. *Phys. Rep.* **267**, 195–373 (1996)
- J.F. Navarro, C.S. Frenk, S.D. White, The structure of cold dark matter halos. *Astrophys. J.* **462**, 563 (1996)
- Peng-Fei Yin et al., Pulsar interpretation for the AMS-02 result. *Phys. Rev. D* **88**, 023001 (2013)

- D.H. Perkins, Proton decay experiments. *Annu. Rev. Nucl. Part. Sci.* **34**, 1–50 (1984)
- T.A. Porter, R.P. Johnson, P.W. Graham, Dark matter searches with astroparticle data. *Annu. Rev. Astron. Astrophys.* **49**, 155–194 (2011)
- S. Profumo. TASI 2012 Lectures on astrophysical probes of dark matter. (2014), [arXiv:1301.0952](https://arxiv.org/abs/1301.0952)
- M. Roos. Dark Matter: The evidence from astronomy, astrophysics, and cosmology. (2010), [arXiv:1001.0316](https://arxiv.org/abs/1001.0316)
- T. Saab. An introduction to dark matter direct detection searches and techniques. (2012), [arXiv:1203.2566](https://arxiv.org/abs/1203.2566)
- V. Trimble, Existence and nature of dark matter in the universe. *Ann. Rev. Astron. Ap.* **25**, 425–472 (1987)

# Index

## Symbols

$\Lambda$ CDM model, 444  
0FGL J1954.4+2838, 299  
2FGL catalog, 268  
2dF Redshift Survey, 207  
3C 279, 290, 308, 310

## A

Absorption length, 343  
Abundances of CRs, 72  
Accelerating cavities, 210  
Acceleration  
  mechanism, 78, 133, 144  
Accelerator, 26, 27, 55, 165, 189  
  data, 65  
  galactic, 199  
Accretion disk, 199  
Accretor  
  in binary system, 199  
Active galaxies, 304  
Active neutrinos, 444  
Adiabatic  
  energy losses, 215  
  invariant, 168  
Aerosol scattering, 226  
Afterglow, 274, 277  
AGASA, 125, 225, 227, 238, 450  
Age, 121, 122  
AGILE, 243, 264, 290, 293, 295, 302, 309  
AGN, 5, 166, 208, 213, 220, 237, 322  
  disk dominated, 304  
  jet dominated, 304  
  thermal dominated, 304  
Air showers, 8, 39, 87, 360  
AIROBICC, 119  
Akeno, 225  
All-particle spectrum, 77, 124, 126  
Alpher, R., 205  
Altitude-azimuth drive, 284  
Aluminum-26, 259  
Alvarez, L., 405  
AMANDA, 345, 393  
Ambient photons, 246  
AMS-01, 82  
AMS-02, 17, 55, 64, 82  
Amundsen-Scott station, 345  
Analog-to-Digital Converters (ADC), 120, 226  
Anderson, C., 26  
Anisotropies  
  large-scale, 134, 153  
  of CRs, 152, 153  
Anisotropy, 123  
  amplitude, 153  
  of CRs, 203, 209, 237, 239  
Ankle, 39, 165, 190, 197, 203, 227, 228, 240  
Annual WIPM modulation, 463  
Antarctica, 61  
ANTARES, 13, 393, 469, 470  
Anticoincidence, 67, 70, 262  
Antideuteron, 80  
Antihelium, 80  
Antimatter, 5, 23, 61, 78  
Antiparticle, 26, 56, 62, 79  
Antiprotons, 78, 148  
Antiquark, 27  
Aperture, 226  
Apparent magnitude, 273  
ARGO-YBJ, 289  
Argon, 405, 464  
Aristotle, 261, 425  
Array trigger, 285  
Astronomy of charged particles, 209

Astrophysical beam dump, 246  
 ATIC, 63, 81  
 Atmosphere, 55, 60, 70, 87, 89, 100, 104,  
 106, 110, 112, 118, 129, 140, 203,  
 220, 224, 231, 282  
 Atmospheric depth, 89, 90, 92, 94, 96, 104,  
 106, 108, 112, 119, 126, 127, 360,  
 363, 364, 368  
 slant, 90  
 Atmospheric muon  
 bundles, 377  
 flux, 368, 373  
 Atmospheric muons, 13, 87, 326, 359, 369,  
 377, 382, 389  
 Atmospheric neutrinos, 3, 18, 87, 321, 325,  
 359, 363, 377  
 Atmospheric scale height, 91  
 Atomic number, 73  
 Atomic opacity, 398, 403  
 Auger, P., 25, 87  
 Avogadro number, 459  
 Axions, 449  
 Azimuth, 35, 122

## B

Baade, W., 52  
 Bacteria, 344  
 Bahcall, J., 401  
 BAIKAL, 345  
 Baikonur cosmodrome, 66  
 Baksan Neutrino Observatory, 20  
 Balloon, 33, 34, 37  
 experiments, 55, 57, 61, 63, 76, 78, 82  
 flight, 81  
 Band spectrum, 274  
 Band-pass filter, 244  
 Bartol neutrino flux, 390  
 Baryon number conservation, 360  
 Baryonic dark matter, 448  
 Baryons, 246  
 BATSE, 7, 259, 274  
 Beam dump, 322  
 Beamed radiation, 158  
 Becquerel, A.H., 4, 23  
 BeppoSAX, 11, 274  
 Bergwitz, K., 24  
 Berkeley Bevatron, 78  
 Beryllium neutrinos, 406  
 BESS, 62, 373  
 Bethe-Block formula, 31  
 Bethe-Heitler formula, 316  
 Big Bang, 75, 204, 205, 238, 276

model, 442  
 Nucleosynthesis, 443, 448  
 Binary systems, 290  
 Binding energy, 73, 74, 176, 192  
 Bioluminescence, 344  
 Bismuth Germanium Oxide (BGO), 63  
 BL Lac blazar, 270  
 BL Lacertae, 310, 314  
 BL Lacs, 306, 308  
 Black body  
 spectrum, 51  
 Black hole, 40, 199, 208, 277, 305, 313, 397,  
 426, 430, 448  
 Black-body  
 radiation, 165, 254  
 Blackett, P., 26, 88  
 BLANCA, 119  
 Blazar, 282, 290, 305–311, 313, 315  
 BL Lac, 270  
 FSRQ, 270  
 sequence, 310  
 Bohr  
 magneton, 437  
 Boltzmann  
 constant, 52, 90, 254  
 law, 44  
 BOOMERanG, 444  
 Boomerang, 299  
 Borexino, 419  
 Boron, 149  
 Boron neutrinos, 406  
 Boulby Palmer Laboratory, 20  
 Branching ratio, 322  
 Bremsstrahlung, 32, 45, 92–95, 144, 149,  
 156, 165, 265, 282, 302, 321, 330,  
 383  
 Brightness temperature, 254  
 Bulge, 40

## C

C.g.s. unit, 28  
 Cabibbo-Kobayashi-Maskawa  
 matrix, 414  
 CALET, 279  
 Calorimeter, 34, 39, 56, 60, 82, 89, 91, 260  
 electromagnetic, 59, 69  
 sampling, 60  
 Canfranc laboratory, 20  
 CANGAROO, 288  
 CAPRICE, 62, 82  
 Capture rate, 406  
 Carbon, 45, 140, 149

- dioxide, 140
- Carbonaceous chondrites, 75
- CASA, 118
- Cascade, 46, 87, 92, 99, 106, 108, 115, 127
  - electromagnetic, 60, 94, 98, 104
  - equation, 95
  - equations, 87
  - hadronic, 58, 60, 100
  - model, 101
  - muon, 92
  - muonic, 88, 112
  - of particles, 55
  - size, 122
- Cassiopeia A, 179, 298, 299, 425
- Catching collision, 171
- CDMS, 463
- Celestial coordinates, 123
- Centaurus A, 237, 269, 290, 308
- Center-of-mass
  - energy, 136
- Central tracker, 68
- CERN, 4, 69, 110, 373
- Chadwick, J., 26
- Chamberlain, O., 78
- Chandra, 7, 259
- Chandrasekhar
  - limit, 426
  - mass, 193, 194
- Charge conjugation, 449
- Charge-asymmetry, 40
- Charged current, 323, 324
- Charmed meson decay, 354
- Chemical composition, 70
  - of CRs, 55, 378
- Chemical cosmology, 75
- Chemical extraction, 405
- Cherenkov
  - angle, 282
  - detector, 56, 63, 119, 228, 282
  - detectors, 88, 112, 118, 129
  - effect, 57, 112, 382
  - emission, 119, 128, 410
  - imaging, 92
  - imaging detector, 282, 285, 286, 288, 292, 297, 311
  - light, 283, 383
  - radiation, 113, 118, 223, 321, 324, 343
  - ring, 383
  - ring imaging (RICH), 57
  - telescope, 18, 92
  - threshold, 118, 410
  - water detector, 378, 379, 384
  - water tank, 229
- Chinese astronomers, 46
- Chlorine experiment, 405
- Chondrites, 75
- Chooz, 417
- CHORUS, 392
- Classical electron radius, 157
- Clay, J., 25
- Cloud chamber, 29
- Cluster of galaxies, 207
- CMB, 154
- CNO
  - cycle in stars, 398, 401
  - cycle in Sun, 400, 401, 404, 424
- COBE, 18, 205
- CoGeNT, 463
- Coincidence, 34
  - time, 114
- Collider, 89, 110, 461
- Column density, 267
- Coma cluster, 446
- COMPTEL, 7, 259, 295
- Compton, 25, 49
  - effect, 97
  - inverse, 149
  - inverse scattering, 249, 251, 255, 264, 294–296, 299, 301, 304, 306, 310, 311, 315
  - scattering, 218, 410
  - wavelength, 193
- Compton Gamma Ray Observatory (CGRO), 7, 243, 259, 274
- Compton–Getting
  - effect, 155
- Computer, 34, 46
- Confinement time, 52
- Constrained MSSM, 452
- Conventional atmospheric neutrino flux, 325, 369
- Conversi, M., 26
- Coordinate space approach, 143
- Coordinated Universal Time (UTC), 70
- Copernican revolution, 40
- Copper, 32
- Core collapse, 176, 426
- Core-collapse supernova, 425
- Corona, 46
- CORSIKA, 104, 108, 110, 124
- COS-B, 7
- Cosmic abundances, 72, 75
- Cosmic accelerators, 52
- Cosmic microwave background, 11, 203, 205, 219, 236, 258
- Cosmic rays, 26, 49, 51, 140, 199



- propagation, 135
  - Cosmic web, 207
  - Cosmochemistry, 75
  - Cosmogenic neutrinos, 338
  - Cosmological constant, 442
  - Cosmology, 51, 78
  - Coulomb
    - barrier, 402
    - multiple scattering, 97, 373, 383, 388
    - repulsion, 398, 438
    - scattering, 32
  - COUPP, 470
  - CP symmetry, 413, 449
  - Crab nebula, 180, 283, 288–290, 294, 295, 314
  - Crab pulsar, 255
  - CREAM, 61
  - CRESST, 463
  - CRIS, 65, 141
  - Critical
    - angular frequency, 159
    - density of matter, 192
  - Critical density, 442
  - Critical energy, 59, 92, 93, 96, 98, 102
  - Critical frequency, 159, 252
  - CRN, 64
  - Cross-section, 58, 73, 98, 108, 129, 217
    - inelastic, 110
  - Crushed cloud model, 301
  - CTA, 288, 303
  - CTB 37B, 299
  - CTEQ6-DIS, 324
  - Curie point, 446
  - Curvature constant, 443
  - Cutoff rigidity, 49
  - Cygnus Loop, 298
- D**
- DAMA, 463
  - Dark energy, 2, 5, 15
  - Dark matter, 3, 15, 56, 61, 67, 81, 83, 208, 441, 446
  - Data acquisition, 113
  - Dating technique, 133, 139
  - Davis, R., 405
  - Daya Bay, 418
  - De Broglie wavelength, 457
  - Decay constant, 364, 367, 370
  - Decay length, 100, 101, 103
  - Decay probability, 370
  - Declination, 342, 350, 354
  - Deep inelastic scattering, 405
  - Degeneracy pressure, 191, 193
  - Delayed shock, 430
  - Density, 89, 93, 100
    - of particles, 114, 115, 121
    - photon, 119
  - Depth-intensity relation, 375
  - Detailed balance, 254
  - Detectors, 23
  - Deuterium, 74, 410
  - Deuteron, 74, 410
  - DICE, 119
  - Differential energy spectrum, 37
  - Differential flux, 35, 37
  - Differential intensity, 35
  - Differential muon intensity, 368
  - Differential number density, 36
  - Differential spectral index, 37
  - Diffuse
    - $\gamma$ -rays, 243, 261, 268
  - Diffuse emission, 134
  - Diffusion
    - coefficient, 146, 152
    - equation, 133, 142, 143, 160
    - model, 133, 142, 162
    - process, 9
  - Diffusion differential equation, 55
  - Diffusion-loss equation, 145
  - Diffusive shock acceleration, 10, 173, 175, 180, 182, 188, 203, 210, 249, 296, 299, 300
  - Digital information, 33
  - Dip model, 236
  - Dipole
    - anisotropy, 153
  - Dipole magnets, 210
  - Dirac delta function, 146
  - Dirac, P.A.M., 23, 26
  - Direct
    - muons, 369
    - neutrinos, 369
  - Direct DM experiments, 454
  - Direct experiments, 39
  - Direct measurements, 125
    - of CRs, 55, 77
  - Direct photons, 344
  - Discovery potential, 349
  - Donor
    - in binary system, 199
  - Doppler effect, 447
  - Double bang, 327
  - Double Chooz, 418
  - DPMJET, 111
  - Drell-Yan process, 98

Drift chambers, 62  
 Dugway Proving ground, 222  
 DUMAND, 345  
 Dust, 40, 42, 44  
 Duty cycle, 88, 225, 283, 307  
 Dwarf galaxy, 208

**E**

Earth, 23, 24, 40, 46, 52, 71, 89, 91  
   magnetic field, 48, 169  
   magnetic moment, 48  
 EAS-TOP, 112, 116, 122  
 Eddington luminosity, 311  
 EDELWEISS, 463  
 Effective area, 245, 262, 279  
 Effective PMT volume, 343  
 Effective temperature, 254  
 Effelsberg radio telescope, 309  
 EGRET, 7, 259, 261, 295, 307, 470  
   field-of-view, 262  
 Einstein  
   cosmological constant, 442  
   general relativity, 442  
 Einstein Observatory, 6  
 Einstein, A., 23  
 Elastic scattering, 405  
 Electric charge, 26  
 Electromagnetic  
   calorimeter, 60  
   cascade, 58, 88, 93, 282  
   shower, 284  
   waves, 42  
 Electromagnetic cascade, 282  
 Electron, 26  
   degenerate matter, 191  
 Electrons, 35, 40  
 Electroweak interaction, 1  
 Eleven-year cycle, 46  
 Elliptic galaxy, 447  
 Elongation rate, 94, 106, 108, 129  
 EM showers, 92  
 Emission, 44  
 Emission lines, 44, 45  
 Emission spectrum, 41  
 Emulsions, 26, 63  
 Energy  
   equipartition, 192  
   loss through excitation, 59  
   loss through radiation, 59  
   threshold, 216  
 Energy density, 50, 52  
   of the magnetic field, 157

Energy loss, 31, 40, 92, 93, 104, 110, 133,  
   141, 148, 157  
   electron, 161  
   muon, 103  
   rate, 160  
   rotational, 196  
 Energy loss length, 215, 217  
 Energy spectrum, 37, 88, 97, 125, 126  
   differential, 190  
   of CR electrons, 155, 161  
   of CRs, 142, 151, 165, 174, 182  
 Energy-per-nucleon, 39, 76  
 Energy-per-nucleus, 39, 76  
 Enhanced magnetic field, 300  
 EPOS, 111, 129  
 Equivalent attenuation length, 362  
 ESA, 7  
 Escape  
   length, 137, 139  
   probability, 153, 183, 184  
   time, 37, 52, 66, 133, 134, 139, 141, 147–  
     149, 151, 152  
 Euler  
   equation, 185  
 Event rate, 35  
 Event topology  
   in neutrino detectors, 384, 386, 387, 389,  
     391  
 Excitation, 31, 33  
   energy loss, 58, 59, 92, 93, 95, 105, 144,  
     151, 156  
 Exosat, 6  
 Exotic particles, 4  
 Exposure, 387  
 Extensive air shower, 87  
 Extensive Air-Showers Arrays, 18  
 External synchrotron radiation, 258  
 Extragalactic background light, 316  
 Extragalactic magnetic field, 219  
 Extragalactic neutrinos, 333

**F**

Faraday  
   law, 166, 167, 198, 210  
   rotation, 42, 209  
 Femi-LAT, 11  
 Fermi  
   acceleration, 335, 349  
   acceleration mechanism, 250  
   energy, 191, 193  
   mechanism, 203  
   spectrum, 336

- Fermi process, 174
    - first-order, 171, 174
    - second-order, 170, 172
  - Fermi, E., 169
  - Fermi-LAT, 82, 243, 262, 268, 276, 278, 290, 293, 295, 296, 298, 300–303, 306–309, 311, 312, 318, 471
  - Fermilab, 392
  - Feynman
    - diagram, 255, 408, 456
    - scaling, 250, 361, 362
  - Fiducial mass, 384
  - Fiducial volume, 384
  - Field of view (FoV), 283, 286
  - Fine structure constant, 218
  - Fine tuning, 1
  - Fine tuning problem, 449
  - FIRAS, 206
  - Fireball, 277
  - First ionization potential, 190
  - Flash Analog to Digital Converters (FADC), 229
  - Flash-ADCs, 120
  - Flavor
    - eigenstates, 414
  - Fluctuation, 87
  - Fluence, 273, 435
  - Fluorescence, 18, 112, 129
    - detector, 18, 118, 220, 222, 229, 230
    - emission, 203, 220
    - telescope, 222
  - Flux, 32
  - Flux density, 245, 253
  - Flux upper limit, 350
  - Fly's Eye detector, 222, 225, 235
  - Form factor
    - nuclear, 460
  - Forward particles, 89
  - Forward production, 110
  - Four-vector, 256
  - Fragmentation, 55, 73, 133, 136, 141, 148
  - Free-free, 45
  - Frejus, 379
  - Frequency
    - critical, 252
  - FRI blazars, 290
  - Friedmann-Lemaître
    - equations, 442
  - FSRQ blazar, 270, 290, 305
  - Fundamental constants, 193
  - Fundamental interactions, 26
  - Fusion
    - in stars, 134, 176
    - in the Sun, 400
    - nuclear, 134
    - reaction, 191
  - Fusion catalyst, 400
- ## G
- Gadolinium, 417
  - Galactic
    - confinement time, 142
    - disk, 139, 150, 155
    - halo, 142
    - magnetic field, 139, 153, 161
    - volume, 148
  - Galactic center, 42
  - Galactic latitude, 292
  - Galactic longitude, 292
  - Galactic magnetic field, 42
  - Galactic magnetic halo, 43
  - Galactic plane, 41, 43, 52
  - Galactic volume, 52, 53
  - Galaxy, 23, 40, 41, 43, 44, 52, 53, 55, 61, 79, 124, 203, 207, 209, 240, 249, 259, 266
  - GALLEX, 14, 407, 415
  - GALPROP, 81, 82, 133, 148, 472
  - GAMMA, 128
  - GAMMA-400, 279
  - Gamma-rays, 35, 87
  - Gamow
    - effect, 398
    - peak, 402
  - Gamow, G., 205
  - Gamow-Teller
    - transition, 407
  - Gauge
    - theory, 445
  - Gauge hierarchy problem, 450
  - Gauge symmetry, 18, 445
  - Geminga, 290, 472
  - Geomagnetic
    - effect, 373
    - field, 23, 121, 373, 378
    - latitude, 371, 373
    - location, 372
  - Geometrical factor, 35, 67, 87
  - Geophysical neutrinos, 12
  - Giacomelli, G., 2
  - Globular cluster, 270
  - Globular clusters, 40, 41
  - GNO, 14, 407
  - Grammage, 136
  - Gran Sasso Laboratory, 20, 389, 392, 463

- Grand Unified Theories, 1, 359, 377, 445
  - Graphite, 44
  - Gravitation, 441
  - Gravitational
    - binding energy, 192
    - collapse, 134, 191, 193
    - coupling constant, 193
  - Gravitational lensing, 447, 448
  - Gravitational radius, 311
  - Graviton, 5
  - Gravity, 1
  - GRB, 5, 166, 214, 243, 264, 272, 322, 335
    - 080319B, 273
    - 090423, 276
    - 980425, 277
    - 990123, 275
    - alert, 274
    - discovery, 273
    - fireball model, 277
    - long, 276
    - model, 277
    - short, 275, 276
    - T90, 276
  - Green catalog, 298
  - Green function, 146
  - Greisen approximation, 96
  - Greisen, K., 92, 97, 98, 215
  - Greisen-Zatsepin-Kuzmin (GZK) cut-off, 215
  - Guest stars, 425
  - Gyrofrequency, 159
  - Gyromagnetic radius, 139
  - GZK
    - cut-off, 227
    - effect, 233, 338
- H**
- Hadron, 87
  - Hadronic
    - calorimeter, 57, 60, 140
    - cascade, 58, 59
    - interaction, 59, 101, 110, 111, 125
    - shower, 57, 70
  - Hadronic accelerator, 251
  - Hadronic interactions, 360, 362, 368, 376, 377
  - Hadronic model
    - of  $\gamma$ -ray production, 247, 249, 281, 297–300, 302–304, 311, 312, 314, 315, 321
  - HAL 9000, 45
  - Half-life, 141
  - Halo, 40, 41, 43
  - Hamamatsu, 325
  - Harmonic analysis, 154
  - Haverah Park, 113, 225
  - HAWC, 289
  - HDFPM, 111, 124
  - Head-on collision, 171, 256
  - HEAO-3, 64
  - HEAT, 62, 82
  - Heavy water, 409
  - Heisenberg uncertainty principle, 191
  - Heitler's
    - model, 93–95
  - Helicoidal motion, 28
  - Helicoidal trajectory, 168
  - Helioseismology, 401, 404
  - Helium, 40, 71
    - energy spectrum, 189
  - HERA collider, 323
  - HERD, 279
  - Hertzprung-Russell
    - diagram, 397, 398
  - HESS, 286, 292, 293, 297, 300, 303, 309, 312, 314, 318, 332
  - Hess, V., 23
  - Higgs boson, 1, 450
  - High-energy (HE)  $\gamma$ -rays, 290
  - High-mass binary, 270
  - Hillas
    - condition, 214
    - criterion, 211
    - plot, 212
  - HiRes, 129, 222, 226, 233, 235
  - History of cosmic rays, 24
  - HKKM
    - neutrino flux, 390
  - Hodoscope, 141
  - Homestake, 14, 20
  - Homestake mine, 405
  - Hubble
    - constant, 204, 215, 218
    - law, 204, 443
    - parameter, 443
    - space telescope, 259
    - time, 204, 334
  - Hubble Space Telescope, 7
  - Hydrocarbons, 434
  - Hydrogen, 42, 45, 149
  - Hyperfine levels, 44
  - Hypernova, 277

**I**

IBL Lac blazars, 290  
 IC 443, 298, 299, 302  
 Ice, 344  
 IceCube, 13, 393, 469, 470  
 ICRC conference, 232, 238, 290  
 Ideal fluid equations, 185  
 Imaging Atmospheric Cherenkov Telescope (IACT), 244  
 IMB, 18, 379  
 IMP, 64, 141  
 India based Neutrino Observatory, 21  
 Indirect DM experiments, 454  
 Indirect measurements of CRs, 55  
 Indirect photons, 344  
 Inelasticity, 99, 101, 129  
 Inflation models, 444  
 INFN, 20  
 Infrared divergence, 254  
 Infrared emission, 44  
 Instrumented volume, 322, 328, 338, 339, 343  
 INTEGRAL, 6  
 Integral flux, 35, 37  
 Integral intensity, 35  
 Integral spectral index, 38  
 Integrating detectors, 118  
 Interaction length, 56, 58, 67, 91, 323  
 Interaction models, 89  
 International Space Station, 16, 279  
 Interstellar  
   matter, 78, 81, 165, 178, 186  
 Interstellar gas, 149, 265  
 Interstellar medium, 40, 55, 56, 73, 79, 81, 84, 133, 135, 142, 147, 162, 243  
 Interstellar space, 9  
 Inverse Compton, 251, 321  
 Inverted mass hierarchy, 415  
 Invisible energy, 231  
 Ionization, 29, 33  
   energy loss, 58, 59, 92, 93, 95, 105, 144, 151, 156  
 Iron peak, 424  
 Isospin conservation, 322  
 Isothermal approximation, 91  
 Isotopic spin, 83  
 Isotropic flux, 36  
 Isotropic radiation, 36  
 Isotropy of CRs, 145  
 ISS, 55  
 Ivuna meteorite, 75

**J**

J-PARC, 417  
 JACEE, 63  
 Jets, 213  
 Jupiter, 45  
 Jupiter-like planets, 448

**K**

K2K, 392  
 Kaluza-Klein  
   theory, 449  
 Kamioka Observatory, 20, 383  
 Kamiokande, 14, 18, 379, 407  
 KamLAND, 412, 415  
 KASCADE, 112, 116, 122, 127  
 KASCADE-Grande, 112, 117, 124, 128  
 Kepler, 425  
 Kernel, 128  
 KGF, 18  
 Kinetic energy density, 50  
 Klein-Nishina  
   cross-section, 257, 304  
 KM3NeT, 13, 348, 469  
 Knee, 10, 16, 37, 39, 52, 88, 110, 112, 119, 124, 125, 128, 165, 177, 190, 197, 300, 303, 325  
 Kohlhörster, W., 87  
 Koshiba, M., 408  
 Kuzmin, V., 215

**L**

Lake Baikal, 345  
 Large Magellanic Cloud, 5, 14, 265, 294, 307, 398, 436  
 Large-scale structures, 40  
 Larmor  
   formula, 156  
   period, 167  
   radius, 43, 142, 157, 165, 181, 189, 203, 208, 240  
 Laser interferometers, 474  
 Lateral particle distribution, 97  
 Latitude effect, 49  
 Lattes, C., 26  
 LBL Lac blazars, 290  
 Lead, 29, 31  
 Leading edge, 158  
 Leading particle, 99, 103  
 Leaky box model, 147, 160  
 LEP, 1, 210, 373, 441  
 Leptonic model

- of  $\gamma$ -ray production, 243, 249, 251, 297–300, 302, 310–312, 314, 315, 321
- LHAASO, 289
- LHC, 1, 89, 110, 210, 211, 236, 373, 441
- Lifetime, 26, 145, 364
- Light absorption, 324
- Light cylinder, 196
- Light elements (Li,Be,B), 133, 135, 138
- Lightest Supersymmetric Particle, 451
- Limited streamer tubes, 389
- Linsley, J., 26, 113
- Liquid scintillator detector, 389
- Local density
  - of DM, 454
- LogParabola, 272
- Long-baseline experiment, 392
- Longitudinal development, 98, 109, 111, 118, 128, 224
- Lorentz
  - boost, 247
  - factor, 100, 101, 121, 156, 172, 252, 277, 313, 331, 336, 369–371
  - force, 27, 48, 168, 196
  - invariance, 153
  - transformation, 171, 248, 256
- Low- $p_t$  processes, 246
- LS 5039, 290
- LSI +61 303, 290
- LSP, 450
  
- M**
- M82, 266, 307
- M87, 290, 308
- MACRO, 13, 121, 375, 377, 388, 415, 446
- MAGIC, 284, 286, 295, 302, 303, 309, 311, 312
- Magnetar, 214
- Magnetic braking, 196
- Magnetic field, 28, 34, 40, 52
- Magnetic field amplification, 299
- Magnetic halo, 53
- Magnetic mirrors, 166, 169
- Magnetic monopole, 19, 359, 446
- Magnetic shielding, 343
- Magnetic spectrometer, 34, 56, 57, 64, 78, 82, 373, 392
- Magnetized clouds, 166, 170
- Magnetohydrodynamic waves, 147
- Magnetosphere, 49, 196, 293
- Main sequence, 397
- Majorana particle, 15, 451
- Markarian 421, 288–290, 308–311
- Markarian 501, 290, 308, 311, 314
- Markov, M, 321
- MASS, 82
- Mass eigenstates, 381, 414
- Mass number, 73
- Massive stars, 134
- Matter density, 53, 58, 80, 332
- Matter-antimatter asymmetry, 3
- MAXIMA, 444
- Maximum detectable rigidity, 69
- Maximum rigidity, 240
- Maximum-likelihood, 122
- Maxwell-Boltzmann
  - distribution, 402
- Maxwell-Boltzmann distribution, 402
- McMurdo, 47
- Mean free path, 58, 137, 151, 170, 218, 360, 361, 363, 364
  - for pions, 61
- Mediterranean Sea, 13, 322, 342, 347, 351
- Medium elements (C,N, and O), 133
- Mesons, 27, 246
- Metal abundance
  - in Sun, 401
- Metal-poor stars, 41
- Metal-rich stars, 41
- Metallicity, 403
- Meteorites, 75
- MIA, 118, 129
- Microgravity, 16
- Microquasar, 84, 200, 313, 322
- Microstrip, 67
- Milagro, 288
- Milky Way, 40, 207, 208, 261
- Millikan, R.A., 24
- MiniCLEAN, 464
- Minimum ionizing particle (m.i.p.), 117
- MINOS, 392, 415
- Mirror reflection in magnetic fields, 168
- Modane laboratory, 20
- Molecular diffusion, 226
- Molecular emission, 149
- Molecules, 44, 45
- Molière
  - radius, 112, 122
  - unit, 98
- Momentum distribution, 89
- Mono-atomic gas, 176, 186
- Monogem, 472
- Monte Carlo, 87, 91, 98, 104, 108, 110, 120, 122, 125, 329, 337, 352, 363, 368, 372, 373, 377, 379
- Moon, 269, 273, 280

- MSSM, 451  
 MSUGRA, 452  
 Multifrequency astrophysics, 244  
 Multimessenger astronomy, 5  
 Multiple muon, 375  
 Multiwavelength astrophysics, 244  
 Muon  
   bundle, 375  
   cascade, 102, 103, 113, 118  
   range, 383  
 Muon decay length, 378  
 Muon energy loss, 329, 352  
 Muon intensity, 371, 375  
   vertical, 376  
 Muon spectrometer, 373  
 Muon telescopes, 373
- N**
- NASA, 7, 61, 64, 205, 259  
 Neddermeyer, S., 26  
 Neper's constant, 58  
 Neutral current, 323, 324, 409  
 Neutral HI, 44  
 Neutralino, 450, 451  
 Neutrino, 35, 49  
   appearance, 392  
   appearance experiment, 409  
   artificial source, 407  
   astronomy, 12  
   astrophysics, 5, 213  
   burst, 429  
   decoupling, 443  
   disappearance experiment, 409  
   effective area, 338  
   elastic scattering, 408  
   flavor, 334  
   flavor oscillations, 378  
   magnetic moment, 437  
   mass, 437  
   matter oscillations, 418, 420  
   mixing, 421  
   mixing angle, 391  
   oscillation length, 382  
   oscillations, 3, 13, 19, 334, 359, 397, 409, 414, 417, 422  
   showers, 238  
   survival probability, 419  
   telescope, 328, 359, 377  
   trapping, 428, 429  
   velocity, 437  
 Neutrino-less double-beta decay, 19  
 Neutrinosphere, 430
- Neutron, 46  
   decay, 246  
   star, 191, 193, 194  
 Neutron detector, 67  
 Neutron monitors, 46  
 Neutron star, 176, 189, 190, 194, 199, 214, 397, 426, 428, 430, 448  
 Neutronization, 428  
 Newton  
   gravitation law, 446  
 NGC 1068, 307  
 NGC 1275, 308  
 NGC 253, 266, 307  
 NGC 3198, 447  
 NGC 4945, 307  
 Nishimura-Kamata-Greisen function, 98  
 Nitrogen, 73, 90, 203, 220  
 NKG function, 98, 114, 121, 123  
 Noise, 34, 114  
 NOMAD, 392  
 Non-baryonic dark matter, 448  
 Non-thermal component, 41  
 Non-thermal emission, 80, 165, 179, 304  
 Non-thermal spectrum, 10, 133, 161  
 Normal mass hierarchy, 415  
 Nova, 270  
 Nuclear binding energy, 74  
 Nuclear drop model, 75  
 Nuclear form factor, 460  
 Nuclear fragmentation, 135  
 Nuclear fusion, 400  
 Nuclear radius, 58  
 Nuclear spallation, 135  
 Nuclear track detector, 389  
 Nuclei, 23, 87  
 Nucleons, 39  
 Nucleosynthesis, 7, 75, 205, 437  
   primordial, 134  
   stellar, 133, 189  
 Number density, 36, 50, 58, 142, 191, 216, 246, 250, 258  
 NUSEX, 18, 379
- O**
- OB associations, 189  
 OB-stars, 189, 432  
 Observational cosmology, 204  
 Occhialini, G., 26  
 On-line computer, 33  
 One-shot acceleration, 211  
 Onion-skin star structure, 424  
 Opacity in the SSM, 401



- OPERA, 391, 415  
 Optical depth, 317  
 Optical module, 325  
 Orphan TeV flares, 315  
 OSO-3, 7  
 OSSE, 7, 259  
 Owens Valley Radio Observatory, 309  
 Oxygen, 73, 90
- P**
- P-process, 438  
 Pacini, D., 24  
 Pair
  - conversion telescope, 260, 262
  - creation, 93, 97
  - electron-positron, 93, 94
  - production, 215, 259
 PAMELA, 55, 64, 82  
 Pancini, E., 26  
 Pandora planet, 75  
 Parity, 449  
 Parsec, 40, 139  
 Particle number density, 36  
 Parton distribution functions, 324  
 Partons, 456  
 Path length, 136, 146, 150, 161, 323  
 Patter recognition
  - of events, 383
 Pauli exclusion principle, 74, 191  
 Payloads, 61  
 Penzias, A., 205  
 Perchloroethylene, 405  
 PeVatrons, 299  
 Phonons, 461  
 Photodisintegration, 176, 213  
 Photometric measurements, 51  
 Photomultiplier, 118, 325, 346  
 Photon decoupling, 205  
 Photoproduction, 246, 322, 334, 338  
 Photosphere, 46, 399, 403, 404  
 Photosynthesis, 140  
 PICASSO, 470  
 Piccioni, O., 26  
 Pierre Auger Observatory (PAO), 129, 155, 203, 224, 228, 233, 237, 238, 335, 450  
 Pion, 27, 61, 92, 99, 102, 107
  - charged, 100
  - decay bump, 248
  - neutral, 100
 Pion decay constant, 364  
 Pitch angle, 157  
 PKS 2155-304, 314  
 Planck, 18
  - constant, 193, 244
  - law, 205
  - mass, 450
  - spectrum, 205
 Planck Satellite, 205, 444  
 Plasma, 46, 166, 199
  - ionized, 175
 Point spread function, 260, 297  
 Poisson
  - equation, 185, 186
  - fluctuation, 282
  - statistics, 227
 Polar cup, 293  
 Polarization, 42, 313  
 Pontecorvo, B., 378, 405  
 Pontecorvo-Maki-Nakagawa-Sakata
  - matrix, 414
 Positron, 27, 56, 64, 78, 80, 87, 93, 113, 118, 148, 323
  - excess, 83
 Positron fraction, 83  
 Potential well, 191  
 Powell, G., 26  
 Power-law, 126  
 PPB-BETS, 81  
 Primary CRs, 7  
 Primordial
  - nucleosynthesis, 134
 Probability distribution function, 329  
 Prompt
  - muons, 369
  - neutrinos, 354, 369
 Prompt decays, 370  
 Prompt neutrino flux, 326  
 Propagation, 133, 135, 148, 156
  - model, 148
  - of CRs, 55, 65, 73, 79, 81, 83, 95, 123
 Proportional counters, 33  
 Proton, 26, 30
  - decay, 3, 18, 377, 380, 445
  - lifetime, 18, 359, 377
 Proton-proton
  - cycle in Sun, 398, 402, 404
 Pseudo-experiment, 329, 349  
 PSK 1222+21, 314  
 PSR J0534+2200, 294  
 Pulsar, 42, 83, 194, 199, 211, 243, 261, 270, 293, 294, 313, 322, 432  
 Pulsar wind nebulae (PWNe), 180, 269, 293  
 Pulse of radiation, 158

**Q**

QED, 92  
 QGSJET, 111, 128, 129  
 Quadrupole magnets, 210  
 Quantum Chromo-Dynamics (QCD), 110, 449  
 Quantum efficiency, 325  
 Quark, 61  
   top, 1  
 Quasar, 208, 243, 255, 304, 308, 313  
 Quasi-elastic scattering, 405  
 Quasi-stellar objects (QSOs), 304  
 Quenching factor, 461

**R**

R-parity, 451  
 R-process, 438  
 Radiation belts, 49  
 Radiation dose, 45  
 Radiation flux, 245  
 Radiation length, 59, 91–94, 96, 117, 263, 330  
 Radiative flux, 245  
 Radio, 41  
   astronomy, 41, 44, 205, 293  
   bright AGN, 301  
   emission, 41, 195, 199  
   galaxy, 166, 270  
   jet, 199  
   loud AGN, 304, 307  
   quasar, 305  
   sources, 41  
   telescopes, 42, 45  
 Radio-frequency cavities, 210  
 Radio-purification, 419  
 Radioactive decay, 133, 140, 145  
 Radioactive isotopes, 139  
 Radioactive nuclei, 37  
 Radioactivity, 4, 24, 25, 114  
 Radioactivity background, 19  
 Radiochemical experiments, 405  
 Radiometric dating, 140  
 Radon, 407  
 Random walk, 139, 146  
 Range, 324  
 Rare phenomena, 19  
 RATAN-600 radio telescope, 309  
 Rayleigh formalism, 154  
 Rayleigh–Jeans  
   limit, 254  
 RCW 86, 299  
 Recombination, 444  
 Recombination epoch, 205

Redshift, 204, 273, 275, 311, 334  
 Reference neutrino flux, 331  
 Regularization, 128  
 Relic particles, 4, 453  
 Remotely operating vehicles, 345  
 RENO, 418  
 Resonance energy, 419  
 Resonant production, 215  
 Response matrix, 128  
 Rigidity, 34, 57, 62, 68, 78, 80, 182, 190  
   maximum, 189, 190  
   maximum detectable, 57, 67  
 ROSAT, 6  
 Rossi, B., 25, 87, 88, 92, 113  
 Rotational  
   energy loss, 196  
 RUNJOB, 63  
 Rutherford scattering, 97  
 RX J1713.7-3946, 297–301, 332  
 RXTE, 7, 309

**S**

S-process, 437  
 SAGE, 14, 20, 407  
 Sample and hold electronic, 225  
 Sanduleak-69202, 436  
 SAS-2, 7  
 Satellite, 33, 34, 37, 45, 49, 60, 64  
   experiments, 81  
 Scalar interaction, 457  
 Scalar WIMP interaction, 457  
 Scarsi, L., 113  
 Schein, M., 25  
 Schmidt telescopes, 425  
 Schrödinger  
   equation, 146  
 Schwarzschild  
   radius, 311, 315  
 Scintillation counters, 26, 34  
 Scintillation light, 461  
 Scintillator, 88, 260  
 Seasonal WIMP modulation, 463  
 Seawater, 344  
 Secondary  
   elements, 133, 137, 148  
 Secondary cosmic rays, 7, 26  
 Secondary-to-primary  
   ratio, 141  
 Sedov  
   phase, 180, 249, 296  
 Segrè, E., 78  
 Self-Synchrotron Compton, 251  
 Sensitivity, 289, 308, 341, 349

- Seyfert galaxies, 270
- Seyferts galaxies, 305
- Shock wave, 53, 166, 173, 177, 178, 186, 194
- Shock-amplified magnetic field, 185, 190
- Short baseline experiment, 392
- Shower, 94, 140
  - age, 96, 97, 122, 128
  - arrays, 37
  - axis, 112, 115, 120, 122, 125
  - detector-plane, 223
  - maximum, 94, 96, 98, 104, 106, 107, 118, 124, 129, 367
- SI units, 28
- SIBYLL, 111, 128
- Silicon
  - tracking system, 67
- Silicon-strip detector, 262
- Simple, 470
- Size
  - electron, 95, 102–104, 122, 127
  - EM, 97, 116, 124
  - muon, 104
  - photon, 95
  - shower, 96, 113, 122, 124
- Slab model, 148
- Sloan Digital Sky Survey (SDSS), 207
- Slow neutron capture, 437
- Small Magellanic Cloud, 265, 307
- SN 1006, 299
- SN 1998bw, 277
- SN remnants, 432
- SN1987A, 14, 398, 433, 435–437
- SNEWS, 435
- SNO, 14, 409
- SNR G353.6-0.7, 299
- Solar abundance problem, 404
- Solar cycles, 372
- Solar flares, 9, 46
- Solar luminosity, 401
- Solar modulation, 46, 77
- Solar neutrino, 19
- Solar neutrino problem, 406
- Solar Neutrino Unit, 406
- Solar system, 9, 23, 70, 134, 142, 152, 165, 177
- Solar wind, 46, 50
- Solid angle, 328, 341
- Solotvina Underground Laboratory, 20
- Soudan, 18
- Soudan 2, 379, 388
- Soudan Underground Laboratory, 20
- Source term, 144
- South Pole, 322, 341, 344
- Soyuz rockets, 16
- Space Shuttle, 16, 259
- Spallation, 56, 73, 135, 145
- Sparticle, 450
- Spatial morphology, 270
- Spectral energy distribution (SED), 245, 250, 258, 266, 269, 279, 289, 300–302, 306, 309–311, 315
- Spectral flux density, 244
- Spectral shape
  - of sources, 271
- Spectroscopy, 5, 41
- Spectrum-weighted moments, 362
- Spin, 27, 44
- Spin-dependent
  - WIMP coupling, 457
- Spin-down power, 292
- Spin-independent
  - WIMP coupling, 457
- Spiral galaxy, 447
- Spitzer Space Telescope, 259, 309
- Standard candle, 295, 426
- Standard Model, 445
  - of particle physics, 1, 18, 441
- Standard Solar Model, 14, 397, 403, 404, 406, 408, 411, 421
- Standard Temperature and Pressure, 59
- Stanley Kubrick, 45
- Star forming regions, 45, 290
- Starburst galaxy, 270, 290, 307
- Starlight, 316
- Statcoulomb, 28
- Steady state
  - of the Universe, 204
- Stella Nova, 425
- Stellar collapse, 19
- Stellar evolution, 397
- Stellar nucleosynthesis, 74, 133, 134, 398
- Stereo reconstruction
  - of showers, 224
- Stereoscopic
  - observation, 285
  - technique, 281, 286
- Sterile neutrino, 449
- Stochastic
  - acceleration, 166
- Stokes theorem, 167
- Straw tubes, 69
- Streaming velocity, 152
- Strong-*CP* problem, 449
- Sudbury laboratory, 20
- SUGAR, 225

Sun, 14, 37, 43, 45, 55, 72, 75, 84, 269  
 structure, 401  
 Sun-Earth distance, 401  
 Sunspots, 46  
 Super-Kamiokande, 13, 382, 415  
 Supercluster  
   of galaxies, 207  
   Virgo, 207  
 Superconducting magnet, 62  
 Superconductive spectrometer, 62  
 Supergravity (SUGRA), 445  
 Superluminal motion, 313  
 Supernova, 52, 53, 75, 176, 177, 193, 203, 249  
   core-collapse, 276  
   explosion, 173, 178, 189, 273, 429  
   model of CR acceleration, 177  
   neutrinos, 12  
   rate, 53, 266  
   remnant, 166, 281, 290, 294, 297, 299, 300  
   remnants, 23, 42, 52, 55, 135, 243, 269, 270, 321  
   shell, 147  
   Tycho, 179  
 Superposition, 106  
   model, 107, 236  
 Supersonic  
   flow, 175  
   velocity, 175, 186  
 Supersymmetry (SUSY), 442, 445, 450  
 Swift, 11, 243, 264, 273, 309  
 Sybill, 129  
 Symmetry breaking, 2  
 Synchrotron, 295, 301  
   emission, 134, 148, 249, 258, 293, 295, 306  
   energy loss, 84, 162, 296  
   frequency, 157  
   nebula, 293  
   peak, 311  
   radiation, 41, 156, 160, 196, 208, 209, 213, 252, 293, 302  
   self-absorption, 254  
   self-Compton (SSC), 258  
   spectrum, 254, 295  
 Synchrotron self-Compton (SSC), 258  
 Systematic uncertainties, 126

**T**

T2K, 417  
 Telescope Array, 203, 224, 231, 233, 240, 335, 450

Temporal variability, 270  
 Tevatron, 1  
 Thermal  
   emission, 41  
   energy, 176, 191  
   population of particles, 189  
   radiation, 304  
   velocity, 175  
 Thermonuclear reactions, 134  
 Thermonuclear supernovae, 426  
 Thomson  
   cross-section, 157, 218, 257, 304  
   scattering, 256, 401  
 Three neutrino flavor oscillations, 414  
 Thyco Brahe, 425  
 Time of flight (ToF), 34, 56, 67, 69, 70, 82, 260, 389  
 Time profile, 120  
 Time projection chambers, 464  
 Time-of-flight system, 67  
 Tokamak, 166  
 Top quark, 1  
 Top-down models, 227, 238  
 Topological defects, 238  
 TRACER, 63  
 Tracker, 262  
 Tracking iron calorimeter, 379  
 Trailing edge, 158  
 Transition probability, 255  
 Transition radiation, 57  
   detector, 63, 69, 82  
 Transparent source, 247  
 Transport equation, 87, 92  
 Trigger, 34, 56, 67, 70, 114, 115, 119, 230, 231, 260, 262, 275, 285, 286, 339  
 Troposphere, 91  
 Tycho Brahe, 179  
 Type I supernovae, 426  
 Type II supernovae, 426

## U

Uhuru, 6  
 Ultra high energy CRs, 203  
 Ulysses, 65, 141  
 Underground detectors, 377  
 Underground laboratories, 13, 18, 359, 377, 445  
 Underground muons, 374  
 Unfolding technique, 127  
 Unipolar generator, 196  
 Unipolar inductor, 210  
 Unitary transformation, 381

Universe, 2, 15, 204, 214, 236, 261, 272, 315,  
333, 352, 400, 431, 441, 474  
Unobtainium, 75

**V**

Véron-Cetty & Véron catalog, 237  
Vacuum energy, 443  
Vacuum gaps, 196, 293  
Van Allen  
  belts, 49, 169, 273  
Van Allen, J., 49  
Vela, 7  
Vela Jr, 298, 299  
Vela satellites, 273  
Vela X, 290  
VENUS, 111  
VERITAS, 284–287, 295, 300, 302, 303,  
309, 312  
Vertical equivalent muon, 230  
Vertical flux of secondary CRs, 363  
Vertical muon intensity, 376  
Very high energy (VHE)  $\gamma$ -rays, 290  
Vibration quanta, 461  
Virgo supercluster, 207  
Virial theorem, 447  
VLBA, 309, 312  
Volcano Ranch, 225  
Voyager, 65, 141

**W**

W Comae, 290  
W28, 290, 303  
W44, 298, 302

W51, 290, 303  
W51C, 298  
Waveform Analyzer (WFA), 120  
Waveform digitization, 346  
Waxman-Bahcall upper limit, 333  
Weak flavor eigenstates, 381  
Weak interactions, 13, 100, 323, 398  
Weighted-slab technique, 148  
Whipple, 294  
White dwarf, 194  
White dwarfs, 190, 191, 426, 448  
Wilson, R.W., 205  
WIMP, 15, 442, 449  
Winston cone, 119  
WMAP, 205, 444  
Wolf-Rayet stars, 189  
Wulf, T., 24

**X**

Xenon, 464  
XMASS, 464  
XMM-Newton, 6

**Y**

Yakutsk array, 117, 225  
Yukawa, H., 26

**Z**

Zatsepin, G., 215  
Zeeman effect, 42  
Zenith, 35, 122  
Zwicky, F., 52, 446